NASA

JPL

FIRST INTERNATIONAL SYMPOSIUM ON SPACE TERAHERTZ TECHNOLOGY

Sponsored by:
NASA Office of Aeronautics and Space Technology (OAST)
University Space Engineering Research Centers Program

Organized Jointly by:
NASA Center for Space Terahertz Technology, The University of Michigan
Center for Space Microelectronics Technology, Jet Propulsion Laboratory

SYMPOSIUM PROCEEDINGS

March 5-6, 1990
Lee Iacocca Lecture Hall, Dow Building
The University of Michigan
Ann Arbor, Michigan

Proceedings of the
FIRST INTERNATIONAL SYMPOSIUM ON SPACE TERAHERTZ TECHNOLOGY

March 5-6, 1990
Lee Iacocca Lecture Hall, Dow Building
The University of Michgan
Ann Arbor, Michigan

Preface

The First International Symposium on Space Terahertz Technology featured papers from academia, government agencies, and industry, summarizing research results relevant to the generation, detection and use of the terahertz spectral region for space astronomy, remote sensing studies of the earth's upper atmosphere and other applications. The presentations covered a wide range of subjects including solid-state oscillators, mixers, harmonic multipliers, antennas, networks, receivers and measurement techniques. Although the discussions focused on the 0.1-1 THz region (3000-300μm), some of the papers examined higher frequencies as well. The program was international in scope, featuring noted researchers from the U.S., Japan, and several European countries.

The Symposium was sponsored by NASA's Office of Aeronautics and Space Technology (OAST) and was organized jointly by The University of Michigan's NASA Center for Space Terahertz Technology and JPL's Center for space Microelectronics Technology. It is our hope that this first symposium will set the stage for future symposia on space terahertz technology to serve as the meeting ground for scientists and engineers interested in this field.

Fawwaz T. Ulaby
Carl A. Kukkonen

Organizing Committee

Fawwaz T. Ulaby, The University of Michigan

Carl A. Kukkonen, Jet Propulsion Laboratory

George I Haddad, The University of Michigan

Gabriel Rebeiz, The University of Michigan

Margaret A. Frerking, Jet Propulsion Laboratory

Barbara Wilson, Jet Propulsion Laboratory

Valerie Franklin, The University of Michigan

Contents

Session 3: Mixers & Multipliers — Chair: Carl Kukkonen

Session 4: Receiver Systems — Chair: Anthony Kerr

Session 5: Applications — Chair: Sam Gulkis

OVERVIEW OF THE UNIVERSITY OF MICHIGAN SPACE TERAHERTZ TECHNOLOGY PROGRAM

Fawwaz T. Ulaby
Department of Electrical Engineering and Computer Science
The University of Michigan

ABSTRACT

In June 1988, NASA established nine university-based Space Engineering Research Centers for the purpose of enhancing and broadening the nation's engineering capabilities to meet the growing demands of the space program. The newly formed centers--which cover a wide range of specialties extending from robotics and propulsion to solid-state electronics--will perform research and develop technologies relevant to the establishment of operational bases on the moon, to manned and unmanned operations on Mars, to space flight missions to other parts of the solar system, and to observations of the Earth's environment from space platforms.

The University of Michigan's NASA Center for Space Terahertz Technology (NASA/CSTT) will focus on the development of terahertz devices, circuits, antenna arrays and heterodyne receiver systems in support of molecular line spectroscopy with particular emphasis on planetary atmospheres, including the Earth's upper atmospheric layer. During Phase I of the program (1988-93), most of the activities will be conducted at frequencies in the 0.1 to 1 THz range, corresponding to the 3 mm to 300 μm wavelength range. The research activities of the Center are divided into three areas: (1) terahertz device modeling fabrication and performance evaluation, (2) terahertz receiver development, including antenna fabrication and integration with the mixer/local oscillator components, and (3) the use of terahertz technology for the study of the Earth's upper atmosphere, astrophysical investigations, and industrial applications.

1. INTRODUCTION

The THz region is one of the least explored segments of the electromagnetic spectrum. Although a number of applications have been identified, primarily in astrophysics and for the study of planetary atmospheres, the potential of the THz region for scientific and industrial applications is yet to be explored. The primary factor that has impeded such an exploration has been technology. The construction of high sensitivity spectral receivers at frequencies above 0.1 THz, and particularly in the 0.3 to 3.0 THz band, is both very difficult and expensive. To detect the presence of a given molecule in interstellar space or to study ozone depletion in the Earth's upper atmosphere, for example, it is necessary to perform spectral line observations with spectral resolutions on the order of 1 MHz or narrower. Moreover, most of the molecules of interest are characterized by weak emission lines with typical antenna temperatures of a few kelvins (Figures 1 and 2), thereby imposing an additional constraint on the required performance sensitivity of THz receivers.

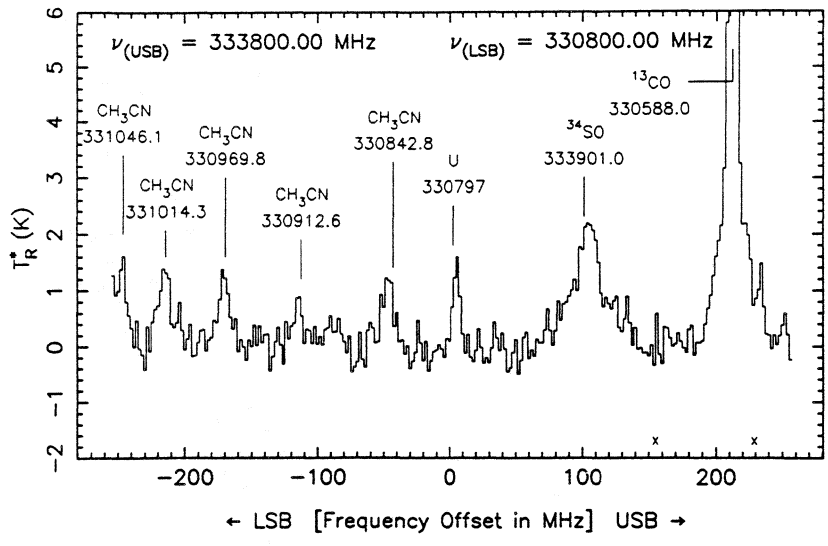

Figure 1. Spectrum of Orion A near 330 GHz measured by the NRAO telescope. (From [1], original data reported in [2].)

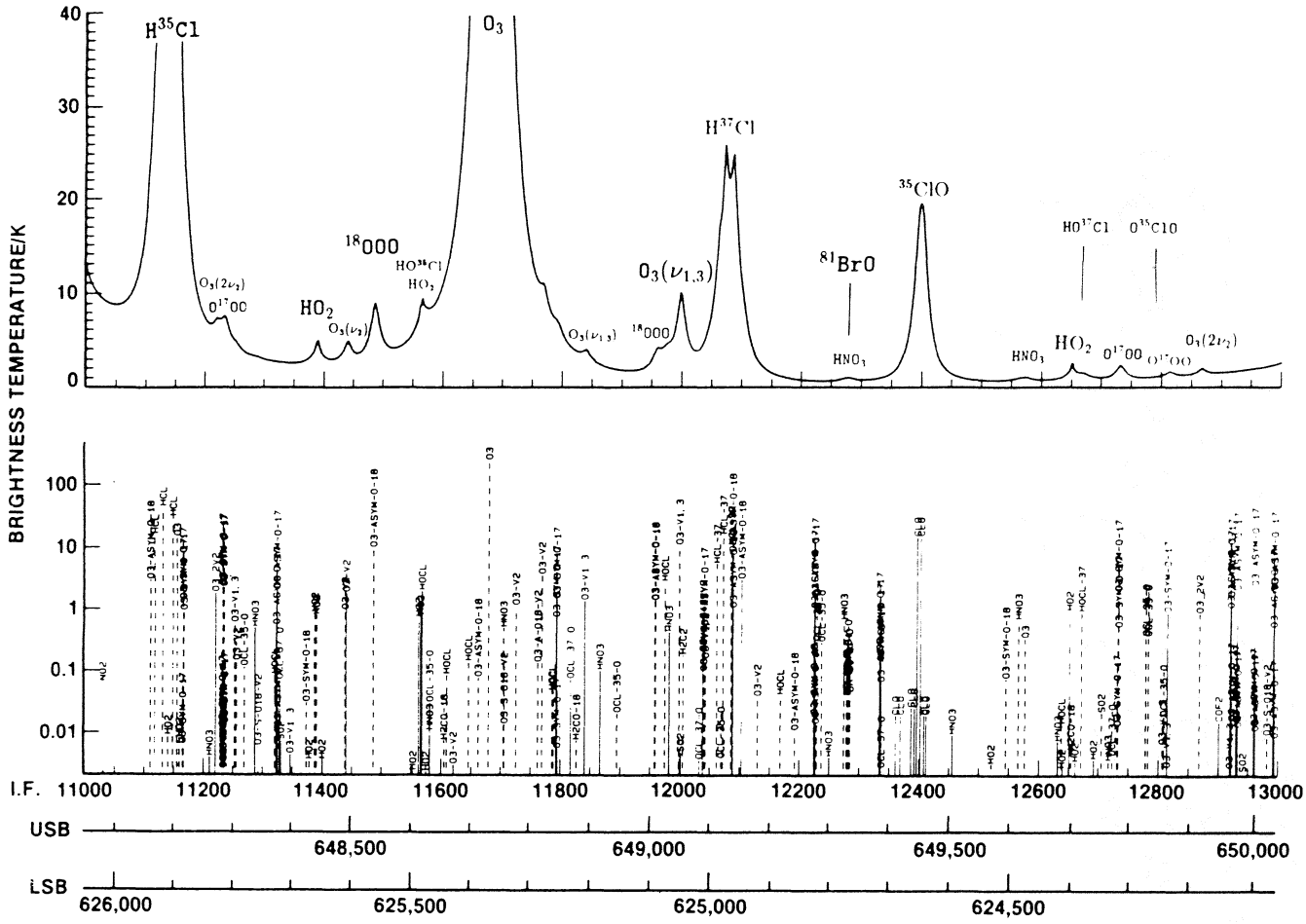

Figure 2. Calculated atmospheric limb emission spectra. The vertical scale is the emission brightness temperature. The horizontal scale is frequency; the calculation is for a radiometer with local oscillator frequency at 637,050 MHz equally receiving radiation from both upper (USB) and lower (LSB) sidebands at 11,000 to 13,000 MHz intermediate frequency (F). The top panel gives results of a full radiative transfer calculation for a limb path with 36 km tangent height; the bottom panel, with much compressed vertical scale, shows all spectral lines from the JPL catalog with the line intensities scaled to account for the limb measurement path and expected abundances for the middle stratosphere. Solid lines in the bottom panel indicate upper sideband; dashed lines indicate lower sideband. (From [3].)

Although successful millimeter and submillimeter spectral observations of the emission from some galaxies and interstellar clouds have been made from Earth telescopes at mountain tops, the attenuating effects of the Earth's atmosphere (Figure 3) impose a major limitation to observations in the THz region. Furthermore, in order to perform these observations, it has been necessary to use

SIS mixers cooled to liquid-helium temperatures or Schottky-diode mixers cooled to 10° to 15° K to achieve the required receiver sensitivity. To circumvent the opacity of the Earth's atmosphere, we need to conduct the observations from space platforms. However, providing very-low temperature refrigeration on board of a space platform is a major, although not impossible, constraint.

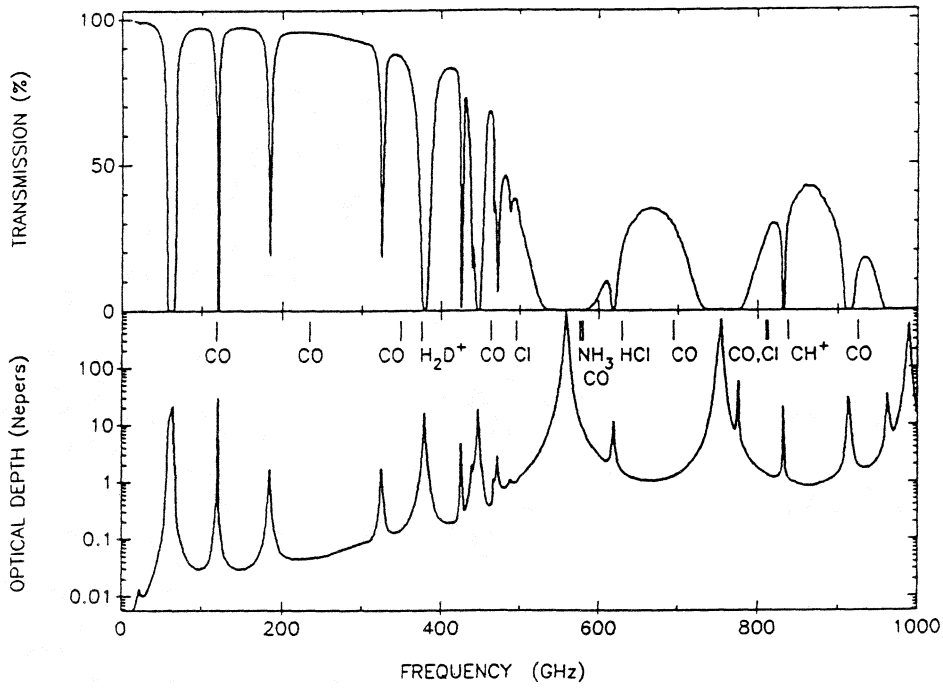

Figure 3. Atmospheric transmission at Mauna Kea at an altitude of 4,200 m, with 1 mm of precipitable water. The 850 GHz (350 μm) window is the highest frequency one available in the submillimeter. Te next window is in the middle infrared at about 30 μm. Also shown are some molecule rotation and atomic fine structure lines. (From [4].)

NASA's Office of Aeronautics and Space Technology (OAST) is supporting an intensive program for the development of THz receiver technology. One component of this program has been to establish a Center for Space Terahertz Technology (CSTT) at The University of Michigan through the University Space Engineering Research Centers Program. The goals of the CSTT are:

a. To accelerate the development of solid-state receivers--including local oscillators, detectors, mixers, and antenna arrays--at THz frequencies, with particular emphasis on room-temperature performance; and

b. To train graduate students in this field.

This paper provides an overview of the research program conducted by CSTT. To place the program in proper perspective from the standpoint of its intended contribution to the development of space THz technology, we will start with a brief review of the present capability of today's receiver technology.

2. REVIEW OF HETERODYNE RECEIVER TECHNOLOGY

Heterodyne detection is the most commonly used technique for making spectral line observations at millimeter and submillimeter frequencies. A traditional heterodyne receiver (Figure 4) uses a local oscillator and a double-ended balanced mixer to downconvert the frequency of the input signal, ω_S, to an IF frequency $\omega_{IF} = |\omega_S - \omega_{LO}|$. The IF output signal is then amplified, and sometimes mixed down again to a still lower frequency, and then fed to a bank of filters to obtain the spectrum of the input signal. The noise performance of the receiver is governed primarily by the RF amplifier, and to a lesser extent by the mixer. Thus, to insure low-noise performance, the RF amplifier should have high gain and low noise. Metal waveguide is used as the standard line for RF connections between the antenna and the RF amplifier, the RF amplifier and the mixer, and the local oscillator and the mixer.

This arrangement works well at frequencies below 100 GHz. As we increase the frequency above 100 GHz, we start to encounter a number of problems. These include:

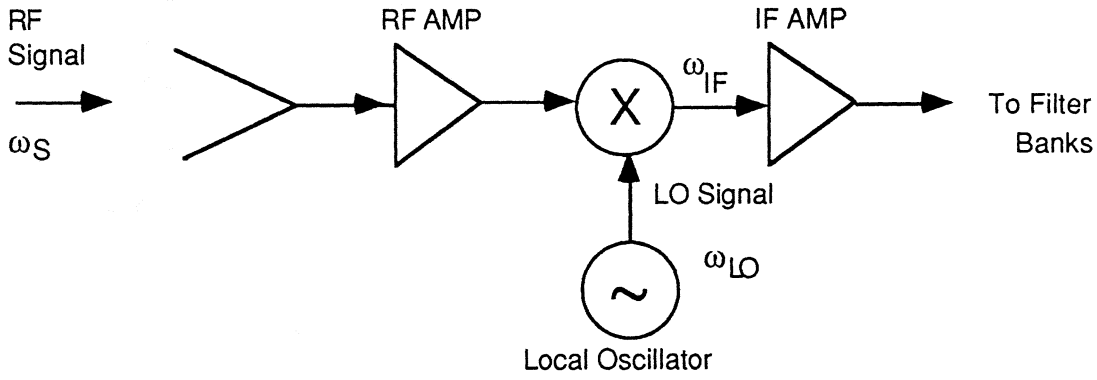

Figure 4. Block diagram of a traditional heterodyne receiver.

a. *Unavailability of RF amplifiers.* In this situation, the noise performance of the receiver becomes dictated by the noise characteristics of the mixer and IF amplifier.

b. *Unavailability of double-ended balanced mixers.* With single-ended mixers, we have to use a quasi-optical diplexer to combine the LO signal with the input RF signal prior to reaching the mixer. An example is shown in Figure 5.

c. *Poor mixer noise performance.* This necessitates cooling the mixer environment to a low temperature. The mixer elements most commonly used today at frequencies above 0.1 THz are the SIS diode and the Schottky barrier diode. Usually, SIS diodes are cooled to liquid-helium temperatures to realize super conductivity, and Schottky diodes are cooled to 15° K to reduce their mixer noise. With the recent advances made in high T_C superconductivity materials, it is hoped that SIS mixers can be made to operate at higher temperatures in the future. Figure 6 shows a plot of typical receiver noise temperatures for SIS mixers, Schottky diode mixers at 20° K and at 300° K, and InSb bolometer mixers. Both the SIS and InSb bolometer mixers were cooled to liquid-helium temperature. The InSb mixers exhibit good noise performance, but they are not desirable for making spectral

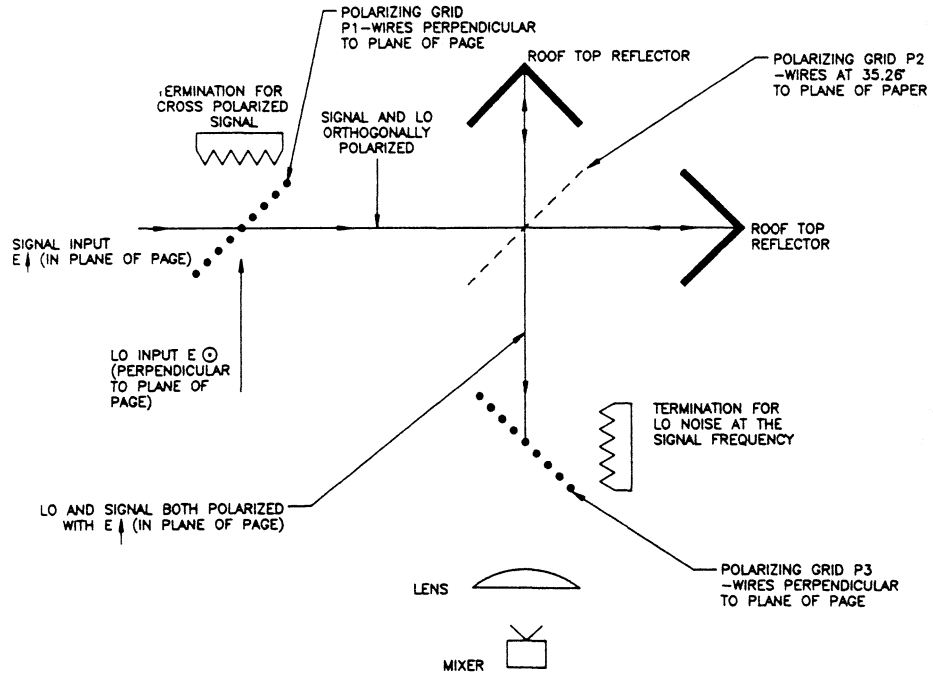

Figure 5. Martin-Puplett interferometer used as diplexer. (From [1].)

observations because they have narrow instantaneous band widths on the order of 1 MHz, which would necessitate scanning the local oscillator frequency in order to cover the desired spectrum.

d. *Unavailability of low-noise solid-state oscillators with sufficient output power to drive the mixer.* Gunn oscillators are now available up to about 120 GHz [5]; and by using doublers and triplers, the frequency range can be extended to about 360 GHz. Quadruplers and quintuplers have also been examined for solving this problem, but the output power of a harmonic multiplier is on the order of $1/n^2$ of the input power (where n is the harmonic order). IMPATT diodes can provide more power than Gunn diodes (Figure 7); but they are far noisier which has detracted from their use in millimeter and submillimeter heterodyne receivers. Using doublers and triplers with Gunn oscillators can provide sufficient power to drive cooled Schottky diode mixers up to about 360 GHz. To extend the range to

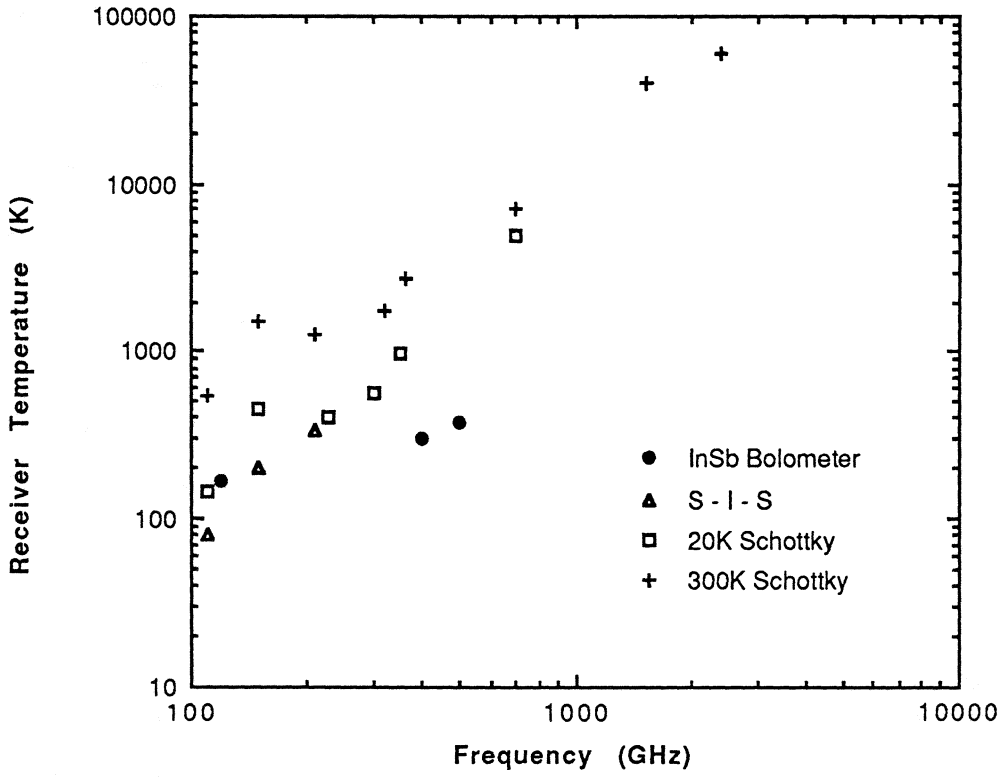

Figure 6. Typical receiver performance in the near millimeter-wavelength band for a number of different types of mixer receivers. (From [5].)

higher frequencies requires the availability of low-noise local oscillators that can produce more than 1 mW of output power at frequencies in the 100 to 400 GHz range. As we will discuss in Section 3, this is one of the major goals of CSTT.

Although SIS mixers require much lower levels of local-oscillator power to function (10^{-7} W, compared to more than I0^{-4} W for Schottky diodes [4]),the liquid-helium refrigeration requirements for superconductivity limit the use of SIS receivers to ground operations. (Schottky diode mixers can operate at room temperature, albeit with poorer noise performance.)

Subharmonic mixing is an alternate technique for operating at frequencies above the fundamental oscillation frequency of available local oscillators. A pair of balanced mixers is used to mix the local oscillator signal with a subharmonic of the

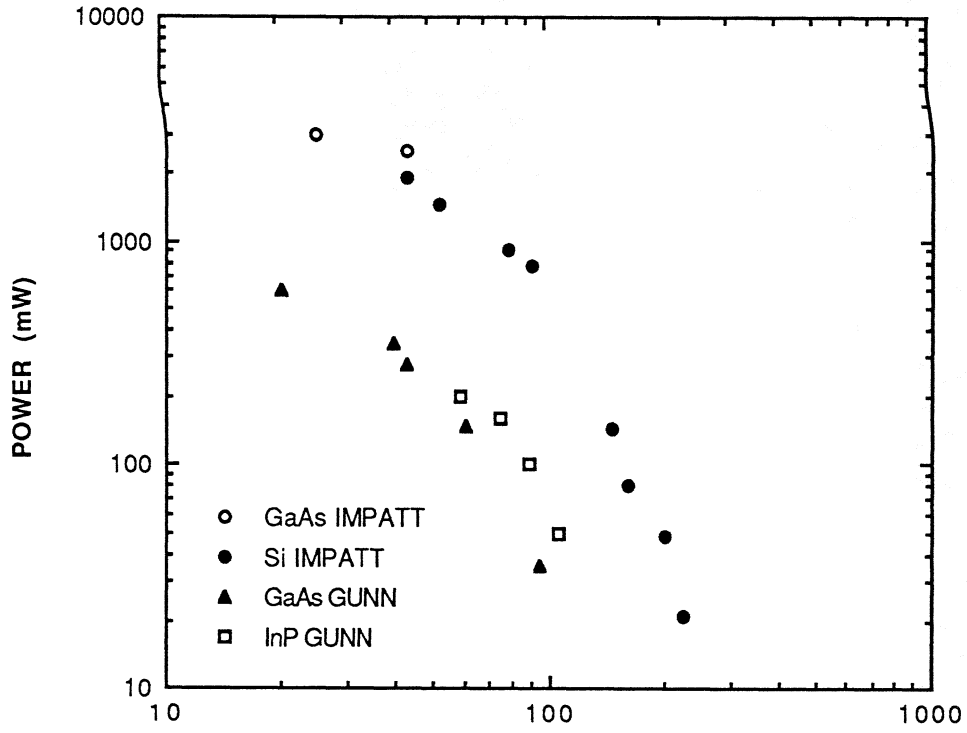

Figure 7. CW performance for IMPATT and Gunn-diode oscillators at near-millimeter frequencies. (From [5].)

input signal to produce an IF output. In general, the signal-to-noise performance of this technique is not as good as that realized with the harmonic-multiplication technique.

e. *Increased ohmic losses in conducting waveguides and increased difficulty of constructing components inside the guide.* For fundamental-mode operation at 300 GHz, for example, the internal dimensions of the waveguide have to be no more than 1 mm x 0.5 mm, and even smaller if it is necessary to reduce the guide height in order to match its wave impedance to a low-impedance component such as a diode detector [5]. A case in point is the Schottky diode mixer (Figure 8); the height of the waveguide carrying the input signal usually is tapered down to about 1/4 of its nominal value as it approaches the diode.

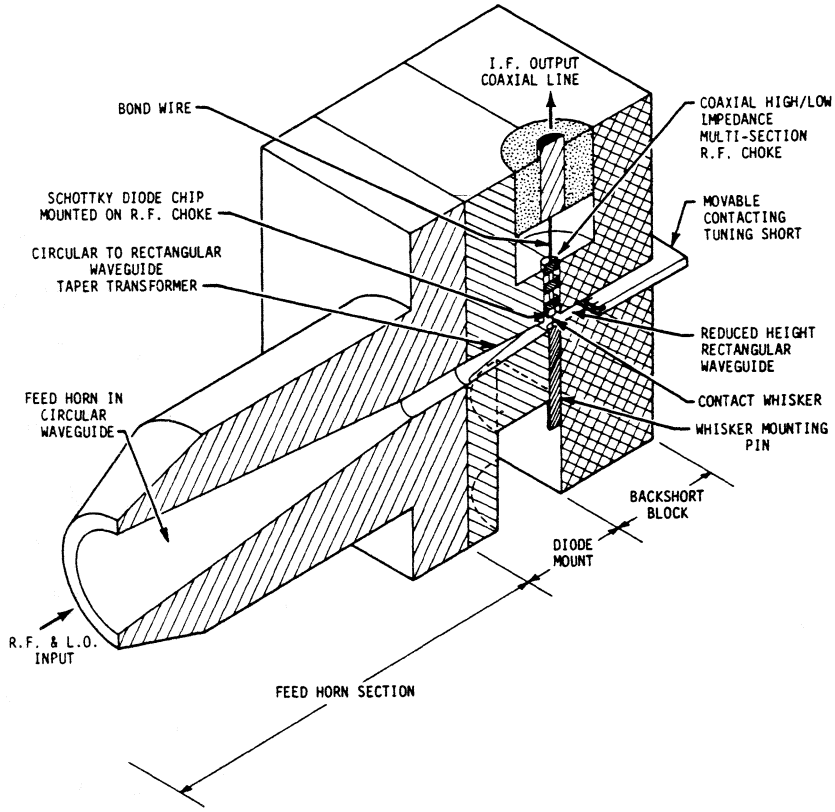

Figure 8. Typical mixer block for millimeter-wave applications. (From [1].)

To avoid the problems associated with waveguides, alternate approaches have been used for coupling RF energy to the mixer, including the planar thin-film antenna configuration shown in Figure 9, and the corner-cube antenna shown in Figure 10. It is also possible to use a half-wave dipole on a thin membrane placed inside a horn antenna and to connect the detector or mixer across the dipole input terminals (Figure 11). This type of configuration is particularly useful for imaging applications, as discussed further in Section 3.3.

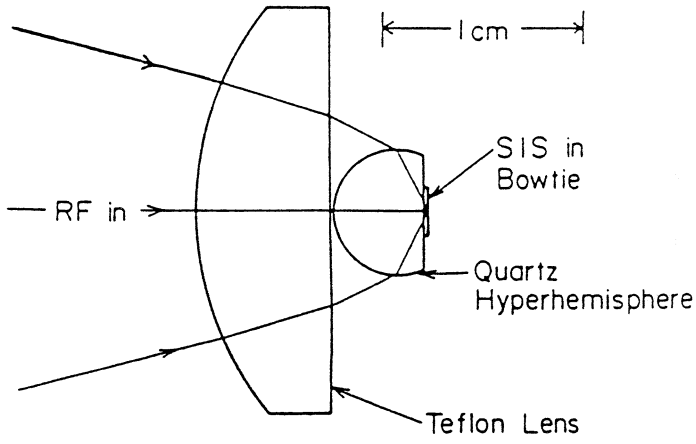

Figure 9. SIS optical-mode coupling for bow-tie antenna structure. (From [4].)

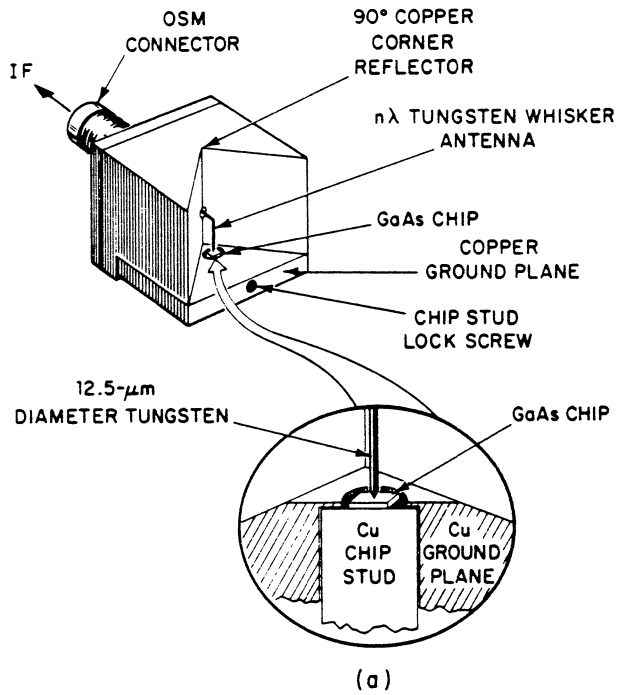

Figure 10. Corner-reflector antenna with quasi-optical mixer mount. (From [6].)

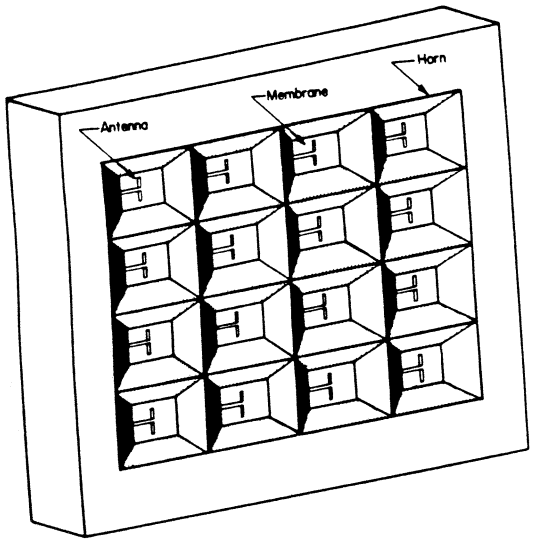

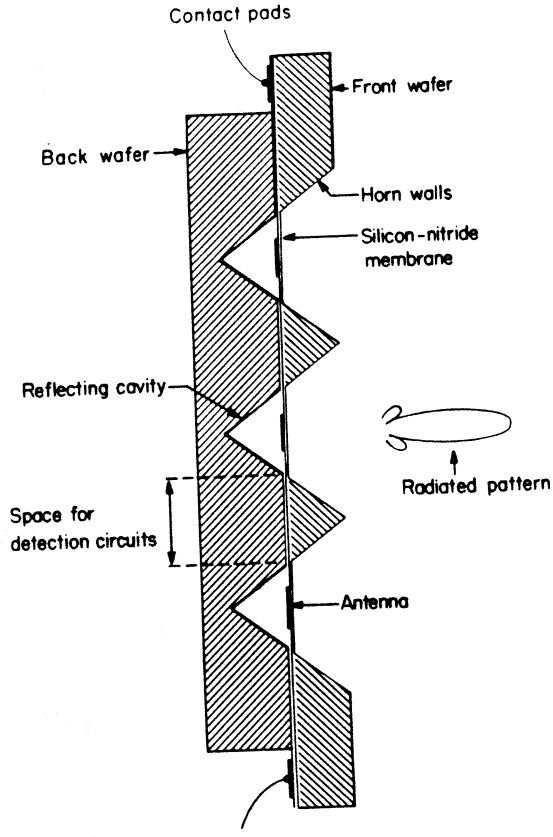

Figure 11. Monolithic antenna horn array. (From [7].)

To incorporate the various aspects peculiar to heterodyne detection at millimeter and submillimeter wavelengths, the receiver is more likely to look like the system shown in Figure 12 than like the traditional configuration shown in Figure 4. This system, which is part of the James Clerk Maxwell Telescope (JCMT) constructed by Cambridge University for operation in Hawaii [8], uses a 75.5 GHz Gunn oscillator and a third harmonic multiplier to provide the local oscillator signal at 226.5 GHz. A quasi-optical diplexer is used to combine the LO and RF signals, and additional optics, including a polarizer, are used to separate the horizontal and vertical polarization components of the input signal and to feed them into the two channels shown in the figure. The mixer elements are Schottky diodes cooled to 20° K.

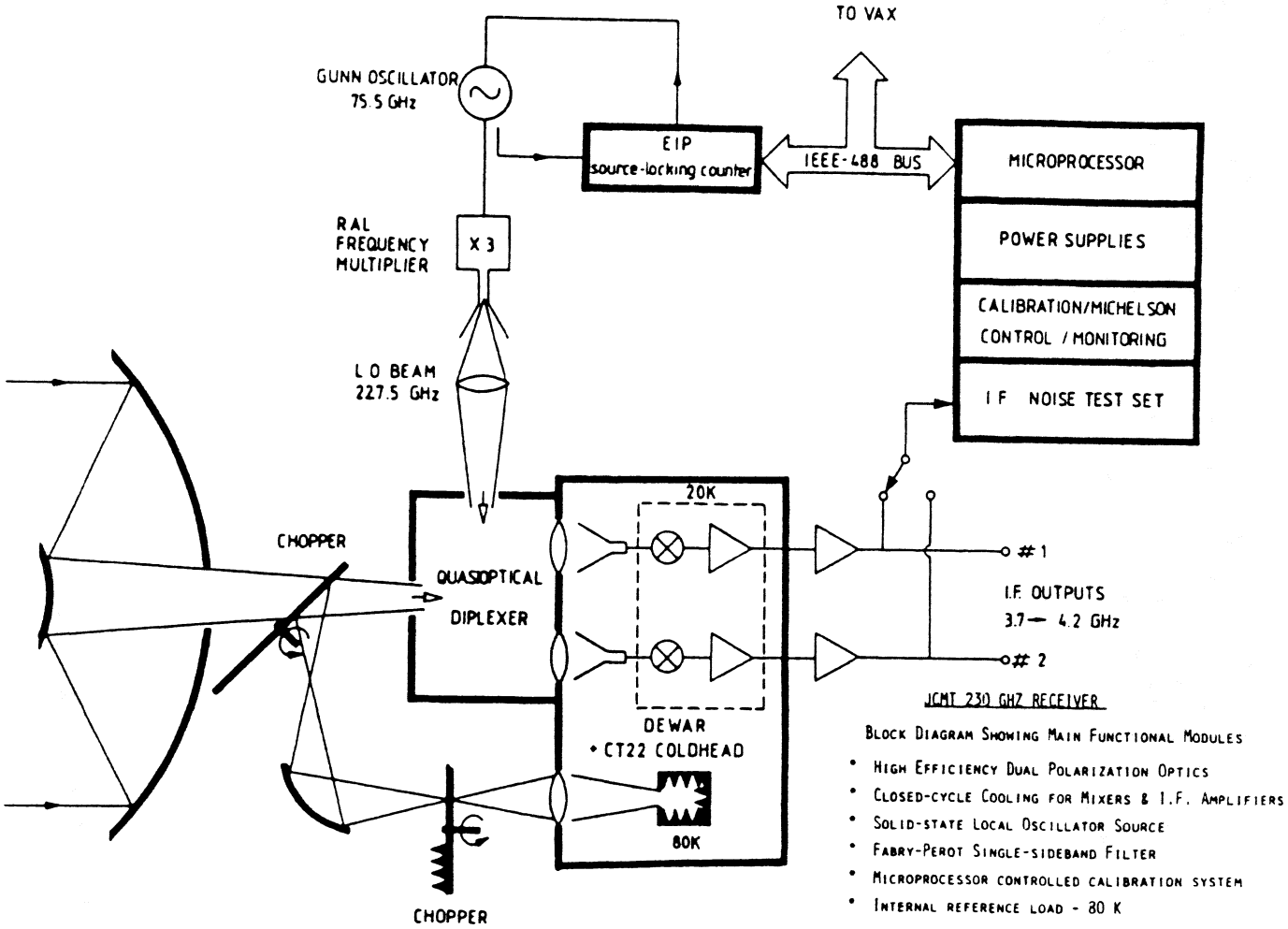

Figure 12. Block diagram of the 230 GHz receiver of the James Clerk Maxwell Telescope. (From [8].)

The cursory review of THz heterodyne receivers given in this section is by design brief in extent and general in scope; for more detailed reviews, the reader is referred to the articles by Archer [5], Payne [1]. Phillips [4], White [8], Goldsmith [9], and other [10-17]. The intent of the review is to provide a framework against which to describe the goals and research activities of the program sponsored by NASA/CSTT at The University of Michigan.

3. NASA/CSTT PROGRAM

3.1 Program Objectives

The program has three inter-related objectives, each of which is of fundamental importance to the program and its long-term viability.

Technology

The goal is to develop the capability to design and fabricate solid-state heterodyne receivers at THz frequencies, with emphasis on room-temperature operation using fundamental local oscillators, but not to the exclusion of liquid-nitrogen cooled receivers or harmonic multiplication and subharmonic mixing techniques. The program will focus on the 0.1 to 1 THz frequency range during Phase I (1988-1993), with the intent to extend the range to higher figures in later phases. The development will be guided by system specifications appropriate for observations of molecular line spectra from space platforms.

Scientific Applications

The use of the technology being developed by NASA/CSTT will be made available to the scientific community at large, including NASA, industry, and other academic institutions. At The University of Michigan, we are exploring the THz spectrum for studying the height profile of the OH number density in the Earth's upper atmosphere, the emission spectra of ^{12}CO, ^{13}CO, and HCN in the Martian atmosphere, and submillimeter-wave interaction with water and ice clouds. These

studies are important in and of themselves, as well as for maintaining a firm connection between the technology component of space THz technology and the scientific-application component.

Academic Objectives

The presence of a broad-based research program in THz science and technology provides graduate students with exposure to many facets of this field through seminar courses, visits by scientists from other institutions, symposia, and interaction with other graduate students in the program. One of the objectives of the program is to produce graduate students who have strong experience with THz instrumentation and measurement techniques, in addition to a firm theoretical foundation in their specific area of specialization. An additional academic objective of the program is to create an atmosphere conducive to novel ideas and interdisciplinary research.

3.2 Organization Structure

The NASA/Center for Space Terahertz Technology draws its technical support from three research facilities: (1) the Center for High Frequency Microelectronics (CHFM), (2) the Radiation Laboratory, and (3) the Space Physics Research Laboratory. Brief descriptions of these facilities are given in Figure 13. A total of 13 research projects are currently being funded by NASA/CSTT, involving 14 research and teaching faculty and 30 graduate students. The projects, which were selected in accordance with a four-year "road map" developed by the Center's Executive Committee and approved by a NASA-appointed oversight committee, cover a wide range of activities extending from growing novel semiconductor materials for heterostructure solid-state devices, to fabricating monolithic imaging arrays and examining the THz emission spectra of planetary atmospheres. In

several cases, the projects are conducted in collaboration with other institutions, such as the Jet Propulsion Laboratory (JPL) and the University of Virginia.

3.3 "Road Map"

The flow diagram shown in Figure 14 represents a road map for the progress of research activities from the component or subsystem level towards the overall receiver-integration level, and Figures 15 and 16 provide more detailed listings of the activities being pursued by the Solid-State and the Antenna and Quasi-Optics groups. No attempt will be made in here to discuss all of these projects in detail; instead, we will use examples to highlight the approach and development process associated with some specific elements of heterodyne-receiver design and fabrication.

a. *Local oscillator power.* Generation of low-noise oscillator power at THz frequencies is probably the single most crucial factor with regard to the development of THz heterodyne receivers today. As was mentioned earlier, Gunn oscillators have served as the primary source of power at frequencies up to about 120 GHz. To operate at higher frequencies has necessitated the use of multipliers or subharmonic mixers. The NASA/CSTT program is investigating four approaches for generating local oscillator power in the 0.1 to 1 THz region: (1) Resonant Tunneling Diodes, (2) Tunnel Transit-Time (TUNNETT) devices, (3) operating a Gunn diode in a second-fundamental mode, and (4) quantum well devices using thermionic emission. The investigations include theoretical-model analyses, fabrication of the devices using novel semiconductor materials and heterostructures, DC analysis of their i-v characteristics, and RF testing. Following a performance evaluation of these four techniques over the next two years, we will then focus our development activity on the most promising candidate in

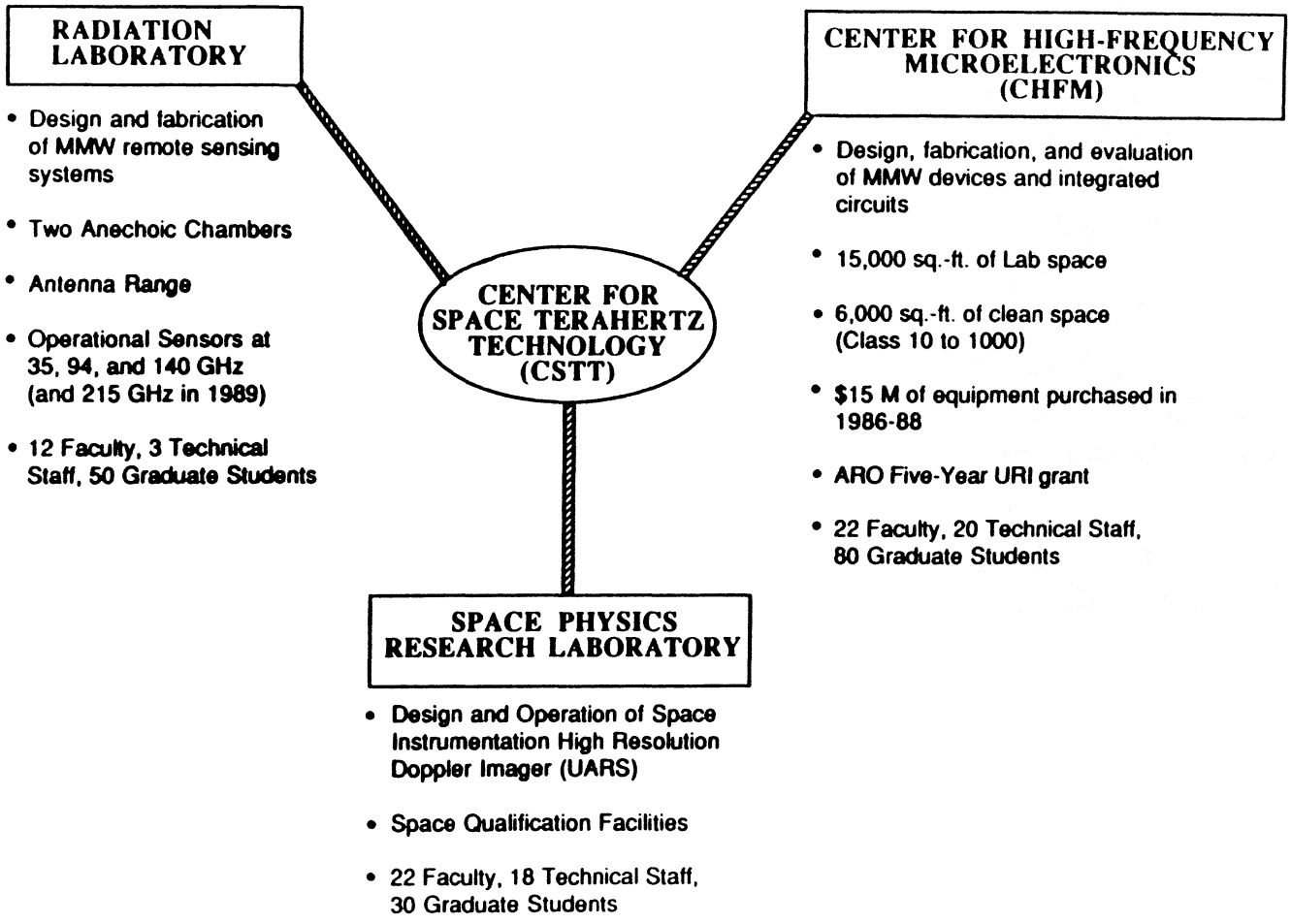

Figure 13. NASA/CSTT couples to three research units.

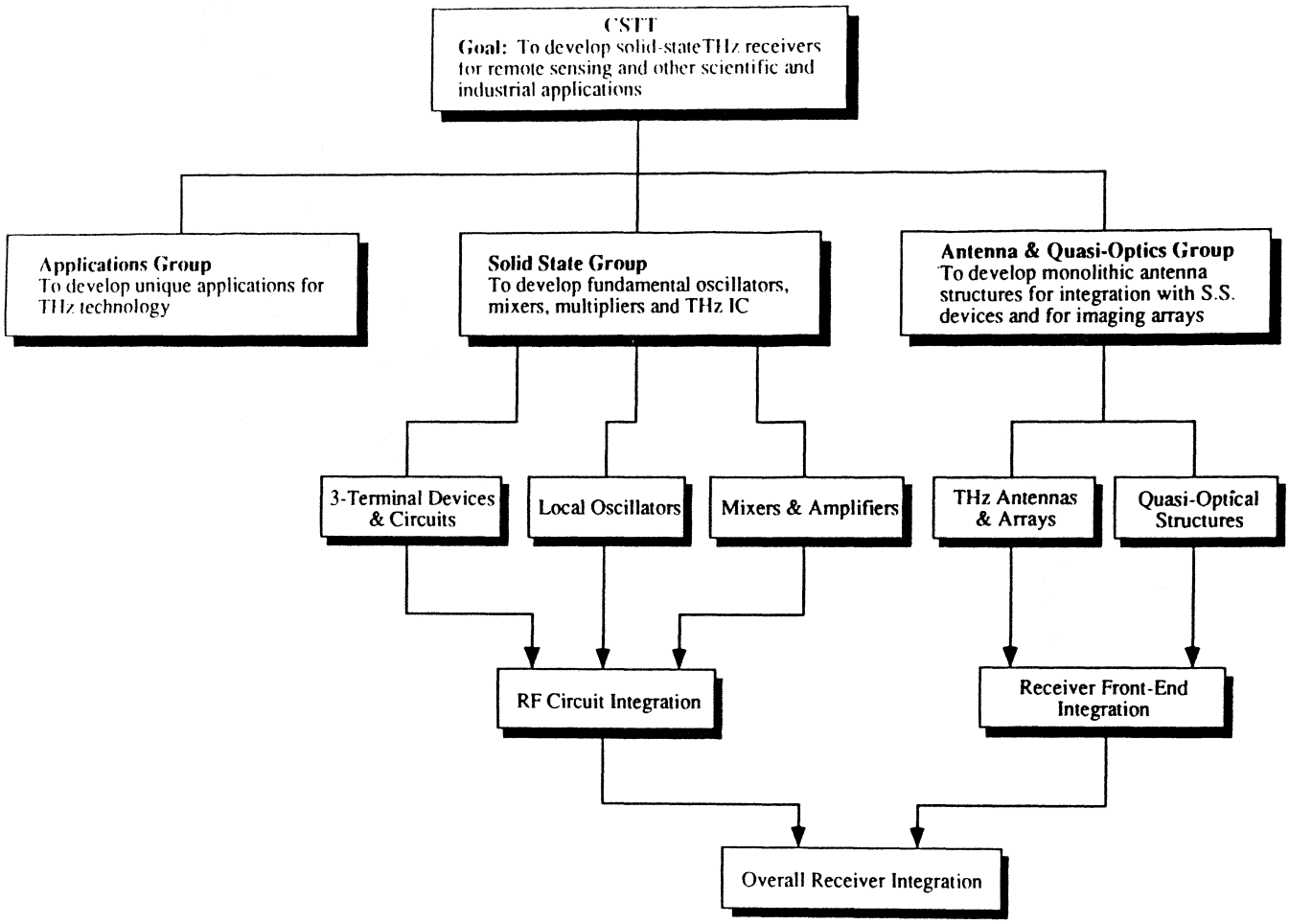

Figure 14. Organizational structure and research plan.

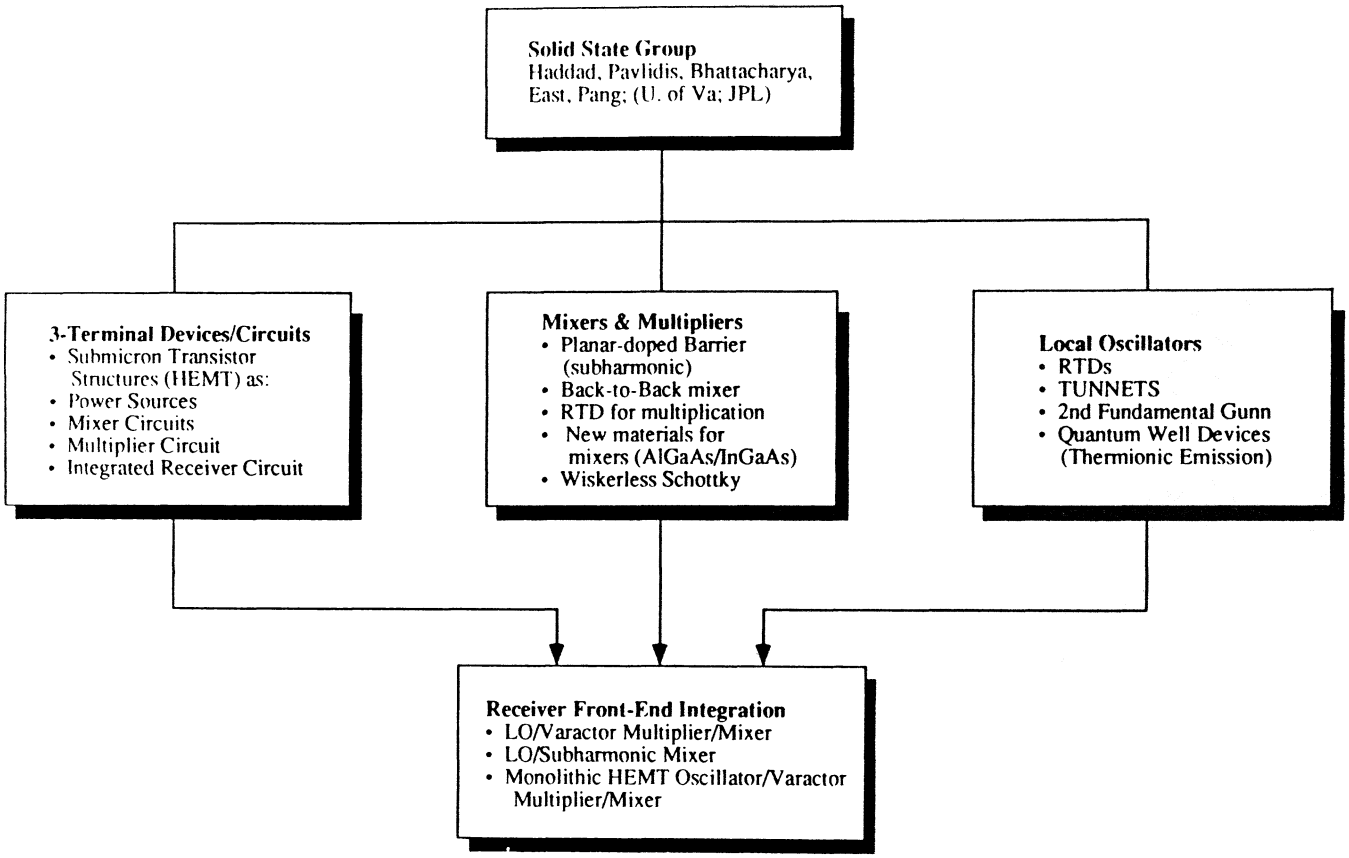

Figure 15. Research activities of the Solid-State Group.

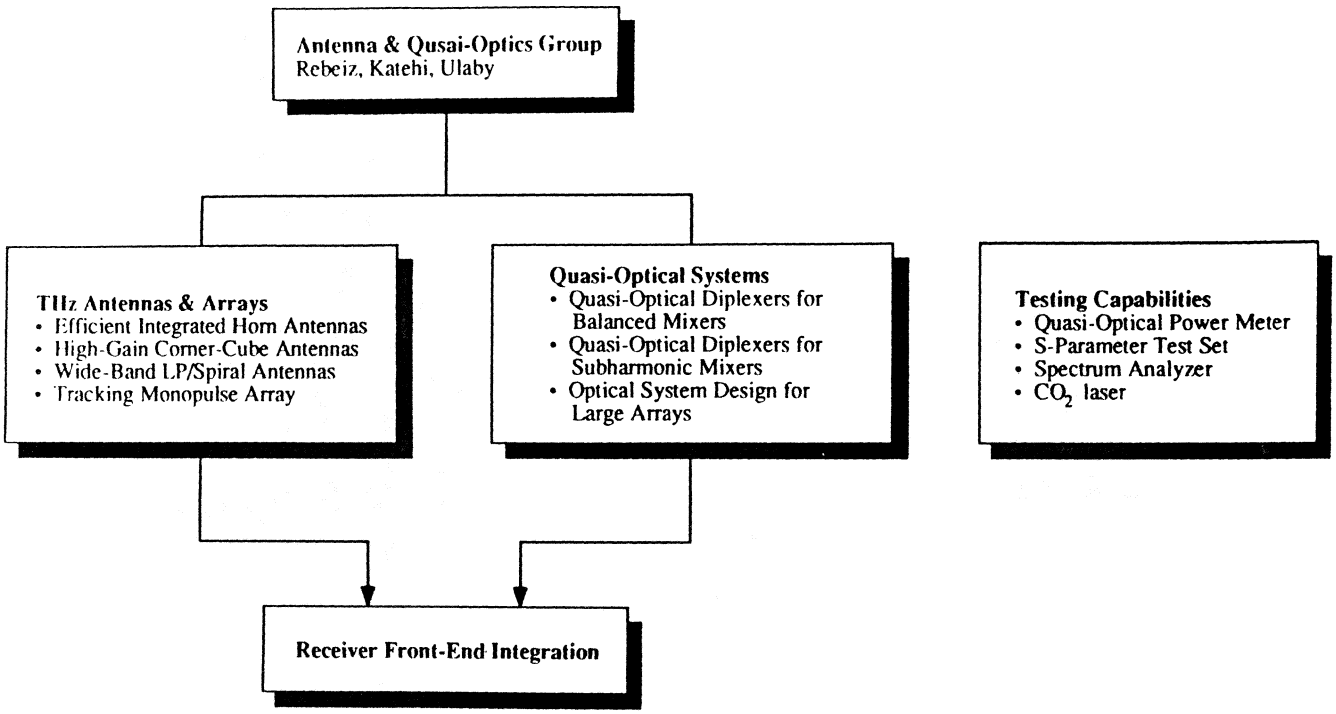

Figure 16. Research activities of the Antennas and Quasi-Optics Group.

subsequent years. Our goal is to develop devices capable of providing 1 mW of power at 1 THz by 1993.

b. *Subharmonic-mixer receiver.* The "traditional" approach used at millimeter and submillimeter wavelengths for designing the front end of a heterodyne receiver is based on single-ended mixers--specifically Schottky diodes and SIS devices--which requires quasi-optical combining of the LO and input RF signals prior to focusing the beam onto the mixer element (Figure 12). A modified version of this approach is shown schematically in Figure 17. Two orthogonally

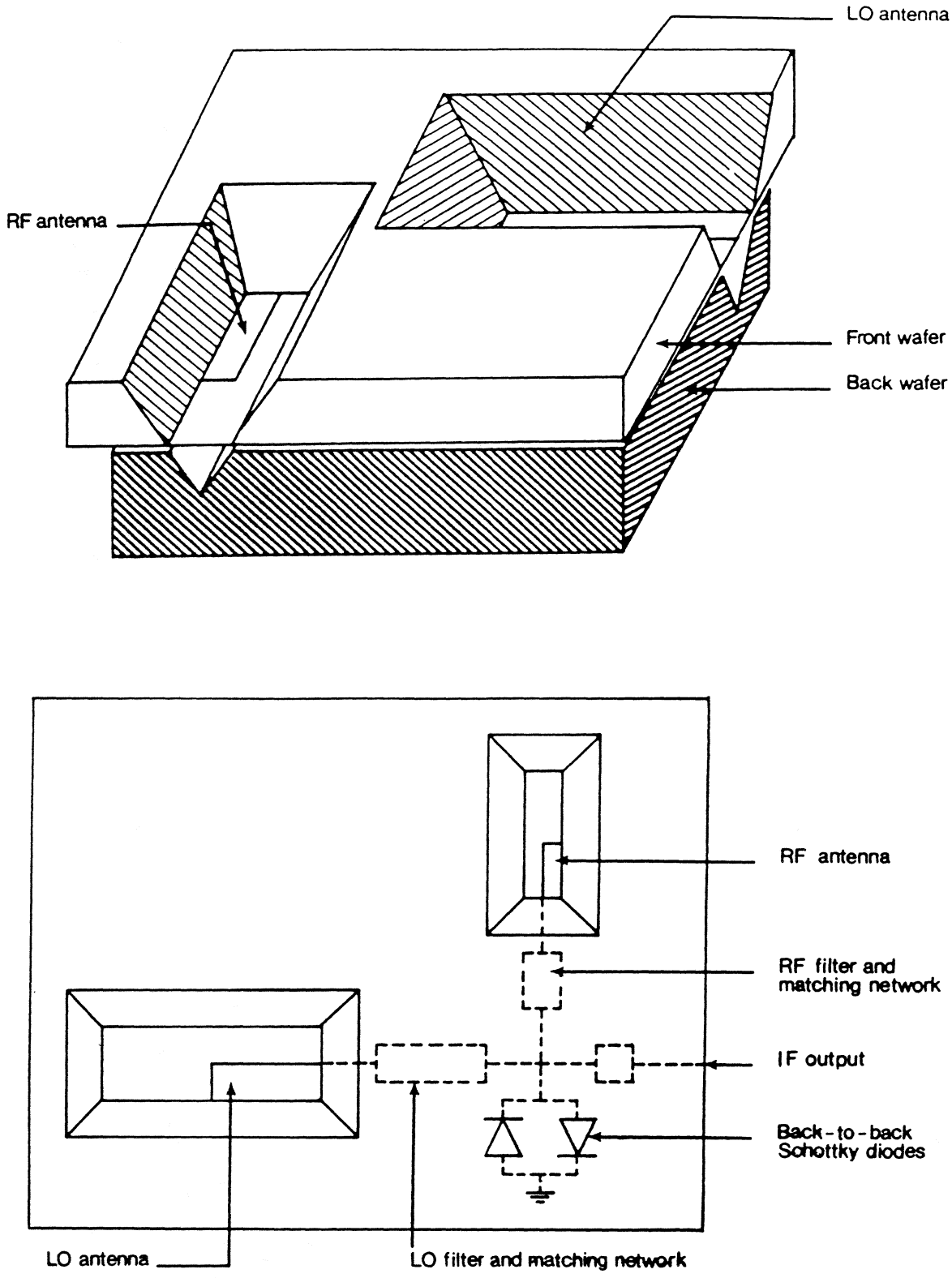

Figure 17. Subharmonic receiver configuration. The RF signal at ω_S and the LO signal at $\omega_{S/2} \pm \omega_{IF}$ are received by orthogonally polarized corner-cube antennas.

polarized corner-reflector antennas are used to couple the RF signal at ω_S and the LO signal at $\omega_{S/2} \pm \omega_{IF}$ to a pair of back-to-back Schottky diodes located on a wafer on the back side of the antennas. A 183 GHz model has been designed and is currently being fabricated and should be ready for performance evaluation soon. This design approach avoids the need for a quasi-optical diplexer as well as the construction difficulties associated with placing the mixer diodes in a reduced-height waveguide structure.

The corner-reflector antennas are particularly suitable for coupling to f/2 reflector systems. To couple the f/1 reflector systems, the pyramidal horn is a preferable choice, in which case orthogonal dipoles can be integrated on a thin membrane located inside the horn cavity (Figure 18), together with a balanced-mixer placed at their terminals.

c. *Monolithic integrated-circuit receiver.* The schematic shown in Figure 19 represents a design for a 180 GHz monolithic integrated-circuit receiver using sub-micron HEMT technology. The local oscillator, doubler, and mixer will all be fabricated as a single circuit. At present, the investigation is examining the performance of each of these three circuit elements individually, as well as modeling the matching networks and examining techniques for coupling the input RF signal to the mixer.

d. *Large-area bolometer for absolute power measurement.* The measurement of power at millimeter-wave frequencies is conventionally made using waveguide power meters. A power meter uses a thermistor or a diode detector suspended in a waveguide, and its frequency coverage is limited to the waveguide band associated with the guide dimensions. At frequencies above 100 GHz, the calibration accuracy is at best ±1 dB, and no power meters are currently available at frequencies above 300 GHz. To remedy this situation, a novel monolithic power meter was developed for THz applications using a 4 x 4 mm

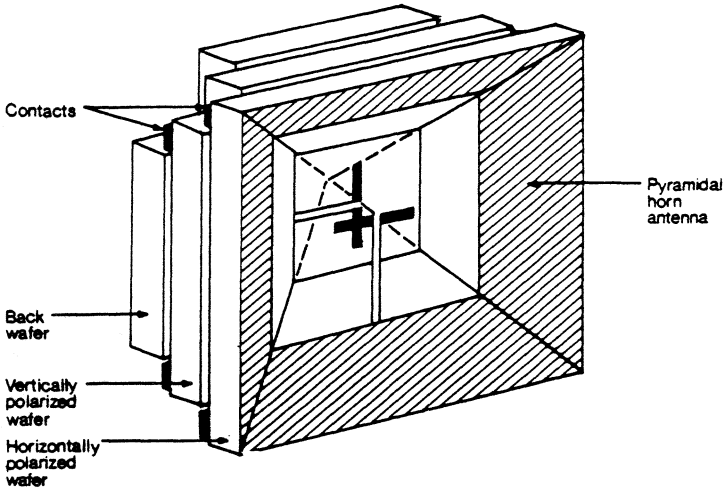

Balanced-Mixers Using Double-Polarized Horns

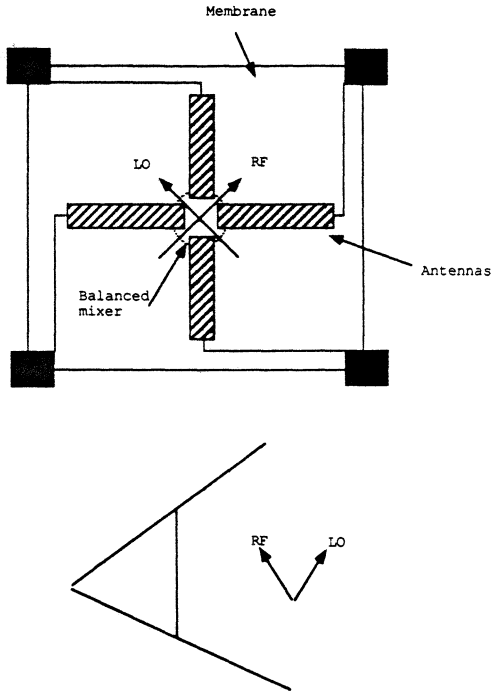

Figure 18. The top figure shows two dipole antennas placed at different locations inside the horn cavity. In the lower design, the two antennas are placed on the same membrane with a balanced mixer between them.

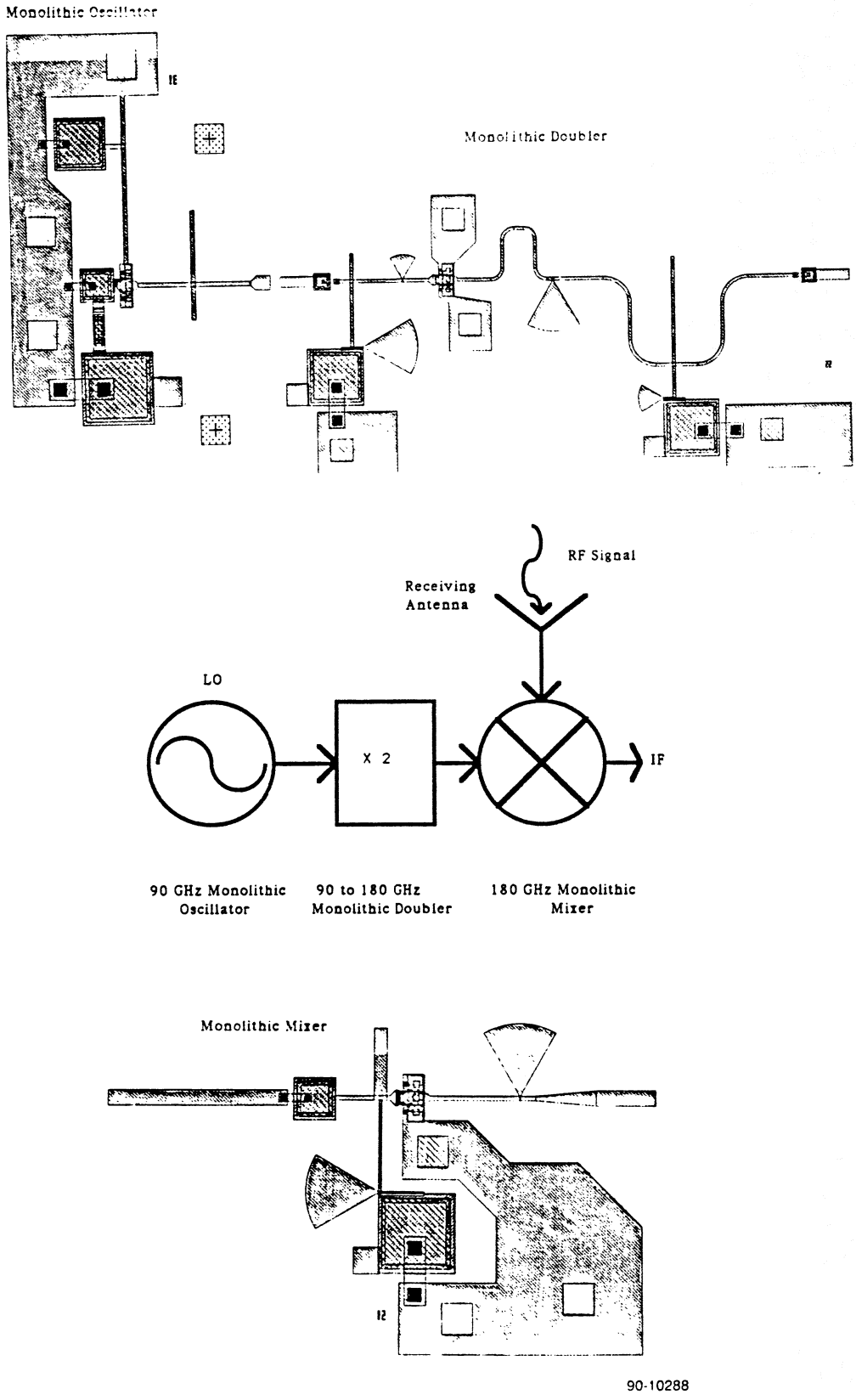

Figure 19. Schematic for a 180 GHz monolithic integrated-circuit receiver.

Bismuth bolometer integrated on a 1.2 mm-thick dielectric membrane (Figure 20). The bolometer is expected to have a wide frequency response extending well into the several THz region. The NEP of the detector was measured to be 3 nW $Hz^{-1/2}$ at a video modulation frequency of 300 Hz. This is the highest sensitivity of a THz-frequency room-temperature power meter reported to date.

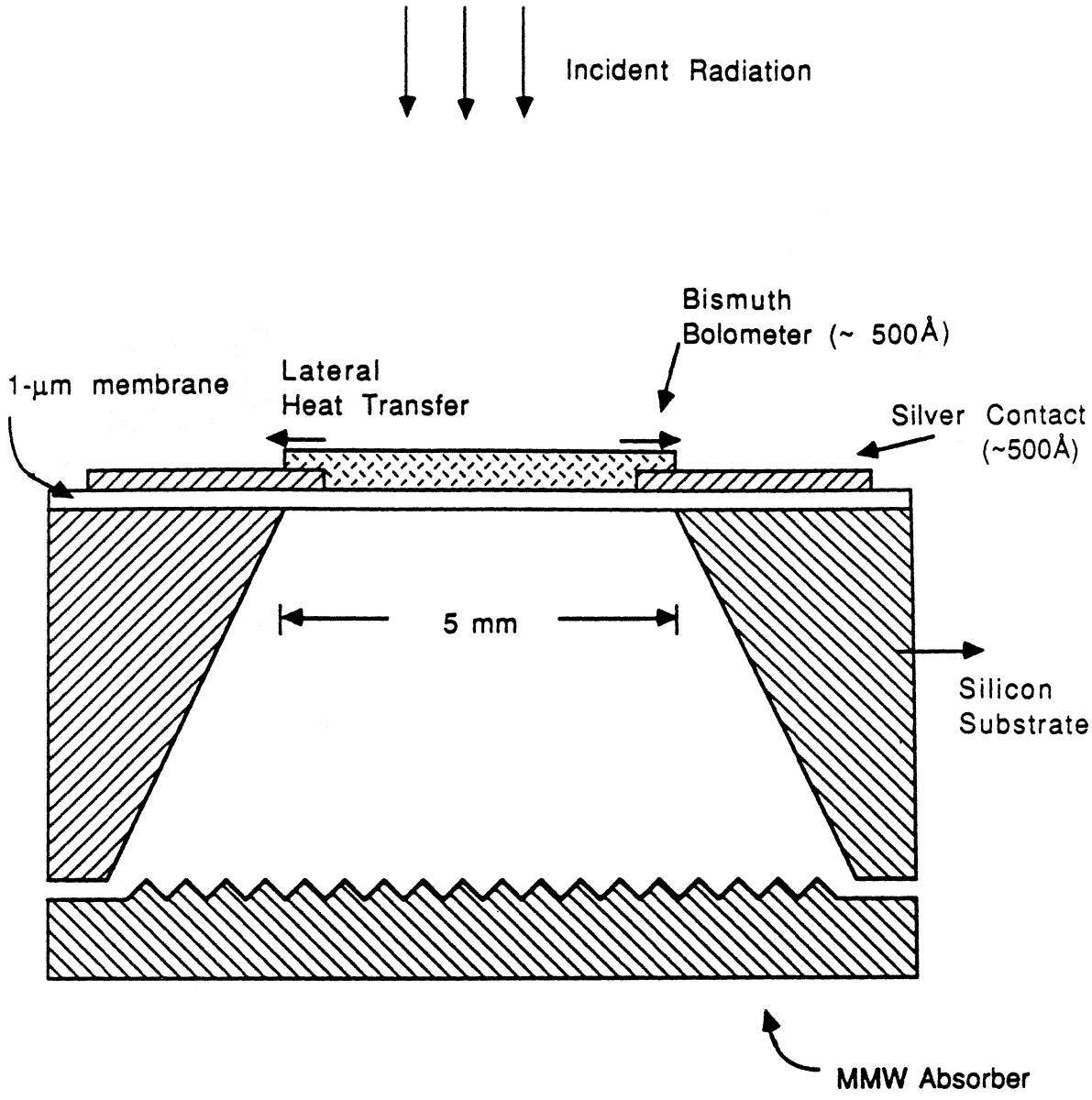

Figure 20. Wideband high responsivity THz power meter.

The preceding examples represent a subset of the research projects being conducted under the Space Terahertz Technology program at The University of Michigan, some of which are treated in more detail in other papers contained in the *Proceedings* of this Symposium.

4. CONCLUDING REMARKS

Within its brief 18-month history, the NASA/CSTT has developed an ambitious plan for developing solid-state technology for the construction of THz heterodyne receivers and their use in support of spectral line observations. The goal of the program is to develop at The University of Michigan a major U.S. facility for research in this field and to establish cooperative relations with NASA, industry, and other academic institutions involved in space THz technology. Holding the First International Space Terahertz Technology Symposium at The University of Michigan is only the first step toward that goal.

REFERENCES

[1] Payne, J. M., "Millimeter and Submillimeter Wavelength Radio Astronomy," *IEEE Proceedings*, Vol. 77, 1989, pp. 993-1017.

[2] Jewell, P. R., J.M. Hollis, F. J. Lovas, and L. E. Snyder, "Millimeter- and Submillimeter-wave Surveys of Orion A Emission Lines in the Ranges 200.7-202.3 GHz, 203.7-205.3 GHz, and 330-360 GHz," *Astrophys. J. Suppl.*, Aug. 1989.

[3] Waters, J. W., "Microwave Limb-Sounding of Earth's Upper Atmosphere," *Atmospheric Research*, 23, 1989, pp. 391-410.

[4] Phillips, T. G., "Techniques of Submillimeter Astronomy," in *Millimeter and Submillimeter Astronomy*, R. D. Wolstencroft and W. B. Burton (editors), Kluwer Academic Publications, Norwell, MA, 1988, pp. 1-24.

[5] Archer, J. W., "Low-Noise Heterodyne Receivers for Near-Millimeter-Wave Radio Astronomy," *IEEE Proceedings*, Vol 73, 1985, pp.109-130.

[6] Fetterman, H. R., G.A. Koepf, P. F. Goldsmith, B. J. Clifton, D. Buhl, N. R. Erickson, D. D. Peck, N. McAvery, and P. E. Tannenwald, "Submillimeter Heterodyne Detection of Interstellar Carbon Monoxide at 434 Micrometers," *Science*, Vol. 211, 1981, p. 580.

[7] Rebeiz, G. M., *et al.*, "Monolithic Millimeter-Wave Two-Dimensional Horn Imaging Arrays," Accepted for publication in *IEEE Transactions on Antennas and Propagation*.

[8] White, G. J., "Receiver Technology", in *Millimeter and Submillimeter Astronomy*, R. D. Wolstencroft and W. B. Burton (editors), Kluwer Academic Publications, Norwell, MA, 1988, pp. 27-93.

[9] Goldsmith, P. F., "Quasi-Optical Techniques at Millimeter and Submillimeter Wavelengths", *Infrared and Millimeter Waves*, Vol. 6, 1982, pp. 277-343.

[10] Tucker, J. R., and M. J. Feldman, "Quantum Detection at Millimeter Wavelengths", *Rev. Mod. Phys.*, Vol. 57, 1985, pp. 1055-1113.

[11] Phillips, T. G., and K. B. Jefferts, "A Low Temperature Bolometer Heterodyne Receiver for Millimeter Wave Astronomy", *Rev. Sci. Instrum.*, Vol. 44, 1973, pp. 1009-1014.

[12] Archer, J. W., "Millimeter Wavelength Frequency Multipliers", *IEEE Transactions on Microwave Theory and Techniques*, Vol. MTT-29, 1981, pp. 552-557.

[13] Rebeiz, G. M., W. G. Regehr, D. B. Rutledge, R. L. Savage, and N. C. Luhmann, Jr., "Submillimeter-Wave Antennas on Thin Membranes", *Infrared and Millimeter Waves*, Vol. 8, 1987, pp. 1249-1255.

[14] Feldman, M. J., "Theoretical Considerations for THz SIS Mixers", *Infrared and Millimeter Waves*, Vol. 8, 1987, pp. 1287-1292.

[15] Tolmunen, T. J., and A. V. Räisänen, "An Efficient Schottky-Varactor Frequency Multiplier at Millimeter Waves. Part I: Doubler", *Infrared and Millimeter Waves*, Vol. 8, 1987, pp. 1313-1336.

[16] Tolmunen, T. J., and A. V. Räisänen, "An Efficient Schottky-Varactor Frequency Multiplier at Millimeter Waves. Part II: Doubler", *Infrared and Millimeter Waves*, Vol. 8, 1987, pp. 1337-1353.

[17] Mattauch, R. J., and T. W. Crowe, "GaAs Schottky Devices for Submillimeter Wavelengths", *Infrared and Millimeter Waves*, Vol. 8, 1987, pp. 1235-1241.

NASA'S TERAHERTZ TECHNOLOGY PROGRAM

DR. MARTIN SOKOLOSKI
Department of Physics
Drexel University
and
Office of Aeronautics, Exploration and Technology
NASA Headquarters

DR. CARL A. KUKKONEN
Director
Center for Space Microelectronics Technology
Jet Propulsion Laboratory
California Institute of Technology

Abstract

NASA is developing submillimeter (terahertz) receivers for use in astrophysics, the study of planetary atmospheres and for Earth observation. The science objectives include the understanding of star formation, the interstellar medium, galactic formation, the composition of planetary atmospheres, and ozone depletion in the Earth's atmosphere. Since the Earth's atmosphere is opaque in most of the submillimeter region, observations must be done from space.

Because submillimeter technology has no significant ground applications, the receiver technology is not available. The NASA Office of Aeronautics, Exploration and Technology is vigorously pursuing a multi-year effort to develop the components needed for a submillimeter heterodyne receiver. The critical components include the antenna, local oscillator and mixer. The technical challenges arise due to the high frequency and short wavelength of the radiation.

Because waveguides and waveguide arrays are difficult to fabricate at these wavelengths, quasi-optical antenna techniques are being actively pursued. The local oscillator is a major challenge, because a terahertz is an order of magnitude higher than frequencies obtainable with conventional electronics. Novel structures such as resonant tunneling devices are used as fundamental oscillators and as frequency multipliers.

The mixer elements being investigated are solid-state planar Schottky diodes for Earth observations and superconducting-insulating-superconducting (SIS) tunnel junctions for low-noise cryogenic astrophysical telescopes.

The University of Michigan Center for Space Terahertz Technology was established by NASA to help develop additional expertise and students trained in this area.

The National Aeronautics and Space Administration (NASA) is developing submillimeter (terahertz) receivers for use in astrophysics, the study of planetary atmospheres and for Earth observation. The science objectives include the understanding of star formation, the interstellar medium, galactic formation, the composition of planetary atmospheres, and ozone depletion in the Earth's atmosphere. Since the Earth's atmosphere is opaque in most of the submillimeter region, observations must be done from space.

For reference, the wavelength of 1 THz (1000 GHz) radiation in free space is one-third of a millimeter or 333 μm. The frequency is 30 times higher than "standard radio waves" used in radars, yet 30 times lower than the frequencies of "standard infrared photons." Technology is available for radar frequencies and detectors are also available in the infrared. However, the technology needed for the terahertz region (0.3-30 THz) has not yet been developed.

There are two reasons for the lack of technology. First, the frequency regime is intrinsically very difficult. The photon energies are small relative to the energy gaps of opto-electronic semiconductors, but the frequencies lie beyond the frequency range accessible with conventional semiconductor electronic devices. Secondly, since the Earth's atmosphere is largely opaque in the terahertz region, there has not been a demand for terahertz receivers for terrestrial applications, and there is no current commercial application of terahertz technology.

The terahertz frequency range is important to NASA because molecular species important in atmospheric chemistry, such as ozone and chlorine oxide, and other molecules found in the interstellar medium, have radiative emissions in this range. The sharp emission lines can be detected readily by a heterodyne receiver. The frequency of an emission line identifies the species; the intensity gives abundance, and the relative intensity of two lines from the same molecule yields the temperature. In addition, Doppler-shifted deviations from laboratory spectra gives information about the dynamics of the interstellar medium.

The NASA Office of Aeronautics, Exploration and Technology is developing technology for potential future terahertz space missions such as the ozone depletion experiment on the Earth Observing System (Eos), the Submillimeter Explorer, the Submillimeter Imaging Line Survey and the Large Deployable Reflector. The focus is on solid-state receiver components that are compact, low power and space-qualifiable.

Limited terahertz data can be obtained from the Earth by observing from high mountains, balloons or aircraft to get above much of the atmosphere, and using frequency bands where the atmospheric absorption is minimum. These Earth-based observations allow the technology to be demonstrated in real systems before actual use in space.

The technology needed to study ozone depletion of the Earth's atmosphere differs from that needed for astrophysics. In ozone depletion studies, the atmospheric signal strength is relatively large, but accurate measurements must be made continuously for 5-10 years to detect small changes. The long mission lifetime precludes the use of stored cryogen refrigeration and dictates that receivers must operate at 65-125K. This leads to a requirement for semiconductor mixers, local oscillators and multipliers, which have limited sensitivity.

A major effort is devoted to improving semiconductor Schottky diode mixer efficiency, and extending performance to higher frequencies. The Microwave Limb Sounder, to be flown on the Upper Atmosphere Research Satellite (UARS) in 1992, operates at 200 GHz. The Eos experiment will be at 650 GHz. Schottky diode mixers require substantial local oscillator power, and this is also a major challenge at 650 GHz.

The signal strengths for astrophysics missions are very small, and ultimate sensitivity is required. This dictates large antennas, and ultra-low noise receivers. Most astrophysical missions will need to carry liquid helium to accommodate use of ultra-sensitive superconducting mixers. The mixer is a superconducting-insulating-superconducting tunnel junction coupled

with the appropriate tuning elements. Lead-based tunnel junctions have been demonstrated on Earth, but lead junctions have very short life time and cannot be space qualified. The focus of the development effort is on niobium nitride, which is a refractory material and NbN junctions have extremely long life. Currently NbN mixers have shown good performance to 200 GHz, with a theoretical limit of 1.5 THz. The major advantages of superconducting mixers are that they have extremely low noise and require much lower local oscillator power than a Schottky diode mixer.

Since astrophysical quantities are not changing rapidly, the mission life requirement is dictated only by the level of "sky search" desired. The science return will be significantly enhanced by array technology being developed by NASA, which will allow arrays of submillimeter receivers to take data in parallel. Current receivers, operating up to 200 GHz or so, all use waveguide technology inherited from the radar community. It is difficult to machine waveguides for terahertz frequencies and it is even more difficult to build waveguide arrays. This is the motivation for the NASA effort in quasi-optical approaches, which utilize lenses, and integrated antenna/mixer structures to facilitate arrays.

NASA

NASA TERAHERTZ (SUBMILLIMETER) TECHNOLOGY PROGRAM

Martin Sokoloski
Department of Physics and Atmospheric Science
Drexel University
and
Office of Aeronautics and Space Technology
NASA Headquarters

and

Carl Kukkonen
Center for Space MicroelectronicsTechnology
Jet Propulsion Laboratory

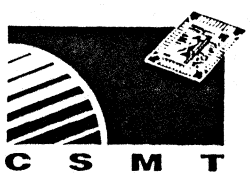

NASA TERAHERTZ TECHNOLOGY PROGRAM

- WHY OBSERVATIONS FROM SPACE ARE REQUIRED
- SUBMILLIMETER SCIENCE OBJECTIVES
  - OZONE DEPLETION IN EARTH'S ATMOSPHERE
  - PLANETARY ATMOSPHERES
  - STAR FORMATION AND INTERSTELLAR MEDIUM
  - GALACTIC FORMATION
  - COSMOLOGY
- CANDIDATE NASA MISSIONS
  - GROUND-BASED
  - AIRCRAFT AND BALLOON
  - SPACECRAFT
  - LUNAR BASE
- NASA SUBMILLIMETER SENSOR PROGRAM
  - HETERODYNE RECEIVER COMPONENTS
    - ANTENNAS AND ARRAYS
    - MIXERS
    - LOCAL OSCILLATORS AND MULTIPLIERS

JPL

SUBMILLIMETER ASTROPHYSICS PROGRAM

ATMOSPHERIC OPACITY

- MOST OF SUBMILLIMETER BAND IS UNOBSERVABLE FROM EARTH DUE TO ABSORBTION IN THE EARTH'S ATMOSPHERE

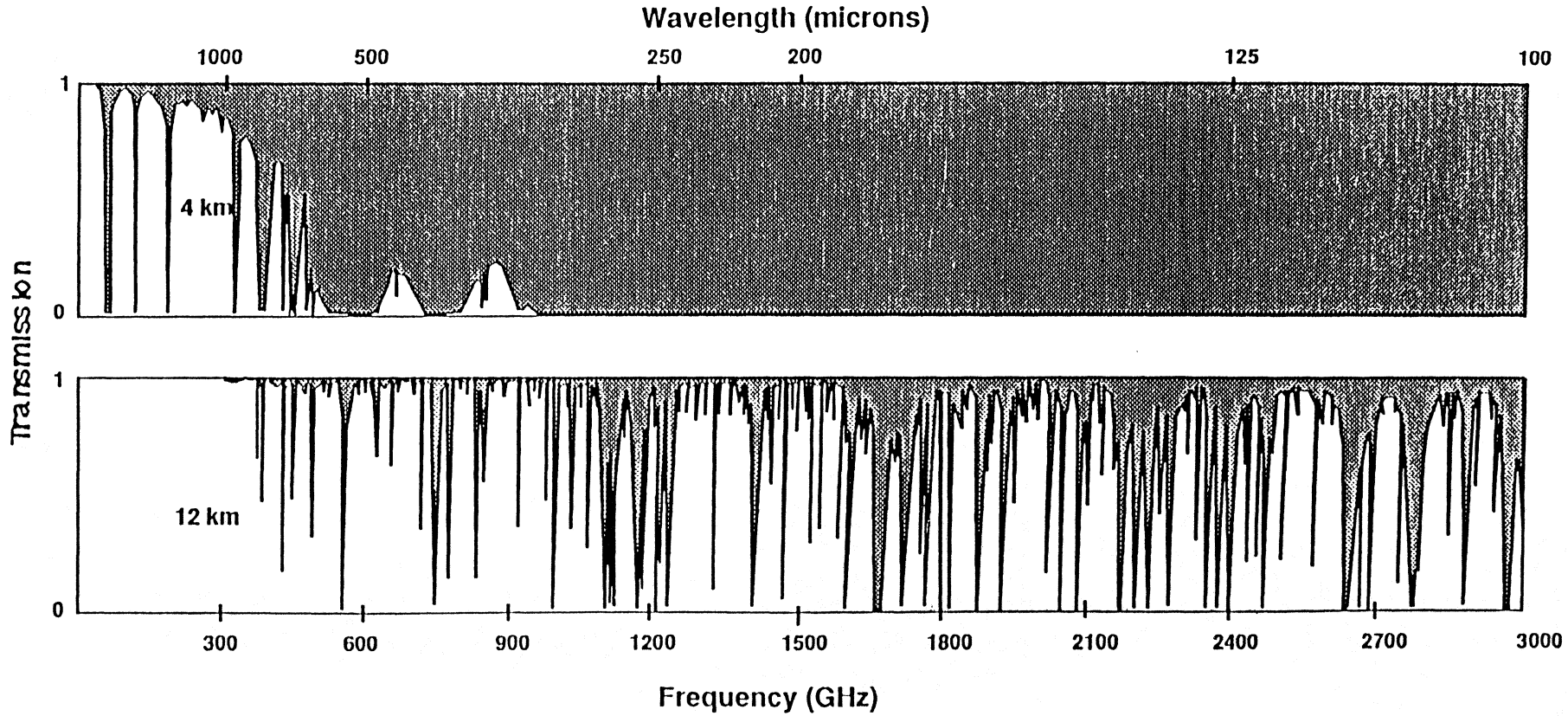

PNS 1/04/90

SUBMILLIMETER ASTROPHYSICS PROGRAM

WHY SUBMILLIMETER ASTRONOMY FROM SPACE?

- SUBMILLIMETER OBSERVATIONS FROM THE GROUND RANGE FROM DIFFICULT TO IMPOSSIBLE DUE TO THE EARTH'S ATMOSPHERE
- EMISSION FROM COLD BODIES IN UNIVERSE PEAKS IN SUBMM SPECTRAL REGION
- PROBES REGIONS WHERE VISIBLE RADIATION IS OBSCURED BY DUST
- SPECTROSCOPY OF MOLECULES CAN DETERMINE COMPOSITION, DENSITY, TEMPERATURE, VELOCITY AND DYNAMICS
- VISIBLE AND INFRARED SPECTRUM OF DISTANT OBJECTS IS RED SHIFTED INTO THE SUBMILLIMETER

OZONE DEPLETION

- SINGLE HETERODYNE RECEIVER AT ~ 650 GHz CAN SIMULTANEOUSLY MEASURE

  - OZONE
  - ClO THE KEY MOLECULE WHICH DESTROYS OZONE
  - HCl THE KEY MOLECULE BY WHICH CHLORINE IS REMOVED FROM THE STRATOSPHERE

<u>1 FREE CHLORINE ACTS AS A CATALYST AND DESTROYS 10,000 OZONE</u>

- MUST MEASURE VERY ACCURATELY AND FOR A LONG TIME
  5 + YEARS

- LONG LIFE MISSION CANNOT USE HELIUM COOLED SIS MIXER AND MUST USE SCHOTTKY DIODE

- OZONE INSTRUMENT - MICROWAVE LIMB SOUNDER ON UARS (200 GHz) and EOS-B (650 GHz) . . . JOE WATERS P.I.

HOW OZONE IS DESTROYED
Chlorofluorocarbon molecule
In the upper atmosphere ultraviolet light breaks off a chlorine atom from a chlorofluorocarbon molecule
Chlorine atom
Ozone molecule
The chlorine attacks an ozone molecule, breaking it apart
Oxygen molecule
An ordinary oxygen molecule and a molecule of chlorine monoxide are formed
After a free oxygen atom breaks up the chlorine monoxide, the chlorine is free to begin the process again (2)
TIME Diagram by Joe Lertola

1987 Ozonesonde Measurements from Halley Bay, Antarctica

(from Jon Farman 7 Dec 87)

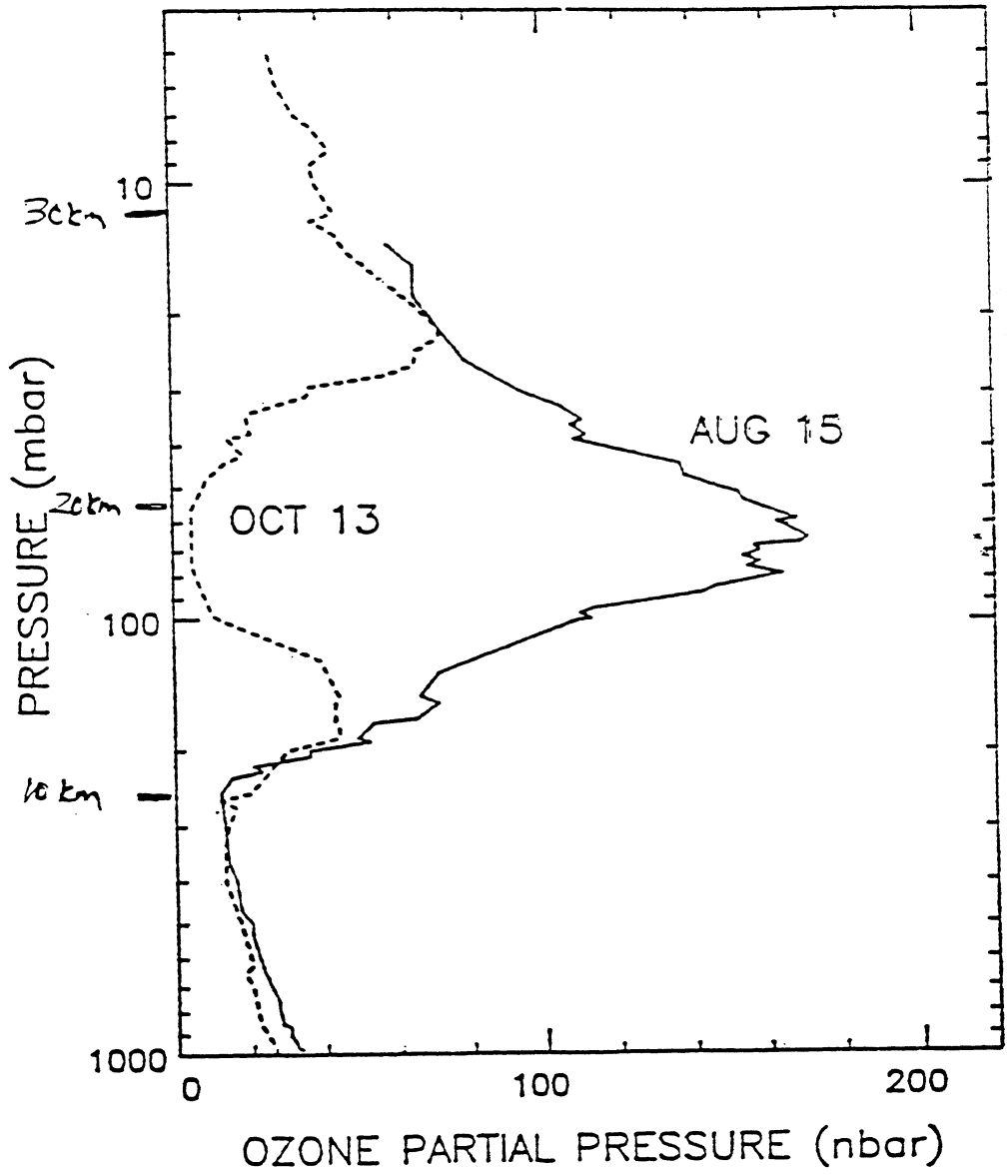

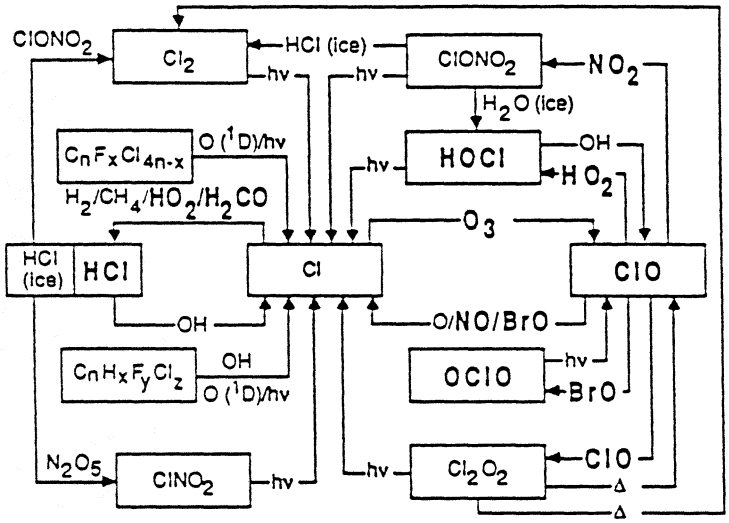

ODD-CHLORINE CHEMISTRY

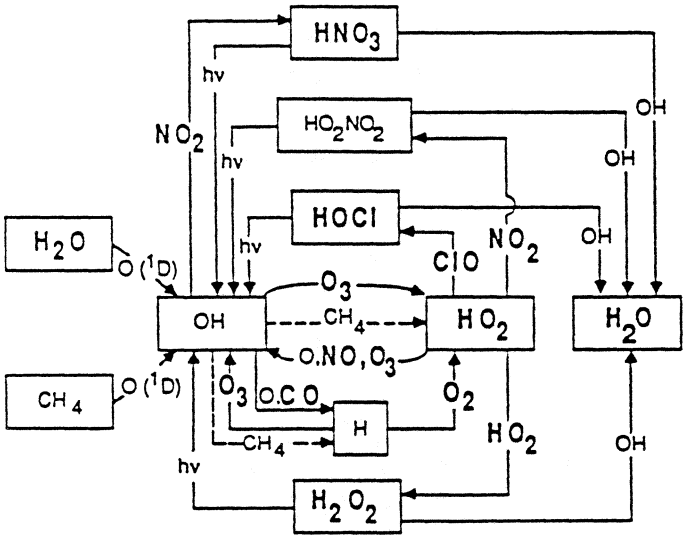

ODD-HYDROGEN CHEMISTRY

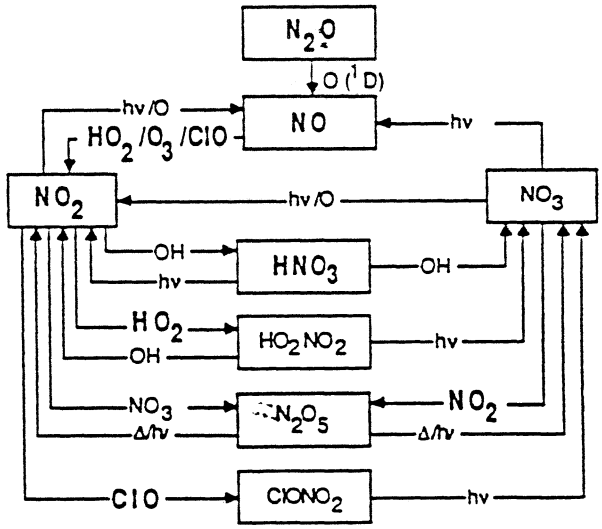

ODD-NITROGEN CHEMISTRY

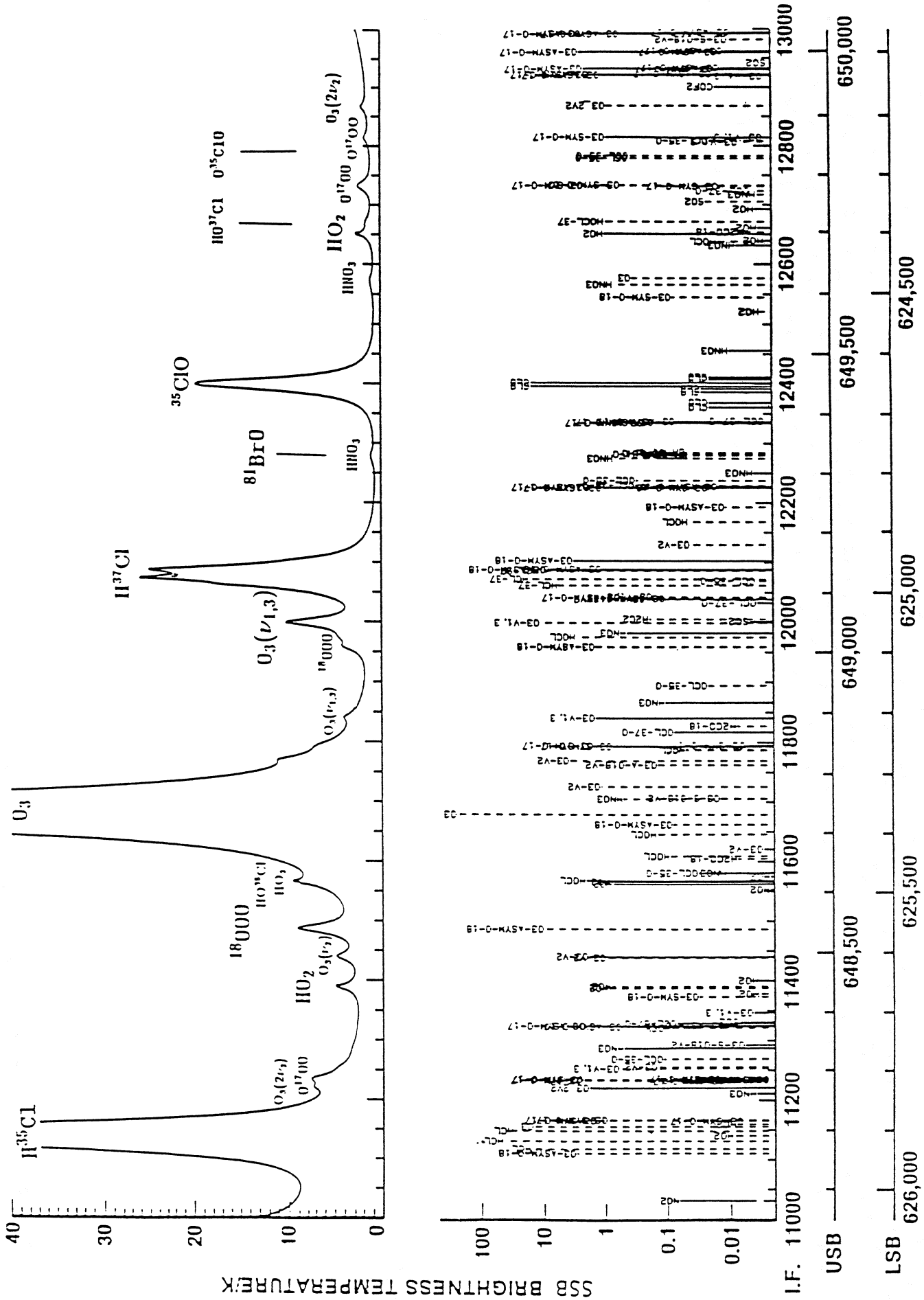
SSB BRIGHTNESS TEMPERATURE/K
40
30
20
10
0
100
10
1
0.1
0.01
I.F.
11000
11200
11400
11600
11800
12000
12200
12400
12600
12800
13000
USB
626,000
625,500
625,000
624,500
LSB
648,500
649,000
649,500
650,000
$H^{35}Cl$
O_3
$O_3(2\nu_2)$
^{18}OOO
$O^{17}OO$
$HO^{37}Cl$
HNO_3
HO_2
$O_3(\nu_1,3)$
$H^{37}Cl$
^{81}BrO
^{35}ClO
$HO^{37}Cl$
$O^{35}ClO$
HNO_3
HO_2
$O^{17}OO$
$O_3(2\nu_2)$

GLOBAL CHANGE TECHNOLOGY: STRATOSPHERIC OZONE DEPLETION

The 550-650 GHz SPECTRAL REGION

- This is the *only* spectral region which allows *simultaneous* measurement of ClO and HCl at all times of day and night
  - ClO is the key molecule by which chlorine destroys stratospheric ozone
  - HCl is the key molecule by which chlorine is removed from the stratosphere
  - Simultaneous measurements of ClO and HCl are needed on a global scale at all times of day and night
    * Abnormally large values of ClO and small values of HCl led to the antarctic ozone hole' — *this may be occuring elsewhere*
- Many additional molecules important for a more complete understanding of ozone depletion can also be simultaneously measured
  - Ozone itself, and all its isotopes: O_3, ^{18}OOO, $O^{18}OO$, ^{17}OOO, $O^{17}OO$
  - Chlorine/bromine destruction cycles: HOCl, OClO, CH_3Cl, BrO
  - Hydrogen destruction cycle: HO_2, H_2O, H_2O_2
  - Nitrogen destruction cycle: NO_2, NO, N_2O, HNO_3
  - Others: temperature, pressure, CO, H_2CO, HCN, SO_2, O_2

550–650 GHz TECHNOLOGY NEEDS

- Need low-noise radiometers operating at ~30–80 K temperature
  - Radiometer noise is given by $\frac{T_{sys}}{\sqrt{(\Delta\nu)(\Delta t)}}$
    - $\Delta\nu$ is required spectral resolution (~0.3–30 MHz), set by atmospheric line widths
    - Δt is allowed integration time (~1 s), set by satellite motion
    - T_{sys} is system 'noise temperature', set by technology
  - The only means available to get low noise is through new technology for low T_{sys}
    - Need: $T_{sys} \leq 3000$ K
    - Current technology: $T_{sys} \geq 6000$ K
  - The following 550–650 GHz technology is needed for low T_{sys}
    - Radiometer architecture to minimize noise
    - Low-noise non-linear device (mixer) for frequency-conversion
    - Local oscillators with ~1 mW power
    - Low-loss method for combining signal and local oscillator
    - Low-loss method for matching ~2–20 GHz mixer output to first stage amplifier

ASTROPHYSICS-INTERSTELLAR MEDIUM

1 mm = 300 GHZ = 15K

- "BLACKBODY" RADIATION FROM DUST
  - DIRECT DETECTORS WITH MODERATE RESOLUTION

- SHARP SPECTRAL LINES FROM ROTATION STATES OF STAR-FORMING SPECIES

  - HETERODYNE DETECTORS
    - IDENTIFY SPECIES
    - DEVIATIONS FROM LABORATORY SPECTRA GIVES DOPPLER SHIFT (DYNAMICS OF MOLECULAR CLOUD)
    - WEAK SIGNALS REQUIRES HIGH SENSITIVITY $\Rightarrow$ SUPERCONDUCTIVITY MIXERS

JPL

SUBMILLIMETER SCIENCE

ANTICIPATED SPECTRUM OF STAR-FORMING CLOUD

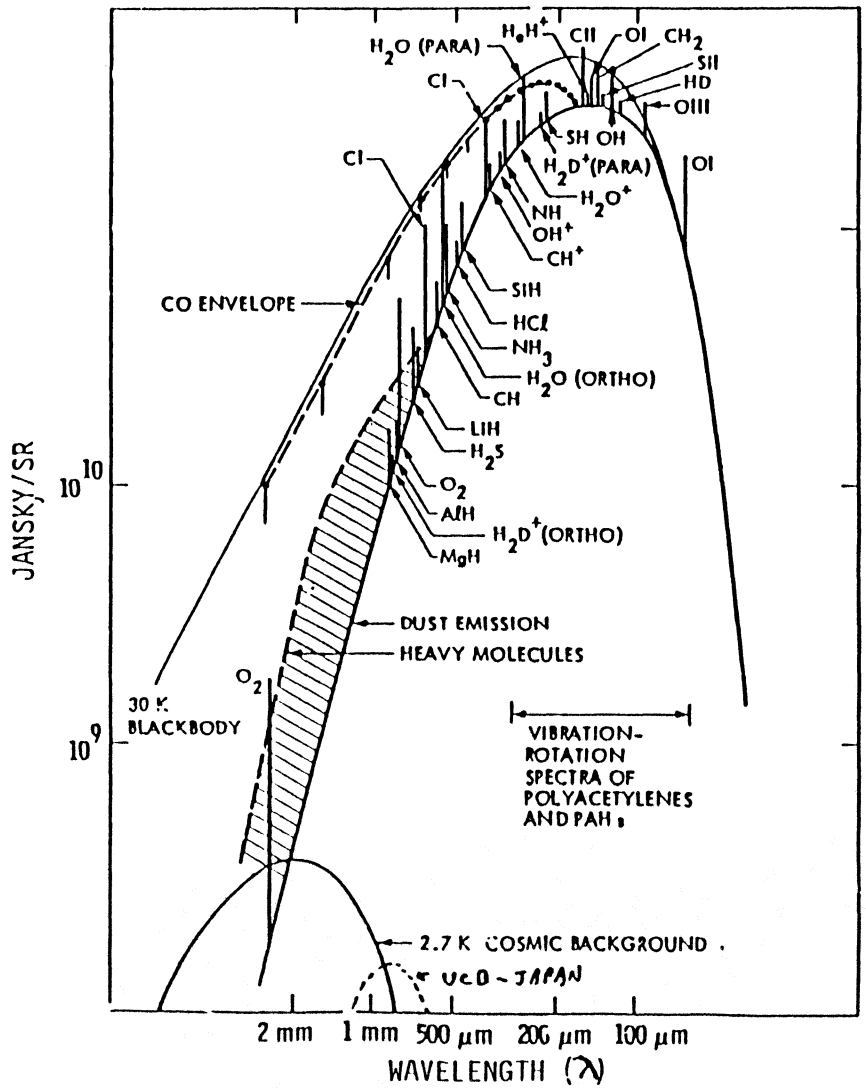

DIRECT DETECTOR SYSTEMS
CONCEPTUAL INSTRUMENT DESIGN

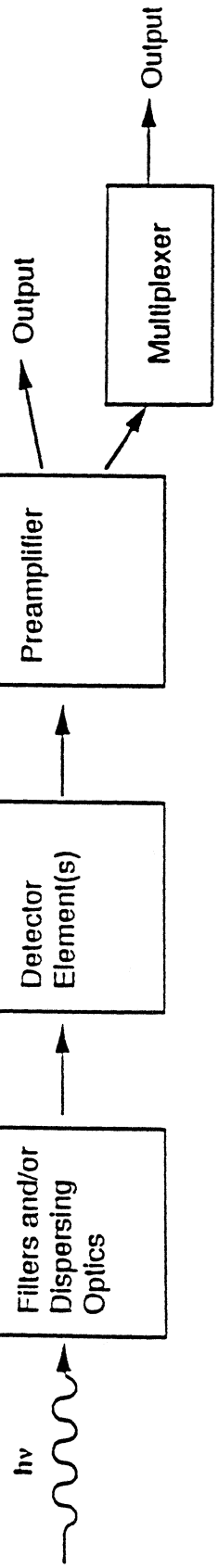

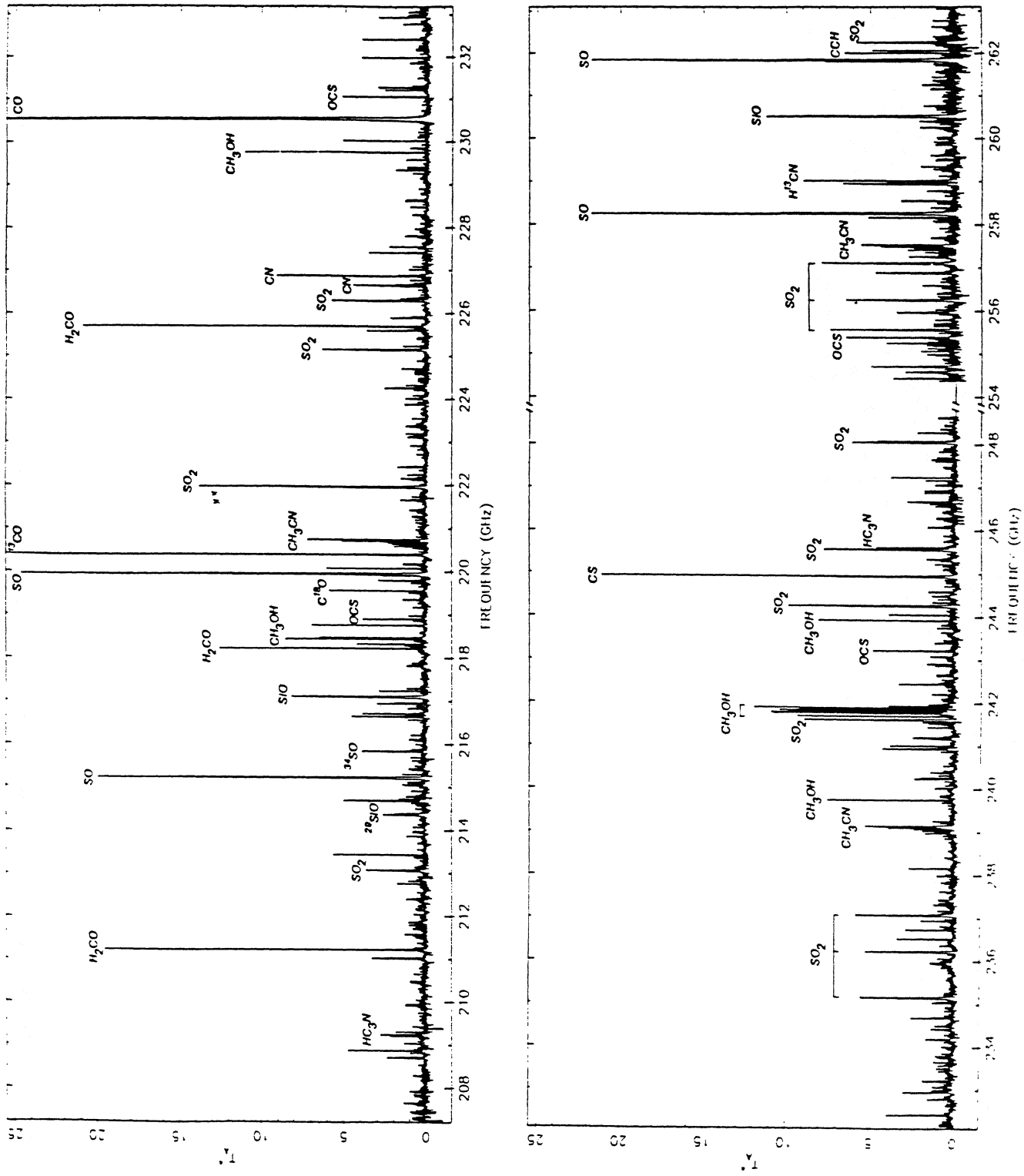
CO
OCS
CH3OH
CN
H2CO
SO2
CN
SO2
SO2
H2CO
CH3CN
13CO
SO
C18O
OCS
H2CO
CH3OH
SIO
34SO
SO
29SIO
SO2
H2CO
HC3N
TA*
FREQUENCY (GHz)
SO
SO
SIO
H13CN
CH3CN
SO2
OCS
SO2
HC3N
CS
SO2
CH3OH
OCS
CH3OH
SO2
CH3OH
CH3CN
SO2
CCH
SO2
TA*
FREQUENCY (GHz)

HETERODYNE RECEIVER TECHNOLOGY

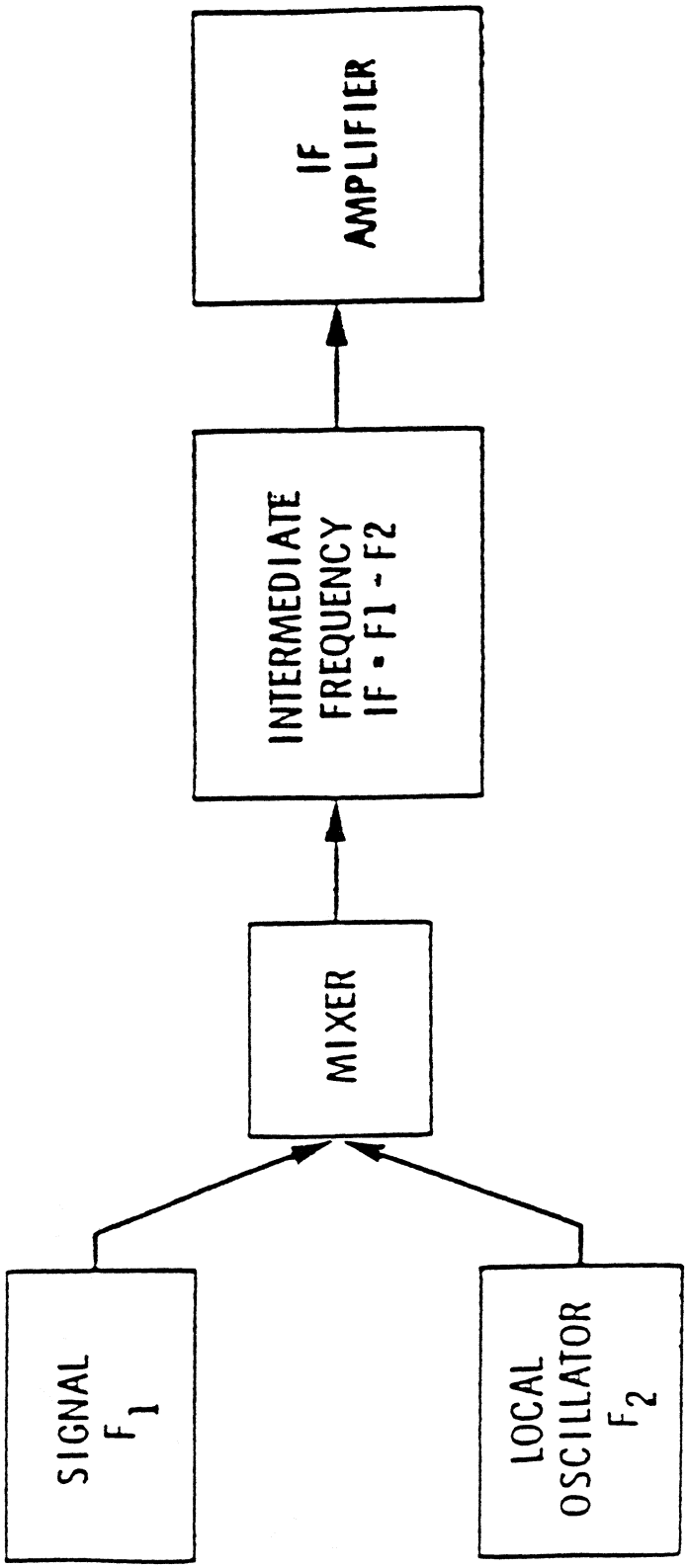

CANDIDATE SUBMILLIMETER APPLICATIONS/MISSIONS

- 10m SUBMM TELESCOPE ON HAWAII
  - AT 14,000 ft.
  - LIMITED TO ATMOSPHERIC "WINDOWS"
- KUIPER AIRBORNE OBSERVATORY
  - 1m TELESCOPE
- BALLOONS
- SPACECRAFT
  - UPPER ATMOSPHERIC RESEARCH SATELLITE, 1991
  - SUBMM WAVE ASTRONOMY SATELLITE, 1994
  - SUBMILLIMETER EXPLORER, 1998?
  - SUBMM IMAGING LINE SURVEY, 1999?
  - EOS-B MILLIMETER WAVE LIMB SOUNDER, 1999?
  - LARGE DEPLOYABLE REFLECTOR, 2004?
- LUNAR-BASED INTERFEROMETER, 2007?

SUBMILLIMETER MODERATE MISSION (SMMM)

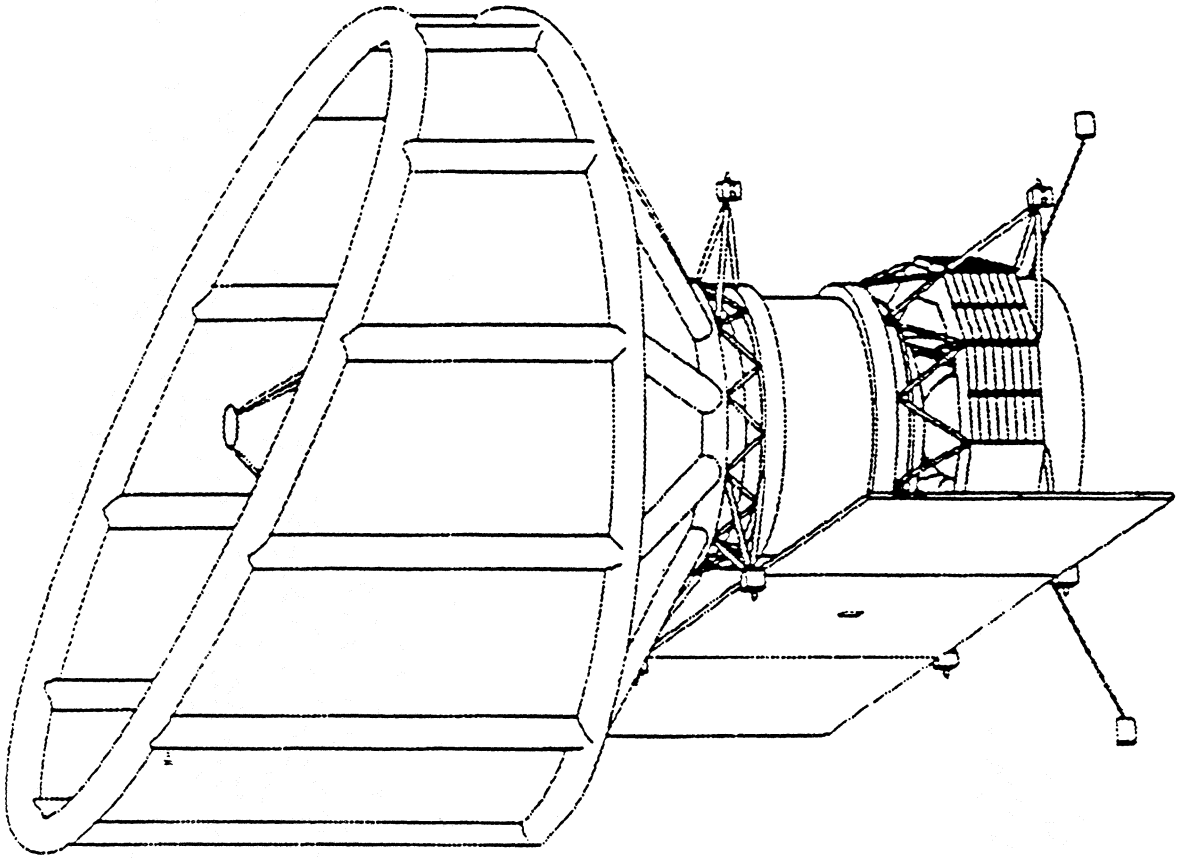

SUBMILLIMETER - INFRARED LINE SURVEY (SMILS)

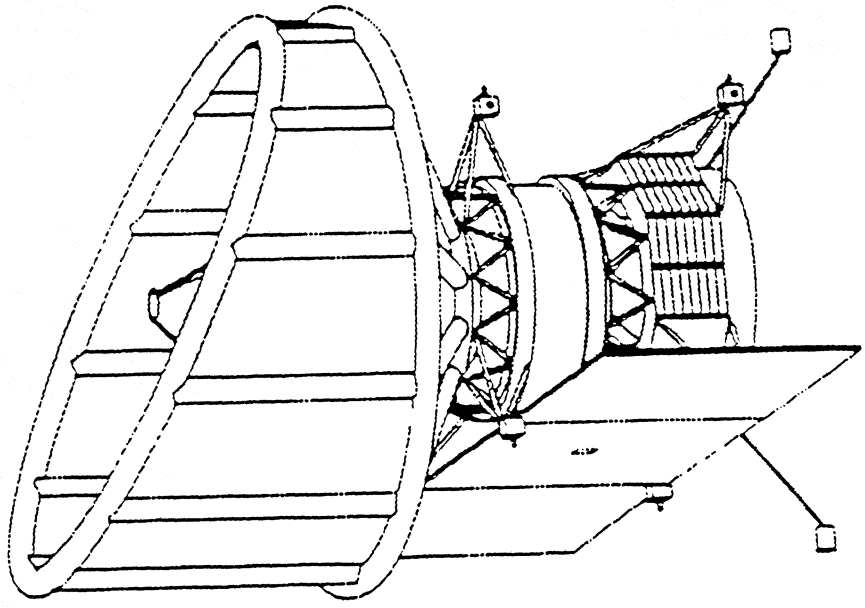

EXPLORER (SMME)

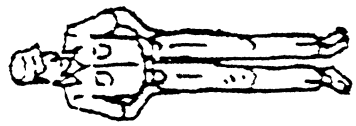

JPL

THE LARGE DEPLOYABLE REFLECTOR

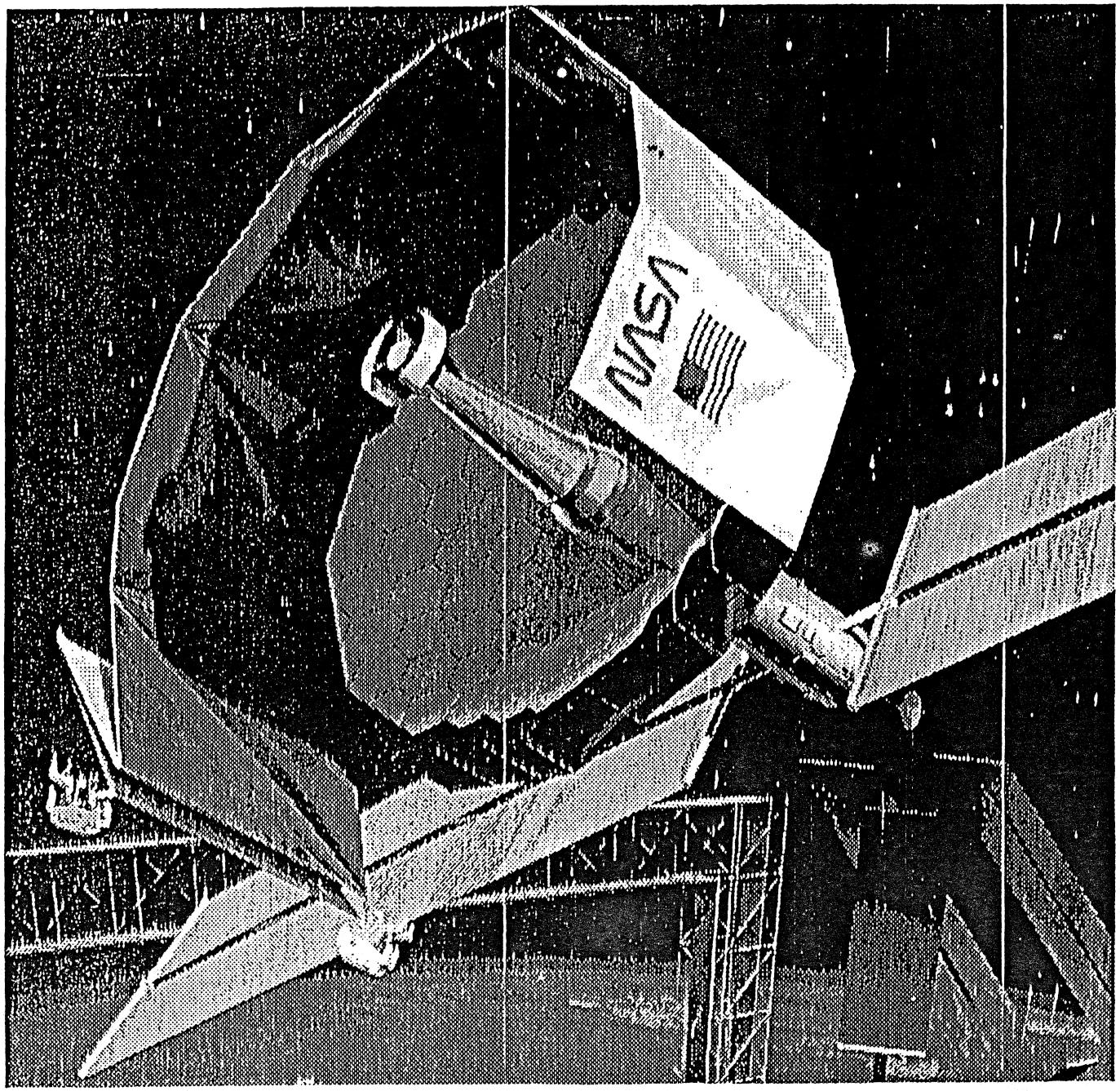

SUBMILLIMETER APERTURE SYNTHESIS ARRAY

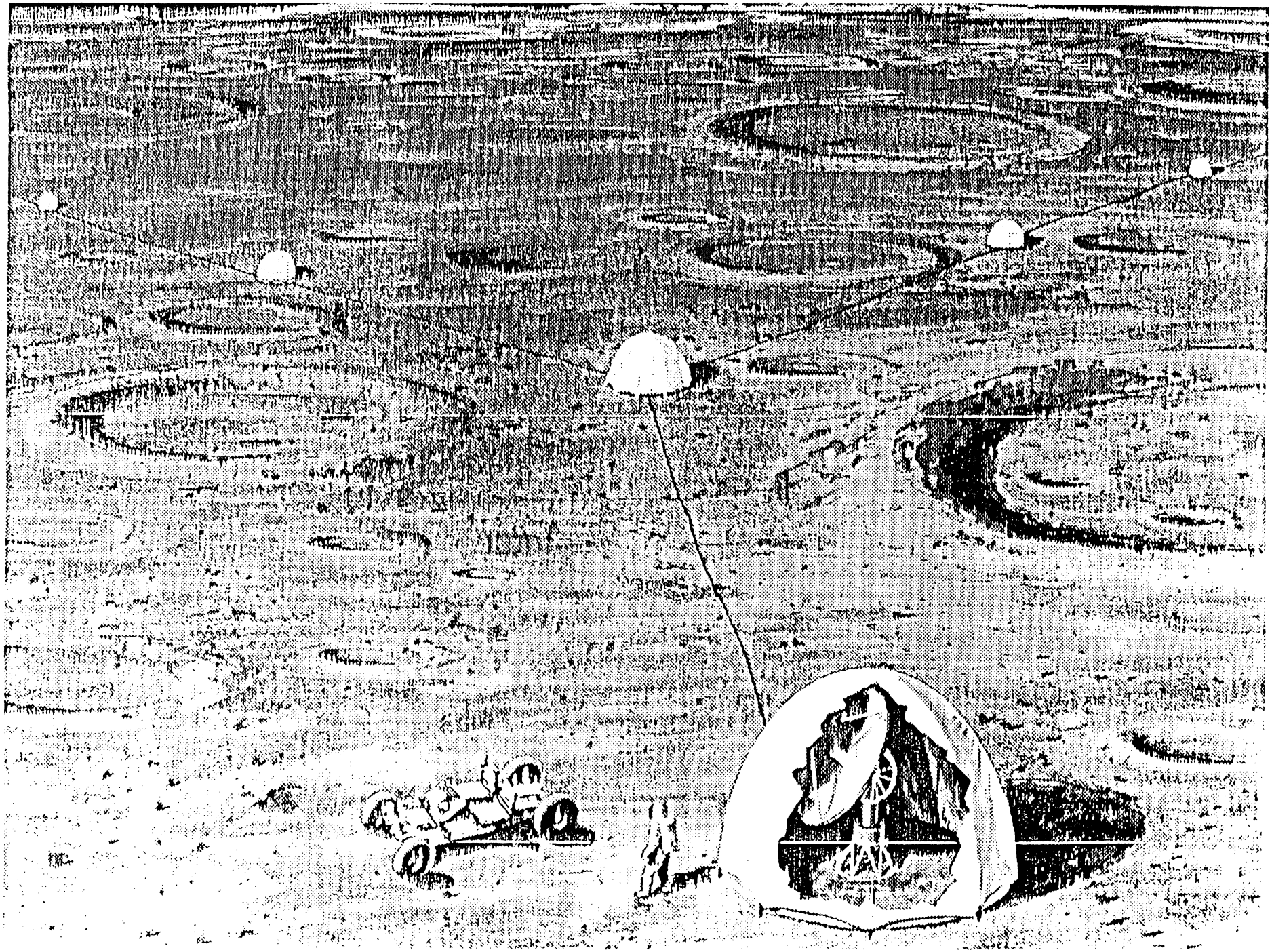

TECHNOLOGY PROGRAM GOALS FOR SUBMILLIMETER MISSIONS

- PROVIDE THE ENABLING TECHNOLOGIES FOR SUBMILLIMETER SPACE ASTRONOMY
- BALANCE THE PACE OF DEVELOPMENT TO MATCH SUBMILLIMETER MISSION SCHEDULES
- ADVANCE THE MATURITY TO A LEVEL OF READINESS APPROPRIATE FOR MISSION BASELINE DESIGN

NASA OAST

COHERENT SENSOR RESEARCH

NEED FOR SUBMILLIMETER COHERENT SENSORS

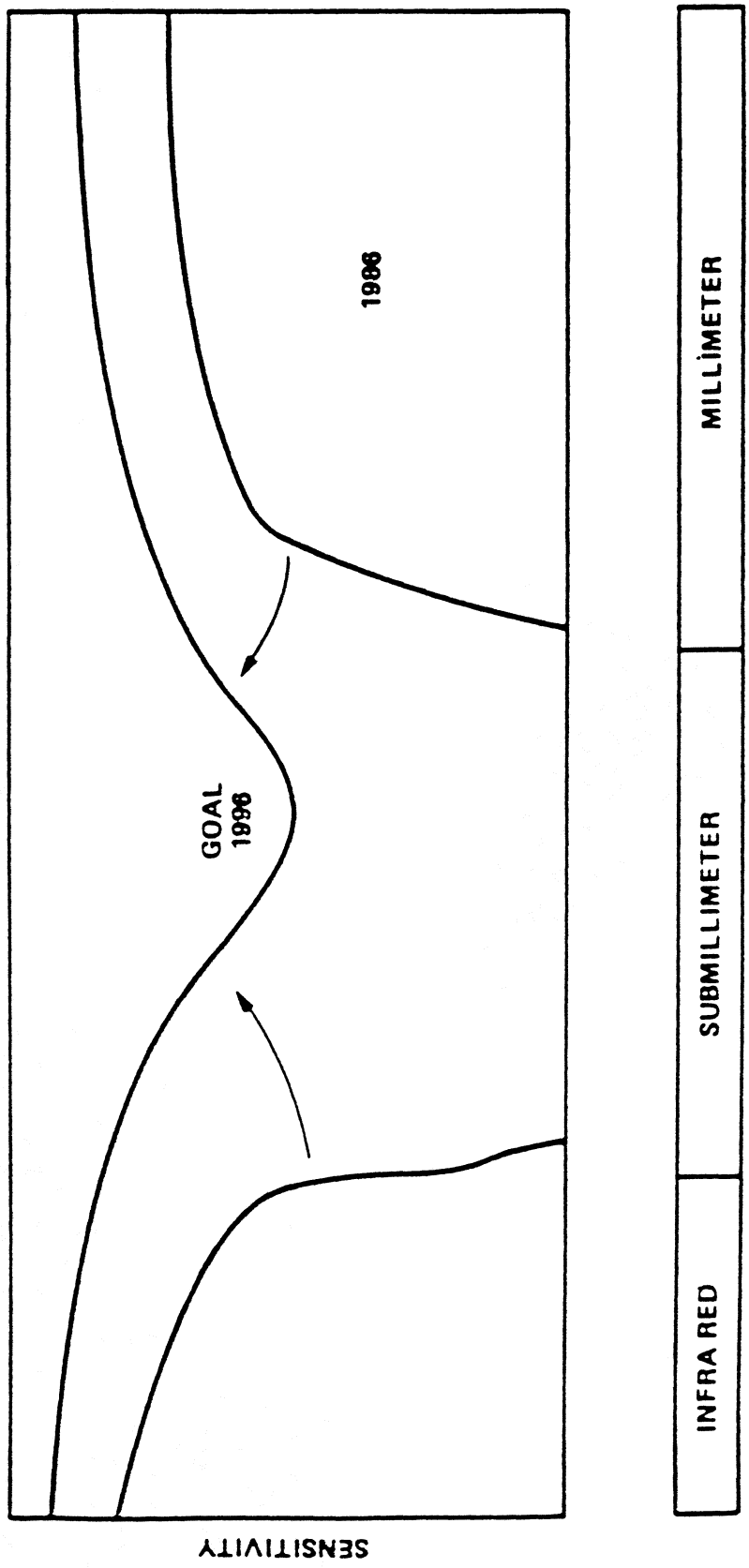

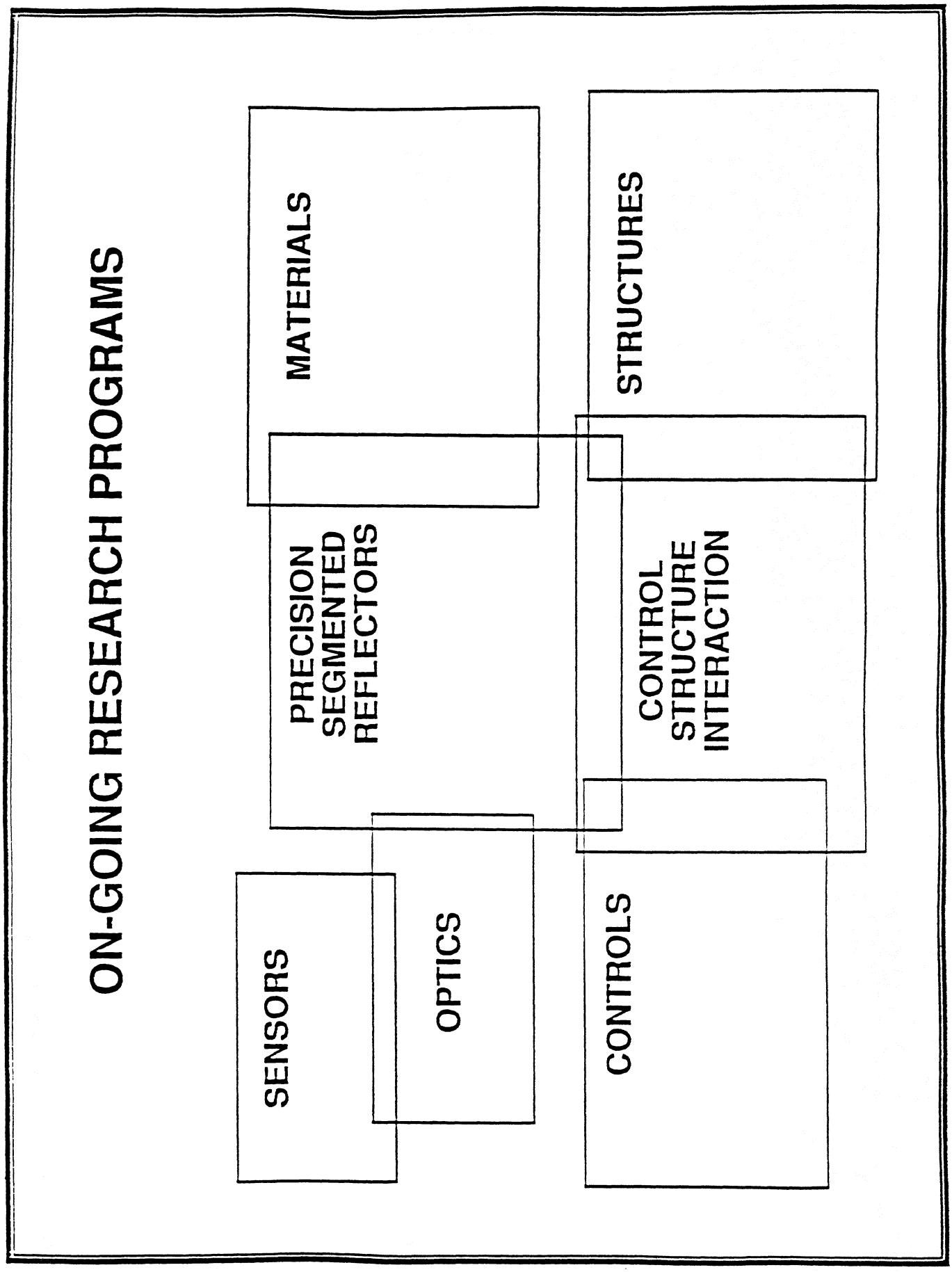
ON-GOING RESEARCH PROGRAMS
MATERIALS
STRUCTURES
PRECISION SEGMENTED REFLECTORS
CONTROL STRUCTURE INTERACTION
SENSORS
OPTICS
CONTROLS

TECHNOLOGY DOMAINS

INSTRUMENT TECHNOLOGIES

- HETERODYNE SYSTEM
- DIRECT DETECTOR SYSTEM
- CRYOGENICS

TELESCOPE TECHNOLOGIES

- PANELS / MATERIALS
- STRUCTURES
- FIGURE SENSING & CONTROL
- OPTICAL SYSTEM

SPACECRAFT TECHNOLOGIES

- POWER & THERMAL
- PROPULSION
- COMMUNICATIONS
- COMPUTING & DATA
- POINTING

SUPPORTING TECHNOLOGIES

- LAUNCH SYSTEMS
- IN-SPACE ASSEMBLY & SERVICE
- MISSION OPERATIONS

SUBMILLIMETER HETERODYNE SENSORS
LDR INSTRUMENTS

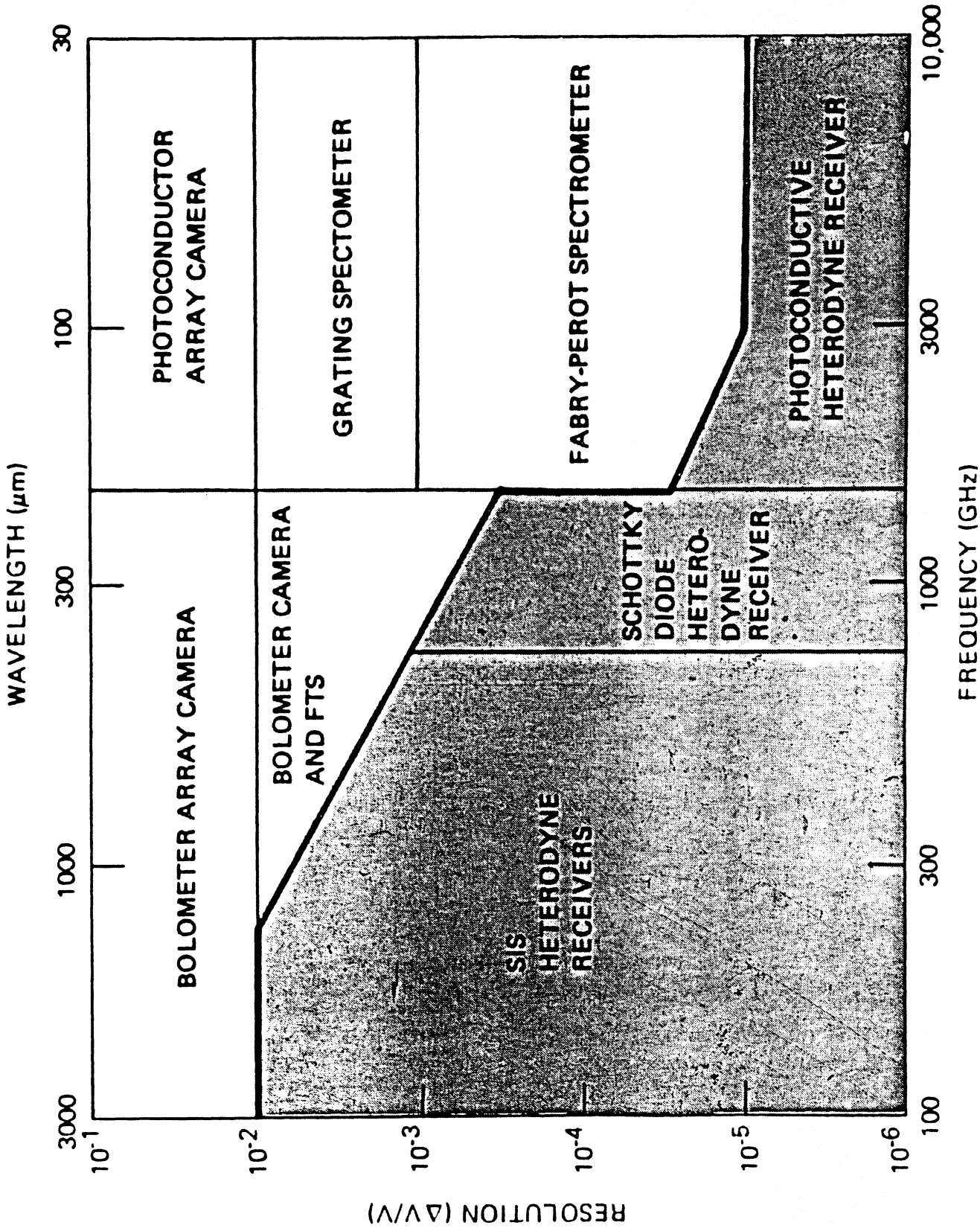

SUBMILLIMETER WAVE SENSOR TECHNOLOGY

JPL QUANTUM WELL MULTIPLIER LOCAL OSCILLATOR OAST

TECHNICAL GOAL

- LOCAL OSCILLATOR SOURCE — 300-1500 GHz
- OUTPUT POWER — 1 μW-1mW
- TUNEABILITY — 10-20%
- LINEWIDTH — $1:10^8$
- FREQUENCY STABLE — $1:10^8$
- SPACE QUALIFIABLE

TECHNICAL APPROACH

- SOLID STATE SOURCE — QUANTUM WELL BASED DEVICE
- FUNDAMENTAL OSCILLATOR — 300-600 GHz
- HARMONIC GENERATOR — 600-1500 GHz

QUANTUM WELL DEVICES

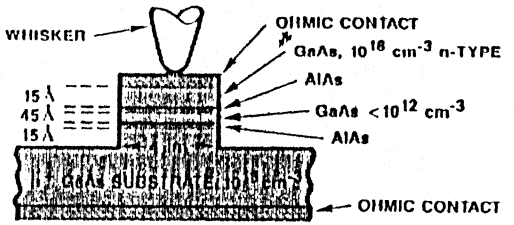

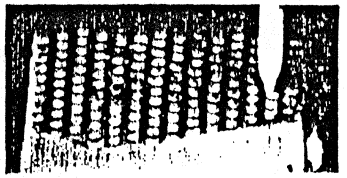

SEM OF DEVICE CHIP MOUNTED IN WAVEGUIDE

PRINCIPLE OF OPERATION

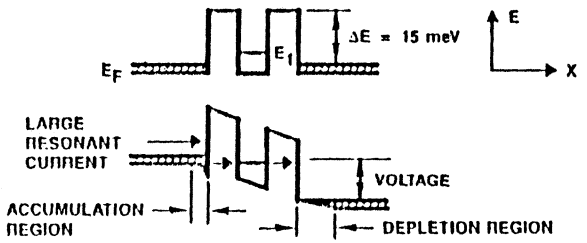

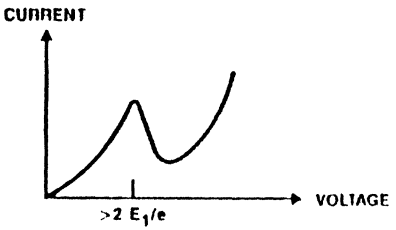

SUBMILLIMETER WAVE MULTIPLIERS

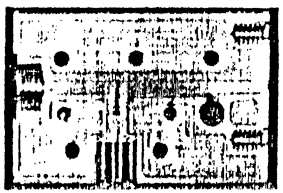

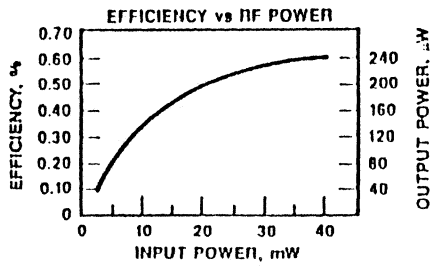

200 GHz TRIPLER PERFORMANCE

THEORETICAL ANALYSIS

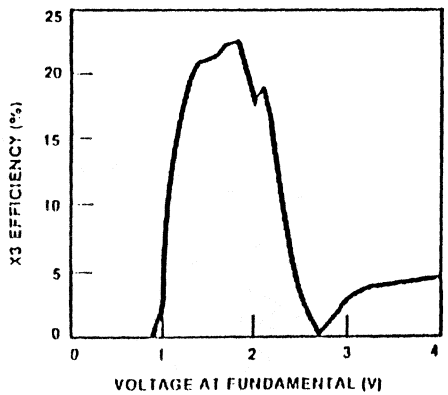

- NEGATIVE RESISTANCE GIVES HIGH EFFICIENCY
- SYMMETRY YIELDS ONLY ODD HARMONICS

200 GHz OSCILLATOR CAP

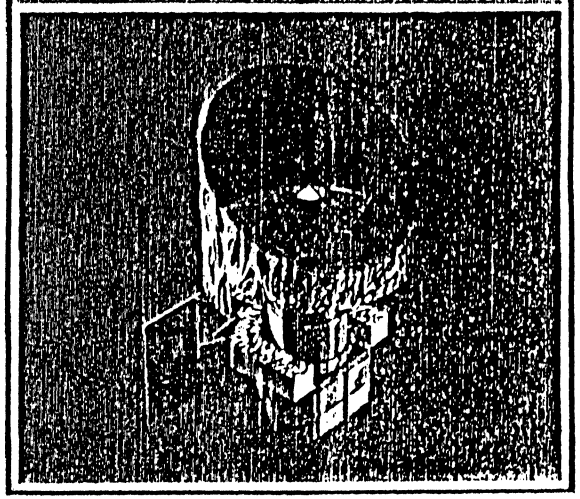

SUBMILLIMETER WAVE SENSOR TECHNOLOGY

SIS MIXERS AND ARRAYS

JPL OAST

TECHNICAL GOAL

- SINGLE ELEMENT MIXERS 600-1500 GHz
- MIXER ARRAYS UP TO 5x5
- SENSITIVITY 10 x QUANTUM LIMIT
- BANDWIDTH 10-20%
- TUNEABILITY
- SPACE QUALIFIABLE

TECHNICAL APPROACH

- SIS JUNCTIONS
- REFRACTORY MATERIAL — NbN/MgO/NbN
- PLANAR ANTENNAS
- PLANAR ANTENNA ARRAYS

NbN/MgO/NbN SIS DEVICES

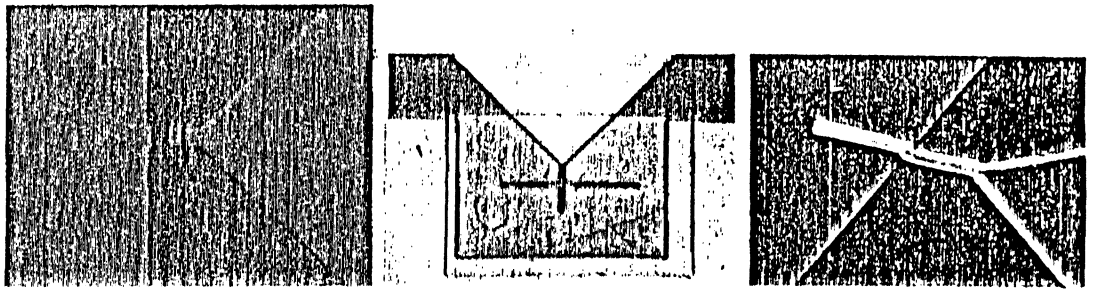

SINGLE MESA SIS JUNCTION | EDGE TUNNEL JUNCTION | CROSSLINE TUNNEL JUNCTION

PRINCIPLE OF OPERATION

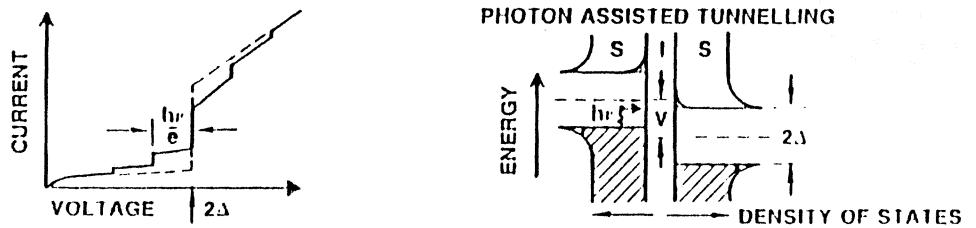

TEST FACILITY

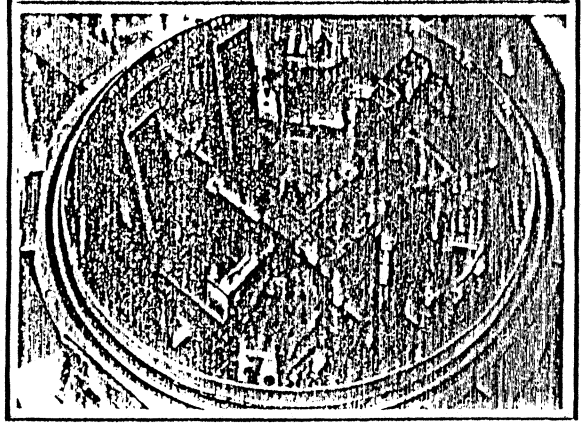

PLANAR ARRAY

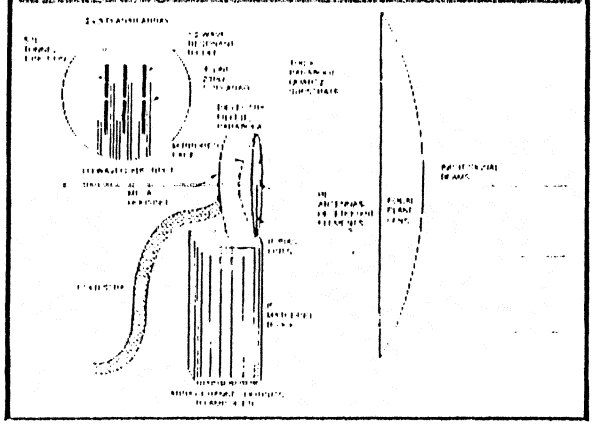

POTENTIAL USE FOR SUBMILLIMETER SPACECRAFT

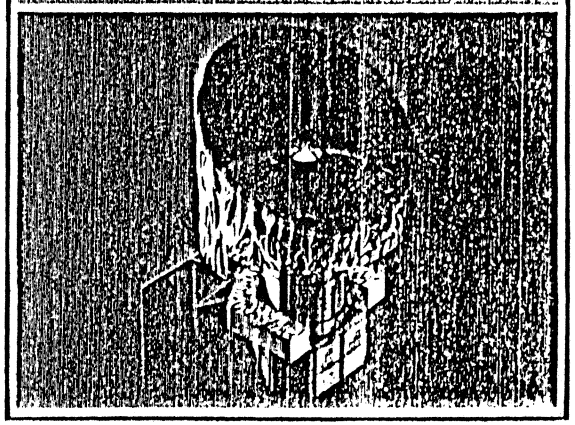

CURRENT-VOLTAGE CHARACTERISTICS OF NbN/MgO/NbN TUNNEL JUNCTIONS

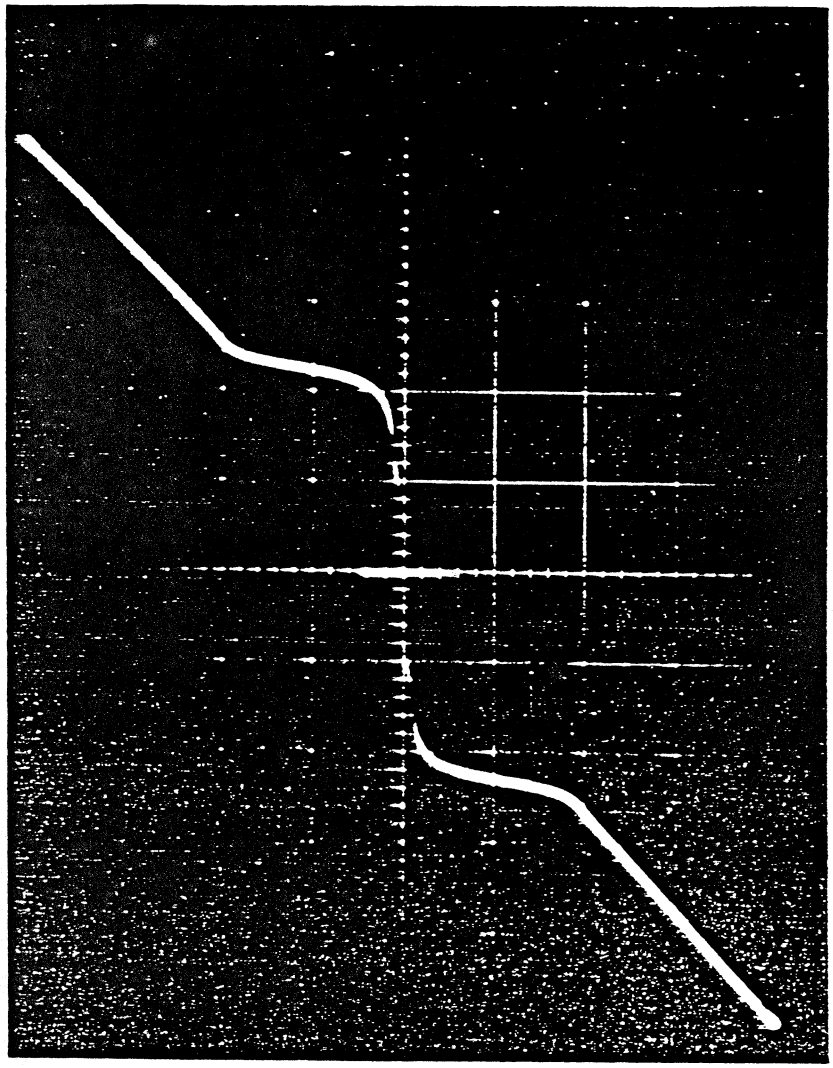

NbN/MgO/NbN SIS Tunnel Junction Geometries

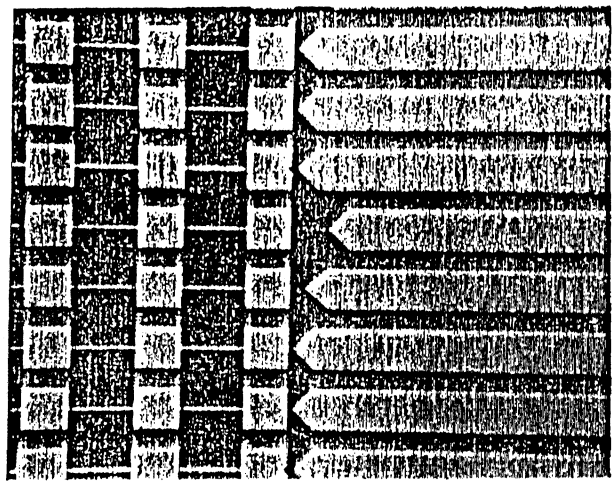

SIS Junction Integrated with Antenna and Filter

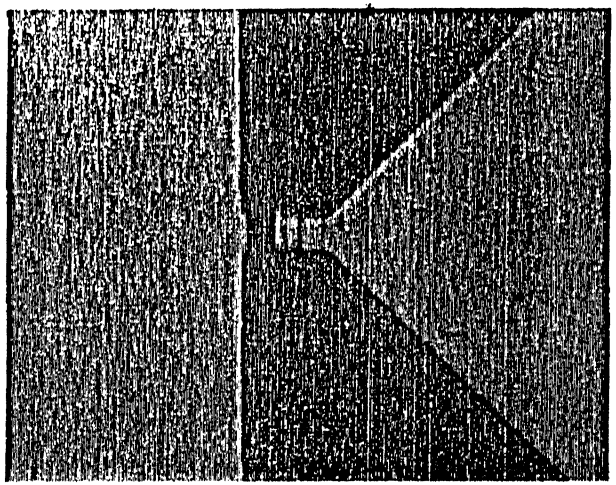

Single Mesa SIS Junction

Mesa Junction Characteristics

Areas	$1\mu m^2$
Eg	4.5 meV
Jc	10 kA/cm^2
R	20 Ω
ωRC(200)	3

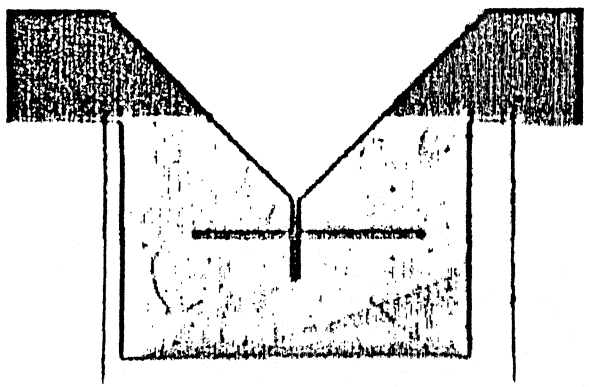

Crossline Tunnel Junction

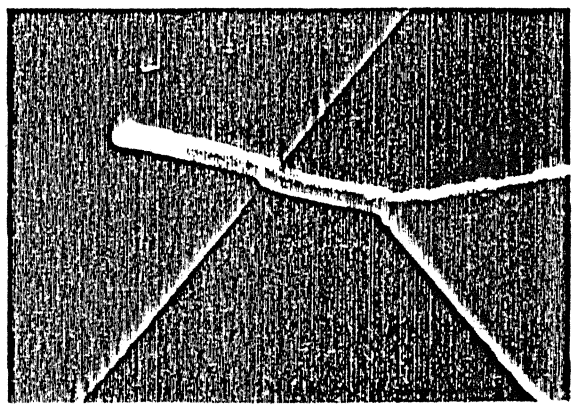

Edge Tunnel Junction

Characteristics

	Cross	Edge
Area(μm^2)	1	0.1
Eg(meV)	5	5
Jc(kA/cm^2)	10	15
R(Ω)	20	150
ωRC(200)	3	2

HIGH TEMPERATURE SUPERCONDUCTIVITY

- PRESENT SIS MIXERS OPERATE BELOW 10K WHICH REQUIRES LIQUID HELIUM COOLANT

- HIGH TC DEVICES HOLD THE PROMISE OF OPERATION AT TEMPERATURES ABOVE 60K WHICH CAN BE ACHIEVED WITH STIRLING COOLERS

JPL

HIGH T_c SUPERCONDUCTING MATERIAL PROPERTIES

	PRESENT S.O.A. TECHNOLOGY	NEAR-TERM TECHNOLOGY	FUTURE TECHNOLOGY BaYCuO
1. MATERIAL	LEAD BASED ALLOYS E.G. PB-IN-AU	NIOBIUM NITRIDE	
2. SUPERCONDUCTING TRANSITION TEMPERATURE (T_c)	6-7°K	16-17°K	94°K
3. SUPERCONDUCTING GAP (2Δ)	2.6 MEV	5.6 MEV	24 MEV
4. UPPER OPERATING FREQUENCY LIMIT	600 GHz	1500 GHz	6000 GHz
5. STABILITY ON THERMAL CYCLING	POOR	EXCELLENT	?
6. MECHANICAL PROPERTIES	SOFT	REFRACTORY, ROBUST	?

SUMMARY

- NASA HAS MANY SCIENTIFIC APPLICATIONS FOR TERAHERTZ INSTRUMENTS
    - 300 GHz TO 3 THz
- ESA ALSO HAS SUBMM APPLICATIONS
- THE TECHNOLOGY FOR THESE MISSIONS IS CHALLENGING AND UNDER DEVELOPMENT

ASTROTECH 21: TERAHERTZ TECHNOLOGY FOR SPACE ASTRONOMY IN THE 21ST CENTURY

James A. Cutts[1]

ABSTRACT

Two major missions are now being considered by NASA for launch in the first decade of the 21st century. The Large Deployable Reflector (LDR) is a filled-aperture telescope 20 meters in diameter which will be erected in space with ultralightweight optical elements and support structures. The Lunar Submillimeter Interferometer (LSI) will be a dilute-aperture phased-array telescope with seven 5-meter aperture elements on a 2-kilometer baseline. Collectively, these observatories will observe emission from cold molecules in the universe on various spatial scales from planet-forming regions to clusters of galaxies providing information about their temperatures, molecular constituents and dynamical motions. They will provide fundamental information on the origin of planets and stars and the evolution of galaxies. To attain these objectives, high performance terahertz receivers operating in the frequency range from 0.3 THz to 10 THz will be needed. Single element mixers and tunable local oscillators for 0.3 to 1 THz will be needed by 1994 in order to demonstrate terahertz technologies in space during the 1990s. Arrays of mixers and local oscillators operating from 0.3 to 10 THz will be needed by the end of the decade to enable the LDR and LSI. The Astrotech 21 program is being formulated by NASA to respond to the technology needs of a broad suit of major astronomy missions launched in the first two decades of the 21st century. An aggressive program of terahertz technology development is anticipated to be included in the program.

---

[1] Dr. Cutts is with Jet Propulsion Laboratory/California Institute of Technology, Pasadena, CA.

INTRODUCTION

Space astronomy is about to embark on a great period of discovery. During the 1990s, four Great Observatory missions will be launched and will probe the universe in spectral regions ranging from gamma radiation to the far infrared. But NASA is already looking beyond the Great Observatories to other major missions in the first decade of the 21st century. To enable its New Century Astronomy program, and thereby assure continued U.S. leadership in space science, a substantial investment in technology will be required during this decade. This will be provided by the Astrotech 21 program. Submillimeter (terahertz) technology will be a major area of emphasis.

ASTROTECH 21

During early 1989, the Astrophysics division at NASA Headquarters determined that significant advances in capability over the Great Observatories would require major advances in the techniques of observation from space. Observations with higher angular and spectral resolution and greater sensitivity are clearly needed. The exploration of new spectral regimes is also needed. Space interferometers located on large space structures or on the lunar surface have been identified as the most promising approach for achieving major advances in angular resolution. Observations of gravitational waves using laser interferometry are seen as a fundamentally new tool for probing the violent accelerations of matter within opaque clouds. In addition, the largely unexplored submillimeter (terahertz) spectral region was identified as particularly promising for investigation. NASA recognized that this capability would require a sustained technology development effort over the next decade, and asked JPL to lead the definition of technology development program. The technology development program is known as Astrotech 21.

The first step in the definition of the Astrotech 21 program was the specification of the observational requirements for future missions. This was followed by the definition of telescopes and science instruments. In many instances, the Astrotech 21 study team has been able to draw on earlier mission studies to streamline the planning process. This is now leading to an assessment of the status of the relevant technologies. At the time of writing, the process of planning an Astrotech technology program is well underway.

The planning and implementation of Astrotech 21 involves a partnership between the Astrophysics Division, which is part of the Office of Space Science and Applications (OSSA) at NASA, and the newly reorganized Office of Aeronautics and Exploration Technology (OAET). Currently, only the planning phase is funded and the implementation phase will require budgetary action by both OAST and OSSA.

SUBMILLIMETER SCIENCE AND TECHNOLOGY

Submillimeter science and technology is already part of the NASA program. The OAET's Information Systems and Human Factors Division is supporting the development of submillimeter technology for space science applications at the Center for Space Microelectronics technology at JPL and other NASA centers. OAET also funds the University Space Engineering Research Centers Program which supports the NASA Center for Space Terahertz technology at the University of Michigan. OSSA, on the other hand, supports the development of flight instruments and the acquisition and analysis of submillimeter science data. Currently, only one submillimeter astrophysical instrument is under development: the Submillimeter Wave Astronomy Satellite (SWAS) which is described at this symposium. The Astrotech 21 submillimeter planning activity will lead to the establishment of technology goals enabling the set of missions beyond SWAS. These missions include the Submillimeter Moderate Mission (SMMM), the Large Deployable Reflector (LDR) and a Lunar Submillimeter Interferometer (LSI). A preliminary schedule for implementing these missions appears in Fig. 1. Illustrations of the SMMM (which includes two possible configurations), the LDR and the LSI appear in Fig. 2.

STATUS

The Astrotech 21 technology plan for submillimeter missions will be completed in late April, 1990. This plan will include not only sensor technology but also cryogenics, telescope technology, space assembly and servicing. In the field of submillimeter heterodyne technology, contributions from the scientific and technical communities have been solicited by Dr. Margaret Frerking of JPL. Dr. Frerking will use thse contributions in formulating a major section of the Astrotech 21 submillimeter plan. The submillimeter plan will be consolidated with plans for other disciplines to form a single integrated plan which will be submitted to the agency by the late spring or early summer.

ACKNOWLEDGEMENTS

The author acknowledges the contributions of a large number of people in the NASA community to the Astrotech 21 planning effort. In particular, the contributions of Dr. Larry Caroff and Mr. Wayne Hudson of NASA Headquarters in the formulation of the Submillimeter planning process are recognized.

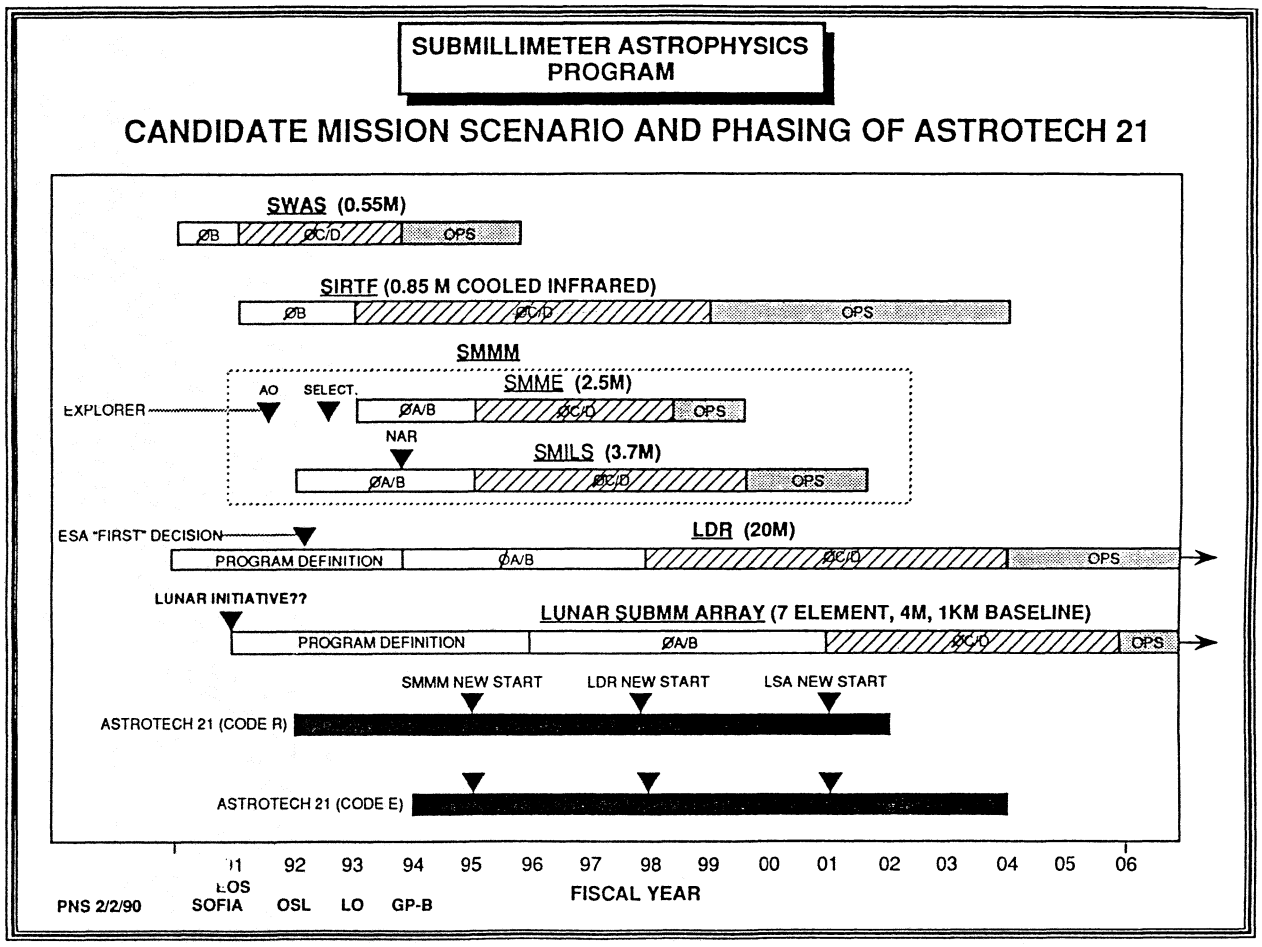

Figure 1

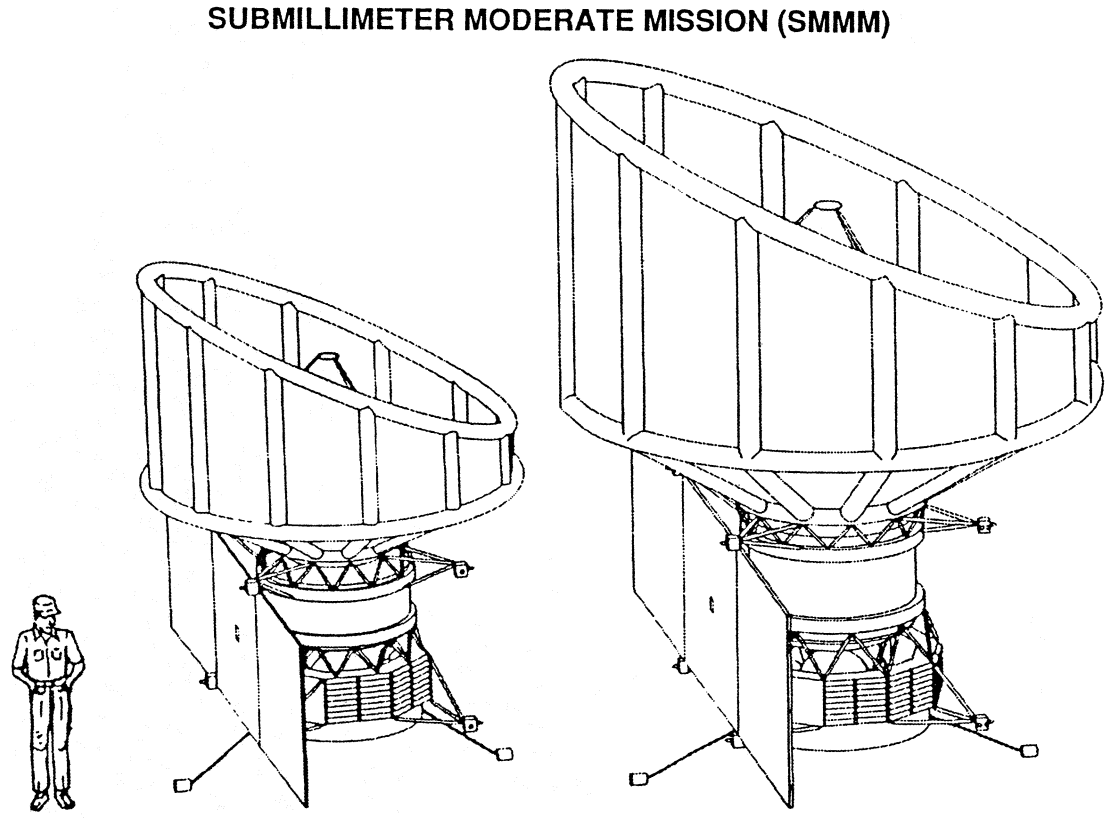

Figure 2a

THE LARGE DEPLOYABLE REFLECTOR

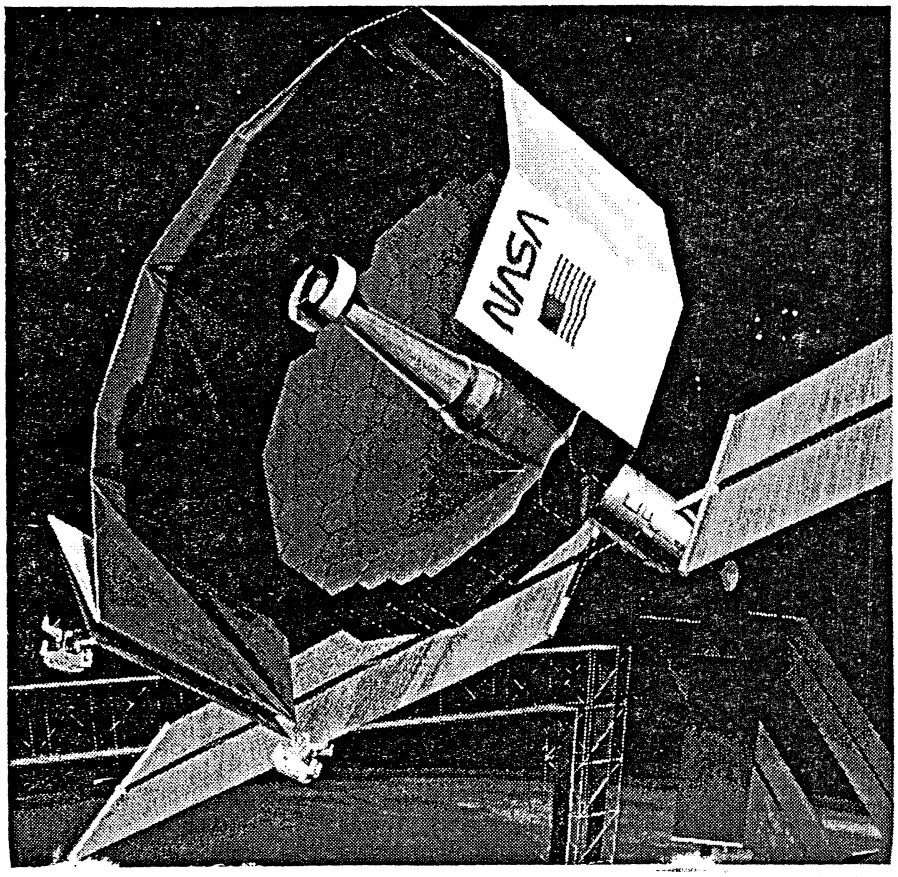

Figure 2b

SUBMILLIMETER INTERFEROMETER

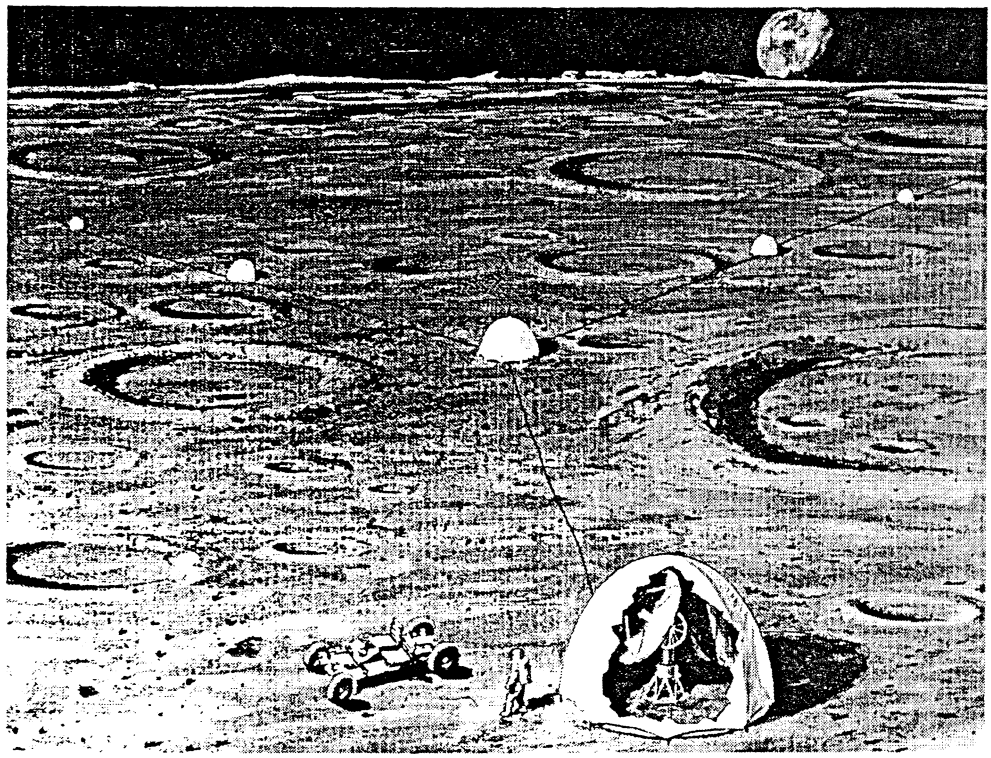

Figure 2c

SUBMILLIMETER-WAVE RESONANT-TUNNELING OSCILLATORS

E.R. Brown
Lincoln Laboratory, Massachusetts Institute of Technology
Lexington, Massachusetts 02173, USA

ABSTRACT

Recent advances in high-frequency resonant-tunneling diode (RTD) oscillators are described. Oscillations up to a frequency of 420 GHz have been achieved in the GaAs/AlAs system. These results are consistent with a lumped-element equivalent circuit model of the RTD. The model shows that the maximum oscillation frequency of the GaAs/AlAs RTDs is limited primarily by high series resistance, and that the power density is limited by low peak-to-valley current ratio. Recent oscillator results obtained with InGaAs/AlAs and InAs/AlSb RTDs show a greatly increased power density and indicate the potential for fundamental oscillations up to about 1 THz.

I. INTRODUCTION

Resonant tunneling in a double-barrier structure can be understood by the diagrams in Fig. 1, which pertain to a quantum well containing only one quasibound-state energy level E_1. If the total energy and momentum of the electrons in the plane of the heterojunctions are conserved during the process, then only those electrons having a longitudinal energy E_L on the cathode side approximately equal to E_1 can traverse the structure with any significant probability. As the bias voltage is increased from zero, the quasibound level drops relative to the electron energy on the cathode side and the current increases. This current increase can be explained in terms of an increase in the number of electrons in the cathode Fermi sphere that have $E_L = E_1$. The current eventually approaches a peak at a voltage close to that which aligns the quasibound level with the conduction band edge in the neutral region on the cathode side. At higher voltages there are no electrons with $E_L = E_1$, so that the current decreases precipitously and a negative differential conductance (NDC) region occurs. This NDC region is the basis for all of the high-speed oscillations observed to date in resonant-tunneling diodes.

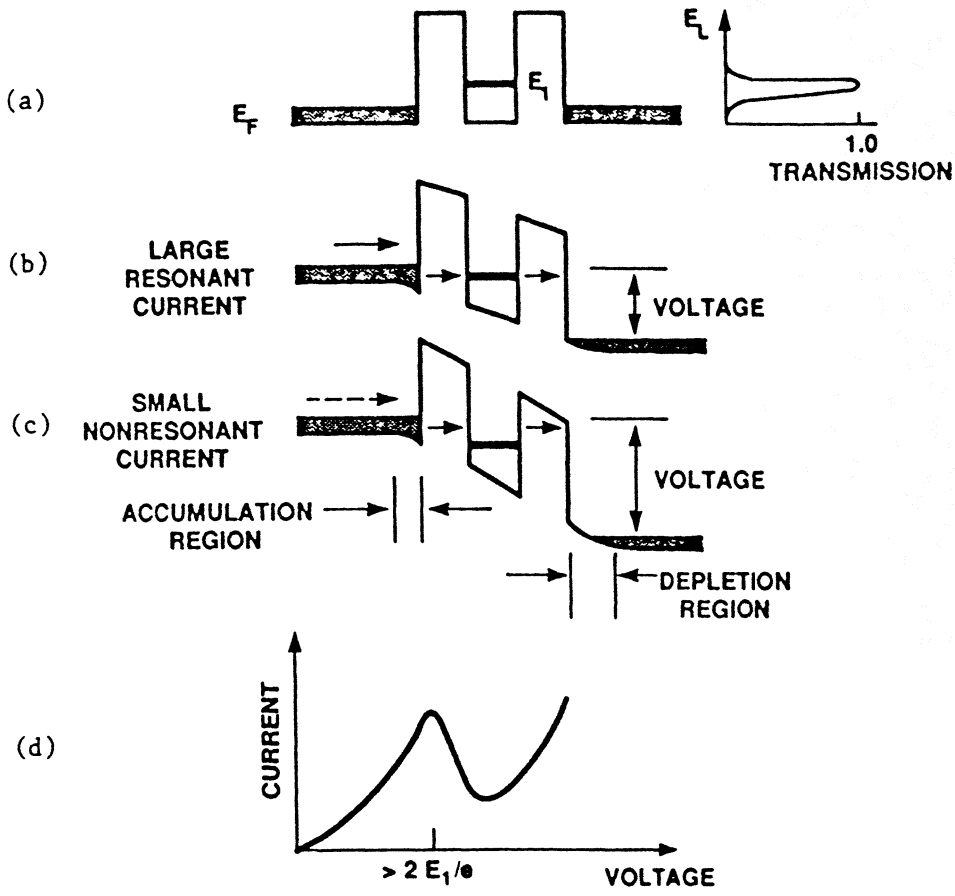

Fig. 1 (a) Band diagram of a generic double-barrier structure with quasibound-state energy E_1. (b) and (c) Schematic diagram of resonant-tunneling transport process. (d) Typical current-voltage curve for a double-barrier diode.

The fundamental requirement for resonant tunneling in a double-barrier structure is spatial quantization, which occurs when $E_1 > \hbar/\tau_s$, where τ_s is the inelastic scattering time. This requirement imposes limits on the size of the structure. For example, the thicknesses of the quantum well and barriers of a GaAs/AlAs structure must be less than roughly 10 and 3 nm, respectively, in order to observe resonant tunneling at room temperature. Fortunately such thin layers can be obtained by modern crystal growth techniques, such as molecular beam epitaxy. In fact these techniques can produce much thinner epilayers, as exemplified by the recent demonstration of double-barrier structures containing 0.8-nm-thick AlAs barriers (i.e., 3 monolayers of the AlAs zincblende lattice) [1]. Such control over layer thickness is a large part of the success of resonant-tunneling devices.

II. MATERIAL CHARACTERISTICS

The quality of a resonant-tunneling diode (RTD) is usually characterized by the peak-to-valley current ratio (PVCR) and the peak current density J_P. Fig. 2 shows the room-temperature current-density vs voltage (J-V) curves obtained for the fastest resonant-tunneling structures in three different material systems.

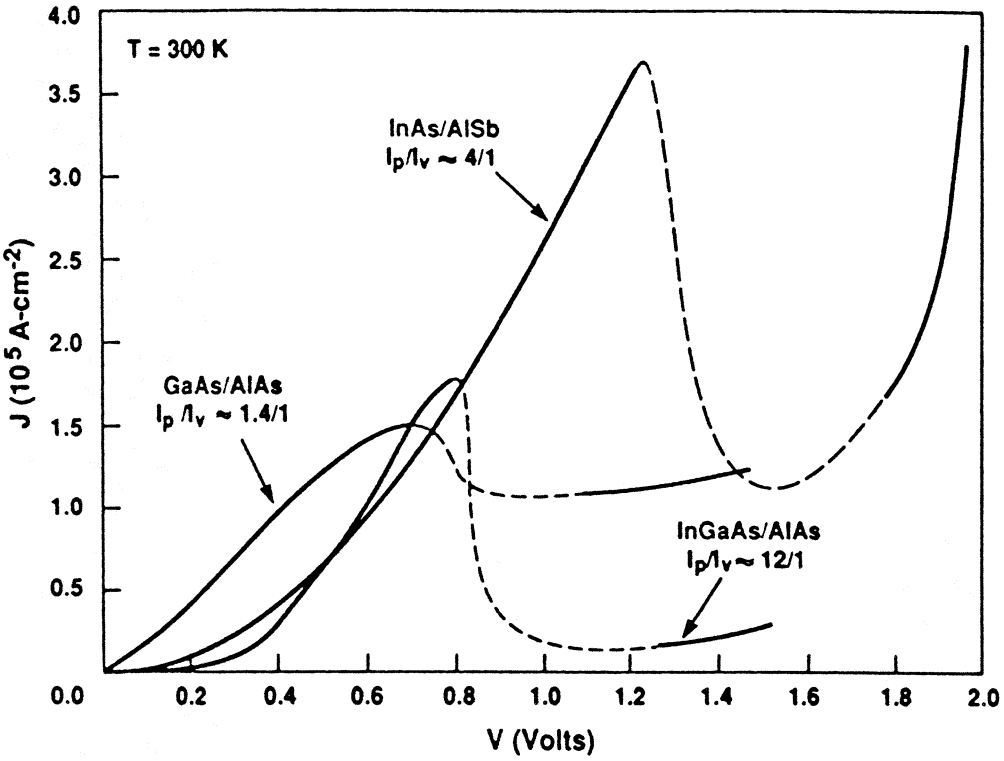

Fig. 2 Current density vs voltage for double-barrier diodes made from three different material systems. The dashed regions of the curves are the result of interpolation through the NDC region, which was highly distorted in the experiments by the occurrence of oscillations.

Each of these structures has a composition and doping profile similar to that shown in Fig. 3. The J-V curve for the GaAs/AlAs structure shows a PVCR $\cong$ 1.5, which is a typical result in this material system for J_P greater than approximately 1×10^5 A cm^{-2}. In contrast, the $In_{0.53}Ga_{0.47}As$/AlAs material system shows a PVCR $\cong$ 12 at a J_P near 2×10^5 A cm^{-2}. These results display a useful empirical rule that has been observed over a large range of peak current densities. That is, $In_{0.53}Ga_{0.47}As$/AlAs and GaAs/AlAs RTDs having the same J_P

differ in PVCR by about a factor of eight.

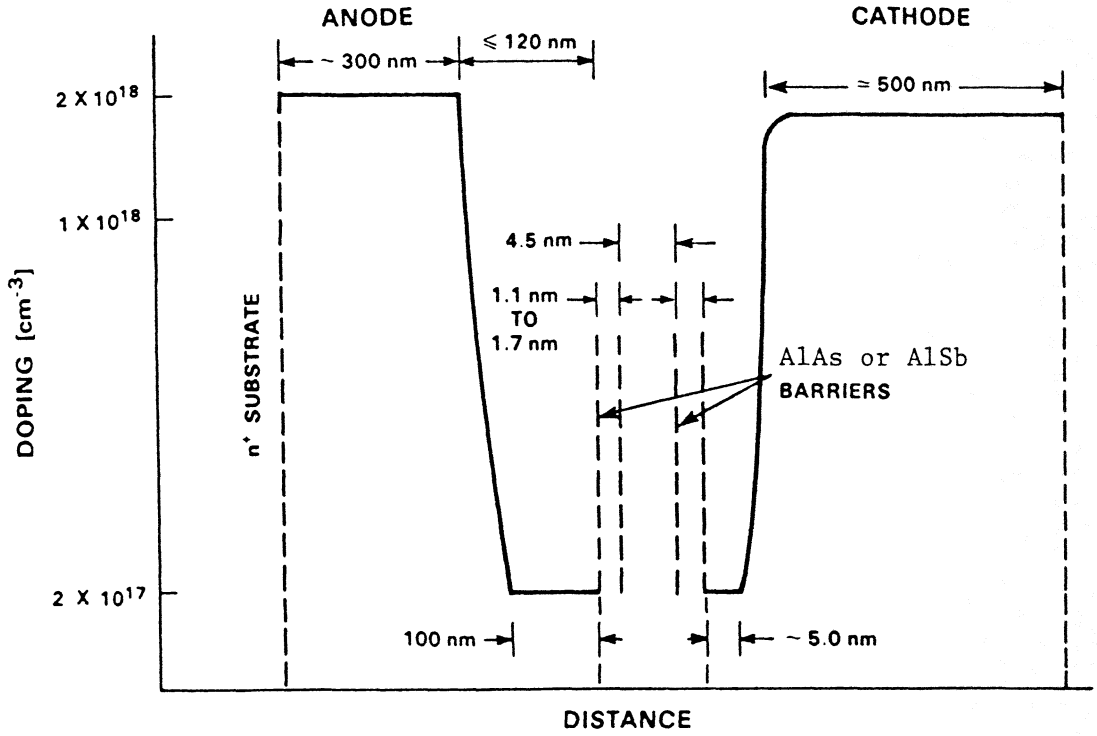

Fig. 3 Composition and doping profile for the fastest double-barrier diodes produced to date.

The InAs/AlSb structure yields the highest J_P of all of our present structures, $J_P = 3.7\times10^5$ A–cm^{-2}, and also shows a PVCR $\cong$ 4, which is satisfactory for many applications. The very high J_P is due mostly to the Type II-staggered band alignment. This causes the electrons to tunnel through the AlSb barriers near the valence band edge where the tunneling wavevector is significantly smaller than at mid gap. Further information can be found in the growing literature on this material system [2].

The layer thicknesses and doping profile of the RTD that has produced the highest oscillation frequency to date is shown in Fig. 3. Very thin (1.1 to 1.7 nm) barriers are used to reduce the resonant-tunneling time and enhance J_P. The asymmetric doping profile is designed to provide an approximately 100-nm-wide depletion layer on the anode side of the double-barrier structure at the bias required for NDC, and also to provide a high bulk electron density (~ 1×10^{18} cm^{-3}) on the cathode side. This density, along with the width Γ_1 of the transmission-probability (T*T) resonance, determines the current density through the structure.

The depletion layer yields a low specific capacitance compared to most other tunnel devices, such as p-n tunnel (Esaki) diodes and Josephson junction diodes, while the high carrier concentration on the cathode side provides a comparable J_P. The ability to separately control the capacitance and current density is an advantage that the RTD has over Esaki and Josephson diodes, which require degenerate carrier concentrations on both sides of the thin tunneling region.

III. SPEED-LIMITATION MECHANISMS

The best measure of the speed of RTD oscillators is the maximum frequency of oscillation, f_{MAX}, which is defined as the frequency above which the real part of the terminal impedance is positive. To determine this frequency accurately, an impedance model of the RTD is required. At sufficiently low frequencies, the impedance is represented by an equivalent circuit consisting of a differential conductance G in parallel with a capacitance C, both in series with a resistance R_S. The capacitance is approximated by $C = \varepsilon A/(d+w)$, where A is the active area, ε is the permittivity of the double-barrier material, and d and w are the lengths of the depletion region and double-barrier structure, respectively. The series resistance arises from various contributions outside the active region of the device, as in a Schottky diode. When G is negative, this circuit implies that oscillations can occur up to a frequency of $f_{RC} = (2\pi C)^{-1}(-G/R_S - G^2)^{1/2} = (2\pi\tau_{RC})^{-1}$. For a given double-barrier structure, f_{RC} represents an upper limit on the maximum oscillation frequency f_{MAX}. The additional time-delay mechanisms described below can only decrease f_{MAX}.

At high frequencies, the quasibound-state lifetime τ_1 and the transit time across the depletion layer must be considered. A straightforward derivation of the effect of the lifetime is given in Ref. [3], and the result is the RCL equivalent circuit shown in the inset of Fig. 4. The new element, the quantum-well inductance, is given by $L_{QW} = \tau_1/G$, where τ_1 is the quasibound-state lifetime. Such an element is expected on physical grounds, since the resonant-tunneling process represents a delay of conduction current with respect to applied

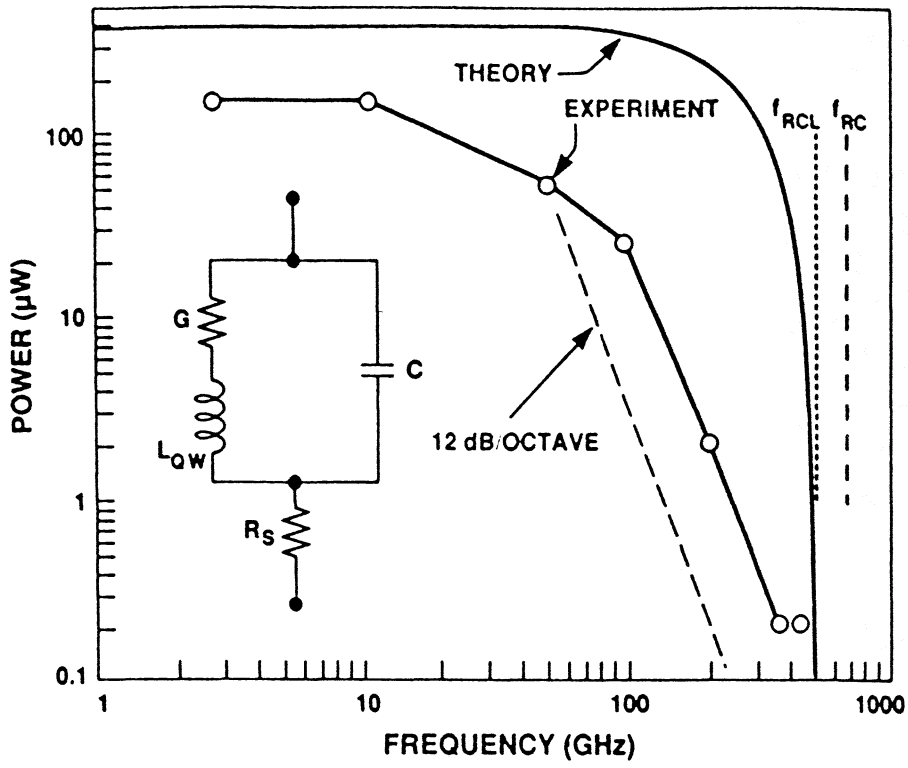

Fig. 4 Experimental and theoretical oscillator results for the fastest double-barrier diode in the GaAs/AlAs material system. The lumped-element equivalent circuit for the diode is shown in the inset.

voltage, similar to the delay that occurs in an ideal inductor. At a fixed bias point, the RCL circuit model yields an f_{MAX} given by

$$f_{RCL} = \frac{1}{2\pi}\left\{\left[\frac{1}{L_{QW}C}\left[1-\frac{C}{2L_{QW}/G^2}\right]\right]\left[1-\left[1-\frac{(GR_S+1)/GR_S}{(C/2L_{QW}G^2-1)^2}\right]^{1/2}\right]\right\}^{1/2} . \qquad (1)$$

In the limit $\tau_1 \ll \tau_{RC}$, this expression reduces to f_{RC} as it should. Note that the imaginary part of the impedance of this circuit in the NDC region is always less than zero because L_{QW} is negative. This means that the diode cannot self-oscillate, i.e., oscillate on an internal resonance. The validity of the RCL circuit has been confirmed recently using several RTDs at Lincoln Laboratory, and in separate experiments at Fujitsu Labs in Japan [4] and the Electronic Technology Laboratory in the U.S. [5].

The second important time-delay mechanism at high frequencies is the transit-time delay across the depletion layer. For diodes having a material profile similar to that shown in Fig. 3, this delay is probably not very important. For example, f_{MAX} calculated using the parameters of the fastest GaAs/AlAs diode is only 10% less than f_{RCL} [6]. This calculation assumes that the average drift velocity across the depletion layer is 4×10^7 cm/s. This velocity is quite plausible in the present GaAs/AlAs double-barrier structure because the kinetic energy of the electrons injected into the depletion layer is high ($\cong$ 0.2 eV), and the mean-free path of the electrons is comparable to the depletion length. For the other two material systems of interest, $In_{0.53}Ga_{0.47}As$ and InAs, the effect of the transit time should be even less. Both the electron LO-phonon scattering time and the L-valley separation from the conduction band edge increase as the In fraction in $In_xGa_{1-x}As$ alloys increases. Consequently, the average drift velocity across the depletion layer should be even higher and the transit-time effects should be less. Based on these considerations, it is anticipated that depletion lengths of InAs RTDs can be significantly longer than those of GaAs RTDs, perhaps by a factor of two or more.

IV. OSCILLATOR RESULTS

The oscillation power vs frequency for a 4–μm–diameter diode made of the fastest GaAs/AlAs resonant-tunneling structure is shown in Fig. 4. The results are consistent with theory in that the maximum observed oscillation frequency 420 GHz is below f_{RCL}, which is calculated to be 506 GHz. This calculation assumes that G is equal to the maximum negative value in the NDC region of Fig. 2, and $\tau_1 = \hbar/\Gamma_1 = 0.11$ ps, where Γ_1 is the full width at half maximum of T*T. A more detailed analysis shows that an increase in the magnitude of G would not significantly speed up the device, but that a three-fold reduction in R_S with the same G would increase f_{RCL} to approximately 900 GHz [4]. This reduction in R_S combined with a two-fold increase in the magnitude of G would further increase f_{RCL} to over 1 THz. Unfortunately, these improvements have not been made because of practical limitations on the

ohmic-contact resistance to GaAs and on the PVCR attainable in GaAs/AlAs double-barrier structures. The other two material systems that have been developed, InGaAs/AlAs and InAs/AlSb, alleviate these deficiencies.

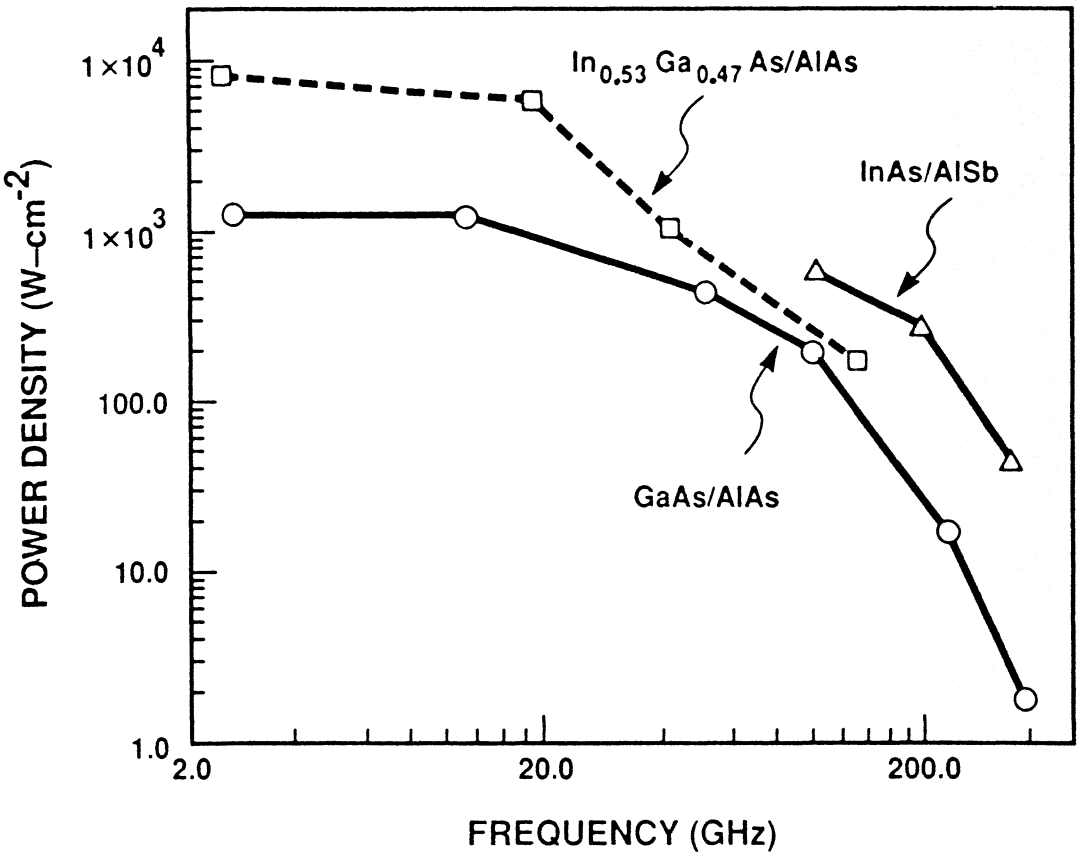

Fig. 5 Experimental oscillation results for double-barrier diodes made from three different material systems.

The oscillation results for the fastest diodes made to date in all three material systems are compared in Fig 5. The relatively poor PVCR of the GaAs/AlAs diode limits the power density to a maximum value just over 1×10^3 W cm^{-2}. The superior PVCR of the $In_{0.53}Ga_{0.47}As$/AlAs diodes provides a low-frequency power density of 1×10^4 W cm^{-2}, which is comparable to that generated by IMPATT diodes. Because of the high PVCR at high current density, the $In_{0.53}Ga_{0.47}As$/AlAs diode will likely be the RTD of choice for high-speed logic applications. At present the InAs/AlSb materials system is the most promising one for

submillimeter-wave oscillator applications. The power density of the InAs/AlSb RTD at 360 GHz is a ten-fold improvement over that of the GaAs/AlAs RTD at the same frequency. We expect that this InAs/AlSb RTD will be capable of oscillating well over 600 GHz. The primary reasons for the superior performance are the low series resistance and the high available current density ($J_P - J_V \cong 2.8\times10^5$ A cm^{-2}) in the InAs/AlSb diodes. The low resistance reflects the nearly ideal ohmic contact that can be formed to InAs. In the present diode the contact resistance is so low that its measurement is difficult, but we estimate from the oscillator results that its specific resistance is less than 2×10^{-7} Ω cm^2.

V. SUMMARY

Resonant-tunneling oscillators in the GaAs/AlAs material system have been demonstrated up to frequencies of 420 GHz. The oscillation characteristics of the fastest diodes, as well as diodes designed for operation at much lower frequencies are consistent with an equivalent circuit model that represents the effect of the time delay in the resonant-tunneling process by a quantum-well inductance. The maximum frequency of oscillation of GaAs/AlAs diodes could be increased significantly by reducing the series resistance and increasing the peak-to-valley current ratio. Alternative material systems such as InGaAs/AlAs and InAs/AlSb should facilitate these improvements, and should produce oscillators operating up to about 1 THz in the near future.

ACKNOWLEDGMENTS

This work was supported by NASA-OAST through the Jet Propulsion Laboratory, the U.S. Army Research Office, and the Department of the Air Force, in part under a program sponsored by the Air Force Office of Scientific Research. The author acknowledges ongoing collaboration at Lincoln Laboratory with T.C.L.G. Sollner, C.D. Parker, W.D. Goodhue, A.R. Calawa, M.J. Manfra, L.J. Mahoney and C.L. Chen, and support from R.A. Murphy and A.L. McWhorter. The InAs/AlSb material used for this work was kindly provided by J.R.

Söderström and T.C. McGill of Caltech.

REFERENCES

[1] T.P.E. Broekaert and C.G. Fonstad, IEDM Technical Digest, Washington D.C., Dec. 1989, p. 559.

[2] J.R. Söderström, D.H. Chow, and T.C. McGill, *IEEE Electron Device Lett.* **11**, 27 (1990).

[3] E.R. Brown, C.D. Parker, and T.C.L.G. Sollner, *Appl. Phys. Lett.* **54**, 934 (1989).

[4] A. Tackeuchi, T. Inata, S. Muto and E. Miyauchi, *Jpn. J. Appl. Phys.* **25**, L750 (1989).

[5] D.W. Whitson, M.J. Paulus, C.E. Stutz, E. Koenig, R. Neidhard and E. Davis, Proc. of 12th Biennial Cornell Conference, Paper V-6, 1989.

[6] E.R. Brown, T.C.L.G. Sollner, C.D. Parker, W.D. Goodhue and C.L. Chen, *Appl. Phys. Lett.* **55**, 1777 (1989).

Potential and limitations of resonant tunneling diodes

C. Kidner, I. Mehdi, J. R. East, and G. I. Haddad
Center for High-Frequency Microelectronics and Center for Space Terahertz Technology
Department of Electrical Engineering and Computer Science
The University of Michigan
Ann Arbor, Michigan 48109

Abstract

The existence of negative resistance in double barrier resonant tunneling structures has led to the proposal of various applications for these devices. For useful applications the bias circuit must be free of low frequency oscillations. Stability criteria for resonant tunneling diodes are investigated showing the effect of different modes of low frequency oscillation. The main results of the paper are (1) stable resonant tunneling diode operation is difficult to obtain, (2) the low frequency oscillation introduces a characteristic signature in the measured dc I-V characteristic, (3) the circuit and device conditions required for stable operation greatly reduce the amount of power that can be produced by these devices.

I Introduction

Though the double barrier structure has become a useful prototype mesoscopic device, its usefulness as an electronic device will be determined by functionality rather than by interesting physics. The proposal [1] and later confirmation [2] of the resonant tunneling concept led to the investigation of double barrier structures for various applications. An important potential application is a two terminal negative resistance device, the Resonant Tunneling Diode (RTD), for microwave and millimeter-wave operation [3,4,5,6]. Since the negative resistance of a resonant tunneling device extends from DC to beyond the operating frequency, potential problems exist with low frequency (LF) bias circuit oscillations. A negative resistance device in combination with the bias circuit should be low frequency stable when biased in the negative resistance region for most practical applications. In mixer and detector applications, the LF oscillations can occur near the IF or video frequencies

introducing additional noise. In high frequency oscillator applications LF bias circuit instabilities introduce unwanted upconverted signals that modulate the carrier, resulting in a signal which is not useful for most applications. The paper is organized as follows. The next section contains an analysis of stability conditions for resonant tunneling diodes. The analysis is similar to earlier work on tunnel diodes. Section III contains experimental data to confirm the predictions of the theory. It is shown experimentally that each instability affects the measured I-V curve in a particular fashion. Requiring stability will reduce the power available from resonant tunneling devices. This effect is discussed in section IV.

II Low frequency stability analysis

Assuming the RTD has the same equivalent circuit as a tunnel diode implies that the stability criteria developed for tunnel diodes [7] will also apply in the RTD case. The RTD and the tunnel diode are voltage controlled negative resistance devices. This means that the device will be connected through a bias circuit to a voltage source. In a practical circuit the bias circuit will include the power supply source impedance and various parasitic elements. If the device with its bias circuit is not short circuit stable there will be unwanted oscillations in the bias circuit. A two terminal circuit is short circuit stable if there are no zeroes of the impedance for complex frequencies with positive real parts. In the early 1960's many papers concerning tunnel diode stability were published. While some applications called for short circuit unstable devices [8] the general advice was to only use devices which are short circuit stable [8,9]. In this section we will describe the requirements for stable RTD operation.

Fig. 1(a) shows an equivalent circuit for a RTD including parasitic elements in a waveguide circuit. The circuit between nodes 0 and 1 represents the intrinsic device. $-R_d$ is the negative differential resistance of the device. C_d is the device capacitance, and R_{sd} is the positive parasitic resistance of the device. The circuit between nodes 2 and 1 represents the coupling of the device to the waveguide circuit with L_p representing the inductance of the whisker contact. A resistance R_p within the waveguide cavity can be introduced to improve the device stability. The RF signal

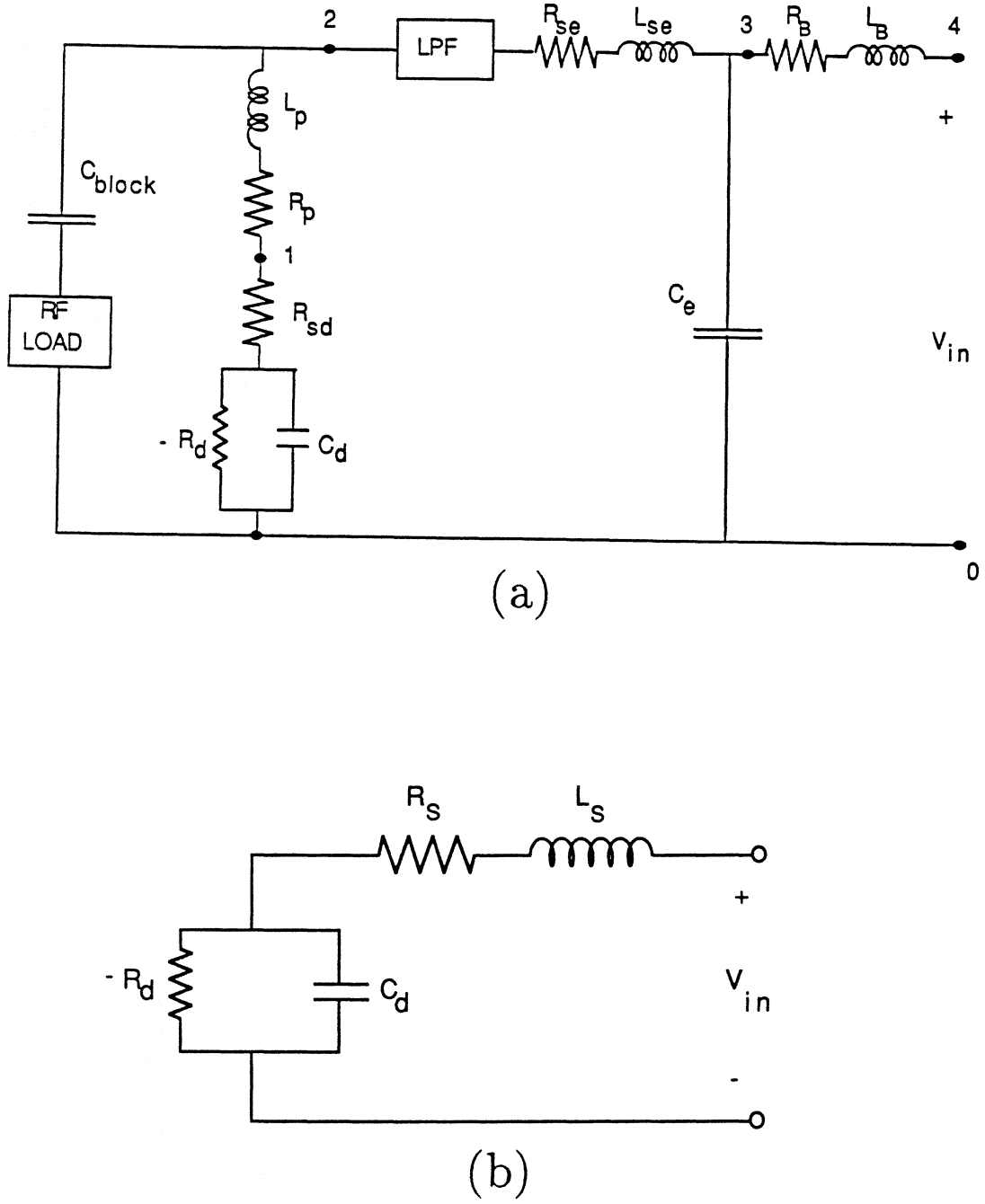

Figure 1: An equivalent circuit for resonant tunneling diodes (a) inside a waveguide circuit, (b) with a simple bias circuit.

is isolated from the bias circuit by a Low Pass Filter (LPF). At low frequencies the LPF can be ignored. The bias signal is isolated from the RF load, modeled here by the blocking capacitor C_{block}. R_{se}, L_{se} and C_e are circuit elements outside of the oscillator cavity. These elements can be used in an attempt to improve the low frequency stability without effecting the RF impedance seen by the device. Finally, R_B and L_B represent the source resistance and inductance of the power supply.

The impedance of the diode coupled to the cavity (across nodes 2 - 0) is

$$Z_{coupled} = R_s + \frac{-G_d}{G_d^2 + \omega^2 C_d^2} + j\omega \left(L_s - \frac{C_d}{G_d^2 + \omega^2 C_d^2} \right), \tag{1}$$

where $G_d = 1/R_d$, $L_s = L_p$ and $R_s = R_p + R_{sd}$. If the magnitude of R_s is less than R_d then the real part of $Z_{coupled}$ is negative at low frequencies and this negative resistance decreases as a function of ω. At the angular frequency ω_r given by

$$\omega_r = \frac{G_d}{C_d} \sqrt{\frac{1}{R_s G_d} - 1}, \tag{2}$$

the real part of the impedance is zero. This frequency corresponds to f_{max}, the cutoff frequency of the diode. Above this frequency the device can no longer supply power to the circuit. At the angular frequency ω_x given by

$$\omega_x = \sqrt{\frac{1}{L_s C_d} - \frac{G_d^2}{C_d^2}}, \tag{3}$$

the imaginary part of Eq. 1 becomes zero. It will be shown that ω_x should be larger than ω_r to prevent spurious oscillations.

For a simple stability analysis the circuit of Fig. 1(a) is approximated by the circuit of Fig. 1(b). This assumes the frequencies of any bias circuit oscillations are low enough that the RF load may be neglected. It also neglects the stabilizing capacitor, C_e. The effect of the stabilizing capacitor will be discussed later. Several of the circuit elements in Fig. 1(a) are in series and thus may be combined to give the elements in Fig. 1(b), $L_s = L_p + L_{se} + L_B$ and $R_s = R_{sd} + R_p + R_{se} + R_B$. The resulting circuit, Fig. 1(b), was studied by Hines [7] for the tunnel diode case.

The circuit in Fig. 1(b) is described by the differential equation

$$L_s C_d \frac{d^2V}{dt^2} + (R_s C_d - L_s/R_d) \frac{dV}{dt} + V(1 - R_s/R_d) = V_{in}. \tag{4}$$

$V_{in} = 0$ for the short circuit case. The characteristic equation of the above differential equation has four possible solutions but it can be shown that only two solutions lead to a stable circuit [7.10]. The four possible solutions are shown as four different areas in the stability diagram of Fig. 2. The circuit is stable when the solution is exponentially decaying (region III) or exponentially decaying sinusoid (region IV). Combining these gives the stability criteria for the circuit of Fig. 1(b) as

$$\frac{L_s}{C_d R_d^2} < \frac{R_s}{R_d} < 1. \tag{5}$$

Algebraic manipulation shows that the first inequality of Eq. 5 is equivalent to

$$\omega_r < \omega_x$$

as a stability criteria, with the frequencies defined in equations 2 and 3.

To obtain stability the ratio R_s/R_d should be just less than one so that both inequalities of Eq. 5 can be satisfied. Not all of R_s has to be part of the rf circuit. R_s consists of four separate positive resistances. R_{sd} is the positive resistance associated with the device and is largely dependent on device design and fabrication. R_p is also part of the rf circuit and may be used to stabilize the RTD. If C_e is not included, R_B is indistinguishable from R_s. The stabilizing load may be inside (R_p) or outside (R_{se}) the rf circuit. Circuit stabilization is often simpler when R_p is sufficient to stabilize the circuit [11]. However, this will degrade the power generation capability of the diode since there will be more positive resistance associated with the device. If the stabilizing load is in the rf portion of the circuit then nearly all the rf power is lost to the stabilizing load. So if possible the bias line stabilizing load should be isolated from the rf circuit.

Typically, for RTDs with peak currents in the mA range R_d is tens of ohms or less and C_d is tens of pF. This constrains L_s to nH's or even tenths of a nH. Since a whisker contact introduces an inductance of this order many RTDs are difficult to stabilize when used with whisker contacts. It is interesting to study the effect of the series inductance L_s. For a given device and circuit, the external inductance in the bias circuit can be varied to sample different portions of the stability plot in Fig. 2. Experimental bias circuit oscillations of a resonant tunneling diode mounted in a low inductance whisker contact cavity with a variable external lead inductance are shown in Fig. 3.

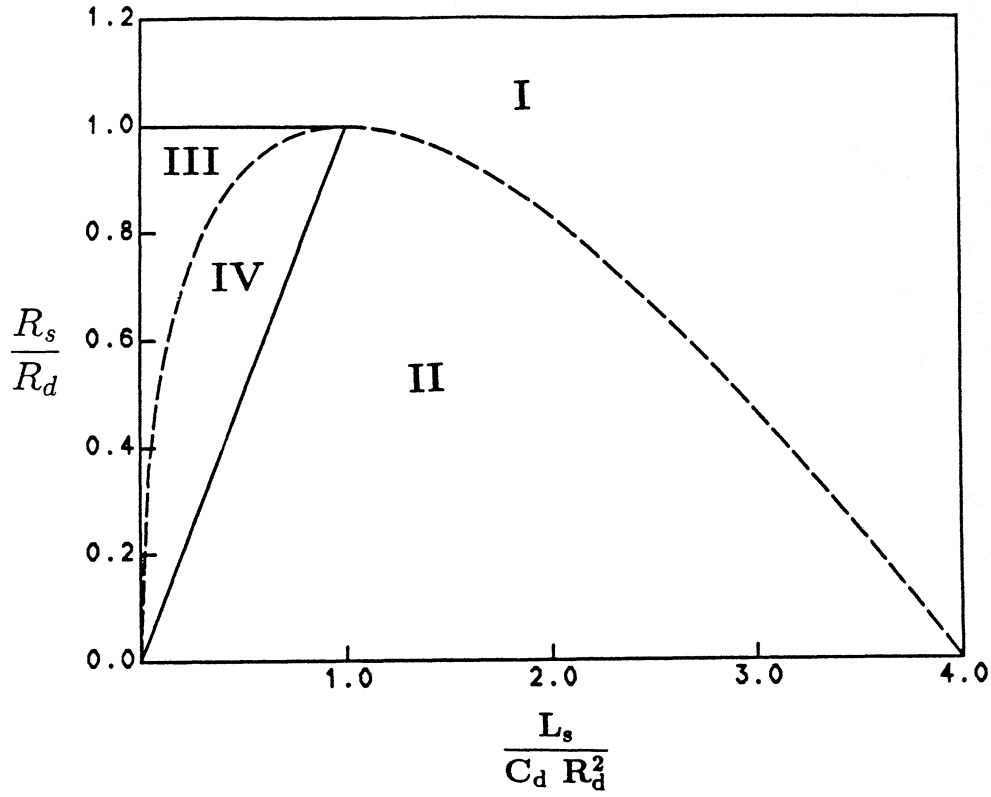

Figure 2: The stability diagram for resonant tunneling diodes based on circuit and device parameters. Regions III and IV correspond to a short circuit stable circuit.

The device is a resonant tunneling diode with AlAs barriers that are 30 Å, thick, an $In_{0.10}Ga_{0.90}As$ deep well that is 70 Å wide, and spacer layers on each side that are 30Å wide. The contact regions are doped to $2 \times 10^{18} cm^{-3}$. Standard photolithiography techniques are used to fabricate diodes of various sizes. The measurements are done on 50 μm by 50 μm diodes.

The circuit is in region I of Fig. 2 for very large L_s. Devices biased in region I should have a growing exponential waveform. In reality,the growth is limited by the extent of the negative resistance region. The result is the well known relaxation oscillation. Similar conditions occur in a tunnel diode [9]. The voltage across the bias terminals of the experimental device is shown in Fig. 3 a). For smaller values of L_s ,the operating point moves to the left on the stability curve in Fig. 2 into region II. The stability diagram predicts growing sinusoidal oscillations, which are also limited by the extent of the negative resistance region. This results in a nearly sinusoidal steady state oscillation and a measured case is shown in Fig. 3(b). In the growing sinusoid region, decreasing L_s causes the frequency of oscillation to increase. This is shown by differentiating the frequency of

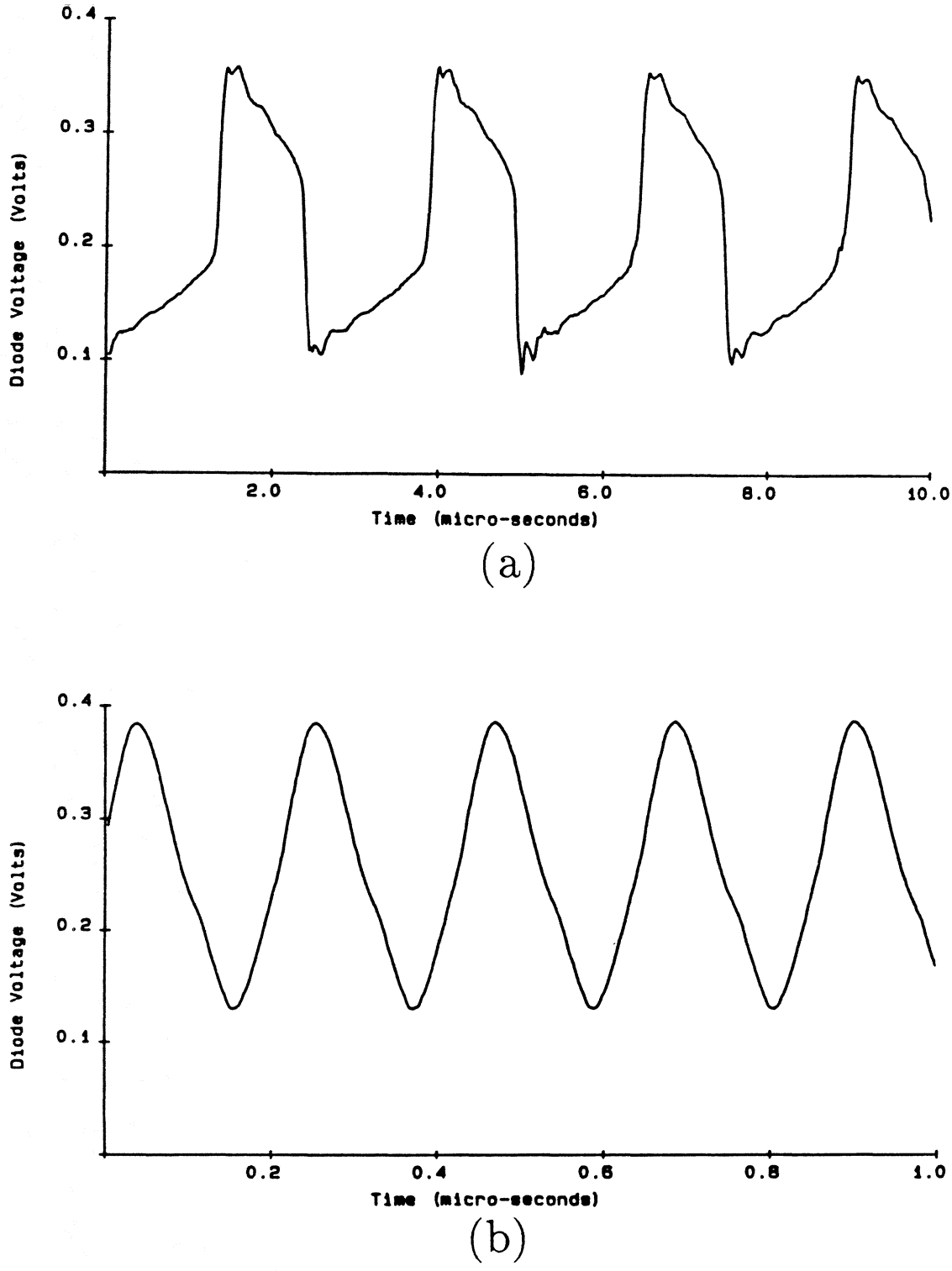

Figure 3: Low frequency oscillation of the RTD as measured by an oscilloscope (a) in the growing exponential region(area I) of the stability diagram. A large RF choke was placed in the bias lines to produce this oscillation. (b) in the growing sinusoidal region (Area II) of the stability diagram. The inductance is from approximately 2 meters of lead wire.

oscillation with respect to the series inductance to obtain

$$\frac{d(\omega^2)}{dL_s} = \frac{1}{4C_d^2 L_s^3}\left(2L_s C_d\left(\frac{R_s}{R_d} - 2\right) + 2R_s^2 C_d^2.\right) \tag{6}$$

For large L_s this is negative since $R_s/R_d < 1$. The extrema is then found by setting the above equation equal to zero and solving for L_s. An extrema occurs when

$$L_s = \frac{R_s^2 C_d}{2 - \frac{R_s}{R_d}} < R_s^2 C_d < R_s R_d C_d.$$

Since the denominator of the derivative is linearly decreasing with L_s this is a maximum. This means that the maximum frequency occurs for values of L_s smaller than the value required for stability. Now, if one calculates the oscillation frequency when L_s is just small enough to give stability one obtains

$$\omega = \frac{1}{R_d C_d}\sqrt{\frac{R_d}{R_s} - 1} = \omega_r. \tag{7}$$

This gives physical meaning to the stability conditions. For a given device R_d and C_d are fixed. Assuming R_s is less than R_d the circuit L_s controls the stability. The idea is to decrease L_s which in turn increases the oscillation frequency until the oscillation frequency is above the resistive cutoff frequency of the device.

A common method for stabilizing a tunnel diode or RTD is to place a capacitor in shunt across the terminals of the device [7,12,13]. From the preceeding analysis it is seen that instability would be overcome if the DC source could be inserted physically near the RTD, minimizing the inductance. Since a large shunt capacitor will appear to the bias circuit oscillations as a DC voltage source the capacitance, C_e shown in Fig. 1(a) effectively accomplishes this. Fig. 4(a) is the same circuit with series elements combined: $L_s = L_p + L_{se}$ and $R_s = R_{sd} + R_p + R_{se}$. To study the effect of C_e the circuit is broken into separate high- and low-frequency equivalents, both of the form of Fig. 1(b). For high frequencies C_e is a short circuit so the combination of L_s, R_s, R_d and C_d in Fig. 4(a) must satisfy the stability criteria, Eq. 5. For the low frequency circuit the element values in Fig. 5(b) become $L_s = L_B$, $R_s = R_B$, $R_d = R_d - R_{sd} - R_p - R_{se}$ and $C_d = C_e$. This low frequency equivalent R_d is different than that given by Hines [7]. The value given here is chosen to give the correct impedance at DC. Plotting the impedance locus vs. frequency for various element values

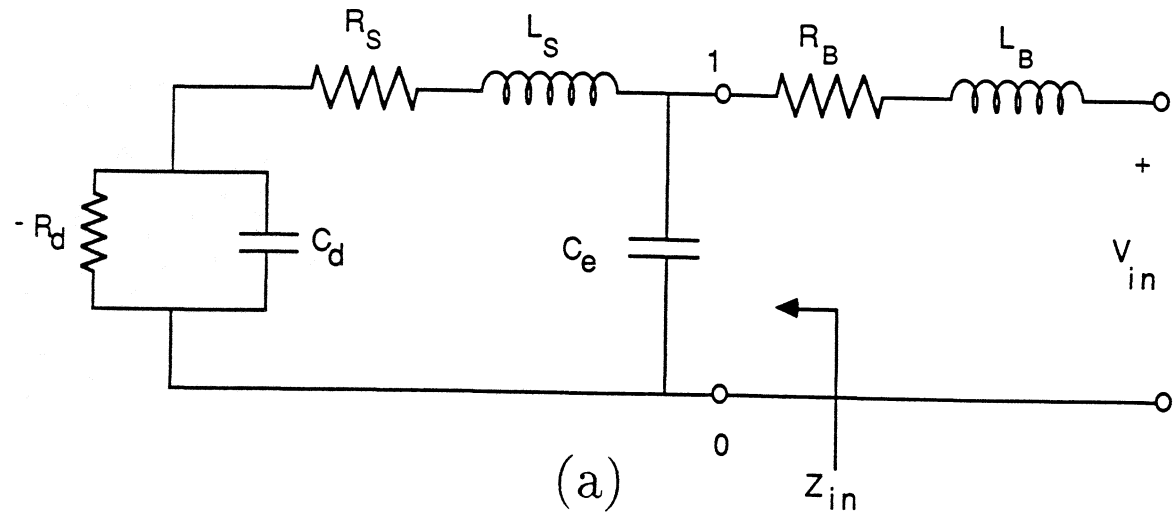

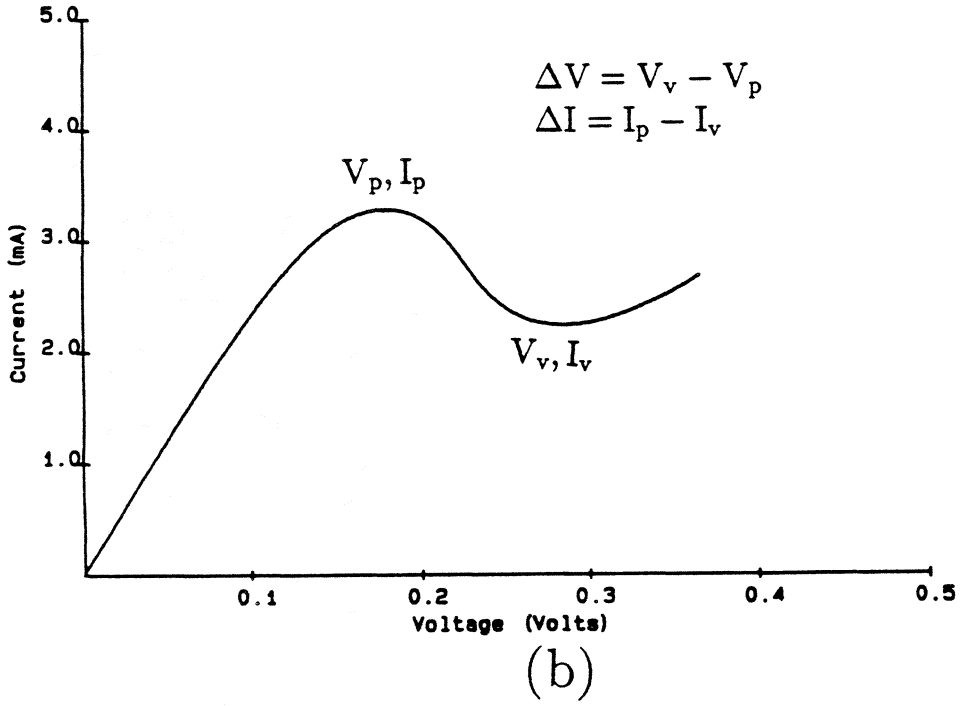

Figure 4: (a) Use of an external capacitance for stabilization, (b)the "true" stable DC I-V curve for the device under consideration as measured on the HP 4145 semiconductor parameter analyzer. Stabilization was attained using $R_s = 33\Omega$ and $C_e = 0.1\mu F$.

indicates that this approximation is very good when the high frequency circuit is stable. Then a sufficient condition for the circuit in Fig. 4(a) to be stable is

$$\frac{L_s}{R_d^2 C_d} < \frac{R_s}{R_d} < 1 \quad AND \quad \frac{L_B}{(R_d - R_S)^2 C_e} < \frac{R_B}{(R_d - R_s)} < 1 \tag{8}$$

The circuit of Fig. 4(a) was used to stabilize the diode discussed earlier with $R_s = 33\Omega$ and $C_e = 0.1\mu F$. The diode was considered stable when no oscillations could be detected using an oscilloscope across the bias leads. Care was taken to ensure that the frequency of the oscillations, usually hundreds of MHz, was not greater than the bandwidth of the oscilloscope. The stable I-V curve of Fig. 4(b) is felt to represent the "true" I-V curve.

The condition of eq. 8 is not necessary. However, Nyquist analysis of the full circuit for different element values indicate that while it is theoretically possible to obtain a stable circuit when the high frequency circuit is unstable, stability requires precise element values and could not be attained in practice. If the simple stability conditions, Eq. 5, are not met by the circuit shunted by the external capacitance, stable operation of the circuit in Fig. 4(a) is virtually unobtainable.

III Low frequency I-V characteristics of unstable devices

The effect of various intrinsic and extrinsic circuit elements on the measured DC I-V characteristics of unstable devices will be discussed in this section. It is shown that from the shape of the I-V characteristic one can tell what kind of instability is present in the circuit. This analysis is not only useful for its own sake but it is necessary since the instability can have severe consequences on the device applications. Some preliminary work on this subject has been described by Young et. al. [3] and Liu [12]. The circuit of Fig. 1(b) will be used for the discussion of DC I-V curves in this section. The same diode as in section II is used to experimentally demonstrate the conclusions. Bias oscillations distort the measured I-V characteristic away from the "ideal" curve of Fig. 4. Three classes of distortions are commonly observed: switching; bistability; and bias circuit oscillations. Sometimes more complex distortions such as double plateau structures are observed which have not been investigated.

An I-V curve displaying switching is shown in Fig. 5. This type of distortion is discontinuous in

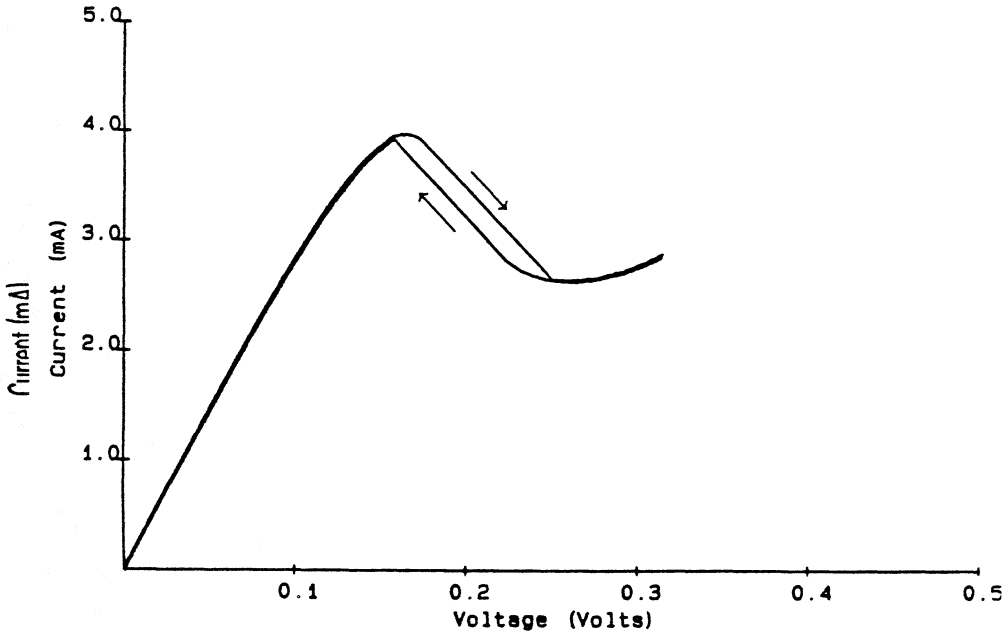

Figure 5: The measured diode I-V curve with an "external" resistance, $R_s \approx 55\Omega$. The "switching" of the diode is obvious.

both current and voltage. This behavior is due to a large series resistance between the voltage source and the point at which the voltage is measured. In the inset of Fig. 6 this corresponds to measuring I vs. V_D with $R_s > |R_d|$ in the NDR region. The resulting I-V curve is apparent from load line analysis on the stable I-V characteristic shown in Fig. 4. As V_{in} is increased from zero to $V_p + R_s I_p$ the measured I-V curve faithfully reproduces the true I-V curve. Since no negative resistance is present the circuit is stable and there is no switching in the region $V_v + R_s I_v < V_{in} < V_p + R_s I_p$ where the load line intersects the I-V curve at three different points. When V_{in} is increased beyond $V_p + R_s I_p$ the only stable point is on the right positive resistance portion of the I-V curve, forcing switching behavior. When V_{in} is swept from $V_{in} > V_p + R_s I_p$ the same argument holds. Hysterisis occurs because the positive going switch point, $V_{in} = V_p + R_s I_p$ is less than the negative going switch point, $V_{in} = V_v + R_s I_v$. Since $R_s > |R_d|$ it follows from the stability diagram, Fig. 2, that the voltage is varying exponentially with time.

An I-V curve showing bistability in the present device due to an internal resistance is shown in Fig. 6. For purposes of demonstration a large series resistance was added which was treated as

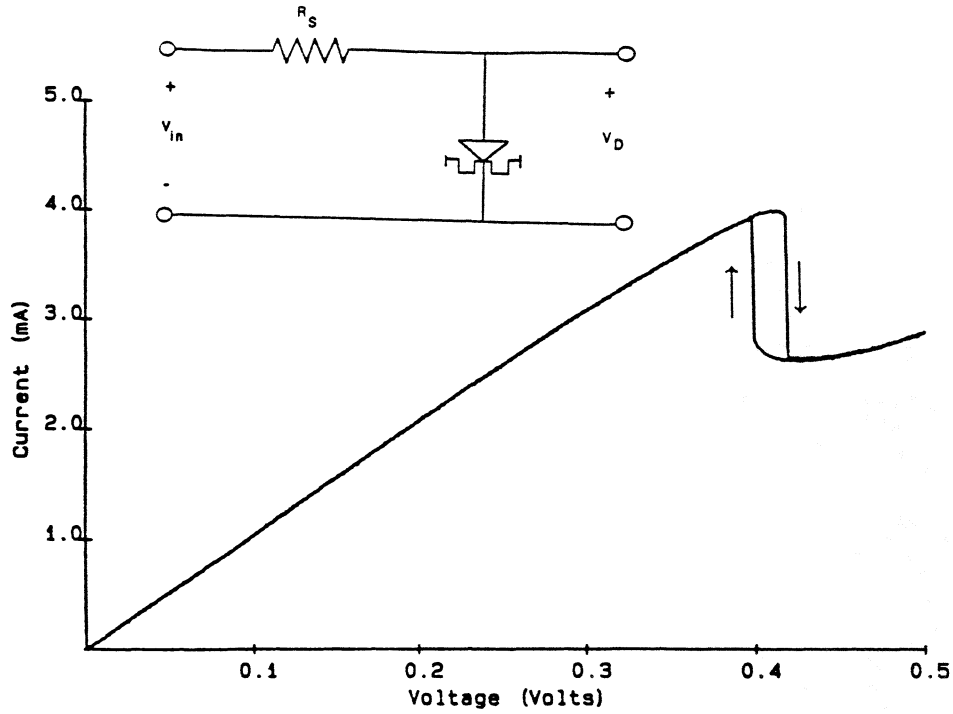

Figure 6: Diode measured I-V curve showing the bistable nature of the device due to an "intrinsic" series resistance ($R_s \approx 55\Omega$).

"internal." In practice the internal series resistance is usually the positive resistance of the device independent of the measuring apparatus. This resistance includes contact resistance and epilayer resistance. The distinctive feature of this distortion is that only the current is discontinuous. This behavior is due to a voltage drop between the point at which the voltage is measured and the NDR device. In the inset of Fig. 6 this corresponds to measuring I vs. V_{in} with $R_s > |R_d|$. Load line analysis follows that presented for the switching case , with similar results. An important difference between the two distortions is that an internal resistance always distorts the I-V curve while an external resistor only distorts the curve if $R_s > |R_d|$.

An I-V curve displaying a plateau structure is shown in Fig. 7. It is a simple matter to show by numerical methods that such a structure is to be expected when bias circuit oscillations are present [2]. The measured current is simply the time average of the current waveform. It does not involve a detection process, so the term "self detection" is a misnomer. These oscillations occur when

$$\frac{R_s}{R_d} < \frac{L_s}{R_d^2 C_d} < 1 \qquad (9)$$

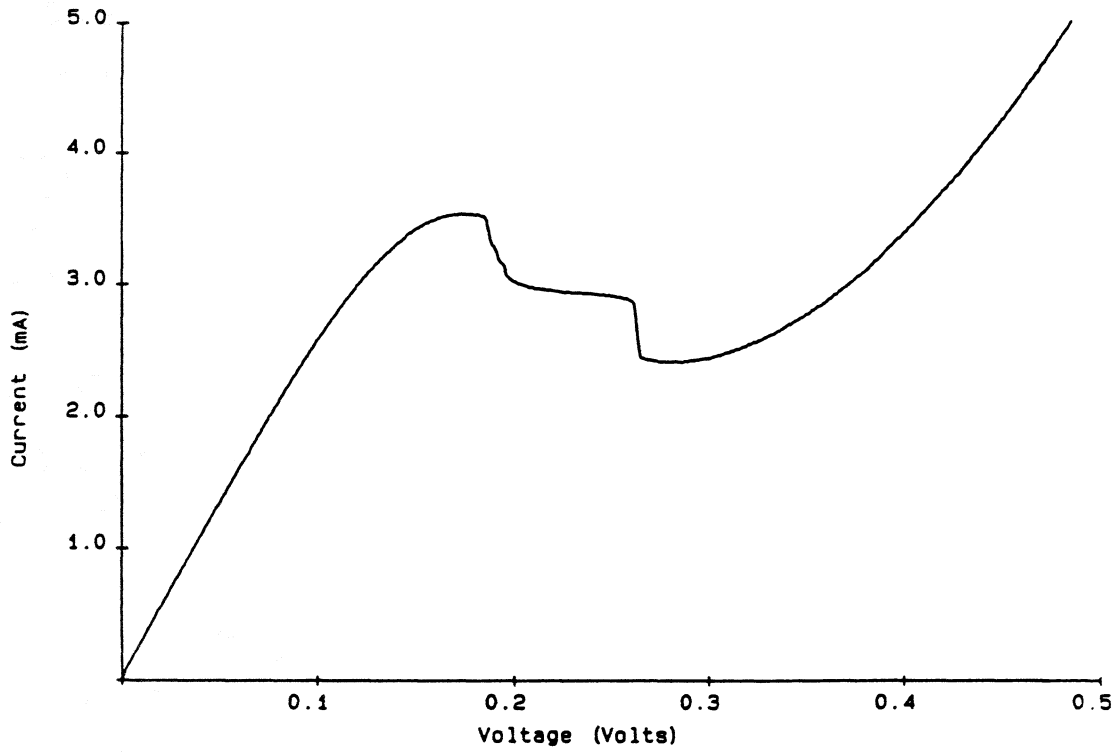

Figure 7: Measured I-V curve showing a plateau structure because of bias circuit oscillations.

For the device tested the DC I-V curve was insensitive to whether the oscillation was sinusoidal or relaxation, Fig. 3(a) or 3(b).

IV Effect of device stability on power generation

The purpose of this section is to show the effect of the stability requirements on the power generation capability of RTDs. Assuming the designer has control of R_s, ($R_s/R_d \approx 1$) the inequality for a stable negative resistance device can be written as

$$C_D > A_D \times G_D^2 \times L_s \tag{10}$$

where now A_D is the device area and the capacitance, C_D , and conductance, G_D, are now per unit area. Thus to obtain stable devices one must decrease the device area, the conductance and the series inductance and increase the device capacitance. Let us now examine each element in more detail regarding stability and high frequency power generation.

Both the negative resistance and the series resistance of the device are frequency dependent. It has been shown from theoretically calculated characteristics that for a particular device the negative

conductance remains constant up to about 200 GHz but then starts to decrease and in the terahertz range becomes about half of the DC value [14]. This is certainly device dependent and for some devices the roll off will be much faster. Similarly the series resistance of the device, assuming contact resistance and epilayer resistance to be constant, increases as a function of frequency mainly due to the behaviour of the skin depth [15]. This behaviour was not considered in the stability analysis, where the circuit values are considered to be constant. Physically it is clear that this will not produce bias circuit oscillations since the effect is to lower the resistive cutoff frequency. Such roll off will, however, further limit the power generating capabilities of RTDs at very high frequencies.

Decreasing the device area is consistent with requirements for high frequency devices. By reducing the device area the device capacitance is reduced which is beneficial in coupling these low impedance devices to the RF load. The limit on device area is imposed by the relevant fabrication technology and packaging restraints. One micron diameter Schottky diodes have been fabricated but diameters much smaller than this might be hard to obtain. Extremely small diodes will be very difficult to contact. Even if the device can be contacted, it may be too small to produce any useable power.

The physical origin of L_s is the inductance due to the lead that connects the device to the measuring apparatus or the device package. For practical applications the devices can be contacted either with bond wires or through whisker contacts. At low frequencies the devices are usually bonded in microwave packages and the associated inductance is at least 1 nH. For high frequency operation whiskers are used and the corresponding inductance depends on the diameter and length of the probe. An approximate inductance value for this configuration is about 0.2 nH [16]. The goal of reducing series inductance for stability is consistent with the requirements for high frequency operation. However, it should be realized that with conventional contacting techniques inductance lower than 0.2 nH can not be easily obtained.

The origin of the device capacitance is the charge distribution in the device. Since the double barrier structure is an undoped region sandwiched between two moderately or heavily doped regions, the device capacitance can be approximated by a parallel plate capacitance model. A

more accurate value of the device capacitance may be found by using a self consistent quantum mechanical simulation to calculate the width of the depletion region. The goal of increasing device capacitance for stability is in direct conflict with performance criteria for high frequency devices [17].

The device negative conductance is given by $\Delta I/\Delta V$, assuming that the negative resistance region is linear. For stability the conductance should be decreased as much as possible implying that ΔI should be reduced and ΔV should be increased.

To calculate the power output from resonant tunneling devices the device area must be selected. One method for calculating the area is to assume that the device is matched to a circuit with resistance of R_L ohms. In that case, the device area can be written as:

$$A_D = \frac{1}{(R_L + R_s)} \times \frac{G_D}{G_D^2 + (\omega C_D)^2} \tag{11}$$

where R_s is the device series resistance, G_D is the conductance per unit area of the device. C_D is the capacitance per unit area of the device under consideration. From the above equation it is seen that the device area becomes larger as $(R_L + R_s)$ is reduced. Since the power scales with device area, it is desirable to reduce the series and circuit resistances as much as possible. In the analysis presented here, it is assumed that the minimum achievable circuit resistance is 1-Ω and the series resistance of the device is negligible. This is an approximation and will be difficult to realize at very high frequencies. However, if a larger load or series resistance is present, then the output power will scale inversely with the load resistance. With the assumption that R_L is equal to 1-Ω and R_s is negligible,

$$A_D = \frac{G_D}{G_D^2 + (\omega C_D)^2}. \tag{12}$$

The rf power achievable from the device for the given area is then calculated as

$$P_{RF} = \frac{1}{2} \frac{{V_{rf}}^2}{1 + \left(\frac{\omega C_D}{G_D}\right)^2}, \tag{13}$$

where V_{rf} is the peak rf voltage. The magnitude of V_{rf} is selected to be half of ΔV and assuming

$G_D = \Delta I/\Delta V$ then the expected power at very high frequencies can be written as [5,17]

$$P_{RF} = \frac{1}{8\omega^2}(\frac{\Delta J}{C_D})^2, \tag{14}$$

where ΔJ is the difference between the peak current and the valley current. Driven by this rule the effort has been to increase the current density and decrease the device capacitance while maintaining a reasonable peak to valley current ratio. However, no consideration was given to stability in that analysis. If stability is considered then the analysis is no longer strictly valid except for an ideal situation where the inductance L_s is negligible. The obvious change is that there is a lower bound on the capacitance of the device. This bound is given by $C_d > L_s/R_d^2$. Decreasing the capacitance beyond this point will make the device unstable.

Moreover, the peak current density is no longer the dominant parameter in the figure of merit. In fact, when the device is limited by stability, the performance becomes inversely related to the ratio of peak current to device capacitance. Rearranging Eq. 10 gives

$$A_D < \frac{C_D}{L_s G_D^2}. \tag{15}$$

So then the stability limited power becomes

$$P_{RF} \leq \frac{1}{8}\Delta V \Delta J \frac{C_D}{L_s G_D^2} \tag{16}$$

which, assuming a linear negative resistance region reduces to

$$P_{RF} \leq \frac{1}{8L_s}(\Delta V)^3 \frac{C_D}{\Delta J}. \tag{17}$$

This clearly demonstrates that ΔV cannot be ignored when designing devices for high frequency power generation.

Thus there are two rf circuit parameters which can limit the power from a device, the minimum achievable load resistance and the minimum achievable lead inductance. The minimum load resistance limits the diode area which can be made to oscillate at the desired frequency. The minimum inductance limits the diode area which will not oscillate with the bias circuit. The power from a device will not be limited by stability concerns if P_{RF} in Eq. 17 is greater than P_{RF} in Eq. 14.

Combining these equations reduces to

$$\Delta V > \frac{\Delta J}{C_D}\left(\frac{L_s}{\omega^2 R_L}\right)^{1/3}. \tag{18}$$

Or, in terms of the circuit parameters

$$\frac{\omega L_s}{R_L} < \left(\frac{\Delta V \omega C_D}{\Delta J}\right)^3. \tag{19}$$

From the above discussion and analysis it can be seen that the criteria for stability do not always coincide with the criteria for high frequency operation.

The effect of requiring stability is demonstrated using a typical device. A self consistent quantum mechanical simulation [18] was used to generate the I-V characteristic. For this particular device the barrier height was selected to be 0.24 eV, the barrier and well width was 23.3 and 43.5 Å respectively. The doping outside the barriers was 1×10^{17} and spacer layers of 50 Å were used. Also a 100 Å drift layer was used on the anode side. These parameters correspond to a GaAs/AlGaAs device which can be fabricated. From the computer simulation this device has a peak current density of $8.6 \times 10^4 \mathrm{A/cm^2}$, peak-to-valley current ratio of 4, a $\Delta V = 0.24\mathrm{V}$, and a depletion region width of 491 Å.

Fig. 8 shows the results of the rf power calculation using Eq. 14 as well as the device area matched for 1 ohm circuit matching (upper curves). This analysis does not take into consideration the series resistance of the device which could further degrade the device performance. Now, for comparison we invoke the stability criteria. We assume that this device can be contacted so that the series inductance is 1 nH. Using this one finds that the device is unstable when matched to a 1 ohm load (the device area is too large to be stabilized). Using Eq. 15 we find that the device will be stable if the area is $3 \times 10^{-9} cm^2$ or less. Thus stabilizing the device places severe constraints on the device size. The maximum area corresponds to a circular mesa of 0.4 μm diameter which would be extremely difficult to contact. If one was somehow able to fabricate and contact this device and assuming that the series inductance is still 1 nH then the available power, from Eq. 17 is shown in Fig. 8 (lower curves) for matching to a non constant load resistor. Note the decrease in output power. The required area and output power assuming that a series inductance of 0.2 nH was obtainable is also shown in Fig. 8.

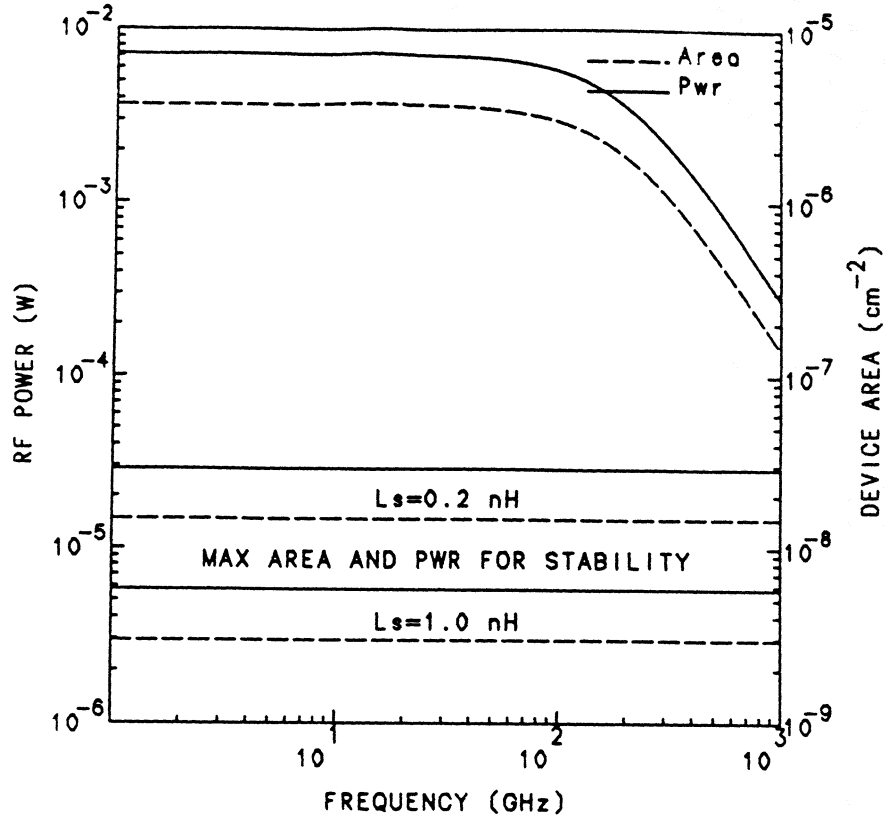

Figure 8: Expected power and area necessary for matching into a 1 ohm resistance (top curves). The lower curves indicate the maximum area and power attainable from the same device if the device was made stable (assuming two different L_s values).

It is apparent from the above results that if one fulfills the requirement for stability the power generation capability of the device is significantly compromised even if it is possible to obtain the required small areas. Since the device conductance and capacitance are fixed the only other circuit element that can be varied is the series inductance. In Table 1 the maximum diode diameter, corresponding power at 1000 GHz and the necessary load resistance are calculated for different values of the series inductance. In all the calculations R_s has been assumed to be negligible when compared to R_L. This approximation is not valid when R_s becomes comparable to R_L. For $R_s = R_L$ the useful power deleivered to R_L will be reduced by half of that shown in the Table. It is also worth noting that decreasing the diode diameter will increase R_s in an actual device.

V Conclusion

The stability criteria for resonant tunneling diodes have been derived. Based on the criteria it is shown that stable operation of resonant tunneling diodes is hard to obtain. The importance

L_s	At 1 THz		
	d_{max}	P_{max}	R_L
nH	μm	μW	Ω
25	0.06	0.23	1191
10	0.10	0.58	476
5	0.14	1.15	238
2	0.22	2.88	95.4
1	0.31	5.75	47.7
0.5	0.43	11.5	23.8
0.2	0.69	28.8	9.54
0.1	0.97	57.5	4.77

Table 1: Maximum diode diameter(in microns), maximum power generation (in microwatts) and corresponding load resistance (in ohms), at 1 THz for various lead inductances when the device is stable.

circuit inductance cannot be over emphasized. In order to stably bias an RTD the lead inductance must be minimized. The diodes can be made stable by using a shunt capacitor but this is only possible if the circuit inductance is very small. It was shown that each instability produces a signature I-V characteristic. The expected I-V curves were experimentally produced using a diode which could be stabilized. Finally, the effect of stability criteria on the potential and capability of RTDs for high frequency power generation has been studied. Requiring stability for devices severly limits the diode area. It is shown that the device parameter ΔV will have a very strong influence on the performance of high frequency RTDs if the lead inductance is not negligible.

Acknowledgments

The authors wish to thank Dr. Richard Mains for many helpful discussions. This work was supported by the NASA Center for Space Terahertz Technology under contract no. NAGW-1334 and the US Army Research Office under the URI program, contract no. DAAL03-87-K-0007.

References

[1] R. Tsu and L. Esaki. *Appl. Phys. Lett.*, 22(11):562–564, June 1973.

[2] L. L. Chang, L. Esaki, and R. Tsu. *Appl. Phys. Lett.*, 24:592–595, 15 June 1974.

[3] T. C. L. G. Sollner, W. D. Goodhue, C. D. Parker P. E. Tannenwald, and D. D. Peck. *Appl. Phys. Lett.*, 43(6):588–590, September 1983.

[4] W. R. Frensley. *Appl. Phys. Lett.*, 51:448–450, 10 August 1987.

[5] R. K. Mains, I. Mehdi, and G. I. Haddad. *Intl. Journal of Infrared and Millimeter Waves*, 10(6):595–620, June 1989.

[6] V. P. Kesan, A. Mortazawi, D. P. Niekirk, and T. Itoh. *IEEE-MTT-S Digest*, 1(L-39):487–490, June 1989.

[7] M. E. Hines. *Bell Syst. Tech. J.*, 39:477–513, May 1960.

[8] H. A. Watson. *Microwave semiconductor devices and their circuit applications.* McGraw-Hill Inc., 1969.

[9] W. F. Chow. *Principles of Tunnel Diode Circuits.* John Wiley and Sons, 1964.

[10] C. Kidner, I. Mehdi, J. East, and G. Haddad. *Submitted to Solid-State Electronics*, Copies available upon request.

[11] J. M. Owens, D. J. Halchin, K. L. Lear, W. S. Lee, and J. S. Harris Jr. *MTT-Digest*, 1:471–474, June 1989.

[12] H. C. Liu. *Appl. Phys. Lett.*, 53(6):485–486, August 1988.

[13] J. F. Young, B. M. Wood, H. C. Liu, M. Buchanan, D. Landheer, A. J. SpringThorpe, and P. Mandeville. *Appl. Phys. Lett.*, 52(17):1398–1400, April 1988.

[14] R. K. Mains and G. I. Haddad. *J. Appl. Phys.*, 64(7):3564–3569, October 1988.

[15] E. R. Brown, W. D. Goodhue, and T.C.L.G Sollner. *J. Appl. Phys.*, 64(3):1519–1529, August 1988.

[16] M. A. Frerking. Personal communication.

[17] I. Mehdi, G. I. Haddad, and R. K. Mains. *Optical and Microwave Tech. Lett.*, 2(5):172–175, May 1989.

[18] R. K. Mains, J. P. Sun, and G. I. Haddad. *Appl. Phys. Lett.*, 55(4):371–373, July 1989.

Tunnel Transit-Time (TUNNETT) Devices for Terahertz Sources*

G. I. Haddad and J. R. East
Solid-State Electronics Laboratory
Department of Electrical Engineering and Computer Science
University of Michigan
Ann Arbor, Michigan, 48109-2122

Abstract

The potential and capabilities of Tunnel Transit-Time (TUNNETT) Devices for power generation in the 100–1000 GHz range are presented. The basic properties of these devices and the important material parameters which determine their properties are discussed and criteria for designing such devices are presented. It is shown from a first order model, that significant amounts of power can be obtained in this frequency range.

*This work was supported by the Center for Space Terahertz Technology under Contract No. NAGW-1334 and U. S. Army Research Office under the URI Program, Contract No. DAAL03-87-K-0007.

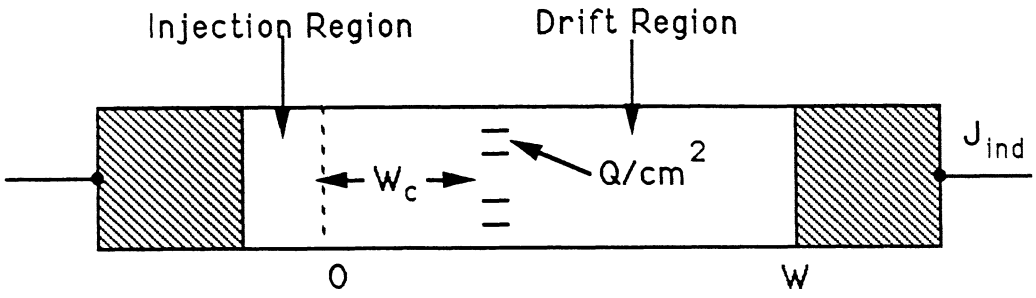

Figure 1 Two-Terminal Negative Resistance Transit-Time Device

1. Introduction

Two-terminal transit-time devices such as IMPATTS are capable of generating significant amounts of power at high-frequencies [1–3]. However, because of the avalanche process, they are very noisy and their efficiency decreases significantly at extremely high frequencies. Also, because of the very narrow drift regions and high doping densities required at such high frequencies, tunneling mechanisms become dominant and effect the performance. Through proper design of the device, we can take advantage of the very fast tunneling process to obtain extremely high frequency and reduce the noise. Such devices have been considered previously [4–7] and preliminary experimental results have been obtained in the 100–300 GHz range. Recent advances in material growth and processing technology will make a significant impact on further development of such devices.

In this paper, the basic principles of two-terminal transit-time devices will be presented and the differences among the various charge injection mechanisms will be discussed. This is followed by an assessment of the R.F. power generation capability of TUNNETTS as well as device design for various operating frequencies.

2. Basic Principles of Two-Terminal Negative Resistance Transit Time Devices

Two-terminal transit time negative resistance devices generally consist of a charge injection region and a drift region as shown in fig. 1. There are several means of injecting the charge Q into the drift region. These include:

a) Thermionic Emission Over a Barrier (BARRITT):
This can be realized from a forward-biased p^+- n or n^+- p junction or by incorporating a wide band semiconductor layer to form a heterojunction barrier.

b) Tunneling Through a Barrier (TUNNETT):
This can be realized by tunneling through a single heterojunction barrier, resonant tunneling through a double barrier [8,9] or tunneling in a reverse-based p^+- n^+ junction.

c) Avalanche Multiplication (IMPATT):
This is realized through avalanche breakdown.

d) Mixed Tunneling or Thermionic Emission and Avalanche Multiplication (MITATT):
This results when two types of mechanisms are involved in the charge generation.

When a pulse of charge of Q coulombs/cm^2 is injected into the drift region and travels with a velocity v_Q in the drift region, the current density induced in the external circuit is given by

$$J_{ind} = \frac{Q}{W}\left[v_Q - \frac{W_c}{W}\frac{dW}{dt}\right] \tag{1}$$

where

W = the width of the depletion layer
and W_c = the location of the charge Q.

For the sake of simplicity and since most of the devices of interest here will be punched through at the bias voltage, and the device is designed to maintain a high field in the drift region, we can assume that W is constant and $v_Q = v_s$, where v_s is the saturated velocity.

Under these conditions, the current voltage waveforms (under large signal conditions which are of interest here) for all of the above devices can be represented approximately as shown in fig. 2. In this figure,

V_{dc} = the d.c. voltage (V)

V_{RF} = the magnitude of the R.F. voltage (V)

Θ_m = the phase angle of charge injection (rad.)

Θ_w = the phase width of the injected charge pulse (rad.)

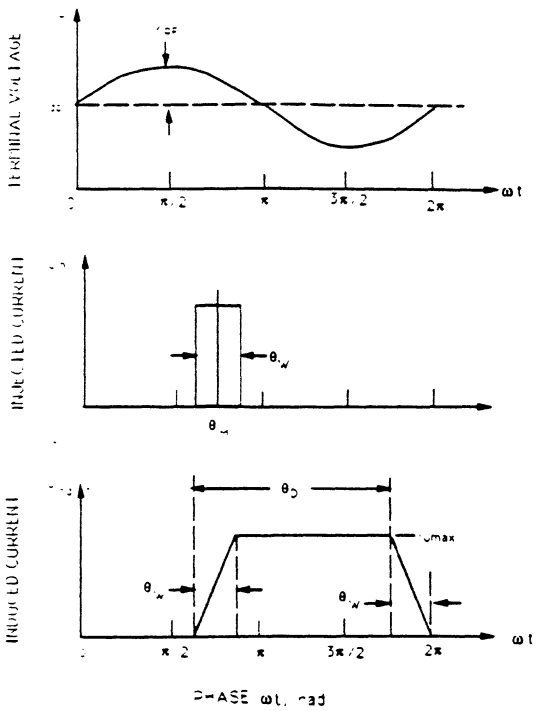

Figure 2 Idealized Voltage and Current Waveforms for Two-Terminal Transit-Time Devices

Θ_D = the drift region transit angle (rad)
$= \omega\tau_D = \omega W/v_s$

τ_D = the transit time through the drift region (sec.)

J = the current density (A/cm^2)

From the waveforms shown in fig. 2, it can be easily shown that the RF power density (watts/cm^2) can be expressed as,

$$P_{RF} = \frac{1}{2\pi} \int_0^{2\pi} J_{ind}(\omega t) V_{RF} \sin(\omega t)\, d(\omega t) \tag{2}$$

which simplifies to

$$P_{RF} = V_{RF} J_{dc} \left(\frac{\sin(\Theta_w/2)}{\Theta_w/2} \right) \left(\frac{\cos\Theta_M - \cos(\Theta_M + \Theta_D)}{\Theta_D} \right) \quad . \tag{3}$$

The device efficiency is

$$\eta \triangleq \frac{P_{RF}}{P_{dc}} = \left(\frac{V_{RF}}{V_{dc}} \right) \left(\frac{\sin(\Theta_w/2)}{\Theta_w/2} \right) \left(\frac{\cos\Theta_M - \cos(\Theta_M + \Theta_D)}{\Theta_D} \right) \quad . \tag{4}$$

Θ_M and Θ_w result primarily from the device design of the generation region and this will determine the particular mode of operation.

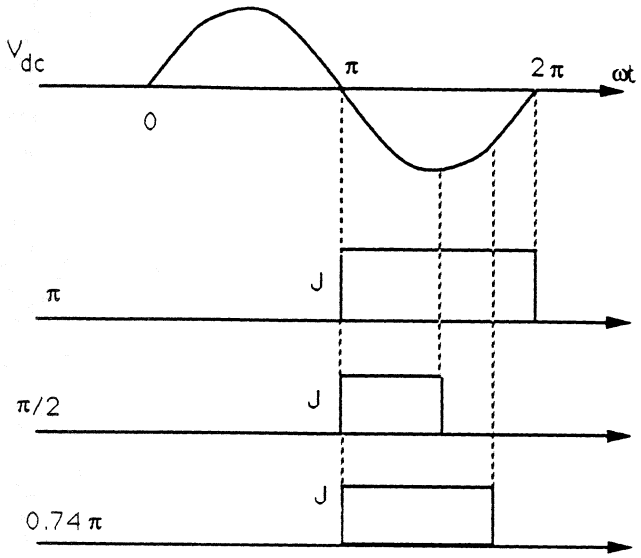

Figure 3 Current Voltage Waveforms for the IMPATT MODE

For IMPATT mode operation, $\Theta_M \cong \pi$ and η becomes

$$\eta = \left(\frac{V_{RF}}{V_{dc}}\right)\left(\frac{\sin(\Theta_w/2)}{\Theta_w/2}\right)\left(\frac{\cos\Theta_D - 1}{\Theta_D}\right) \quad . \tag{5}$$

For maximum η (negative for power delivery), we would like Θ_w to be as small as possible. This implies a small charge-generation region width, small voltage drop across the generation region and V_G/V_D as small as possible, where V_G is the voltage across the generation region and V_D is the voltage across the drift region.

As an ideal case, let $\Theta_w \rightarrow 0$ (very sharp pulse). This assumption is made for simplicity since we are interested here in a first order estimation. Even if Θ_w is $\pi/2$ (which is quite wide for most cases), the estimates will be reduced by a factor of $2/\pi$ which is small relative to the estimates of interest here.

For this case we have

a. $\Theta_m \cong \pi$ (IMPATT mode)

$$\eta = \frac{V_{RF}}{V_{dc}}\left(\frac{\cos\Theta_D - 1}{\Theta_D}\right) \quad . \tag{6}$$

For $\Theta_D = \pi$, $\eta = -(2/\pi)(V_{RF}/V_{dc})$, for $\Theta_D = \pi/2$, $\eta = -(2/\pi)(V_{RF}/V_{dc})$, and for $\Theta_D = 0.74\pi$, $\eta = -(2.27/\pi)(V_{RF}/V_{dc})$. The current voltage waveforms for these cases are illustrated in fig. 3.

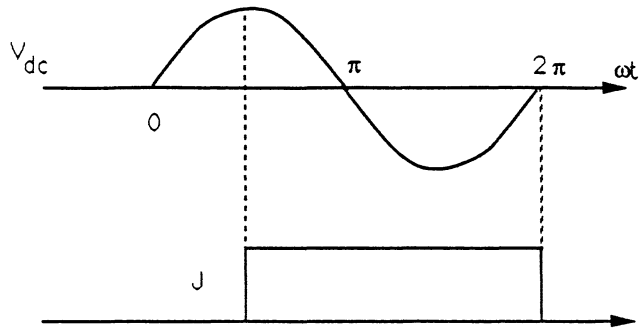

Figure 4 Current-Voltage Waveforms for TUNNETT and BARRITT Devices

It is worth noting that the d.c. voltage is directly proportional to the width of the drift region and thus to Θ_D. Since the R.F. voltage is directly proportional to the d.c. voltage, then the R.F. power density will be directly proportional to Θ_D. Also the capacitance of the device is inversely proportional to Θ_D (or W) and thus it is desirable (as will be shown later) from an impedance matching consideration to make Θ_D or W as large as possible for maximizing power. Thus even though the efficiency for $\Theta_D = \pi/2$ or π is the same, the power generation capability will be much higher for the $\Theta_D = \pi$ case.

It is also important to point out that in an actual device, Θ_m will be less than π and thus a minimum drift angle is required before the device exhibits a negative resistance. Therefore a frequency will exist, usually referred to as the avalanche frequency ωa, below which the resistance will be positive. This is desirable since it will then be easier in such a device to eliminate bias-circuit oscillations which would be difficult to suppress if the negative resistance extended all the way to d.c. Such a device will then exhibit a negative resistance (and thus is capable of oscillation) between ωa and $\omega\tau_D = 2\pi$. It will also have islands of negative resistance at higher frequencies but with much reduced power generation capability.

b. For $\Theta_m = \pi/2$ (TUNNETT, BARRITT)

$$\eta = (V_{RF}/V_{dc})(\sin\Theta_D/\Theta_D) \quad . \tag{7}$$

For $\Theta_D = (3\pi/2)$, $\eta = -(2/3\pi)(V_{RF}/V_{dc})$. The current voltage waveforms for this case are shown in fig. 4. It is seen that, compared to an IMPATT device, the efficiency is approximately 1/3 for this case. However, the voltage will be approximately 3/2 because $\Theta_D = 3\pi/2$ instead of π and the capacitance will be lower which is also

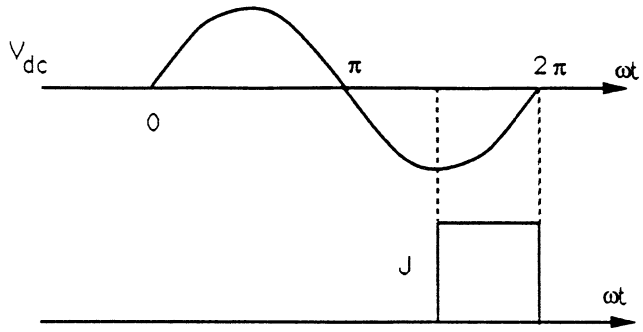

Figure 5 Current-Voltage Waveform for a QWITT Device

desirable. It is also seen that the device will exhibit a negative resistance between $\omega\tau_D = \pi$ and 2π and thus will not exhibit a negative resistance at low frequencies which is an important consideration for bias-circuit oscillations.

c. For $\Theta_m = 3\pi/2$ (Resonant-Tunneling Injection: QWITT)

$$\eta = (V_{RF}/V_{dc})\frac{\sin\Theta_D}{\Theta_D} \quad . \tag{8}$$

For $\Theta_D = \pi/2$, $\eta = -\frac{2}{\pi}\frac{V_{RF}}{V_{dc}}$. The current-voltage waveform for this case is shown in fig. 5.

It is worth noting for this case that if this particular mode of injection is employed, the negative resistance will exist all the way to d.c. This makes it difficult to stabilize such devices and spurious oscillations and in particular bias circuit oscillations will be extremely difficult to suppress. In addition the magnitude of the R.F. voltage swing for this case will be extremely small and thus the power generation capability will be very limited. Also depending on the bias point, if the R.F. voltage magnitude is increased, injection at $\Theta_m = \pi/2$ will take place which will be out of phase with the $\Theta_m = 3\pi/2$ case and will decrease the negative resistance and thus the power output significantly. Therefore, operation of such a device in the transit-time mode is not desirable and is probably best to minimize transit-time effects and utilize the inherent negative resistance property. However, the problems of small power output and spurious oscillations will persist.

d. Ideal case for η.

The maximum η is obtained for $\Theta_w = 0$, $\Theta_m = 3\pi/2$ and $\Theta_D \approx 0$. For this case, $\eta = -(V_{RF}/V_{dc})$. The current voltage waveform for this case is shown in fig. 6. However, the R.F. power generated will be small because Θ_D and thus V_{dc} will be very

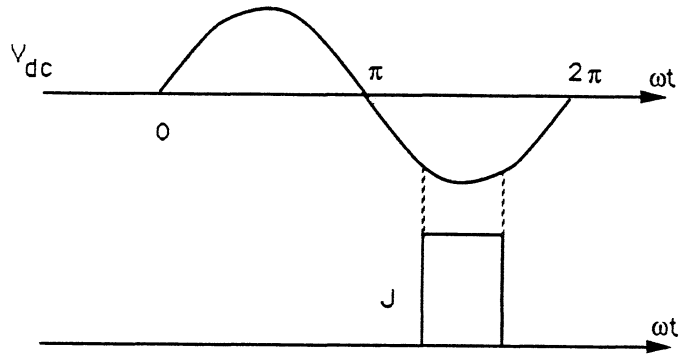

Figure 6 Current-Voltage Waveform for Ideal Efficiency

small. This does point the way, however, to shape the current-voltage characteristic to optimize η if that becomes an important factor.

Since we will be mostly concerned here with TUNNETT devices, fig. 7 shows a heterojunction structure for optimizing the efficiency by inserting spacer layers of GaAlAs. Since v_s in GaAlAs is approximately 1/5 of the saturated velocity in GaAs, the current voltage waveform will be approximately as shown in fig. 7(b), where the induced current during the transit of electrons in the GaAlAs portion of the drift region will be directly proportional to the saturated velocity in this material. This would result in enhanced efficiency [5,7] as shown in fig. 8. It is seen, for example, that for $\beta = 0.2(v_{s_{GaAlAs}} = 0.2v_{s_{GaAs}})$, the efficiency of a heterojunction-type device can approach that of a conventional IMPATT. Thus, heterojunctions can be employed effectively and in several different configurations to enhance the efficiency and power output of TUNNETT devices. This is an extremely important aspect of recent advances in material growth technology which will aid in improved performance of such devices.

3. TUNNETT Device Design

The basic structure and electric-field profile at the bias point for a basic device are shown in fig. 9. The i-layer between the p^{++} and n^{+} regions is not necessary and can be eliminated. The drift region doping can be designed to optimize performance. This basic structure can operate in several modes depending on the i-layer thickness, x_A. It has been shown [5] that for a GaAs structure (which will be considered here), if $x_a > 1,000$ Å, $E_c x_A = 1$ and avalanche breakdown occurs and this results in an

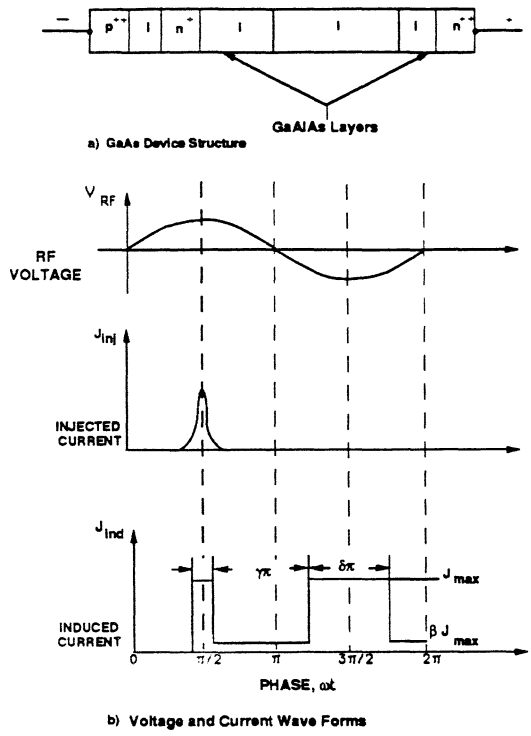

Figure 7 Heterojunction TUNNETT Device

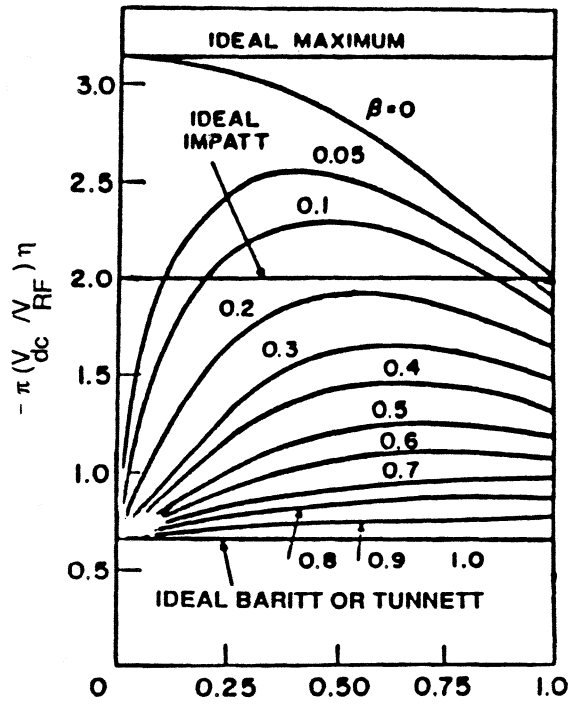

Figure 8 Efficiency as a Function of δ and β. ($\gamma = 0$)

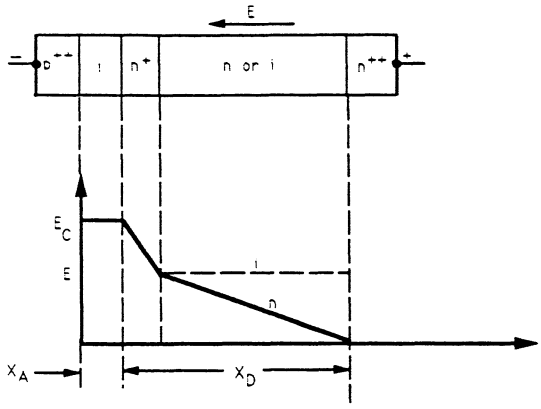

Figure 9 TUNNET Device

IMPATT device. If $x_A < 500$ Å, $E_c > 10^6$ V/cm, injection of carriers will be through tunneling and this results in a TUNNETT device. If 500 Å $< x_A <$ 1,000 Å, both tunneling and avalanche will be present and this results in a MITTAT device.

It is worth noting here that several means for improving the performance of such two-terminal negative resistance devices exist and such devices have the capability of generating significant amounts of power in the 100–1,000 GHz range. Such basic structures also result in very highly nonlinear capacitance-voltage characteristics before breakdown or tunneling occurs and thus will make excellent varactors for harmonic multiplication particularly when low power levels are available at the fundamental. Such devices do not exhibit an inherent negative resistance at low frequencies (except for rectification effects) and thus would be much easier to stabilize and suppress bias circuit oscillations.

4. Estimation of Expected Power Output From Conventional Single Drift TUNNETT Devices

Since we are interested in a first order estimate of the power generation capability, we will consider here a basic TUNNETT structure. As indicated earlier more complicated structures including hereojunctions and double-drift can be employed to improve performance. From the previous current-voltage waveform (fig. 4) for a TUNNET device ($\Theta_w = 0$, $\Theta_m = \pi/2$ and $\Theta_D = 3\pi/2$), the admittance per unit area can be expressed as,

$$Y_D = -G_D + jB_D$$

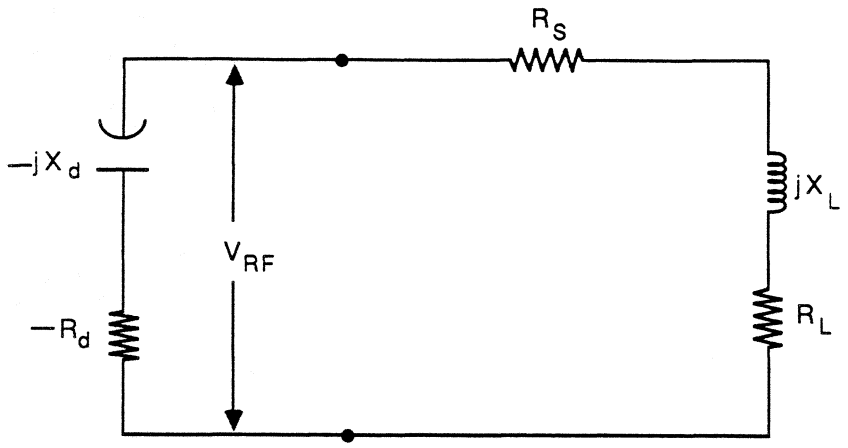

Figure 10 Oscillator Equivalent Circuit

$$= -\frac{4J_{dc}}{3\pi V_{RF}} + j\left[\frac{\omega\epsilon}{x_D + x_A} - \frac{4J_{dc}}{3\pi V_{RF}}\right] \tag{9}$$

$$Y_d = \text{the total admittance}$$

$$= AY_D = A[-G_D + jB_D] \tag{10}$$

where A = the area of the device (cm^2)

$$Z_d = \text{the total impedance of the device} = -R_d - jX_d$$

$$= \frac{1}{Y_D} = \frac{1}{A}\left[\frac{-G_D}{G_D^2 + B_D^2} - j\frac{B_D}{G_D^2 + B_D^2}\right] \quad . \tag{11}$$

The equivalent circuit for an oscillator is shown in fig. 10

where R_s = the parasitic diode resistance and circuit loss
R_L = the useful load resistance
and X_L = the load reactance.

From the oscillation conditions, we have

$$X_L = X_d \; ; \; R_d = R_s + R_L$$

$$\therefore \quad \frac{1}{A}\left[\frac{G_D}{G_D^2 + B_D^2}\right] = R_s + R_L$$

and

$$A = \left(\frac{G_D}{G_D^2 + B_D^2}\right) \frac{1}{R_s + R_L} \tag{12}$$

$$P_{RF}(Gen.) = \frac{V_{RF}^2}{2} G_d = \frac{V_{RF}^2}{2}(AG_D)$$

$$= \frac{V_{RF}^2}{2}\left(\frac{G_D^2}{G_D^2 + B_D^2}\right) \frac{1}{R_s + R_L} \tag{13}$$

$$P_{RF}(R_L) = \text{the power delivered to the load}$$

$$= P_{RF}(Gen.) \frac{R_L}{R_s + R_L}$$

$$= \frac{V_{RF}^2}{2}\left(\frac{G_D^2}{G_D^2 + B_D^2}\right) \frac{1}{R_L(1 + R_s/R_L)^2} \quad . \tag{14}$$

For finite R_s, the maximum power delivered to R_L occurs when $R_s = R_L$. For this case we have,

$$P_{RF}(R_L)_{max} = \frac{V_{RF}^2}{2}\left(\frac{G_D^2}{G_D^2 + B_D^2}\right) \frac{1}{4R_L} \tag{15}$$

and

$$A = \left(\frac{G_D}{G_D^2 + B_D^2}\right) \frac{1}{2R_L} \quad . \tag{16}$$

Next we need to estimate V_{RF} and J_{dc}. For this we assume the following approximate electric-field profile at the d.c. bias point (as shown in fig. 11).

where x_A = the effective generation region width
x_D = the drift-region width
E_m = the maximum electric field in the tunneling region
E_D = the field in the drift region

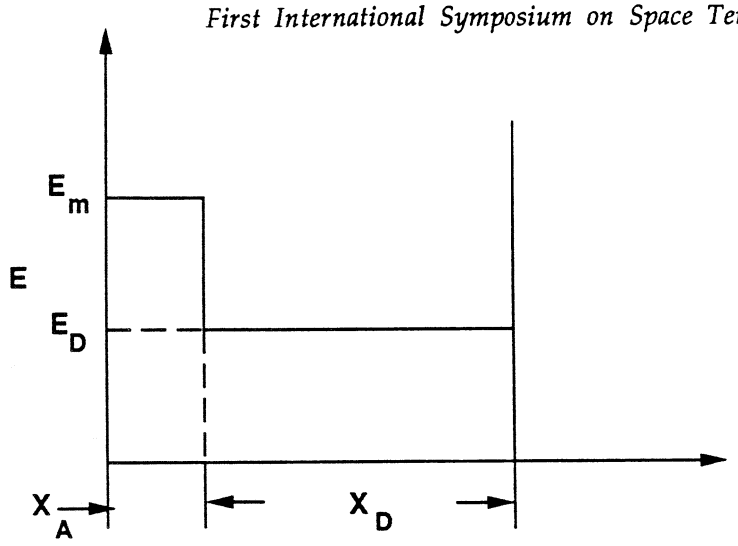

Figure 11 Approximate Electric Field Profile at the d.c. Bias Voltage

and

$$V_{dc} = (E_m - E_D)x_A + E_D(x_A + x_D) \quad . \tag{17}$$

If we assume that at V_{min} (the minimum dynamic voltage at $\omega t = \frac{3\pi}{2}$) $E = E_s$ where $v \geq v_{sat}$ for $E \geq E_s$, we find that,

$$V_{RF} = V_{dc} - V_{min} = E_D(x_A + x_D) - E_s(x_D + x_A) \tag{18}$$

and

$$\frac{V_{RF}}{V_{dc}} = \frac{E_D - E_s}{E_D + (E_m - E_D)\frac{x_A}{x_A + x_D}} \quad . \tag{19}$$

For the magnitude of current densities which will be encountered $E_M \cong 1.6 \times 10^6 \mathrm{V/cm}$. With present technology $x_A = 100$ Å can be easily achieved. For TUNNETT devices $\omega\tau_D = \frac{3\pi}{2}$ and thus

$$x_D = \frac{3v_s}{4f} \quad . \tag{20}$$

It is important to keep carrier generation in the drift region very low. We will therefore assume that

$$\int_0^{x_D} \alpha \, dx = 0.1 \tag{21}$$

where α = ionization rate = $Ae^{-(b/E)^m}$.

For GaAs: $A = 3.85 \times 10^5/cm.$, $b = 6.85 \times 10^5 V/cm$ and $m = 2$

$$\therefore \quad Ae^{-(b/E_D)^2} \, x_D = 0.1 \tag{22}$$

and

$$E_D = \frac{b}{\left[ln\left(\frac{Ax_D}{0.1}\right)\right]^{1/2}} \quad . \tag{23}$$

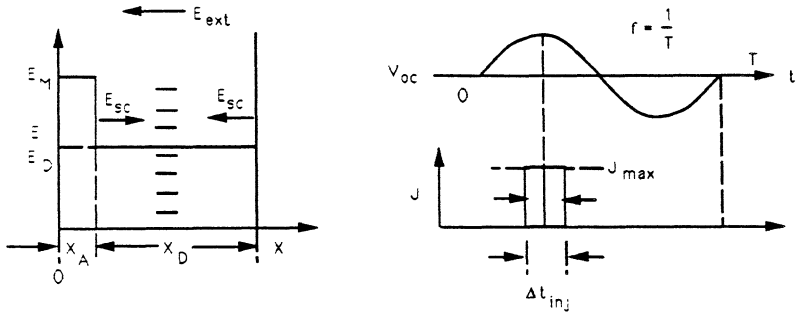

Figure 12 Electric Field and Injected Current Pulse for Estimating J_{dc}

Assuming $E_s = 3 \times 10^3$ V/cm. and an effective velocity $v_s = 10^7$ cm/sec. we then have the parameters shown in Table I for devices operating at different frequencies.

Next we estimate J_{dc} by considering space charge effects as shown in fig. 12. Assume $\Delta t_{inj} = R_{inj}T$ where R is a constant fraction $= \Theta w/2\pi$.
The total charge in the drift region $= AJ_{max}\Delta t_{inj}$

$$= qA\int_0^{x_D} n(x')\,dx' \tag{24}$$

$$\frac{dE_{sc}}{dx} = \rho/\epsilon = \frac{-qn(x)}{\epsilon}$$

$$\Delta E(x) = E(x) - E(o) = \frac{-q}{\epsilon}\int_0^x n(x')dx' \tag{25}$$

$$\Delta E = \Delta E(x_D) = E(x_D) - E(o) = \frac{-q}{\epsilon}\int_0^{x_D} n(x')dx' = \frac{-q}{\epsilon}\left[\frac{J_{max}\Delta t_{inj}}{q}\right] \tag{26}$$

$$|\Delta E| = \frac{J_{max}R_{inj}T}{\epsilon} \leq E_D \tag{27}$$

$$J_{DC} = \frac{J_{max}\Delta t_{inj}}{T} = J_{max}R_{inj}$$

$$\therefore J_{DC} \leq \epsilon\, E_D\, f \quad . \tag{28}$$

From an estimate of V_{dc}, V_{RF} and J_{dc}, the equations given above can be employed in a straightforward manner to estimate the R.F. power which can be expected from such devices.

We will first assume that $R_s + R_L = 1\Omega$, which is unrealistic but serves as a good reference for other more realistic cases. The pertinent parameters for this case are shown in Table II.

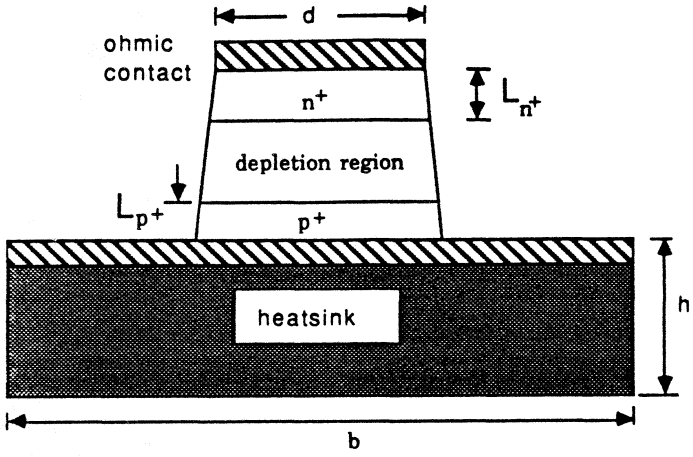

Figure 13 Mesa Diode Structure

The series resistance represents power loss and is extremely important for these devices. Figure 13 is a cross-sectional view of a mesa diode. The total positive resistance, R_s, associated with the mesa diode is given by [10]

$$R_s(f) = \frac{\rho_c + \rho_e L_e}{A} + \frac{\rho_s}{\pi\sigma}[0.5 \ln (b/d) + h/b] \quad . \tag{29}$$

Where,

ρ_c is the specific contact resistance in $\Omega - cm^2$ (1×10^7)
ρ_e is epilayer resistivity in ohms-cm ($\rho_n = 0.00037$, $\rho_p = 0.0015$)
ρ_s is the resistivity of the heatsink (gold) in ohms-cm (0.00024)
L_e is the length of the undepleted epilayers ($L_{n^+} = 0.5\mu$m, $L_{p^+} = 0.1\mu$m)
A is the area of the diode
σ is the skin depth given by $\sqrt{\frac{2\rho_s}{\mu\,\omega}}$
b is the length of the chip (0.02 cm)
h is the height of the substrate or heatsink (0.005 cm)
d is the diode diameter.

The series resistance is given in Table III. Taking into account the series resistance, the amount of useful power delivered to R_L is reduced. The results for different diameter devices at the center frequencies of 100, 500 and 1,000 GHz are shown in Tables IV, V and VI respectively.

Another important parameter for cw operation is the thermal resistance which is approximately given by

$$R_{th} = \frac{2}{\pi K_{hs} d} + \frac{4L}{\pi d^2 K_{sc}} \tag{30}$$

where,

K_{hs} : Thermal conductivity of the heatsink in $W/\text{cm}\ ^\circ\text{K}$ (3.9 for Cu and 11.7 for diamond)

K_{sc} : Thermal conductivity of the semiconductor in $W/\text{cm}\ ^\circ\text{K}$ (0.3 for GaAs)

L_{p+} : The distance from the junction to the heatsink in cm (0.1 μm)

d : is the diode diameter in cm.

The thermal resistance is given in Table VII for different diameters and heat sinks.

From the thermal resistance values given in Table VII, we can estimate the temperature rise in the device for various operating conditions and device diameters. This is done in Table VIII. It can be seen from this table that the diameters chosen for the 100 and 500 GHz operation result in a temperature rise of less than 225°K which is a safe value. However, for 1,000 GHz a diamond heatsink is required to remain below the 225°K temperature rise. Therefore, for this case, $J_{d.c.}$ must be reduced for a copper heatsink. For example for a 4 μm-diameter device $\Delta T = 363^\circ$K. In order to limit ΔT to 225°K and maintain the same load impedance, we can reduce $J_{d.c.}$ by a factor of 0.62. This will reduce the R.F. power by a factor of 0.38 and thus result in an output power of 2.8 mw which is still significant.

5. Conclusions

Preliminary estimates of the power generation capability of TUNNETT devices in the 100–1,000 GHZ range are promising. It is believed that an output power of 1 mw at one terahertz is feasible.

Acknowledgement: The authors are grateful to R. Mains and I. Mehdi for their contributions to this work.

REFERENCES

[1] R. K. Mains and G. I. Haddad, "Properties and Capabilites of Millimeter-Wave IMPATT Diodes," *Infrared and Millimeter-Waves*, K. J. Button (Ed.), vol. 10, Part III, Chap. 3, Academic Press, Inc., New York, 1963.

[2] R. K. Mains, G. I. Haddad, and P. A. Blakey, "Simulation of GaAs IMPATT Diodes Including Energy and Velocity Transport Equations," *IEEE Trans. on Electron Devices*, vol. Ed-30, No. 10, pp. 1327–1338, October 1983.

[3] M. El-Gabaly, G. I. Haddad, and R. K. Mains, "Effect of Doping Profile Variation on GaAs Hybrid and Double-Read IMPATT Diode Performance at 60 and 94 GHz," *IEEE Trans. on Microwave Theory and Techniques*, vol. MTT-32, No. 10, pp. 1342–1352, October 1984.

[4] J. Nishizawa, K. Mofoya, and Y. Okuno, "GaAs TUNNETT Diodes," *IEEE Trans. on Microwave Theory and Techniques*, vol. MTT-20, No. 12, pp. 1029–1035, December 1978.

[5] M. Elta and G. I. Haddad, "High-Frequency Limitations of IMPATT, MITATT, and TUNNETT Mode Devices," (Invited Paper) *IEEE Trans. on Microwave Theory and Techniques*, vol. MTT-27, No. 5, pp. 442–449, May 1979.

[6] M. E. Elta, H. R. Fetterman, W. V. Macropoulas, and J. J. Lambert, "150 GHz GaAs MITATT Source," *IEEE Electron Device Letters*, vol. EDL-1, No. 6, pp. 115–116, June 1980.

[7] N. S. Dogan, J. R. East, M. E. Elta, and G. I. Haddad, "Millimeter-Wave Heterojunction MITATT Diodes," *IEEE Trans. on Microwave Theory and Techniques*, vol. MTT-35, No. 12, pp. 1308–1317, December 1987.

[8] T.C.L.G. Sollner, E. R. Brown, W. D. Goodhue, and H. Q. Le, "Observation of millimeter-wave tunneling diodes and some theoretical considerations of ultimate frequency limits," *Appl. Phys. Lett.*, vol. 50, No. 6, pp. 332–334, February 1987.

[9] V. P. Kesan, D. P. Neikirk, B. G. Streetman, and P. A. Blakey, "A New Transit-Time Device Using Quantum-Well Injection," *IEEE Electron Device Letters*, vol. EDL-8, No. 4, pp. 129–131, April 1987.

[10] L. E. Dickens, "Spreading Resistance as a Function of Frequency," *IEEE Trans. on MTT*, vol. MTT-15, No. 2, pp. 101–109, February 1967.

TABLES

Table I. Important Device Parmeters for Different Center Frequencies

f(GHz)	$x_D(\mu m)$	$E_D(V/cm)$	$V_{dc}(V)$	$V_{RF}(V)$	V_{RF}/V_{dc}
100	0.75	2.1×10^5	17.4	15.7	0.90
500	0.15	4.13×10^5	7.8	6.5	0.84
1000	0.075	6.6×10^5	6.5	5.5	0.83

Table II. Estimated $P_{RF}(Gen.)$ and Other Operating Parameters for a 1-Ω Reference ($R_s + R_L = 1\Omega$)

f(GHz)	$V_{dc}(V)$	$V_{RF}(V)$	$J_{dc}(A/cm^2)$	$G_D\left(\frac{mho}{cm^2}\right)$	$B_D\left(\frac{mho}{cm^2}\right)$	A (cm^2)	$D(\mu m)$
100	17.4	15.7	22.3×10^3	0.6×10^3	8.2×10^3	8.87×10^{-6}	34
500	7.8	6.5	2.2×10^5	1.4×10^4	1.9×10^5	3.9×10^{-7}	7
1000	6.6	5.5	7×10^5	5.4×10^4	7.3×10^5	1.0×10^{-7}	3.6

f	I_{dc}(ma)	P_{dc}(W)	η (%)	$P_{RF}(Gen.)$T(mW)
100	198	3.44	19	650
500	85.8	0.67	18	120
1000	70	0.46	17.5	80

Table III. Series Resistance of Mesa Diode

diameter	diode series resistance (Ω) at		
μm	100 GHz	500 GHz	1000 GHz
1	13.6	14.6	15.4
2	3.9	4.8	5.5
3	2.0	2.9	3.5
4	1.4	2.2	2.7
5	1.1	1.8	2.3
7	0.79	1.4	1.9
10	0.60	1.2	1.6
15	0.46	0.96	1.3
20	0.39	0.84	1.2
25	0.35	0.75	1.0
30	0.31	0.68	0.95

Table IV. Estimated Power Output Including R_s
$f = 100$ GHZ
$J_{dc} = 22.3 \times 10^3 A/cm^2$; $V_{dc} = 17.4V$; $V_{RF} = 15.7V$

Diode Diam. (μm)	Area (cm^{-2})	$R_s(\Omega)$	$-R_d(\Omega)$	$R_L(\Omega)$	$I_{dc}(ma)$	P_{dc}(w)	P_{RF} (Gen.) (mw)	P_{RL} (R_L) (mw)	$\eta\%$
20	2.9×10^{-6}	0.39	3	2.61	66	1.15	217	189	16.4
25	4.5×10^{-6}	0.35	2.4	2	100	1.75	271	225	13
30	6.5×10^{-6}	0.31	2	1.69	145	2.52	325	275	11
30	6.5×10^{-6}	1	2	1	145	2.52	325	162	6.4

Table V. Estimated Power Output Including R_s
$f = 500$ GHz
$J_{dc} = 2.2 \times 10^5 A/cm^2$; $V_{dc} = 7.8V$; $V_{RF} = 6.5V$

Diode Diam. (μm)	Area (cm^{-2})	$R_s(\Omega)$	$-R_d(\Omega)$	$R_L(\Omega)$	I_{dc}(ma)	P_{dc}(mw)	P_{RF} (Gen.) (mw)	P_{RL} (R_L) (mw)	η%
4	1.16×10^{-7}	2.2	3.36	1.16	25.5	200	35	12	6
5	1.8×10^{-7}	1.8	2.16	0.36	39.6	309	55	9.2	3
7	3.9×10^{-7}	1.4	1	–	–	–	–	–	–

will operate at a lower V_{RF}

Diode Diam. (μm)	Area (cm^{-2})	$R_s(\Omega)$	$R_L(\Omega)$	$-R_d(\Omega)$	$V_{RF}(V)$	I_{dc}(ma)	P_{dc}(mw)	P_{RF} (Gen.) (mw)	P_{RL} (R_L) (mw)	η%
4	1.16×10^{-7}	2.2	2.2	4.4	4.96	25.5	200	27	13.5	6.75
5	1.8×10^{-7}	1.8	1.8	3.6	3.9	39.6	309	33	16.5	5.3
7	3.9×10^{-7}	1.4	1.4	2.8	2.32	86	670	42.3	21	3
10	7.2×10^{-7}	1.2	1.2	2.4	1.46	158.4	1,235	49	24.5	2

Table VI. Estimated Power Output Including R_s
$f = 1000$ GHz
$J_{dc} = 7 \times 10^5 A/cm^2$; $V_{dc} = 6.6V$

(Because of series resistance, the device cannot oscillate at $V_{RF} = 5.5V$s where maximum η is obtained, but will oscillate at a lower V_{RF})

Diode Diam. (μm)	Area (cm^{-2})	$R_s(\Omega)$	$R_L(\Omega)$	$-R_d(\Omega)$	$V_{RF}(V)$	I_{dc}(ma)	P_{dc}(w)	P_{RF} (Gen.) (mw)	P_{RL} (R_L) (mw)	$\eta\%$
4	1.16×10^{-7}	2.7	2.7	5.4	0.88	81	535	15	7 .5	1.4
5	1.8×10^{-7}	2.3	2.3	4.6	0.66	126	832	17.6	8.8	1
7	3.9×10^{-7}	1.9	1.9	3.8	3.7	273	1,800	21	10.5	.5

Table VII. Thermal Resistance of a Mesa Diode

Diameter	R_{th} = Diode Thermal Resistance (10^2 °K/W)	
μm	Copper heatsink	Diamond heatsink
1	58.7	47.9
2	18.8	13.3
3	10.2	6.53
4	6.73	4.01
5	4.96	2.79
7	3.20	1.64
10	2.06	0.97
15	1.28	.055
20	0.92	0.38
25	0.72	0.29
30	0.59	0.23

Table VIII. Estimated CW Power

f(GHz)	Diode Diam. (μm)	$P_{dc}(w)$	$R_{th}(°/w)$ Cu	$R_{th}(°/w)$ Diamond	$\Delta T(°K)$ Cu	$\Delta T(°K)$ Diamond	$P_{RF}(mw)$
100	20	1.15	92	38	106	48	189
	25	1.75	72	29	126	51	225
	30	2.52	59	23	150	58	275
500	5	0.31	496	278	154	86	16.5
	7	0.67	320	164	214	110	21
	10	1.24	205	97	254	120	24.5
1000	4	0.54	673	401	363	216	7.5
	5	0.83	496	278	411	230	8.8
	7	1.8	320	164	576	295	10.5

WATT-LEVEL QUASI-OPTICAL MONOLITHIC FREQUENCY MULTIPLIER DEVELOPMENT

R. J. Hwu, N. C. Luhmann, Jr., L. Sjogren, X. H. Qin, W. Wu
Department of Electrical Engineering
University of California, Los Angeles
Los Angeles, California 90024

D. B. Rutledge
Division of Engineering and Applied Science
California Institute of Technology

B. Hancock, J. Maserjian, U. Lieneweg
JPL

W. Lam
TRW

C. Jou
Chiao-Tung University

ABSTRACT

Sources of millimeter wavelength power for heterodyne receiver local oscillator applications conventionally have been expensive and short-lived klystrons, or Gunn devices (both of which are limited to relatively low frequencies). An alternate approach is to use efficient, broad band frequency multipliers in conjunction with more reliable, lower frequency oscillators to provide power. To obtain sufficient power for large receiver arrays we have employed quasi-optical arrays of devices which have been fabricated monolithically. Multipliers devices under investigation include both varactor diodes and negative resistance devices.

This work has been supported by TRW under the California MICRO Program, the Army Research Office and the Caltech President's Fund.

INTRODUCTION

Increased interest in the millimeter region has stimulated the development of receiver technology for a wide range of applications including radio astronomy[1], atmospheric radiometry[2], plasma diagnostics[3], millimeter wave imaging[4], nondestructive testing[5], radar[6], and high density, high directivity communications and data transmission[7].

The realization of a simple tunable local oscillator (LO) source, with adequate output power for use in Schottky diode mixer receiver systems at millimeter wavelengths presents a difficult problem. The traditional choice at longer wavelengths has been the reflex klystron. However, its highest operation frequency is limited to about 220 GHz with less than 10 mW output and it possesses limited tunability. In addition, the cost, today, of a tube, power supply and cooler is about thirty five thousand dollars[8]. Conventional high-frequency 0-type carcinotrons or vane type backward-wave oscillators (BWOs) have been successfully developed at frequencies up to 1 THz[9]. However, BWOs are noisy and therefore require sophisticated phase lock systems. In addition, they are expensive ($\succ$ \$100 k for tube and high voltage supply), and the lifetime is only about one or two thousand hours. Furthermore, the output power is only about 50 mW at 400 GHz dropping to about 1 mW at 1 THz[9]. These problems may be eliminated with the development of planar interdigital slow wave circuit BWOs currently under way at NASA Lewis.

A solid state solution to the LO problem would be highly desirable since it can be expected to be low cost, compact and light weight, and to possess excellent reli-

ability. Since the power of these solid-state sources falls off dramatically at higher frequencies, the combination of a high-power low-frequency source with a harmonic multiplier is an attractive alternative. The use of a frequency multiplier allows one to take advantage of the more favorable characteristics of low frequency sources: lower noise, larger tuning range, lower cost, and improved reliability. Current single Schottky diode multipliers are highly developed, and have achieved impressive conversion efficiency. Considerable effort has been made to combine the output power of these single multipliers.

Although multipliers with one or two diodes have been highly developed, they are basically limited to output power levels of milliwatts at frequencies of $\simeq$ 200 GHz with the power falling off dramatically at 1 THz. However, many applications call for significantly more power. For example, there is currently interest in developing focal-plane imaging arrays for radio astronomy and plasma diagnostics[11]. These arrays might contain from 10-100 Schottky diodes[10], and would require a total local oscillator power ranging from 100 mW to 1 W. Other applications in radar, and high order multiplier chains[12] also require higher power.

The major task of the present work is the development of quasi-optical millimeter-wave monolithic planar multiplier arrays for watt-level frequency multipliers[13,14]. This is an attractive approach to combine the power of each device by using monolithic integrated circuit techniques, thereby resulting in potentially low cost fabrication and small-size realization. Such a circuit has the inherent property of having a large number of identical devices which may then be combined to increase output power. Low-loss quasi-optical structures are used for filtering, matching, and terminating the

multiplier circuit, because waveguide, stripline or coaxial structure become lossy and extremely difficult and expensive to fabricate as the frequency is increased beyond 100 GHz. In addition, the quasi-optical structures are eminently suited to LO applications in millimeter and submillimeter systems in which quasi-optical diplexing structures are commonly employed. The resulting array satisfies the need for a compact, low-cost, low-loss local oscillator for large heterodyne detector arrays.

WATT-LEVEL QUASI-OPTICAL MONOLITHIC FREQUENCY MULTIPLIERS

1. Schottky Diode-Grid Doubler Array

Monolithic Schottky diode grids have been fabricated on 4 cm^2 GaAs wafers in a proof-of-principle test of a quasi-optical varactor millimeter wave frequency multiplier array concept[13] (see Figs. 1 and 2). Efficiencies of 9.5% and output power levels of 0.5 W were achieved at 66 GHz when the diode grid was pumped with a pulsed source at 33 GHz. Furthermore, the diode-grid equivalent circuit model based on a transmission line analysis of plane wave illumination has been verified experimentally over a frequency range from 33 GHz to 140 GHz[14]. The equivalent circuit model together with a large-signal multiplier analysis of the nonlinear varactor impedances were used to predict the doubler performance and to facilitate detailed comparison between theory and experiment.

Excellent agreement was found between experiment and theory for a number of diode grids with a ratio of pump to cutoff frequencies ranging from 0.1 to 0.32. The

major limitations to the proof-of-principle diode grid arrays were the low diode breakdown voltage ($\approx$ -3 V) and the high diode series resistance (= 25 Ω - 50 Ω). Currently, we are beginning fabrication of Schottky diode doubler arrays with increased voltage and decreased series resistance.

2. Silicon MOS Diode Doubler

In parallel with the GaAs Schottky diode doubler array studies, we investigated the use of a MOS structure having an undoped epitaxial layer, which is grown on a heavily doped substrate and isolated by a thin oxide layer (see Fig. 3). The space-charge-limited current which is injected into the epilayer from the heavily doped substrate produces a step-like capacitance-voltage characteristic resulting in increased harmonic generation efficiency (see Fig. 4). The thin MOS concept was tested by fabricating honeycomb arrays which were mounted in crossed waveguide mounts and whisker contacted. The experimental results show good agreement with the theoretical predictions[15,16] and the large-signal multiplier analysis. A maximum efficiency of 17% was predicted for the $3\mu m$ radius device which is in good agreement with the 14.7% obtained experimentally.

Another important feature of these devices is that, due to the blocking barrier, two diodes can be operated back-to-back generating a sharp spike in the capacitance-voltage curve. The height and width of this capacitance-voltage characteristic can, in principle, be adjusted by doping control alone thus eliminating the need for an external dc bias. This arrangement needs no external ohmic contact resulting in a highly efficient frequency tripler. However, defects in the epitaxial silicon layer deteriorated

the thin oxide and limited the yield of the devices making array construction difficult.

3. Barrier-Intrinsic-N^+ Diode-Grid Tripler Array

Device Concept

Recently, a GaAs barrier-intrinsic-N^+ (BIN) diode has been developed[17] as shown in Fig. 5. This structure has an aluminum metal gate in intimate contact with a layered GaAs structure consisting of a 300 $\AA$ thickness of undoped GaAs, a 100 $\AA$ thickness of $2 \times 10^{18}\, cm^{-3}$ heavily doped n^+ GaAs, another 1000 $\AA$ thickness of undoped GaAs, and a 3 μm thick $6 \times 10^{18}\, cm^{-3}$ heavily doped n^+ GaAs region grown on top of a semi-insulating GaAs substrate. The GaAs BIN diode eliminates the problem of low fabrication yield associated with the thin MOS structure and takes advantage of the higher mobility of GaAs. It does not require an insulator layer as in the thin MOS structure, but instead relies on a Mott-type barrier formed between the metal gate and a sheet of positive charge created by a thin (100 $\AA$) heavily doped n^+ region in the GaAs. The 3 μm thick layer is required to reduce the series resistance. The active region is the intrinsic layer between the Mott barrier and the 3 μm heavily doped ($6 \times 10^{18}\, cm^{-3}$) electron injection zone. An intrinsic cut-off frequency of 960 GHz can be achieved. A tripling efficiency of 35% at an output frequency of 100 GHz is predicted (as seen in Fig. 1) [15,16].

In summary, the advantages of the BIN diode over the Schottky diode are seen in (1) the stronger nonlinearity of the C-V curve, which generates harmonics more efficiently (especially the third harmonic without using an idler) and (2) the ability to reach a high capacitance state before forward conduction sets in, making possible

the capacitive tripler[18,19].

Metal Grid Design

The metal grid employed for the BIN diode tripler consists of a columnar mesh of aluminum strips with Schottky electrodes on each end as shown in Fig. 6. The period of the grid is chosen to be about half the dielectric wavelength to avoid exciting substrate modes. A reasonable grid inductance is then achieved by choosing a strip width of 20 μm. The small dimension and rectangular shape of the Schottky electrode are designed to minimize the zero-voltage capacitance and series resistance of the device, respectively. This arrangement leads to a high cut-off frequency of the BIN diode. The two neighboring Schottky barrier electrodes are designed to provide the back-to-back configuration for two BIN diodes. The design requires only one metal pattern, which greatly facilitates the case of fabrication.

The initial BIN diode structure was grown with a 1500 $\AA$ epitaxial layer using a conservative fabrication design with relatively large dimensions ($\sim 2 \times 5\ \mu m$ diode area). This gives an intrinsic cut-off frequency of $\approx$ 600 GHz. The experimentally measured C-V curve is shown in Fig. 7. Figure 8 shows the symmetric capacitance-voltage characteristic measured from the back-to-back configuration of two BIN diodes. This measurement demonstrates the concept of tripling operation with two back-to-back connected BIN diodes. As can be seen from this figure, the capacitance measured from two diodes under a back-to-back configuration, which is only half of that from a single diode, again, proves the back-to-back configuration employed should result in efficient tripling operation.

Device Performance

A quasi-optical diode-grid tripler coupling and filter circuit design has also been developed as shown in Fig. 9, where power at the fundamental frequency enters from the bottom, through an input tuner. The blazed grating plate (which functions as a high-pass transmission filter) reflects the incident pump power at the fundamental frequency to the diode grid on the left of it, and the metal mirror behind the diode grid again reflects all the harmonics back to the grating plate. Different harmonics are then diffracted in different directions. The third harmonic is designed to exit in the desired direction passing through an output tuner. One should remember that due to the symmetric capacitance-voltage characteristic of two back-to-back connected GaAs BIN diodes, even harmonic currents cancel; therefore even harmonic idler circuits are unnecessary.

It should also be mentioned that the projected cut-off frequency of the experimental device is determined to be 600 GHz with the calculated series resistance of 35 Ω. A maximum tripling efficiency of 24% at an output frequency of 99 GHz is predicted for this GaAs BIN array that has recently been fabricated. Using the quasi-optical diode-grid tripler configuration, watt level output at 99 GHz with an efficiency 8.5% has been experimentally achieved from a total of approximately 6000 BIN diodes on the 15 cm^2 wafer. This experimental measurement is in good agreement with the theoretical prediction.

Large – Signal Multiplier Analysis Results

From the large-signal multiplier analysis study, using the measured capacitance-

voltage data of two back-to-back connected BIN diodes, the tripling efficiency versus the input power level at various input frequencies is shown in Fig. 10. Both input and output tuning were optimized at each frequency. As also shown in Fig. 10, the efficiency is highest with low input power levels (5-10 mW). Over the output frequency range of 99-120 GHz, an efficiency greater than 20% is predicted for the GaAs BIN array which has recently been fabricated. The highest efficiency is 24% at 99 GHz obtained with an input power of 9.0 mW, which shows excellent agreement with the theoretical predictions[15,16].

Substantial improvements are possible for the performance of the BIN diode. Figure 11 shows the simulated tripling efficiency results as a function of the series resistance. The input and output impedances are the optimized values. The simulated results are in excellent agreement with the theoretical values predicted in standard references[15,16]. The simulation predicts 35% tripling efficiency for $R_a = 15\ \Omega$.

SUMMARY AND CONCLUSIONS

The submillimeter or terahertz wavelength region (300 GHz to 3 THz) is one of the last major windows in the electromagnetic spectrum to be explored. Its major application has been scientific research including astrophysics, atmospheric physics, plasma diagnostics,and laboratory spectroscopy. More recently, space-based radar and communications systems are emploring this spectral range to combine the frequency resolution and agility available in the microwave regime with the high spatial resolution of modest apertures typical of optical technology. Various methods have

been proposed for generating submillimeter wave radiation using solid-state devices. The most probable solution, however, will be based on harmonic multiplication of lower frequency solid-state sources. This is due to the fact that the technology for both the low-frequency fundamental sources as well as that of frequency multipliers are fairly mature. Arrays of devices to increase power handling are also required to increase power. Quasi-optical monolithic solid-state diode-grid frequency multipliers are, therefore, highly desirable for generating submillimeter or terahertz wavelength radiation. Based on the studies of watt-level solid-state frequency multiplier arrays, prospectives of two-stage monolithic frequency tripler arrays are shown in Fig. 11 for obtaining watt-level submillimeter or Terahertz wavelength power.

ACKNOWLEDGMENTS

Work supported by U.S. ARO, California MICRO and the Cal Tech Presidents Fund.

REFERENCES

(1) H.I. Cong, A.R. Kerr and R.J. Mattauch, IEEE Trans. on Microwave theory and Tech., MTT-27, No. 3, pp. 245-248, 1987.

(2) J.W. Waters, Journal of Geophysical Research, Vol. 84, c11, pp. 7034-7040, 1979.

(3) Luhmann, N.C. Jr., Peebles, W.A. "Laser Diagnostics of Magnetically Confined Thermonuclear Plasmas," Chapter 5 in the Laser Handbook,Vol. 5 edited by M.L. Stitch and M. Bass, North Holland-Physics Publishing (Amsterdam) pp. 455-636 (1985); and Brower, D.L., Park, H.K., Peebles, W.A., Luhmann, N.C.Jr. "Multichannel Far-Infrared Collective Scattering System for Plasma Wave Studies," an invited Chapter in the Academic Press (New York) series on Topics in Millimeter Wave Guided Propagation, Volume II, Chapter 3, Pgs. 83-172, ed. by K.J. Button, April, 1988.

(4) T.S. Hartwick, D.T. Hodges, D.H. Barker and T.B. Foote, Appl. Opt., Vol. 15, p. 1919, 1976.

(5) P.K. Cheo, 7th Int'l Conf. on Infrared and Millimeter Waves, p. w3-1, 1983.

(6) E.K. Reedy and W. Emell, Infrared and Millimeter Waves, Vol. 4, Chap. 2, Academic Press, Inc., New York, 1982.

(7) K. Mlyanchi, Infrared and Millimeter Waves, Chap. 1, Academic Press, Inc., New York, 1983.

(8) Varian of Canada Catalog #3478, Klystron Oscillator and BWO catalog, 1976.

(9) G. Kantorowicz, P. Palluel, Infrared and Millimeter Waves, Vol. 1, Chap. 4, Academic Press, Inc, New York, 1979.

(10) C.E. Zah, W.W. Lam, J.S. Smith, and Z. Rav-Noy, 9th Int'l Conf. on Infrared and Millimeter Waves, 1984.

(11) P.E. Young, D.P. Neikirk, P.P. Tong, and N.C. Luhmann, Jr., Rev. Sci. instrum., Vol. 56, pp. 81-89, 1985.

(12) J.W. Archer, IEEE Trans. on Microwave Theory and Tech., MTT-33, No. 6, pp.533-538, 1985.

(13) C.F. Jou, W.W. Lam, H. Chen, K. Stolt, N.C. Luhmann, Jr., and D.B. Rutledge, "Millimeter-Wave Monolithic Schottky Diode-Grid Frequency Doublers," IEEE Trans. on Microwave Theory and Tech., MTT-36, No. 11, pp. 1507-1514, 1988.

(14) W.W. Lam, C.F. Jou, H. Chen, K. Stolt, N.C. Luhmann, Jr., and D.B. Rutledge, "Millimeter-Wave Monolithic Schottky Diode-Grid Phase Shifters," IEEE Trans. on Microwave Theory and Tech., MTT-36, No. 5, pp. 902-907, 1987.

(15) R.P. Rafuse and D.H. Steinbrecher, "Harmonic Multiplication with Punch-Through Varactors," Int'l Solid-State Circuit Conf., Tech. Dig., pp. 68-69, 1966.

(16) K. Schunemann and B. Schiek, "Optimal Efficiency of Charge-Storage Multipliers II," A.E.U. 22, 293-302, 1968.

(17) Lieneweg, B.R. Hancock, and J. Maserjian, "Barrier-Intrinsic-N^+ (BIN). Diodes for Near-Millimeter Wave Generation," 12th Intl. conf. Infrared and Millimeter Waves, Tech. Dig., pp. 6-7, 1987.

(18) R.J. Hwu, L.P. Sadwick, N.C. Luhmann, Jr., D.B. Rutledge, and M. Sokolich, "Quasi- Optical Watt-Level Monolithic diode-Grid Frequency Tripler Arrays in the Millimeter- Wave Region," 1989 IEEE International MTT-S International Microwave Symposium, Long Beach, California, June 13-15, 1989.

(19) R.J. Hwu, L.P. Sadwick, N.C. Luhmann, Jr., and D.B. Rutledge, "DC and Millimeter- Wave Performance of Watt-Level Barrier- Intrinsic-N^+ Diode-Grid Frequency Multiplier Fabricated on III-V Compound Semiconductor," 1988 International Electron Device Meeting, San Francisco, California, December 11-14, 1988.

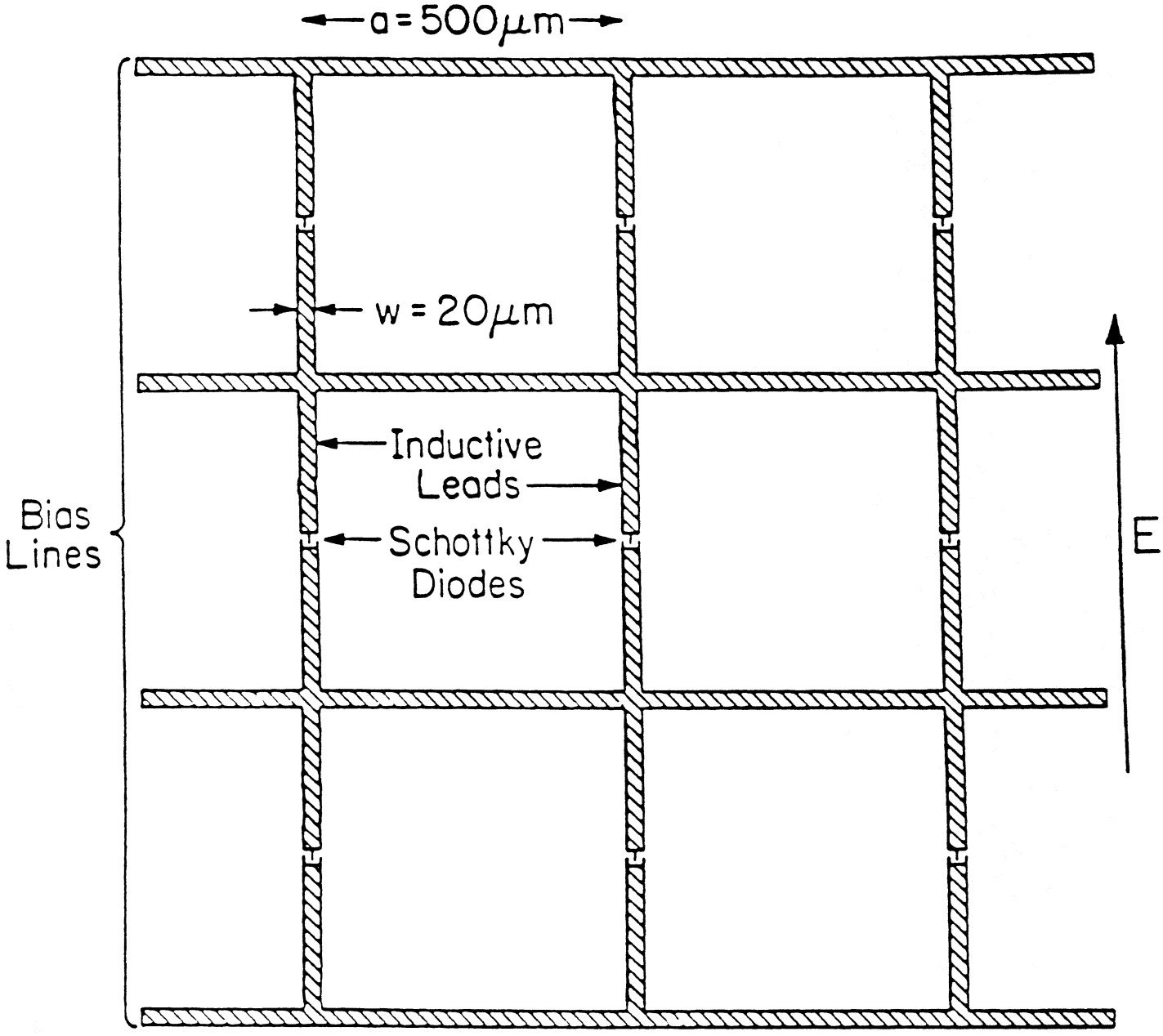

Figure 1. Metal grid design for Schottky diode doubler.

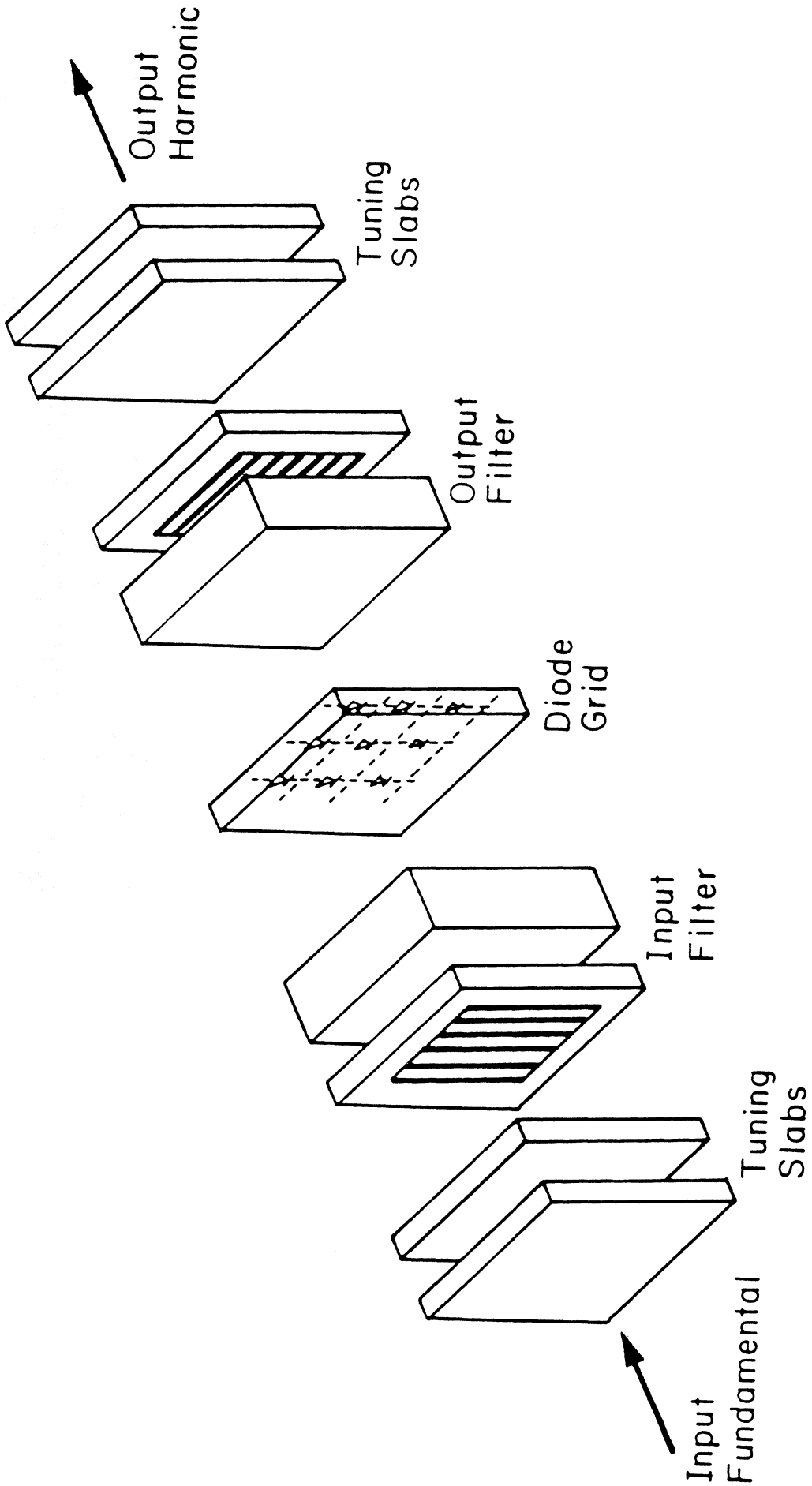

Figure 2. Quasi-optical diode-grid doubler configuration.

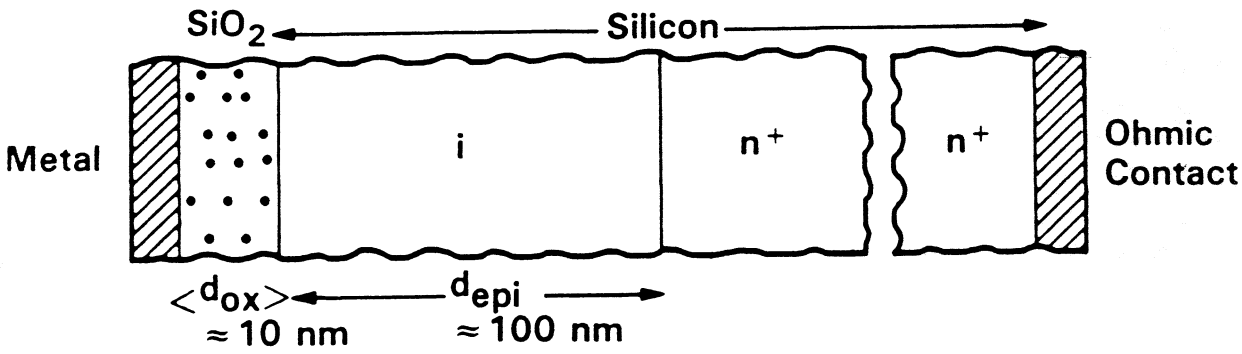

Figure 3. Structure of the thin MOS diode.

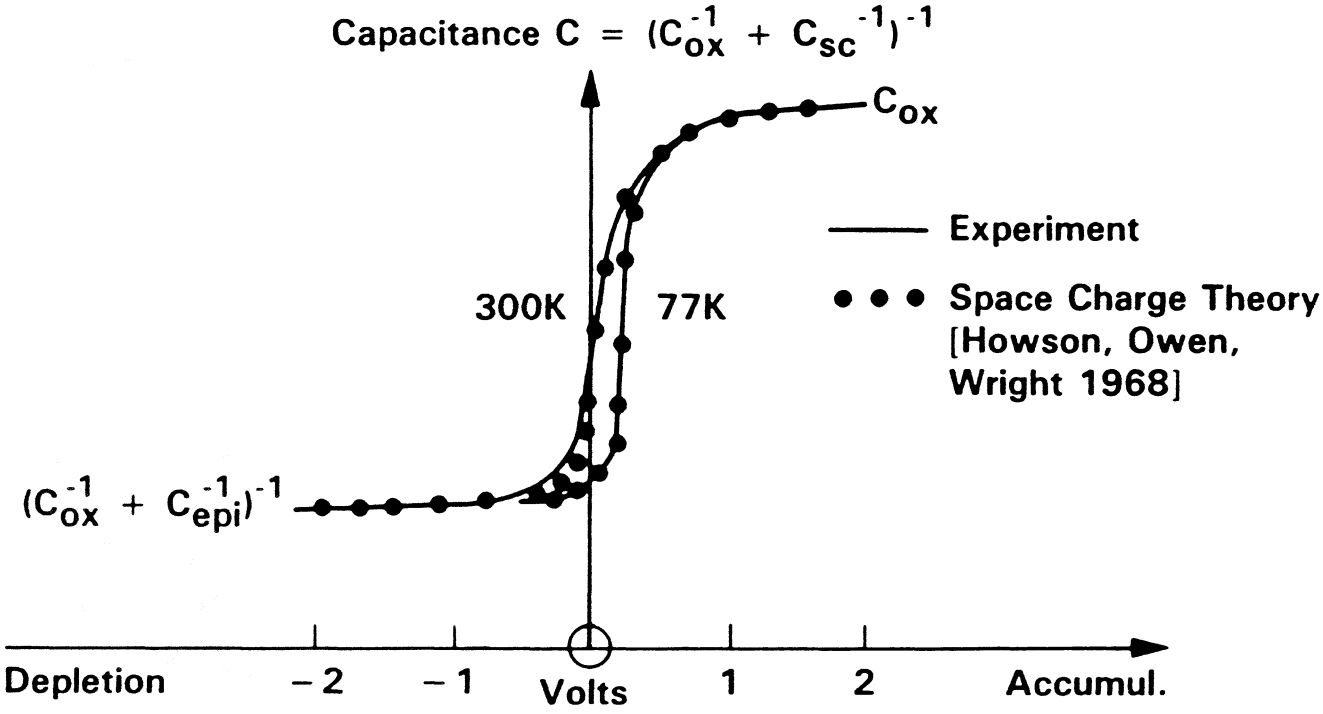

Figure 4. Capacitance-voltage characteristic from the thin MOS diode.

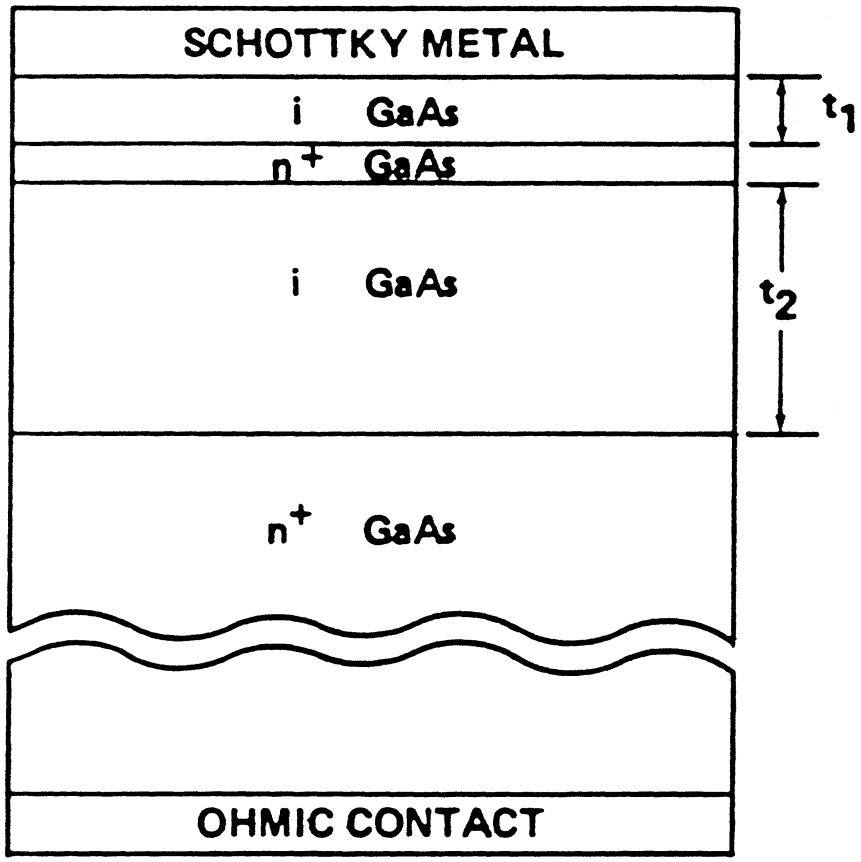

Figure 5. Structure of the GaAs BIN diode.

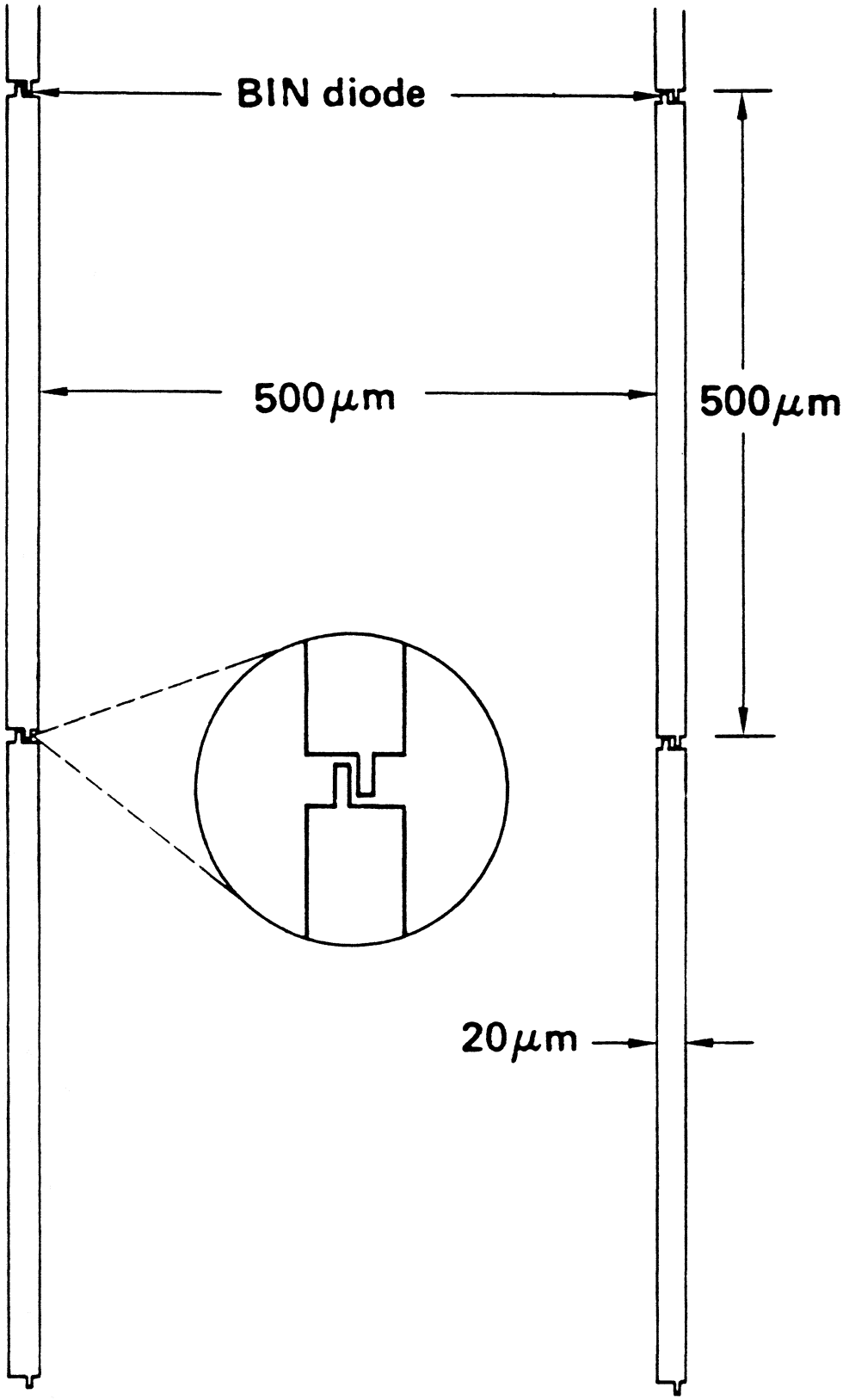

Figure 6. Metal grid design for BIN diode tripler.

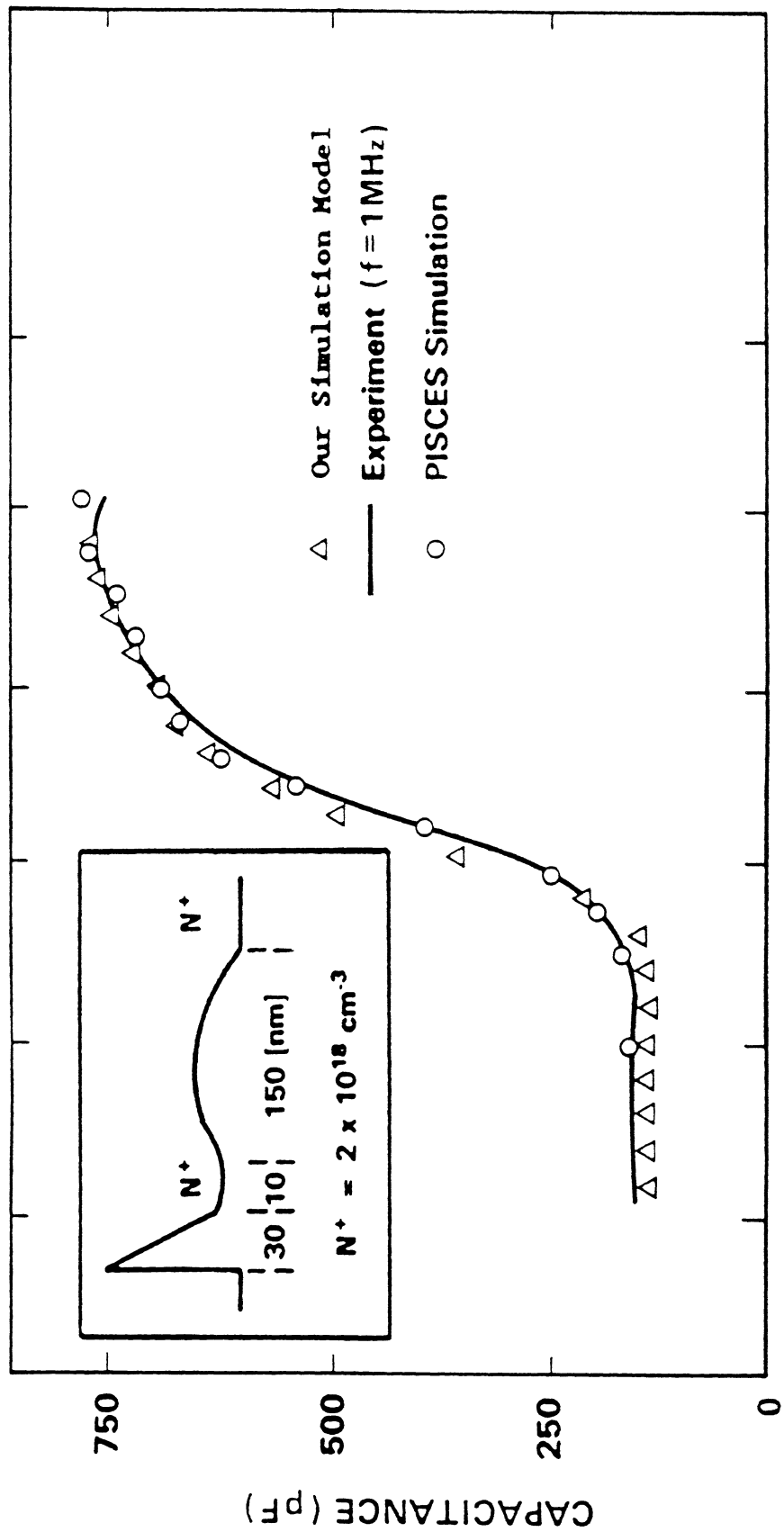

Figure 7. Capacitance-voltage characteristic from the GaAs BIN diode.

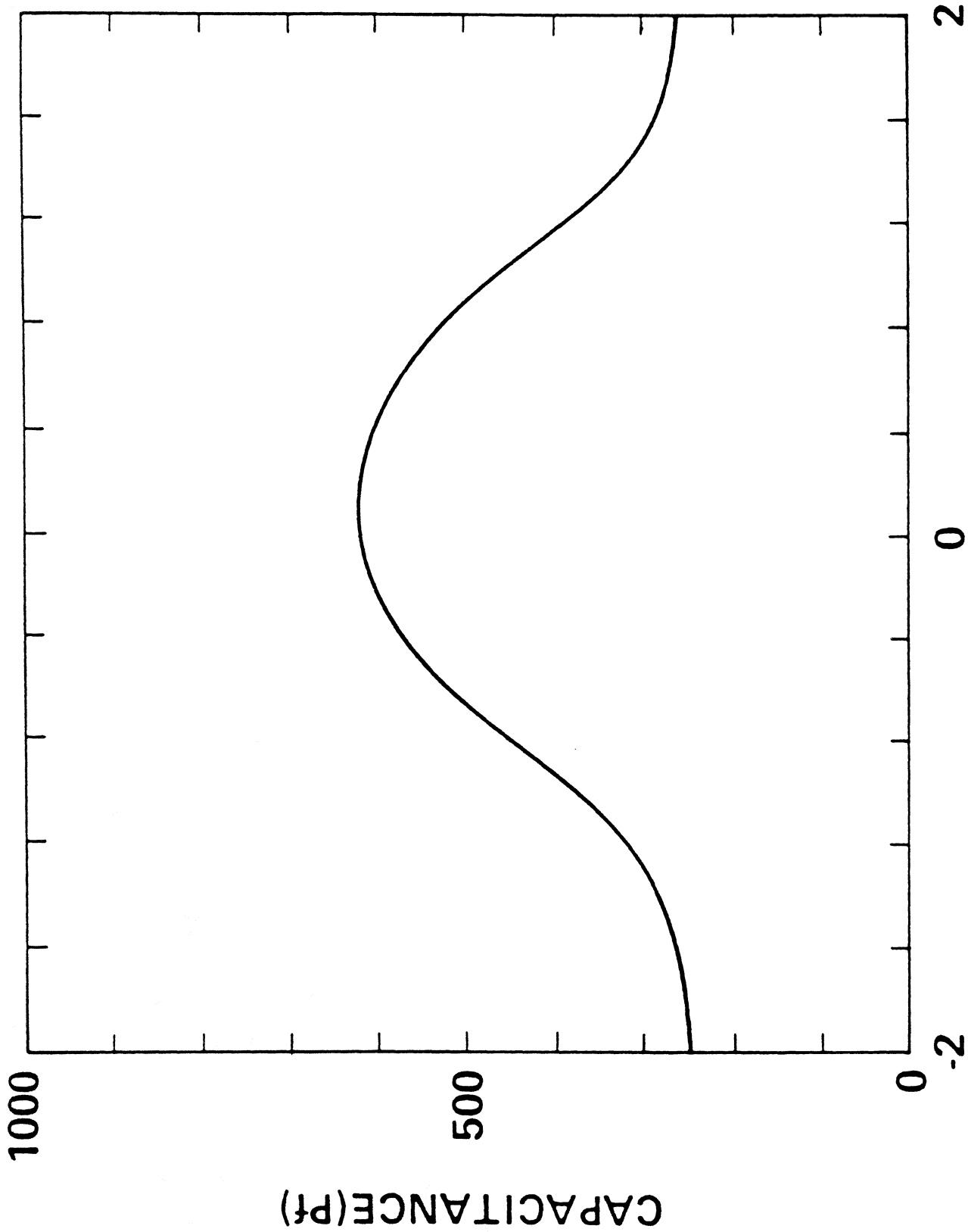

Figure 8. Symmetrical capacitance-voltage characteristic from two back-to-back connected BIN diodes.

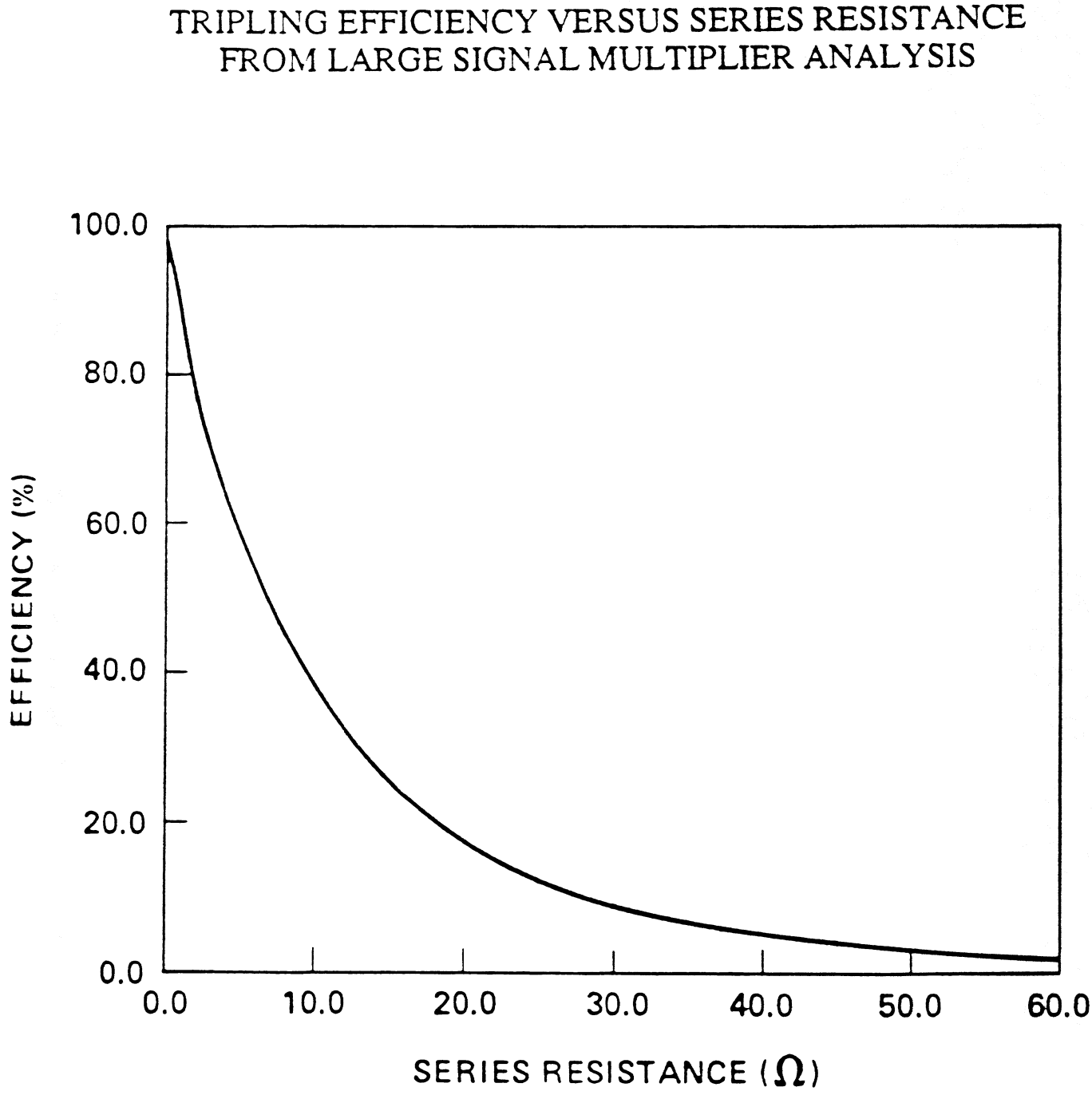

back connected BIN diodes.

Figure 11. Two-stage frequency tripler for submillimeter and Terahertz wave generation.

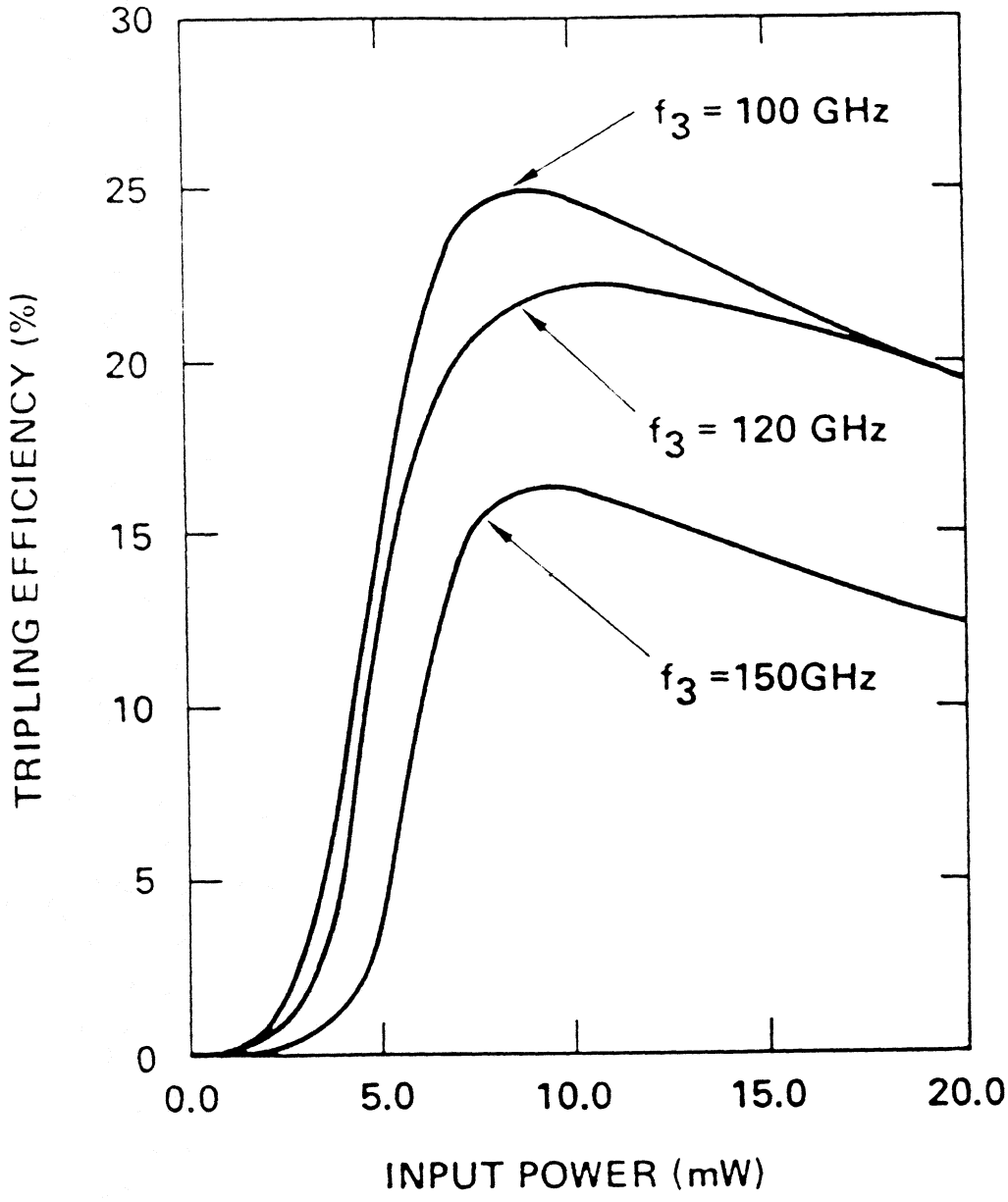

Figure 10. Tripling efficiency versus input power at different output frequencies.

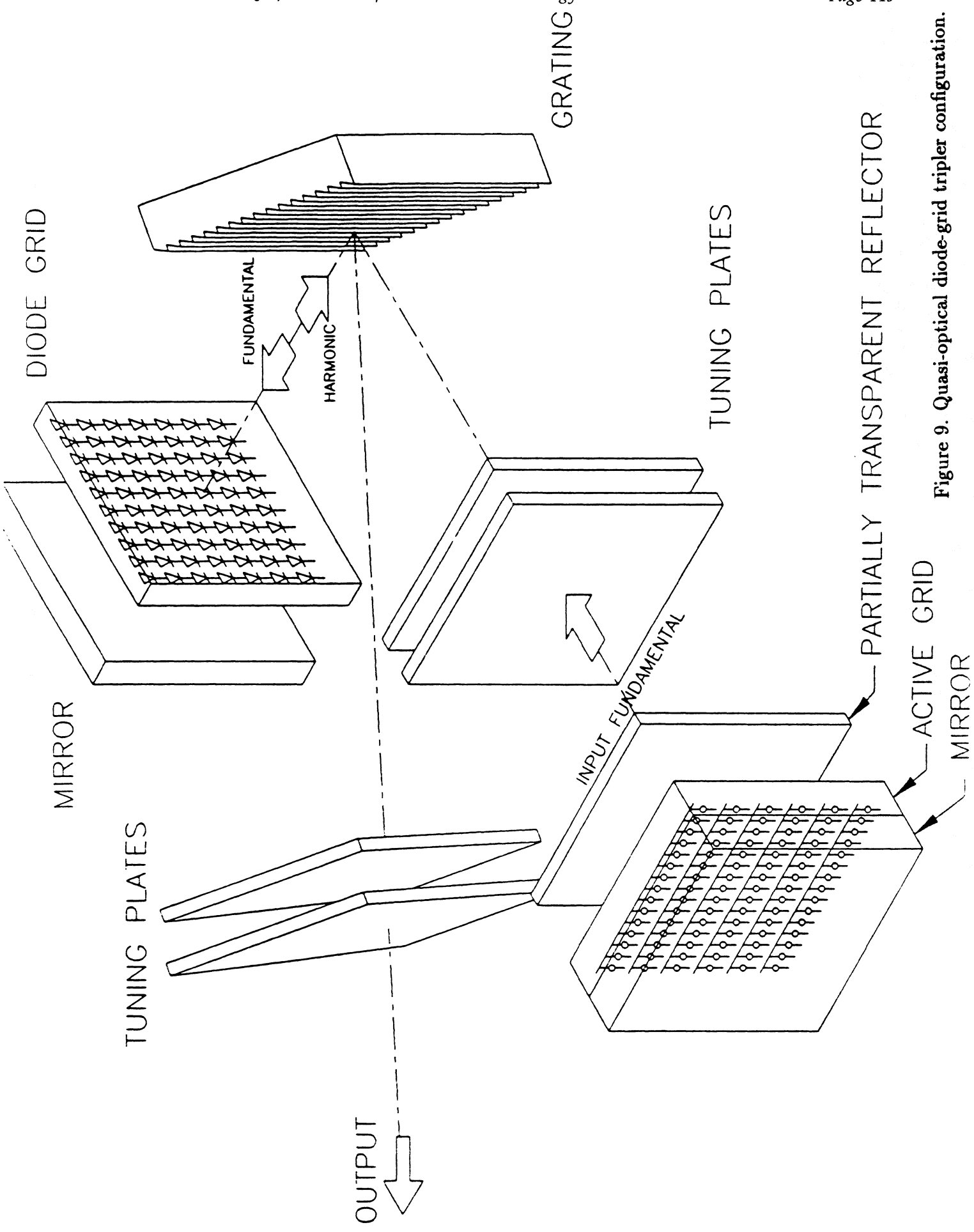

Figure 9. Quasi-optical diode-grid tripler configuration.

SUBMICROMETER DEVICES AND MONOLITHIC FUNCTIONS USING InAlAs/InGaAs HETEROSTRUCTURES

Geok Ing Ng, Youngwoo Kwon and Dimitris Pavlidis
Center for Space Terahertz Technology
Solid State Electronics Laboratory
The University of Michigan
Ann Arbor, MI 48109-2122.

ABSTRACT

A monolithic integrated circuit technology is reported using submicrometer HEMT's made with InAlAs/InGaAs heterostructures. The maximum oscillation frequency measured for 0.25μm devices is 148GHz. Good characteristics are also shown for devices subjected to all the steps of the integrated technology.

Monolithic heterostructure oscillators, doublers and mixers have been fabricated with this technology. They are designed for fundamental signal generation at 90GHz, frequency doubling to 180 GHz and mixing at 90 GHz. An analysis of the design procedures and characteristics is presented.

This first generation novel heterostructure monolithic circuits are designed for implementation in receiver/sensor components operating in the THz region.

Work supported by NASA (contract No. NAGW-1334), US Army Office (contract NO. DAAL-03-87-k-0007), and Wright Patterson Air Force Base (contract No. F33615-87-C-1406).

1. Introduction

$In_{0.52}Al_{0.48}As/In_{0.53}Ga_{0.47}As$ High Electron Mobility Transistors (HEMT's) have demonstrated extremely high cutoff frequencies (f_T) and very low noise figures [1]. The addition of excess Indium in the channel results in strained devices with better carrier confinement and improved characteristics [2]. Double-heterojunction strained $InAlAs/In_{0.65}Ga_{0.35}As$ HEMT's with 1μm long gates showed even further enhancement in carrier confinement and demonstrated lower output conductance than single channel devices with the same In content [3]. This paper, presents the technology and electrical characteristics of submicron strained InAlAs/InGaAs HEMT's and heterostructure monolithic integrated circuit functions made with them. Double and single heterojunction designs were used for these studies.

Monolithic integrated circuits use primarily conventional MESFET technology on GaAs. Recently AlGaAs/GaAs and pseudomorphic AlGaAs/InGaAs/GaAs devices have been implemented in integrated designs and very encouraging results were obtained in terms of bandwidth [4] and noise figure characteristics [5]. Unlike these GaAs based approaches, InAlAs/InGaAs designs are based on InP substrates and as mentioned already, discrete components made with them demonstrate excellent properties. Their integrated characteristics have not, however, been fully explored. Only few reports exist on this subject [6] which could lead to new avenues for analog applications.

First integrated designs using 0.8μm long-gate InAlAs/InGaAs HEMT's have demonstrated the possibility of building high gain amplifier blocks at X-band [7] and broadband control circuits up to 26.5 GHz [8]. Submicron HEMT's with optimized design and technology characteristics are, however, expected to perform

up to frequencies which lie in the submillimeter frequency region. A maximum oscillation frequency (f_{max}) of 405 GHz [9] already has been reported for discrete devices and it is expected that the f_{max} limits could be pushed above 500 GHz. These devices are consequently potential candidates for building basic functions such as oscillators, multipliers and mixers operating at extremely high frequencies. Space based sensor applications where gas molecule resonances are studied at several hundred GHz could consequently take direct advantage of monolithic integrated circuits made with InAlAs/InGaAs. Circuits of this type are currently under study and first results on their technology and design are reported in this paper.

Section 2 describes the technology of submicron discrete and integrated monolithic circuits. Integrated designs for oscillators, doublers and mixers are reported in Sections 3, 4 and 5, respectively.

2. Technology and Electrical Characteristics of Submicron InAlAs/InGaAs HEMT's for Monolithic Integrated Applications.

A cross section of $In_{0.52}Al_{0.48}As/In_xGa_{1-x}As$ InAlAs/InGaAs HEMT's is shown in Fig.1. The design corresponds here to the double heterojunction (DH) scheme [3] which is found to show larger carrier occupation in the strained quantum well and therefore better carrier confinement than single channel designs. The channel where the Two-Dimensional Electron Gas (2DEG) is formed has a high Indium composition (x) which exceeds the lattice matched (x=0.53) value. Unlike single channel designs employing only one donor layer between gate and channel, the DH-HEMT has a second donor layer in the bottom. This provides more carriers

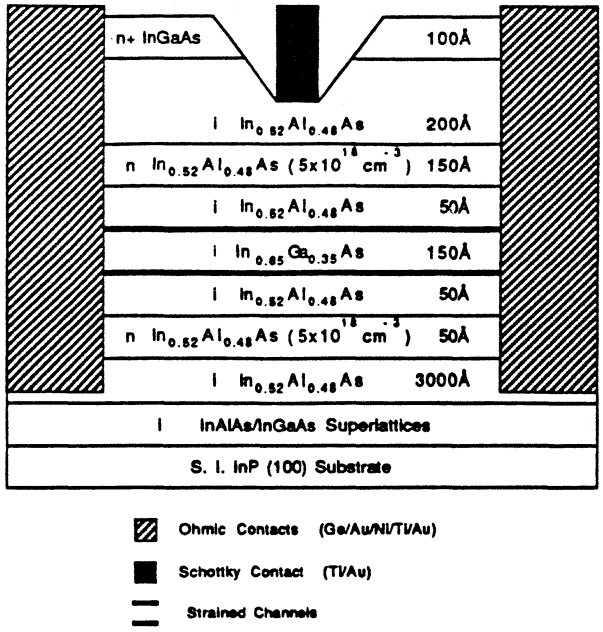

Figure 1 Cross section of double-heterojunction InAlAs/InGaAs HEMT.

and requires special attention in its design (smaller thickness than the top donor layer and appropriate doping) to avoid parasitic conduction.

The introduction of additional Indium in the channel improves the device properties. A transconductance and cutoff frequency improvement has already been reported by increasing the In content from 53% to 65% [2]. Further increases of Indium do not seem to enhance further the device properties. Our recent studies have for example demonstrated that devices with 75% or more In have smaller f_T and f_{max} values. By way of example an increase of In from 60% to 80% in 5% steps shows f_{max} values of 40GHz, 52GHz, 62GHz, 47GHz and 50GHz, respectively. The degradation of device characteristics with In content above certain value is related to their growth mode and the resulting interface characteristics.

Based on the above analysis, it was concluded that a 65% Indium content in the channel is a good compromise for improved electrical characteristics and controlled growth conditions suitable for integrated applications. The latter demand good

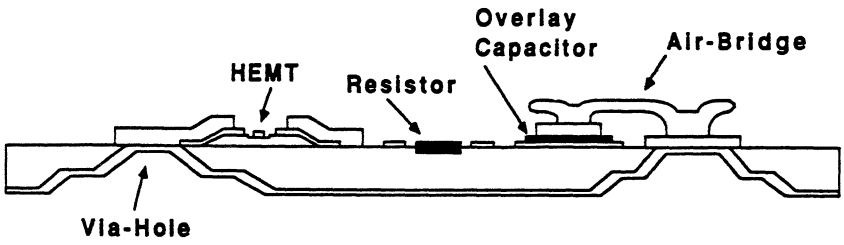

Figure 2 Cross section of heterostructure Monolithic Integrated Circuit using InAlAs/InGaAs HEMT's.

wafer uniformity and reproducibility to guarantee the compliance of performance with the predicted design characteristics.

A cross section of a InAlAs/InGaAs heterostructure monolithic integrated circuit is shown in Fig.2. Their technology of fabrication uses wet-etched (H_3PO_4:H_2O_2:H_2O-1:1:38) mesas for isolation. This solution has an etch rate of 20$\AA$/sec and results in small orientation dependence and no undercut. The quality of ohmic contacts (Ge/Au/Ni/Ti/Au) was improved from 0.3Ωmm in first runs to 0.1Ωmm by increasing the cap doping density ($5 \times 10^{18}cm^{-3}/100\AA$ instead of $3 \times 10^{18}cm^{-3}/200\AA$), and reducing the i-layer thickness of InAlAs from 400$\AA$ to 200$\AA$; the smaller thickness helps also in increasing the device transconductance. An image reversal lithography (Shipley 5214) was used for better reproducibility, edge definition and uniformity of the ohmic contacts; the chlorobenzene based lift-off originally employed, was eliminated for this step.

The submicron gate was defined using single 4500$\AA$ thick PMMA layer exposed by E-beam at 5.5nC/cm, 25kV. A citric acid etchant was used for gate recess in a mixture of 11:1:44 with H_2O_2 and H_2O. This results in relatively low etch rates

($\sim 300\mathring{A}$/min) and acceptable control of recess depth. The HEMT gates (Ti/Au) fabricated in this way have a length of 0.2 to 0.25μm.

The reticle for the investigated monolithic integrated functions was relatively large (6.3mm $\times$ 6.7mm) to allow simultaneous fabrication and comparison of characteristics of several functions. Submicron devices of different topology were necessary in order to satisfy the distinct requirements of each function. The reticle was for this reason subdivided in 11 subfields and some layout optimization was necessary to comply with the E-beam subfield size while maintaining the appropriate circuit topology.

Following the gate definition, a TiAu layer was deposited for the bottom plates of overlay capacitors. A thick SiO_2 layer $\sim 2500\mathring{A}$ was deposited by lift-off for the overlays. The sputtered lift-off technique developed specifically for the MMIC's allows selective overlay fabrication without deposition on the active area of the device and therefore no influence on its characteristics.

Active bias resistors for gate bias were recessed separately from the devices in order to control their values in the 5KΩ range. Air-bridges were fabricated in a two-step process. The wafers were then thinned down to 100μm (thickness for which all microstrip stubs were designed) and diced. The integrated ciruits were finally mounted and bonded in a specially designed test fixture operating from 70 to 100 GHz.

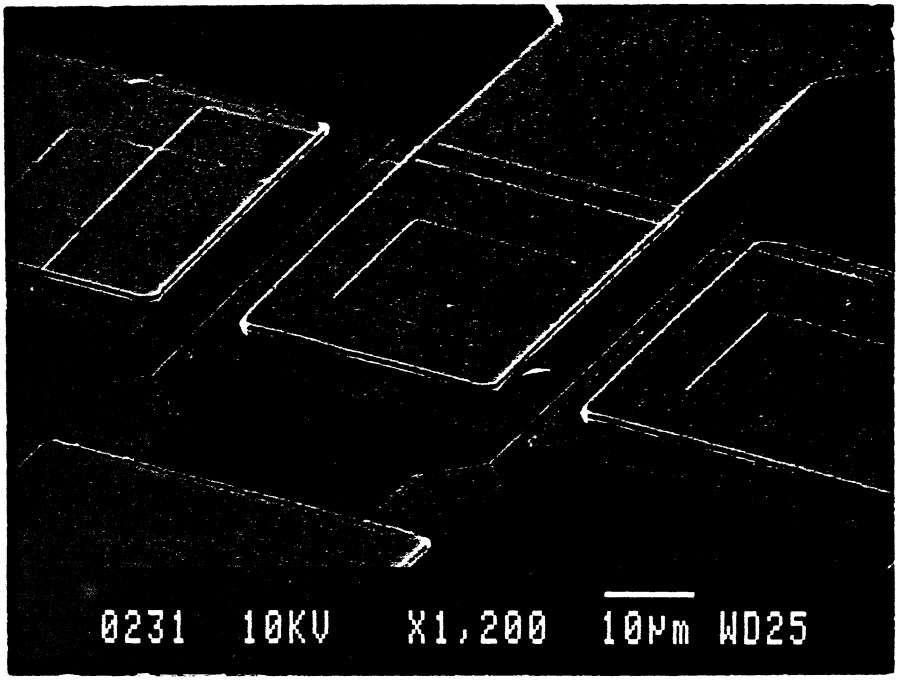

Figure 3 Photograph of submicron InAlAs/InGaAs HEMT in a monolithic integrated circuit.

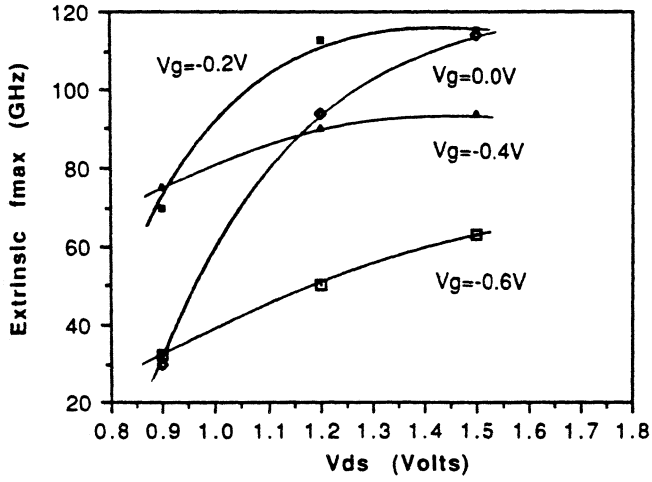

Figure 4 Bias dependence of current gain cutoff frequency (f_T) and maximum oscillation (f_{max}) frequency of a single channel (60%) HEMT from "integrated-circuit" wafer.

A photograph of the submicron InAlAs/InGaAs HEMT of an integrated circuit is shown in Fig. 3. Its gate is 0.2μm long. Fig. 4 shows the bias dependant f_T and f_{max} characteristics of such an integrated device fabricated with single channel (60% In) design. The maximum f_T and f_{max} values are 100GHz and 115GHz respectively. The device had 12dB gain at 26.5GHz. Better performance (f_T = 82GHz, f_{max} = 148GHz with 14dB of gain at 26.5GHz) could be obtained with a double heterojunction design of 65% In composition in the channel.

3. 90GHz Monolithic Oscillator Design Using InAlAs/InGaAs HEMT Technology.

The monolithic oscillator design was intended for implementation in a more complex integrated function as shown in Fig. 5. The frequency of the local source (monolithic oscillator) is doubled and subsequently mixed with the receiving signal. The resulting IF lies in the microwave region (1.0GHz to 10.0GHz) and can be processed using conventional existing technologies. Although fundamental oscillation frequencies should in principle be feasible in the several hundred GHz region using this technology, the design frequency of this first iteration was selected to be 90 GHz. This allows immediate use of presently available monolithic device characteristics and allows indentification of possible problems related with such realizations.

The oscillator design was based on measured small-signal characteristics of submicron HEMT's. A common source topology was selected with capacitive feedback in the gate and a combination of capacitive-inductive feedback in the source to induce oscillation conditions.

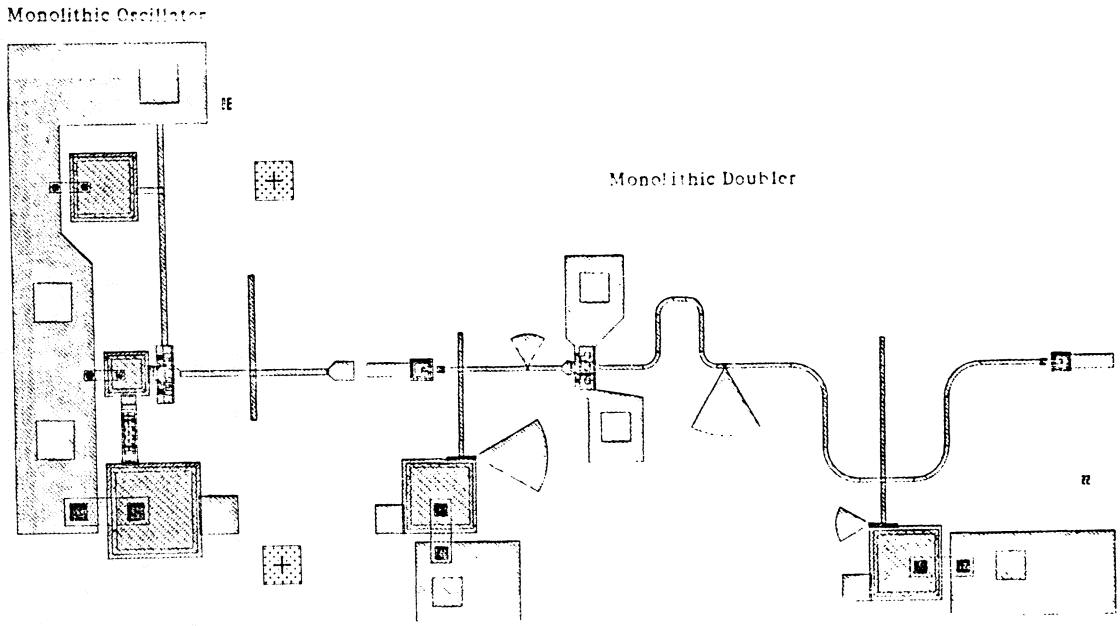

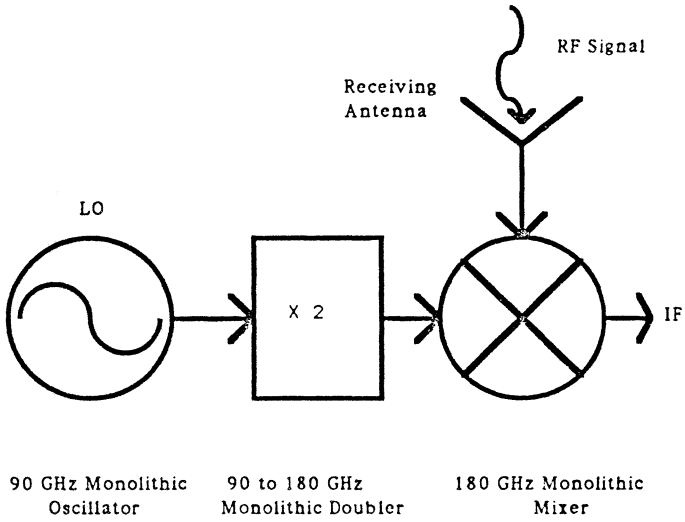

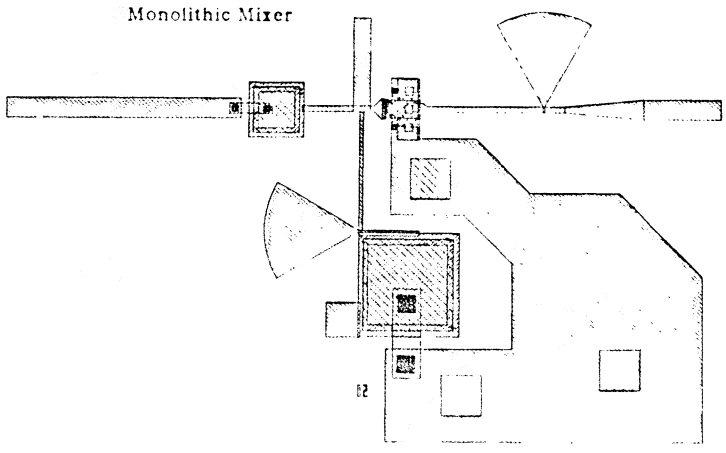

Figure 5 Schematic and layout of monolithic integrated sensor module.

Oscillation can be initiated if the following conditions are satisfied:

$$|\Gamma_{in}| \times |\Gamma_{osc}| \geq 1$$

$$\leq \phi_{in} + \leq \phi_{osc} = 0$$

where $|\Gamma_{in}|$, ϕ_{in} and $|\Gamma_{osc}|$, ϕ_{osc} denote magnitude and phase of the reflection coefficient at a reference plane looking towards the load and oscillator, repectively. This condition, is equivalent to a total resistance ($R_{tot} = R_{in}$ - R_{osc}) and reactance ($X_{tot} = X_L + X_{osc}$) equal to zero. Additionally to guarantee sustained steady-state oscillation it is necessary to satisfy the following conditions:

$$\frac{\partial R_{tot}}{\partial \omega} > 0 \quad , \quad \frac{\partial X_{tot}}{\partial \omega} > 0$$

As in every monolithic realization it is particularly important to aim towards process tolerant designs where the oscillation and steady-state conditions can be satisfied over a broad enough frequency range independent of active or passive element variations in their characteristics.

The integrated oscillator chip was fabricated using the monolithic submicron HEMT technology described in Section 2. A photograph of the fabricated monolithic chip is shown in Fig. 6.

The inductive feedback elements were realized using 16μm wide microstrips with 90Ω characteristic impedance on 100μm thick substrates. A 50Ω output port was considered and integrated matching was provided using again microstrip stubs. Overlay capacitors are used either for feedback or for RF grounding the bias pad of the gate. This pad was connected to the gate through an integrated 5kΩ resistor. Via holes are finally incorporated in the design for reducing parasitic inductances

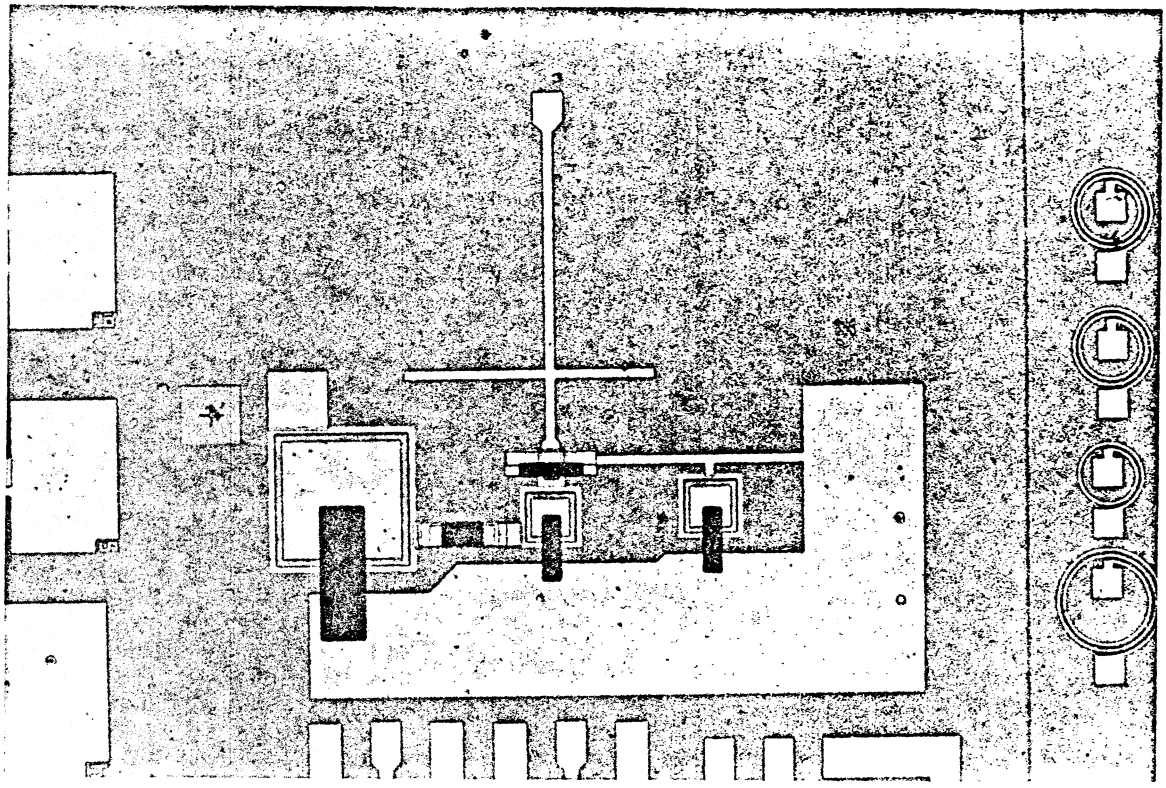

Figure 6 90GHz Monolithic Integrated Oscillator chip.

of the chip to ground.

4. 90GHz to 180GHz Monolithic Doubler using InAlAs/InGaAs HEMT Technology.

Signal multiplication is usually performed using two-terminal multiplier diodes. The high frequency characteristics of HEMT's suggest the possibility of three-terminal devices too for such applications. In fact, the transistor approach can allow larger bandwidth and better DC to RF efficiency than diodes which normally require relatively high power drive levels.

For multiplier applications, similarly to high efficiency power amplifiers, the HEMT's are operated with dc gate bias voltage (V_{gb}) close to pinch-off (V_p), i.e. under class B conditions. To obtain a high frequency harmonic at the output, the load is tuned at the desired harmonic. Suitable networks need to be incorporated at the gate and drain terminals to short-circuit all out-of-band harmonics.

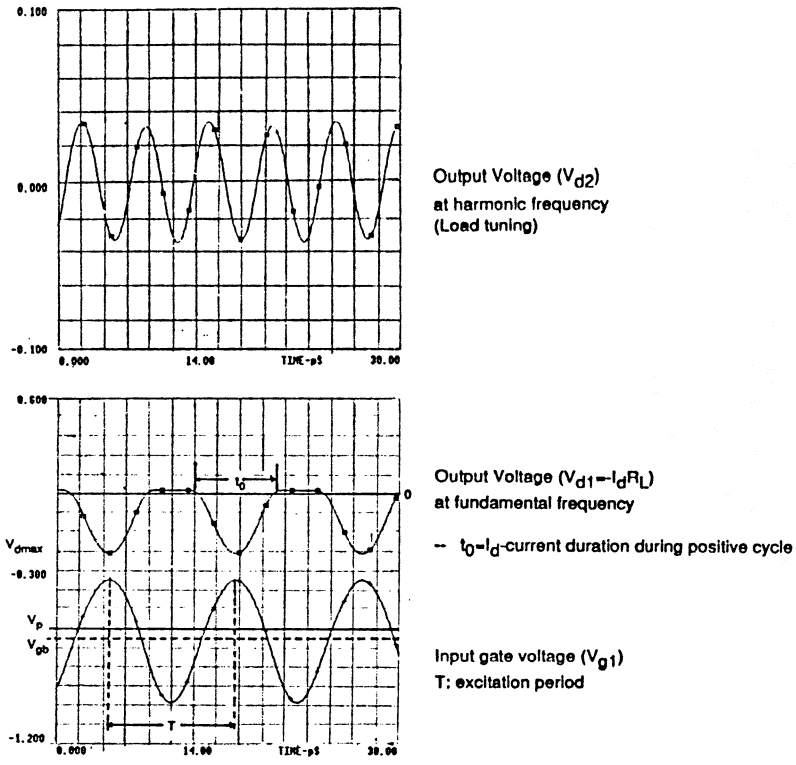

Figure 7 Voltage waveforms at various terminals of a 90GHz to 180GHz doubler.

A harmonic-balance technique (LIBRA^R) was used to analyze the doubler characteristics. The time domain characteristics of the output/drain voltage V_{d1}, V_{d2} at the fundamental and doubled frequency respectively, as well as, the input/gate voltage (V_{g1}) are given in Fig. 7; the frequency of the V_{d2} waveform across the load is consequently 180GHz. The amplified input voltage V_{g1} results in a waveform V_{d1} which ideally should be set to zero during the negative voltage ($V_{g1} \geq V_p$) excursion. This is not, however, true in practice, due to the high frequency operation displacement current which leaks through the gate capacitance and contributes to a V_{d1} "parasitic" signal (positive "square-like" waveform in Fig 7). The time duration of the V_{d1} cycle t_o where the transistor is conductive and more precisely the ratio t_o/T, where T is the period of the excitation signal V_{g1}, need to be optimized in order to achieve a good conversion efficiency i.e. large $I_{ddoubler}(2f)/I_{dmax}(f)$ value. If t_o is made too small compared to T then the magnitude of the resulting $I_d(2f)$

current is small. On the other hand, very large t_o values risk to produce $I_d(2f)$ signals with small harmonic content and are therefore undesirable.

The dc gate voltage is selected close to pinch off so that good class B operation is possible. Furthermore, the large signal swinging of I_d from zero to it's I_{dmax} value (in response to maximum V_{g1} excursions), can result under $V_{g1} \sim V_p$ bias condition in more efficient high harmonic generation. In fact, by exceeding slightly V_p one can ensure that not only I_d is set closer to zero but also C_{gs} reaches its minimum value. The $V_{g1} \geq V_p$ condition is, however, incompatible with the small gate leakage requirement for reduced risk of device breakdown. InGaAs HEMT's have unfortunately high gate leakage compared to other devices (typically 100μA at -6.5V for a 1.0μmx 75μm device) and risk therefore to be sensitive to this bias requirement for multipliers. Except this, gate leakage is not a real fundamental limitation in the circuit performance because its level at the input gate terminal turns out to be small compared to the displacement current in the gate capacitance at high frequency operation.

For increased power levels the conversion loss is seen to reduce and subsequently increase. This is due to the initially larger amplitude of signal I_d at the output due to the increased input gate voltage V_{g1} and larger transconductance g_m. At higher V_{g1}'s approaching forward operation I_d reaches a maximum I_{dmax} and does not therefore, improve any more. Furthermore g_m starts reducing considerably in HEMT's due to parasitic "MESFET"-type conduction. The conversion loss vs. input power characteristics depend on the selected gate bias and are minimum for $V_{g1} \sim V_p$. A different gain power tendency is observed for diode doublers where the conversion loss improves over a larger range of input power levels. Due to the

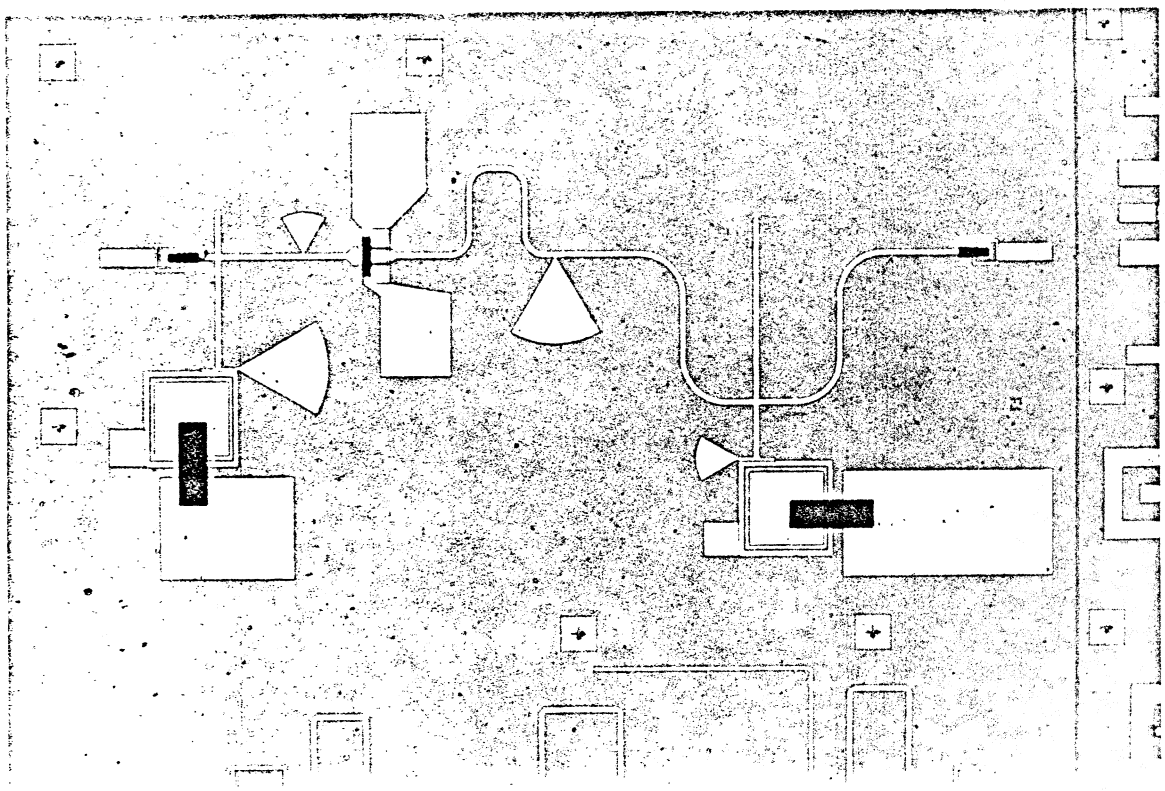

Figure 8 90GHz to 180GHz Monolithic Integrated Doubler chip.

gate-leakage increase with input power this should be selected for the best possible compromise of conversion loss and leakage.

A photograph of the fabricated monolithic doubler chip is shown in Fig. 8. Right next to the HEMT one distinguishes two radial stubs used to realize band-reject filter characteristics. The left stub acts as a 180GHz resonator prohibiting the doubled signal from leaking towards the input, while the right one is a 90GHz resonator cutting off the fundamental 90GHz from the output terminal. Gate bias is achieved through an overlay capacitor connected to 90GHz radial stub which is $\lambda/4$ transformed to yield perfect open conditions at the input line. A matching network with a $\lambda/4$ stub (180GHz) is finally incorporated at the output for drain

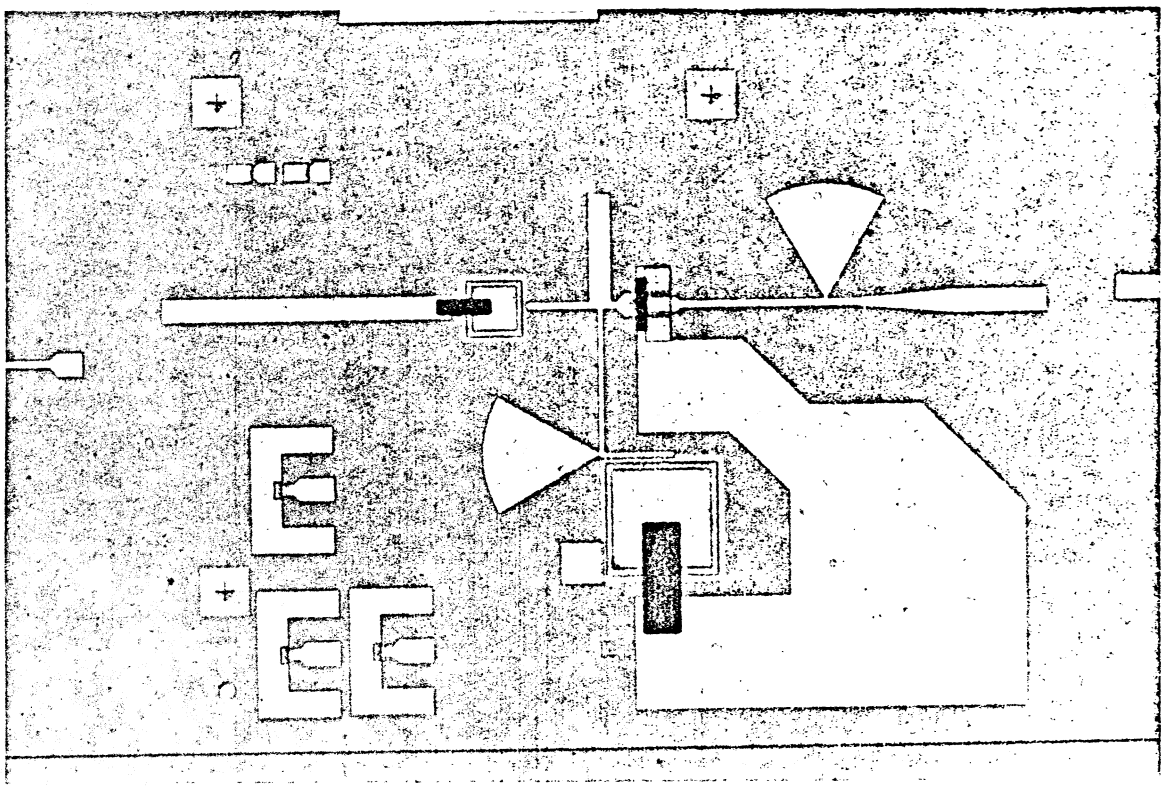

Figure 9 90 GHz Monolithic Integrated Mixer chip.

bias. The monolithic doubler is designed for 13.5dB conversion loss with 1dBm LO power level. The fundamental frequency rejection at the output is of the order of 38dB.

5. 90GHz Monolithic Mixer using InAlAs/InGaAs HEMT Technology.

Monolithic mixers can be built using InAlAs/InGaAs HEMT's instead of diodes. The transistor approach allows lower conversion loss and lower power levels for the LO signal. Unless a balanced design is used, various responses generated by non-linearities and LO noise cannot be rejected to a satisfactory level. The balanced approach becomes of particular importance in monolithic integrated designs where the oscillator is built without any resonator stabilizing networks. Frequency conversion is achieved by the nonlinearity of the transconductance-input-voltage (V_g)

characteristics. Best characteristics are obtained when other V_g dependent parameter, such as for example output conductance shows less nonlinear characteristics. HEMT's are consequently ideally suited for such applications due to the very nonlinear g_m-V_g characteristics.

A photograph of the fabricated 90GHz monolithic chip is shown in Fig. 9. The RF and LO signals are applied simultaneously at the input. Matching is achieved by the same input network for both LO and RF with best characteristics in the center of the L0-RF band (92.5GHz). A $\lambda/4$ transformer connects a radial stub to the input line for gate bias. The overlay capacitor enhances the short circuit conditions of the $\lambda/4$ transformer at its end (90 GHz design). Furthermore, it short-circuits the IF signal by series resonance with the stub and eliminates consequently the IF from the input port. A radial stub design is also used at the output to filter out the RF and LO signals.

In addition to the 3GHz IF, a signal response is also found at $\sim$ 6GHz. This is eliminated by a low pass filter design employing lumped elements and being integrated onto the same chip. Matching of the complete circuit to 50Ω load is finally achieved by the same integrated lumped network. The conversion loss of the circuit is 10dB using 91GHz(LO)/94GHz(RF) signals and 5dB of LO power.

Conclusions

An sumbmicron monolithic integrated technology is reported for receiver/sensor applications in the THz region. The results of the first study are obtained using 0.20-0.25μm long HEMT's made with InAlAs/InGaAs heterostructures. Maximum oscillation frequencies of 148GHz were obtained and good performance was

demonstrated for devices subjected to all the monolithic integrated process steps. The technology steps used for monolithic fabrication have also been discussed.

Monolithic integrated functions using the submicron HEMT's have been studied and circuits were fabricated. Fundamental signal generation is at first attempted at 90GHz. Signal doubling from 90GHz to 180GHz and mixing at 90GHz is also studied using the submicron HEMT's.

Acknowledgement

The authors would like to acknowledge the great help provided by Y. J. Chan, J. Pamulapati, and P. K. Bhattacharya for MBE growth. T. Brock, H. F. Chau, J. Hu, R. Lai, D. Pehlke and K. Studer-Rabeler for submicron and MMIC fabrication. Special thanks are also given to J. Morgan, M. Tutt and P. Marsh for their continuous and creative effort in the area of microwave and millimeter-wave device and circuit characterization.

REFERENCES

1. U. K. Mishra, A. S. Brown and S. E. Rosenbaum, C. E. Hooper, M. W. Pierce, M. J. Delaney, S. Vaughn, K. White: "Microwave Performance of AlInAs/GaInAs HEMT's with 0.2 and 0.1μm gate length", IEEE Electron Device Letters, Vol. 9. pp 647-640, Dec. 1988.

2. G. I. Ng. D. Pavlidis, M. Jaffe, J. Singh and H. F. Chau, "Design and Experimental Characteristics of Strained $In_{0.52}Al_{0.48}As/In_xGa_{1-x}As$ (x > 0.53)" IEEE Transactions on Electron Devices, Vol. 36, No. 10, pp. 2249-2259, Oct. 1989.

3. G. I. Ng. D. Pavlidis, M. Tutt, J. Oh and P. K. Bhattacharya, "Improved device characteristics using strained double channel $In_{0.65}Ga_{0.35}As/In_{0.52}Al_{0.48}As$ HEMT's" IEEE Trans. on Electron Devices, Vol. 10, No. 3, pp. 114-116, March 1989.

4. C. Nishimoto, R. LaRue, S. Bandy, M. Day, J. Ecusfein, C. Webb, C.Yuen, Z. Zdasiuk "A 2-20 GHz High Gain Monolithic HEMT Distributed Amplifier" IEEE, 1987 Microwave and Milllimeter Monolithic Circuits Symposium, June 1987, pp. 109-114.

5. G. Metze, A. Cornfeld, J. Singer, II. Carlson, E. Chang, T. Kirkendall, G. Dahrooge, J. Bass, H.-L. Hung, T. Lee: "Monolithic V-Band Pseudomorphic-MODFET Low-Noise Amplifiers" IEEE 1980 MMIC-Symposium, Conference-Digest pp. 111-116.

6. M. Tutt, D. Pavlidis, G. I. Ng, M. Weiss, J. L. Cazauz: "Monolithic Integrated Circuit Applications of InGaAs/InAlAs HEMTs", GaAs IC-Symposium. 1988, pp. 293-296.

7. M. Weiss, G. I. Ng and D. Pavlidis: "InP Based Monolithic Integrated HEMT Amplifiers and their Material Sensitivity", Submitted to "20th European Microwave Conference."

8. M. Weiss, G. I. Ng and D. Pavlidis: "HEMT Control Circuits for Monolithic InP Applications", Submitted to "20th European Microwave Conference."

9. A. J. Tessner, P. C. Chao, K.H.G. Duh, P. Ho, M. Y. Kao, S.M.J. Liu, P.M. Smith, J. M. Ballingall, A. A. Jabra, T. H. Yu: "Very High Performance 0.15μm gate-length InAlAs/InGaAs/InP lattice-matched HEMT's", 12th Biennial IEEE/Cornell University Conference in "Advanced Concepts in High Speed Semiconductor Devices and Circuits."

Aperture Efficiency of Integrated-Circuit Horn Antennas

Yong Guo, Karen Lee, Philip Stimson
Kent Potter, David Rutledge

Division of Engineering and Applied Science
California Institute of Technology
Pasadena, CA 91125

Abstract—**We have improved the aperture efficiency of silicon integrated-circuit horn antennas by optimizing the length of the dipole probes and by coating the entire horn walls with gold. To make these measurements, we developed a new thin-film power-density meter for measuring power density with accuracies better than 5%. The measured aperture efficiency improved from 44% to 72% at 93 GHz. This is sufficient for use in many applications which now use machined waveguide horns.**

INTRODUCTION

Rebeiz *et al.* [1] developed an integrated-circuit horn array based on anisotropic etching of silicon (Figure 1a). The etch forms pyramidal cavities bounded by (111) crystal planes. Gold is evaporated on these walls to make them highly conducting. The power received by the horns is picked up by dipole probes suspended on 1-μm silicon-oxynitride membranes inside the horns. The power is detected by bismuth microbolometers. Horns were demonstrated at 242 GHz and at 93 GHz, and the technology appears to be quite suitable for scaling to the terahertz frequency range. These horns have several potential advantages for use in millimeter and submillimeter arrays. The array is fully two-dimensional, and the horns are made simultaneously by integrated-circuit processing techniques. It should be possible to integrate superconducting tunnel junction devices with the horns. An isotropic etching technology is also available in gallium arsenide, which suggests that it should be possible to make horns that would include monolithic Schottky diodes. The membranes appear fragile, but we have been able to mount beam lead diodes on them, and they have passed standard industrial temperature and vibration tests. However, the measured aperture efficiency was low; Rebeiz *et al.* reported a value of 44% at 93 GHz for a array with a period of 1 λ. This efficiency is not good enough for most applications.

Rebeiz' measured and calculated losses are summarized in Figure 1b. The two major loss components are mismatch loss (2.2 dB) and horn-sidewall loss (0.7 dB). The mismatch loss was estimated from 7-GHz modeling experiments that indicated that

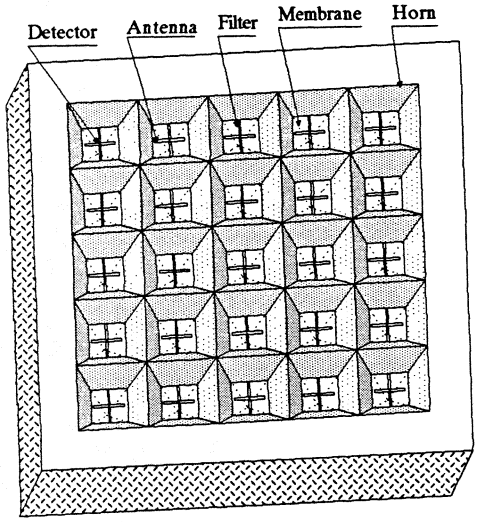

(a)

Loss component	loss, dB
Intrinsic pattern loss	0.2
Mismatch loss	2.2
Cross-polarization loss	0.2
Horn-to-horn coupling loss	0.1
Horn sidewall loss	0.7
Total calculated loss	3.4
Measured loss	3.6

(b)

Figure 1. Integrated-circuit horn array made by anisotropic etching of silicon (a), and the summary of measured and calculated losses (b) reported by Rebeiz *et al* [1].

the antenna impedance is $54 + j95\,\Omega$, compared with the bolometer resistance, $138\,\Omega$. The horn-sidewall loss arose from fact that the entire horn was not coated with gold; part was bare silicon with a resistivity of $0.5\,\Omega$cm. The horn arrays are made as a stack of 4 wafers. One of these wafers includes the membranes; this wafer was not coated with gold because the membranes would also have been covered over during the evaporation. The goal of this work was to eliminate these two sources of loss.

Another difficulty with the previous measurements was measuring the aperture efficiency. A 10% accuracy was claimed, but this is not adequate for testing antennas with higher efficiencies. Although the measurement is fundamentally only the ratio of received power to incident power density, there were many factors that complicated the measurement and affected the accuracy. The power density was calculated from the reading of a waveguide power meter connected by a calibrated directional coupler, together with the calculated gain of a standard gain horn. The received power was measured for a chopped signal, and this required an accurate knowledge of the effective value of the modulation waveform and the frequency roll-off of the bismuth microbolometer. To simplify the measurements and improve the accuracy, we developed a new thin-film power-density meter and used only four-wire DC electrical measurements in the calibration and measurement.

Horn fabrication

A range of horns with dipole probes varying in length from $0.32\,\lambda$ to $0.50\,\lambda$ were constructed. In addition, the horn walls on the membrane wafer were coated with

gold by evaporating at an extreme angle so that the walls of the horns formed a shadow over the membrane. The bolometers were fabricated by a photoresist bridge technique [2]. They had resistances in the range 50 to 100 Ω, with typical resistance responsivities of 20,000 Ω/W.

Power-Density Meter

Recently there has been renewed interest in developing quasi-optical power meters. Professor Derek Martin has recently developed an approach where the power is absorbed in a metallic thin film suspended in a closed gas cell [3]. The accuracy is reported to be 10%. Professor Gabriel Rebeiz is pursuing a design on a silicon-oxynitride film [4]. Our power meter (Figure 2) consists of an evaporated bismuth film with a sheet resistance of 189 Ω on a 50-μm thick mylar sheet. A film with this sheet resistance absorbs half the incident power and transmits half. The device is surrounded by a 5-cm thick layer of styrofoam to reduce the convection heat loss and to block infrared radiation. The transmitted power is absorbed by a pyramidal beam dump lined with absorber. The power-density meter works as a bolometer. It absorbs power, heats up, and we measure the change in resistance by a 4-wire measurement. The bolometer has an active area of 4 cm^2, and the typical resistance responsivity to RF radiation is 20 Ω/(W/cm^2). We have carefully considered and tested for different sources of error: resistance drift, edge effects, time constants, varying angle of incidence, and absorption in the styrofoam, and feel that the measurements are accurate to better than 5% for incident power densities greater than 100 μW/cm^2.

Measurements

Both the power-density meter and the horn microbolometers were calibrated by a plot of the resistance R versus DC power P. This plot is of the form

$$R = R_0 + \mathcal{R}P$$

where $\mathcal{R}$ is the resistance responsivity in Ω/W. The resistance responsivity is calculated from the slope of the plot. There is one additional correction factor for the proportion of power that is absorbed by the power-density meter.

In the measurements, the signal source was a 93-GHz klystron with an output power of 170 mW feeding a horn 60 cm from the array. The resistance changes in the horn microbolometers were measured, and then the horn array was replaced by the power-density meter. The aperture efficiency η can then be written as a simple formula

$$\eta = \frac{A_m \mathcal{R}_m \Delta R_h}{A_h \mathcal{R}_h \Delta R_m}$$

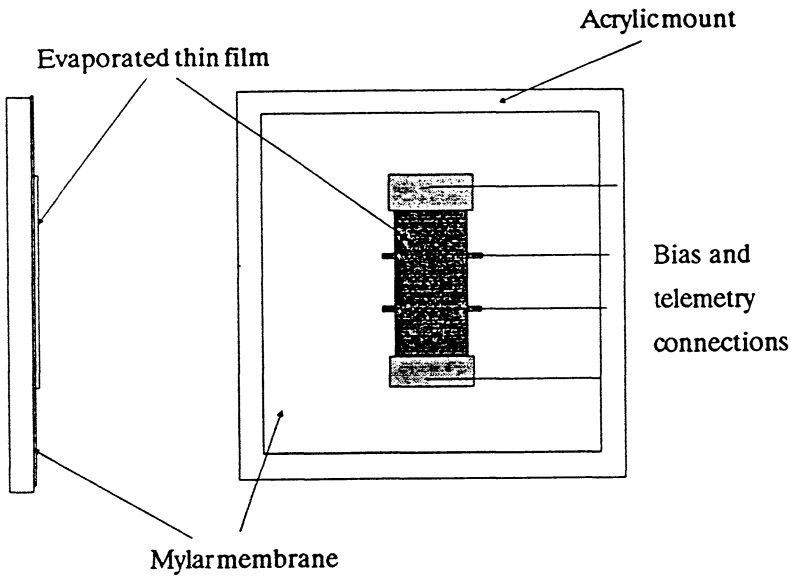

(a)

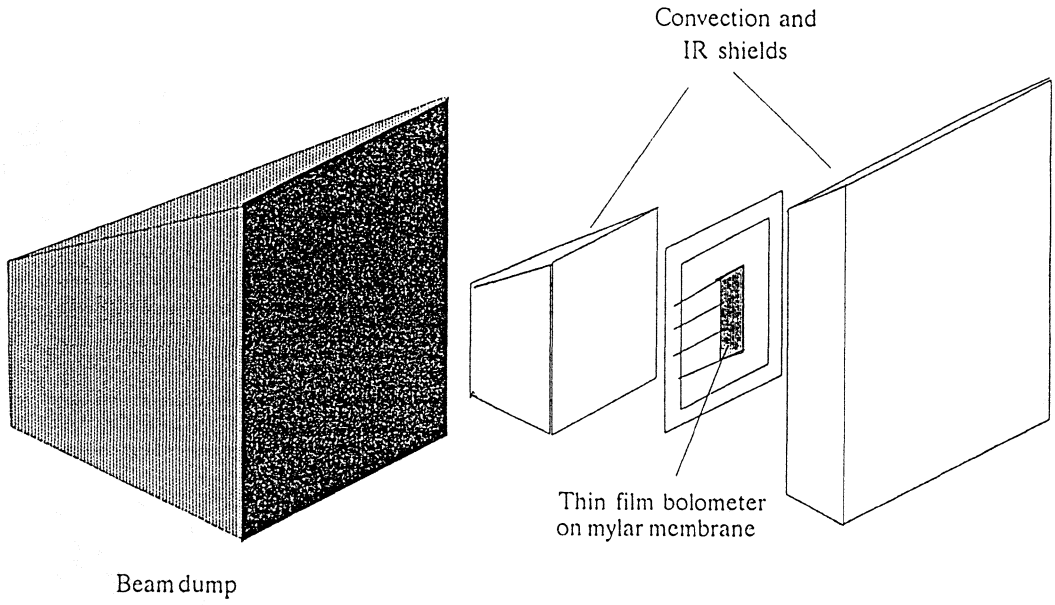

(b)

Figure 2. Thin-film power-density meter (a), and assembly (b).

where A_m is the area of the power-density meter, $\mathcal{R}_m$ is the corrected resistance responsivity of the meter, ΔR_h is the resistance change of the horn microbolometer, A_h is area of the horn, $\mathcal{R}_h$ is the responsivity of the horn microbolometer, and ΔR_m is the resistance change of the power-density meter.

Figure 3a shows the measured efficiencies for different antenna lengths. Measurements were made first for membrane wafers without gold coating. After the membrane wafers were coated with gold, the efficiencies were measured again. The efficiency reaches its

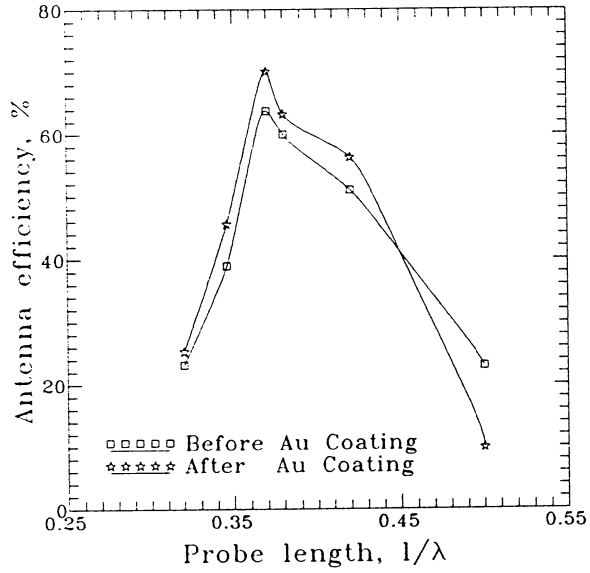

(a)

Loss component	loss, dB
Intrinsic pattern loss	0.2
Mismatch loss	0.4
Cross-polarization loss	0.2
Horn-to-horn coupling loss	0.1
Total calculated loss	0.9
Measured loss	1.4

(b)

Figure 3. Measured aperture efficiencies at 93 GHz versus antenna length (a). The efficiencies were measured before and after coating the membrane wafer with evaporated gold. Summary of measured and calculated losses (b).

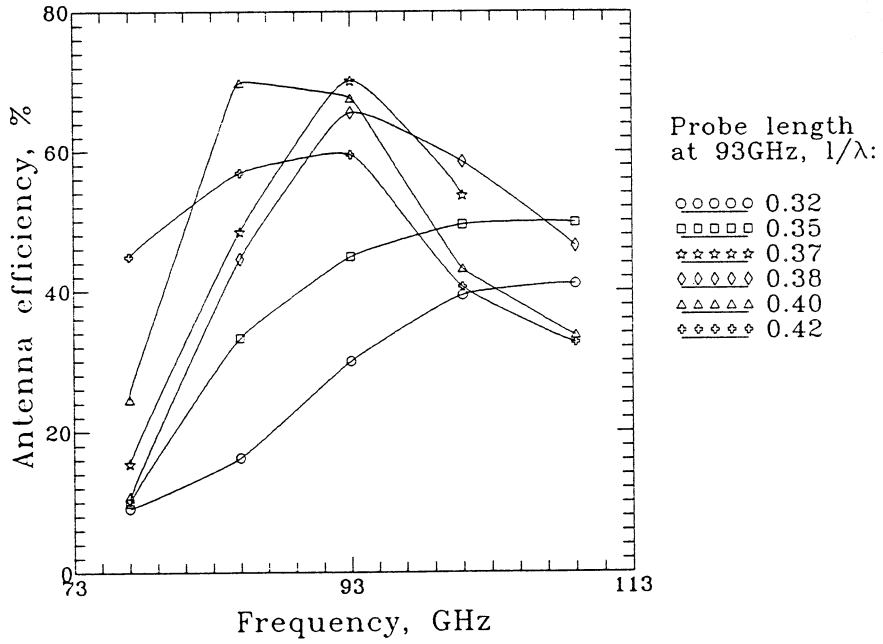

Figure 4. Aperture efficiency versus frequency for different dipole probe lengths.

maximum value, 72%, for a length of 0.37 λ. For all but the longest probe, gold coating the walls of the membrane wafer improves the efficiency. The typical improvement is 6%. Figure 3b shows the estimated loss breakdown. The total calculated loss is 0.9 dB, compared with the measured value, 1.4 dB. There is still some mismatch loss (0.4 dB), because the bolometer resistance in the measurements was 90 Ω, compared with the resonant antenna resistance of 50 Ω that was measured on the microwave model. We also made a plot of efficiency for the frequency range from 77 GHz to 109 GHz for antennas of various lengths, and this is shown in Figure 4. Probes with lengths in the range from 0.37 to 0.40 λ gave efficiencies better than 60%. The 3-dB bandwidths are of the order of 10 GHz.

Finally, we made measurements of the system coupling efficiency with a lens (Figure 5). This system coupling efficiency is the ratio of the detected power to the power incident on the lens. In the measurement, various stops were used to change the half angle subtended by a 100-mm diameter lens with an f-number of 0.75. The highest system coupling efficiency with a lens is 36% for an f-number of 0.75. We estimate that the loss from reflection and absorption in the lens is 28%, so that it should be possible to achieve a coupling efficiency of 50% in a f-0.75 system with reflecting optics, compared with 24% reported by Rebeiz *et al.* [2].

Conclusion

We have improved the aperture efficiency of silicon integrated-circuit horn antennas by optimizing the length of the dipole probes and by coating the entire horn walls

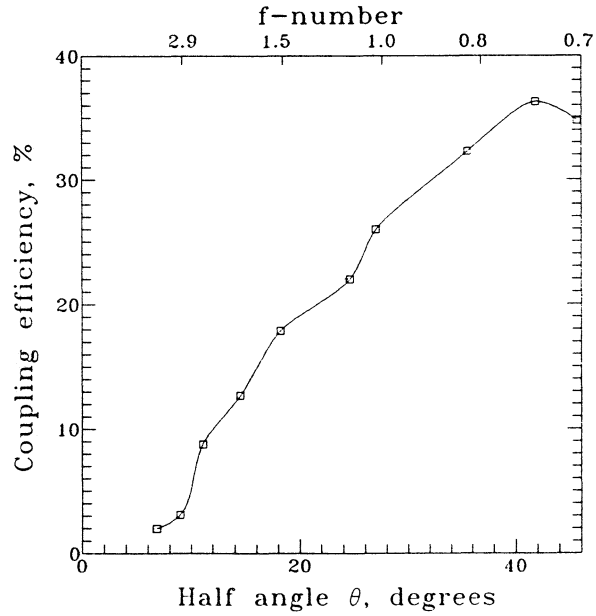

Figure 5. System coupling efficiency with a lens. The horizontal axis is the half angle subtended by the lens, which is varyied by changing stops in front of the lens.

with gold. To make these measurements, we developed a new thin-film bolometer power-density meter for measuring power density with accuracies better than 5%. The measured aperture efficiency improved from 44% to 72% at 93 GHz. These horns are now efficient enough to be considered for use in remote sensing, plasma diagnostics, and radio astronomy.

ACKNOWLEDGEMENTS

We appreciate the support of Aerojet Electrosystems, who also performed the temperature and vibration tests and mounted the beam-lead diodes. We also appreciate the support of NASA's Office of Aeronautics and Space Technology, and the Strategic Defense Initiative's Terahertz Technology Program, contract F19628-87-K-0051. The swept-frequency measurements were performed on a backward-wave oscillator at UCLA's Center for High-Frequency Electronics.

REFERENCES

[1] G. M. Rebeiz, D. P. Kasilingam, Y. Guo, P. A. Stimson, D. B. Rutledge, "Monolithic Millimeter-Wave Two-Dimensional Horn Imaging Arrays", to be published in the *IEEE Transactions on Antennas and Propagation.*

[2] D. P. Neikirk, W. W. Lam, and D. B. Rutledge, "Far-infrared microbolometer detectors," *International Journal of Infrared and Millimeter Waves 5*, 1984, pp. 245–278. The bridge technique described in this paper uses a CF_4 plasma to make a buffer layer for the bridge. We are currently using a thin layer of aluminum as the buffer layer.

[3] Professor Martin's power meter is now commercially available from Thomas Keating Ltd., Billinghurst, West Sussex, England.

[4] C. C. Ling and G. M. Rebeiz, "A wide-band monolithic submillimeter-wave quasi-optical power meter," to be presented at the 1990 IEEE MTT-S International Microwave Symposium.

INTEGRATED TAPERED SLOT ANTENNA ARRAYS AND DEVICES

K. Sigfrid Yngvesson

Department of Electrical and Computer Engineering
University of Massachusetts
Amherst, MA 01003

ABSTRACT

The potential advantages of integrating antenna elements/arrays with active devices has made this into an area which has received increasing emphasis among millimeter wave/submillimeter wave researchers. This paper reviews the status of one type of antenna element which shows great promise for such applications - the Tapered Slot Antenna (TSA). We will cover some recent advances in this area, with particular emphasis on the potential application of TSA arrays in THz Space Technology. Examples are given of applications with relevance to THz Space Technology in three areas: (1) Focal plane arrays for imaging; millimeter wave prototypes at 35 and 94 GHz have demonstrated system aperture efficiencies (i.e. total coupling efficiencies) of over 50%, with angular resolution close to the Rayleigh criterion. (2) Quasi-optical power-combining with high radiative efficiency, as demonstrated by a 32 GHz prototype developed together with JPL. (3) Integrated receivers, such as SIS mixers, and a new two-dimensional electron gas element.

REVIEW OF TSA ELEMENTS AND ARRAYS

Endfire antenna elements of the tapered slot antenna (TSA) type can be employed both as single elements and in arrays. TSAs utilize a tapered slot in the metalization on a thin dielectric substrate, to radiate in the "end-fire" direction (along the tapered slot, see Figure 1). The special case of air dielectric also has been investigated. Some distinctive advantages of the TSA elements are (1) the 3 dB beamwidth can be varied over a wide range, down to about 15 degrees (2) ease of fabrication by photoetching, and integration with active elements (3) high packing density when used in arrays (4) high efficiency in phased arrays even with element spacings greater than 1 λ.

Integrated millimeter wave TSA elements were pioneered by Gibson [1] who demonstrated a bandwidth of 8–40 GHz for an exponentially tapered ("Vivaldi") single element, matched to a detector. Since that time, theoretical work by Schaubert and co-workers [2, 3] as well as Johansson [4] has provided a fairly complete picture of the process by which single element TSAs radiate. While TSA elements have many features in common with the general class of traveling-wave antennas, there are some differences: for example, the H-plane beamwidth often follows the $(1/L^{1/2})$ dependence expected for traveling-wave antennas (L = antenna length), while the E-plane beamwidth also depends on the aperture size, and varies more slowly with L [2, 3, 5]. A complete moment-method solution has been presented for the air-dielectric case, and a simplified linearly tapered geometry [4]. Radiation patterns (both co-polarized and cross-polarized) are predicted correctly. An unsolved case is the single element on a dielectric, with a finite substrate width.

As indicated by both theoretical and experimental studies, TSA patterns can have high cross-polarization levels in the diagonal (D) plane. The lowest X-pol levels (10–15 dB below the Co-Pol peak) are obtained for exponentially tapered elements, with an optimum dielectric thickness. For these elements, the integrated power lost to X-Pol, is about 10%. Phase centers have also been predicted and measured in recent work — typically, the E-plane phase center is somewhat behind the aperture, while the H-plane one is further toward the feed-point. A Vivaldi element has been used in one experiment as the feed for an f/D = 1 paraboloid reflector. The dependence of the gain on the axial displacement indicated that for this element E- and H-plane phase centers were close. The aperture efficiency of this system was estimated to be ~55% by direct substitution with a waveguide horn. TSA elements used as feeds for reflectors or lenses, thus yield comparable system aperture efficiency to typical waveguide feeds.

Arrays of TSA elements (Figure 2 shows an example) have a number of useful advantages. They have been employed in the focal plane of a reflector, in order to form a multi-beam system for millimeter wave imaging. One such system demonstrated resolution of two point sources at the Rayleigh distance [6]. When compared at the same beamwidth (to illuminate a specific reflector optimally), elements in a TSA array occupy about 1/4 of the area of a typical waveguide feed element. Thus, imaging systems with TSA focal plane arrays (Figure 3) can be designed to yield high angular resolution (due to small element spacing) while retaining high aperture efficiency. In other multi-beam systems, TSA arrays could be used if a high cross-over level is desired.

Most of the work on TSA elements and arrays thus far has utilized substrates such as low-ε_r Duroid, or Kapton (ε_r = 3.5), and has been limited to 35 or 94 GHz. Recent work has emphasized techniques for enabling TSA arrays to be used at THz frequencies. Kollberg et al are developing a 16 element TSA array for 100 GHz, with integrated SIS mixers, to be used as a focal plane array in a 20 meter diameter radio

telescope. The Chalmers University group is also developing TSA elements to be integrated with SIS mixers at 300 GHz [5]. The substrates used are quartz and silicon. The University of Massachusetts group is developing TSAs on GaAs and silicon, to be integrated with Two-dimensional electron gas elements to be described below. The most important constraint is that there is an optimum substrate thickness, which decreases as the dielectric constant goes up. As a rule of thumb, one can use the following relationship:

$$\frac{t_{eff}}{\lambda_0} = .03 - .04 \qquad (1)$$

where,

$$t_{eff} = t \times (\varepsilon_r - 1) \qquad (2)$$

The optimum thickness (t) of a silicon substrate (with ε_r = 11.8) for a 100 GHz TSA is about 5-10 micrometers. One approach for achieving the required thickness of the substrate is to etch semiconductor substrates, such as silicon or GaAs. The optimum thickness is considerably greater than the typical membrane thickness in the work of Kevin C. Lee, J. Silcox, et al. [7]. A design being tested at the University of Massachusetts is shown in Figure 5. This design includes a cross-bar for added mechanical strength. Model experiments showed that the cross-bar has negligible effect on the radiation pattern of the element.

QUASI-OPTICAL POWER-COMBINING WITH TSA ARRAYS

Power-combining of a number of sources or power amplifiers is a promising approach to the problem of obtaining higher power output for a number of millimeter wave applications. Traditional designs employ microstrip or waveguide combining networks. If a fairly large number (10-100) of sources are to be combined, microstrip networks become very lossy at millimeter waves. We have demonstrated an active array approach, which is predicted to have an efficiency which is essentially independent of the number of elements. The combiner is intended to be used with the spacecraft transmitters in the NASA deep-space communication network, which is being extended for operation at 32 GHz. The transmitter power will first be split into a number of channels, and amplified by MMIC power amplifiers. The output from the amplifiers will be fed to the elements of a phased array, designed with TSA (Tapered Slot Antenna) radiators. The array thus combines the power of the amplifiers, and feeds it into a near-field Cassegrain reflector system, as illustrated in Figure 5. Circular polarization will be obtained from the linearly polarized array via a polarizer, indicated in Figure 5. The array is also designed for scanning ($\pm 10^o$) by incorporating MMIC phase-shifters in each channel – the corresponding scan for the reflector system is $\pm 1^o$.

The optimum element spacing depends in an array of this type on a number of factors, such as the optical system, packing density of the MMIC chips, etc. A spacing of $d = 1.22\lambda_0$ has been chosen based on such considerations. Element 3 dB beamwidths of 30–40^o are being used to effectively cut down the grating lobes which arise at this spacing. We have studied the predicted array directivity which can be achieved when elements with ideal $(\cos\theta)^q$ active element patterns are used. The array directivity has been calculated for a 21 element two-dimensional array configuration which is presently being developed. The

predicted directivity (D) should be compared with the maximum directive gain (G_{max}) allowed by the total array area for a given element spacing. The area efficiency can be defined as $\eta_A = D/G_{max}$, and is plotted in Figure 7. It is clear that very high area efficiencies are feasible.

A transition to microstrip has been developed for the TSA elements as shown in Figure 7. One of the several substrates (10 mil Duroid 5880) which are used in the two-dimensional array is shown. Dummy TSA elements are used as edge elements to ensure that all active elements have similar patterns.

We have tested a two-dimensional array, fed from a microstrip power divider. The measured E-plane pattern, as shown in Figure 8, is very close to the predicted pattern.

Power-combining arrays of the above type are best used with power amplifier elements, or with injection-locked oscillators. Power-amplifiers and injection-locked oscillators are generally found to have higher output power, and have lower noise, than when a device of the same family (MESFET, IMPATT, etc.) is used as a free-running oscillator. A TSA array quasi-optical power-combiner therefore has considerable potential as a high-power millimeter wave source, which could also have low near-carrier noise. The power-divider would most conveniently be accomplished by using quasi-optical techniques, as shown in Figure 9. Such a power-combiner could be a convenient future source of THz power, especially if the active devices could be fabricated monolithically.

TWO-DIMENSIONAL ELECTRON GAS ELEMENTS FOR MIXING AND HARMONIC GENERATION

While both SIS and Schottky-barrier ixer diodes have been integrated with TSA elements, we would like to emphasize a more novel type of integrated receiver which uses the nonlinear characteristics of an element which is essentially a HEMT device without the gate, i.e. a two-terminal device. As in the HEMT, the current is carried by the two-dimensional electron gas (2 DEG) in a quantum well, which has been formed near a heterojunction. The structure of the device is shown in Figure 10. The microwave equivalent circuit essentially consists of a nonlinear resistance. Due to the two-dimensional nature of the electron gas, the microwave resistance will be independent of the area of the element, if the length/width ratio is held constant. Conversely, the resistance may be tailored by changing the length/width ratio. A typical device size may be of the order of 10-20 micrometers, and it is clear that the capacitance of such a device will be much smaller than for an SIS or Schottky-barrier element. The latter have to be made extremely small, in order to operate in the THz region.

The nonlinearity of the resistance arises because increasing RF power heats the electron gas above the lattice temperature; this in turn causes a change in electron mobility. This type of nonlinearity was first utilized in the InSb "hot-electron" detector and mixer. Its main disadvantage has always been the slow response time of the electrons in InSb, about 1 microsecond, which limits the IF frequency to 1 MHz. The response time of the 2DEG is much faster, of the order of .1 to 1 nanoseconds, which should result in a mixer with bandwidth in the range 1 – 10 GHz, as first pointed out by Smith et al. [8]. We are presently fabricating elements of this type for use in mixers, which could be extended to the THz region. A design in which a 2DEG element is integrated with a TSA antenna is shown in Figure 11. The original proposal for a 2DEG mixer by Smith et al., was for a liquid-helium temperture device, tuned to cyclotron resonance by a magnetic field. We have also shown that a nonlinear device at temperatures of 50–80 Kelvin, wihtout a

magnetic field, should be feasible [Yngvesson, Lau and Yang, to be published]. It is also clear that the nonlinearity could be employed for harmonic generation, as well as mixing.

CONCLUSION

We have shown in this paper that TSA antenna arrays can be used with high efficiency in focal plane imaging as well as power-combining systems. The prototype systems so far have operated in the 30-100 GHz range. It appears entirely feasible to extend these prototypes to the THz range, however, and much of the interesting work in the area of integrated TSA arrays in the next few years is likely to be concentrated on such efforts.

References

[1] P.J. Gibson, "The Vivaldi Aerial," in *Proc. 9th European Microwave Conf.* (Brighton, U.K.), 1979, pp. 101–105.

[2] R. Janaswamy, D.H. Schaubert, and D.M. Pozar, "Analysis of the Transverse Electromagnetic Mode Linearly Tapered Slot Antenna," *Radio Sci.*, vol. 21, pp. 797–804, 1986.

[3] R. Janaswamy and D.H. Schaubert, "Analysis of the Tapered Slot Antenna," *IEEE Trans. Antennas Propagat.*, vol. AP-35, p. 1058–1065, 1987.

[4] J.F. Johansson, "A Moment Method Analysis of Linearly Tapered Slot Antennas," *IEEE Antennas and Propagat. Symposium*, pp. 383–386, 1989.

[5] K.S. Yngvesson et al, "The Tapered Slot Antenna — A New Integrated Element for Millimeter Wave Applications," *IEEE Trans. Microw. Theory Techn.*, MTT-37, 365–374, 1989.

[6] J.F. Johansson, E.L. Kollberg, and K.S. Yngvesson, "Model Experiments with Slot Antenna Arrays for Imaging," *SPIE Proceedings*, Vol. 598, pp. 118–125, 1985.

[7] K. C. Lee, et al. "Schottky Barrier Diode on a Submicron–Thick Silicon Membrane Using a Dual Surface Fabrication Technique," *J. Appl. Phys.* 60, 4038–4040, 1986.

[8] S.M. Smith, et al., "Millimeter and Submillimeter Detection Using $Ga_{1-x}Al_xAs$/GaAs Heterostructures," *Int. J. of Infr. and MMW*, Vol. 8, No. 8, 793–802, 1987.

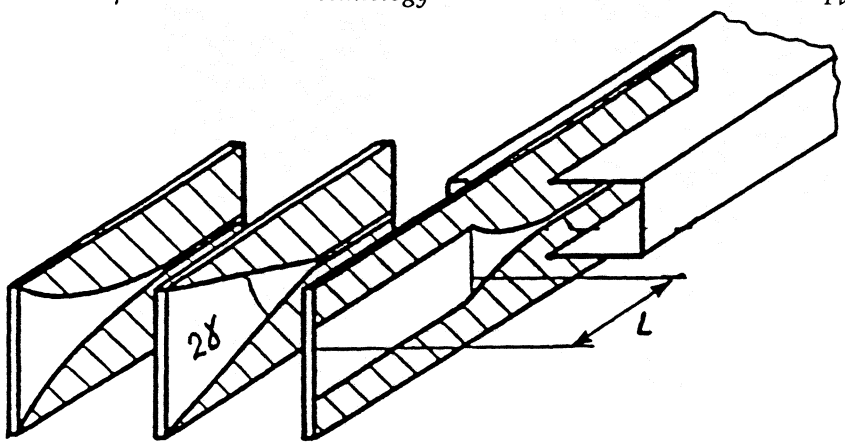

Vivaldi LTSA CWSA

Figure1. The three different types of end-fire tapered slot antennas (TSA)

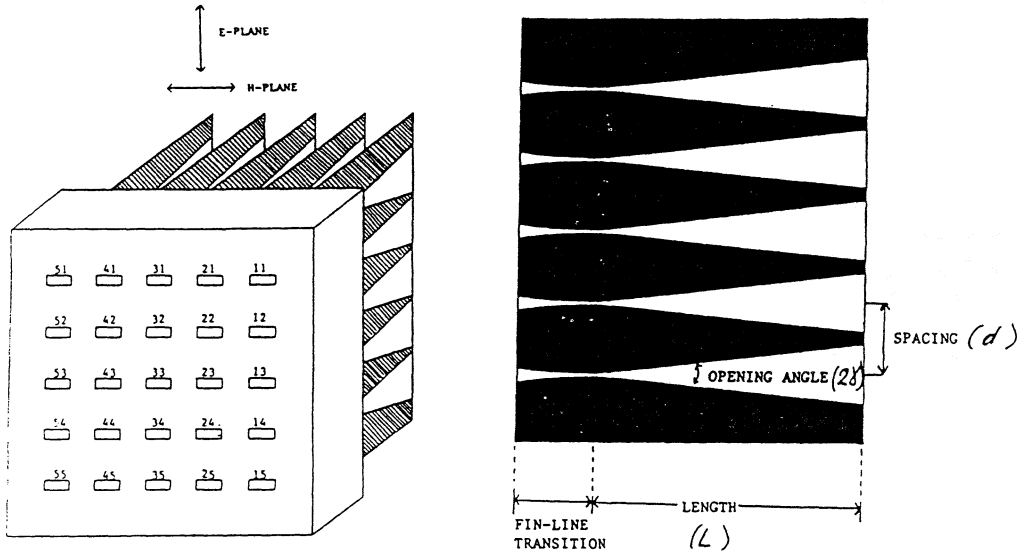

Figure 2. A typical TSA array with a fin-line to waveguide feeding block. The metal pattern made on one of the substrates is shown to the right.

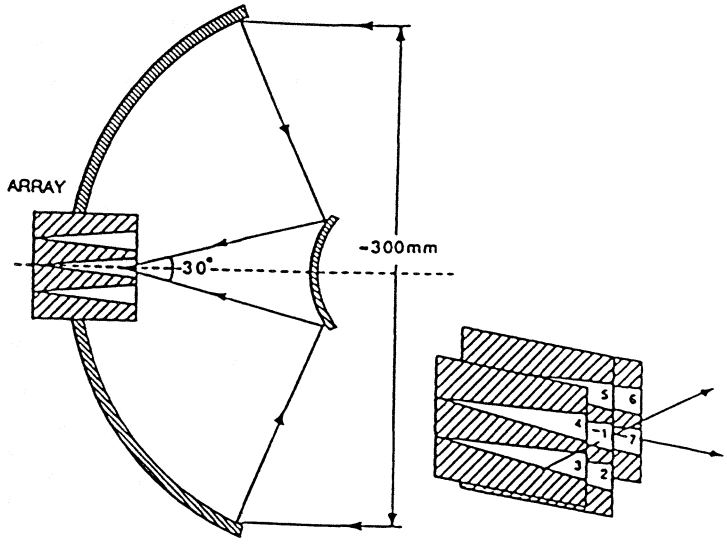

Figure 3. Schematic diagram of 94 GHz seven-element imaging system.

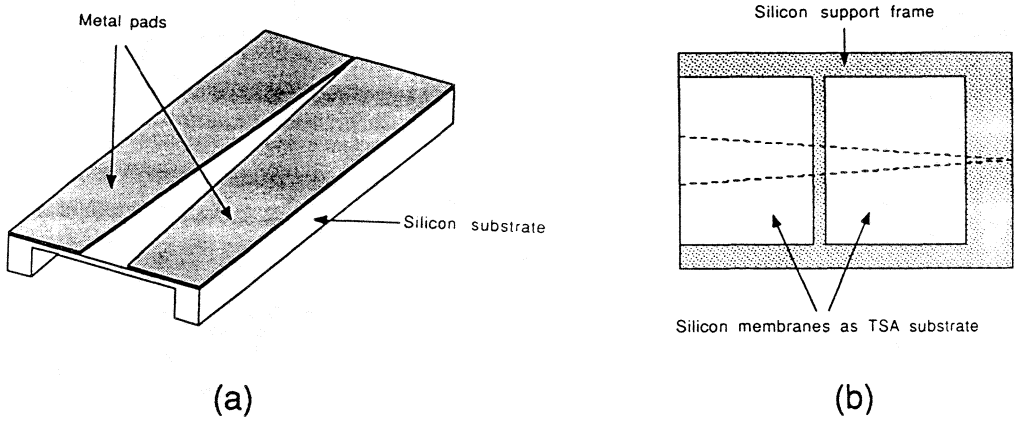

Figure 4. Silicon membrane TSA. (a) Metal pattern side; (b) Membrane side.

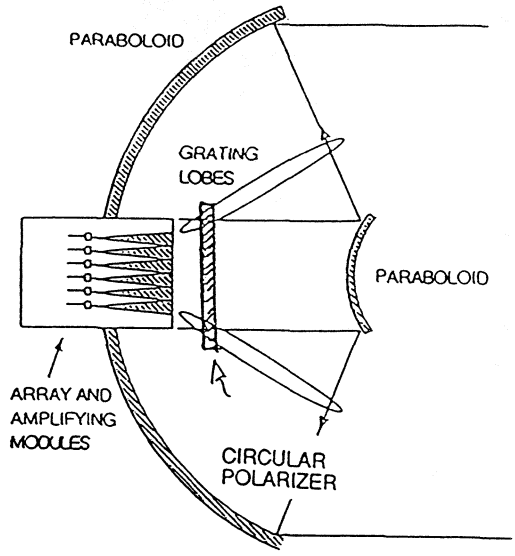

Figure 5. Overview of near-field Cassegrain reflector system with power-combining array.

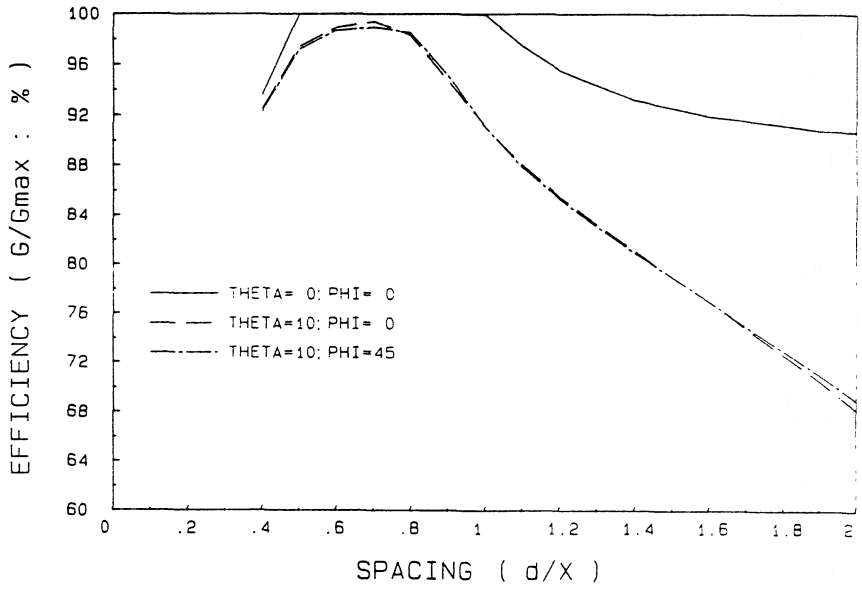

Figure 6. Calculated area efficiency of 21 element array, employing elements with $(\cos\theta)^q$, as a function of element spacing (d/λ_o). The value q has been chosen to result in maximum allowed directive gain for each element, based on its area.

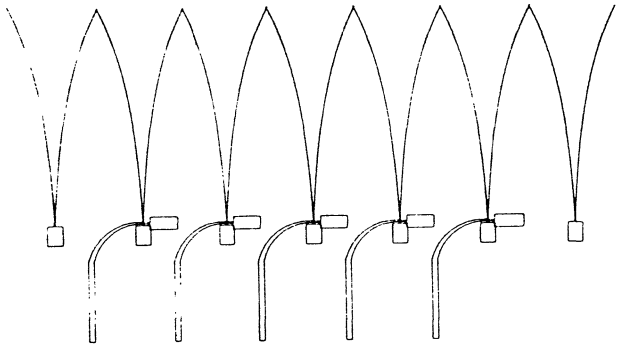

Figure 7. Slot-line to microstrip transition used in TSA array.

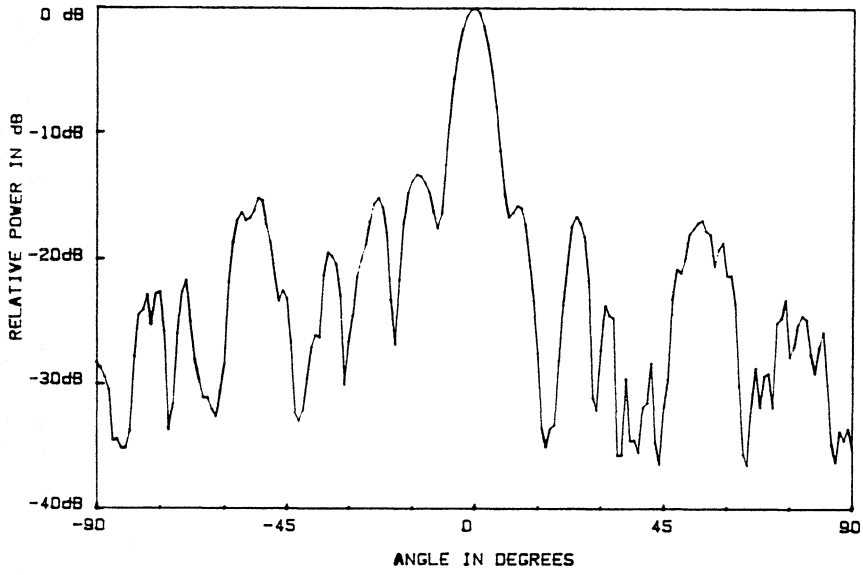

Figure 8. Measured E-plane radiation pattern for a 21-element array.

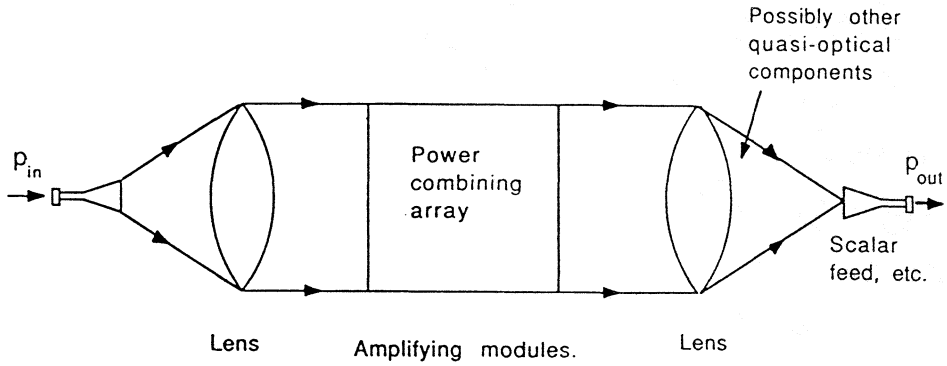

Figure 9. Schematic diagram of a focussing power combining quasi-optical system.

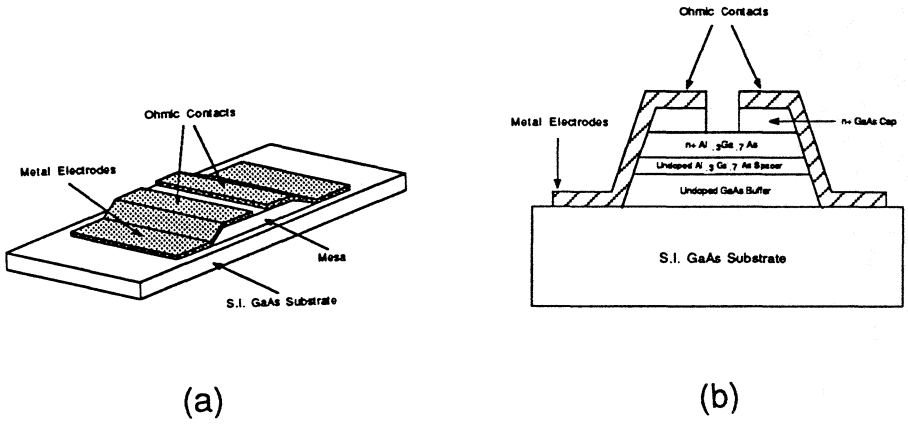

(a) (b)

Figure 10. Schematic diagram of a 2DEG device element. (a) overview; (b) cross section.

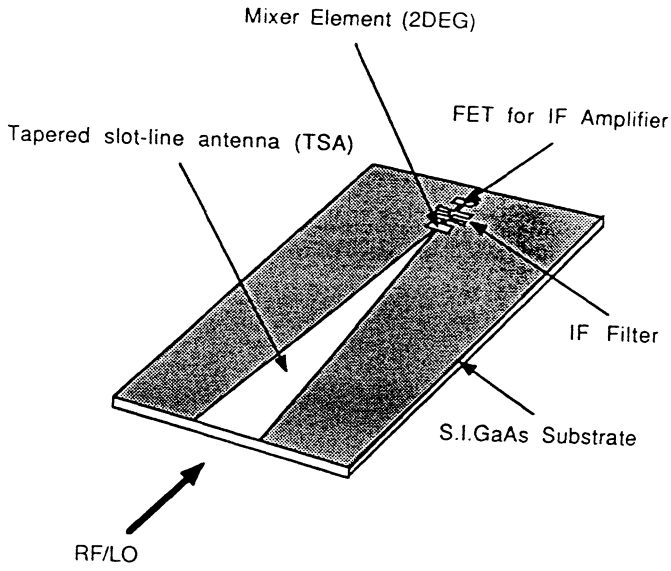

Figure 11. Monolithic millimeter / submillimeter wave TSA mixer with IF amplifier.

THEORETICAL ANALYSIS OF A DIPOLE-FED HORN ANTENNA

G.V. Eleftheriades, Walid Ali-Ahmad, L.P.B. Katehi, G.M Rebeiz

Center for Space Terahertz Technology,
University of Michigan, Ann Arbor, MI

March 1990

Abstract

This antenna consists of a strip dipole printed on a membrane and suspended in an etched pyramidal silicon cavity. The entire fabrication is monolithic. For the theoretical characterization, the horn is approximated by a stepped structure of multiple rectangular waveguide sections. The fields in each section are given by a linear combination of waveguide modes, and the fields in air are given by a continuous plane wave spectrum. To evaluate the Green's function for this problem, an infinitesimally small electric dipole is considered in one of the waveguide sections. Then, the fields inside the silicon cavity are evaluated, and the far-field patterns are found from the Fourier transforms of the electric field on the aperture of the horn.

1. INTRODUCTION

In millimeter wave imaging systems the use of a single detector with electronic or mechanical scanning is inadequate. The events may be too fast, or the required integration time too long. The way to eliminate this limitation is to image all points simultaneously. In 1987, G.M. Rebeiz fabricated a monolithic millimeter-wave imaging array consisting of a large number of silicon horns with detectors placed at the focal plane of the imaging system. For the design of this array, the radiating elements were characterized experimentally and mutual coupling was neglected. As a result, the efficiency of the array was approximately 45 percent. To improve the performance of the array, the elements have to be modeled accurately. This paper presents the development of a rigorous method for the theoretical characterization of the isolated elements.

The procedure for rigorously generating the Green's function for a dipole-fed metallic rectangular horn radiating in free-space is being described. The method allows for step discontinuities to be included in the horn geometry and is not limited by large flaring angles or short axial lengths.

2. THEORY

The procedure which has been employed in the formulation of the problem consists of five steps:

1. The geometry of the horn is approximated by a cascade of rectangular waveguide steps. One of the waveguide steps contains an infinitesimal dipole excitation.
2. The field on the apex and aperture of the horn is transfered, via appropriate transmission matrices, on the excitation (source) plane.
3. The aperture field is matched to free space using plane-wave expansion.
4. The transfered fields of step two are matched over the excitation plane.
5. Finally steps (3) and (4) combined together result in a linear system of equations. The solution of this system provides the required Green's function in discrete form inside the horn and in continuous form in the half space.

2.1 Approximation of the horn geometry

The horn is approximated by a multistepped discontinuity consisting of N sections as shown in Figure 1.

The horn aperture lies on an infinite-metallic screen. Furthermore, it is assumed that there is no reflection from the apex of the horn, since any reflection will be at cut-off.

2.2 Transfer of the apex and Apperture Field on the source plane

Each step discontinuity is characterized by a transmission matrix $[T_b]$:

$$\begin{bmatrix} B^{(2)} \\ D^{(2)} \\ A^{(2)} \\ C^{(2)} \end{bmatrix} = [T_b] \begin{bmatrix} B^{(1)} \\ D^{(1)} \\ A^{(1)} \\ C^{(1)} \end{bmatrix} \tag{1}$$

where the elements of the column matrices denote the unknown coefficients of the field next to the discontinuity. The field in each waveguide is represented in a modal expansion as shown below :

$$\begin{aligned} \bar{E}_t^{(i)} &= \sum_{m,n}^{\infty} \left[\bar{e}_{mn}^{(i),TE}(x,y) \left\{ A_{mn}^{(i)} e^{-\gamma_{mn}^{(i)} z} + B_{mn}^{(i)} e^{\gamma_{mn}^{(i)} z} \right\} \right. \\ &+ \left. \bar{e}_{mn}^{(i),TM}(x,y) \left\{ C_{mn}^{(i)} e^{-\gamma_{mn}^{(i)} z} + D_{mn}^{(i)} e^{+\gamma_{mn}^{(i)} z} \right\} \right] \end{aligned} \tag{2}$$

$$\begin{aligned} -\hat{z} \times \bar{H}_t^{(i)} &= \sum_{m,n}^{\infty} \left[\bar{e}_{mn}^{(i),TE}(x,y) Y_{mn}^{(i),TE} \left\{ A_{mn}^{(i)} e^{-\gamma_{mn}^{(i)} z} - B_{mn}^{(i)} e^{\gamma_{mn}^{(i)} z} \right\} \right. \\ &+ \left. \bar{e}_{mn}^{(i),TM}(x,y) Y_{mn}^{(i),TM} \left\{ C_{mn}^{(i)} e^{-\gamma_{mn}^{(i)} z} - D_{mn}^{(i)} e^{\gamma_{mn}^{(i)} z} \right\} \right] \end{aligned} \tag{3}$$

where i takes the values 1 or 2.

In the above representation both TE and TM modes are included to support the analysis of an arbitrary planar excitation current. A cascade of such transmission matrices, along with associated phase delay transmission matrices is used to transfer the apex and aperture field on the excitation plane :

$$\begin{bmatrix} B^I \\ D^I \\ A^I \\ C^I \end{bmatrix} = [T_B] \begin{bmatrix} B^{(1)} \\ D^{(1)} \\ 0 \\ 0 \end{bmatrix}_{apex} \qquad \begin{bmatrix} B^{II} \\ D^{II} \\ A^{II} \\ C^{II} \end{bmatrix} = [T_A] \begin{bmatrix} B^{(N)} \\ D^{(N)} \\ A^{(N)} \\ C^N \end{bmatrix}_{apperture} \tag{4}$$

Referring to fig.1, the source interface divides the source section #K into two subsections. one on the left, having length l_I and one on the right, having length l_{II}. Accordingly, in equations (4) above, the modal coefficients of the left subsection are denoted with the index (I) and those of the right subsection with the index (II).

2.3 Matching to Half space

This task matches the discrete field spectrum of the aperture section of the horn to the continuous field spectrum of free space, over the horn aperture. The field in free-space is expressed as a plane wave superposition:

$$\bar{E}(x,y,z) = \frac{1}{2\pi} \int_{-\infty}^{\infty} \int_{-\infty}^{\infty} \bar{g}(k_x,k_y) e^{-ik_x x} e^{-ik_y y} e^{-ik_z z} dk_x dk_y \tag{5}$$

with the transverse component of $\bar{g}(k_x,k_y)$ given by:

$$\bar{g}_t(k_x,k_y) = \frac{1}{2\pi} \int\int_{\text{aperture}} \bar{E}_t(x,y,0^+) e^{ik_x x} e^{ik_y y} dx dy \tag{6}$$

Field continuity on the aperture of the horn leads to the following matrix equation :

$$\begin{bmatrix} F_{11} & F_{12} & F_{13} & F_{12} \\ F_{21} & F_{22} & F_{21} & F_{24} \end{bmatrix} \begin{bmatrix} B^{(N)} \\ D^{(N)} \\ A^{(N)} \\ C^{(N)} \end{bmatrix} = \begin{bmatrix} 0 \\ 0 \\ 0 \\ 0 \end{bmatrix} \tag{7}$$

The submatrices F_{ij} contain reaction integrals involving the discrete modes of the aperture field. There are three kind of reaction integrals as shown below :

$$I^{pq}_{1ijmn} = \int_{-\infty}^{\infty} \int_{-\infty}^{\infty} \frac{(k^2 - k_y^2)}{k_z} \tilde{e}^p_{xij}(k_x,k_y) \tilde{e}^{*q}_{xmn}(k_x,k_y) dk_x dk_y \tag{8}$$

$$I^{pq}_{2ijmn} = \int_{-\infty}^{\infty}\int_{-\infty}^{\infty} \frac{(k^2 - k_x^2)}{k_z} \tilde{e}^{p}_{yij}(k_x,k_y)\tilde{e}^{*q}_{ymn}(k_x,k_y)dk_x dk_y \quad (9)$$

$$I^{pq}_{3ijmn} = \int_{-\infty}^{\infty}\int_{-\infty}^{\infty} \frac{k_x k_y}{k_z} [\tilde{e}^{p}_{yij}(k_x,k_y)\tilde{e}^{*q}_{xmn}(k_x,k_y) + \tilde{e}^{p}_{xij}(k_x,k_y)\tilde{e}^{*q}_{ymn}(k_x,k_y)]dk_x dk_y \quad (10)$$

where p, q take the values 1 ($\rightarrow TE$) or 2 ($\rightarrow TM$).

In order to facilitate the numerical evaluation of the integrals it is advantageous to transform them in the space-domain. Their transformation from the spectral-domain to the spatial-domain is accomplished via the application of Parseval's theorem leading to :

$$I^{pq}_{1ijmn} = \frac{1}{2\pi}\int_{x_N}^{x_N}\int_{-y_N}^{y_N} \frac{ie^{-ik\rho}}{\rho}(k^2 + \frac{\partial^2}{\partial y^2})$$
$$[e^{p}_{x1ij}(-x) \otimes e^{q}_{x1mn}(x)][e^{p}_{x2ij}(-y) \otimes e^{q}_{x2mn}(y)]dxdy \quad (11)$$

$$I^{pq}_{2ijmn} = \frac{1}{2\pi}\int_{x_N}^{x_N}\int_{-y_N}^{y_N} \frac{ie^{-ik\rho}}{\rho}(k^2 + \frac{\partial^2}{\partial x^2})[e^{p}_{y1ij}(-x) \otimes e^{q}_{y1mn}(x)]$$
$$[e^{p}_{y2ij}(-y) \otimes e^{q}_{y2mn}(y)]dxdy \quad (12)$$

$$I^{pq}_{3ijmn} = -\frac{1}{2\pi}\int_{x_N}^{x_N}\int_{-y_N}^{y_N} \frac{ie^{-ik\rho}}{\rho}\frac{\partial^2}{\partial x \partial y}[(e^{p}_{y1ij}(-x) \otimes e^{q}_{x1mn}(x))$$
$$(e^{p}_{y2ij}(-y) \otimes e^{q}_{x2ij}(y)) + (e^{p}_{x1ij}(-x) \otimes e^{q}_{y1mn}(x))(e^{p}_{x2ij}(-y) \otimes e^{q}_{y2mn}(y)]dxdy \quad (13)$$

where $\rho = \sqrt{x^2 + y^2}$.

2.4 Matching on the source interface

The point excitation is assumed to be a y-directed surface current given by:

$$\bar{K}(x,y) = \delta(x - x')\delta(y - y')\hat{y} \quad (14)$$

Upon matching over the source interface we derive the matrix equation :

$$[A]\begin{bmatrix} B^{(I)} \\ D^{(I)} \\ A^{(I)} \\ C^{(I)} \end{bmatrix} = [A]\begin{bmatrix} B^{(II)} \\ D^{(II)} \\ A^{(II)} \\ C^{(II)} \end{bmatrix} + \begin{bmatrix} 0 \\ 0 \\ e^{TE}_{1mn}(x',y') \\ e^{TM}_{2mn}(x',y') \end{bmatrix} \quad (15)$$

where matrix [A] above involves the mode admittances of the source section as shown below :

$$\begin{bmatrix} I & O & I & O \\ O & I & O & I \\ -Y^{TE,K} & O & Y^{TE,K} & O \\ O & -Y^{TM,K} & O & Y^{TM,K} \end{bmatrix} \tag{16}$$

2.5 Derivation of the final system of equations

The equations that have been generated so far are summarized below :

- Apex-aperture field transfered on the source plane through transmission matrices:

$$\begin{bmatrix} B^{(I)} \\ D^{(I)} \\ A^{(I)} \\ C^{(I)} \end{bmatrix} = [T_B] \begin{bmatrix} B^{(1)} \\ D^{(1)} \\ 0 \\ 0 \end{bmatrix}_{apex} \qquad \begin{bmatrix} B^{II} \\ D^{(II)} \\ A^{(II)} \\ C^{(II)} \end{bmatrix} = [T_A] \begin{bmatrix} B^{(N)} \\ D^{(N)} \\ A^{(N)} \\ C^{(N)} \end{bmatrix}_{apperture} \tag{17}$$

- Matching of the aperture field :

$$[F] \begin{bmatrix} B^{(N)} \\ D^{(N)} \\ A^{(N)} \\ C^{(N)} \end{bmatrix} = \begin{bmatrix} 0 \\ 0 \\ 0 \\ 0 \end{bmatrix} \tag{18}$$

- Matching of the fields on the source interface :

$$[A] \begin{bmatrix} B^{(I)} \\ D^{(I)} \\ A^{(I)} \\ C^{(I)} \end{bmatrix} = [A] \begin{bmatrix} B^{(II)} \\ D^{(II)} \\ A^{(II)} \\ C^{(II)} \end{bmatrix} + \begin{bmatrix} 0 \\ 0 \\ e^{TE}_{1mn}(x', y') \\ e^{TM}_{2mn}(x', y') \end{bmatrix} \tag{19}$$

The above equations are merged together to form a single matrix equation involving the modal coefficients of the apex and aperture sections :

$$\begin{bmatrix} [A][T_B]' & -[A][T_A] \\ O & [F] \end{bmatrix} \begin{bmatrix} B^{(1)} \\ D^{(1)} \\ B^{(N)} \\ D^{(N)} \\ A^{(N)} \\ C^{(N)} \end{bmatrix} = \begin{bmatrix} O \\ O \\ e_1 \\ e_2 \\ O \\ O \end{bmatrix} \tag{20}$$

Note that the block-submatrix $([A][T_B])'$ consists only of the half first columns of $[A][T_B]$. This is a consequence of the assumption of no reflections from the apex of the horn. Having found the modal coefficients of the apex and aperture sections, the Green's function inside the horn is represented as a discrete Fourier series whereas outside the horn as a Fourier integral. Specifically the transverse component of the Green's function for a y-directed current inside the horn can be represented in a quadratic form as shown below :

$$\bar{G}_t(x,y,x',y') =$$

$$\left[\bar{e}^{TE}_{mn}(x,y)\ \bar{e}^{TM}_{mn}(x,y)\ \bar{e}^{TE}_{mn}(x,y)\ \bar{e}^{TM}_{mn}(x,y)\right][T_B][SM1] \begin{bmatrix} 0 \\ 0 \\ e^{TE}_{mn}(x',y') \\ e^{TM}_{mn}(x',y') \end{bmatrix} \tag{21}$$

In the above representation [SM1] is an appropriate submatrix of the inverse of the system matrix defined in (19).

3. NUMERICAL RESULTS

The aperture field and the far-field for a specific horn geometry has been evaluated. For this purpose the aperture coefficients are calculated from the solution of matrix equation (20). For a vertical point source only modes of the form (m,n) [m=1,3,5, ... and n=0,2,4, ...] are excited. Numerical convergence for the far-field was achieved when TE and TM modes up to the order (7,7) were included. The magnitude of the co-polarized aperture field

shown in fig.4 is recognized to be a perturbed dominant mode field distribution. Furtermore,the utilization of both TE and TM modes in the theory enabled the calculation of the cross-polarized aperture field which has a level of -16dB for the case under consideration. The phase of the aperture field is depicted in fig.5. Of interest is the cross-polarization phase which divides the aperture ,along its geometrical axes of symmetry, into four quadrants. Each quadrant is out of phase with its adjacent quadrants.

4. CONCLUSION

This paper presented a riqorous method for the characterization of a monolithic horn antenna excited by an infinitesimal small dipole printed on a membrane. Using this method, the fields on the aperture of the silicon horn were evaluated and transformed to the Fourier domain in order to derive the far-field patterns. The developed method may easily be extended to compute input impedance and resonant properties of these radiating structures for feeding dipoles of finite size.

5. AKNOWLEDGMENTS

The work was sponsored by the Center for Space Terahertz Technology, the University of Michigan, Ann Arbor, MI.

REFERENCES

1. Thomas Wriedt, Karl-Heinz Wolff, Frint Arndt and Ulrich Tucholke, "Rigorous Hybrid Field Theoretic Design of Stepped Rectangular Waveguide Mode Converters Including the Horn Transitions into Half-Space," *IEEE Transactions on Antennas and Propagation*, Vol. 37, No. 6, June 1989.

2. Amir I. Zaghloul and Robert H. MacPhie, "Cross-Correlation Formulation of the Complex Power from Planar Apertures," *Radio Science*, Vol. 10, No. 6, pp. 619-624, June 1975.

3. Robert H. McPhie and Amir I. Zaghloul, "Radiation from a Rectangular Waveguide with Infinite Flange-Exact Solution by the Correlation Matrix Method," *IEEE Transactions of Antennas and Propagation*, Vol. AP-28, No. 4, July 1980.

4. Jose A. Encinar and Jesús Rebollar, "A Hybrid Technique for Analyzing Corrugated and Non-Corrugated Rectangular Horns," *IEEE Transactions on Antennas and Propagation*, Vol. AP-34, No. 8, August 1986.

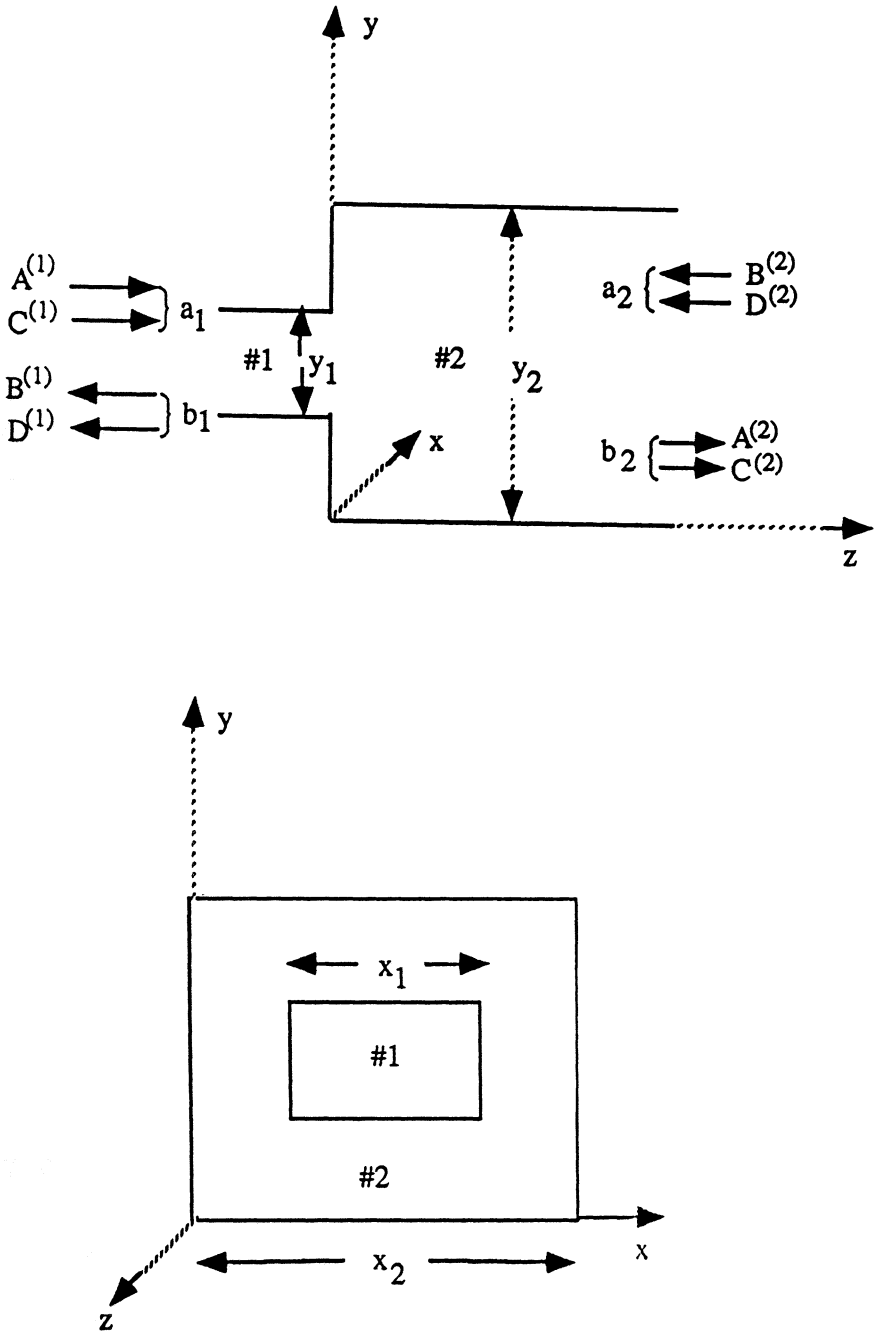

Fig.1 A waveguide step discontinuity.

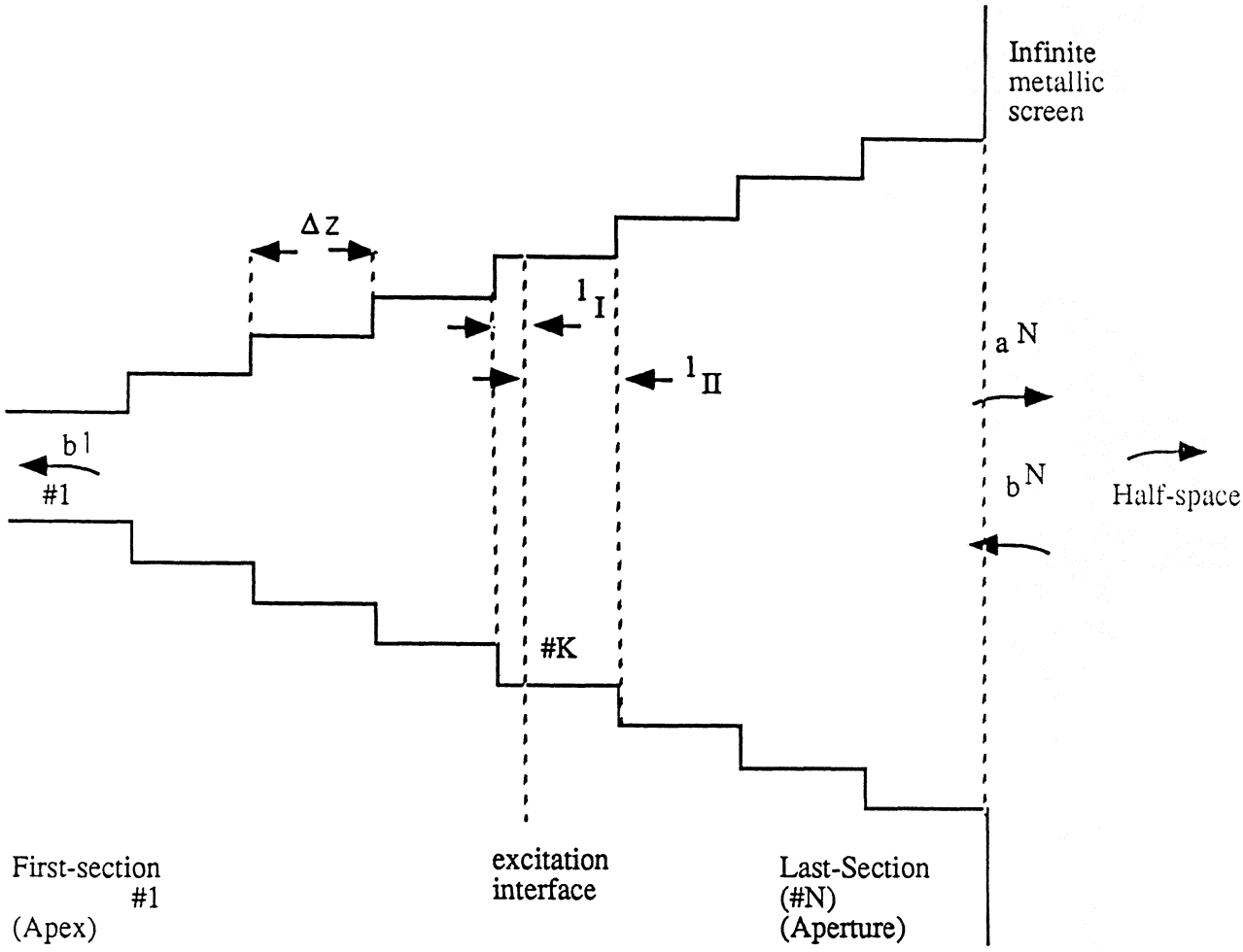

Fig.2 Approximation of the horn geometry by cascaded step discontinuities.

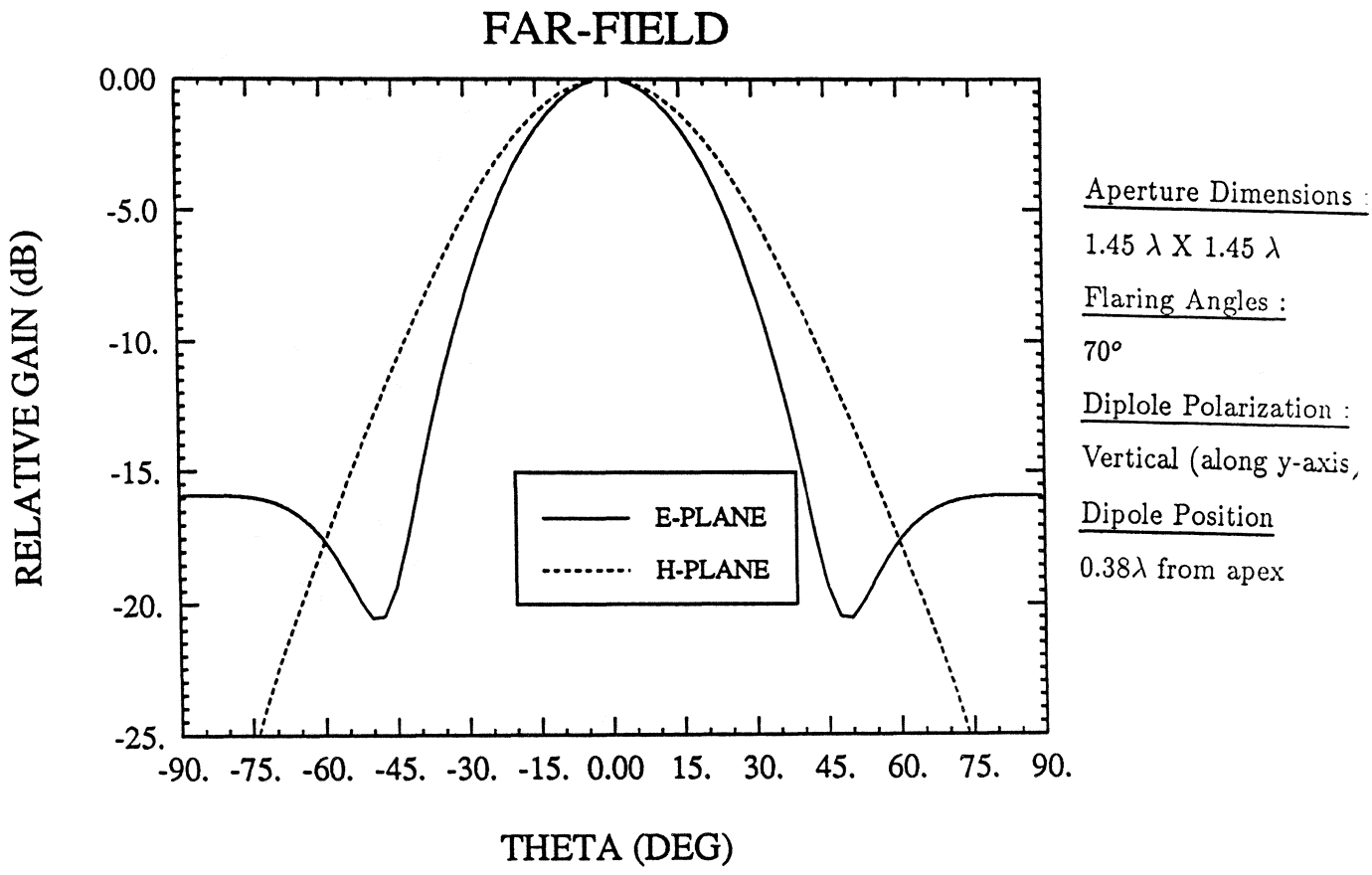

Fig.3 Far-field.

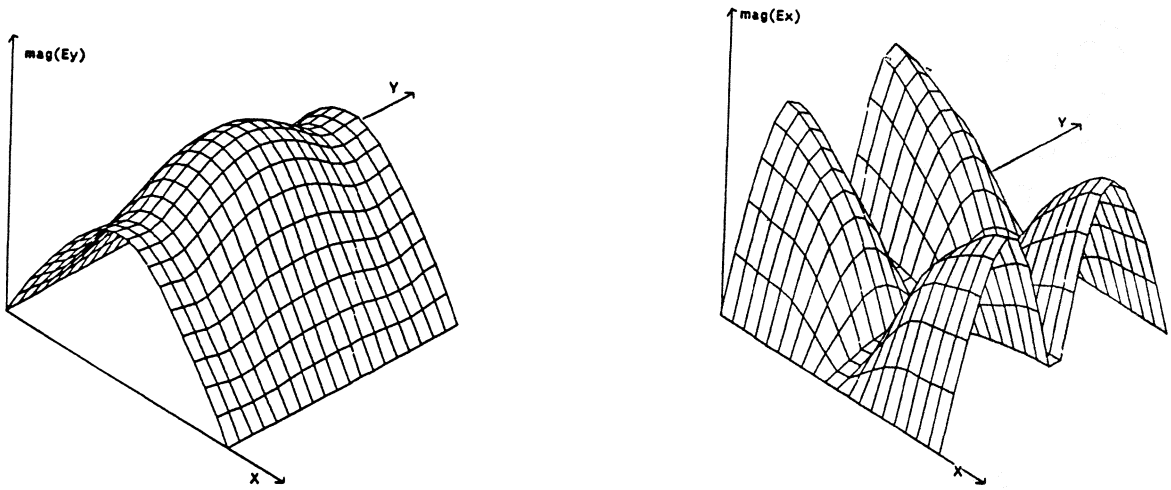

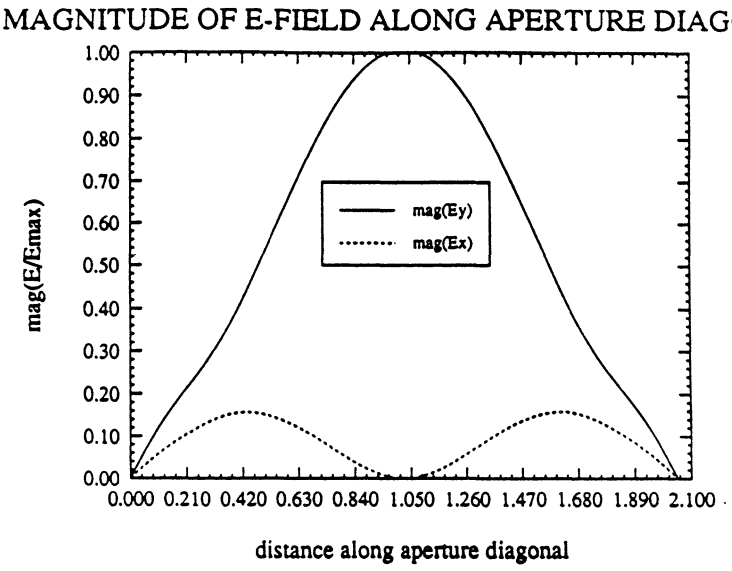

Fig.4 Magnitude of aperture field. (a) The co-polarazized field. (b) The cross-polarized field. (c) Comparison of the co-polar and cross-polar magnitude along the aperture diagonal.

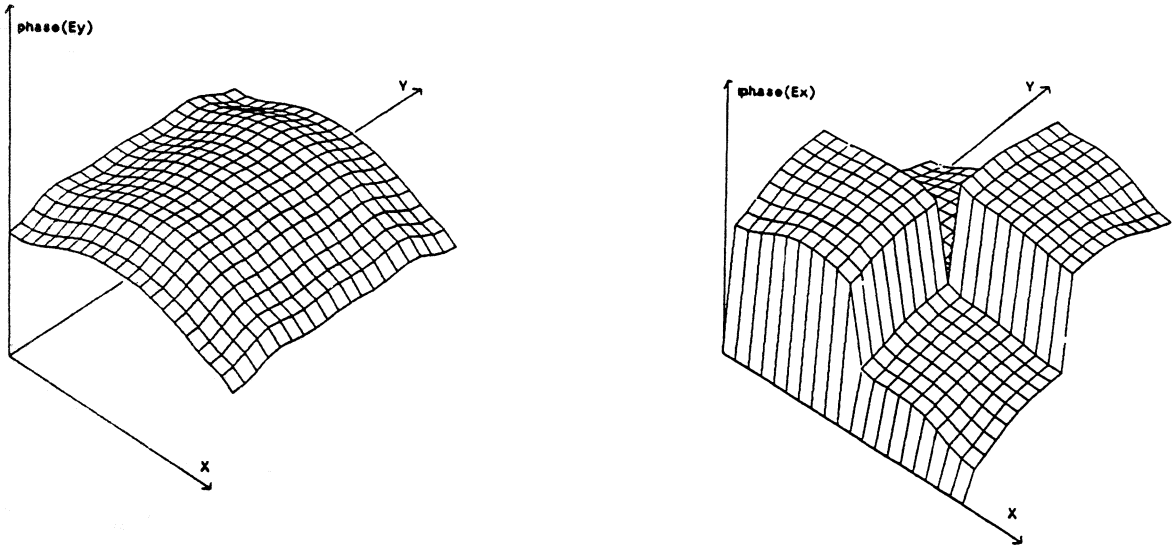

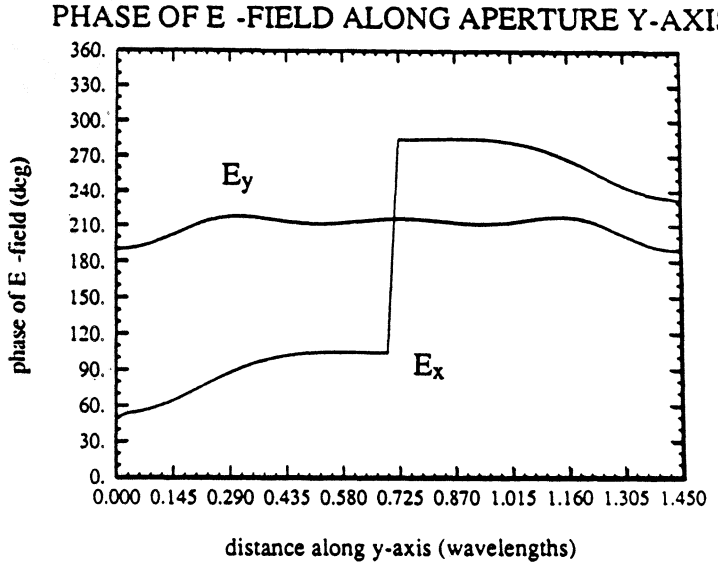

Fig.5 Phase of aperture field. (a) The co-polarized field. (b) The cross-polarized field. (c) Comparison of the co-polar and cross-polar phase along the aperture diagonal.

Twin-slot Multi-layer Substrate-supported Antennas and Detectors for Terahertz Imaging

Stuart M. Wentworth, Robert L. Rogers, John G. Heston,
and Dean P. Neikirk
The University of Texas at Austin
Austin, TX 78712

Planar antenna arrays with integrated detectors have proven to be very useful for millimeter and submillimeter wave receiver systems. One problem with planar antennas is their tendency to couple significant power into guided modes (also called surface waves) when the substrate is a significant fraction of a dielectric wavelength λ_d thick [1]. Coupling into these surface waves can be avoided by making the substrate very thin (on the order of 50 μm or less for far-infrared radiation), or by making the substrate appear infinitely thick by placing a focusing lens on back of the substrate [2]. Unfortunately, substrate lenses tend to be quite lossy in the terahertz regime, while membrane-supported devices present difficult fabrication challenges. A third approach involves the use of electrically thick substrates of carefully chosen thickness, in conjunction with an antenna design which suppresses surface wave coupling.

In this paper we will discuss twin-slot antennas supported on a multilayer dielectric stack, which show both good patterns and efficiencies. The dielectric layers used are thick enough to be handled with conventional fabrication equipment. The appropriate choice of dielectric stack also allows the beamwidth to be adjusted, providing a good match between the antenna and optical system feed patterns. In addition, we will also discuss new integrated microbolometer configurations which should be more sensitive than conventional microbolometers for terahertz detection. The combination of these antennas and detectors may allow the fabrication of imaging arrays with higher sensitivities than those currently available.

Twin slot antenna structure

The theory underlying a twin slot antenna on a dielectric stack (Fig. 1) has been covered in extensive detail by Rogers *et al.* [3-5]. In this theory, it is much easier to treat the twin slot antenna structure as a source of radiation rather than as a receiver. By reciprocity, efficiencies and beam patterns will be the same for both source and receiver. Briefly, the total power emitted by a twin slot antenna consists of the power radiated through the dielectric (the "front side" of the structure), the power lost to surface waves,

and the power radiated directly to air (the "backside" of the structure). To calculate radiated power, equivalent transmission line models of the dielectric stack are used, and each slot is modeled as a voltage source. To calculate power lost to surface waves, a reciprocity method described by Rutledge *et al.* is used [6].

Planar antennas placed on a dielectric substrate tend to radiate more power through the dielectric than directly into air [7]. For most efficient operation, it is desirable that the power radiated through the dielectric side be much larger than that radiated directly to air (i.e., to the backside of the stack). For a slot antenna, the use of an odd number of $\lambda/4$ thick dielectric layers, with high-low-high alternating dielectric constants, will maximize the frontside radiation [3,8]. The dielectric substrate which supports the antenna also forms a waveguide structure which will cause undesirable loss of power to guided (or surface) waves. However, if the substrate consists of an odd number of $\lambda/4$ thick layers, alternating from high to low to high dielectric constant, it is possible to restrict the surface wave losses to one dominant mode, usually the TM_0 mode [9]. If a pair of slots is placed one half a TM_0 wavelength apart in the broadside direction, and the slots are driven in-phase, then the TM_0 modes from each slot will superimpose and cancel [4]. Thus, the same dielectric stack which maximizes radiated power through the dielectric can also be used to suppress surface wave losses when used in conjunction with twin slots. Similar twin slot antennas have been used in the past as a component in a quasi-optical mixer operating at 100 to 120 GHz [10].

In order to test the performance of the dielectric stack structures twin slot antennas have been fabricated on a 2.5 cm x 2.5 cm square 406 μm thick fused quartz substrates for operation near 94 GHz [11]. The slot ground plane was deposited by thermal evaporation of ~300 Å of chromium for adhesion followed by ~6000 Å of gold (slightly more than two skin depths at 94 GHz). Slots were then chemically etched into the ground plane. The feed network was separated from the ground plane by a 2 μm thick polyimide layer (DuPont Pyralin PI-2556 polyimide), cured at 250 °C for a duration of 1.5 hours. Fabrication of bismuth microbolometer detectors and microstrip feed line network was accomplished using a bilayer photoresist bridge technique [12,13]. The Bi microbolometer was approximately 1000 Å thick, 3 μm long and 3 μm wide. The feed lines are 25 μm wide,with a 1000 Å thick layer of Ag topped by a 2000 Å thick layer of Bi, and finally a 2000 Å thick layer of Ag (the much higher conductivity of Ag essentially shorts the Bi in the feed line). Bi microbolometer resistance was measured to be about 80 Ω, and the microstrip impedance was calculated to be about 13-16 Ω based on empirical formulas [14-16]. The series resistance of the microstrip line between the innermost filters was

measured as 18 Ω (~0.23 Ω/square). For the fused quartz structure, the room temperature microbolometer responsivity was measured to be about 7.2 V/W when biased at 0.1 V.

Electrical connection was achieved by placing the chip on a small microwave laminate board, and connecting pads on the chip to copper pads on the board using silver paint. The chip was placed in a positioning mount with the twin slot antenna at the center, allowing the antenna to pivot in the E- and H-planes. A Hughes IMPATT W-band oscillator connected to a standard gain horn was placed approximately 36 cm from the antenna. Laser alignment was used to determine boresight and to align the chip plane parallel with the plane of the horn. The radiation was chopped at 200 Hz, and the signal was measured with a Stanford Research Systems SR530 lock-in amplifier. Measurements were taken at 4° increments in both E- and H-planes, and the detected signals ranged from 6 μV down to the background noise level of about 0.02 μV.

Figure 2 shows both measured and calculated receiver gain beam patterns for the single fused quartz substrate operating at 90.5 GHz. There is considerable asymmetry between the E- and H-planes, which would be undesirable for optical system feeds. The shape of the measured E-plane agrees reasonably well with the theoretical model. We conjecture that the slightly jagged peaks are associated with finite ground plane effects, and with interference from surface waves reflecting back from the edges of the ground plane. The shape of the H-plane beam pattern shows only rough agreement with theory. We again assume that this is primarily a result of guided waves reflecting off the ground plane edge. There may also have been interference from adjacent pairs of slots, which were 0.5 cm distant from the center element in the H-plane. The sudden drop for the H-plane pattern at -56° is due to shadowing from the antenna positioner mount.

Placement of a quarter wavelength thick quartz layer one quarter of a wavelength above the substrate tested above results in a "resonant" structure similar to those described in [8]. The quartz-air-quartz stack, corresponding to $\varepsilon_{high} = 3.8$ and $\varepsilon_{low} = 1.0$ in Fig. 1, was made by placing a 1/4 λ_d thick (406 μm) fused quartz chip over the substrate, using small spacers 860 μm thick placed at the corners of the chip. Figures 3 and 4 show beam patterns for this multilayer stack at 90.5 and 94 GHz, respectively. Although the antenna is designed for 94 GHz, the air gap was slightly thicker (~864 μm) than the 1/4 λ_d design thickness (787 μm). Experimentally, the narrowest beam pattern was found at 90.5 GHz, which matched the predicted resonant frequency for the actual layer thicknesses used. In both figures, the calculated beam pattern shapes are approximately matched by experiment. The boresight gain does not change noticeably between 94 and 90.5 GHz. This could be quite convenient in lens-coupled receivers where the beam pattern is not critical, but where the gain is desired constant over some appreciable bandwidth.

Comparing the single and multilayer 90.5 GHz results of Figs. 2 and 3, the theory predicts a boresight gain about 6 dB higher for the multilayer case. This increase is indeed observed since the boresight detector signal increases from 1 μV to 4 μV when the additional layer and air gap are added. It is also observed that compared to the single layer case, the measured and calculated patterns for the multilayer case are much narrower, and would thus match an optical system of higher f-number.

Our model predicts at least a 10 dB higher receiver gain than is achieved by any of the experimental cases. However, the theory does not consider losses in the feedline, nor does it consider mismatch losses between the detector and the feed line. Our measurements indicate 6 dB of feedline loss. Another 3 dB mismatch loss is expected between the detector (80 Ω resistance) and the microstrip feedline (13-16 Ω impedance). Another possible loss mechanism is rf power loss through the low pass filters, which may not have a low enough impedance compared to the microstrip line.

Composite Microbolometers

The twin slot antennas discussed above made use of integrated microbolometer detectors. These detectors are relatively simple to fabricate, present a purely real impedance, and can easily be calibrated to make absolute power measurements. Figure 5 shows the dependence of resistance on ambient temperature for microbolometers made of bismuth and of tellurium [17]. These devices were about 1000 Å thick and roughly 4 μm x 4 μm in area, and were fabricated on glass substrates. The slopes for both materials stay fairly constant throughout the temperature range measured. The dR/dT of Te is roughly 3 orders of magnitude higher than that of Bi. Calculations show that a microbolometer made with Te could approach responsivities of magnitude 2000 V/W, or a hundred times higher than a comparable Bi microbolometer. Although the Te looks promising because of its high responsivity, its high resistance makes direct coupling to a planar antenna difficult. However, alternative composite structures for impedance matching could be developed to utilize such high resistance detectors. The combination of new antenna structures and high responsivity microbolometers may allow a significant improvement in far-infrared detector sensitivity.

One solution to the mismatched load problem is to separate the load from the detector in a composite microbolometer structure, as shown in Fig. 6 [18]. The load, which is impedance-matched to the antenna, is in intimate thermal contact with, but is electrically isolated from, the detector element. Changes in load temperature will be quickly followed by changes in detector temperature, and hence by changes in detector resistance.

Composite microbolometers have been fabricated on glass substrates consisting of nichrome as the load, Te as the detector, and SiO_x as the insulator. The 80% Ni-20% Cr load was approximately 1500 Å thick, in contact with a 1500 Å thick gold bow-tie antenna. Following deposition of an 1800 Å thick SiO_x layer, the signal line/detector layer was fabricated. The Te detector was about 1200 Å thick, contacted to a 2000 Å thick gold signal line. The lengths and widths were about the same for both NiCr and Te elements, ranging from 4.5 to 5.0 μm. Fabrication will be detailed elsewhere [18].

Figure 7 shows the responsivity curve generated for the composite microbolometer at a Te detector bias of 0.75 V. This figure also shows the noise voltage measured across the Te detector element at the same voltage. The noise is measured with a PAR 124A lock-in amplifier with 117 preamp over a bandwidth of 10% of the selected center frequency. Since the Johnson noise floor is about 10^{-8} V/$\sqrt{\text{Hz}}$, it is clear from this figure that a 1/f-type noise is dominant. The NEP plot in Fig. 8 is calculated by dividing the noise by the responsivity. The device has a minimum NEP of 6.7 x 10^{-9} W/$\sqrt{\text{Hz}}$ at 30 kHz. For comparison, a Bi microbolometer typically has an r_{dc} of 20 V/W, and minimum NEP of 10^{-10} W/$\sqrt{\text{Hz}}$ at 10 kHz. Although the NEP of our composite microbolometer is somewhat higher than a conventional Bi device, the higher responsivity produces signals of much larger magnitude, thus reducing the requirements for very small signal amplifiers. Also, it is somewhat easier to build low noise amplifiers which match the higher input impedance of the composite detectors.

Conclusions

A planar receiver has been demonstrated which consists of a twin slot antenna on a dielectric stack and a microbolometer detector. As expected from theory, a higher gain beam pattern was obtained when a quartz-air-quartz dielectric stack was used. Both theoretical models and experimental measurements show that although all the dimensions used for this antenna structure (i.e. the dielectric layer thicknesses, slot length, slot separation, and microstrip feed network length) are referenced to a single design frequency, the operating bandwidth is reasonably broad, without dramatic changes in either gain or pattern over at least a 5% variation in frequency.

A composite microbolometer has also been developed using a NiCr load and a Te detector element. Such a structure removes the constraint of impedance matching to the antenna impedance, and opens the way for the use of a variety of new materials with considerably larger temperature coefficients of resistance than bismuth.

References:

1. B. Roudot, J. Mosig, and F. Gardiol, "Surface Wave Effects on Microstrip Antenna Radiation," *Microwave Journal*, pp. 201-211, March 1988.

2. D.P. Neikirk, D.B. Rutledge, M.S. Muha, H. Park, and C.X. Yu, "Progress in millimeter-wave integrated circuit imaging arrays," *Proc. SPIE*, 317, p. 206, 1981.

3. R.L. Rogers and D.P. Neikirk, "Radiation Properties of Slot and Dipole Elements on Layered Substrates," *Int. J. Infrared and Millimeter Waves*, Vol 10, No. 6, pp. 697-728, 1989.

4. R.L. Rogers and D.P. Neikirk, "Use of Broadside Twin Element Antennas to Increase Efficiency on Electrically Thick Dielectric Substrates," *Int. J. Infrared and Millimeter Waves*, Vol. 9, No. 11, pp. 949-969, 1988.

5. R.L. Rogers, S.M. Wentworth, D.P. Neikirk, and T. Itoh, "A Twin Slot Antenna on a Layered Substrate Coupled to a Microstrip Feed Line," to be published in *Int. J. Infrared and Millimeter Waves.*

6. D.B. Rutledge, D.P. Neikirk, and D.P. Kasilingam, "Integrated Circuit Antennas," Infrared and Millimeter Waves, Vol. 10, Academic Press, pp. 1-90, 1983.

7. N.G. Alexopoulos, P.B. Katehi, and D.B. Rutledge, "Substrate Optimization for Integrated Circuit Antennas," *IEEE Trans. MTT*, Vol. 31, No. 7, pp. 550-557, 1983.

8. N.G. Alexopoulos and D.R. Jackson, "Fundamental Superstrate Effects on Printed Circuit Antennas," *IEEE Trans. Antennas and Propagation*, Vol. AP-32, No. 8, pp. 807-816, Aug. 1984.

9. R.L. Rogers, D.P. Neikirk, H. Ling, and T. Itoh, "Antennas on Layered Substrates," *13th Annual Conf. on Infrared and Millimeter Waves*, pp. 33-34, Dec. 1988.

10. A.R. Kerr, P.H. Siegel, and R.J. Mattauch, "A simple quasi-optical mixer for 100-120 GHz," in *1977 IEEE MTT-S Int. Microwave Symposium Dig.*, pp. 96-98.

11. S.M. Wentworth, R.L. Rogers, J.G. Heston, D.P. Neikirk, and T. Itoh, "Millimeter Wave Twin Slot Antennas on Layered Substrates," to be published in *Int. J. Infrared and Millimeter Waves*, Vol. 11, No. 2, Feb. 1990.

12. D.P. Neikirk, W.W. Lam, and D.B. Rutledge, "Far-Infrared Microbolometer Detectors," *Int. J. Infrared and Millimeter Waves*, Vol. 5, No. 3, pp. 245-278, 1984.

13. D. M. Dobkin and B. D. Cantos, "Plasma Formation of Buffer Layers for Multilayer Resist Structures," *IEEE Electron Device Lett.*, Vol. EDL-2, No. 9, pp. 222-224, Sept. 1981.

14. T.C. Edwards, Foundations for Microstrip Circuit Design, Wiley and Sons, New York, 1981, pp. 44-47.

15. K.C. Gupta, R. Garg, I.J. Bahl, Microstrip Lines and Slotlines, Artech House, Inc. 1979, p. 11.

16. I. Bahl and P. Bhartia, Microwave Solid State Circuit Design, Wiley and Sons, New York, 1988, p. 18.

17. S.M. Wentworth and D.P. Neikirk, "Far Infrared Microbolometers Made with Tellurium and Bismuth," *Electronics Letters*,Vol. 25, No. 23, pp. 1558-1560, 9 Nov. 1989.

18. S.M. Wentworth and D.P. Neikirk, "Far-Infrared Composite Micro-bolometers," to be presented at the *1990 IEEE MTT-S International Microwave Symposium*, Dallas, May 8-10, 1990.

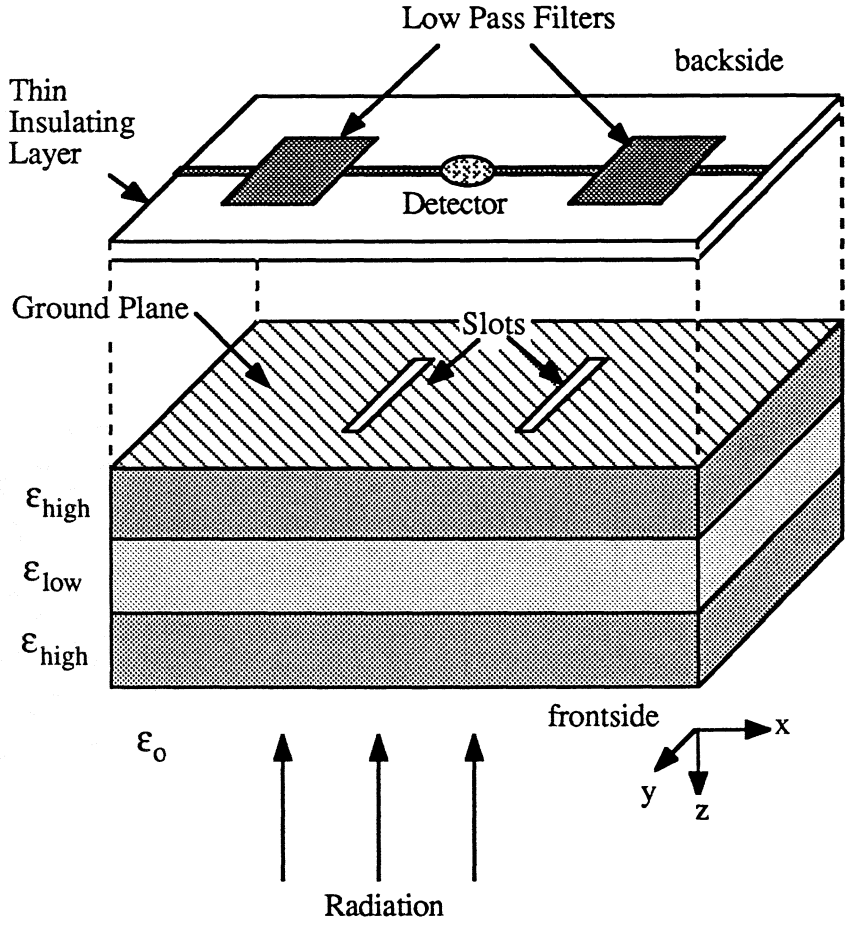

Fig. 1: Twin slot antenna on a dielectric stack, where each layer is 1/4 wavelength thick. The slots couple power into a microstrip line supported over the slots by a thin insulator. This power is dissipated in a detector, and is isolated from the rest of the feed network by low pass filters.

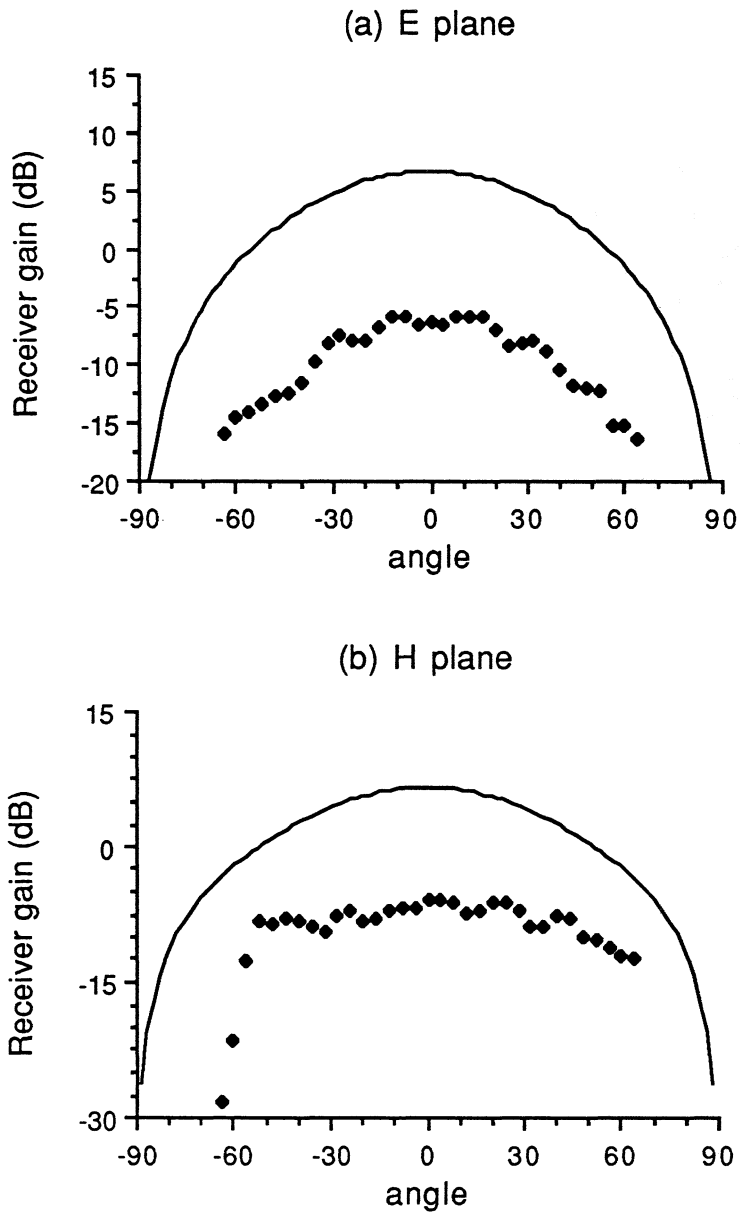

Fig. 2: (a) E-plane and (b) H-plane beam patterns for a twin slot antenna on a single 1/4 λ_d thick fused quartz substrate for 90.5 GHz radiation. Theory (solid line) is compared with experiment.

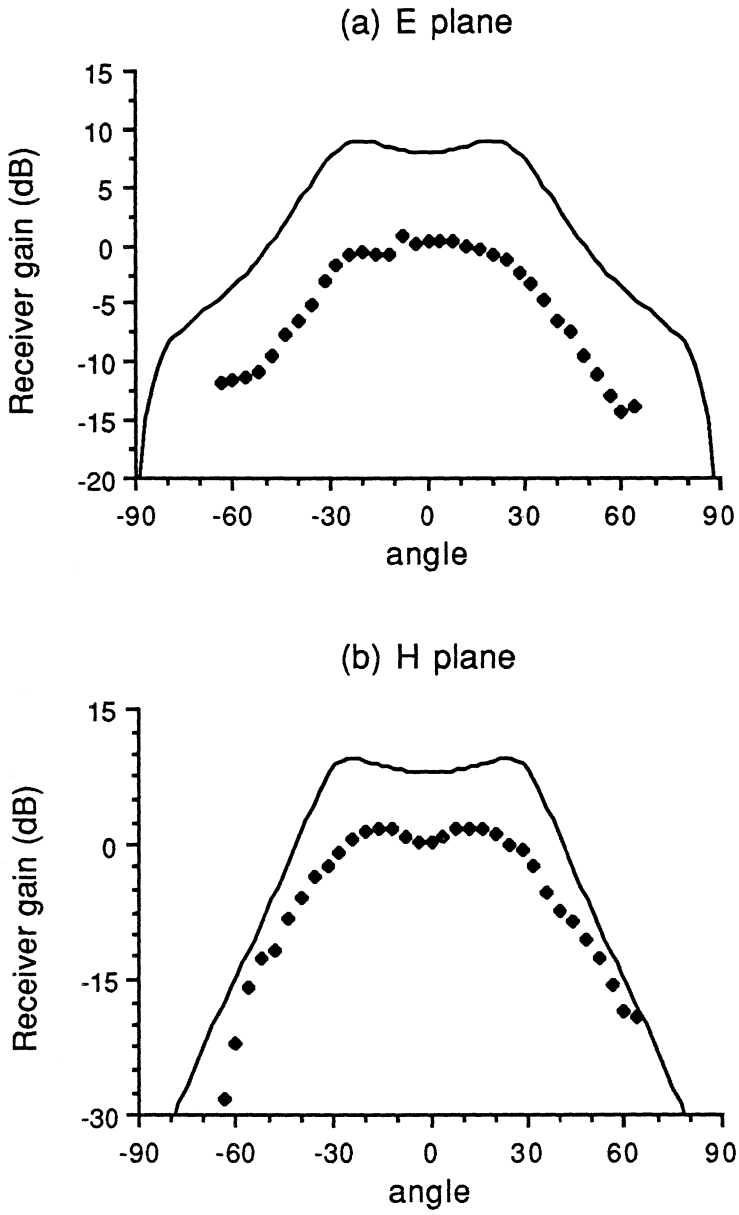

Fig. 3: (a) E-plane and (b) H-plane beam patterns for a twin slot antenna on a multilayer stack (dielectric constants 3.8,1, and 3.8) for 94 GHz radiation. Theory (solid line) is compared with experiment.

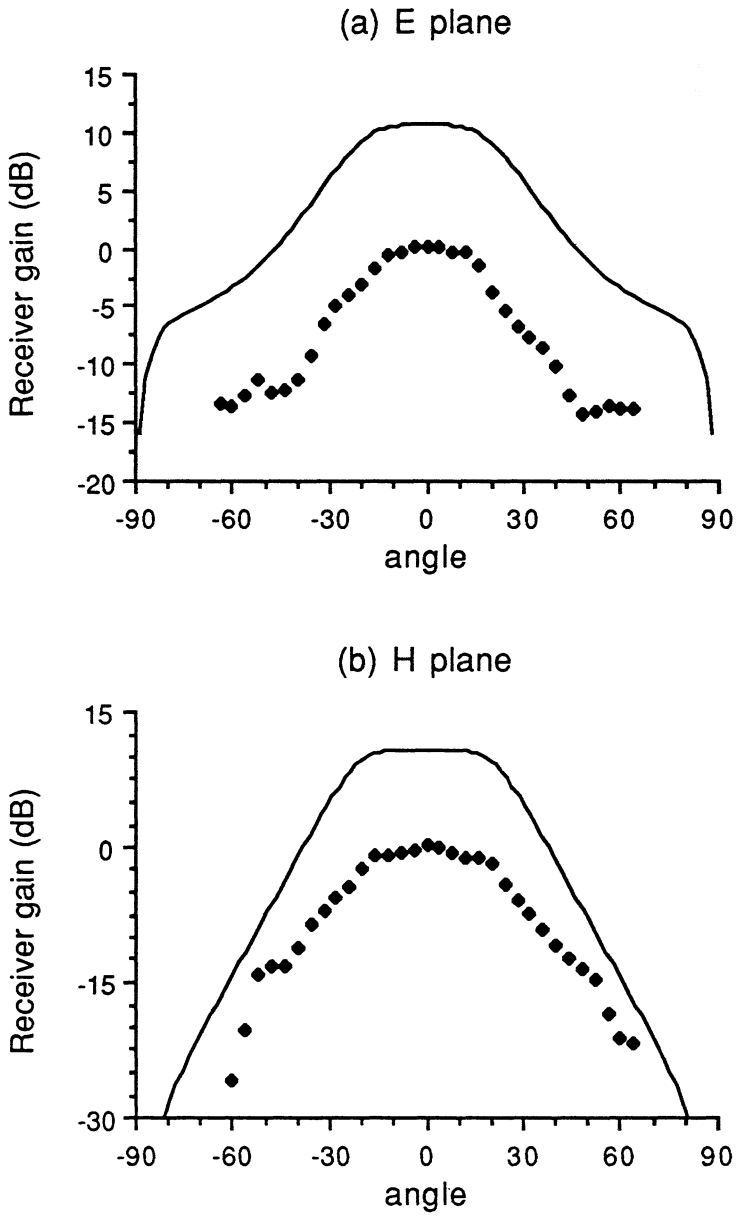

Fig. 4: (a) E-plane and (b) H-plane beam patterns for a twin slot antenna on a multilayer stack (dielectric constants 3.8,1, and 3.8) for 90.5 GHz radiation. Theory (solid line) is compared with experiment.

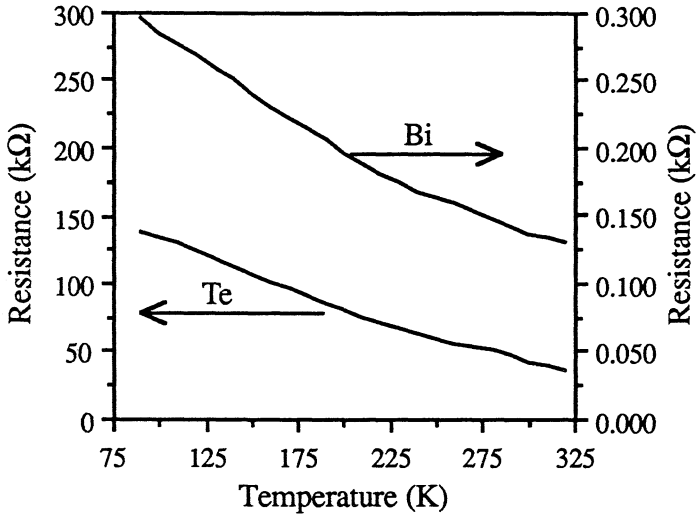

Fig 5: Resistance as a function of temperature for Te and Bi microbolometers.

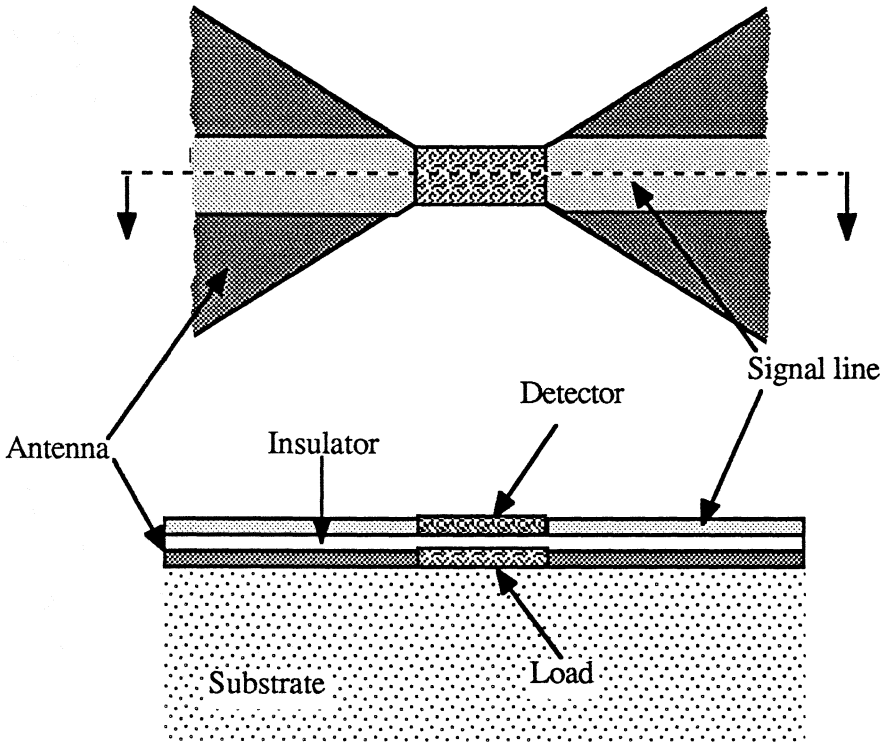

Fig. 6: Top view and cross section of a composite microbolometer. The load is impedance-matched to the bow-tie antenna, and is thermally coupled to a detector.

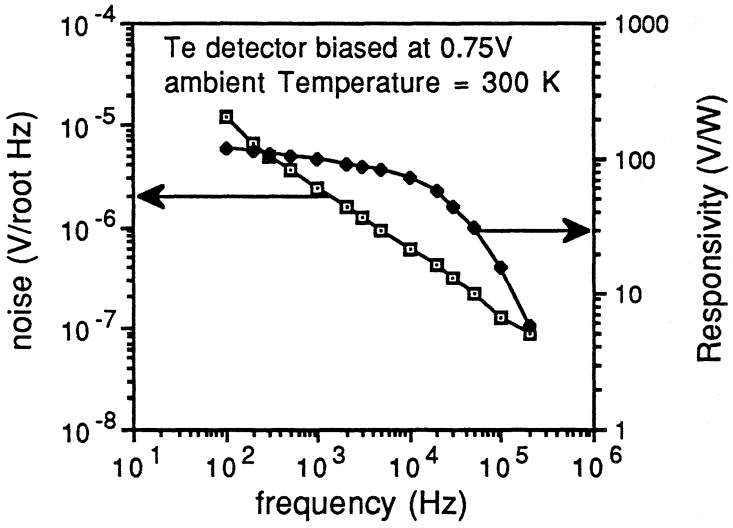

Fig. 7 Noise and responsivity are plotted versus beat frequency for a composite microbolometer with the Te detector element biased at 0.75V.

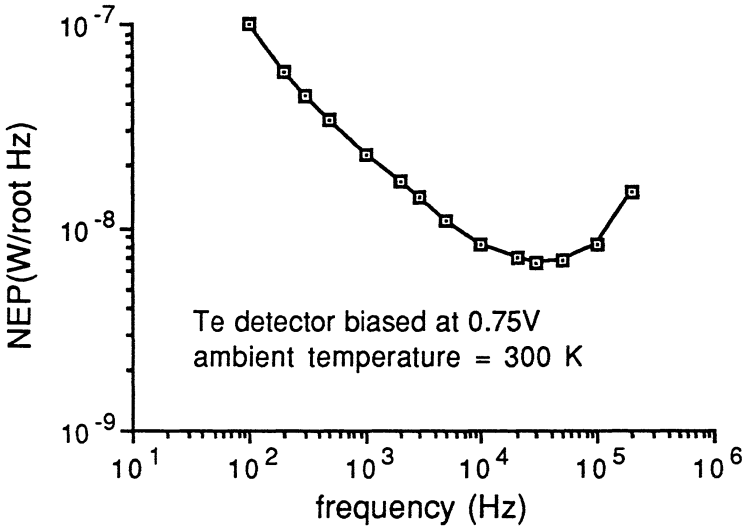

Fig. 8: Sensitivity for the composite microbolometer versus beat frequency, with the Te detector element biased at 0.75V. Best performance occurs at about 30 kHz, where NEP = 6.7 x 10^{-9} W/$\sqrt{\text{Hz}}$.

A Wideband Monolithic Submillimeter-Wave Quasi-Optical Power Meter

Curtis C. Ling and Gabriel M. Rebeiz,

NASA / Center for Space Terahertz Technology / Radiation Laboratory
Electrical Engineering and Computer Science Department
The University of Michigan, Ann Arbor, MI 48109-2122

ABSTRACT- A novel monolithic power meter has been developed for submillimeter-wave applications (100GHz to 10THz). The detector is a 4x4 mm Bismuth bolometer integrated on a 1.2 μm thick dielectric membrane. This approach results in a wideband high-responsivity detector. The power meter is simple to fabricate, inexpensive, and can be easily calibrated using a low-frequency network. Quasi-optical measurements at 185GHz show that the bolometer is polarization independent, acts as a lambertian surface, and could be modelled by a simple transmission line model. The measured low-frequency responsivity for a 70Ω bolometer, at a bias of 1V. and a video modulation of 300Hz, is around 1V/W. The NEP of the detector is around $3nWHz^{-1/2}$. Potential application areas are antenna coupling efficiency measurements and absolute power measurements at submillimeter wavelengths.

INTRODUCTION

Power measurements at millimeter-wave frequencies is conventionally done using waveguide power meters. These employ a thermistor or a diode suspended in a waveguide [1]. They are calibrated at the factory, limited to a waveguide band, and become very expensive for frequencies above 100GHz. They also become inaccurate near 200GHz (+/-1dB), and are simply not available for frequencies above 300GHz. Neikirk and Rutledge [2] developed a Bismuth microbolometer for millimeter-wave and far-infrared detection. The microbolometer is very small compared to wavelength, and needs a millimeter-wave antenna to gather the incident energy. Although this detector is easily calibrated, it is not suited for absolute power measurements because one must deimbed the antenna gain and mismatch from the measurements. Indeed, this topic is an active area of antenna research by itself. Other submillimeter wave power meters include the calibrated water calorimeter [3] and the new Keiting (acoustic based) power meter [4]. However, all these units are expensive and accurate to within +/-2dB. In fact, there is a lack of simple and accurate power meters at submillimeter-wave frequencies, and our detector is specifically intended to fill this need.

QUASI-OPTICAL POWER METER

We have developed a high-responsivity quasi-optical power meter optimized for measurements at submillimeter wavelengths (Fig.1). In contrast to a waveguide power meter which measures the total incident power, this device is "quasi-optical", and measures the power density of an incident plane wave. The bolometer is larger than a wavelength, and this allows the use of a transmission-line (T.L) equivalent circuit to determine the fraction of the incident power absorbed by the bolometer. The bolometer can be modeled by a resistive sheet with an RF impedance equal to its DC resistance [5]. The bolometer is integrated on a 1-μm thick dielectric

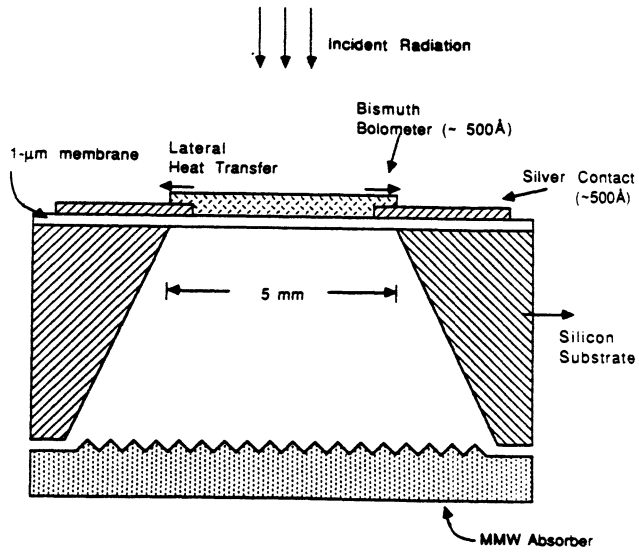

Figure 1: Quasi-optical membrane power-meter

membrane. The use of a membrane offers two important advantages: 1) It results in a low thermal conductance path between the bismuth bolometer and the supporting silicon wafer thereby yielding a high-responsivity detector, and 2) it is much thinner than a wavelength so that the bolometer is effectively suspended in free space. This yields a frequency independent transmission-line model, and results in a wideband submillimeter-wave detector. The low-frequency cutoff is given by the size of the bolometer; that is, when diffraction becomes severe and the TL model breaks down. The high frequency cutoff is given by the electronic properties of thin film bismuth, and this occurs in the far-infrared range [5]. A 4x4 mm bolometer should cover the frequency range from 100GHz to 10THz. Finally, the bolometer is a thermal detector with a slow time constant (around 100msec), and responds only to the average absorbed power. Therefore, it can be easily calibrated using a low-frequency (10MHz) network, and an absolute power-density measurement can be made at submillimeter frequencies.

FABRICATION

A 3-layer $SiO_2/Si_3N_4/SiO_2$ structure with respective thicknesses of 5000Å/3000Å/4000Å is deposited on both sides of a <100> silicon wafer. The first layer is grown using wet oxidation at 1100°C, and the top two layers are deposited in a high temperature chemical-vapor-deposition furnace at 700°C. The silicon-dioxide layers are in compression while the silicon-nitride layer is in tension. This combination yields a 1.2 μm thick dielectric layer in tension with a tensile stress of $2x10^7$ dynes/cm^2 [6]. The layer must be in tension to yield flat and rigid self-supporting membranes. These are fabricated in two steps. First, an opening is defined on the back of the wafer, then the silicon is etched until a transparent 5x5 mm membrane is exposed. The etching process is anisotropic and forms a pyramidal cavity bounded by the <111> crystal planes [7]. Next, the bolometer and contacts are defined on the top side of the wafer. The contacts are evaporated silver 500Å thick, and the bolometer is evaporated bismuth 500-700Å thick with a DC resistance of 70-100Ω. The process is monolithic and compatible with standard IC fabrication techniques.

LOW-FREQUENCY MEASUREMENTS

The frequency response and responsivity of the bolometer is measured using a low-frequency network. An amplitude modulated 10MHz signal is applied to the bolometer. The frequency response is found by varying the modulation frequency from 50Hz to 10KHz, and measuring the bolometer response using a lock-in amplifier. The frequency response can also be found using the millimeter-wave system shown in Fig. 3. In this case, a 90.7GHz Gunn source is modulated from 80Hz to 2KHz, and the bolometer response is measured. The output signal drops as 1/f in the LF and 90.7GHz measurements (Fig. 2). In order to calibrate the bolometer at low-frequencies, the 10MHz power absorbed must be accurately measured. This is done by monitoring the instantaneous voltage across the bolometer. Several 4x4 mm bolometers with resistances between 70Ω and 95Ω were measured, and absolute responsivities between 0.6V/W and 2.0V/W were obtained, at a bias of 1V. and a modulation frequency of 300Hz. The output was also a linear function of the applied RF power at 90.7GHz, and of the bias voltage. All of the above experimental data indicate that the bolometer is behaving as a standard high-responsivity thermal detector. Finally, the noise of several 4x4 mm bolometers was measured from 20Hz till 100KHz. The noise spectrum exhibits a 1/f rolloff till 300Hz, and is limited by the Johnson noise for higher frequencies. The NEP is around $3nWHz^{-1/2}$ at a bias of 1V. and a video modulation of 300Hz.

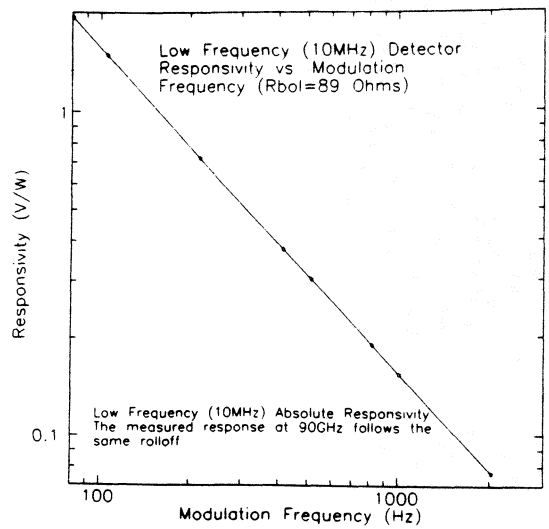

Figure 2: Measured low-frequency responsivity vs. modulation frequency. The 90GHz response has an identical rolloff.

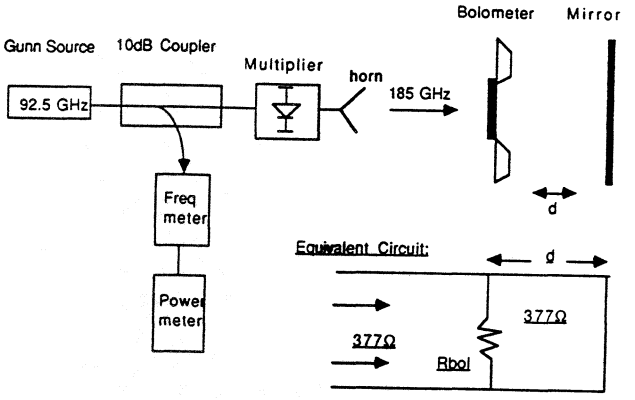

Figure 3: Millimeter-wave setup with back shorting mirror and TL equivalent circuit

SUBMILLIMETER-WAVE MEASUREMENTS

The bolometer response vs. incidence angle was measured at 185GHz. The vertical and horizontal patterns are identical, follow a cosine-law, and are independent of the polarization of the incident signal (Fig. 4). The transmission-line equivalent circuit is checked by measuring the bolometer response at 182GHz with a sliding ground plane behind the silicon substrate. The power absorbed by the bolometer is given by $(1-S_{11}{}^2)$, where S_{11} is calculated using the TL equivalent circuit (Fig. 3) [8]. The preliminary measurements agree with the TL model, although there is a strong standing wave riding on the predicted response (Fig. 5). The measured minima occur at a half-wavelength period, and the measured frequency using the mirror data agree exactly with the waveguide frequency meter. These experiments indicate that the bolometer behaves as a quasi-optical power meter, although still not a calibrated one.

The absolute responsivity can also be found at 140GHz, by measuring the source power with an accurate waveguide power meter, and using a calibrated horn antenna. This gives a plane-wave with an absolute power density incident on the bolometer. The responsivity is then found from the measured voltage. It should be noted that in a practical setup, the bolometer is calibrated using a LF network, and the LF responsivity is used to measure the millimeter-wave power. However, by measuring the absolute responsivity at 140GHz, one can determine the validity of the LF calibration. We are now in the process of calibrating our millimeter-wave system at 140GHz using an Anritsu power meter.

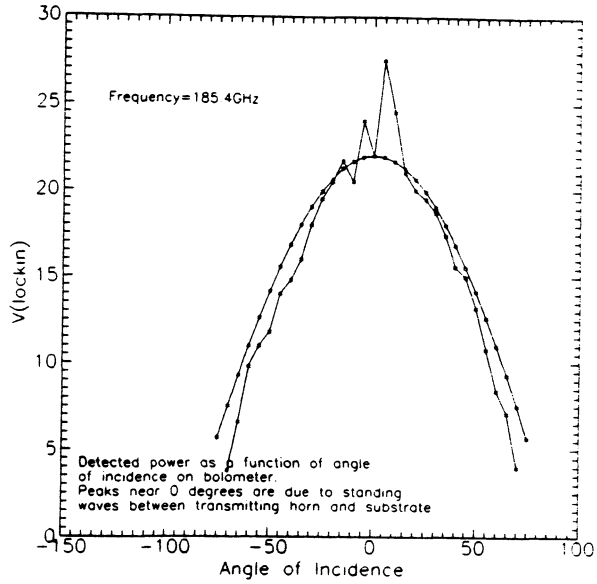

Figure 4: Measured response vs. incidence angle at 185GHz. The peaks are standing waves between the bolometer and the horn transmitter.

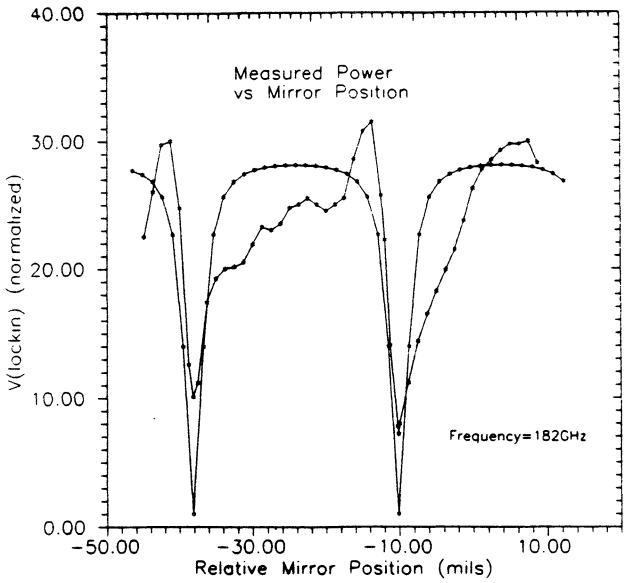

Figure 5: Measured response vs. mirror position at 182GHz. The peaks and dips are due to standing waves in the bolometer-mirror setup.

CONCLUSIONS

A wideband high responsivity quasi-optical power meter has been developed for submillimeter-wave applications. The integration of the detector on a thin 1.2 m dielectric membrane results in a novel wideband high responsivity detector. Preliminary experiments indicate that the detection is of thermal nature, and the large-area bolometer behaves as a quasi-optical detector. Current experiments are being done to reduce the standing waves, and to calibrate the system at 140GHz. The bolometer has been routinely used to detect power in the range of 10nW to 40nW at 200GHz. Within our knowledge, this is the least expensive and most sensitive room temperature laboratory power meter. A two-dimensional detector array is also under construction at the University of Michigan.

ACKNOWLEDGEMENTS

This work was supported by NASA-Center for Space Terahertz Technology. The authors would like to thank Prof. David Rutledge and Karen Lee at the California Institute of Technology for valuable discussions.

REFERENCES

[1] Anritsu America Inc., 15 Thornton Rd, Oakland, New Jersey, 07436

[2] D. P. Neikirk, W. W. Lam and D. B. Rutledge, " Far-infrared microbolometer detectors," Int. J. of Infrared and Millimeter Waves, vol. 5, No. 3, pp. 245-277, 1984.

[3] Foot, Hodges and Dyson, " Calibration of power and energy meters for the FIR/Near MMW spectral regions," Int. J. of Infrared and Millimeter Waves, vol. 5, No. 4, pp. 773-782, 1981.

[4] Thomas Keating Ltd., Billingshurst, West Sussex, England.

[5] W. H. Block and O. L. Gaddy, " Thin metal-film room-temperature IR bolometers with nanosecond response times," IEEE Journal Quantum Electronics, vol. QE-9, # 11, 1973.

[6] L.I. Maissel and R. Glang, "Handbook of thin film Technology," pp. 12-21 to 12-30, McGraw Hill, New York, 1970.

[7] K. E. Peterson, "Silicon as a mechanical material," Proc. of the IEEE, vol. 70, pp. 420-457, 1982.

[8] Ramo, Whinnery and Van Duzer, "Fields and Waves in Communication Electronics," Second Edition, ch. 6, Wiley and Sons, 1984.

A SUBMILLIMETER-WAVE HETERODYNE ARRAY RECEIVER USING A DIELECTRIC-FILLED PARABOLA: CONCEPT AND DESIGN

Peter H. Siegel

Jet Propulsion Laboratory
California Institute of Technology
Pasadena, California

Abstract

A novel quasi-optical receiver architecture with planar integrated antenna/active device capability has been described [1,2] which combines the features of a dielectric substrate lens and a parabolic reflector in a single structure termed a *dielectric-filled parabola*. This design can be used to form both single element and small array receivers operating in heterodyne or direct detection modes or can be configured as a transmitter for planar oscillator or frequency multiplier circuits.

In this presentation the heterodyne applications of the dielectric-filled parabola will be examined with an emphasis on small array systems. Measurements and calculations based on a microwave model of a single element receiver and a 10 element array will be given as well as some early details on a soon to be operating millimeter-wave system.

I. Introduction

At microwave and millimeter-wave frequencies the most sensitive heterodyne receivers generally make use of rectangular waveguide and some form of scalar feed horn for coupling energy into or out of a discrete nonlinear element usually mounted in close proximity to the guide. Over the years such systems have been highly optimized, originally for use with GaAs Schottky barrier diodes and later for integration with superconducting-insulator-superconducting tunnel junctions. The same basic waveguide structure has been used to produce heterodyne down-converters and frequency multipliers up to wavelengths as short as 0.5mm (600 GHz). Unfortunately, these waveguide systems are very difficult to fabricate at submillimeter wavelengths due to their small physical size and the necessity of coupling efficiently into a separately mounted mixer, multiplier or oscillator element. For this reason alternative mounting structures have been sought for some years.

One means of simplifying the fabrication of submillimeter wavelength receiver systems is to integrate the mixer or multiplier element with an appropriate photolithographically produced planar antenna thus eliminating both the feed horn and waveguide. Such systems are fairly common at microwave

frequencies and are beginning to be reported upon more frequently at millimeter [3-13] and even submillimeter wavelengths [14-16]. However, there are some drawbacks to using planar integrated antenna structures at high frequencies. First, if the antenna is integrated on a substrate with a dielectric constant greater than 1, unless it is very thin (<0.1 wavelength), much of the input (or output) power can end up being lost in substrate modes [11] rather than being coupled to the nonlinear element. At 1 THz a typical planar antenna integrated on a quartz substrate would have to have a dielectric thickness of less than 15 microns. Second, most planar antennas have small effective apertures and hence very low directivity and therefore require very fast (low f#) optics for beam shaping and matching to the higher gain systems with which they are frequently associated. Finally, unlike waveguide systems, planar antennas have no dynamic tuning capability making intrinsic matching to a transmit or receive element essential.

The planar integrated receiver system which is referred to in this presentation has been described in a previous proceedings [1,2]. It is a variation on a concept originally proposed by Rutledge and Muha [7] to take advantage of the fact that a planar antenna on a dielectric half-space radiates preferentially into the dielectric. In their design a planar bow-tie antenna containing a detector at its apex was integrated on a dielectric substrate which was in turn attached to the flat surface of a hemispherical lens. Rays leaving this 'hyperhemisphere' are oriented near normal to the surface and hence trapped waves are eliminated. Our design combines the features of this dielectric-lens antenna system with the high gain of a parabolic reflector in a single structure which we have been calling a *dielectric-filled parabola* (DFP).

In the first part of the presentation the DFP characteristics will be summarized. This is followed (Section III) by microwave scale model measurements showing the beam patterns and input impedances of several common planar antenna structures when integrated on a DFP. Section IV contains a comparison of the measured and computed field distribution of a thin half-wave resonant dipole on a DFP at 10 GHz. In Section V the beam patterns of a small 2X5 element array on a DFP are presented and finally, in Section VI, we conclude with a description of a submillimeter-wave system now in the final stages of fabrication.

II. Design Concept

Fig. 1 shows a conceptual picture of a heterodyne array receiver system employing a dielectric-filled parabola. The DFP is formed from a plano-convex dielectric lens whose convex surface has been shaped into a parabola and metallized. The planar antenna and receiver elements are integrated onto the center of the flat surface of the dielectric lens; the focal point of the parabola (in practice it is more convenient to integrate the antenna elements on a separate planar dielectric substrate and glue it to the main assembly). The f/D ratio of the system is 0.25 but as we shall see the planar antennas do not fully illuminate the parabola and hence the effective f# is somewhat higher.

Some of the properties of the dielectric-filled parabola are listed below (for additional details see [1]):

1). The parabola and dielectric lens are combined into a single structure which produces a collimated output beam from a very broad beamed radiator with no additional optical components.
2). The parabola has an f/D ratio of 0.25 and thus can accommodate planar antennas with beamwidths approaching 180 degrees.
3). The parabolic face is in the far field of the planar antenna elements.
4). All paraxial rays entering the parabola travel an equal distance in the dielectric to the focal point.
5). There is an extensive flat dielectric surface which allows for the placement of integrated bias and or input/output transmission line structures for communicating with the receiving or transmitting element.
6). The planar antenna and receiver or transmitter element can be fabricated on a separate and relatively thick dielectric plate then glued in place on the dielectric-filled parabola facilitating fabrication, testing and optimization.
7). Signal power is incident on the flat side of the dielectric and so it is very easy to incorporate a quarter-wave matching layer to reduce input reflection loss.
8). For heterodyne receiver operation the local oscillator may be injected via a through hole at the center of the parabola's mirrored surface without additional signal beam blockage or complicated diplexing elements.
9). There are no struts or other free standing structures in front of the beam, only the integrated planar antenna elements themselves, making the whole unit self contained, compact and inherently robust.
10). For cryogenic operation the dielectric and hence the antenna elements can be very readily heat sunk to the cold plate through the metallic face at the rear of the parabola.
11). Off-axis antenna elements produce beams inclined to the optical boresight as in multi-beam phased array systems. For imaging applications the DFP should be placed behind the focal plane with an additional collimating lens out front to re-image the sky onto the antennas.
12). Refraction at the air-dielectric interface increases the extent of off-axis beam tilt for a given lateral displacement of the antenna in the focal plane.
13). The number of array elements which can be accommodated in the focal plane of the parabola is a function of the aperture illumination and the effective f/D ratio and is limited by the acceptable levels of astigmatism and coma. These aberrations can be reduced by forming a shallower parabola on a thicker substrate (increasing the f/D ratio and using higher gain planar antenna elements) but at the expense of increased dielectric loss.

III. Microwave Model Measurements

In order to measure easily the performance of the DFP with a wide variety of antenna structures a microwave scale model of the feed system was fabricated. The parabola itself was machined on a numerically controlled lathe from two one-inch thick sheets of Emerson and Cuming Stycast HiK ϵ_r=4 material to simulate fuzed quartz. The pieces were glued together with Eccobond 45 mixed to a semi-rigid formulation. The diameter of the parabola was 8.4" and a separate 0.1" thick, 8.4" diameter plate for holding the antenna elements was added to the 2" thick lens to bring the f/D to 0.25. The parabolic surface was electroplated with a thin layer of silver and then electroformed copper was grown to a thickness of about 0.002".

The more complex shaped planar antennas (spirals and log-periodics) were fabricated from 0.005" thick sheets of copper using photolithography directly through rubylith masks and subsequent chemical etching. The rubylith masks were generated on an HP7550A digital plotter using a single point diamond scribe (available from EESOF) held in a custom made aluminum cartridge. The final antennas were either glued or taped in place on the dielectric-filled parabola. Measurements were made on thin and thick half-wave resonant dipoles, self-complementary and broad-toothed planar log-periodic antennas, bow-tie antennas, and log-spiral antennas.

Antenna power patterns were measured in an anechoic chamber using an automated position system constructed for this purpose and a specially modified HP415E SWR meter [17]. In all cases (except for the polarization measurements on the log-spiral) the transmit antennas were standard gain rectangular horns. The overall dynamic range was 40 dB over the frequencies considered.

Antenna input impedances were measured on an HP8410A network analyzer through feed cables (always a .047" diameter semi-rigid coaxial line) on the air side of the dielectric surface. The test signal reference plane was established at the end of the coaxial feed line by shorting the cable with silver paint (Silver Print type 22-201) which produced as good a short as pure indium even at 10 GHz. No error correction algorithms were employed and as the impedance measurements were affected somewhat by the feed cables, they should be taken as approximations only.

A summary of the data collected can be found in Figs. 2 and 3. For more details the reader is referred to [2]. In general, depending upon the application, any of the measured antennas might be used at high frequencies. The dipoles have the lowest input impedance (generally preferred for matching to most nonlinear elements used in low noise receivers), the log-spiral has the broadest bandwidth and the most circularly symmetric patterns. If cross polarization is a consideration, the log-periodic antennas are likely to give less satisfactory performance. The bow-tie has the most compact impedance locus but its H-plane patterns vary widely with frequency. For arraying, antenna physical size must be considered as well as desirable configurations for biasing and, if heterodyning, for intermediate frequency removal.

All of the antennas slightly underilluminate the dielectric-filled parabola. At submillimeter wavelengths this is not a serious problem as the parabola is

physically small. At lower frequencies one could increase the focal length of the dielectric-filled parabola (improve the illumination efficiency) by using a thicker substrate to hold the antenna and forming a much shallower lens on the opposite surface of the dielectric. This will of course result in a longer dielectric path length and hence more transmission loss. Alternate optical systems with lower off-axis aberration are currently under investigation.

The input impedances of the antennas on the dielectric-filled parabola differ from those of the same antennas in free space and in general the real part decreases. The resonant frequency of the dipole antennas did in fact shift by approximately the square root of the mean dielectric constant of air and quartz as predicted in [18].

IV. Measured and Computed Field Distribution

To see how well we could predict the performance of a given antenna on a DFP we compared the measured far-field patterns of the thin dipole antenna (Fig.2A) with the patterns derived from the computed field distribution of a thin dipole on an infinite dielectric half-space [19-21]. The E and H plane field patterns published in [19] were applied to the surface of our parabolic lens (assuming no reflection at the edge) and the results are shown in Fig. 4 as dashed lines. We then used the equations in [22] to calculate the far field patterns. Unfortunately, the calculated patterns did not match our measurements as well as we had hoped. To determine why, we probed the field across the face of our 8.4" diameter parabolic stycast lens (with the metallization removed) at 10 GHz and obtained the field distributions shown in Fig. 4 as solid lines (the high frequency ripple is the result of reflections off the lens surface). The differences in the measured and calculated fields is quite marked and shows that the theoretical model we used is over simplified. The projected far field patterns from the probe measurements are shown in Fig. 5. Even here the agreement is only fair and further work in this area, both theoretical and experimental, is indicated.

V. Array Patterns

Of the antennas studied, the half-wave resonant dipole has an input impedance which most closely matches that of an SIS tunnel junction or Schottky diode element. It also satisfies the spacing requirements (in one plane) for contiguous beams on the sky and can be readily mated with surface oriented TEM transmission line (twin lead) for IF removal. A 2X5 element array of 10 GHz dipoles (length to width ratio of 10 to 1) was fabricated on our 0.1" thick, 8.4" diameter stycast plate using photolithography directly on the stycast which was first metallized with 50,000Å of evaporated copper. A beam lead detector diode (TRW A2S255) was silver epoxied to the terminals of each antenna and RF blocking capacitors (Dielectric Labs 1pF high frequency gap-caps) were placed at appropriate points across the IF lines to prevent RF leakage down the lines. Power was measured with an HP415E SWR meter [17] by modulating the transmitter at 1kHz.

Sample patterns for the extreme elements of the array are given in Fig. 6.

The rapid rise of the coma lobe for the extreme off-axis elements is expected but its absolute level is somewhat higher than predicted by the Ruze analysis [22]. Cross polarization levels (not shown) were also higher than expected (up to 10 dB below the peak for the corner elements). Mutual coupling has not as yet been measured. Some of these problems may be due to the fact that the array model is operating at one-half the lower frequency limit of intended use where the parabola is only 7 free space wavelengths in diameter. At this frequency diffraction effects are sure to be significant. We are currently fabricating a 20 GHz array with the same parabola to reduce the influence of diffraction.

VI. Fabrication

At the time of this symposium our first submillimeter-wave DFP units are being fabricated and testing should begin in a couple of months. Our initial design has an RF center frequency of 230 GHz and an IF of 1.4 GHz but the mount has been fabricated so that operation at a higher frequency simply requires changing out a separate antenna/diode plate. The same mixer mount is used for single antennas and for arrays of up to 10 elements. Measurements are planned using both SIS tunnel junctions and planar GaAs Schottky barrier diodes as the downconverting elements.

A machinist's drawing of the ten element heterodyne array system is shown in Fig. 7. The receiver subsystem is fabricated in five parts; 1) the dielectric-filled parabola, 2) a separate substrate (of the same dielectric material) containing the planar antennas, receiver elements and biasing and intermediate frequency removal lines and RF filters, 3) a separate quarter-wavelength thick matching layer, 4) a metallic holder for the parabola containing the local oscillator feed (a pyramidal horn), a balun transformer and matching section and a standard 50 ohm OSSM connector for output coupling and 5) a cover plate which clamps the antenna substrate and matching layer to the flat side of the parabolic lens and encloses the IF matching network.

The dielectric parabola is ground onto one side of a flat, .788" (2cm) diameter, 0.197" (0.5cm) thick disk of fuzed quartz (Infrasil T17) using lathe shaped meehanite cast iron laps. The laps are machined on a numerically controlled lathe. Three separate laps are used during the lens grinding process which is accomplished by impregnating the lap with aluminum oxide (30, 10 and 5 micron grits were used) and pressing it up against the fuzed quartz disk which is slowly turned about its axis on a small lathe. The final parabola is thinned to .187" to allow room for the .010" thick quartz substrate containing the planar antennas and downconverting elements. Infrasil T17 was used as the substrate material because it has an especially low water content and thus a fairly low loss tangent in the submillimeter-wave band. Any low loss dielectric which can be machined or ground could be used bearing in mind that the incident radiation will undergo a substantial reflection upon hitting the surface of the dielectric unless a suitable matching layer is added.

Once ground and polished the parabolic substrate lens is vacuum coated with a 50Å thick chromium adhesion layer followed by several skin depths of gold. A small rectangle (sized to match the LO feed horn aperture) was masked off at the center of the parabola before plating. The parabola described here has an intended lowest operating frequency of 200 GHz. The choice of diameter is a compromise between aperture size and dielectric loss.

The substrate containing the antennas, downconverting elements and IF lines is composed of .010" thick .788" diameter polished quartz disks of Infrasil T17. For our initial tests and to facilitate optimization the mixing elements and planar antenna structures were fabricated separately. The antennas and IF lines are formed in a chrome-gold lift-off process. They consist of half-wave resonant dipoles 0.002" wide by 0.016" long with a terminal gap of 0.001" at the center. Coplanar lines (twin lead) are used for IF removal. The lines are each 0.0005" wide and are spaced 0.001" apart and have an impedance of about 200 ohms to match the IF output impedance of the downconverting elements. Separate RF blocking capacitors composed of a 3000Å SiO insulating layer and a top layer of aluminum were formed across the IF lines $\lambda/4$ and $3\lambda/4$ back from the dipoles. The ends of the coplanar line flare out to bonding pads at the edge of the quartz wafer where they are wire bonded to planar balun transformers which surround the parabola. The transformers [23] convert the balanced 200Ω twin lead directly to 50Ω coax through a quarter wavelength long coplanar waveguide section. They are formed on Epsilam 10 (ϵ_r=10) and are designed to work from 1-2 GHz.

The first downconverting elements to be tested will be JPL fabricated NbN/MgO/NbN SIS edge junctions [24] which have been formed on .010" thick quartz wafers and diced into chips of .002"x.005"x.001" (width x length x thickness). The junctions have typically an area of $<.2\mu m^2$, a current density of $\approx 3x10^5 A/cm^2$, a resistance of 50Ω and an ωRC product <1 at 230 GHz. The chips are placed device side down across the terminals of the planar antennas and soldered in place. Soldering is facilitated by evaporating a 3000-5000Å thick layer of indium over the SIS tunnel junction leads during fabrication. Mixing measurements with separately mounted planar GaAs Schottky diodes of similar dimensions are also planned.

The holder for the parabola is fabricated from brass and contains a parabolic depression for accurately mating to the quartz lens. The center of the housing contains a pyramidal feed horn (for LO injection) which is wire electro-discharge machined (EDM) into the block as the first step of the machining process. The feed horn tapers to the face of a standard WR-3 waveguide flange on the rear of the holder. Higher frequency waveguide LO injection is accomplished by mating a transition which continues the taper to a desired final waveguide size. The holder also contains the stripline channels for the balun transformer/impedance matching sections.

A brass top plate holds the quarter-wave matching layer and serves to clamp the whole assembly together. It also encloses the balun transformers and coax connectors. The matching layer for 230 GHz is a 0.010" thick teflon disk with a small hole at the center which surrounds the antennas.

VIII. Summary

A novel planar integrated antenna feed system has been described. Although intended for submillimeter wavelength heterodyne applications it can be used over a wide range of frequencies and in a variety of modes; as a receiver or transmitter, in a heterodyne or direct detection mode, with a single element or with a modest focal plane array. It combines the high directivity of a parabolic reflector with the convenience of a substrate lens on which both planar antenna elements and receiving or transmitting devices can be integrated. It allows some control over the output beam and can match very broad beamed radiators to high f-number systems. The design is inherently robust, easy to fabricate, can be scaled to very high frequencies and is cryogenically coolable.

The beam patterns and antenna input impedances have been measured for a number of different planar antenna elements on this dielectric-filled parabola from 4 to 12 GHz using a frequency scaled model. The results of these measurements show clearly that the system performs well. The patterns of a small array of 10 dipole elements were also presented and show somewhat higher than expected off axis aberrations. Our first attempts at analysis have been only partially successful and more work is indicated.

A millimeter/submillimeter wave system has been fabricated and detailed assembly procedures are given. RF measurements using both NbN SIS tunnel junctions and GaAs Schottky barrier diodes will be performed over the next several months.

Acknowledgements

The author would like to thank the following people who significantly contributed to this work: R.J. Dengler for making all the microwave model measurements, Dr. B.D. Hunt, Dr. H.G. LeDuc and S.R. Cypher for fabricating the SIS tunnel junctions and the planar antennas, Dr. M.A. Frerking and Dr. W.R. McGrath for many valuable discussions and technical advice, R. McMillan for suggesting the method and ultimately fabricating the quartz parabolic substrate lens and J. Lichtenberger for electroplating the stycast lens.

This work was performed by the Microwave Observational Systems Division, Jet Propulsion Laboratory, California Institute of Technology under sponsorship of the National Aeronautics and Space Administration, Office of Aeronautics and Space Technology (NASA/OAST).

References

[1]. P.H. Siegel and M.A. Frerking, "The dielectric-filled parabola: A new high frequency integrated receiver/transmitter front end," IEEE Int. Sym. on Antennas and Propagation, pp. 1191-94, June 1989.

[2]. P.H. Siegel and R.J. Dengler, "Measurements of dipole, bow-tie, log-periodic and log-spiral antennas on a dielectric-filled parabola," IEEE Int. Sym. on Antennas and Propagation, pp. 94-97, June 1989.

[3]. A.R. Kerr, P.H. Siegel and R.J. Mattauch, "A simple quasi-optical mixer for 100-120 GHz," IEEE MTT-S International Microwave Symposium Digest, pp. 96-98, June 14-16, 1977.

[4]. T.L. Hwang, D.B. Rutledge and S.E. Schwarz, "Planar sandwich antennas for submillimeter wave applications," Applied Physics Letters, vol. 34, no. 1, pp. 9-11, Jan. 1, 1979.

[5]. B.J. Clifton, G.D. Alley, R.A. Murphy and I.H. Mroczkowski, "High-performance quasi-optical GaAs monolithic mixer at 110 GHz," IEEE Transactions on Electron Devices, ED-28, pp. 155-157, Feb. 1981.

[6]. L. Yuan, J. Paul and P. Yen, "140 GHz quasi-optical planar mixers," IEEE MTT-S International Microwave Symposium Digest, pp. 374-375, June 15-17, 1982.

[7]. D.B. Rutledge and M.S. Muha, "Imaging antenna arrays," IEEE Transactions on Antennas and Propagation, AP-20, pp.535-540, July 1982.

[8]. C. Yao, S.E. Schwarz and B.J. Blumenstock, "Integration of a dielectric millimeter-wave antenna and mixer diode: an embryonic millimeter-wave IC," IEEE Transactions on Microwave Theory and Techniques, MTT-30, pp. 1241-1247, Aug. 1982.

[9]. T. Thungren, E.L. Kollberg and K.S. Yngvesson, "Vivaldi antennas for single beam integrated receivers," 12th European Microwave Conference, pp. 361-366, Sept. 1982.

[10]. H.R. Fetterman, T.C.L.G. Sollner, P.T. Parish, C.D. Parker, R.H. Mathews and P.E. Tannenwald, "Printed dipole millimeter-wave antenna for imaging array applications," Electromagnetics, vol. 3, pp. 209-215, 1983.

[11]. D.B. Rutledge, D.P. Neikirk, and D.P. Kasilingam, "Integrated-Circuit Antennas," Infrared and Millimeter Waves, vol. 10., Academic Press, pp.1-90, c.1983.

[12]. K.D. Stephan and T. Itoh, "A planar quasi-optical subharmonically pumped mixer characterized by isotropic conversion loss," IEEE Transactions on Microwave Theory and Techniques, MTT-32, pp. 97-102, Jan. 1984.

[13]. K.S. Yngvesson, J.F. Johansson and E.L. Kollberg, "A new integrated feed array for multi-beam systems," IEEE Transactions on Antennas and Propagation, AP-34, pp. 1372-1376, Dec. 1986.

[14]. M.J. Wengler, D.P. Woody, R.E. Miller and T.G. Phillips, "A low noise receiver for submillimeter Astronomy," SPIE Proceedings Vol. 598, Instrumentation for Submillimeter Spectroscopy, pp.27-32, 1985.

[15]. G.M. Rebeiz, W.G. Regehr, D.B. Rutledge, R.L. Savage and N.C. Luhmann Jr., "Submillimeter-wave antennas on thin membranes," International Journal of Infrared and Millimeter Waves, vol. 8, no. 10, pp.1249-1255, Oct. 1987.

[16]. T.H. Buttgenbach, R.E. Miller, M.J. Wengler, D.M. Watson and T.G. Phillips, "A broad-band low-noise SIS receiver for submillimeter Astronomy," IEEE Transactions on Microwave Theory and Techniques, MTT-36, pp.1720-1726, Dec. 1988.

[17]. R. Dengler and P.H. Siegel, Self-Operating Range Changer for Computer Interfacing the HP415E SWR Meter", JPL New Technology Report, Docket #17822, Jan. 11, 1989.

[18]. N.G. Alexopoulos, P.T. Katehi and D.B. Rutledge "Substrate Optimization for Integrated Circuit Antennas," IEEE Trans. on Microwave Theory and Techniques, MTT-31, pp. 550-557, July 1983.

[19]. C.R. Brewitt-Taylor, J. Gunton and H.D. Rees, "Planar antennas on a dielectric surface," Electronics Letters, vol.17, no.20, October 1, 1981, pp. 729-730.

[20]. N. Engheta, C.H. Papas and C. Elachi, "Radiation patterns of interfacial dipole antennas," Radio Science, vol. 17, no. 6, pp.1557-1566, Nov.-Dec. 1982.

[21]. M. Kominami, D.M. Pozar and D.H. Schaubert, "Dipole and slot elements and arrays on semi-infinite substrates," IEEE Trans. Antennas and Prop., AP-33, no.6, pp. 600-607, June 1985.

[22]. J. Ruze, "Lateral feed displacement in a paraboloid," IEEE Trans. Antennas and Prop., vol. AP-13, pp. 660-665, Sept. 1965.

[23]. R.E. DeBrecht, "Microwave transmission line and devices using multiple coplanar conductors," patent no. 3835421, issued Sept. 10, 1974, 12 pages.

[24]. B.D. Hunt, H.G. LeDuc, S.R. Cypher, J.A. Stern and A. Judas, "NbN/MgO/NbN edge-geometry tunnel junctions," Appl. Phys. Lett., vol. 55 (1), pp. 81-83, 3 July 1989.

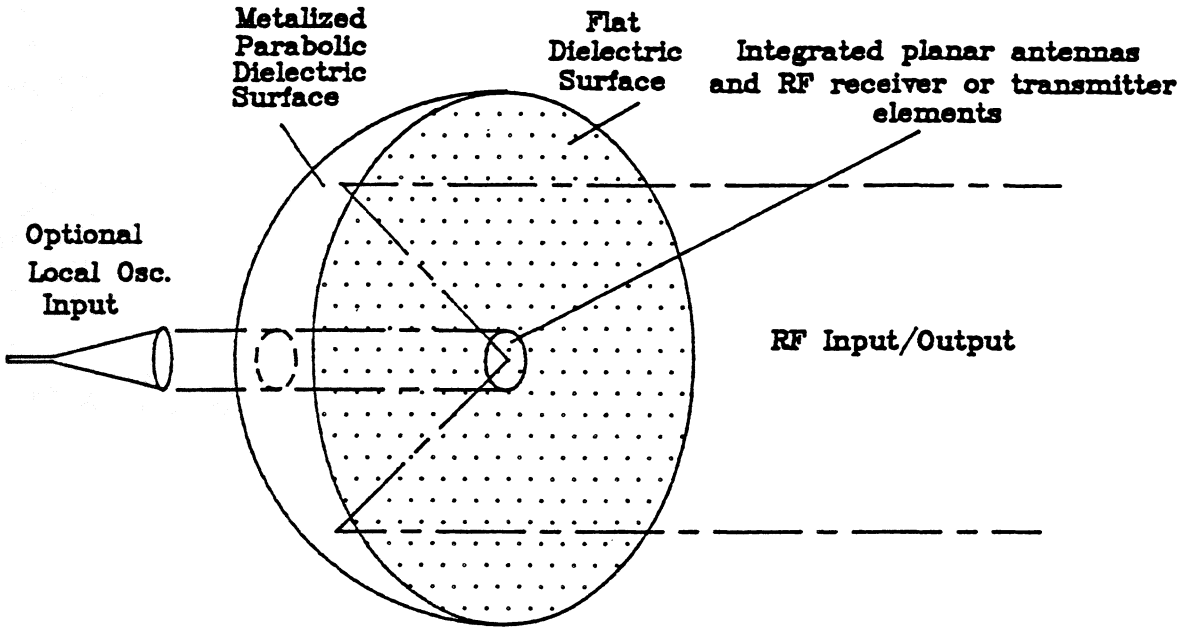

Fig. 1: Sketch of the dielectric-filled parabola used in a heterodyne receiver configuration. The down converting elements and associated antennas lie on the focal plane of the parabola (f/D=.25). Radiation from the antenna elements predominates in the dielectric (as opposed to the air) approximately in the ratio $\epsilon_r^{3/2}$ [11]. Bias and intermediate frequency lines are integrated on the flat surface of the dielectric. A quarter-wavelength thick dielectric matching layer can be placed over the existing surface to minimize reflective losses.

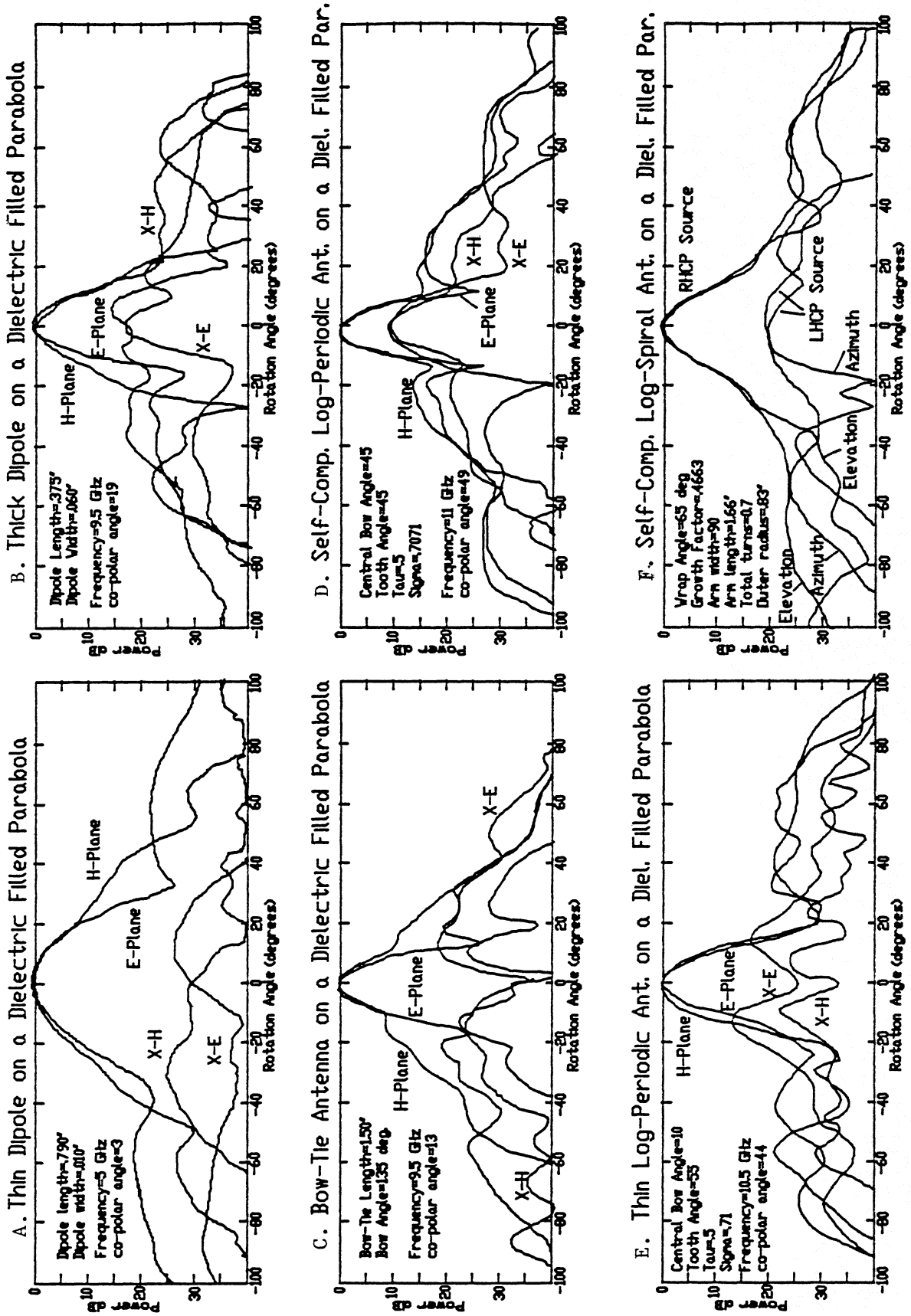

Fig. 2: Principle and cross polar plane antenna power patterns of six planar antennas on a dielectric-filled parabola. In each case the measurement was performed by sampling the field with a coaxial line brought in on the air side of the lens (ϵ_r=4). No matching layer was present. The beam width in 2a. is larger than the other plots because the measurement frequency was halved.

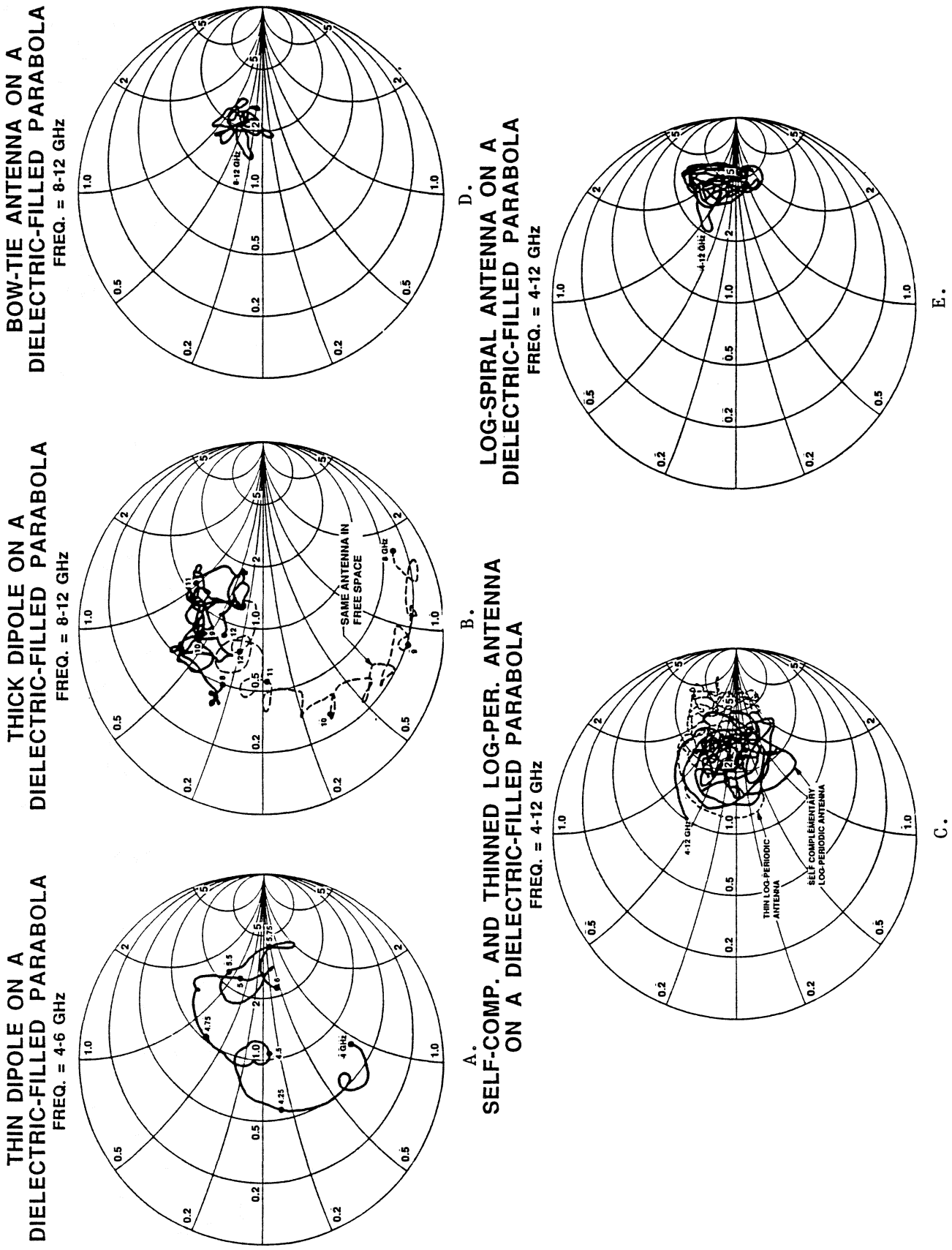

Fig. 3: Smith chart plots showing the input impedances for the six antennas shown in Fig. 2 on a dielectric filled parabola. An 8410A network analyzer was used for the measurements with the reference plane formed by shorting the end of the coaxial sampling cable. The dipoles contained a bazooka balun transformer and a short length of balanced line between the reference plane of the test cable and the antenna terminals. No correction algorithms were performed on the data.

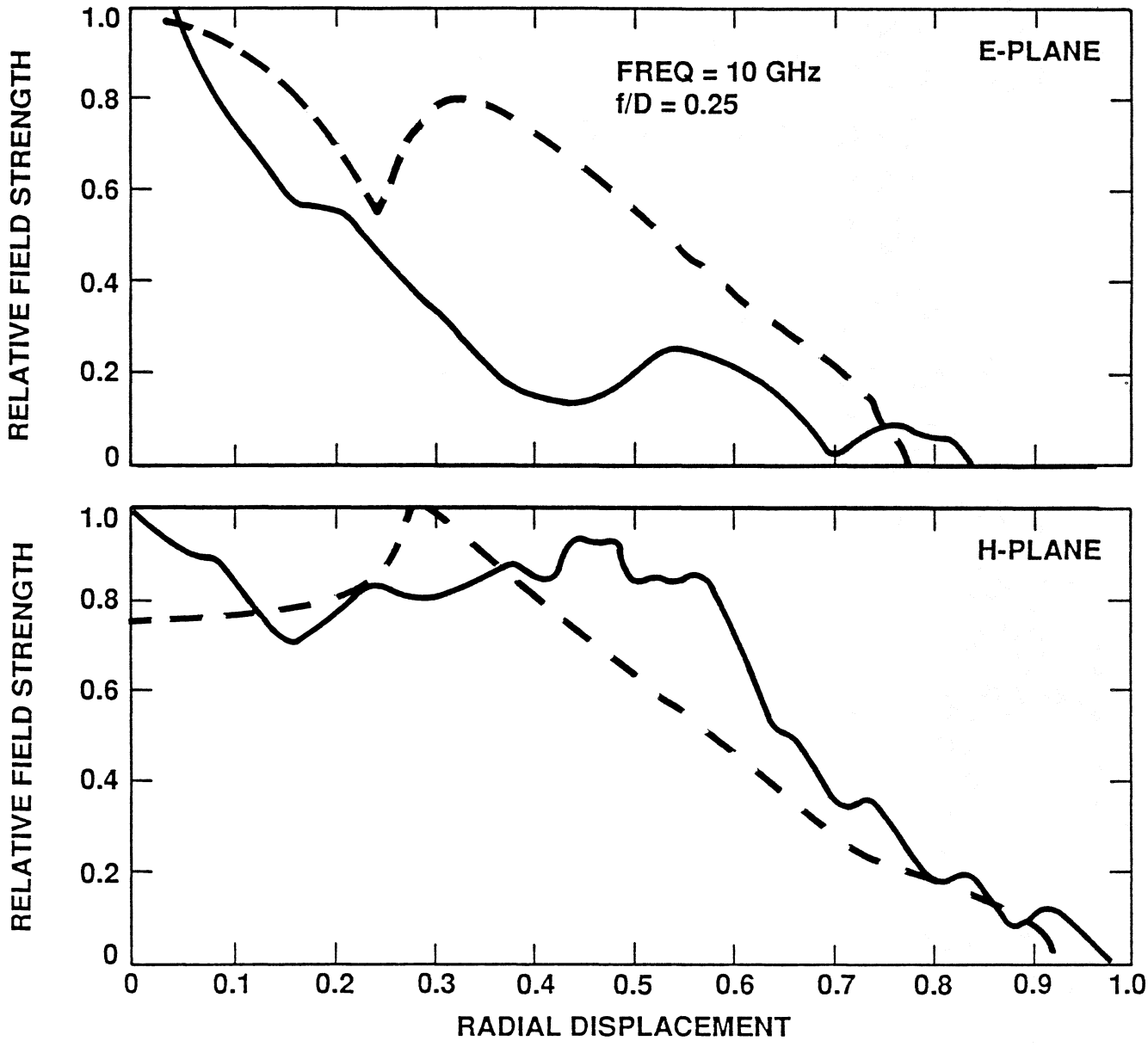

Fig. 4: A comparison of the calculated (dashed) and measured (solid) field strength along the surface of a dielectric-filled parabola with a thin dipole antenna at the focal point at 10 GHz. The calculations are based on data published in [19]. The measurements were made with a dipole probe placed in intimate contact with the lens surface. The excessive ripple is due to reflections off the air-dielectric interface.

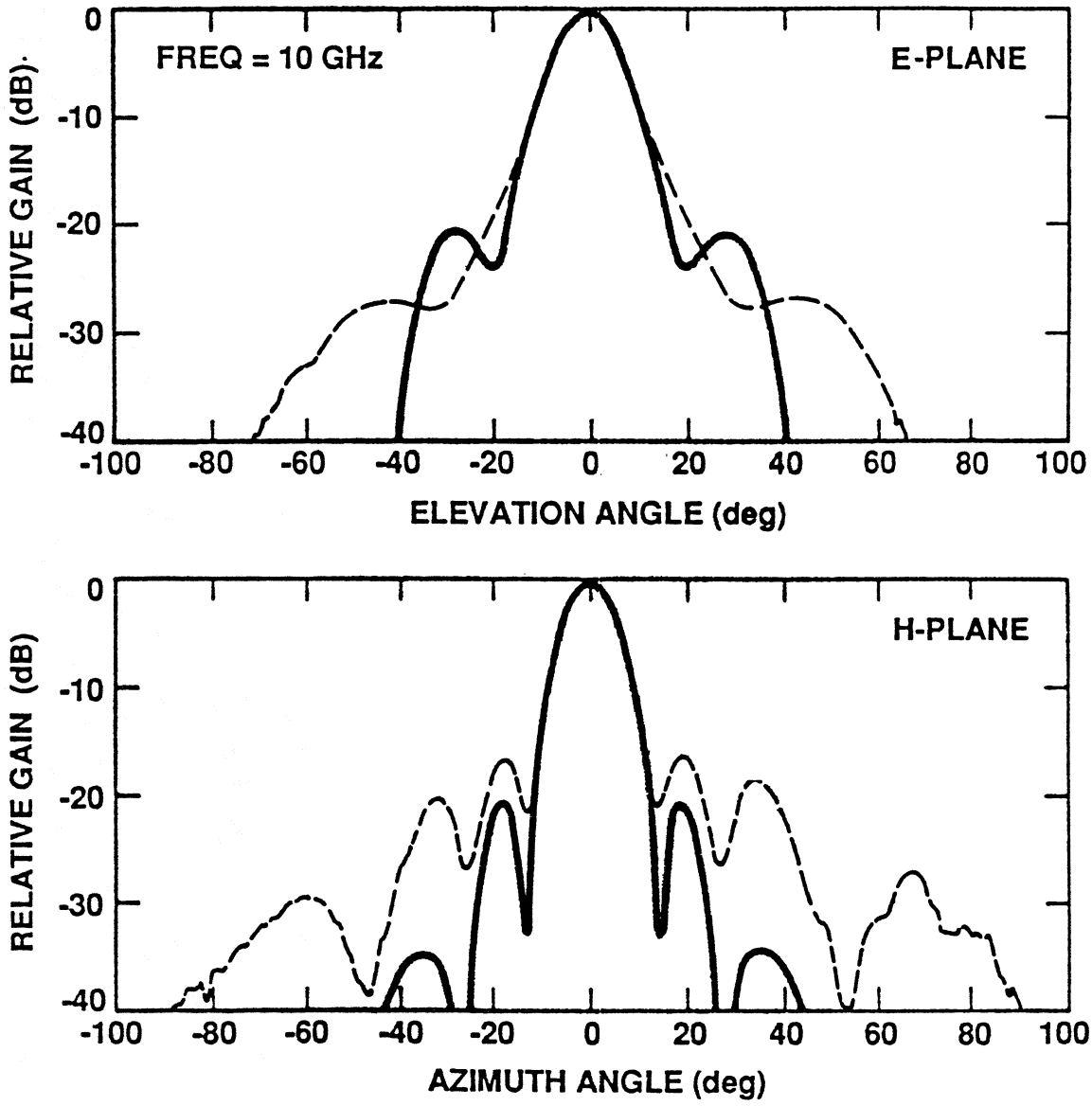

Fig. 5: The far field patterns of a thin dipole on a dielectric-filled parabola calculated from the measured field distributions of Fig. 4 (solid) and those actually measured at 10 GHz (dashed).

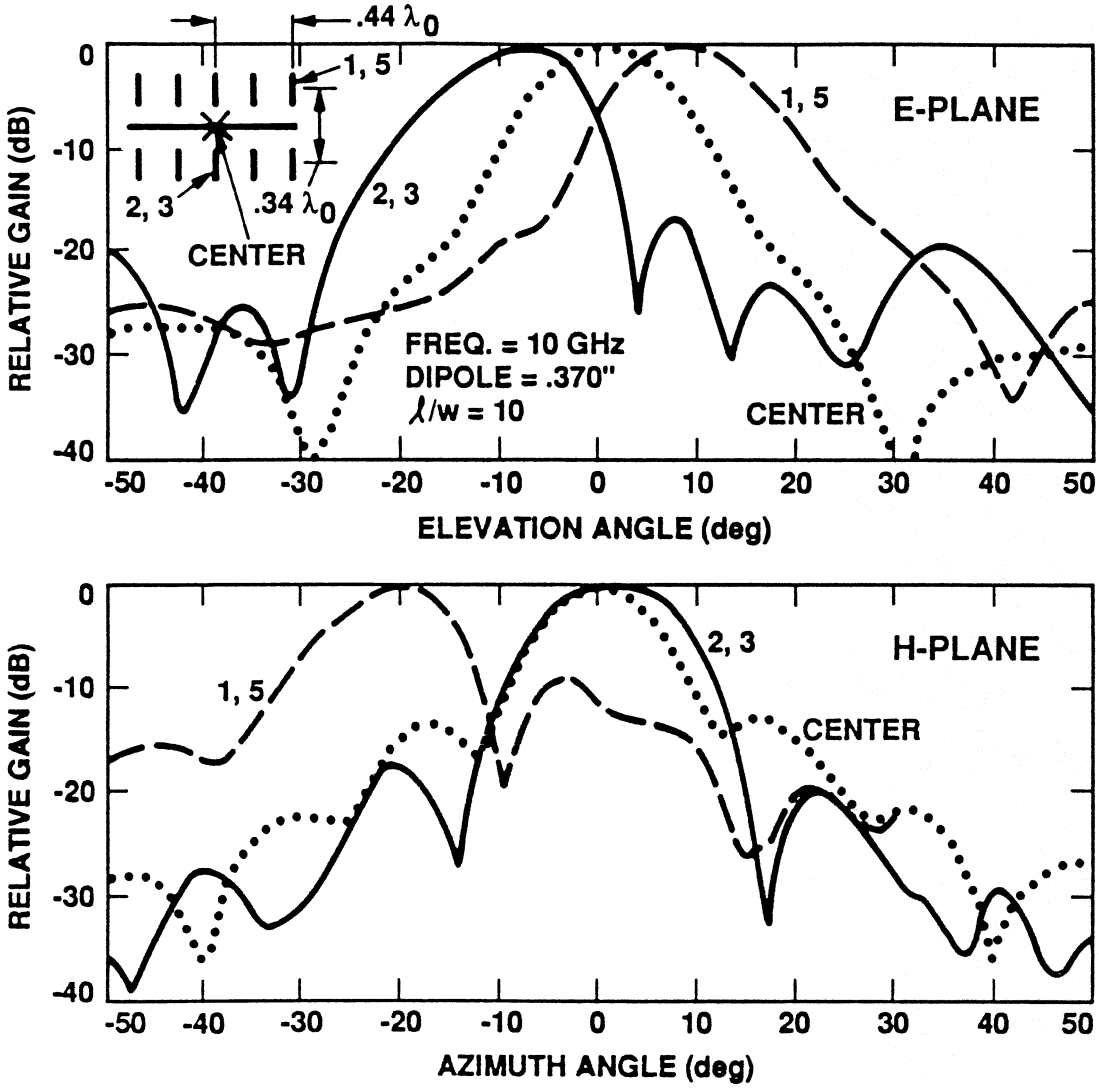

Fig. 6: The measured power patterns of several of the offset antennas of a 2x5 10 element thick dipole array (length to width = 10) on a dielectric-filled parabola at 10 GHz. At this frequency the parabola is only 7 wavelengths in diameter and diffraction effects may be significant.

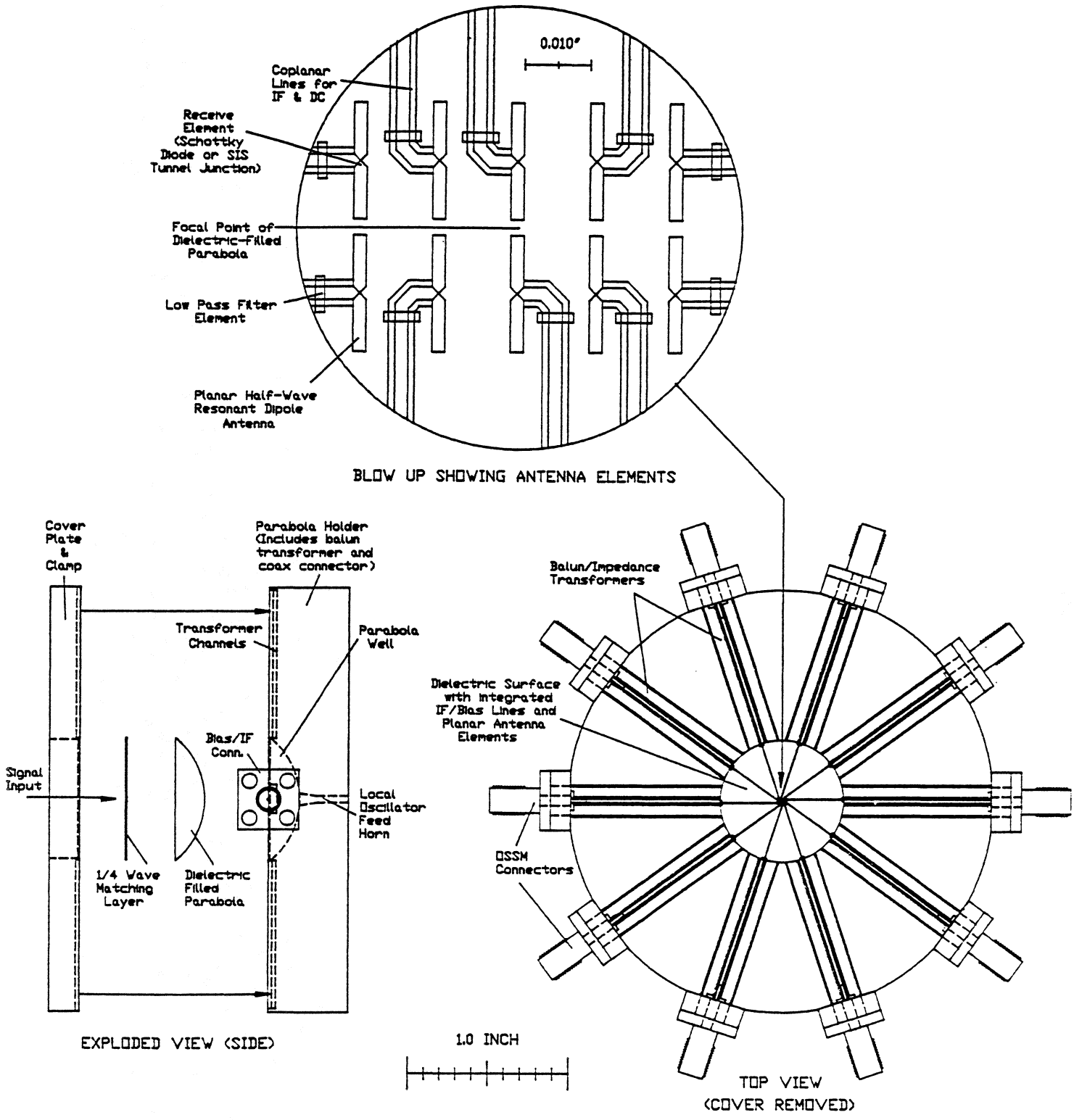

Fig. 7: Machinist's views of a complete millimeter/submillimeter wavelength heterodyne array receiver using a dielectric-filled parabola. Each array element has an SIS tunnel junction at its apex. The SIS junctions and antennas have initially been formed separately (for 230 GHz operation) but will eventually be fully integrated. The junction parameters are chosen so as to be well matched at both the RF and IF frequencies. LO injection is via a feed horn integrated into the rear of the holder. Coplanar lines (twin lead) containing low pass filter elements (gap-caps) are used for IF removal and DC biasing. Balun transformers surrounding the parabola convert the 200Ω twin lead to 50Ω coax. A teflon matching layer reduces input signal reflection loss.

Millimeter and Submillimeter Studies of Planar Antennas

H. van de Stadt, Th. de Graauw, A. Skalare[1],

R. A. Panhuyzen*, R. Zwiggelaar[2]

National Institute for Space Research, Landleven 12,

P.O. Box 800, 9700 AV Groningen, The Netherlands

*Department of Applied Physics, University of Groningen,

Groningen, The Netherlands

Abstract.

We report measurements of the properties of planar logperiodic and double dipole antennas in scale models around 10 GHz and in real size over the frequency range of 100 to 500 GHz.

In the scale model measurements we used an automated antenna range facility. We investigated single antennas as well as antenna arrays, mounted on substrates and on the backsurface of plano-convex lenses. The results of double-dipole antennas are superior to the logperiodic in the sense of slide lobe patterns, bandwidth and polarization behavior.

In the measurements between 100 and 480 GHz, we used an array of 3x3 logperiodic antennas in the focal plane of a lens with aspherical surfaces. All was mounted inside a dewar for liquid

---

[1]Present address: Chalmers Technical University, Göteborg, Sweden.

[2]Present address: University College, London, England.

helium temperatures, as planar Nb SIS junctions were used as detecting elements. We measured nice beam patterns at the lower frequencies, both on-axis, as well as off-axis. At higher frequencies, we had high side lobe levels of irregular shape. Results are presented on the polarization properties and the influence of a reflecting, adjustable backshort.

1. Introduction.

Planar antennas have a number of properties that make them suitable for application in mm/submm heterodyne receivers. In this paper we will study some properties of broadside planar antennas, where the radiation is directed normal to a flat metal structure. The following properties are of interest:

- Sensitivity: Planar antennas can have high efficiencies and can easily be integrated with planar SIS or SIN junctions, which are presently the most sensitive kind of heterodyne mixer for mm/submm wavelengths down to .8 mm and possibly for smaller values.

- Bandwidth: Several types of planar antennas (logperiodic and logspiral) can be made nearly frequency independent and can be used over many octaves. Some associated properties are: their effective antenna size varies linearly with wavelength and they

have relatively large feed angles. However, to effectively use the large bandwidth the local oscillator (LO or combination of LO's) must be tunable over the same bandwidth. For most oscillators a tunability of 30 % is already very difficult to realize. Thus the multi-octave bandwidth of some planar antennas seems to be not of much practicle interest for application in heterodyne receivers. This also implies that the limited bandwidth of dipole antennas seems to be not a severe drawback.

- Polarization: All commonly used LO's are linearly polarized. This does not automatically comply with logspiral antennas (circularly polarized) and logperiodic antennas (elliptically polarized and changing orientation with frequency). In this respect the arrangement of dipole antennas, as we have investigated, seems to be a good choice.

- Imaging: Planar antennas lend themselves for multi-element, imaging detector arrays much simpler than a multiplicity of horn-waveguide combinations. Some form of quasi-optical arrangement is required for optimum coupling of aperture ratios and to avoid problems with undersampling and/or crosstalk. The whole arrangement must be such that different elements of the imaging array should be easily servable and replacable. We looked for a structure where each antenna element can have its own lens, detector, IF output coupling leads and a fixed backshort. Also, the construction must be suitable for the implementation of SIS or SIN mixers, as their low LO power requirement allows application in mm/submm imaging arrays.

In this paper we first describe measurements on logperiodic antennas. Some of the less favourable properties led us to investigate some arrangement of dipole antennas. Several papers

have been published (e.g. refs.2 to 4) using combinations of two full-wavelength dipoles as elements in an imaging array. In chapter 4 we will motivate our preference for an arrangement of four half-wave dipole antennas.

2. Scale Model Measurements of Logperiodic Planar Antennas.

Log-periodic antenna structures have been attracting attention for radio and microwave applications ever since the fifties, ref. 1. In recent years, some of the early designs have again become of interest for applications in the mm- and sub-mm-wave regime. The main reason is a desire for a broadband antenna, that lends itself well to integration with microcircuitry and active planar components, such as superconducting SIS and SIN mixers. In this chapter we present some of our scale model measurements at frequencies centered around 10 GHz.

For our study we have chosen the types of logper antennas as given in figure 1: 1a has symmetrical sectors 45°/135°; 1b is a slightly different version of 1a with 10°/120° sectors; 1c has straight and more denser teeth; 1d has teeth on only one side of the "core". In this chapter we discuss only a selection of many measurements. More detailed information can be found in ref.7.

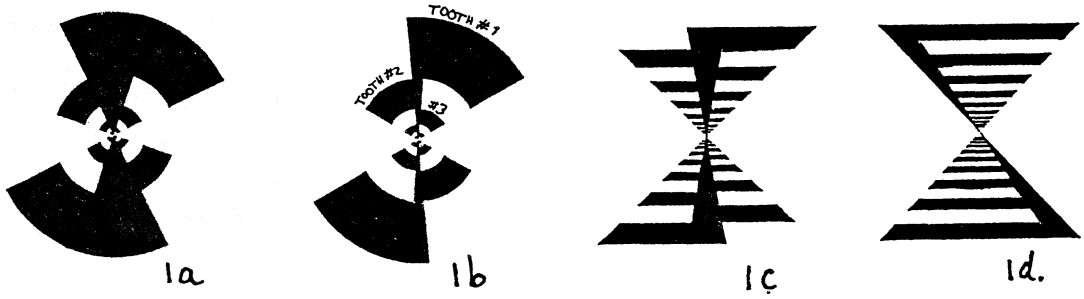

Fig. 1: Four different types of logperiodic patterns, as investigated in this study.

A large (154 mm diameter) model was made of the 10°/120° degrees antenna to study the reflection at various resonant frequencies. The reflection S_{11} was measured (Fig. 2) with a coaxial cable probing the antenna. It shows radiating resonances as dips in the trace. The size of the antenna is such as to put the resonance of the outer edge of the second tooth close to 2 GHz, i.e. the outer edge corresponds to roughly one quarter wavelength at that frequency. The sharp resonance at .64 GHz is due to an (unwanted) dipole resonant mode. Three of the desired tooth resonances occurred, but the one at the outside of the outermost tooth was very weak. The reason for this is the different boundary conditions for the resonating edge. The existence of a low-frequency limit for logperiodic antennas was mentioned already in ref.1, where a value of .9 GHz was mentioned for a 254 mm radius antenna. From the measurements we can deduce that the input impedance of our antenna varies between 120 and 225 Ohm.

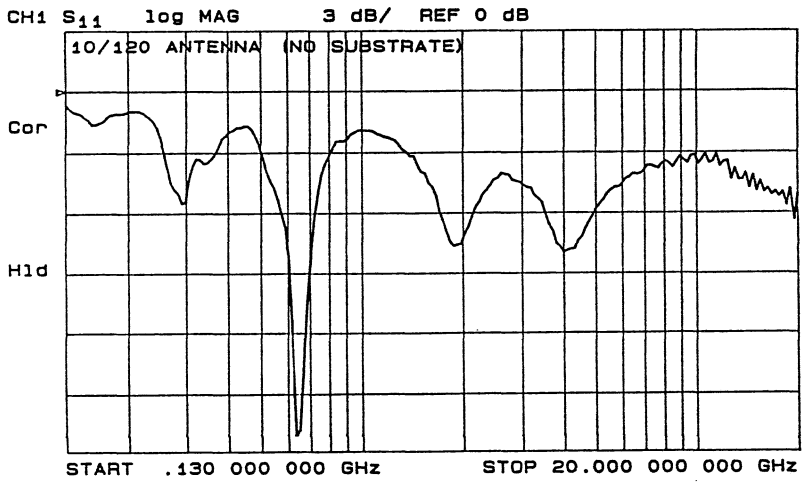

Fig. 2: The S11 reflection coefficient of antenna model 1b. There are 4 major dips in the trace. The two lower ones are unwanted dipole modes, the two higher ones (at 2 & 4 GHz) are the correct log-per modes in tooth#2 and tooth#3.

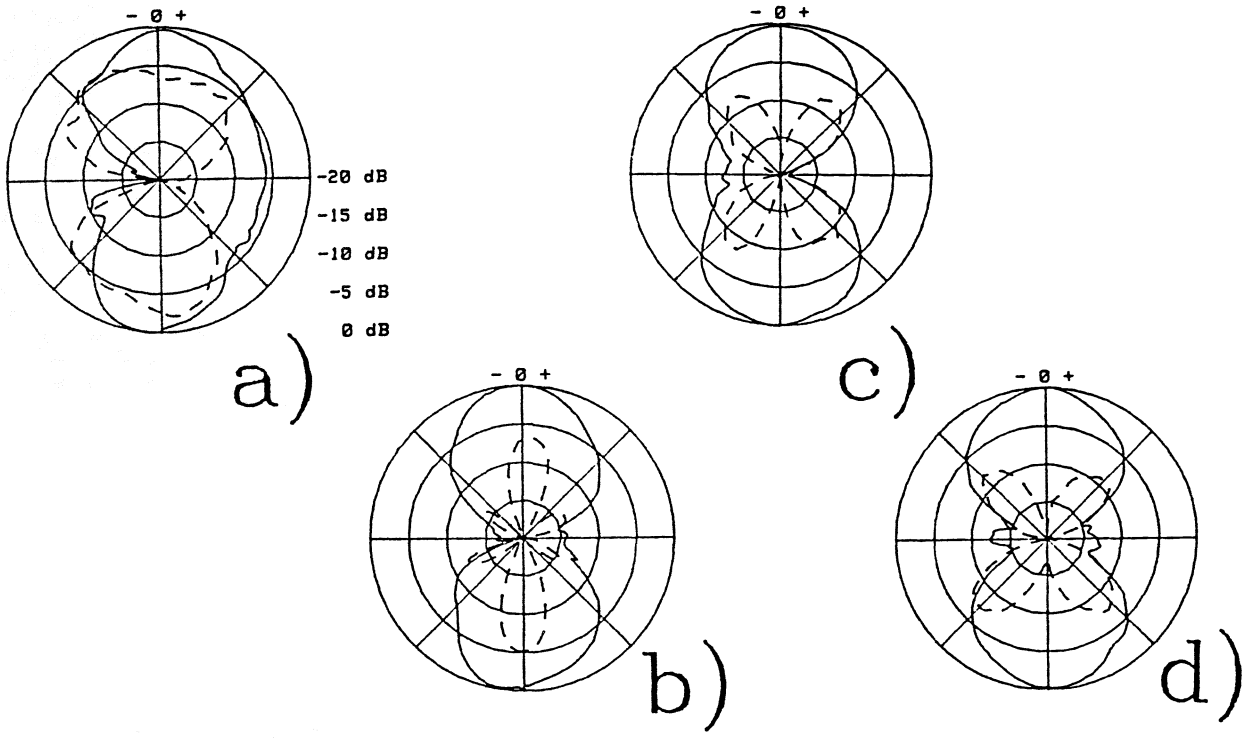

Fig. 3: H-plane radiation patterns of antenna 1a. The measurements were done in two different models, but the a/b/c/d figures can be compared by referring them to a frequency CF : a) 0.7CF, b) 1.0CF, c) 1.25CF, d) 1.5CF .

The dips in the S11 diagram at .64 GHz and lower frequencies are below the desired operating range of the antenna. As mentioned, they are caused by a type of dipole resonance, where the electrical currents are perpendicular to those in the correct log-per modes, and they give rise to cross-polarized patterns as shown in Figs. 3 and 5.

For the measurements of Fig. 3 the antenna structure 1a was supported by an electrically thin Kapton film. HP beam-lead diode detectors were used as power detectors. We actually used two models with diameters of 40 and 28 mm in order to cover an effective total bandwidth of one octave with an antenna measurement set-up suitable for frequencies between 8 and 12 GHz. Antenna patterns are measured 360 degrees round. In total more

than 80 scans were made per antenna type. In Fig.3 we only show the H-plane data for structure 1a at 4 frequencies. E-plane and D-plane (diagonal) data show similar characteristics. The "CF" frequency roughly corresponds to the resonance frequency of the outer edge of the second tooth, counting from the perimeter of the antenna.

In Fig.3 co-polarized and cross-polarized patterns are indicated with continuous and dotted lines, respectively. Apart from the pattern at the lower end of the band (at .7 CF) the co-polarized radiation patterns are between 55 and 60 degrees wide (halfwidth at -10 dB level) and have fairly good quality. The level and shape of the cross-polarized patterns indicate that a strong dipole mode was excited. The lobes at +/- 45 and +/-135 degrees also occur in the H-plane.

The addition of a dielectric substrate has the general effect of directing the radiation into the dielectric, giving sometimes as much as 8 dB difference between the peaks of the front and back lobes of the antenna.

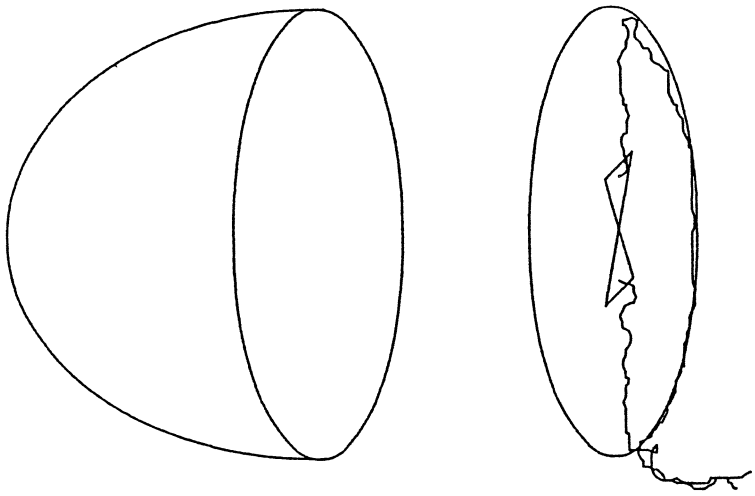

Fig. 4: Schematic view of the High Density Polyethylene (HDP), ellipsoidal lens (dielectric constant 2.31) + antenna-on-Kapton.

A series of measurements has been made with a log-periodic antenna on a thick dielectric lens, see Fig. 4, in order to increase the directivity. Fig. 5 shows this is indeed the case. However, two other effects are also visible: 1) there is a rather high sidelobe pattern in the backward direction and 2) the cross-polarization is rather high over the whole band. The reason is partly that the current distribution in the antenna structure varies with frequency, which makes the main polarization plane change with frequency. Independent measurements showed that the main polarization plane actually varies more than +/-20 degrees. The other effect is the generation of a circularly polarized component. This was confirmed by measuring patterns in a series of different planes relative to the antenna. If the antenna beam had been plane polarized, one of the planes would radiate all the power into one of its two polarizations. In the lens-antenna combination this is not the case.

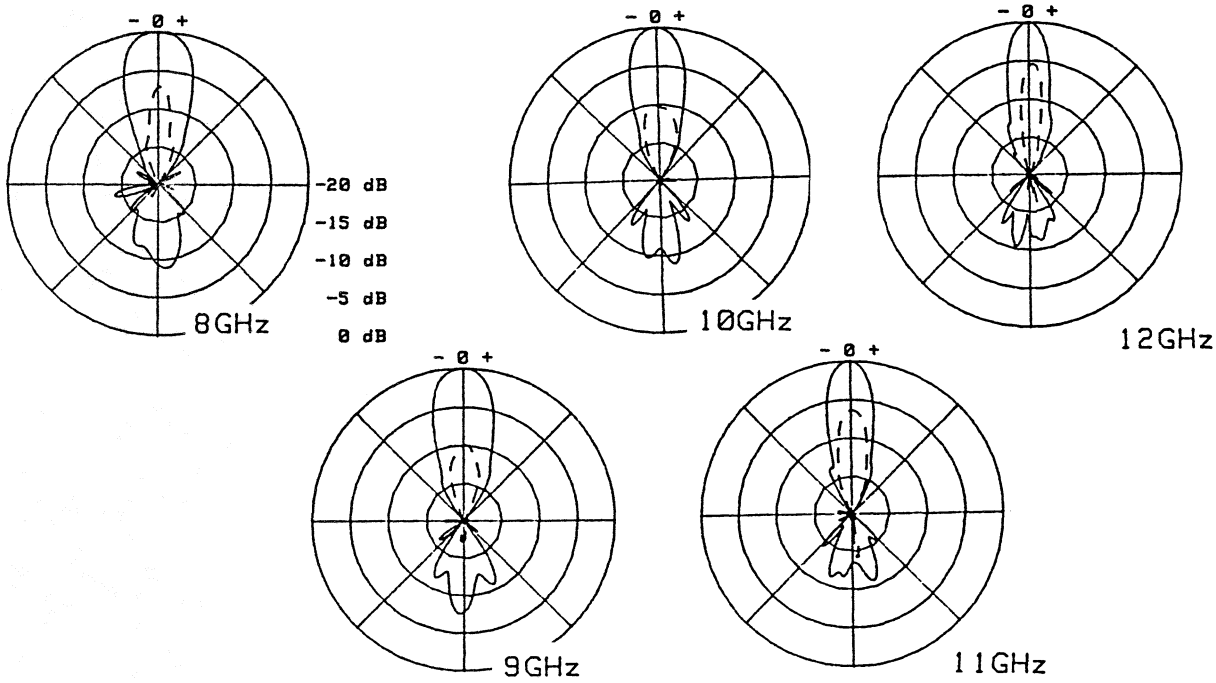

Fig. 5: E-plane measurement of antenna model 1a with a poly-ethylene lens at frequencies of 8, 9, 10,11 and 12 GHz.

An improvement in the polarization properties was expected from the antenna with straight and denser teeth, Fig. 1c. But the resulting radiation patterns look very much like the ones in the previous Fig. For the antenna with straight teeth on only one side (Fig. 1d) it turned out that a dipole resonance was excited along the free edge of the antenna and therefore the polarization properties were also not improved.

3. Mm and Submm Measurements of a Logperiodic Array.

We have built a 3x3 element array of logperiodic antennas. The diameter per element is 4.6 mm in order to study properties for frequencies of 100 GHz and higher. The inter-element spacing is 6 mm, the substrate 200 μm thick glass. Measurements were done using beam lead diodes, bismuth bolometers and Nb SIS mixers as detectors.

In order to be able to use SIS mixers we have constructed an optical arrangement in a cryostat of Infrared labs., Tucson, with an enlarged body so that we have an internal height of 10 cm available, see Fig. 6. The arrangement uses a 40 mm diameter polyethelene window and a movable reflecting backshort. We can use reflectors of 14 mm diameter for single antenna elements or 20 mm diameter for an array of 3x3 elements. The reflector can be moved over 4 mm distance. Efficient cooling of the SIS detector substrate is achieved by four clamping springs, to be mounted (but not present) on the four inner screws of Fig. 7.

As shown in Fig. 6 we have chosen for an optical arrangement with a single-element, free-standing lens, made of HDP. It was machined on a standard lathe and uses higher order, aspheric lens surfaces in order to get good off-axis imaging quality.

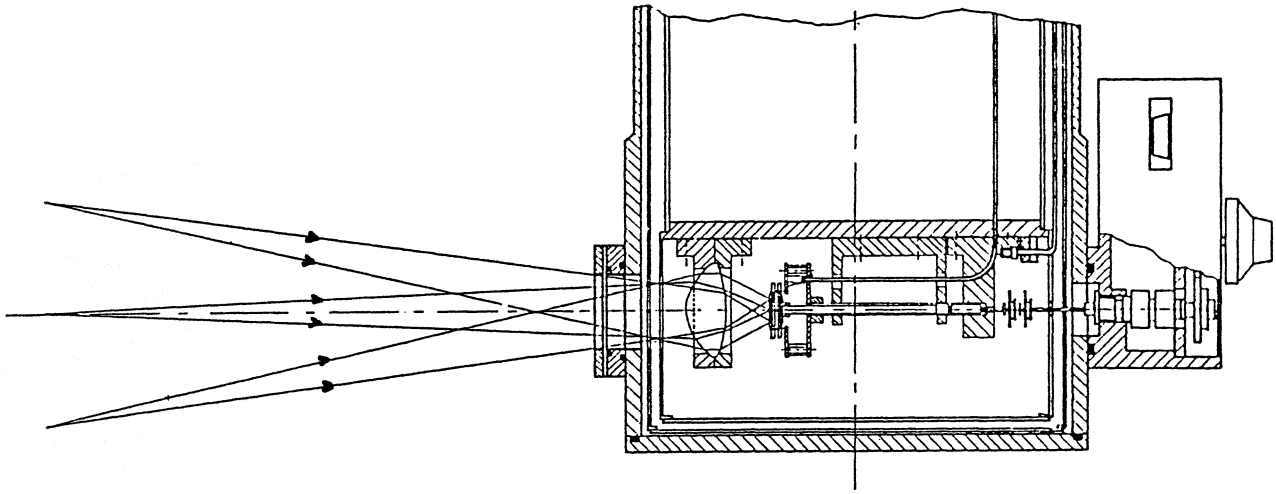

Fig. 6: Schematics of the array dewar with lens, planar antenna array and adjustable backshort on cold plate of He vessel.

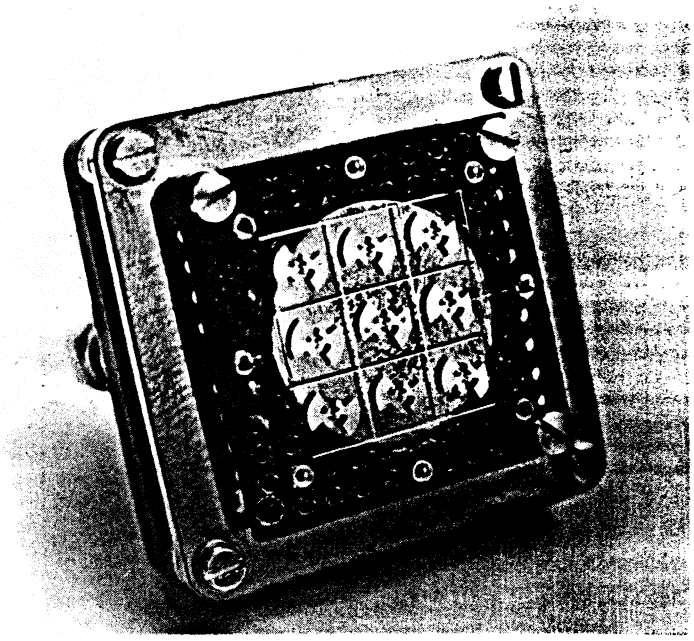

Fig. 7: Photograph of 3x3 element logperiodic planar array in a mounting with a reflecting backshort. The wires (25μm Au) to the centre element are visible

In Fig. 8a we show the antenna pattern of a single on-axis antenna element (without neighboring elements) for 106 GHz. The reflecting backshort was adjusted for optimum signal level. The pattern shows good agreement with a computed Airy pattern, which is based on diffraction as it occurs due to the 40 mm diameter dewar window. The half power beam width is 8.5° for the -10 dB points. The side lobe levels are at a quite acceptable level of ≈-17 dB.

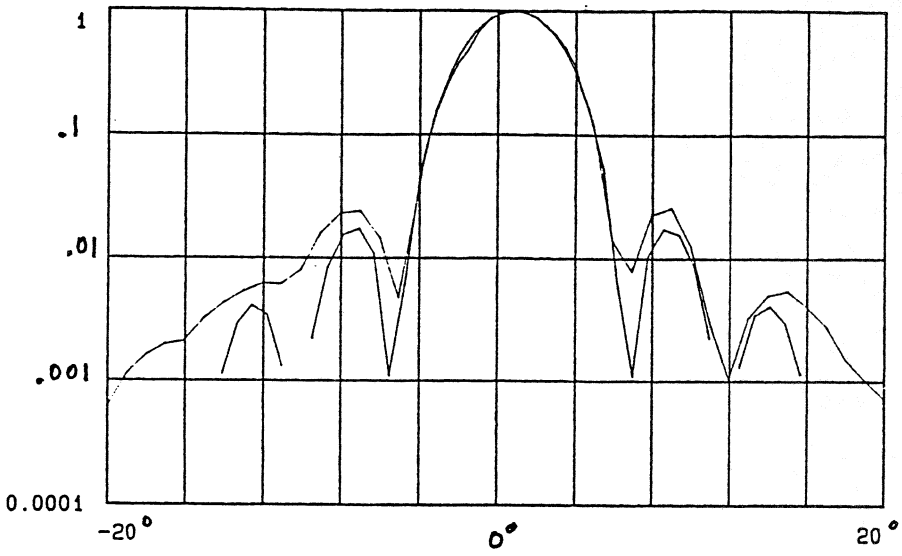

Fig. 8a: E-plane pattern of on-axis logper element at 106 GHz with a beam lead planar Schottky diode as a detector. Data are compared with a computed Airy pattern.

In Fig. 8b we show the antenna patterns for an on-axis and an off-axis array element at 106 GHz. The circumstance that the elements are surrounded by other array elements seems to broaden the beam width (to 10.6°). Also, the distinct side lobes of Fig. 8a have disappeared.

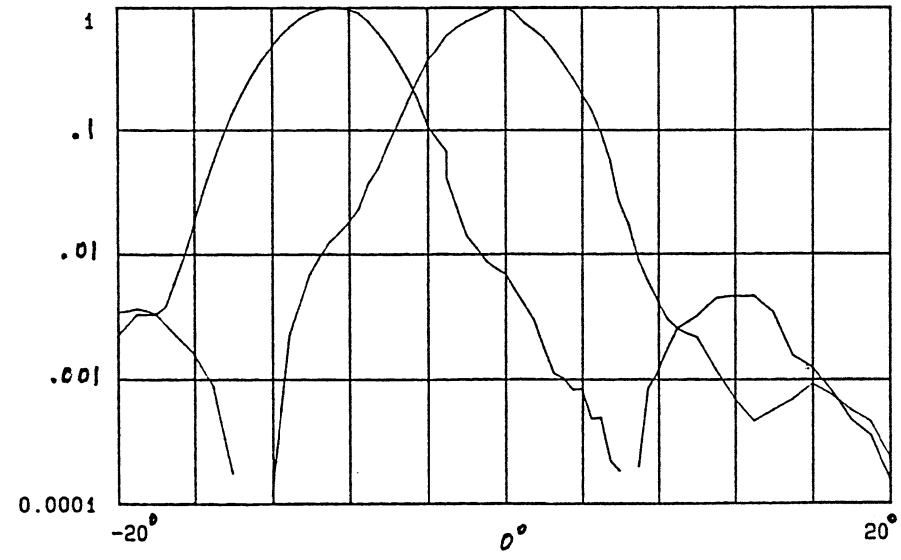

Fig. 8b: E-plane antenna patterns of on-axis and off-axis logper elements measured at 106 GHz with bismuth bolometers as detectors. No off-axis degradation is apparent.

In Fig. 8c we show the same results as Fig. 8b, but now at a frequency of 220 GHz. Compared with a computed Airy pattern at that frequency shows that the array element yields now the same diffraction limited resolution as an isolated element and there is no degradation when we go off-axis.

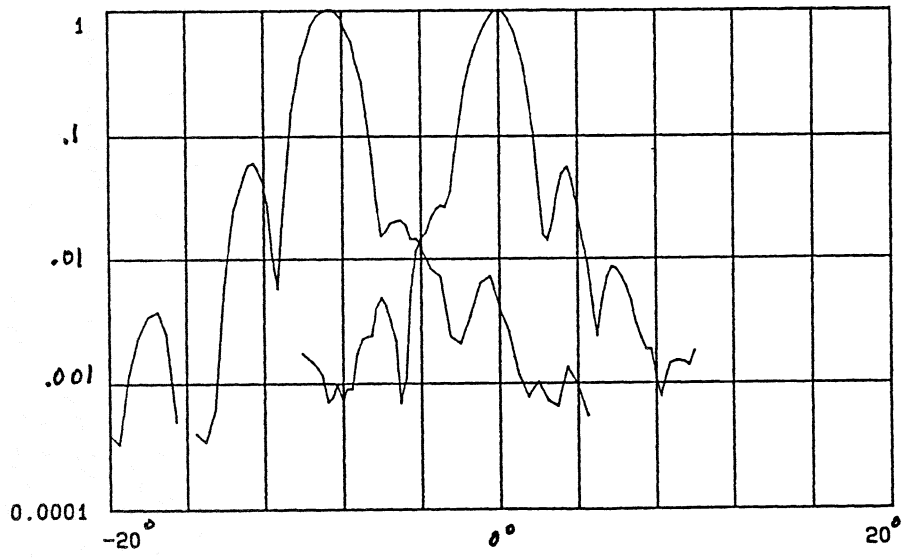

Fig. 8c: E-plane antenna patterns of on-axis and off-axis logper elements measured at 220 GHz with bismuth bolometers as detectors. No off-axis degradation is apparent.

In Fig. 8d we show the same results as in Figs. 8b and 8c, but now at a frequency of 483 GHz. Here we see a considerable degradation of the beam quality as compared to the diffraction limited beam quality. The central beam gets much wider and the level of the sidelobes is increasing considerably. Two reasons can be the origin of these phenenomena: 1) substrate effects (the substrate thickness is 200 μm, while the wavelength is 621 μm); 2) interference effects. The latter may be due to detection or reradiation of more than one set of teeth. Also the presence of the backshort can give rise to unwanted interference effects.

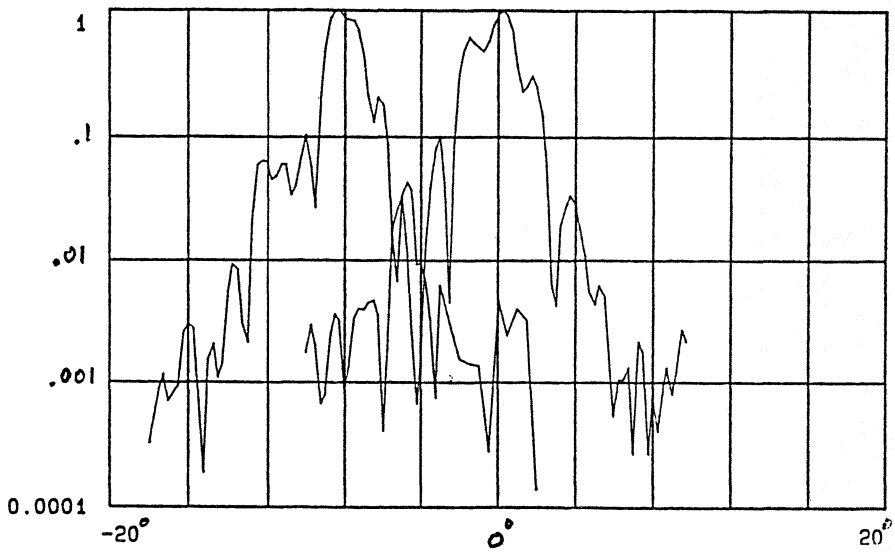

Fig. 8d: E-plane patterns of on-axis and off-axis logper elements measured at 483 GHz with bismuth bolometers as detectors. Considerable off-axis degradation is present.

Some antenna patterns were also measured with a Nb SIS mixer as a detecting element. Essentially the same patterns were measured as with bismuth bolometers.

Finally we analyzed the polarization behaviour as a function of frequency. Due to the curvature of the teeth in logper antennas one can expect a considerable change in orientation of the optimum detection angle for linearly polarized radiation. In Fig. 9 we present this angle as a function of frequency. We used two carcinotrons covering a range of 182 to 273 GHz. The change in orientation at 211 GHz is probably because the effective part of the antenna changes from one tooth to a smaller tooth. This is a worrying aspect of logper antennas, as was already clear from the scale model measurements in the preceding chapter.

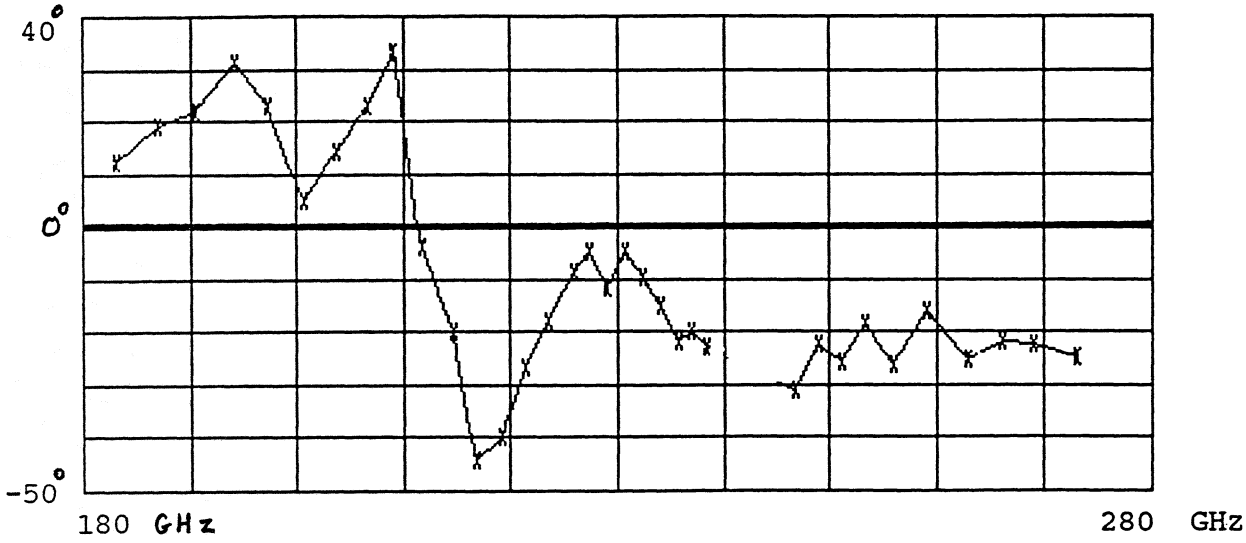

Fig. 9: Measured orientation of the linear polarization angle of a logper antenna as a function of frequency.

4. Scale Model Measurements of a Planar Dipole Array Antenna.

Several designs have been published of planar full-wave dipole antennas for imaging applications (refs. 2 to 4). In this paper we present a modified configuration using two half-wave dipoles at a spacing of about one half wavelength from each other (Fig. 10). The good sides of this antenna are its polarization properties and the fact that the beamwidth can be balanced in the E- and H-planes. The main beam, which is rather wide, is symmetrical in the forward and backward directions. This means that the antenna has to be backed by a reflector plane, and that it is useful primarily for illumination of reflectors.

We have studied the antenna in two configurations. In the first it was supported only by a thin Kapton™ film, thus simulating its free space properties. In the second the antenna was mounted between a thick polyethylene lens, and a quarter wavelength thick polyethylene slab ($\epsilon_r \approx 2.3$) backed by a metallic reflector (Fig. 12). The diameter of the lens was 110 mm. All measurements were

made in a 7-14 GHz computer controlled antenna measurement range. A Hewlett-Packard HSCH-5330 beam lead diode was bonded into each design with indium solder and used for direct detection of the signal.

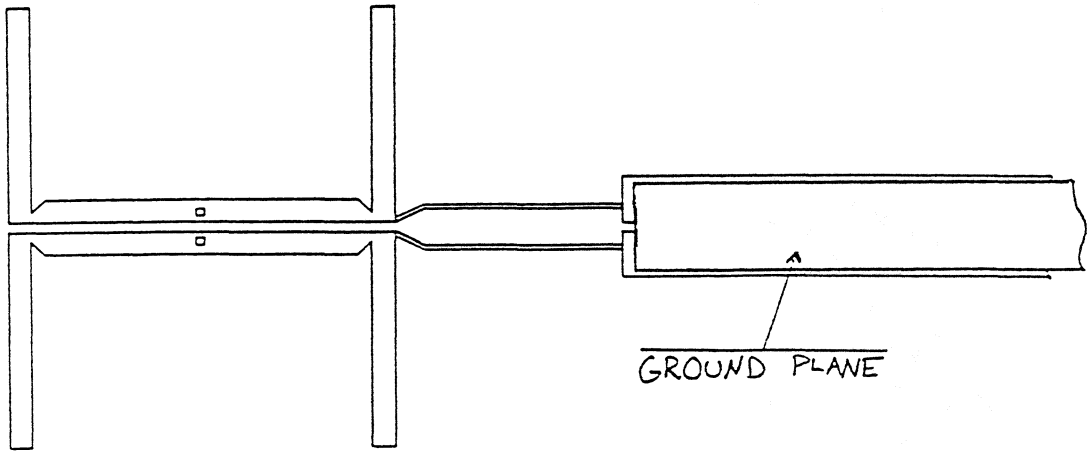

Fig. 10: The antenna with two (half-wave) dipoles. A conducting backshort plane at a quarter wave behind this plane creates an image of two more elements. Detectors are mounted midway between the two dipoles, DC and IF leads are on the right.

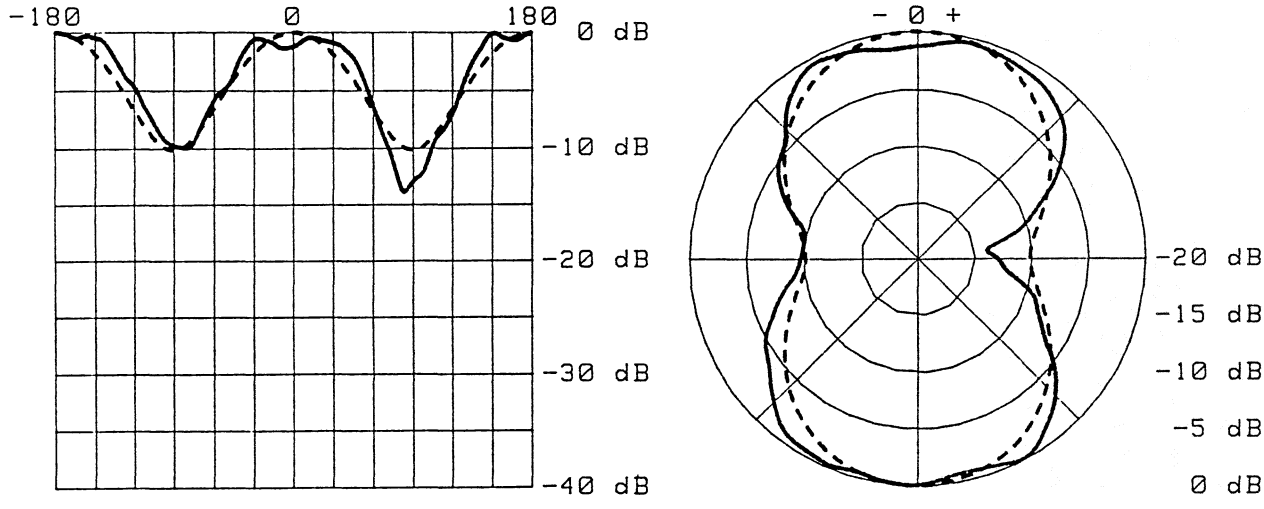

Fig. 11: Comparison between the calculated (dashed) and the measured (continuous) H-plane radiation patterns of the antenna without lens.

In the measurements of the model on the Kapton film the DC bias line turned out to make the H-plane antenna pattern slightly assymetrical. The characteristic impedance of the line was therefore lowered by a piece of copper tape which was placed on the back side of the Kapton film. (This arrangement Fig.10 was also used in the measurements with the lens). The antenna pattern was measured at several frequencies between 8 and 12 GHz and found to be satisfactory at 9.5 to 12 GHz. As an example the H-plane pattern at 10 GHz is shown in Fig.11 together with the theoretical diffraction pattern.

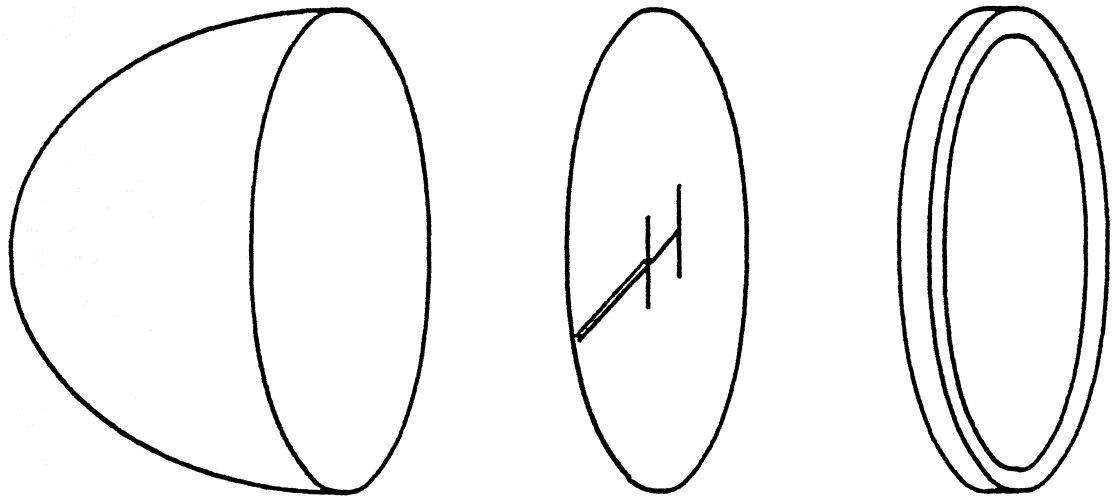

Fig. 12: An exploded view of the HDP lens, the kapton film with dipoles and a quarter wavelength slab with ground plane.

The purpose of using a lens and a reflector was to focus the main beam and remove the back lobe of the dipole feed. The lambda quarter slab was made from the same material as the lens to avoid problems with substrate modes. The physical size of the dipole array was scaled down to correct for the dielectric constant of the plastic. Since many antenna types have large amounts of cross-polarization in the 45° diagonal (D-) planes, we also did measurements in that plane.

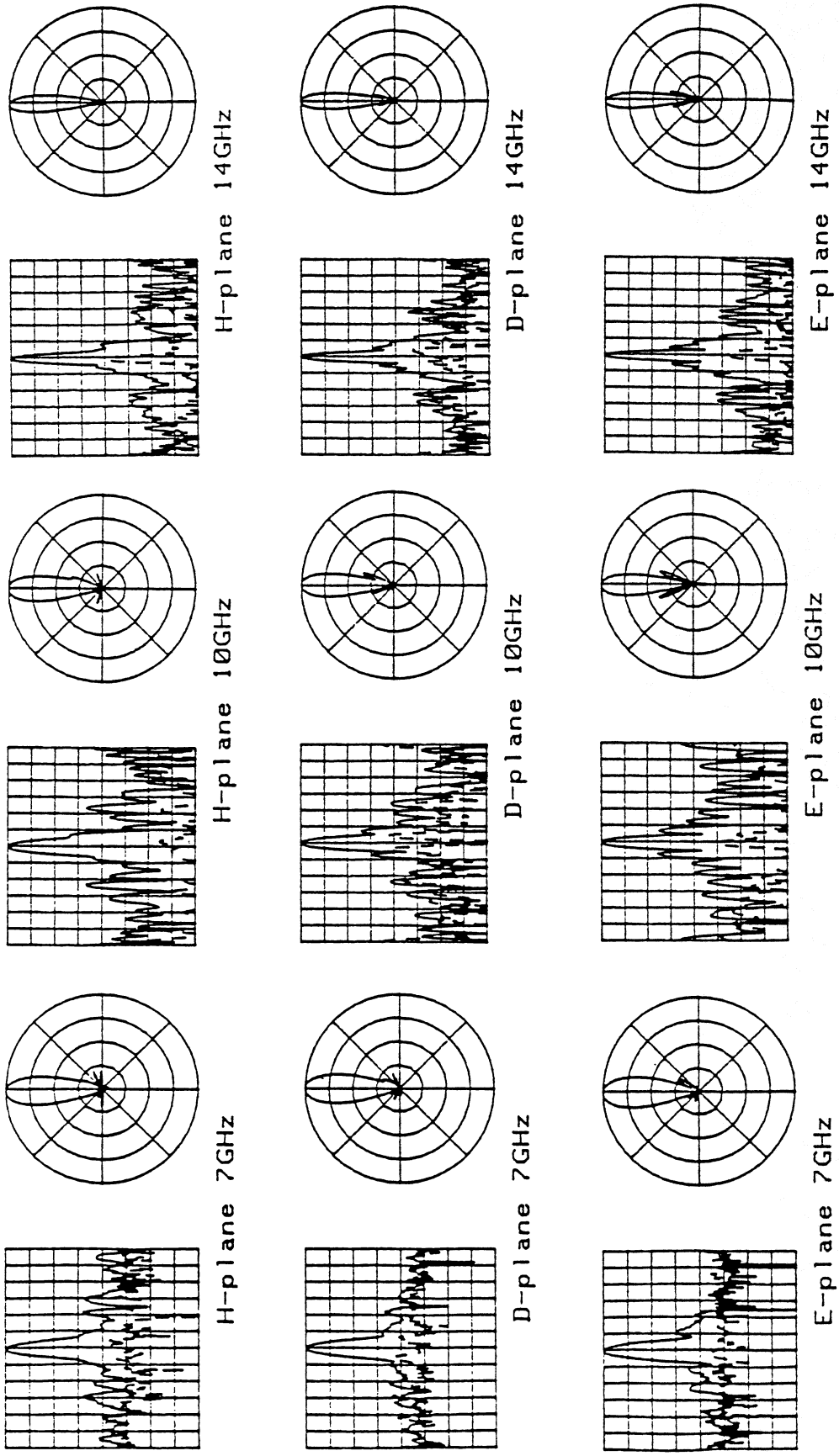

Fig. 13: Measured co- and cross-polarized patterns in H-, D- and E-planes for dipole arrangement with lens and fixed backshort at frequencies of 7, 10 and 14 GHz. Data are over 360° with 5dB/div.

Measurements were made in the 3 planes at 8 different frequencies from 7 to 14 GHz, but to conserve space only the patterns at 7, 10 and 14 GHz are shown in Fig. 13. The patterns are of good quality over the whole octave with sidelobe levels in most cases below -15 dB and cross-polarization below -20 dB. The E/H/D-plane beam widths are well balanced, but since they are diffraction limited, they decrease as the frequency increases.

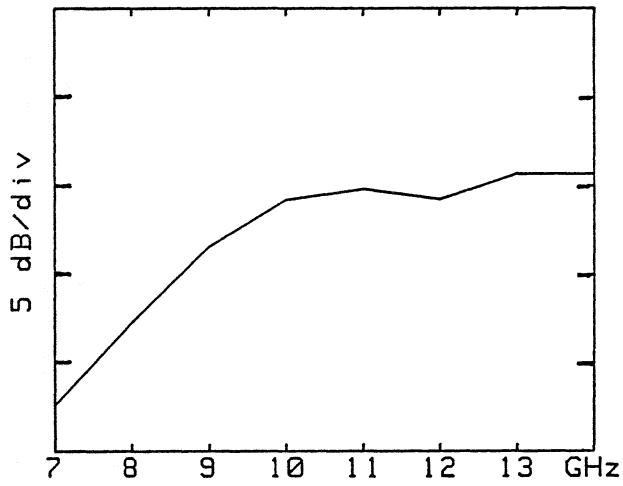

Fig. 14: Detected power as a function of frequency for the dipole antenna with lens and backshort. Systematic errors resulting from frequency dependence of the source power and detector sensitivity have not been corrected for.

The radiation pattern of the antenna is good over the whole octave of bandwidth available in the antenna range. However, the detected signal level is affected by the frequency, Fig. 14. The coupling drops off below 10 GHz, probably because the dipoles are not resonating properly there. Towards the higher end of the band it looks better. Here, the coupling is probably helped a bit by the narrowing beamwidths of both the dipole/lens antenna and the transmitting horn in the antenna range.

It is our feeling that the dipole array + lens antenna may be a good alternative for sub-mm wave low noise mixer applications. Therefore, we are currently planning two experimental recivers at 100 and 350 GHz, using SIS junctions as mixer elements.

5. Conclusions.

From our study of planar logperiodic antennas we come to the following conclusions with respect to bandwidth (see chapter 2): The lower bandwidth limit was defined by two effects: 1) the occurrence of low frequency "dipole" resonance modes, which produce cross-polarized radiation, and 2) the lowest proper "log-per" resonance occurs when the second tooth in the structure is active. The upper bandwidth limit occurs when the dielectric substrate of the antenna is a quarter wavelength (in the substrate material) thick, where the radiation pattern starts breaking up into several lobes.

Within their usable bandwidth log-per antennas radiate very wide beams (see chapter 2). A lens directly in front of a logper antenna improves the beamwith to acceptable values. However, the cross-polarization properties are not good. The generation of a circularly polarized component and a frequency dependent orientation further complicate the picture. A free standing lens with a logper antenna and reflecting backshort in its focus shows roughly the same polarization behaviour (see chapter 3).

We have investigated an antenna consisting of an arrangement of four half-wave dipoles (see chapter 4). We have demonstrated the following properties: It has strictly linear polarization, more than 30 % bandwidth, easy connection to IF leads and excellent beam patterns. For applications where the extreme bandwidth of log-periodic structures is not needed, these properties make the dipole arrangement much to be preferred.

The dipole arrangement can be positioned at the flat back surface of a thick lens. Together with a fixed backshort it yields a simple, rugged and easily replaceable construction. For imaging arrays the individual lenses per element mimimize crosstalk that could otherwise occur via reflections in a common lens or a common substrate. The absence of moving backshorts results in a particularly simple construction.

Acknowledgements.

We want to acknowledge the financial support of the European Space Agency through contracts 6648/86/NL/PB/(Sc) and 7898/88/NL/PB/(Sc). Advice and support by Dr. J. Inatani from Nobeyama Observatory in Japan was of vital importance for the SIS detector fabrication. We thank A. van Ardenne (then at the Radio Observatory in Dwingeloo, The Netherlands) for originally starting up this study. The contributions of C.E. Honingh, T.M. Klapwijk, H. Schaeffer and J. Wezelman of our institutes are much appreciated.

References.

1. R.H. DuHamel and D.E. Isbell, "Broadband Logarithmically Periodic Antenna Structures", 1957 IRE National Convention Record, pp. 119-128, 1957.

2. P.T. Parrish, T.C.L.G. Sollner, R.H.Mathews, H.R.Fetterman, C.D. Parker, P.E. Tannenwald and A.G. Cardiasmenos, "Printed Dipole-Schottky Diode Millimeter Wave Antenna Array", SPIE Millimeter Wave Technology, 337, 49-52, 1982.

3. W. Chew and H.R. Fetterman, "Printed Circuit Antennas with Integrated FET Detectors for Mm-Wave Quasi-Optics", IEEE Transact. on Microw. Theory and Techn., 37, 593-597, 1989.

4. J.A. Taylor, T.C.L.G. Sollner, C.D. Parker and J.A. Calviello, "Planar Dipole-Fed Mixer Arrays for Imagig at Millimeter and Submillimeter Wavelengths", 1985 Intl. Conf. IR and Mm Waves, p.187-188, W1.7, 1985.

5. G.M. Rebeiz, W.G. Regehr, D.B. Rutledge, R.L. Savage and N.C. Luhman, " Submillimeter-wave Antennas on thin Membranes", Int.J. IR and MM Waves, 8, 1249-1255, 1987.

6. H. van de Stadt, "Test of Planar Imaging Array", SRON internal report, Groningen, october 1989.

7. A. Skalare, "Scale Model Measurements of Log-Periodic Antenna Structures", SRON internal report, Groningen, january 1990.

8. A. Skalare, "A Dipole Antenna Feed for a Dielectric Lens Surface", SRON internal report, Groningen, january 1990.

GaAs Schottky Barrier Diodes for Space Based Applications at Submillimeter Wavelengths †

Thomas W. Crowe, W.C.B. Peatman and W.L. Bishop

Semiconductor Device Laboratory
Department of Electrical Engineering
University of Virginia
Charlottesville, VA 22903

ABSTRACT

Recent technological advances have made possible the development of heterodyne receivers with high sensitivity and high spectral resolution for frequencies up to 3,000 GHz (3 THz). These receivers, which rely on GaAs Schottky barrier mixer diodes to translate the high-frequency signal to a lower frequency where amplification and signal processing are possible, have found a variety of important scientific applications. Recently there has been a great deal of interest in developing submillimeter wavelength receivers for space based applications involving both radio astronomy and remote sensing of the Earth's atmosphere. Such receivers must be much more compact, reliable and power efficient than those presently available. This will be achieved through the development of a new generation of planar Schottky diodes that will be driven by solid-state local oscillator sources and have parasitic capacitances as low as those of the best whisker contacted diodes. This paper reviews the status of submillimeter wavelength heterodyne receivers and the ongoing work at the University of Virginia which is focussed on the development of improved diode structures.

† *This work has been supported by the National Science Foundation under contract ECS-8720850, the Jet Propulsion Laboratory, and the U.S. Army.*

I. INTRODUCTION

Technological advances have made possible the development of heterodyne receivers with high sensitivity and high spectral resolution for frequencies up to 3,000 GHz (3 THz) [1,2,3]. These receivers are opening a major region of the electromagnetic spectrum to spectroscopic investigation and are thus having an important impact on radio astronomy. They are also finding increasing applications in fields such as plasma diagnostics, chemical spectroscopy and remote sensing of the Earth's atmosphere. Recently there has been a great deal of interest in the development of receiver systems that are suitable for deployment in satellites. Such a space based system would clearly be an advantage for submillimeter wavelength radio astronomy and investigation of the Earth's upper atmosphere. This paper is an attempt to review briefly the current state-of-the-art of submillimeter wavelength Schottky diode receivers and consider the development that is needed for these receivers to be suitable for space based applications. The ongoing research at the University of Virginia is highlighted.

A simplified block diagram of a heterodyne receiver is shown in Fig. 1. The receiving antenna and optical components couple the signal and local oscillator (LO) power into the mixer structure. The mixer consists of a non-linear element that "mixes" these two frequencies to

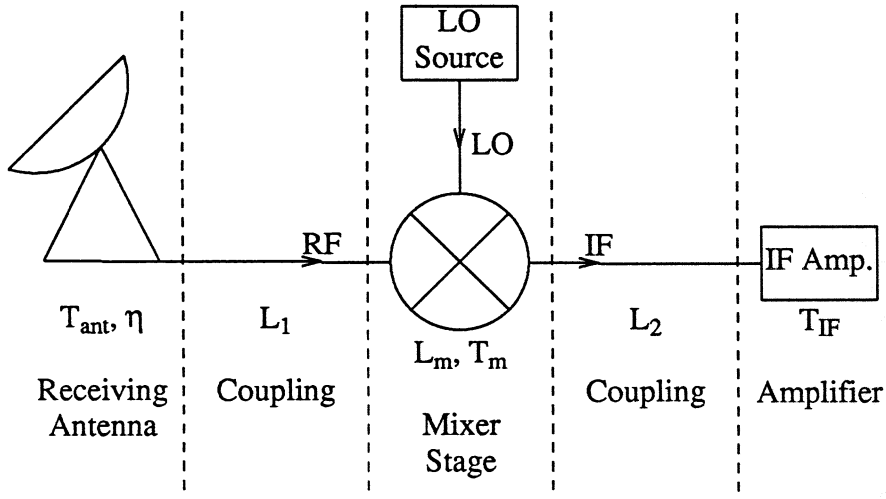

Fig. 1. A simplified block diagram of a typical heterodyne receiver.

generate the intermediate frequency, ν_{IF}, given by

$$\nu_{IF} = | \nu_{sig} - \nu_{LO} | . \quad (1)$$

If the LO source is spectrally pure, the resulting IF signal will have the same frequency spectrum as the original signal, except that it will be at a much lower center frequency that can now be amplified and analyzed by standard microwave techniques. The first stage of the IF amplifier is typically either a cooled GaAs FET or a high electron mobility transistor[4].

The most important figure-of-merit of the receiver is the system noise temperature, which can be approximated as

$$T_{sys} = T_{ant} + \frac{1}{\eta} L_1 T_{rec} \quad (2)$$

where T_{ant} and η are the noise temperature and efficiency of the receiving antenna, L_1 represents the loss between the receiving antenna and the mixer due to coupling losses and attenuation in the signal path, and T_{rec} is the noise temperature of all components from the mixer back. T_{rec} can be expressed as

$$T_{rec} = T_m + L_m L_2 T_{IF} \quad (3)$$

where T_m and L_m are the mixer noise temperature and conversion loss respectively, L_2 is the IF signal loss between the mixer and the amplifier due to coupling losses and attenuation, and T_{IF} is the noise temperature of the IF amplifier stage. Noise sources beyond the IF amplifier have only a marginal effect and are not considered here.

The two most important components for consideration in this paper are the mixer and the LO source. At millimeter wavelengths the LO source is typically a Gunn diode in combination with a solid-state multiplier. The output from the Gunn diode, which can be as high as 120 GHz, is coupled into the multiplier circuit where the non-linear capacitance of a Schottky varactor diode is used to generate harmonics. By proper design of the multiplier circuit the unwanted harmonics are suppressed and the desired frequency is coupled to the mixer input. This LO system is noted for its simplicity, compactness, reliability and low cost. However, as is discussed

more generally in the next section, the power available from such systems drops drastically at submillimeter wavelengths, and is presently insufficient for many applications.

GaAs Schottky barrier diodes are used in the mixer for a wide variety of applications due to their excellent mixing properties and their relative ease of use and reliability. There are two main figures-of-merit for the diodes. The first is the figure-of-merit cut-off frequency, defined as

$$\nu_{co} = \frac{1}{2\pi R_s C_{jo}}, \tag{4}$$

where R_s and C_{jo} are the diode series resistance and zero-bias junction capacitance, respectively. For good receiver performance ν_{co} must be much greater than the signal frequency. The second figure-of-merit is the diode slope parameter, V_o, which is a function of the sharpness of the diode's I-V curve. The I-V curve is generally assumed to be exponential with a series resistance,

$$I = I_{sat} e^{(\Phi - V - IR_s)/V_o} \tag{5}$$

where I_{sat} is the diode saturation current and Φ is the barrier height. A lower value of V_o yields a sharper I-V curve and less diode noise. At frequencies above about 600 GHz the overall receiver performance is more dependent on the cut-off frequency than V_o so that it is most important to minimize the $R_s C_{jo}$ product. At lower frequencies the state-of-the-art diodes already have a high enough cut-off frequency so that the major emphasis is in the reduction of V_o [5]. To date Schottky diodes have been used in radio astronomy applications at frequencies as high as 3 THz, and it is quite reasonable to consider how these diodes need to be improved to make them available for space based applications.

II. THE STATE OF THE TECHNOLOGY

The development of Schottky diode receivers for heterodyne spectroscopy in the submillimeter wavelength region has been quite rapid. As of 1982 the highest reported operating frequency was roughly 700 GHz with a noise temperature of 8000K (SSB) [6]. Since then several newer versions of the original corner cube receiver [7] have improved the receiver sensitivity and the operating frequency [1,2,3]. A good example of this technology is the receiver

developed at the Max Planck Institute for Radioastronomy in Bonn, West Germany [1]. This system was reported in 1986 having noise temperatures of only 4,850 K SSB at 693 GHz and 17,000 K SSB at 2,500 GHz. The increased sensitivity can be traced mostly to improvements in the coupling of the signal into the diode and to improvements in the diode itself. Also, there has been much development in the laser local oscillator systems. This has improved the coverage of the submillimeter wavelength region and the system reliability. In fact, several of these systems now meet airborne specifications and have been used very successfully on the Kuiper Airborne Observatory [1,2]. In the remaining part of this section the present status of the Schottky diodes for submillimeter wavelength applications is considered.

A. GaAs Schottky Barrier Mixer Diodes

A cross-sectional sketch of a typical high-frequency diode chip is shown in Fig. 2. These diodes are in essence quite similar to the original "honeycomb" diodes first produced by Young and Irvin in 1965[8]. However, with increased understanding of diode operation their basic structure has been greatly optimized. Also, the improvement in fabrication technology has made possible the development of high-quality devices with much smaller feature sizes for reduced capacitance. A comparison of the original diodes of Young and Irvin and several state-of-the-art

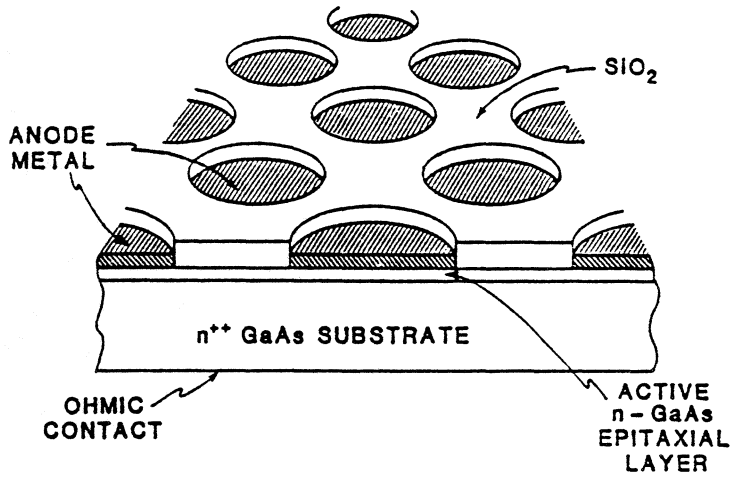

Fig. 2. A cross-sectional sketch of a typical high-frequency diode chip (not to scale).

devices is given in Table I. The new diodes have thinner epitaxial layers and reduced anode diameters. More importantly, the doping density of the epitaxial layers is now optimized for the specific frequency of operation. The result is greatly increased cut-off frequency and reduced diode noise. An SEM photograph of a diode chip with 0.5 μm diameter anodes is shown in Fig. 3.

In a typical mixer, an individual anode on the diode chip is contacted with a pointed metal wire, or whisker. Although the whisker contact technique is fraught with difficulties, it yields the lowest possible shunt capacitance (of order 1fF) and is thus necessary for the highest operating frequencies. For comparison several planar diodes are also included in Table I. These diodes have integrated anode contacts (i.e. they are whiskerless) and thus are much easier to install in the mixer and much more reliable. However, this comes at a cost in shunt capacitance, as is seen in the table. An SEM of a planar diode developed at the University of Virginia is shown in Fig. 4 [9]. The major component of the shunt capacitance is between the large anode and cathode pads. This shunt capacitance must be significantly reduced if this diode is to be used at submillimeter wavelengths.

Some recent high-frequency results are presented in Table II. These results have been compiled from a quick survey of several research teams and thus do not necessarily represent the best results obtained to date, but rather a cross-section of results that have been achieved. It is clear from this table that Schottky diodes are useful for scientific applications throughout all of the submillimeter wavelength region (0.3 - 3 THz), and perhaps to higher frequencies. It should also be noted that all of these results were obtained with whisker contacted Schottky diodes. Planar diode technology has not yet reached the submillimeter region. This is a problem that will be discussed in more detail later.

Throughout most of the submillimeter wavelength region the most common local oscillator source has been the submillimeter gas laser. A gas discharge CO_2 laser is used to pump the submillimeter wavelength laser, whose active medium is an organic molecule that is chosen to

Table I
Characteristics of GaAs Schottky Barrier Mixer Diodes

Diode	R_s (Ω)	C_{jo} (fF)	ν_{co} (GHz)	V_o@ 10–100μA (mV)	diameter (μm)
Original[8]	15	15-20	530-700	31	3
2I2-150	10	6.5	2,400	28	2
1I1	9	1.5	11,800	33.4	1
1T6	≈35	0.4	11,400	35.6	0.45

Planar Diodes	R_s (Ω)	C_{jo} (fF)	C_{shunt} (fF)	ν_{co} (GHz)	V_o@ 10–100μA (mV)	diameter (μm)
SC2R2	5.5	5.5	14	-	31.0	2.5
SC2R4	5-6	6.0	9-10	-	30.4	2.5

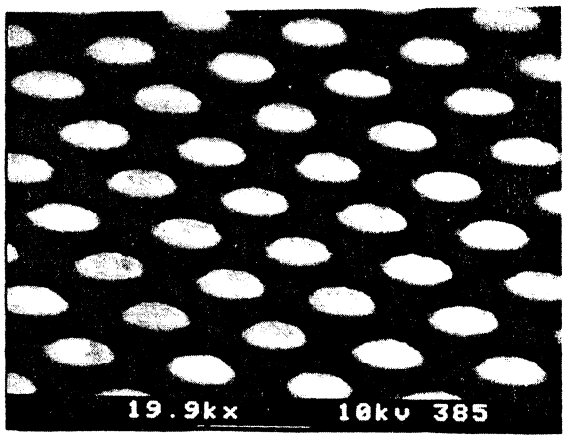

Fig. 3. An SEM photograph of the surface of a 1T6 diode chip. The anode diameter is roughly 0.45 microns.

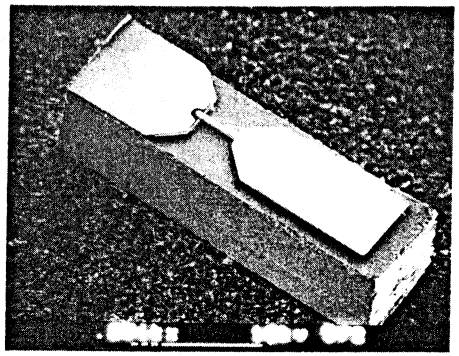

Fig. 4. An SEM photograph of a planar Schottky barrier mixer diode developed at the University of Virginia. It has yielded excellent performance at 100 GHz [9].

Table II
Submillimeter Wavelength Performance of Some Whisker Contacted Schottky Barrier Mixer Diodes

ν_{RF} (GHz)	T_{rec}^{SSB} (K)†	ν_{IF} (GHz)	BW_{IF} (GHz)	Temp.(K)	Reference
460-490	1740	1.45	0.3	20	Keen, 1986 [10]
693	4850	1.4	1	300	Röser, 1986 [1]
800	3150	6.4	1	77	Harris, 1989 [3]
1,963	21,000*	6.7	0.2	77	Boreiko, 1989 [11]
2,520	17,000	1.4	1	300	Röser, 1986 [1]

† *In order to express all of the data in a uniform manner it is assumed that* $T^{SSB} = 2T^{DSB}$ *for all instances where the actual values are quoted as DSB in the references.*

* *Measured on the Kuiper Airborne Observatory.*

have an emission line close to the desired signal frequency. These systems are large, heavy, consume lots of power and are quite difficult to maintain. In fact, the sole virtue of these systems is that they generate sufficient power to drive a Schottky receiver at essentially any frequency from 300 to over 3000 GHz. Although these systems are airborne qualified, it is doubtful that they will be space qualified at any time in the near future. (This would require months/years of continuous operation without manual adjustment.) This is the most significant obstacle to the development of space based receivers.

B. GaAs Schottky Barrier Varactor Diodes

As was mentioned in Section I, varactor diodes are used to multiply the output frequency of Gunn diodes to frequencies well into the submillimeter wavelength region. To date these devices have generated sufficient output power to drive Schottky mixer diodes at frequencies as high as 600 GHz. A comparison of the characteristics of several varactor diode batches is presented in Table III. The data in this table shows a very important trend that gives some indication of the difficulty involved in the fabrication of varactor diodes for THz applications. Specifically, as the cut-off frequency of the diodes is increased the reverse breakdown voltage, V_{bd}, is decreased, thus reducing the capacitance modulation. This means that diodes optimized for high-frequency operation will be less efficient multipliers and will not be able to handle large input powers. The most recent varactor diodes (2T2) have been used by Erickson at the University of Massachusetts

Table III
Characteristics of Several Schottky Barrier Varactor Diodes

Diode	N_{epi} (cm^{-3})	R_s (Ω)	C_{jo} (fF)	C_{min} (fF)	V_{bd} (V)	ν_{co} (GHz)	C_{max}/C_{min}
6P2	$3x10^{16}$	9.5	20.1	5.2	19.5	833	3.9
5P8	$5x10^{16}$	12	13	5	16	1,020	≈3.5
2T2	$1x10^{17}$	11.5	5.5	1.9	10.7	2,500	2.8

to generate as much as 0.7 mW of power at 500 GHz [12]. This is a very encouraging result, but much more development in this area is necessary.

III. Technology Needed for Space Based Applications

The requirements for a space based receiver system are quite easily stated. The receiver must be compact, light in weight, consume the smallest amount of power possible, be able to withstand high vibration (during launch for example) and, most importantly, it must be highly reliable without system maintenance. The current generation of submillimeter wavelength receivers fails to meet each one of these constraints. There are two main problems that must be overcome. The submillimeter wavelength laser must be replaced with a solid-state source and the whisker contacted diode must be replaced with a planar diode structure.

The elimination of the laser LO system can be achieved by increasing the output power of varactor diodes and/or decreasing the power required to drive Schottky diodes. As will be shown in the next section there has been significant progress in both of these areas. Another method to extend the frequency range of multipliers is to use subharmonically pumped mixers. This type of mixer uses an LO frequency that is roughly one-half of the signal frequency. There are two ways to do this. The first is to simply drive a standard diode with the LO and let the mixer diode itself generate upper harmonics that are then mixed with the signal. Although these devices do not, in general, achieve the sensitivity that is available from fundamental mixers, they are quite good and have been demonstrated up to about 600 GHz with solid-state sources [13]. The second type of subharmonically pumped mixer incorporates two Schottky barrier mixer diodes that are in anti-parallel configuration. The I-V of such a diode combination is symmetric. If the LO power is strong enough to turn on both of the diodes the conductivity will peak twice during each LO cycle. This will allow the signal to see an impedance that varies at a frequency of $2\nu_{LO}$, thereby generating an IF at $\nu_{sig} - 2\nu_{LO}$. Such a device can have sensitivity very close to that achieved in fundamental mixers, but they are quite difficult to build with whisker contacted diodes.

The second difficulty in putting today's receiver technology into space is the stability of the whisker contact. Although several satellites incorporating whisker contacted Schottky diodes have been successfully space qualified, the fabrication and qualification of these receivers is time consuming, labor intensive and quite expensive. (An example of an upcoming launch is the Microwave Limb Sounder on the Upper Atmosphere Research Satellite scheduled to be launched in 1991.) A better solution is the development of planar Schottky diodes for this frequency range. Planar Schottky diodes are being developed at a number of research laboratories and substantial progress has been made over the past several years [9,14]. Although these devices have given quite good results at 100 GHz, they are not yet competitive with whisker contacted diodes at submillimeter wavelengths. This is due to the large shunt capacitance that is inherent in the planar diode structure and the difficulty in fabricating sub-micron anodes. The planar diode research at the University of Virginia is outlined in the next section. It is the goal of this research to develop planar diodes that have the same performance as whisker contacted diodes throughout the submillimeter wavelength region.

IV. Recent Advances at the University of Virginia

Research at the University of Virginia Semiconductor Device Laboratory is focussed on the development of improved solid-state devices for high frequency applications. Recently, several important advances have been made which greatly improve the prospects for the development of solid-state heterodyne receivers for space based applications. These advances are in the areas of reduced LO power requirement for Schottky mixer diodes, increased cutoff frequency of Schottky barrier varactor diodes, and fabrication of planar Schottky devices with greatly reduced parasitic capacitance.

A. Reduced LO Power Require for Submillimeter Wavelength Schottky Barrier Mixer Diodes

In a mixer, the local oscillator power is used to drive the non-linear mixer element between its high and low impedance states. For good conversion efficiency, the ratio of these impedances

must be as large as possible. If there is not sufficient LO power available to drive the element over its full impedance range, the conversion loss will be degraded. Thus, the non-linear device requires a certain amount of power in order to achieve an acceptably low conversion loss. Since solid-state LO sources generate very low power levels it is important to reduce the amount of power that the mixer element requires. There are two ways to do this, either increase the coupling efficiency between the source and the diode or reduce the power needed in the diode itself.

In an attempt to reduce the LO power requirement of the Schottky diodes we have tried to reduce the diode parasitic elements as much as possible. The series resistance dissipates much of the LO power before it reaches the non-linear junction impedance and the junction capacitance tends to short power around the junction. Also, it is important to make the junction capacitance as small as possible, even at the cost of a slight increase in series resistance. This is done in an attempt to increase the coupling efficiency between the diode's antenna structure and the diode itself. For example, at 1 THz a diode with 1 fF of capacitance has a maximum impedance magnitude of 160 Ω ($1/\omega C_{jo}$) and a minimum impedance equal to the diode's series resistance (roughly 10 - 30 Ω). The effective impedance of the diode at the LO frequency is bounded by these two values, and as a rule of thumb is assumed to be equal to their geometric mean, for this example 60 Ω †. Since the high-frequency impedance of the antenna is typically of the order of 100 - 200 Ω, it is expected that a large fraction of the LO power is reflected by the diode. A reduction of the junction capacitance while maintaining the series resistance - junction capacitance product constant should help to reduce this reflection.

We have fabricated Schottky diodes with half micron anodes to test this hypothesis. A comparison of receiver noise temperature as a function of LO power at 1,400 GHz for a standard

---

† *It is quite complicated to calculate the diode's actual high-frequency impedance when it is dc biased and LO power is applied. However, it is reasonable to assume that this impedance is between the maximum and minimum diode impedances and as a rule of thumb it is assumed to be near the geometric mean of these values. For the case described above* $Z_{geom} = \sqrt{160 \cdot 20} = 60\,\Omega$.

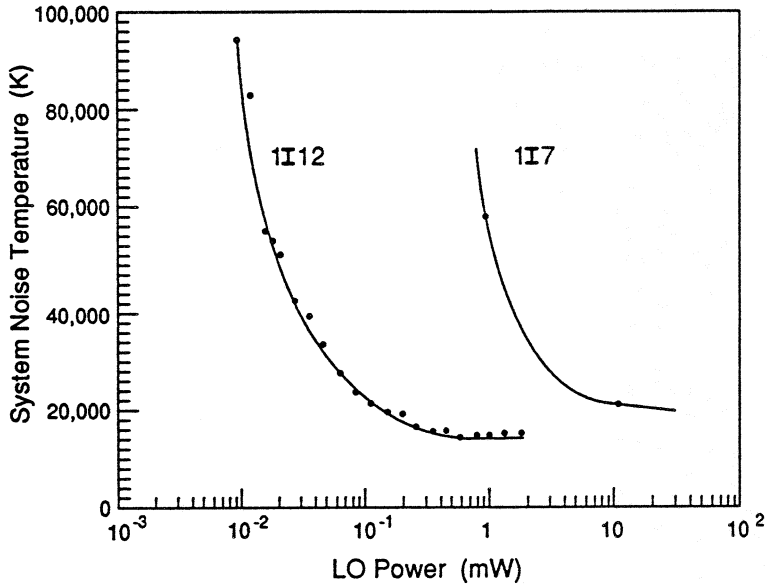

Fig. 5. A comparison of receiver noise temperature versus LO power for two diodes at 1,400 GHz. The newer 1I12 diode has one-half the capacitance of the 1I7 diode and requires an order of magnitude less LO power. The diodes were mounted in identical corner cubes and tested in the same receiver system.

Schottky diode (1I7, C_{jo}=1.0fF) and the half-micron diode (1I12, C_{jo}=0.5fF) is presented in Fig. 5 [15]. The new diode requires only about 0.1 mW of LO power to attain the same performance level that the old diode achieved at nearly 5 mW. This is a very substantial improvement. However, solid-state sources can not yet generate even this small amount of power at THz frequencies.

B. Increased Cut-off Frequency of Varactor Diodes

Until recently the maximum cut-off frequency of Schottky barrier varactor diodes was limited to values below 1 THz. This is substantially below the cut-off frequency of mixer diodes because the varactor's epilayer must be low doped and thick enough to yield a large reverse breakdown voltage. However several recent batches of devices have cut-off frequencies in the THz range. This has been achieved by judiciously increasing the epilayer doping density to reduce the R_sC_{jo} product and accepting a small decrease in reverse breakdown voltage. A summary of dc results was presented in Table III.

A novel doping structure for varactor diodes, called the Barrier-Intrinsic-N^+ (BIN) diode, is also quite encouraging. This work was pioneered at UCLA and the Jet Propulsion Laboratory [16]. These devices have extremely sharp capacitance-voltage (CV) characteristics, and may be very useful at high-frequencies where efficiency is much more important than power handling capability. This is provided that the new diodes can be fabricated with low enough series resistance and zero-bias junction capacitance. The result of a first attempt to fabricate a BIN-like diode is summarized in Fig. 6, which shows the capacitance modulation of the BIN-like diode compared to a standard varactor diode. The improved sharpness of the CV curve is clear. These devices may become very useful for harmonic multiplication into the THz range.

C. Planar Schottky Diodes with Reduced Parasitic Capacitance

The major problem with all planar Schottky barrier diodes is the excessive shunt capacitance caused by the large contact pads which overlay the high dielectric constant GaAs substrate ($\varepsilon_r = 13$). To improve this situation the substrate must be replaced with a low dielectric constant material or entirely removed. This is exactly what has been done [17]. Fig. 7 shows an SEM photograph of a planar diode that is fabricated on a quartz substrate. The only remaining GaAs is a thin layer below each of the contact pads and below the anode itself. The rest of the material is simply a quartz substrate that is adhered with a thin adhesive layer.

To achieve the minimum possible capacitance for this diode structure it would be desirable to remove even the quartz substrate. This is easily achieved provided that the adhesive is properly chosen so that it can be dissolved without damaging the diode itself. Fig. 8 is an SEM photograph of a chip that has been soldered to a quartz stripline and then had the substrate removed. All that remains is the metal contact pads and a thin layer of GaAs (a few microns thick). There is no GaAs near the anode finger itself. This structure has very low shunt capacitance and, in fact, the pad capacitance should be thought of as part of the stripline impedance and thus should not degrade high-frequency performance. Also, the pads can be used as part of a planar antenna

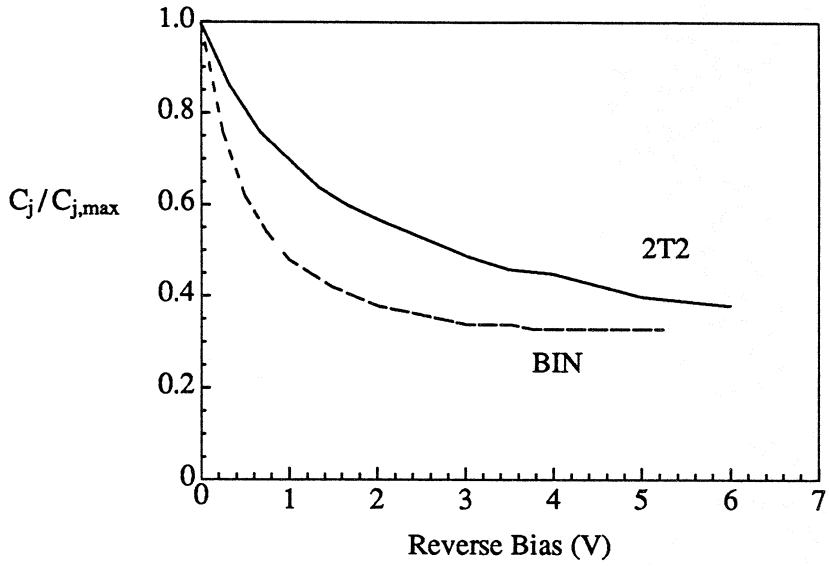

Fig. 6. *The capacitance-voltage characteristics of two varactor diodes of similar capacitance and series resistance. The 2T2 is a standard varactor diode with* $C_{jo}=5.5\,fF$ *and* $R_s=11.5\Omega$. *The BIN-like diode has* $C_{jo}=3.9\,fF$ *and* $R_s=18\,\Omega$. *The BIN-like diode has a much sharper CV curve and better overall capacitance modulation.*

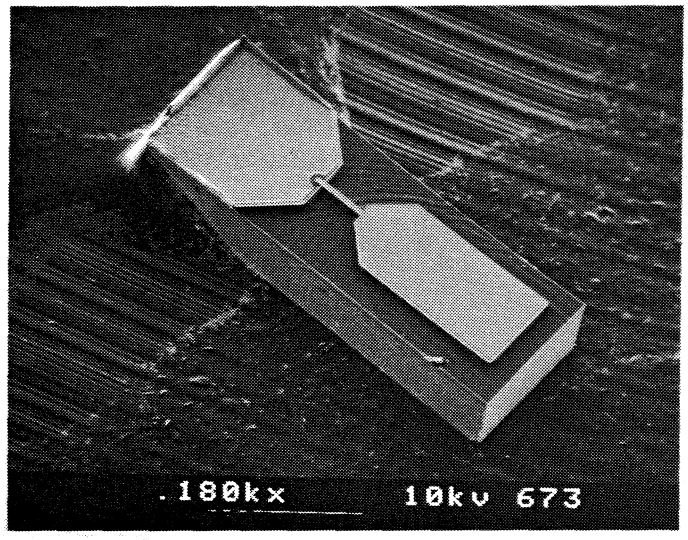

Fig. 7. *An SEM photograph of a planar GaAs Schottky barrier diode on a quartz substrate [17]. The only remaining GaAs is a thin layer below each contact pad and below the anode.*

structure for a quasi-optical coupling system. This type of planar diode structure will yield performance that is equivalent to the best whisker contacted devices, or perhaps better.

A planar diode chip with two anodes connected in anti-parallel is shown in Fig. 9. This prototype device has been designed for subharmonic mixing in the millimeter wave range and is now available for evaluation. The fabrication process has been designed so that the shape of the contact pads and the anode finger length and spacing can be easily changed. This chip will also be fabricated on a quartz substrate for high-frequency applications.

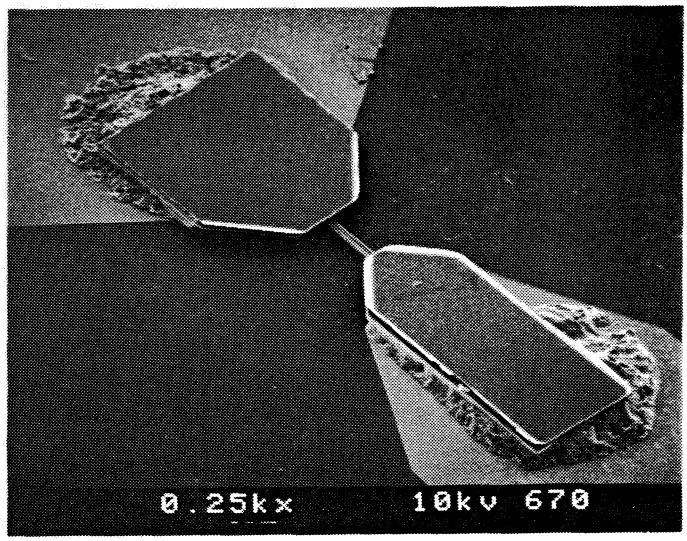

Fig. 8. An SEM photograph of a planar GaAs Schottky barrier diode without any substrate [17]. The chip was soldered to a quartz stripline before the substrate was removed.

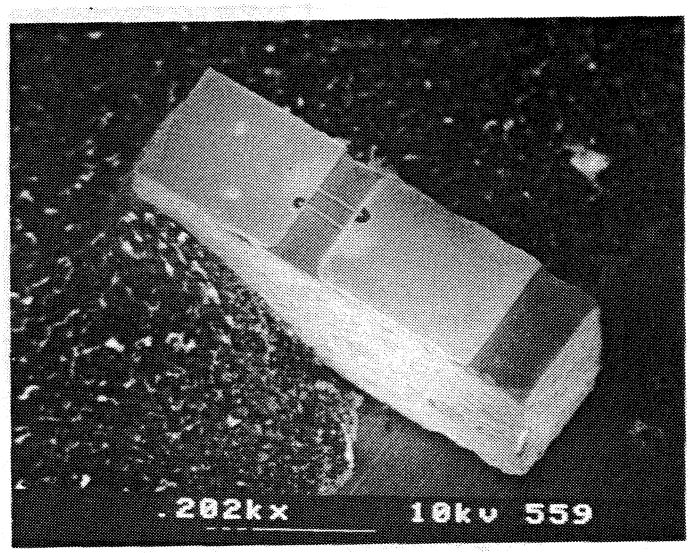

Fig. 9. An SEM photograph of a planar dual-diode structure. The diodes are in anti-parallel configuration for subharmonic pumping applications.

V. FUTURE RESEARCH AND CONCLUSION

GaAs Schottky barrier diodes are used in heterodyne receivers throughout the submillimeter wavelength region. Although receivers based on these devices have been highly successful, and have met airborne requirements, a great deal of work remains to be done before they can be routinely space qualified. First the laser local oscillator must be replaced by an solid-state source. This is already possible at frequencies up to about 600 GHz, but development of improved varactor diodes is necessary to increase this into the THz frequency range. Investigation of novel varactor diode structures, such as the BIN diodes and perhaps high electron mobility varactors, may yield the required improvement. Also, development of mixer diodes that require less LO power will help to lessen the burden on the varactor diodes. Further work in this area is necessary to determine if the significant improvements that have recently been achieved can be extended.

Although whisker contacted diodes can be space qualified, this is a costly, and to some extent risky, process. The development of planar Schottky diodes for THz frequencies is thus very important. New planar diodes with greatly reduced shunt capacitance are now becoming available. These devices will eventually yield better performance than the present whisker contacted diodes. However, a substantial amount of further research is necessary before this is achieved. The major problems to overcome are the reduction of the anode diameter to sub-micron dimensions and detailed optimization of the chip design to improve the coupling of the high-frequency signal into the diode. The new substrateless diode should be ideal for incorporation into waveguide or open structure mixer designs. This planar technology will greatly simplify the space-qualification process for submillimeter wavelength receivers, improve the receiver reliability and extend the maximum frequency of operation of space based receiver systems.

REFERENCES

[1] H.P. Röser, R. Wattenbach, E.J. Durwen, and G.V. Schultz, "A High Resolution Spectrometer for 100 μm to 1000 μm and Detection of CO (J=7-6), CO (J=6-5) and ^{13}CO (J=3-2)," Astron. Astrophys., 165, 287-299, (1986).

[2] J. Zmuidzinas, A.L. Betz, and R.T. Boreiko, "A Corner-Reflector Mixer Mount for Far Infrared Wavelengths," Infrared Phys., Vol. 29, No. 1, pp. 119-131, (1989)

[3] A.I. Harris, D.T. Jaffe, J. Stutzki, and R. Genzel, "The UCB/MPE Cassegrain Submillimeter Heterodyne Spectrometer," Int. J. IR and MM Waves, Vol. 8, No. 8, pp. 857-883, (1987).

[4] M.W. Pospieszalski, S. Weinreb, R.D. Norrod, and R. Harris, "FETs and HEMTs at Cryogenic Temperatures, Their Properties and Use in Low Noise Amps," IEEE Trans. Microwave Theory Tech., Vol. MTT-36, No. 3, pp. 552-560, (1988).

M.W. Pospieszalski, J.D. Gallego, W.J. Lackatosh, "Broadband, Low-Noise Amplifiers in the 1-50 GHz Range," To be presented at the 1990 IEEE MTT-S International Microwave Symposium, Dallas, TX, May 1990.

[5] T.W. Crowe and R.J. Mattauch, "Analysis and Optimization of Millimeter- and Submillimeter-Wavelength Mixer Diodes," IEEE Trans. Microwave Theory Tech., Vol. MTT-35, No. 2, pp. 159-168, (1987).

[6] P.L. Goldsmith, N.R. Erickson H.R. Fetterman, C.D. Parker, B.J. Clifton, D.D. Peck, P.E. Tannenwald, G.A. Koepf, D. Buhl, and N. McAvoy, "Detection of the $J=6 \rightarrow 5$ Transition of Carbon Monoxide," Ap. J. Lett., Vol. 243, pp. L79-L82, Jan. 1981.

[7] H. Kräutle, E. Sauter and G.V. Schultz, "Antenna Characteristics of Whisker Diodes Used as Submillimeter Receivers," Infrared Physics, Vol. 17, p. 477, (1977).

[8] D.T. Young and J.C. Irvin, "Millimeter Frequency Conversion Using Au-n-Type GaAs Schottky Barrier Epitaxial Diodes with a Novel Contacting Technique," Proceedings of the IEEE, pp. 2130-2131, (1965).

[9] W.L. Bishop, K. McKinney, R.J. Mattauch, T.W. Crowe, and G. Green, "A Novel Whiskerless Schottky Diode for Millimeter and Submillimeter Wave Applications," Proceedings of the 1987 IEEE MTT-S International Symposium, Las Vegas, Nev., 607-610, June 1987.

[10] N.J. Keen, K.-D. Mischerikow and G.A. Ediss, "Three Facility Low-Noise Receivers for Millimeter and Submillimeter Radio-Astronomy," 16th European Microwave Conf., Dublin, Sept. 1986.

[11] R.T. Boreiko and A.L. Betz, "Heterodyne Spectroscopy of the J=17-16 CO Line in Orion," Astrophys. J., Vol. 337, No. 1, pp. 332-341, Feb 1989.

[12] N.R. Erickson, "High Efficiency Submillimeter Frequency Multipliers," To be presented at the 1990 IEEE MTT-S International Microwave Symposium, Dallas, TX, May 1990.

[13] N.R. Erickson, "Low Noise 500- to 700-GHz Receivers Using Single-Diode Harmonic Mixers," First International Symposium on Space Terahertz Technology, Ann Arbor, MI, March 1990.

[14] J.W. Archer, R.A. Batchelor, and C.J. Smith, "Low-Parasitic, Planar Schottky Diodes for Millimeter-Wave Integrated Circuits," IEEE Trans. Microwave Theory Tech., Vol. MTT-38, No. 1, pp. 15-22, Jan. 1990.

[15] W.C.B. Peatman and T.W. Crowe, "Design and Fabrication of 0.5 Micron GaAs Schottky Barrier Diodes for Low-Noise Terahertz Receiver Applications," To appear in Int. J. Infrared and Millimeter Waves, 1990.

[16] R.J. Hwu, N.C. Luhmann, Jr., D.B. Rutledge, D. Streit, T. O'Neill, U. Lieneweg, "Monolithic Watt-Level Millimeter-Wave Barrier-Intrinsic-N$^+$ (BIN) Diode-Grid Frequency Tripler," Conference Digest: Thirteenth Int. Conf. Infrared and Millimeter Waves, pp. 328-329, Honolulu, HI, 1988.

[17] W.L. Bishop, E.R. Meiberg, R.J. Mattauch and T.W. Crowe, "A Micron Thickness, Planar Schottky Barrier Diode Chip for Terahertz Applications with Theoretical Minimum Parasitic Capacitance," To be presented at the 1990 IEEE MTT-S Int. Microwave Symp., Dallas, TX, May 1990.

RECENT RESULTS ON: SURFACE-CHANNEL SCHOTTKY, InGaAs SCHOTTKY, AND Nb BASED SIS MIXER ELEMENT RESEARCH+

R. J. Mattauch, W. L. Bishop and A. W. Lichtenberger

Semiconductor Device Laboratory
Department of Electrical Engineering
The University of Virginia
Charlottesville, VA 22903-2442

ABSTRACT

The Schottky barrier diode is the mixer element of choice for heterodyne receivers operating at frequencies in excess of 100 GHz and above superconducting transition temperatures. While ground based systems can tolerate a whisker contacted structure due to its minimum value of shunt capacitance, space based systems require the mechanical integrity of a whiskerless structure. The Surface Channel Diode, a new structure which exhibits simplicity of fabrication along with minimum parasitic element values, will be reported upon. Both DC and RF performance will be presented.

GaAs has been the material of choice for Schottky barrier mixer and varactor diode fabrication for the past 20 years. As frequencies of operation reach the terahertz range the need for less LO power and lower mixer temperature become more severe. The InGaAs system offers great promise in relaxing these needs due to its lower barrier potential and higher electron mobility. Preliminary results obtained in an investigation of the use of InGaAs in Schottky barrier fabrication will be reported upon.

The promises of conversion gain, quantum limited noise, and minimal LO power requirement are held for SIS mixer elements. Recent calculations indicate Nb elements should operate well past 1 THz with only minimal degradation. Niobium based trilayer research which has produced devices exhibiting excellent electrical results (Vm > 1.5V, and extremely low sub-gap leakage current) will be described.

+ This work was supported in part by the National Science Foundation under grant ECS 8802881*, the Jet Propulsion Laboratory, the National Radio Astronomy Observatory which is operated by Associated Universities, Inc., under contract with the National Science Foundation, and the University of Michigan Center for Space Terahertz Technology.

* in conjunction with the U.S. Army, Fort Monmouth ETDL

1. INTRODUCTION

The needs of high sensitivity heterodyne receivers of the future operating at frequencies in excess of 100 GHz are dependent on the receiver operating temperature. Those operating above the critical temperature, Tc, of operational superconducting materials will require semiconductor diodes exhibiting highly nonlinear electrical parameters as mixing elements; while those operating at temperatures below Tc will require superconductive elements. At present, the semiconductor element of choice is the Schottky barrier diode. and the superconductive element having yielded the best receiver results to date is the superconductor-insulator-superconductor, SIS, junction. This paper treats device requirements and recent results obtained in each of these areas at the University of Virginia Semiconductor Device Laboratory.

Submillimeter wave applications of Schottky barrier mixer diodes will require a device devoid of contact with a sharpened metal wire, a whiskerless diode, for ease of integration into subharmonic mixers, MMIC's, and imaging arrays. Also required will be a diode needing a minimum of LO power due to its attendant scarcity with increasing frequency. Our most recent advances in the whiskerless diode technology are presented in Section 2. A report on research toward lowering needed LO power by reducing diode forward turn-on voltage is presented in Section 3.

Superconductive mixer elements must exhibit a minimum value of sub-gap current, an abrupt change in conductance at the gap sum voltage, minimum proximity effects, excellent mechanical robustness, immunity to change with temperature cycling, and the highest possible gap frequency. At this time SIS elements yielding the best DC and RF results and the greatest promise are those employing Nb or NbN. Results on a $Nb/Al_2O_3/Nb$ trilayer technology and a NbCN edge-junction technology, both yielding excellent electrical characteristics, are presented in Section 4.

2. THE SURFACE CHANNEL DIODE

Certain radio astronomy applications requiring optimum performance in the THz range will tolerate whisker contacted diodes. The vast majority of receivers utilizing Schottky diodes, however, will require the mechanical integrity of whiskerless structures. This will be especially true of receivers employed in space, balloon, and airborne applications. In addition to mechanical rigidity, such device technology can provide ease of

integration into MMIC's and arrays for imaging applications.

Work on whiskerless diodes has been ongoing for approximately 15 years. M. V. Schneider of Bell Labs was one of the early contributors to the beginning of this work (1) and to whiskerless diode investigation in general (2). An article by Garfield (3) on the RF testing of the device of this section, the surface channel diode, presents a rather complete listing of the papers pertinent to this topic. Cross-section and isometric views of a general whiskerless diode are shown in Fig. 1.

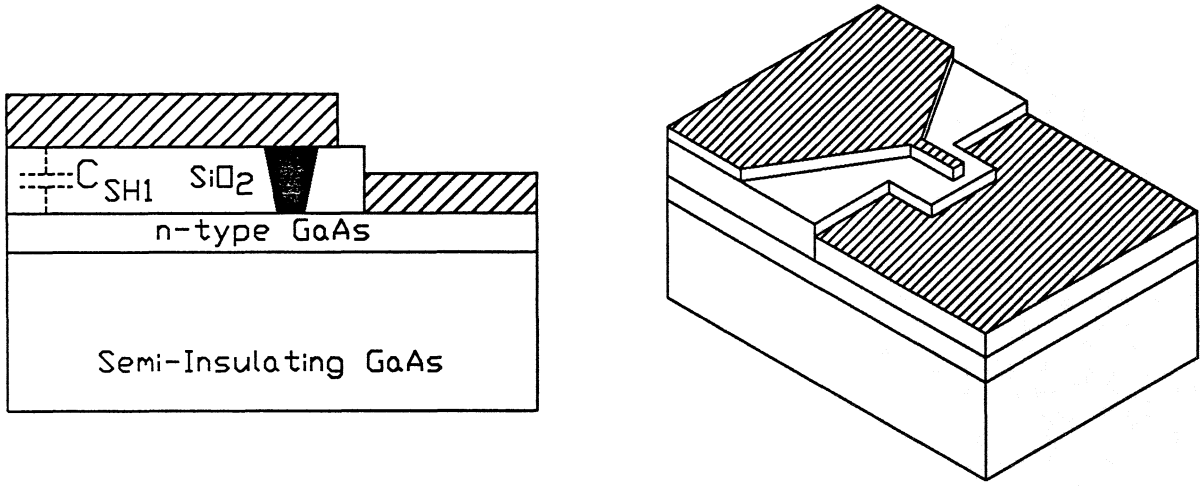

Figure 1 A general whiskerless Schottky diode structure.

The shunting effect of the conducting GaAs layers underlying the anode contact area and connected to the cathode presents a severe limitation at high frequencies. Several fabrication techniques have been employed in an attempt to lessen this effect and are shown pictorially in Fig. 2.

Bishop(4) recently presented an innovative approach[1] which results in the surface-channel diode shown in both pictorial cross-section and SEM views in Fig. 3.

This surface-channel technology is felt to be superior to the others in that it is straightforward, less costly, and yields a planar device. Relative disadvantages of the other

[1] NASA patent application case no. GSC 13063-2CU

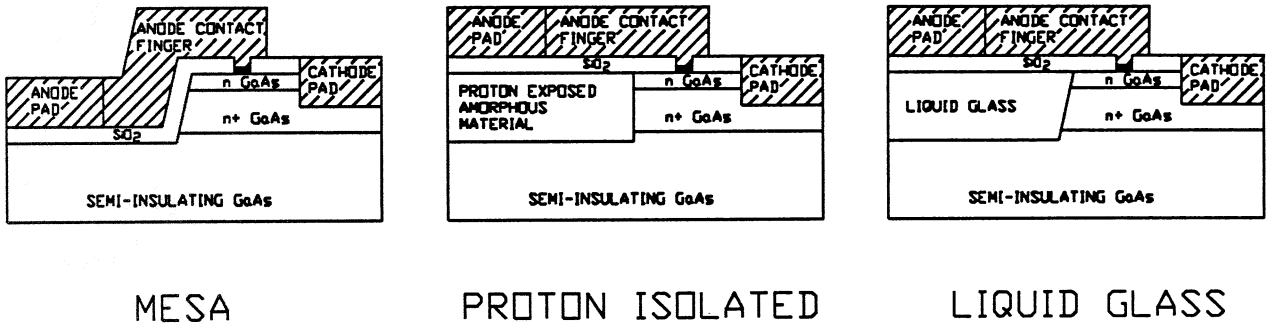

Figure 2 Pictorial views of (a) mesa, (b), proton isolated, and (c) liquid glass whiskerless diode structures.

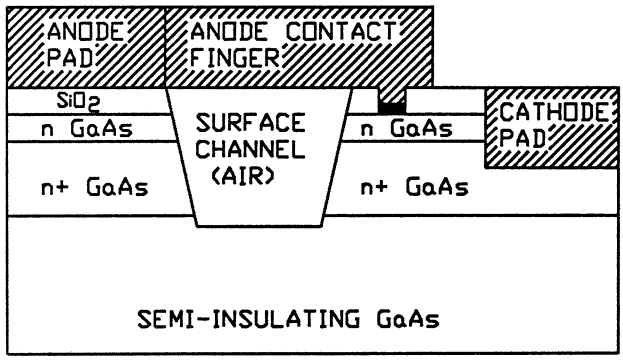

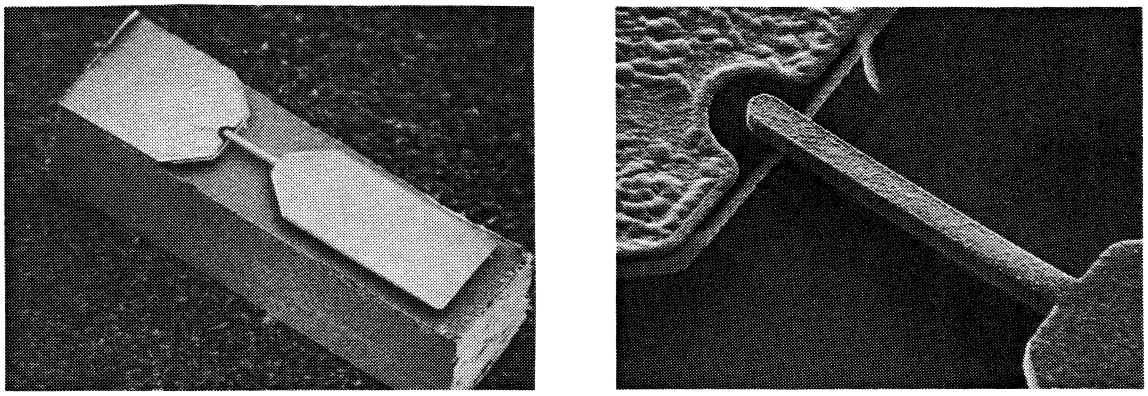

Figure 3 Surface-channel diode structure shown in pictorial cross-section and SEM views.

mentioned technologies are: the non-planar nature and resulting lack of precise photolithographic definition in the case of the mesa device, the added complexity of the proton bombardment process, and the intolerance to gross temperature change of the liquid glass isolated device.

A further extension of the surface-channel technology which permits complete removal of the substrate or its replacement with a lower dielectric material will be presented by Bishop(5). This advancement, which we feel brings the hybrid technology to its ultimate limit, is presented along with the basic surface-channel technology in the following section.

2.1 Fabrication Technology. Not only does the surface-channel technology yield a novel method for isolating devices, or device sections, on the same semiconductor substrate; but also it is quite straightforward. The four basic processing steps required for formation of a surface-channel Schottky barrier diode are shown pictorially in Fig. 4. Here the surface channel separates the anode contact pad from the junction region thus greatly reducing the capacitance shunting the junction. This disconnects the shunt capacitance, Csh1, (Fig. 1) from the Schottky diode region. Another advantage of this technology is that the surface channel is formed in the last step of the process thus allowing previous lithography steps to be carried out on a planar surface. The advantage can be appreciated from Fig. 3.

2.2 Electrical Performance. We found no substantial difference, with the exception of the shunt capacitance, between the standard whisker-contacted diode and its surface channel counterpart. Measured electrical parameters for diodes from two surface channel batches and for a whisker contacted diode, having nearly the same diameter and formed on GaAs of nearly the same donor concentration and layer thickness, are presented in Table I.

The only substantive difference between diodes of the two technologies is shunt capacitance. Figure 5 shows pictorial and circuit schematic representations for a surface-channel diode along with approximate capacitance values for 2.5 micrometer diameter test device.

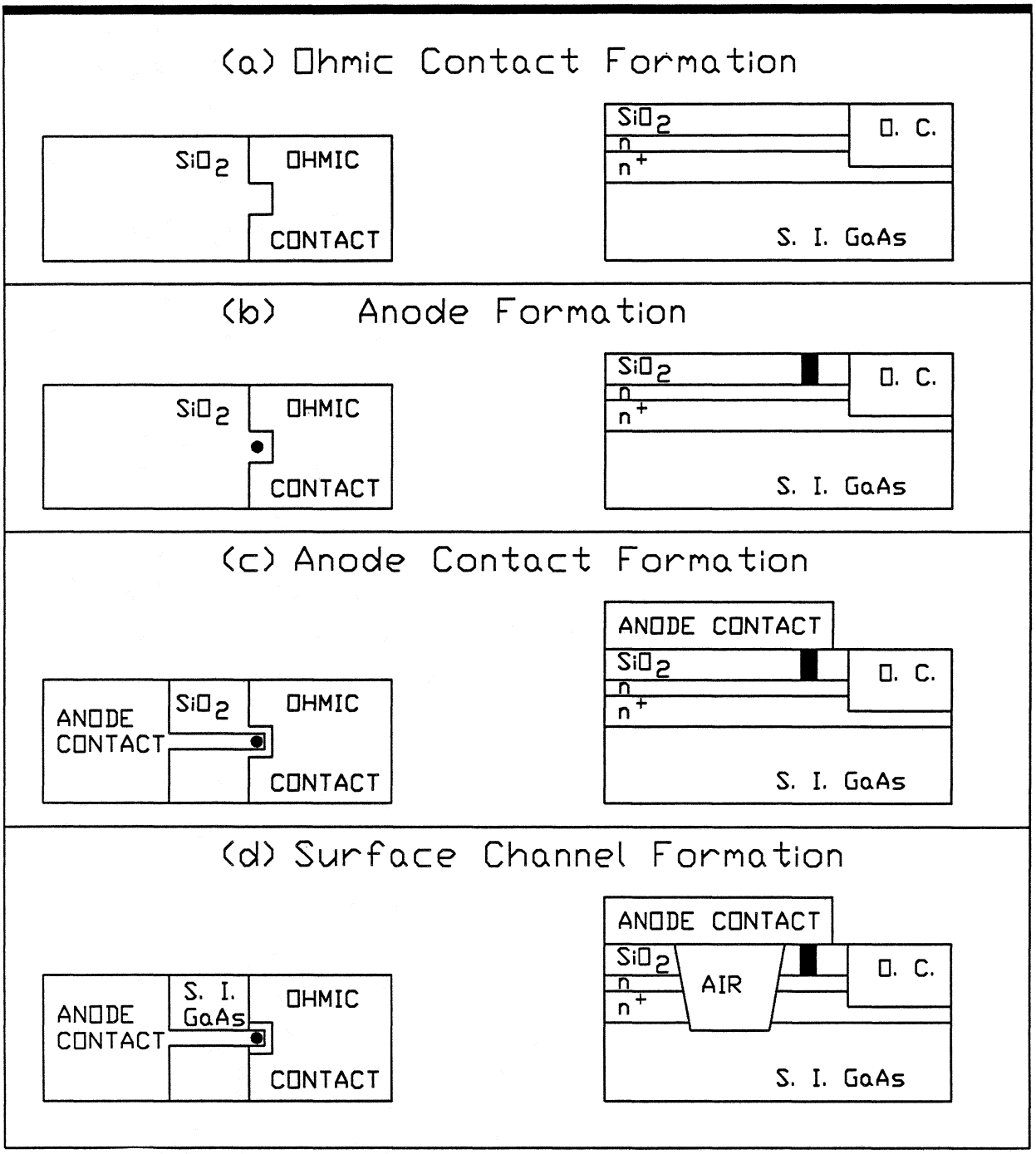

Figure 4 Surface-channel diode fabrication steps: (a) ohmic contact formation, (b) anode formation, (c) anode contact formation, and (d) surface channel formation.

Table I

Electrical Parameters of Surface-Channel and Comparable Whisker-Contacted Schottky barrier Diodes.

	Surface-Channel (SC2R4)	Whisker Contacted (2P14)
Diameter (μm)	2.5	2.3
Rs (ohms)	5.4	4.4
Δ (mV)	70	69
Cj (fF)	6	7
V_{br} (V)	6.2	6.2

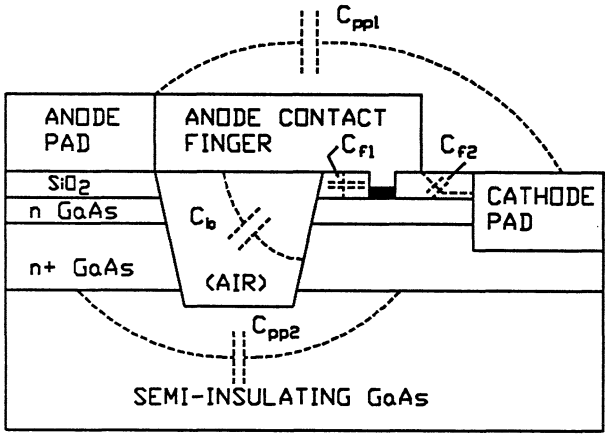

$C_{PPT} = C_{PP1} + C_{PP2} \cong 8.6fF$

$C_b + C_{f1} + C_{f2} \cong 1.7\ fF$

Figure 5 Pictorial and schematic diagrams for a surface-channel diode. Capacitance values are for a 2.5 micron diode structure.

In the case of the surface-channel diode the importance of the pad-to-pad capacitance is mount dependent. That of an isolated device may well become a part of the RF circuitry (e.g. as part of a coplanar waveguide circuit) once the device is mounted. Thus the beam capacitance, Cb, and the finger capacitance, Cf, are the shunt elements of importance. This total shunt capacitance value has been shown to

be on the order of 1.7 fF for a specific 2.5 micrometer diameter test diode structure. Furthermore this value was shown experimentally to decrease by approximately 1 fF upon removal of the SiO_2 surrounding the anode. This resulting value of approximately 1 fF is very near that of a comparable whisker contacted diode as shown by Kerr et al.(6), and leads to the conclusion that the surface-channel structure holds great promise for application in the THz frequency range.

Characterization of test surface-channel structures at 100 GHz was carried out by Garfield (3) using a technique similar to that of Weinreb and Kerr (7). Mismatch at both RF and IF ports was taken into account and harmonic conversion was shown to be negligible. Device DC excited noise temperature was shown to be comparable to that of an equivalent whisker contacted device which performed well in room temperature mixer applications. Mixer conversion loss and noise temperature performance were also found to compare favorably with the best obtained at room temperature in that frequency range with whisker contacted diodes as is shown in Table II.

Table II

Mixer noise temperature and conversion loss at 94 GHz for comparable surface-channel and whisker contacted diodes.

Diode Type	Tmixer (SSB) @94 GHz	Lmixer (SSB) @94 GHz
Surface-Channel (SC2R1)	555 K	5.8 dB
Surface-Channel (SC2R2)	518 K	5.3 dB
Whisker-Contacted (2D2)	560 K	5.3 dB

2.3 Substrate Replacement/Removal. Use of any conventional whiskerless diode in a hybrid application will cause a disturbance of the field pattern surrounding the transmission structure due to the diode substrate. A GaAs substrate with a dielectric constant of 13 would cause an even greater disturbance than would a quartz

substrate with a dielectric constant of 3.8. Scale model studies have shown that the pad-to-pad capacitance of such a device can be reduced by a factor of ten by elimination of the GaAs substrate. It was this realization which prompted the development by Bishop(5) of a practical and simple method of device substrate replacement or removal.

This novel technique[2] involves fabrication of the device, removal of the original semiconductor substrate, and bonding of the remaining epitaxial layers to a replacement substrate of lower dielectric constant such as quartz. Its basic steps are depicted in Fig. 6. This process yields a single device or multiple device configuration attached to a replacement substrate by an adhesive layer, A2. Resulting devices can then be easily manipulated and bonded into circuits as desired. The final step, if desired, is the removal of the replacement substrate by dissolution of adhesive layer, A2. This step results in a device layer consisting of metallization and semiconductor material only a few microns thick bonded into the microwave integrated circuit. Figure 7 shows a photomicrograph of a Schottky barrier diode bonded into a circuit and the substrate removed by this process.
The resulting structure consists of a 80x175 micron anode contact metallization pad connected by a 4x50 micron gold beam to a Schottky anode. That anode is formed on a two micron thick layer of single crystal GaAs which also bears an alloyed 125x125 micron ohmic contact pad.

In summary, the surface channel technology provides a simple, straightforward method of fabrication of Schottky barrier mixer and varactor diodes exhibiting excellent electrical characteristics, excellent mechanical stability, ease of integration into MMIC's, and reduced shunt capacitance. In addition, the substrate replacement/removal technology yields near monolithic integrated circuit results while maintaining the flexibility of hybrid technology. These two technologies provide a means of producing Schottky barrier diodes which meet or exceed the above mentioned needs of whiskerless diodes. The one remaining need, reduction of the forward turn-on voltage of the mixer diode, is addressed in the next section.

---

[2] NASA disclosure case no. GSC 13205

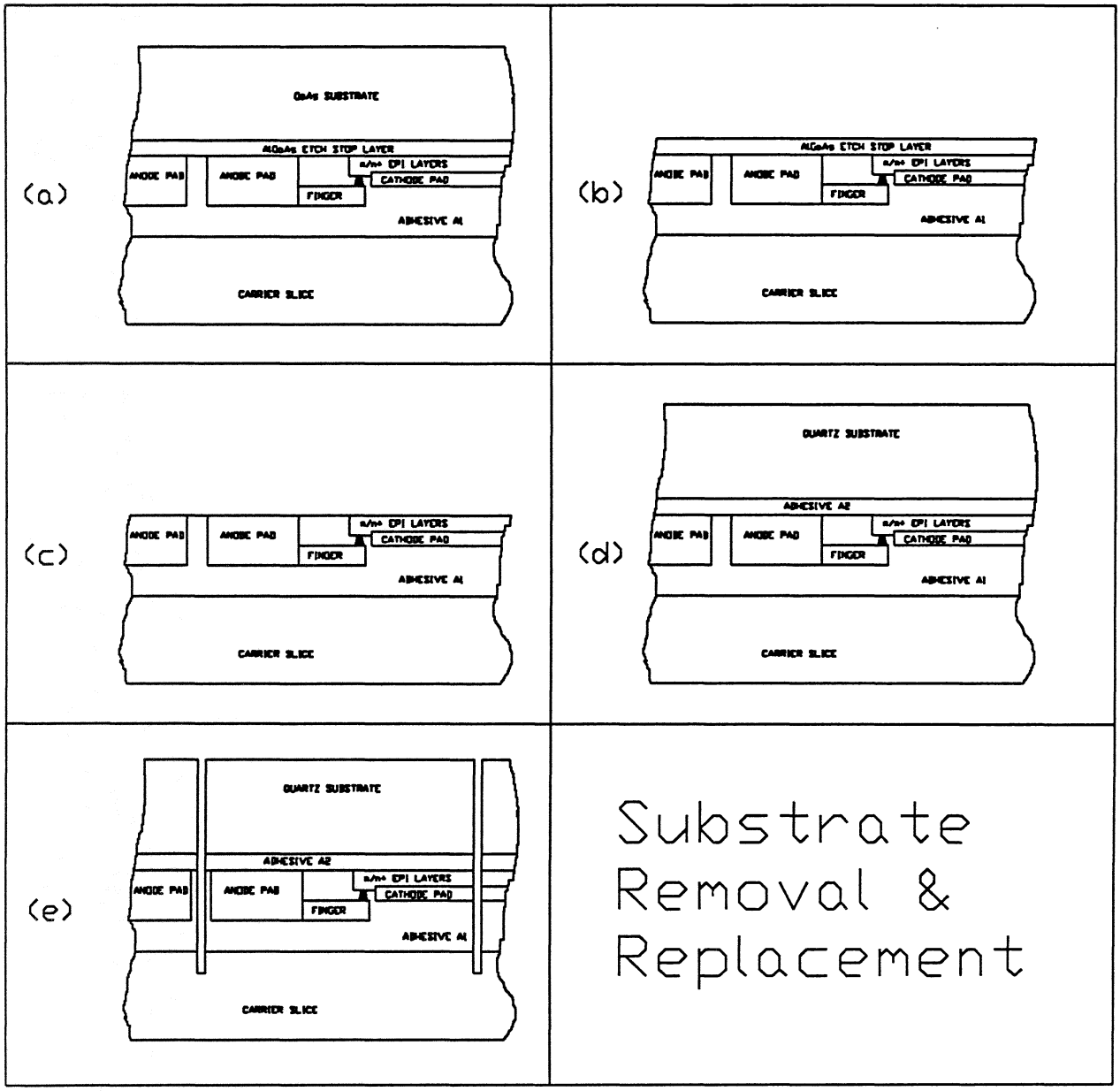

Figure 6 Basic steps in the substrate removal process: (a) bonding the diode shown in Fig. 4 to a carrier with adhesive layer, A1, (b), and (c) removal of the semiconductor substrate, (d) attachment of a 'replacement substrate' with adhesive layer, A2, (e) dicing of the wafer, and (f) (not shown) removal of individual device or circuit element chips from the carrier slice.

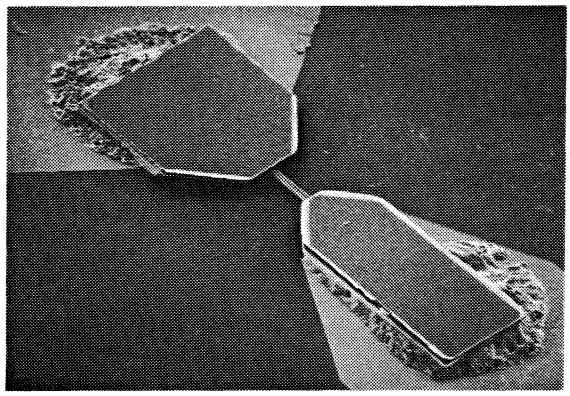

Figure 7 A 2.5 micron diameter surface-channel diode with its substrate removed mounted into a microwave circuit, on a quartz substrate.

3. InGaAs SCHOTTKY BARRIER MIXER DIODES

As was indicated in the introduction, the higher the receiver frequency the lower the available LO power. For this reason harmonic mixing, requiring LO power at half the mixer LO frequency, is commonly used. LO power needs can be further reduced by reducing the forward turn-on voltage of the Schottky diode pair. This is accomplished by reduction of the height of the Schottky barrier formed by the anode metal contact to the semiconductor. In general III-V compounds form a Schottky barrier which is very weekly dependent on the anode metal work functions. Most such electron barrier heights are very near 2/3 the electron energy gap, Eg. Thus, the Schottky barrier height can be lowered by choosing a semiconductor material with a smaller energy gap.

The ternary compound, In(x)Ga(1-x)As, offers very great promise in this application since; (a) variation of the In mole fraction, x, of the compound causes a

variation in Eg and thus Schottky barrier height ϕ_B, (b) InAs, resulting from a mole fraction equal to unity, forms a Schottky barrier of negative height, critical for low resistance non-alloyed ohmic contacts, and (c) the electron mobility of the InGaAs system is generally slightly higher than that of GaAs. A plot of Schottky barrier height, ϕ_B, versus In mole fraction is given in Fig. 8. This translates nearly directly

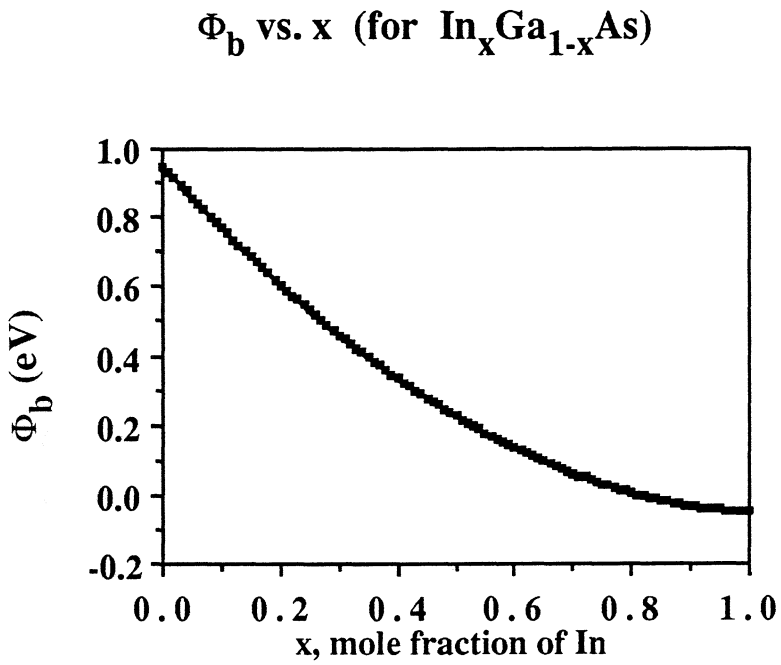

Figure 8 Predicted Schottky barrier height, ϕ_B, versus In mole fraction, x. (From Kajiyama (8))

to the forward turn-on voltage of the resulting Schottky diode. With InGaAs offering such great promise we can envision a surface-channel Schottky barrier mixer diode formed on that material which is graded to InAs for the purpose of formation of a non-alloyed ohmic contact. Such a device can exhibit a forward turn-on voltage of the desired value, series resistance slightly less than that of an equivalent GaAs device, and permit formation of a non-alloyed ohmic contact having reduced specific contact resistance; a step highly desirable in nanofabrication. Investigation of the feasibility of such devices is being carried out through device modeling, and development of a compatible fabrication process.

3.1 Device Modeling. Modeling of basic device parameters such as junction capacitance, series resistance, ideality factor, and reverse breakdown voltage is quite straightforward and similar to that for GaAs diodes. Lowering of the Schottky barrier height, ϕ_B, by increasing of the In mole fraction, x, is accompanied, however, by an increase in diode reverse saturation current, Jsat. This is related to a device parameter of critical importance to mixing efficiency: the ratio of diode off-state to on-state impedance Zoff/Zon. The theoretically desirable value is infinity. Zoff is controlled by the diode parallel junction capacitance, Cj(v), and conductance, Gj(v). Since Gj(v) is directly proportional to Jsat, increasing Jsat increases device conductance. In present GaAs mixer diodes the device off-state impedance is dominated by the junction capacitive reactance. Analysis shows that too great a reduction of the device turn-on voltage through reduction of the electron barrier height can cause attendant reduction in Zoff/Zon, and thus increase mixer conversion loss. Initial indications are that an In mole fraction of .2 will not seriously degrade Zoff/Zon. This analysis is accompanied by parallel development of a compatible device fabrication technology.

3.2 Device Fabrication Technology. Major device fabrication steps are:

1. Thinning of the device active layer by anodic oxidation,
2. Feature patterning by dielectric deposition, photolithography, and etching (wet and dry),
3. Ohmic contact formation, and
4. Anode formation.

Steps 1,3, and 4 are most sensitive to change of materials. Each has been developed and characterized separately. None exhibited great deviation from the equivalent step used in GaAs diode fabrication. A test batch of InGaAs devices was fabricated from material having non-ideal electrical parameters. All processing proceeded as expected and the resulting diode current-voltage characteristics were quite encouraging in that they exhibited device parameters expected for that material.

4. SUPERCONDUCTIVE MIXER ELEMENTS

The SIS quasiparticle tunnel junction mixer is very attractive due to its extremely low shot noise, potential for conversion gain, and low LO power requirement. In the last few years SIS mixers have been established as having the highest sensitivity at millimeter wavelengths, with mixer noise temperatures comparable to the photon noise temperature, 5 K at 100 GHz.(9). Detailed theoretical analysis, however, has shown that an optimized SIS receiver should be capable of near quantum-limited performance to nearly twice the gap frequency; typically on the order of 1-2 THz. (10) Thus, the goal of this facet of our research to carry out work necessary to yield excellent mixer elements for application from 100 GHz to 1 THz for radio astronomy and associated applications. Fabrication processes are being developed for two types of junctions which are attractive for this application: Nb/Al-Al_2O_3/ Nb trilayer devices, and NbCN edge structures. The results of this research are presented in the following sections.

4.1 Trilayer Junction Fabrication. Nb/Al-Al_2O_3/Nb trilayer SIS junctions are physically robust and exhibit stable electrical characteristics with time and thermal cycling between 4.2 and 300 K. Integral to the fabrication process is the formation of a 'trilayer' film composed of a thin (20 Å) layer of insulating Al_2O_3 sandwiched between two thicker layers of Nb, all deposited in a system during one vacuum cycle. The deposition system used is modelled after that of Huggins and Gurvitch (11) but achieves a base pressure of 5 x 10^-10 Torr. A sputtering pressure of 14 mTorr is utilized to obtain stress-free Nb films. Intrinsic stress existing in the electrode films has been found to be detrimental to SIS junction quality (12).

Junction areas can be simply defined by anodization of the upper Nb film, however the resulting junctions are not acceptable for millimeter wave application due to the relatively high dielectric constant of Nb_2O_5 which gives an unacceptably high shunt capacitance. It is also highly desirable for the junctions to have individual tuning elements for optimum performance. A common alternative to the utilization of anodization is a technique by which a lift-off resist feature is machine aligned to be positioned inside the perimeter of a previously defined junction area. The subsequently deposited insulation layer covers the critical perimeter of the junction. The main disadvantage of this and other machine-aligned techniques is the

alignment difficulty experienced for devices having feature sizes smaller than three microns.

We have chosen to develop a trilevel resist self-aligned technique which is depicted in Fig. 9.

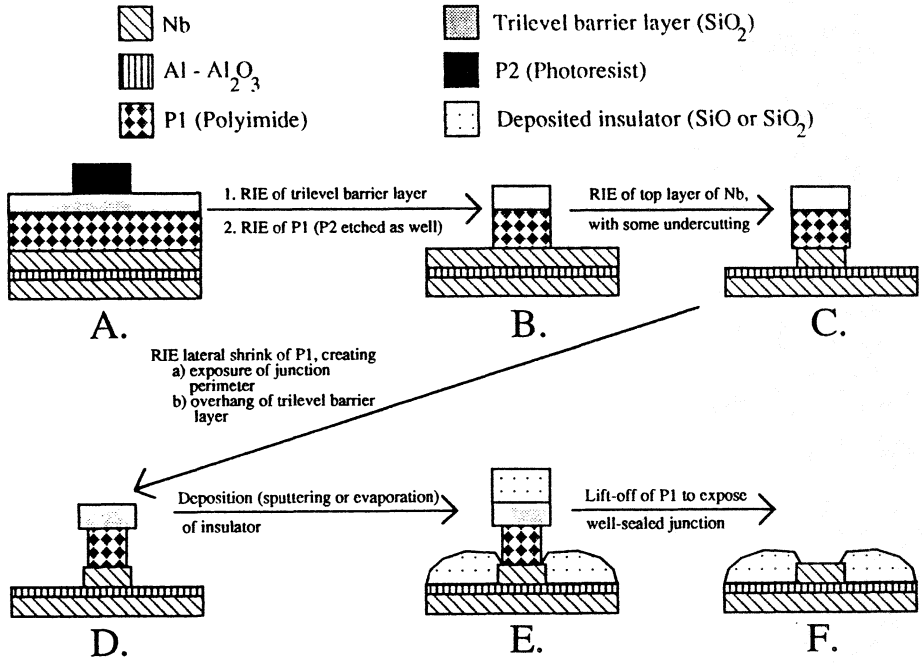

Figure 9 Trilevel resist self-aligned process.

In this process the patterned Nb/Al-Al_2O_3/Nb trilayer film is covered with a planarization layer upon which a thin layer of SiO_2 is deposited. This composite layer is then photolithographically patterned and etched in a two step reactive ion etching process. After definition of the junction area by reactive ion etching, RIE, we reduced the lateral dimension of the planarization layer, revealing the perimeter of the junction area and simultaneously forming an excellent liftoff stencil shown in Fig. 10. The subsequently deposited insulation layer actually overlaps the top Nb electrode and seal the junction. A portion of a wafer showing this insulation layer and associated tuning element electrodes in a six junction array is given in Fig. 11.

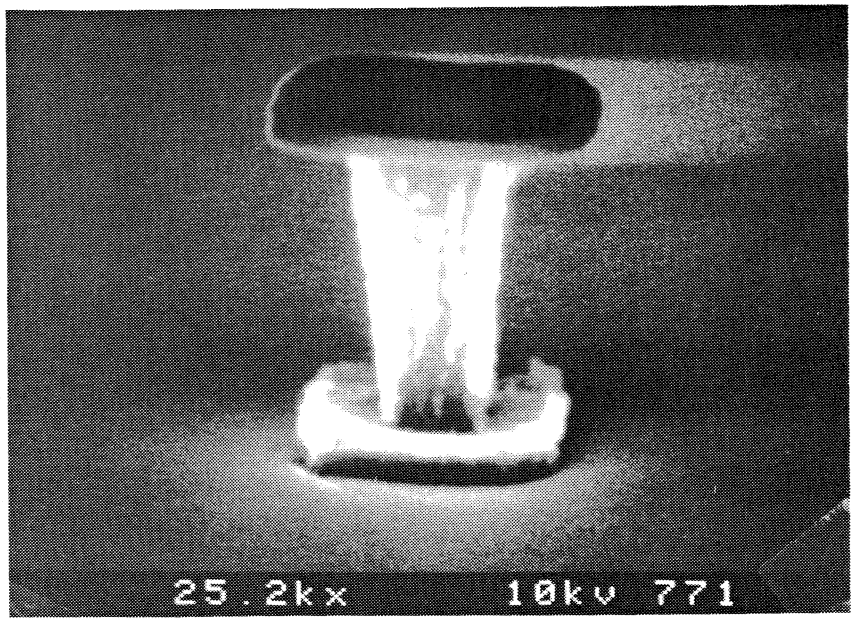

Figure 10 SEM photograph of trilevel resist overhang.

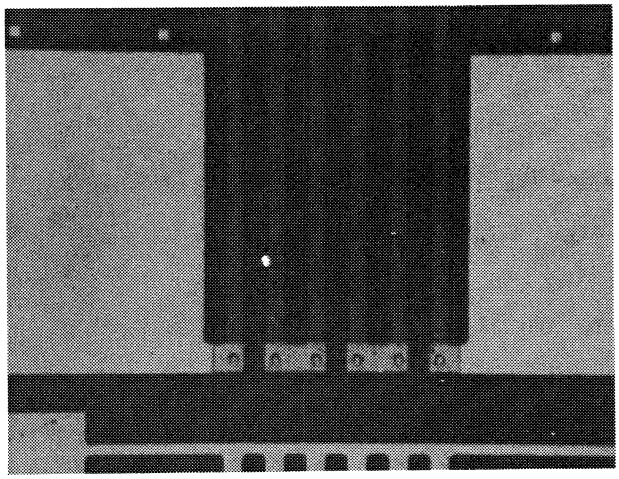

Figure 11 A micrograph of a six junction array with the overlapping SiO insulating layer in place. Also shown are the tuning element electrodes.

4.2 Trilayer Device Electrical Performance. The most striking feature of SIS junctions produced in our lab by this process is their low leakage current, a property critical to mixer elements. Figure 12 shows the I-V characteristics of a three element series array of 1.5 x 1.5 micron junctions exhibiting critical current density of 1400 A/cm^2.

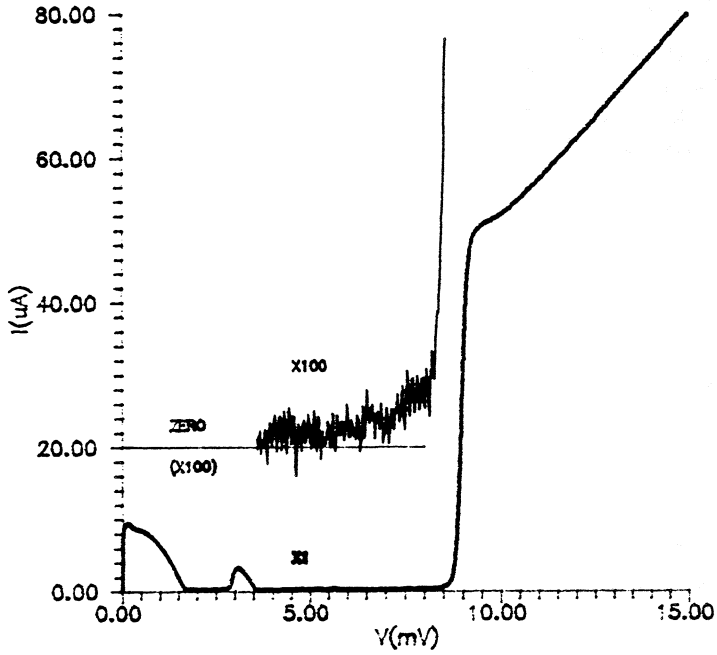

Figure 12 Current-voltage characteristics of a series array of three 1.5x1.5 micron $Nb/Al_2O_3/Nb$ junctions.

As can be seen, each junction has a turn-on voltage of 2.93 mV, a gap width of 100 microvolts, and a very weak 'knee'. This extremely low leakage current is clearly less than 0.1% of the quasiparticle current rise, and corresponds to a quality parameter, Vm, value greater than 1.5 V. This leakage current is considerably less than that reported for any small SIS junction made from any superconductor material to date.

Work is presently proceeding toward improving the reliability of this fabrication technique. The primary difficulty encountered involves repeatability and uniformity in lateral etching of the planarization layer which provides the lift-off stencil. Various planarization materials and chemical treatments are being examined.

4.3 NbCN/Si:H/NbCN Edge Junctions. NbCN possesses one of the largest superconducting energy gaps, 2.6 mV. Since twice the gap frequency is roughly the upper limit for near quantum-limited receiver sensitivity, NbCN is very attractive for high frequency applications. Our work in this area has centered on developing an

edge junction process since it provides a very straightforward method of fabricating small area junctions required for submillimeter wave use. Most of this work has focussed on NbCN/Ox/PbBi edge junctions. Such devices resulting from our work have exhibit the highest quality factor, Vm(3mV), values, >100 mV at 4.2 K, of any edge junctions of which we are aware (13). An all-NbCN edge junction would, however, be more desirable than our present PbBi counterelectrode structure due to its refractory nature. We are presently developing a NbCN/Si:H/NbCN edge junction fabrication process in collaboration with E. J. Cukauskas of the Naval Research Laboratory. A pictorial drawing of this structure is shown in Fig. 13.

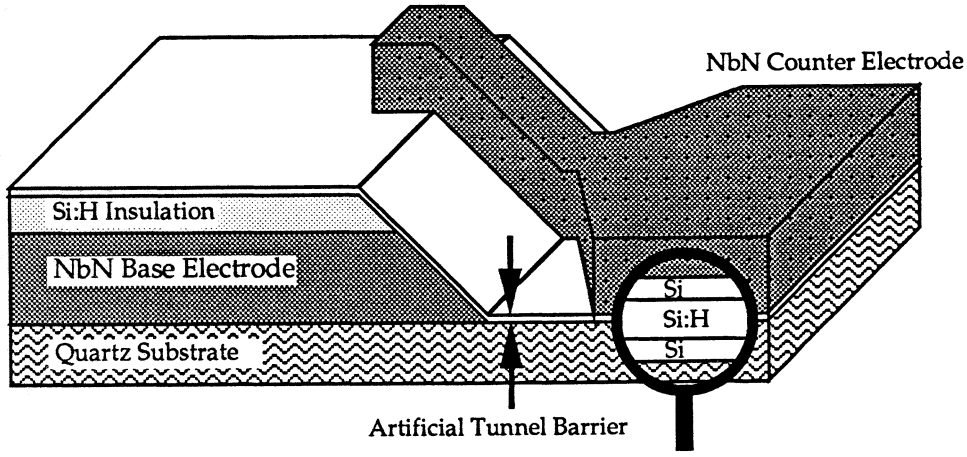

Figure 13 Pictorial drawing of NbCN/Si:H/NbCN edge junction.

The hydrogenated Si barrier, which is deposited at 700 K, has a specific capacitance approximately two times smaller than that obtained in using MgO, which is the typical barrier employed in the NbCN system. The Si barrier technology, therefore, has the advantage of permitting deposition of a superior 'hot' NbCN counterelectrode and the use of junction areas which are twice those of equivalent devices employing MgO as the barrier material. The research on this structure has focused primarily on the barrier deposition and counterelectrode RIE steps. Completion of the first set of devices is anticipated in the near future.

5. SUMMARY

Presented in the above sections are the primary needs perceived for mixer elements of highest sensitivity heterodyne receivers operating at frequencies in excess of 100 GHz, along with research efforts oriented at direct fulfillment of those needs. The mixer element of choice depends on the mixer operating temperature.

In the case of semiconducting mixer elements it was pointed out that a Schottky diode having excellent mechanical stability (devoid of a whisker contact), and easily formed in conjunction with other diodes or in circuits is essential. Presented in answer to this need is the surface-channel diode having record low shunt capacitance. Also presented is the new substrate removal technology which permits near MMIC performance with the flexibility of hybrid technology. The need for reduced LO power will be met by use of mixer elements having a lower turn-on voltage. The InGaAs technology yields great promise in this area and will permit formation of non-alloyed ohmic contacts having reduced specific contact resistance. This material-device system is being investigated.

In the case of superconductive mixer elements the need for mechanical stability and robustness in temperature cycling is answered by refractory materials. The Nb trilayer technology meets this need quite well. In addition, need for materials having potential for operation in the THz region is answered by the NbN system.

While the above mentioned are perceived needs which will, most certainly, be joined by others, unforseen at this time; it is felt that the presented technologies and suggested study areas will answer the presently perceived needs of heterodyne receiver elements for operation above 100 GHz in the near future.

REFERENCES

[1] Schneider, M.V., private communication, August 1975.

[2] Carlson, E.R., M.V. Schneider, and T.F. McMaster, "Subharmonically pumped millimeter wave mixers," IEEE Trans. on Microwave Theory and Tech., Vol. MTT-26, no. 10, pp. 706-715, Oct. 1978.

[3] Garfield, D.G., R.J. Mattauch, and S. Weinreb, to be published.

[4] Bishop, W.L., K. McKinney, R.J. Mattauch, T.W. Crowe, and G. Green, "A novel whiskerless Schottky Diode for Millimeter and Submillimeter Wave Applications," IEEE Proc. International Microwave Symposium, pp. 607-610, 1987.

[5] Bishop, W.L., E.R. Meiberg, R.J. Mattauch, and T.W. Crowe, "A micron-thickness, planar Schottky diode chip for terahertz applications with theoretical minimum parasitic capacitance," accepted for publication in IEEE 1990 International Microwave Symposium Digest.

[6] Kerr, A.R., J.A. Grange, and J.A. Lichtenberger, "Contact Whiskers for Millimeter Wave Diodes," NASA Technical Memorandum 79616, August 1978.

[7] Weinreb, S. and A.R. Kerr, "Cryogenic Cooling of Mixers for Millimeter and Centimeter Wavelengths," IEEE J. Solid-State Circuits, Vol. SC-8, No. 1, Feb 1973.

[8] Kajiyama, K., Y. Mizushima, and S. Sakata, "Schottly barrier Height of n- In_x $GA_{(1-x)}$ As Diodes, Appl. Phys.Lett., Vol. 23, No. 8, pp. 458-459, Oct. 15, 1973.

[9] Pan, S.-K., A.R. Kerr, M.J. Feldman, A. Kleinsasser, J. Stasiak, R.L. Sandstrom, and W.J. Gallagher, "An 85-116 GHz SIS receiver using inductively shunted edge-junctions," IEEE Trans. Microwave Theory Tech., MTT37, Mar. 1989.

[10] Feldman, M.J., "Theoretical considerations for THz SIS mixers," Int. J. Infrared & Millimeter Waves, 8, 1287-1292, 1987.

[11] Huggins, H.A. and M. Gurvitch, "Magnetron sputtering system equipped with a versatile substrate table," J. Vac. Sci. Techol. A., vol. 1, pp. 77-80, Jan.-March 1983.

[12] Kuroda, K. and M. Yuda, "Niobium-stress influence on Nb/Al-oxide/Nb Josephson junctions," J. Appl. Phys. 63 (7), 2352-2357, 1988.

[13] Lichtenberger, A.W., M.J. Feldman, and R.J. Mattauch, "The effects of ion gun beam voltage on the electrical characteristics of NbCN/PbBi edge junctions," IEEE Trans. Magnetics, MAG-25, 1243, 1989.

CAPABILITY OF SCHOTTKY DIODE MULTIPLIERS AS LOCAL OSCILLATORS AT 1 THz

Antti Räisänen and Mikko Sironen
Helsinki University of Technology
Radio Laboratory
SF-02150 Espoo, Finland

ABSTRACT

There is a strong need of all-solid-state local oscillators at mm- and submm-waves especially in spaceborne applications such as remote sensing of the atmosphere and radio astronomy. Up to 150 GHz this need can be satisfied with fundamental (second harmonic) sources such as Gunn oscillators. Up to about 600 GHz Schottky varactor multipliers with sufficient output power have been built. In the 1 THz region the efficiency and output power of the varactor/varistor multipliers becomes very low.

In the Radio Laboratory of the Helsinki University of Technology sponsored by the European Space Agency and Farran Technology Ltd. extensive studies on the theoretical performance of Schottky varactors and varistors as multipliers of a frequency around 100 GHz to submm region (300-1200 GHz) have been carried out. The performance of a commercially available diodes as well as experimental diodes have been analyzed in various direct and cascaded configurations of low and high order multipliers using harmonic balance analysis. Also optimum diode structures for multiplier applications have been searched. Because of high circuit losses ($\geq$ 10 dB) in a multiplier chain producing 1 THz, the output power seems to stay at or below 100 μW even in the best multiplier configurations when the available input power at 100 GHz is 50 mW.

INTRODUCTION

Currently, there is a lot of interest in developing high-efficiency multipliers for 1 THz range and above. One of the corner stone missions of the European Space Agency (ESA) is the Far Infrared and Submillimeter Space Telescope (FIRST) [1]. Therefore, the ESA has recently awarded a stydy contract "Development of Critical Detection Technologies for Spaceborne Submillimeter Heterodyne Receivers" in which several companies, universities and research institutes are involved in Ireland, Sweden, the Netherlands, Great Britain, France, Italy, West Germany and Finland.

At the Helsinki University of Technology, generation of 1 THz signals using Schottky-varactors/varistors has been studied by computer simulations. The study is based on the use of harmonic balance analysis, where the harmonic balance is solved by using multiple reflection technique [2-4]. A major problem is the modelling of the Schottky diode used as a multiplier.

The validity of the existing simple modelling of the diode (see Figure 1 and equations (1)–(7)) in the harmonic balance analysis has been tested with several multipliers of various orders at frequency range of 100-200 GHz at the Helsinki University of Technology [5-9]. The multipliers utilize Farran Technology VD010, VD011 and VD012 varactors. Nonlinear analysis and scaled modeling have been utilized in design. In the case of a doubler for 80-100 GHz the peak efficiency abtained is as high as 45%. A tripler for 100-115 GHz has produced a peak efficiency 28%, a quadrupler for 140-155 GHz an efficiency 11% and a quintupler for 165-170 GHz an efficiency of 4.3%. A doubler for 160-193 GHz gives maximum efficiency of 23%. All of these results are in reasonable agreement with the theory when waveguide losses and other nonidealities are taken into account.

At submillimeter frequencies the diode modelling is more complicated [10] and no good comparisons between the theory and experiment exist.

An efficient way of producing signals in the range of 1 THz is first to double the 100 GHz signal, which can be obtained from a Gunn oscillator at a power level of 50 mW, and then to quadruple the 200 GHz signal to 800 GHz, or to quintuple it to 1000 GHz, or to sextuple it to 1200 GHz.

Theoretically varactor VD012 gives an efficiency of about 25% for a doubler from 100 to 200 GHz. Experimentally 15% efficiency or maximum power of 7 mW can be obtained. Therefore, the input power to higher order multipliers at 200 GHz is assumed to be 7mW.

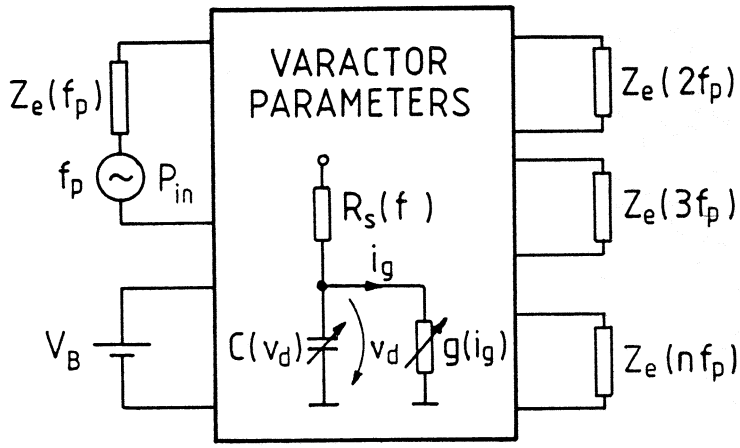

Figure 1. Equivalent circuit of a Schottky-varactor frequency multiplier.

DIODE MODEL

Varactor capacitance is assumed to be

$$C_j(V) = \frac{C_0}{(1 - v/\phi_{bi})^{\gamma_0(1+kV)}} \ , \tag{1}$$

where $C_0 = C_j(0)$, ϕ_{bi} is the built-in potential and γ_0 and k are dependent on the doping profile. Usually the varactor capacitance is less nonlinear with high reverse bias. This is taken into consideration by choosing a positive value for parameter k. Typical values are $\gamma_0 = 0.45 - 0.5$ and $k = 0 - 0.01$. Varistors are assumed to have a constant capacitance below approximately 0.25 V and ϕ_{bi} is artificially chosen to be 1.3 V to emphasize resistive multiplication.

For both varactors and varistors the I-V characteristic is assumed to be

$$I_d(V) = I_0\left(\exp\left(\frac{qV}{\eta kT}\right) - 1\right) \ , \tag{2}$$

where I_0 is saturation current, q is elementary charge, k is Boltzmann's constant, T is absolute temperature and η is ideality factor.

The series impedance is modelled as the following [12]:

$$Z_s(\omega) = Z_{epi}(\omega) + Z_{sub}(\omega) \tag{3}$$

$$Z_{epi}(\omega) = \frac{\rho t_e}{A}\left[\frac{1}{1+\jmath\omega/\omega_s} + \jmath\frac{\omega}{\omega_d}\right]^{-1} \tag{4}$$

$$Z_{sub}(\omega) = \frac{\rho}{2\pi\delta}\ln\left(\frac{b}{r_a}\right)\frac{\sqrt{2\jmath}}{\sqrt{\frac{1}{1+\jmath\omega/\omega_s} + \jmath\frac{\omega}{\omega_d}}} + \frac{\rho}{4r_a}\frac{1}{\frac{1}{1+\jmath\omega/\omega_s} + \jmath\frac{\omega}{\omega_d}}, \tag{5}$$

where t_e is thickness of epilayer, ρ is resistivity, A is anode area, r_a is anode radius and b effective radius of the chip. ω_s and ω_{ds} are the scattering and dielectric relaxation frequency defined as

$$\omega_s = \frac{q}{m^*\mu} \tag{6}$$

$$\omega_d = \frac{1}{\epsilon_s\rho}, \tag{7}$$

where m^* is effective carrier mass, μ is carrier mobility and ϵ_s is dielectric constant of the chip.

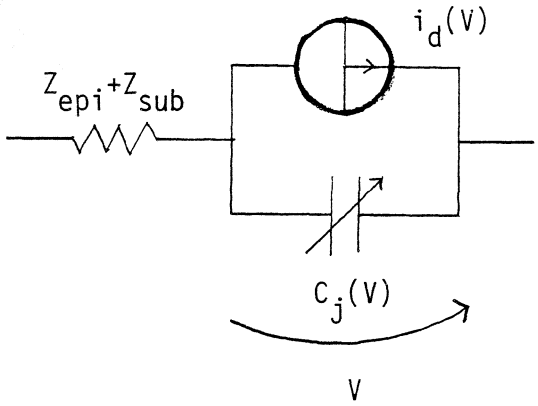

Figure 2. Simple Schottky barrier diode model.

MULTIPLICATION OF 200 GHz TO 1 THz RANGE

4 x 200 GHz

Theoretical calculations were carried out for seven different realizable diodes presented in Table 1, where r_a, N_D and t_e correspond anode radius, epilayer doping concentration and epilayer thickness, respectively. Varactor VD012 is commercially available, while all other diodes are experimental diodes by Farran Technology Ltd. The input power was assumed to be 7 mW in each case.

Table 1. Diode characteristics.

type	diode	C_{jo} [fF]	R_S [Ω]	V_B [V]	r_a [μm]	N_D [cm^{-3}]	t_e [μm]
varactor	VD012	12.5	11.0	14.0	1.8	$6.5 \cdot 10^{16}$	0.8
	A	9.5	7.2	9.0	1.5	$2 \cdot 10^{17}$	0.25
	B	3.4	30.0	17.0	1.1	$9 \cdot 10^{16}$	0.49
	C	5.1	11.5	9.0	1.0	$2 \cdot 10^{17}$	0.25
	D	3.3	12.0	6.9	0.8	$3 \cdot 10^{17}$	0.18
varistor	054	2.8	12.0	8.0	0.65	$6.5 \cdot 10^{16}$	0.11
	074	4.2	12.0	8.0	0.85	$6 \cdot 10^{16}$	0.11

Table 2. Optimum performance and parameters of quadruplers 4 x 200 GHz.

Diode	η [%]	P_{out} [mW]	$V_{b\ opt}$ [V]	R_1 [Ω]	X_1 [Ω]	X_2 [Ω]	X_3 [Ω]	R_4 [Ω]	X_4 [Ω]
VD012	0.2	0.014							
A	9.0	0.63	-2.0	24	126	66	38	17	23
B	6.2	0.43	-4.0	91	427	211	124	67	82
C	15	1.1	-1.7	53	224	144	85	35	45
D	12	0.84	-0.8	159	283	181	123	50	64
057	2.2	0.15	-1.8	116	268	47	21	30	39
074	0.94	0.066	-1.4	60	166	19	4	26	23

In Table 2 also the optimized termination impedances are given. With a varistor the best performance is obtained if the intermediate harmonics are nearly short or open circuited. The efficiency decreases if these harmonics are terminated with an inductance which resonates with the varistor capacitance at that particular frequency. Although a similar procedure normally improves the efficiency in the case of reactive multiplication, a weak nonlinearity of the $C - V$-curve of the varistor causes an opposite effect. The reactive multiplication is ineffective and the permitted current flow at the intermediate harmonics only increases losses in the varactor series resistance decreasing conversion efficiency to the 4th harmonic.

5 x 200 GHz

Theoretical calculations were made for varactors VD012 and C assuming 7 mW of input power. With varactor VD012 a quintupler with all idlers was analyzed. With varactor C two cases were analyzed. Firstly (I) a quintupler with all idlers and secondly (II) a quintupler with 2. and 3. optimum idlers and open circuited 4. harmonic. The optimized theoretical efficiencies are 0.03%, 10.3% and 3.4% for VD012, CI and CII, respectively.

6 x 200 GHz

Again similar theoretical calculations were carried out for varactors VD012 and C. For VD012 varactor the calculation was made with all idlers. In the case of varactor C three different cases were analyzed: (I) all idlers, (II) 2. and 3. optimum idler and 4. and 5. harmonic open circuited, and (III) 2. and 4. optimum idler and 3. and 5. harmonic open circuited. The optimized theoretical efficiencies are 0.0003%, 6.9%, 0.87% and 2.1% for VD012, CI, CII and CIII, respectively.

DIODE OPTIMIZATION

Varactor optimization was carried out for 4x, 5x and 6x200 GHz using the diode model above, but for the junction capacitance the following expression [11]:

$$C_j(V) = \frac{A\epsilon_s}{w(V)}\left(1+\frac{3}{2}\frac{w(V)}{r_a}\right) \tag{8}$$

$$w(V) = \sqrt{\frac{2\epsilon_s}{qN_D}\left(\phi_{bi}-V-\frac{kT}{q}\right)}, \tag{9}$$

$w(V)$ stands for the width of the depletion region. The epilayer thickness was determined according to equation (9) by using the break-down voltage for V, which means that at break-down voltage the epilayer is completely depleted.

The overall optimum diode for all high-order multipliers described above has an epilayer thickness of about 0.3 μm, anode radius of 1.2 μm and epilayer doping density of $1.6\cdot10^{17}\mathrm{cm}^{-3}$. The optimum diode parameters are quite similar to those of varactor C, and the optimum diode gives only slightly better performance.

COMPARISON OF VARIOUS MULTIPLIERS PRODUCING 800 GHz

Comparison of the performance of four differrent multiplier configurations producing 800 GHz signal was made by computer simulations. In these configurations 100 GHz signal is multiplied: 8x, 2x2x2x, 4x2x and 2x4x.

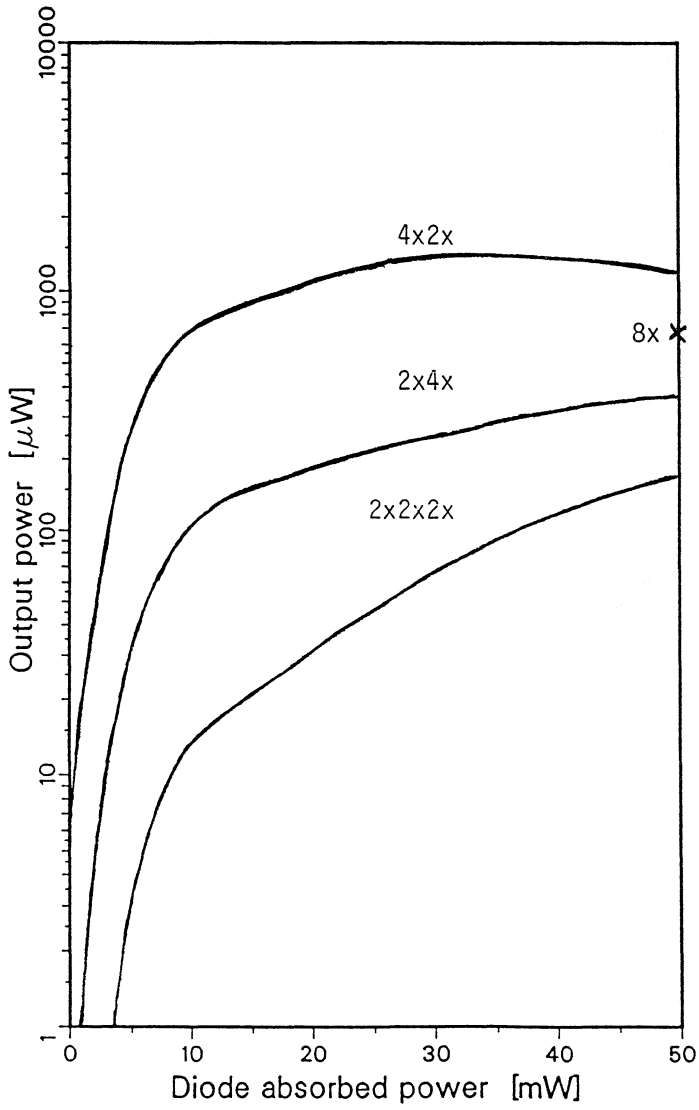

Figure 3. Comparison of theoretical performance of various multipliers producing 800 GHz.

as an octupler

Theoretical efficiencies were calculated for varactors VD012, B and C. The input power was assumed to be 50 mW. In the case of diode B this high input power causes the rectified current to rise up to 15 mA, which may burn the diode.

The calculation show that diode C is not able to handle 50 mW input power, but will break-down. Therefore, varactor VD012 is the best choice giving 1.3% efficiency with 50 mW input power.

Figire 3 shows the performance of three other configurations, where VD012 is used for multipliers 2x100 GHz, 4x100 GHz and 2x200 GHz, and the optimized diode (as described above) is used for 4x200 GHz and 2x400 GHz. At 50 mW input power 4x2x100 GHz cascaded multiplier gives by far the best result. The octupler is also clearly more efficient than the other two configurations. These performances are purely theoretical, because no metal losses are assumed and all ideal idler terminations are assumed in the higher-order multipliers. However when nonidealities are reasonably taken into account, the cascaded multiplier 4x2x100 GHz is still by far the best and can produce about 100μW at 800 GHz.

In fact the Schottky barrier diode is more complicated than assumed above. Reactive elements of the diode series impedance due to dielectric relaxation and carrier scattering in epilayer have also voltage dependence. Also the series recistance in epilayer is voltage modulated. These nonlinearities can be presented in following fashion [10] :

$$R_e(V) = \rho \frac{t_e - w(V)}{A} \tag{10}$$

$$L_i(V) = R_e(V) \frac{1}{\omega_s + v_d/t_e} \tag{11}$$

$$C_e(V) = \frac{\epsilon_s A}{t_e - w(V)}, \tag{12}$$

where v_d is (maximum) drift velocity. Figure 4 shows this diode model.

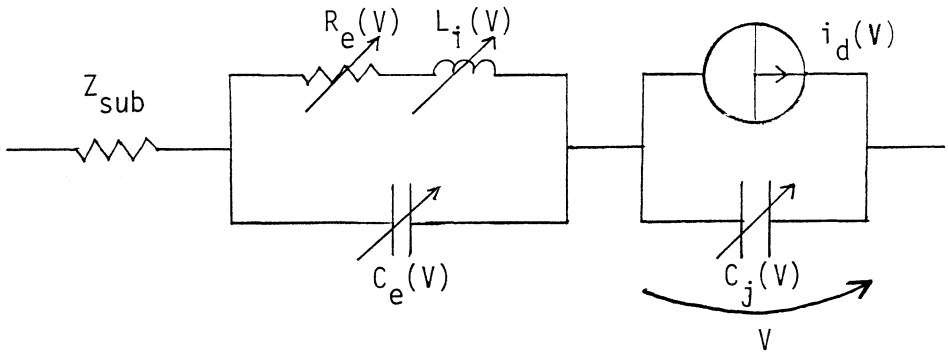

Figure 4. Schottky barrier diode model including nonlinearities of the undepleted part of the epilayer.

Taking these extra nonlinearities into account improves the theoretical efficiency of the multipliers considerably at low input power levels, but only slightly at high input power levels. The efficiency improvement increases as a function of frequency.

CONCLUSIONS

A quadrupler, quintupler and sextupler utilizing an optimized realizable varactor pumped with 7 mW power at 200 GHz can produce theoretical efficiencies of 17.8%, 11.8% and 7.8%, respectively. This optimum varactor is quite similar to a varactor already realized, varactor C, which gives theoretical efficiencies of 15%, 10.3% and 6.9%, respectively. In practice, the nonidealities in idler circuits and metal losses are expected to drop the efficiencies by 10 dB or more.

An octupler 8 x 100 GHz utilizing a commercially available varactor can give theoretically an efficiency of 1.3% when pumped with 50 mW power. In this case the nonidealities in idler circuits and mount losses are expected to be so high, that in practice only 10 μW power would be obtained. The output power at 800 GHz from a doubler-quadrupler-combination is expected to be about 100 μW.

Varistors are clearly much less effective than varactors. However, in practice designing a high-order varistor multiplier is much easier than that of a varactor multiplier. A few microwatts can be obtained also from varistor multipliers at 1 THz and that is enough for SIS mixers.

Results presented here are only preliminary. Clearly a lot of work must be done for the proper modelling of Schottky diodes at 1 THz.

ACKNOWLEDGEMENTS

This study was partly supported by the European Space Agency, Farran Technology Ltd. and the Academy of Finland.

REFERENCES

[1] FIRST, Far Infrared and Submillimeter Space Telescope, Assesment Study, ESA document SCI(83)1, September 1983.

[2] A.R. Kerr, "A technique for determing the local oscillator waveforms in a microwave mixer," *IEEE Trans. Microwave Theory Tech.*, Vol. MTT-23,

828–831, (1975).

[3] D.N. Held and A.R. Kerr, "Conversion loss and noise of microwave and millimeter-wave mixers: Part I – Theory," *IEEE Trans. Microwave Theory Tech.*, Vol. MTT-26, 49–55, (1978).

[5] P.H. Siegel, A.R. Kerr and W. Hwang, "Topics in the optimization of millimeter-wave mixers," NASA Technical Paper 2287, 512 p., 1984.

[5] T.J. Tolmunen and A.V. Räisänen, "An efficient Schottky-varactor frequency multiplier at millimeter waves, Part I: Doubler," *Int. J. Infrared and Millimeter Waves*, Vol. 8, no. 10, 1313–1336, (1987).

[6] T.J. Tolmunen and A.V. Räisänen, "An efficient Schottky-varactor frequency multiplier at millimeter waves, Part II: Tripler," *Int. J. Infrared and Millimeter Waves*, Vol. 8, no. 10, 1337–1353, (1987).

[7] T.J. Tolmunen and A.V. Räisänen, "An efficient Schottky-varactor frequency multiplier at millimeter waves, Part III: Quadrupler," *Int. J. Infrared and Millimeter Waves*, Vol. 10, no. 4, 475–504, (1989).

[8] T.J. Tolmunen and A.V. Räisänen, "An efficient Schottky-varactor frequency multiplier at millimeter waves, Part IV: Quintupler," *Int. J. Infrared and Millimeter Waves*, Vol. 10, no. 4, 505–518, (1989).

[9] T.J. Tolmunen and A.V. Räisänen, "Design, construction and test of a doubler for 183 GHz," Helsinki University of Technology, Radio Laboratory, Report S178, 1989.

[10] Th.W. Crowe, "GaAs Schottky barrier diodes for the frequency range 1-10 THz", *Int. J. Infrared and Millimeter Waves*, Vol. 10, no. 7, 765-777, (1989).

[11] J.A. Copeland "Diode edge effect on doping-profile measurements ", *IEEE Trans. Electron Devices*, Vol. ED-17, 404-407, (1970).

[12] E. Bava, G.P. Bava, A. Godone, and G. Rietto, "Analysis of Schottky-barrier millimetric varactor doublers", *IEEE Trans. Microwave Theory Tech.*, Vol. MTT-26, no. 11, 1145-1149, (1981).

Planar Doped Barrier Devices for Subharmonic Mixers

J.R. East, T. Lee and G.I. Haddad
Center for Space Terahertz Technology
Dept. of Electrical Engineering and Computer Science
The University of Michigan, Ann Arbor, Michigan

Abstract

Mixers are a critical component of most millimeter wave and THz systems. Often, the front end mixer performance determines the overall system performance. At higher millimeter wave and THz frequencies, mixer performance can be limited by the lack of low cost solid state sources. A subharmonic mixer with a pumping frequency at half the signal frequency would reduce the source power requirements at these higher frequencies. Typical subharmonic mixers use back to back Schottky barrier diodes. The resulting structures are difficult to fabricate, and the performance can be degraded if the diodes are not matched and by parasitics associated with the various connections. One possible solution is to use an integrated Schottky barrier structure. Another possible solution is to use a planar doped barrier (PDB) as a single device subharmonic mixer. This paper will present an analysis of PDB subharmonic mixer performance.

I. Introduction

The PDB is a device that uses a symmetric doping structure to produce the anti-symmetric current vs. voltage characteristic required for subharmonic mixer operation. PDB structures can be modified to vary the barrier height, the capacitance per unit area and the space charge resistance. This allows a wide range of possible device structures. The device capacitance is approximately constant over a large RF voltage range. One potential disadvantage of the PDB is the "ideality factor". Since the structure is a series connection of two junctions the "ideality factor" is at least two. A variety of PDB structures have been studied to find the device characteristics and the performance as subharmonic mixers. Computer results show that the PDB has a conversion loss within 1.5 db of similar Schottky structures. This paper will present these results and a preliminary experimental characterization of the PDB structures. The organization of the paper is as follows. The next section contains a brief review of conventional Schottky barrier diode based subharmonic mixers. This information can form a basis of comparison for the PDB mixers. Section III contains a simplified description of PDB characteristics and a more complete numerical analysis of the current vs. voltage and capacitance vs. voltage characteristics of typical structures. This analysis points out the tradeoff's between the device structure and the resulting characteristics that are important for mixer performance. Section IV gives preliminary low frequency characterization results for the device structures discussed in section III. Section IV presents a computer analysis of subharmonic mixer parameters and

performance for the structures of section III and IV. The paper is summarized in section V.

II. Conventional Subharmonic Mixers

Conventional Schottky barrier based subharmonic mixers have been the subject of a number of theoretical investigations and have be used in a variety of systems at frequencies at 100 GHz and above. Kerr[1] used the large signal time and frequency domain method developed by Held and Kerr[2] to analyze the performance of subharmonic mixers. This analysis described the performance of a dual Schottky barrier subharmonic mixer. The result predict conversion losses of 6 to 7 db and mixer noise temperatures of approximately 500 K for 100 GHz operation. The diodes and associated circuit were assumed to be matched in this study. The effects of unmatched diodes or circuits were studied by Hicks and Khan[3]. They found that small mismatch in the diode capacitances and lead inductance could greatly degrade the mixer performance. This study shows the importance of careful mounting structure design for these mixers.

Some of the best experimental results are described by Schneider and his coworkers[4-6]. These references describe subharmonic mixers operating between 65 and 100 GHz with conversion losses and noise figures in the 7 to 11 db range. The diodes used were individual notch-front GaAs mixer diodes. As the frequency increases the diodes become more difficult to match. One possible solution is an integrated structure. Marsh et.al.[7] describe a monolithic diode integrated circuit operating at 183 GHz. This mixer had a conversion loss of 5 db and a double sideband noise temperature of 600 K. These mixers use two waveguides and a quartz carrier to bring the signal and pump frequencies to the diodes and to extract the IF frequency. Some of this complexity can be overcome by using quasi-optical techniques to apply the signal and pump frequencies. A microwave frequency example of a quasi-optical mixer is described by Stephan and Itoh [8]. Another possible solution is to use a single planar doped barrier device to produce the required anti-symmetric current vs. voltage characteristic.

III. Planar Doped Barrier Devices

The planar doped barrier is an MBE growth technique that uses thin doping layers between more lightly doped regions to introduce or modify potential barriers in semiconductor structures. The technique was introduced by Malik et. al.[9]. A typical structure would have a p^+ doping spike between two intrinsic i layers with heavily doped n^+ contacts. The current vs. voltage characteristic of an asymmetric PDB is similar to a Schottky barrier characteristic. The PDB can be used as a Schottky barrier replacement with the additional advantage of barrier height control[10-11]. At 94 GHz a PDB single ended mixer had a noise figure of approximately 6 db and required only 280 μwatts of local oscillator power. If the p+ doping spike is placed in the middle of the structure, the current vs. voltage characteristic can be made anti-symmetric. Dixon and Malik[12] first showed subharmonic PDB operation at microwave frequencies. A millimeter wave

PDB subharmonic mixer with a 25 GHz signal bandwidth was described by Chen and Wong[13]. This device had a relatively large turn on voltage of 1.7 volts and a conversion loss of approximately 15 db. The purpose of this paper is to develop designs for PDB devices for operation at higher millimeter wave frequencies where low oscillator power is an important consideration.

An idealized planar doped barrier structure is shown in Fig. 1. The device designer has control of the material profile and dimensions. The device capacitance per unit area is determined by the width of the two i layers

$$C_{pdb} = \frac{\epsilon}{2l_i}, \tag{1}$$

where l_i is the width of one of the i regions in Fig. 1 and ϵ is the dielectric constant. Since the i layer width is controlled by the material structure and not by the bias conditions, the PDB capacitance is approximately constant with bias. The potential barrier height V_{pdb} is determined by the combination of the i layer width and the amount of charge in the p^+ doping spike,

$$V_{pdb} = \frac{qP_{spike}l_i}{4\epsilon} \tag{2}$$

where P_{spike} is the sheet density of charge in the doping spike and q is the electronic charge. A range of barrier heights are possible with proper choice of layer thickness and spike charge. The current vs. voltage characteristic of the PDB is

$$J_{pdb} = J_0 exp(\frac{qV}{2kT}) \tag{3}$$

where J_0 is a saturation current that depends on the barrier height. In a conventional Schottky barrier diode the "ideality factor" is a measure of the physics of the current transport across the barrier. It is near 1 for a good device at temperatures where tunneling current is small. The equivalent "ideality factor" for the PDB is two. The PDB is two junctions in series. The biased device acts as a voltage divider , with half of the applied bias appearing across the region to the right of the p^+ doping spike and the other half appearing to the left. This higher n factor is a potential limitation on the mixer performance of these devices. These approximations can be used to get an approximate device design. A more complete numerical analysis is needed to predict the device performance under large signal bias operation and to confirm these simple approximations.

A large signal computer program that solves Poissons' equation and the electron transport equation was developed to confirm the simple results given in equations 1 through 3. The capacitance vs. voltage characteristic of PDB structures with total i layer lengths of 500 and 1500 Å at 300 k is shown in Fig. 2. The capacitance is dependent on the i layer length and is approximately constant with bias voltage. The capacitance approximation given by equation 1 is correct except for a depletion of the contact regions. The increases the effective length and lowers the capacitance. The

barrier height predicted by equation 2 depends on materials constants and the $P_{spike}l_i$ product. In fact the barrier height depends on the structure since there is charge redistribution near the edges of the i layers at the n^+ contacts. The barrier height of a PDB structure with a constant $P_{spike}l_i$ product and a variable i layer length is shown in Fig. 3. There is an approximately 20% variation in the barrier height as the i layer length is increased from 500 to 2000 $\AA$.

The current vs. voltage characteristics of the PDB show the largest deviation from the simple theory. The current vs. voltage characteristic of two PDB structures with the same $P_{spike}l_i$ product and with total i layer thicknesses of 500 and 1500 $\AA$ are shown in Fig. 4. The difference in the current at low bias voltages is due to differences in the barrier height as shown in Fig. 3. The difference in the current at larger biases is due to space charge effects in the i layers of the device under high level injection conditions. The derivative of the electric field in the structure depends on the combination of the doping in the structure, and the density of the injected electrons. For low level injection conditions, the injected electron density is small, and the field slope is constant. As the density of injected electrons increases, the field slope is reduced and the change in voltage across the n^+ contacts required for a change in barrier height increases. The amount of injected charge in a long device is larger than in a short device, so the effect on the current vs. voltage characteristic is larger. The effect of this "space-charge resistance" is similar to series resistance in conventional mixer diodes and limits the minimum on resistance of the PDB device. The effect can be reduced by using shorter devices. A 500 $\AA$ long PDB has about the same depletion layer width and zero bias capacitance as a conventional epitaxial mixer diode with a doping of $2 \times 10^{17} cm^{-3}$.

With an i layer length of 500$\AA$ to reduce the space charge resistance, the P^+ doping can be varied to vary the barrier height and the turn on voltage. The current vs. voltage characteristics for three 500$\AA$ structures with P^+ sheet charges of $0.75, 1.0$ and $1.25 \times 10^{12} cm^{-12}$ are shown in Fig. 5. These curves show the wide range of barrier heights and turn on voltages possible with these structures and also show the reduced space charge resistance of the shorter structures. Structures with the material parameters of Fig. 5 were grown in GaAs using MBE. The experimental results are discussed in the next section.

IV. Planar Doped Barrier Device Characteristics

Initial work on the fabrication of PDB structures has begun to confirm the prediction of the last section. The devices are fabricated using the process sequence as follows:

Device Fabrication Sequence

1. GaAs MBE wafer growth with AlGaAs etch stops on GaAs substrate,
2. GeAuNi/Ti/Au ohmic contact deposition,
3. Au plated heat sinks,

4. Removal of substrate and etch stop layer,
5. Back side ohmic contact formation,
6. Mesa formation using chemical or RIBE etching,
7. Ohmic contact anneal.

We have started the initial characterization of three PDB structures. The 0.3 volt structure is shown in Fig. 6, the 0.5 volt structure in Fig. 7 and the 0.7 volt structure in Fig. 8. In these figures the current vs. voltage characteristics are for two mesa structures in series with contact to the top and unalloyed ohmic contacts. This initial characterization shows the basic device designs are correct. Work on complete device structures with the process sequence shown above is in progress.

V. Planar Doped Barrier Mixer Performance

We have started an initial characterization of the large signal mixer performance of PDB structures. This work used a large signal mixer analysis described by Maas[14]. This program is similar to the Held and Kerr program[2]. There are several tradeoffs in the performance in the performance of a PDB subharmonic mixer in comparison with a back to back Schottky barrier based mixer. The PDB has an n factor of at least two, in comparsion with an n factor of near one in a conventional diode. This higher n factor reduces the current modulation of the PDB. The effect of the n factor on the conversion loss of a subharmonic mixer is shown in Fig. 9. The figure shows the conversion loss of a subharmonic mixer vs. available local oscillator power for n factors between one and two and a constant barrier height of 0.7 volts. The higher n factor increases the amount of pump power required and slightly degrades the minimum conversion loss. The effect of the n factor can be overcome to some degree by control of the barrier height. Fig. 10 shows the conversion loss vs. local oscillator power for the range of barrier heights chosen for the experimental structures. The reduction of the barrier height reduces the required local oscillator power, even with the higher n factor. The lower barrier height slightly reduces the on to off ratio of the device and slightly degrades the conversion performance. For some applications, the Schottky mixer can be biased, which in effect lowers the barrier height. However, for high frequencies and for subharmonic operation, having two bias paths in the small waveguide structure would produce a complex structure than would not easily be matched. The unmatched structure would degrade the mixer performance. Although these are initial results, this data indicates that the PDB is a promising device for subharmonic applications.

Conclusions

This paper has given an overview of planar doped barrier devices for subharmonic mixer applications. These devices have a simple structure that will be useful for subharmonic operation. The simple design theory predicts the device capacitance and

barrier height. The device current vs. voltage characteristic is strongly effected by space charge resistance. For best mixer operation the PDB should be as short as possible. Initial experimental results confirm the device designs. A large signal analysis was used to study PDB subharmonic mixer performance. The performance is a tradeoff between the advantages of lower pump power because of barrier height control and higher conversion loss due to a higher n factor. The devices under consideration had conversion losses within 1.5 db of a comparison Schotthy diode pair and required a quarter of the local oscillator power.

References

1. "Noise and Loss in Balanced and Subharmonically Pumped Mixers: Part I - Theory, Part II - Application," by A. Kerr, *IEEE Trans. on Microwave Theory and Techniques*, vol. MTT-27, No. 12 Dec. 1979, pp. 938–950.

2. "Conversion Loss and Noise of Microwave and Millimeter Wave Mixers: Part I - Theory, Part II - Experiment," by D. Held and A. Kerr, *IEEE Trans. on Microwave Theory and Techniques*, vol. MTT-26, Jan. 1978, pp. 49–61.

3. "Numerical Analysis of Subharmonic Mixers Using Accurate and Approximate Techniques," by R. Hicks and P. Khan, *IEEE Trans. on Microwave Theory and Techniques*, vol. MTT-30 , Dec. 1982, pp. 2113–2119.

4. "Subharmonically Pumped Millimeter-Wave Mixers," by E. Carlson, M. Schneider and T. McMaster, *IEEE Trans. on Microwave Theory and Techniques*, vol. MTT-26, Oct. 1978, pp. 706–715.

5. "Harmonically Pumped Stripline Down-Converter," by M. Schnieder and W. Snell, *IEEE Trans. on Microwave Theory and Techniques*, vol. MTT-23, March 1975, pp. 271–275.

6. "Millimeter-Wave Receivers with Subharmonic Pump," by T. McMaster, M. Schnieder and W. Snell, *IEEE Trans. on Microwave Theory and Techniques*, vol. MTT-24, Dec. 1976, pp. 948–952.

7. "183 GHz Monolithic Subharmonic Mixer," by S. Marsh, N. Cronin and P. Reece, *IEEE International Microwave Symposium Digest,* 1987, pp. 121–122.

8. "A Planar Quasi-Optical Subharmonically Pumped Mixer Characterized by Isotropic Conversion Loss," by K. Stephan and T. Itoh, *IEEE Trans. on Microwave Theory and Techniques*, vol. MTT-32, Jan. 1984, pp. 97–102.

9. "Planar Doped Barriers in GaAs by Molecular Beam Epitaxy," by R. Malik, T. AuCoin, R. Ross, K. Board, C. Wood and L. Eastman, *Electronics Letters*, vol. 16, 23 Oct. 1980, pp. 836–837.

10. "Asymmetric Planar Doped Barrier Diodes for Mixer and Detector Applications," by by M. Kearney, M. Kelly, R. Davies, T. Kerr and P. Rees, *Electronics Letters*, vol. 25, 12 Oct. 1989, pp. 1454–1456.

11. "Planar Doped Barrier Mixer and Detector Diodes as Alternatives to Schottky Diodes for Both Microwave and Millimeter Wave Applications," by by I. Dale, A. Condle, S. Neylon and M. Kearney, *IEEE Microwave Symposium Technical Digest*, 1989, pp. 467–470.

12. "Subharmonic Planar Doped Barrier Mixer Conversion Loss Characteristic," by S. Dixon and R. Malik, *IEEE Trans. on Microwave Theory and Techniques*, vol. MTT-31, Feb. 1983, pp. 155–158.

13. "W-Band Beam Lead Planar Doped Barrier Subharmonic Mixer," by by J. Chen and D. Wong, *IEEE Microwave Symposium Technical Digest*, 1985, pp. 178–180.

14. *Microwave Mixers*, by Stephen A. Maas, Artech House, 1986, Appendix A.

List of Figures

1. PDB structure, potential and design considerations.

2. Capacitance vs. Voltage Characteristics for PDB structures i layer length = 500, 1000 and 1500 $\mathring{A}$.

3. Barrier height vs. i layer thickness for constant $P_{spike}l_i$ product.

4. Current vs. Voltage characteristic comparison for two i layer lengths(top = 500Å, bottom = 1500Å).

5. Current vs. Voltage characteristic for 500$\mathring{A}$ i layer lengths and different P^+ sheet dopings($top = 0.75\, middle = 1.0\ and\ bottom = 1.25^{12} cm^2$.

6. 0.3 volt barrier PDB current vs. voltage characteristic

7. 0.5 volt barrier PDB current vs. voltage characteristic

8. 0.7 volt barrier PDB current vs. voltage characteristic

9. n factor effect on mixer performance

10. barrier height effect on mixer performance

PLANAR DOPED BARRIER
(details)

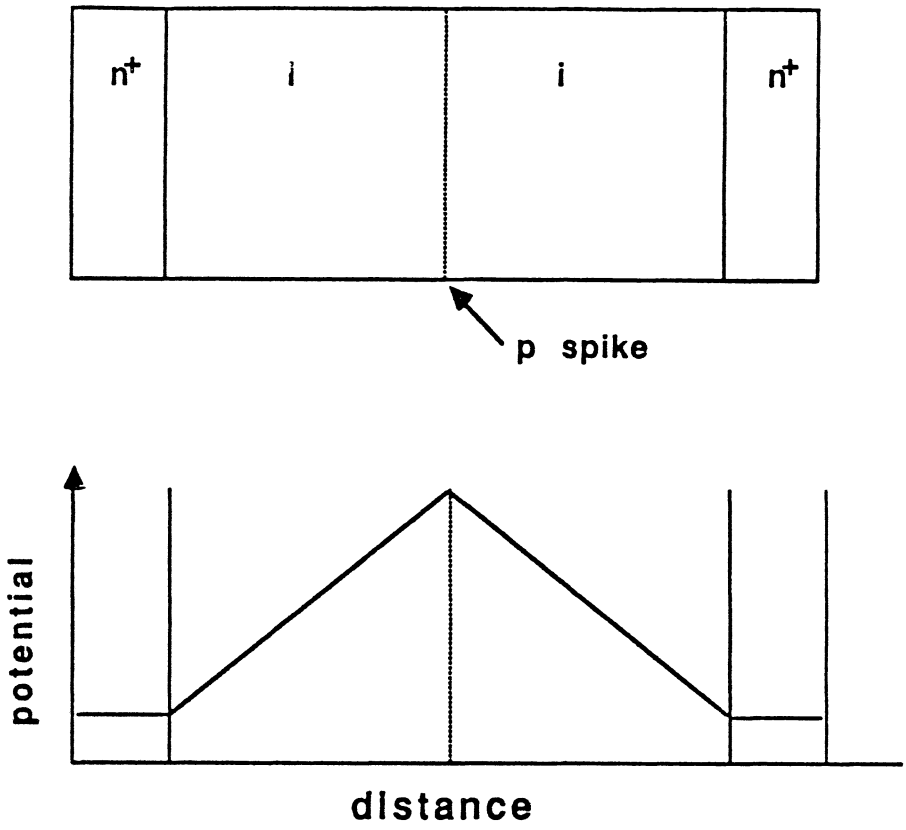

Choice of

1) width
2) doping
3) material

Control

1) barrier height
2) resistance
3) capacitance

Figure 1

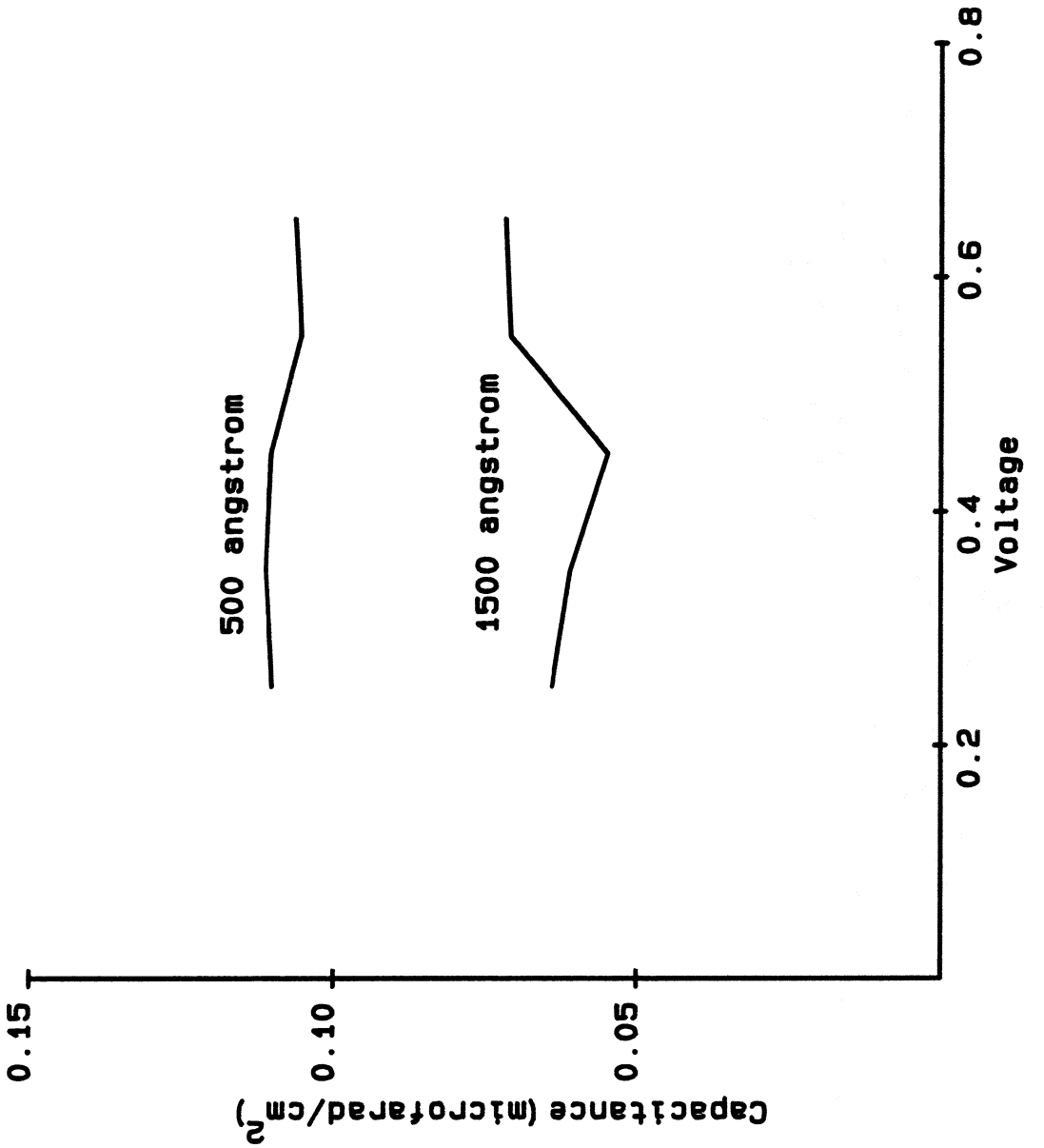
0.15
0.10
0.05
Capacitance (microfarad/cm²)
0.2
0.4
0.6
0.8
Voltage
500 angstrom
1500 angstrom

Figure 2

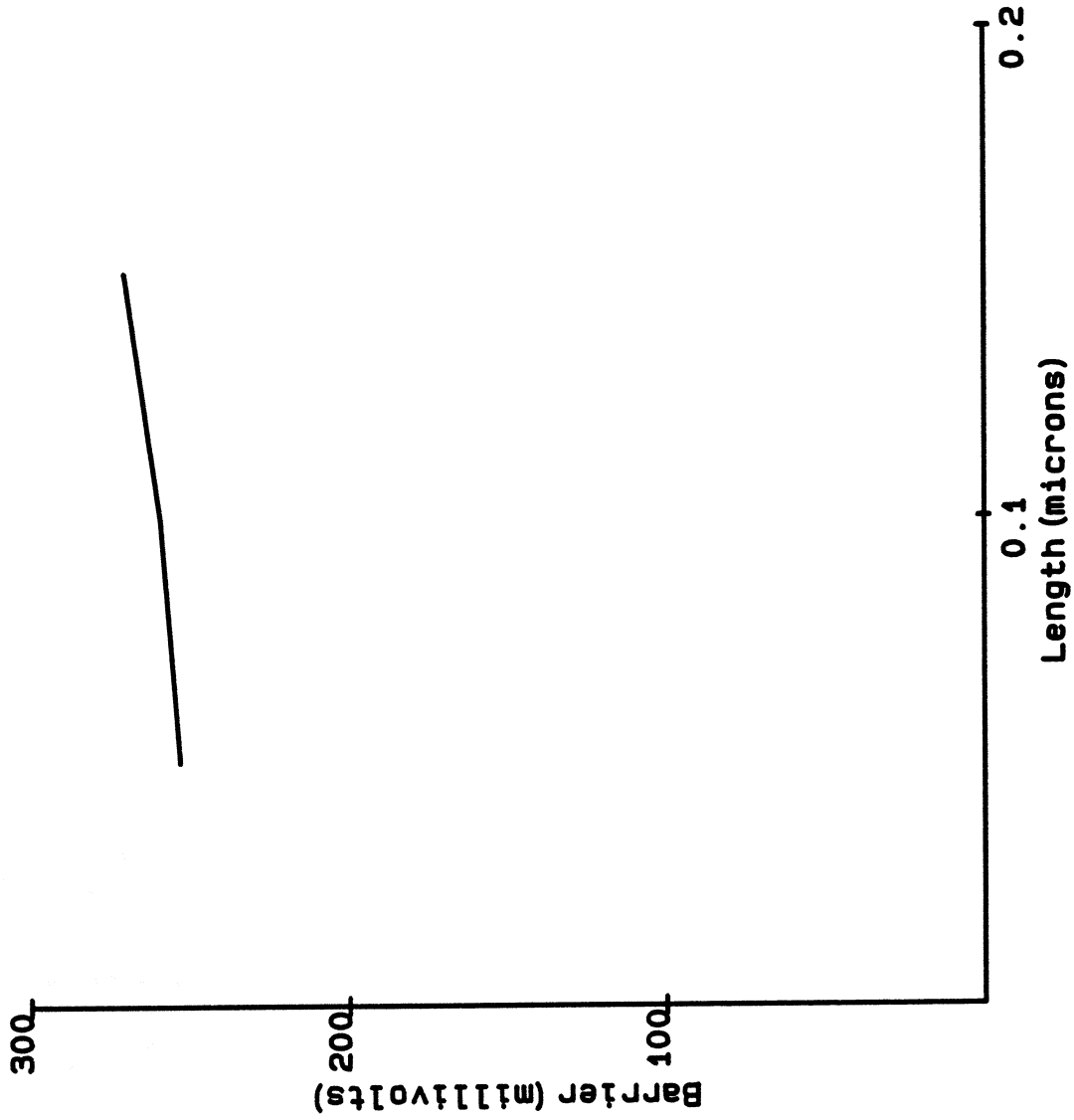

Figure 3

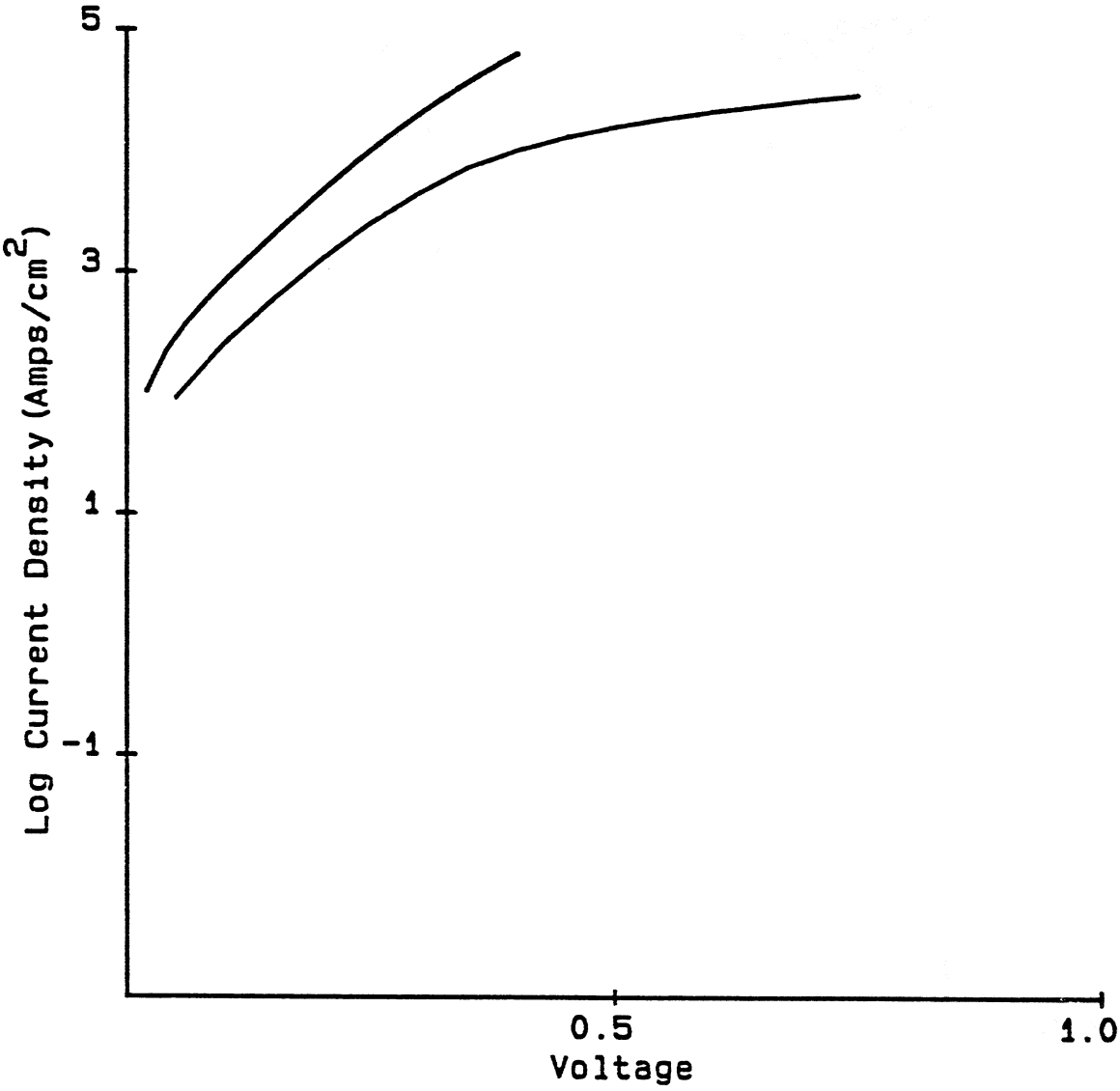

Figure 4

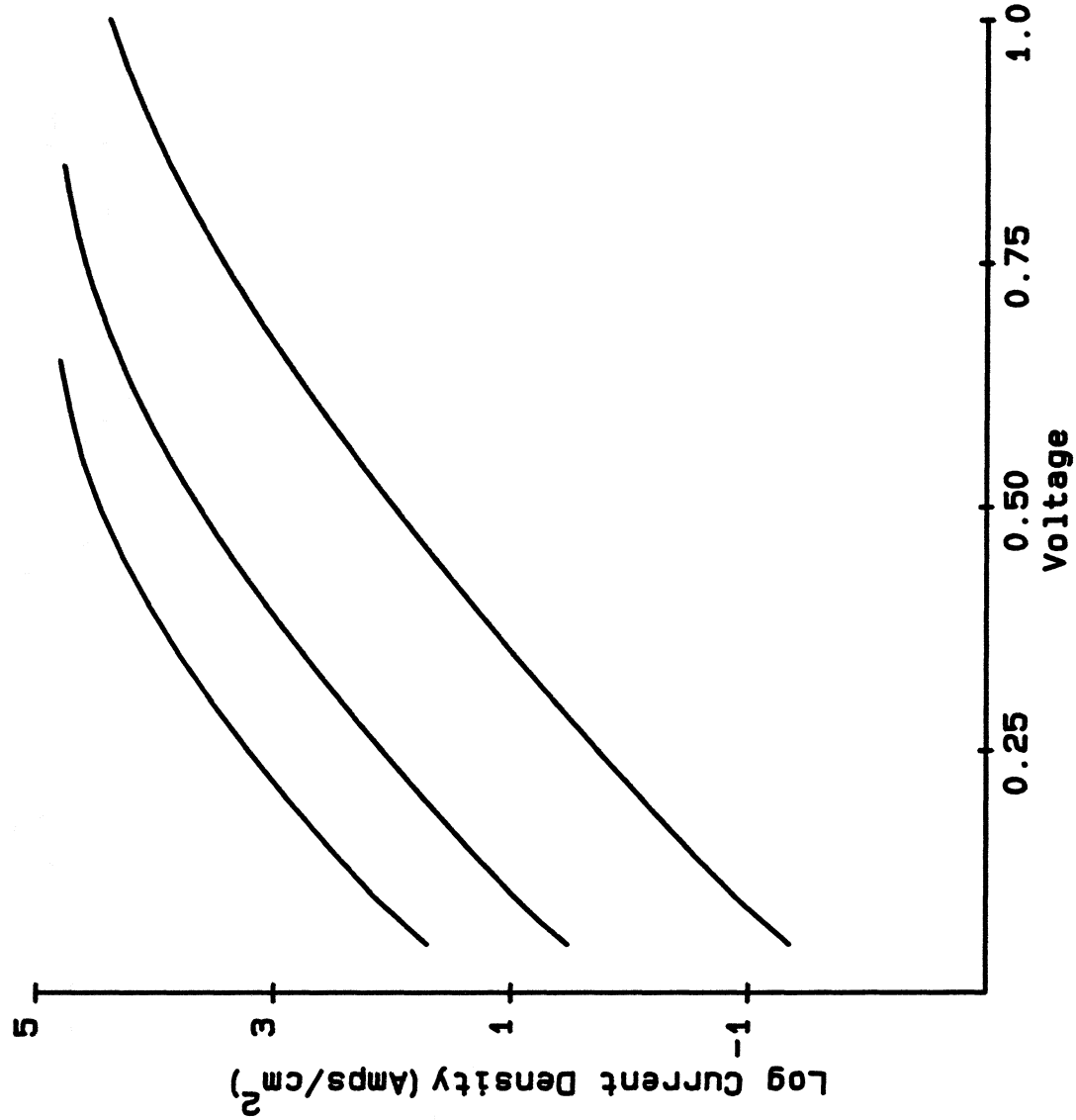

Figure 5

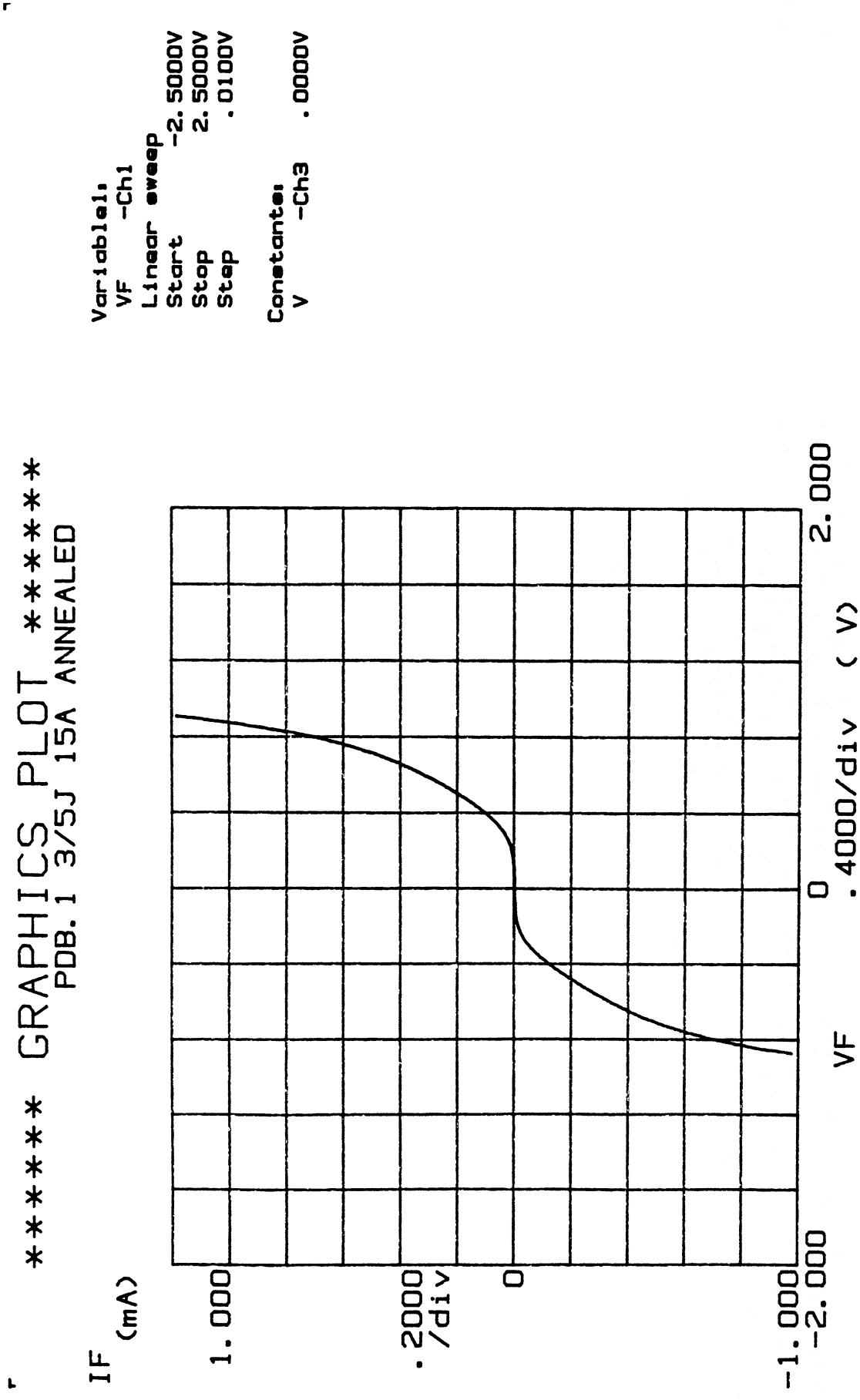
Variable1:
VF -Ch1
Linear sweep
Start -2.5000V
Stop 2.5000V
Step .0100V
Constants:
V -Ch3 .0000V
******* GRAPHICS PLOT *******
POB.1 3/5J 15A ANNEALED
IF (mA)
1.000
.2000 /div
0
-1.000
-2.000
2.000
0
VF .4000/div (V)

Figure 6

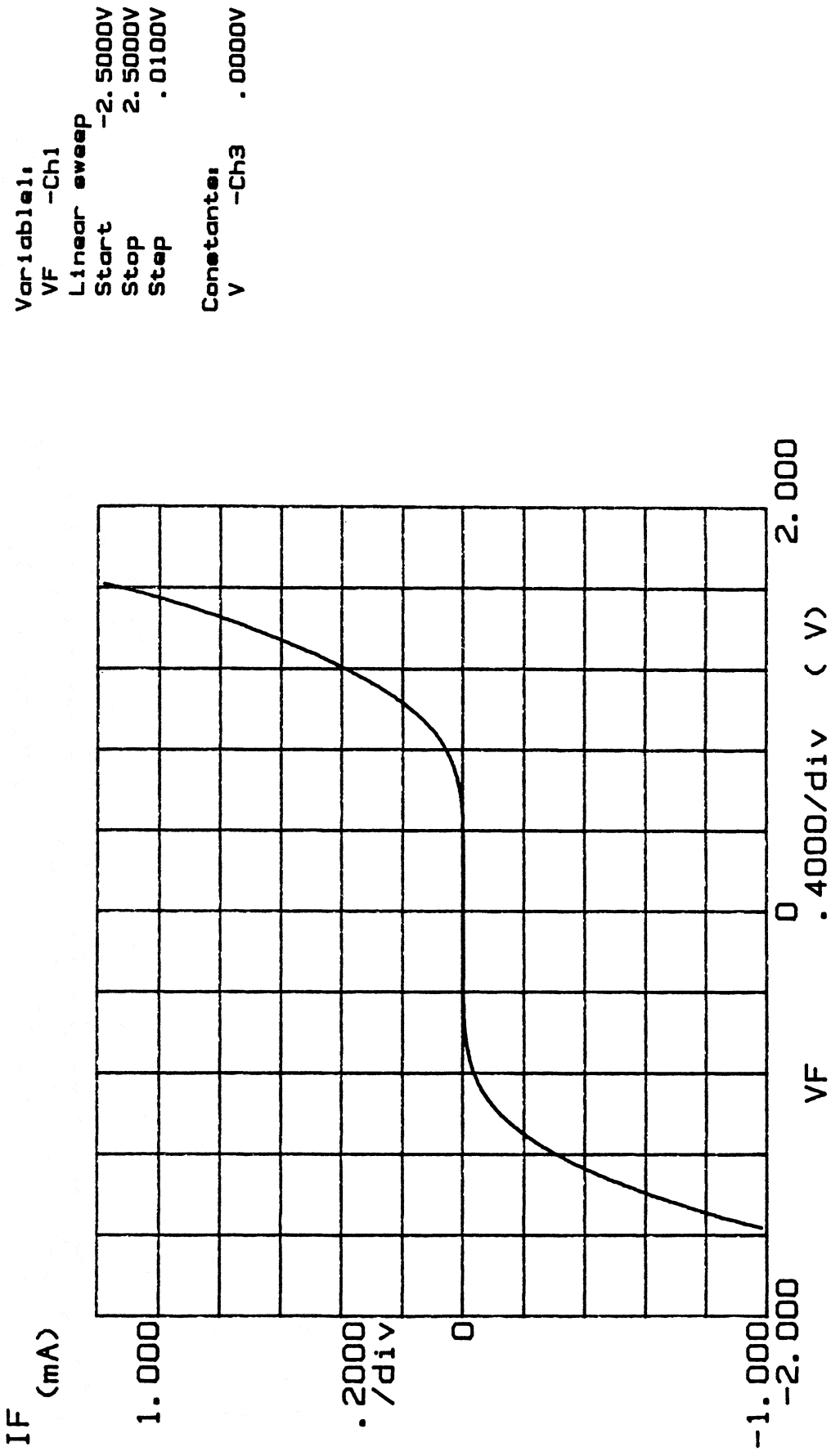
Variable1:
VF -Ch1
Linear sweep
Start -2.5000V
Stop 2.5000V
Step .0100V
Constants:
V -Ch3 .0000V
******* GRAPHICS PLOT *******
PDB.1 3/5A 20A ANNEALED
IF (mA)
1.000
.2000 /div
0
-1.000
-2.000
2.000
0
VF .4000/div (V)

Figure 7

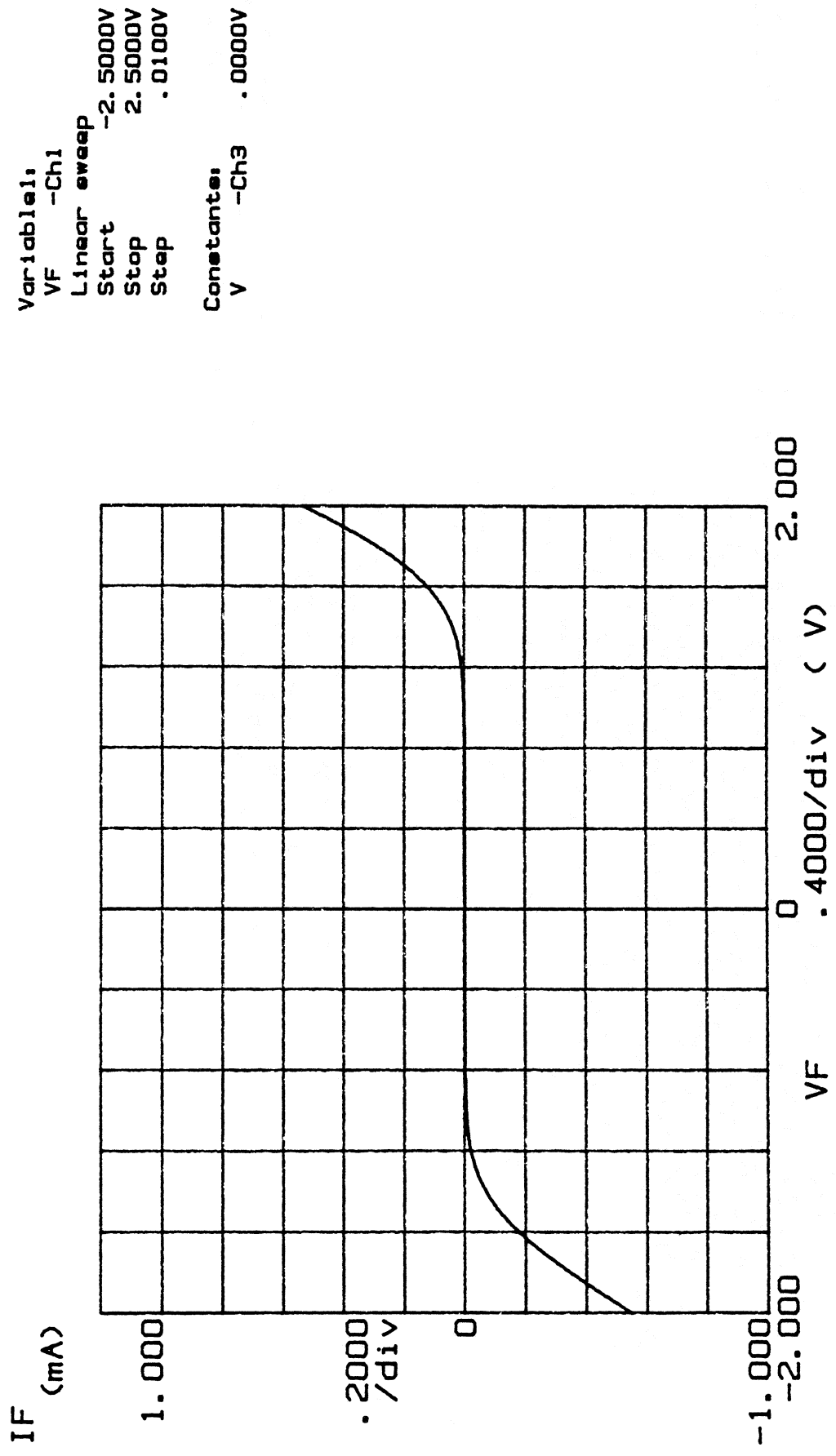
Variable1:
VF -Ch1
Linear sweep
Start -2.5000V
Stop 2.5000V
Step .0100V
Constants:
V -Ch3 .0000V
******* GRAPHICS PLOT *******
PDB.1 3/5L 25A ANNEALED
IF (mA)
1.000
.2000 /div
0
-1.000
-2.000
-2.000
0
2.000
VF .4000/div (V)

Figure 8

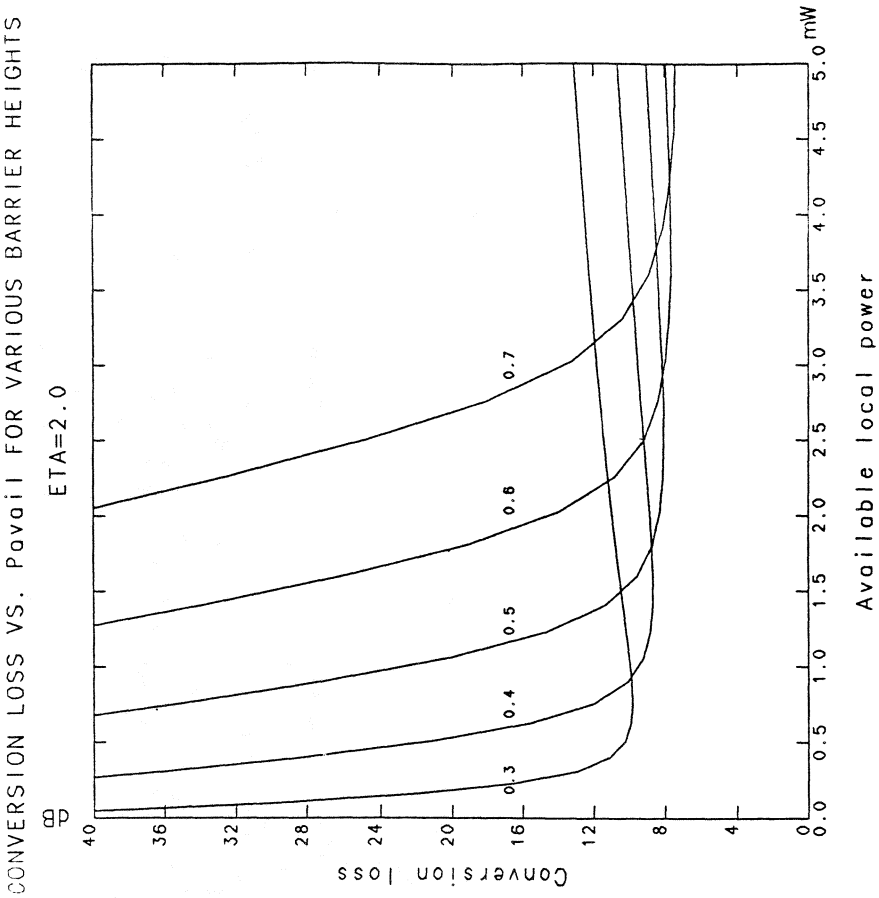

Figure 10

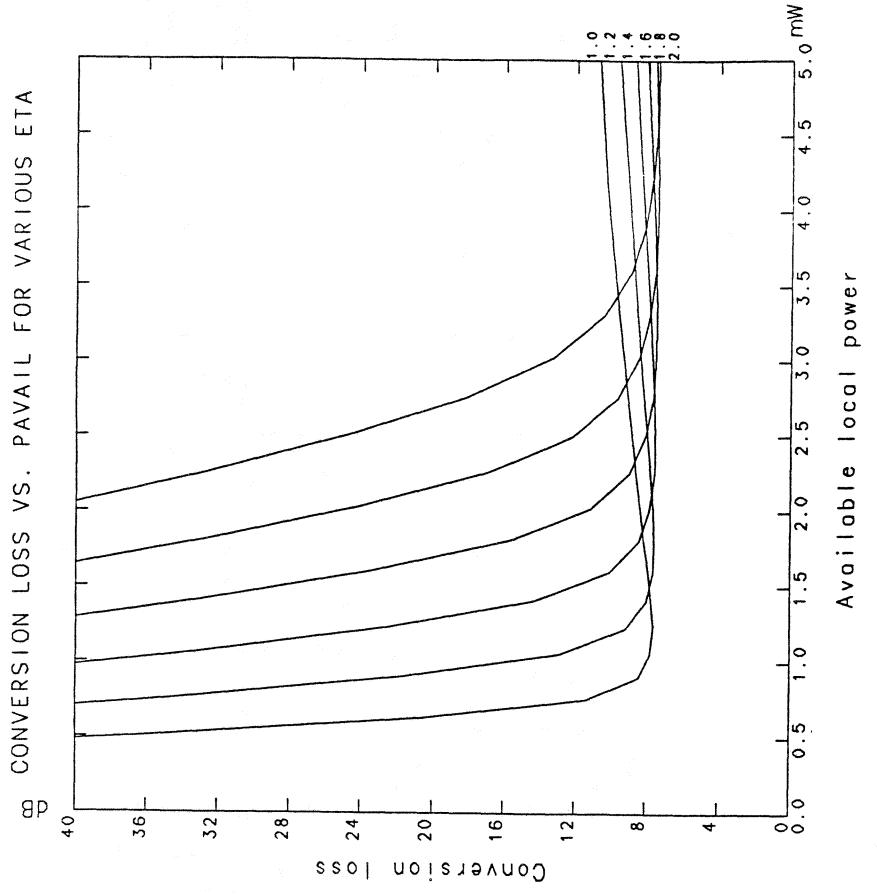

Figure 9

QUANTUM WELL MULTIPLIERS: TRIPLERS AND QUINTUPLERS

M. A. Frerking

Jet Propulsion Laboratory
California Institute of Technology
Pasadena, California

Quantum well devices are a promising new type of non-linear device for harmonic generation in the millimeter and submillimeter wave regime. Two types of non-linear impedances have been employed for harmonic generation: the varactor with a non-linear capacitance-voltage characteristic and the varistor with a non-linear current-voltage (I-V) relationship. The harmonic generation efficiency of the varactor theoretically exceeds that for a varistor since an ideal varactor suffers no resistive losses. However, above about 400 GHz, currently available varistors are more efficient because they have considerably higher cutoff frequencies. The maximum conversion efficiency to the nth harmonic for an ideal varistor with a monotonically increasing I-V characteristic has been shown to be $1/n^2$ [1,2]. The quantum well double barrier diode is a varistor which exhibits a negative resistance in its I-V curve at frequencies as high as 2.5 THz [3]. Since its I-V curve is no longer monotonically increasing, it can generate harmonics with higher efficiency than the $1/n^2$ limit. Tripling to 200 GHz has been demonstrated with these devices with output powers in excess of 200 μW [4,5, viewgraph 6 (VG-6)]. The capacitance - voltage characteristic of these devices is also highly non-linear and may provide efficient varactor operation. Theoretical analysis yields high efficiencies for tripling and quintupling of GaAs/AlAs and InGaAs/AlAs quantum well devices with optimized embedding impedances.

A quantum well resonant tunneling diode (RTD) is formed of two thin layers of a material with a high energy band gap on either side of a lower energy gap material. As shown in VG-2 this structure has a potential energy distribution consisting of a potential well sandwiched between two barriers. In such a structure a bound state can occur. When no voltage is applied to the RTD, no current flows. As the voltage is increased across the device electrons tunnel through the barriers. When the voltage equals that of the bound state resonant tunneling occurs greatly enhancing the current. As the voltage increases further, the resonance is passed and the current drops. When the voltage exceeds the barrier height the current again increases. Since the RTD structure is symmetric the I-V curve is antisymetric about zero voltage.

Thin barrier RTDs are very fast devices. The charge-transport time can be less than 100 fs, while the intrinsic parasitics are low. Current densities as high as 2×10^5 A/cm^2 have been achieved [6] and the specific capacitance of 0.1 μF/cm^2 is comparable to high speed GaAs Schottky barrier diodes.

Frequency multiplication using these devices was first suggested by Sollner [7]. The shape of the I-V curve suggest that there should be large harmonic content to the current waveform, and the antisymmetry implies that only odd harmonics should be present. The differential negative resistance allows efficiency greater than $1/n^2$ the limit for monotonically increasing I-V curves.

To design a multiplier using a quantum well RTD as the non-linear device, a large signal analysis was carried out using a modified version of GISSMIX [8, VG-8] to optimize terminations at the various harmonics. The large signal analysis was carried out at three output frequencies; DC, 183 GHz, and 1000 GHz. In addition three quantum well RTD devices were modelled; one GaAs/AlAs RTD and two InGaAs/AlAs RTDs. The device details are summarized in the VG-10,

VG-11, and VG-12.

At DC, where parasitics can be ignored so that the RTD is operating in a purely varistive mode, the 3rd and 5th harmonics had comparable efficiencies; 2.5% for the GaAs/AlAs RTD and 7% for the InGaAs/AlAs RTD [VG-15, VG-16].

To verify the large signal theoretical analysis, measurements of multiplication efficiency were also performed at low frequencies. The agreement between experiment and theory is excellent, not only for the 3rd and 5th harmonics, but also for the 7th, 9th , and 11th harmonics [VG-15].

In the submillimeter wavelength regime, the effect of parasitics is critical. The two most important parasitics are the series resistance and the shunt capacitance [VG-17]. The series resistance arises from the ohmic contact, the resistance of the undepleted epilayers on both sides of the double barrier structure, and spreading resistance from the mesa into the much wider substrate material. The voltage variable capacitance occurs in the depletion region. The functional form indicated in VG-17 is a simple solution to Poisson's equation. C_{jo} is the capacitance of the double barrier structure when no voltage is applied.

For varistor operation to dominate, the time averaged impedance due to the capacitance must be less than the resistive impedance of the quantum well device. These limits are shown graphically in VG-18. The resistive impedance of the device depends on the detailed shape of the I-V curve and the voltage swing of the pump power. For the devices we have tested, it is in the range 100 - 300 Ωs. An average capacitance of less than 5 fF is required for varistor operation at 100 GHz while an average capacitance of less than 1 fF is needed for varistor operation at 1000 GHz.

The predicted voltage variable capacitance of the quantum well device is highly non-linear, suggesting that these devices may perform extremely well as varactors. VG-20 and VG-21 show the predicted performance of the InGaAs/AlAs RTD at three frequencies, DC, 183 GHz, and 1000 GHz. At DC the device is operating in the purely varistor mode whereas at 183 GHz it is functioning primarily as a varactor. The 5th harmonic generation efficiency is greater at 183 GHz (about 25%) than at DC (about 7 %) since varactor operation allows the build up of higher instantaneous current in the device. This can be seen by comparing the current waveforms at DC (VG-13) and at 183 GHz (VG-19). At 1000 GHz the series resistance is limiting the performance as a varactor yielding lower efficiencies.

With the existing GaAs/AlAs and InGaAs/AlAs RTDs, power levels on the order of 0.25 to 0.5 mW can be generated at the 5th harmonic when provided the proper embedding circuit. The output power scales with current density. Current densities almost an order of magnitude higher have recently been demonstrated in the new material system InAs/GaAlSb [6].

In summary, quantum well devices are a promising new millimeter and submillimeter wave frequency multiplier device. They can be optimized to maximize performance as a high order harmonic generator. In particular 5th order harmonic generation is very efficient. Since their inherent symmetry produces only odd harmonics, circuit design is greatly simplified. We have verified varistor multiplication at very low frequencies by comparing large signal theoretical analysis with experimental measurement. Understanding the parasitics is critical to optimizing for high frequency performance. The voltage variable capacitance of quantum well devices may in fact make them a very good candidate varactor.

References

1. C. H. Page, "Frequency conversion with positive nonlinear resistors," *J. Res. Nat. Bur. Stand.*, vol. 56, no. 4, p. 179, Apr. 1956.

2. C. H. Page, "Harmonic generation with ideal rectifiers," *Proc. IRE*, vol. 46, pp. 1738-1740, Oct. 1958.

3. T. C. L. G. Sollner *et. al.*, "Resonant tunneling through quantum wells at frequencies up to 2.5 THz," *Appl. Phys. Lett.*, vol. 45, p. 1319, 1984.

4. P. D. Batelaan and M. A. Frerking, "Quantum well multipliers," Twelfth International Conference on Infrared and Millimeter Waves Digest, p. 14-15, Dec. 1987.

5. A. Rydberg and H. Gronqvist, "Quantum-well high-frequency millimetre-wave frequency tripler," *Electronics Letters*, Vol 25, No. 5, p. 348, Mar. 1989.

6. T. Broekaert and C. Fonstad, *IEEE Int. Electron Devices Meeting Tech. Digest*, (IEEE, New York), paper 21.5, 1989.

7. T. C. L. G. Sollner, E. R. Brown, and H. Q. Le, "Microwave and Millimeter-Wave Resonant-Tunneling Devices," *Lincoln Laboratory Journal*, Vol. 1, No. , 1988.

8. P. H. Siegel, "Topics in the Optimization of Millimeter-Wave Mixers," NASA Technical Paper 2287, Mar.1984.

QUANTUM WELL MULTIPLIERS

JPL

M. A. Frerking

March 7,1990

Collaborators:

JPL

P. Batelaan

T. Tolmunen

Lincoln Laboratory

E. Brown

G. Sollner

Sponsor:

NASA OAST Sensors Program

SUBMILLIMETER WAVE LOCAL OSCILLATOR

- TECHNICAL GOALS
  - Local Oscillator Sources for 300 - 1500 GHz
  - Output Power 1 μW - 1 mW
  - Tuneability 10-20 %
  - Linewidth 1:10^8
  - Frequency Stability 1:10^8
  - Space Qualifiable
- TECHNICAL APPROACH
  - Solid State Source - Quantum Well Device
  - Fundamental Oscillator 300 - 600 GHz
  - Harmonic Generator 600 - 1500 GHz

MAF 2-28-90

DOUBLE BARRIER TUNNELING IN QUANTUM WELL DEVICES

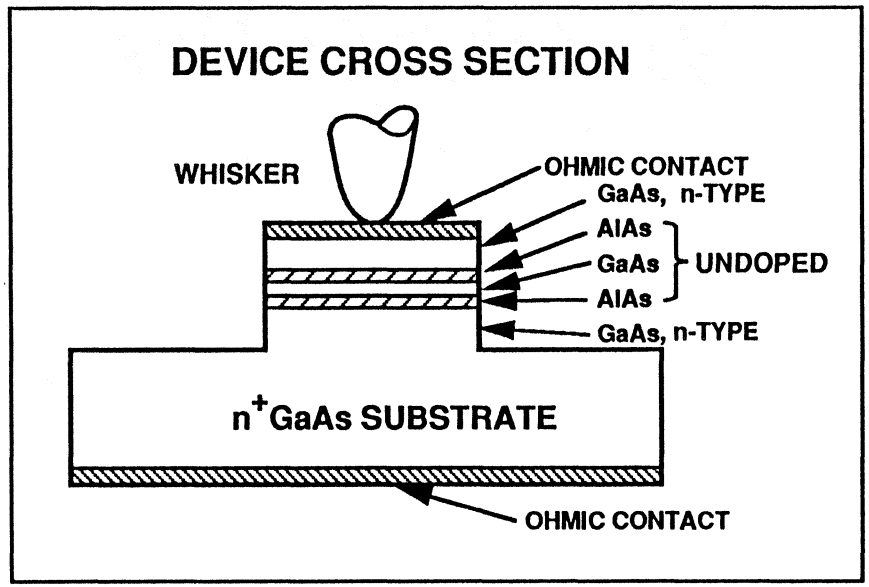

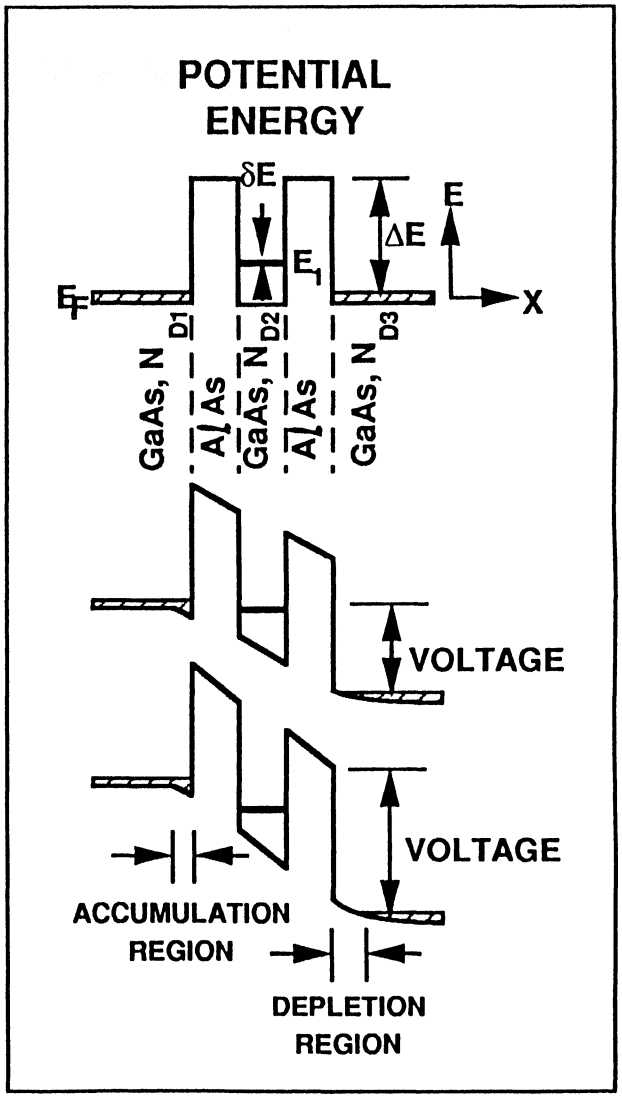

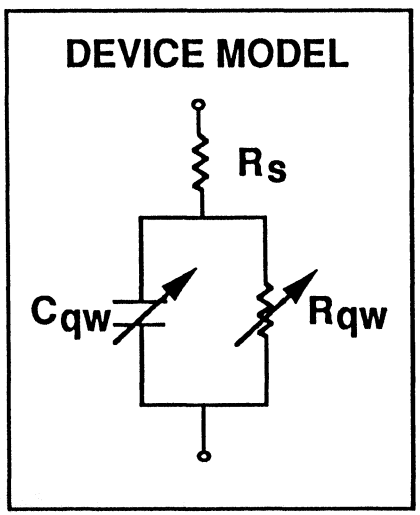

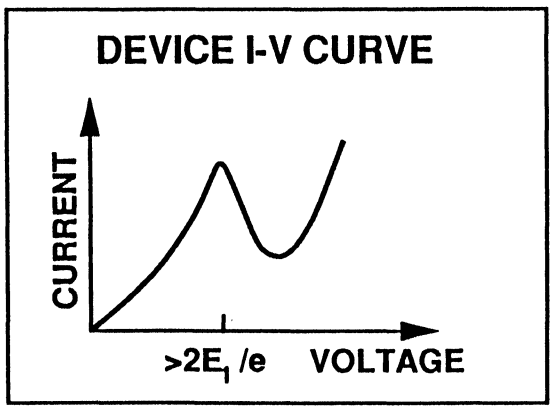

MAF 2-28-90

ADVANTAGES OF QUANTUM WELL DEVICES

- High Speed
  - Quantum Limit< 100 fs
  - $\tau \sim 2h/\Delta E$
- Low Parasitics
  - High Current Density $\sim 1.5 \times 10^5 A/cm^2$
  - Low Capacitance $\sim 0.1\ \mu F/cm^2$
- Unique Current Voltage Characteristic
  - Negative Differential Resistance
  - Antisymetric about zero
- Engineered Device

MULTIPLICATION USING QUANTUM WELL DEVICES

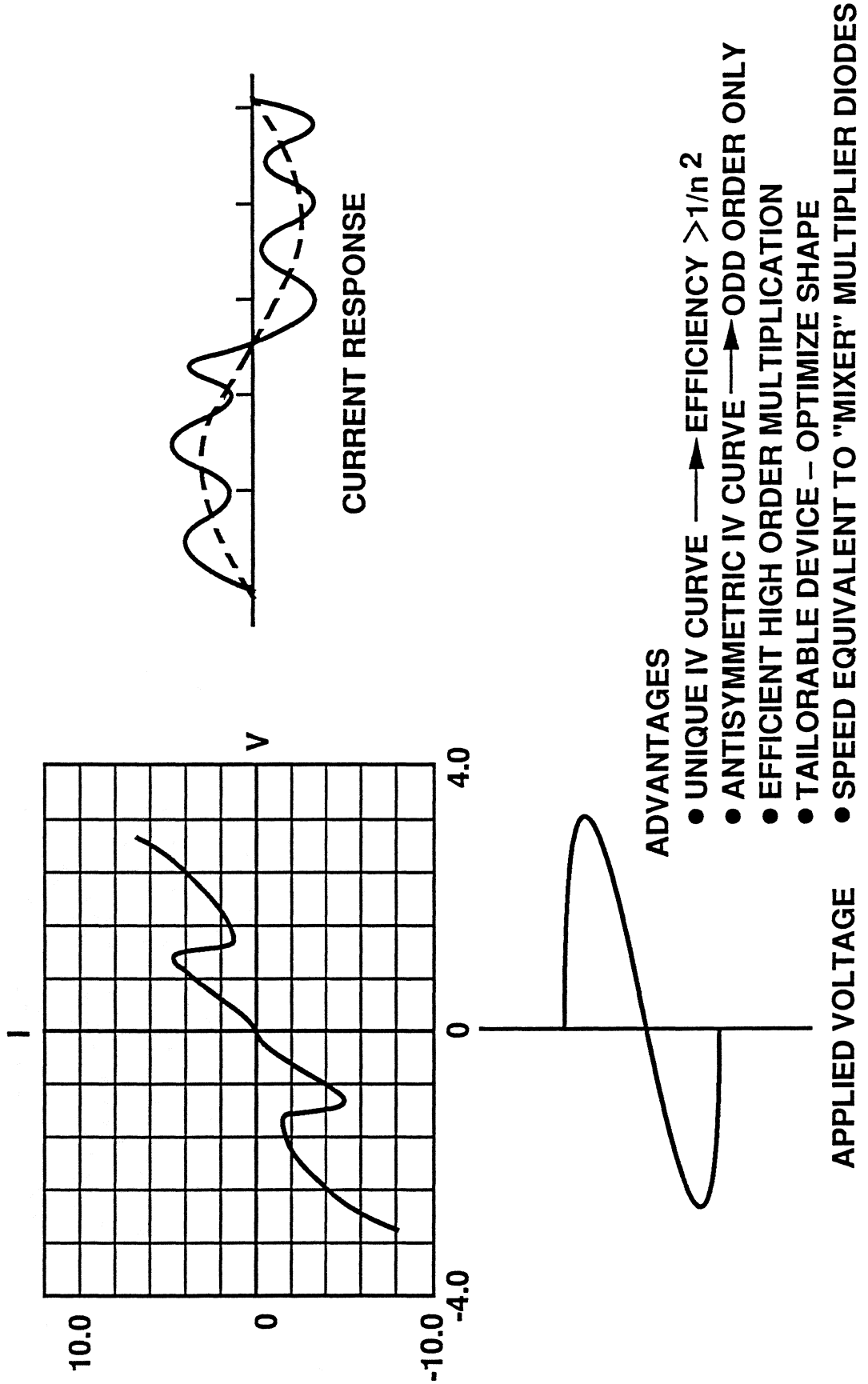

QUANTUM WELL TRIPLER

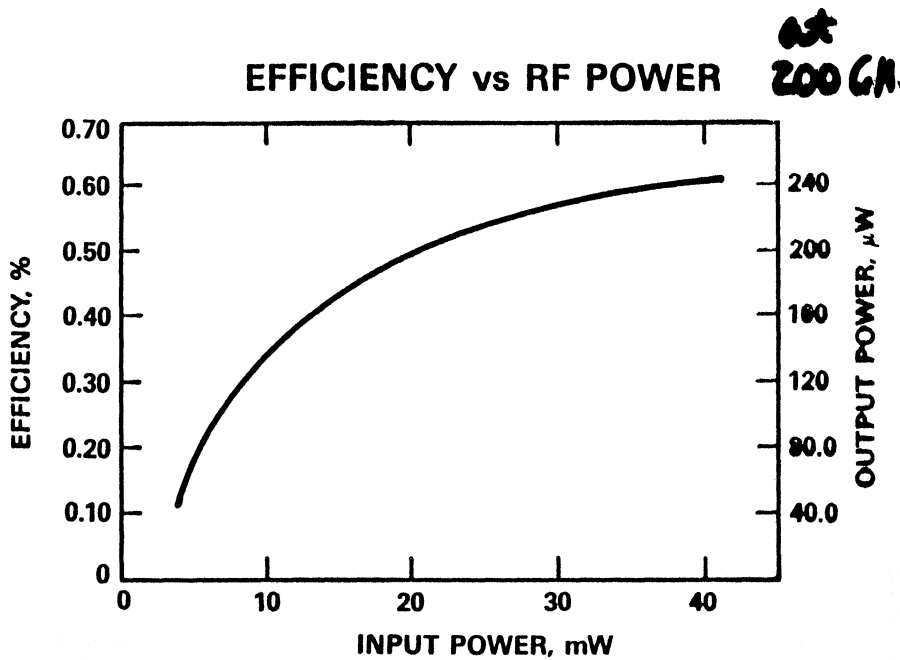

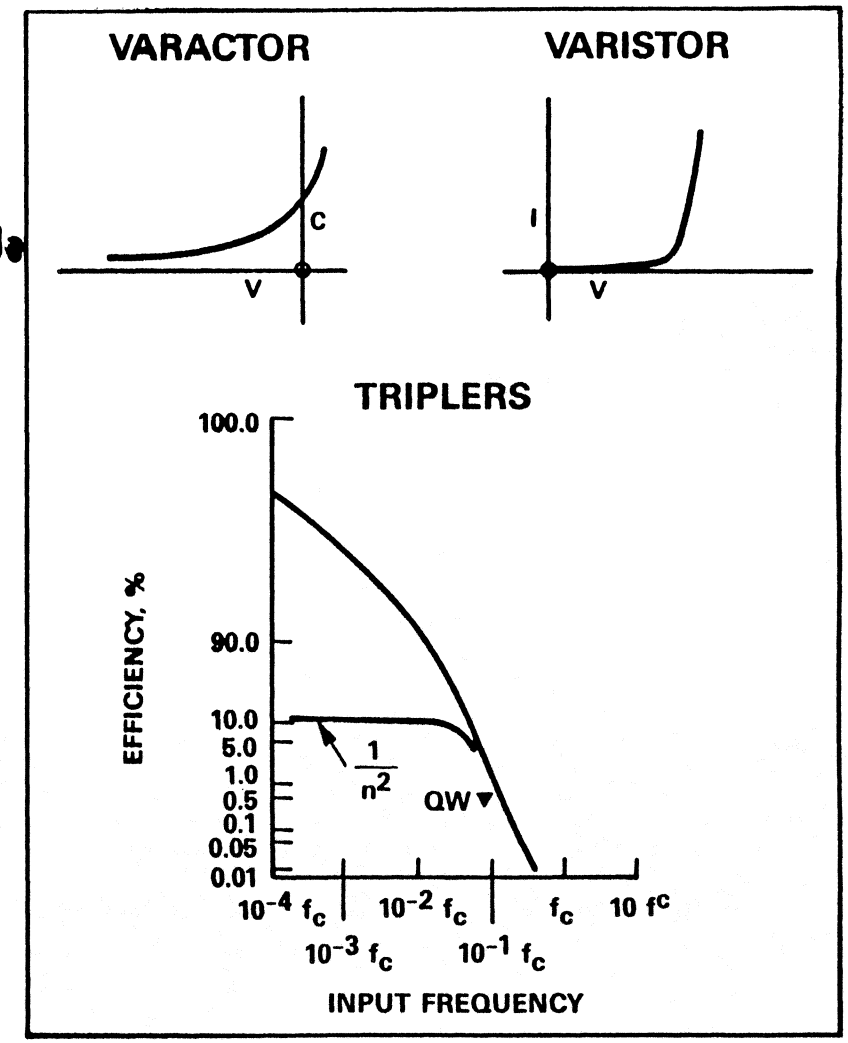

LARGE SIGNAL ANALYSIS

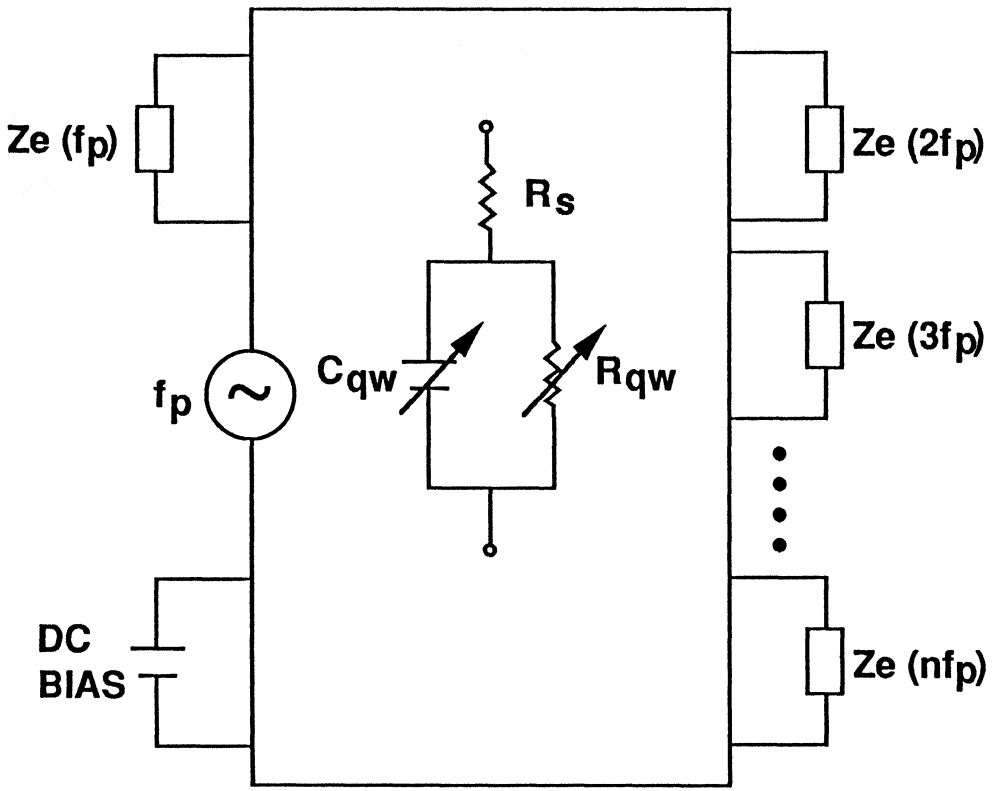

- USE MODIFIED GISSMIX PROGRAM TO OPTIMIZED TERMINATIONS AT VARIOUS HARMONICS
- INPUTS
  - QW MEASURED IV CURVE
  - QW CALCULATED CV CURVE
  - PUMP POWER
  - DC BIAS POWER
  - CIRCUiT EMBEDDING IMPEDANCES
- OUTPUTS
  - VOLTAGE AND CURRENT WAVEFORMS
  - HARMONIC GENERATOR EFFICIENCY
  - HARMONIC POWER
- VERIFIED PROGRAM BY COMPARISON TO ANALYTICAL SOLUTION FOR PURELY RESISTIVE DEVICE

LARGE SIGNAL ANALYSIS

- Frequencies
  - Low Frequency - no parasitics
  - Millimeter Wave - Quintupler to 183 GHz
  - Submillimeter Wave - Quintupler to 1000 GHz
- Quantum Well Devices
  - GaAs/AlAs RTD - existing device
  - InGaAs/AlAs RTD - existing device
  - InGaAs/AlAs RTD - hypothetical, but possible

GaAs/AlAs Quantum Well Resonant Tunneling Diode

Devices obtained from Lincoln Laboratory

Device Detail

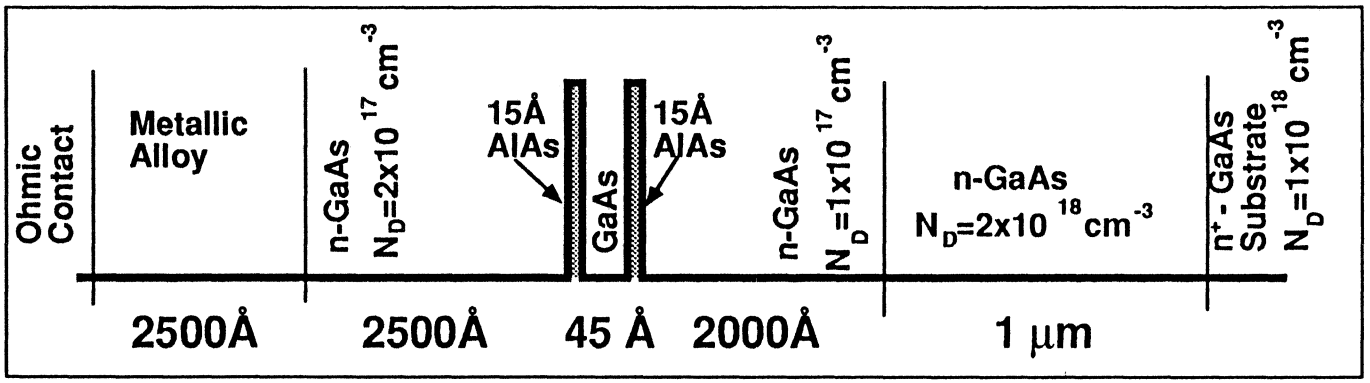

Device Parameters

Jp = 4x10^4 A/cm^2

Ip/Iv = 3.5:1

Diameter = 4 μm

Rs = 12 Ω

Ceff = 1/{1/Cmin - 1/Cmax} = 12 fF

fc = 1/2πRsCeff = 1140 GHz

Device I-V Curve

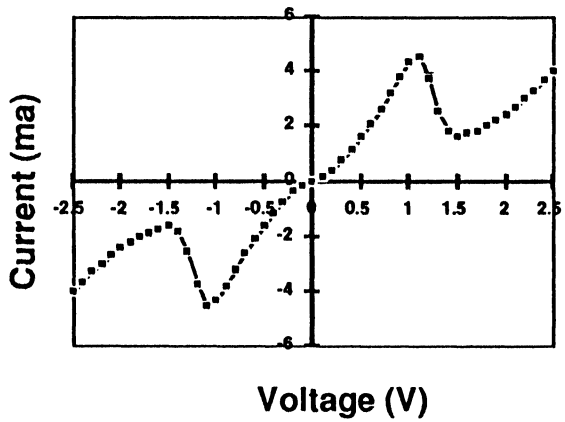

InGaAs/Aℓ As Quantum Well Resonant Tunneling Diode

DEVICES OBTAINEDFROM LINCOLN LABORATORY

DEVICE DETAIL

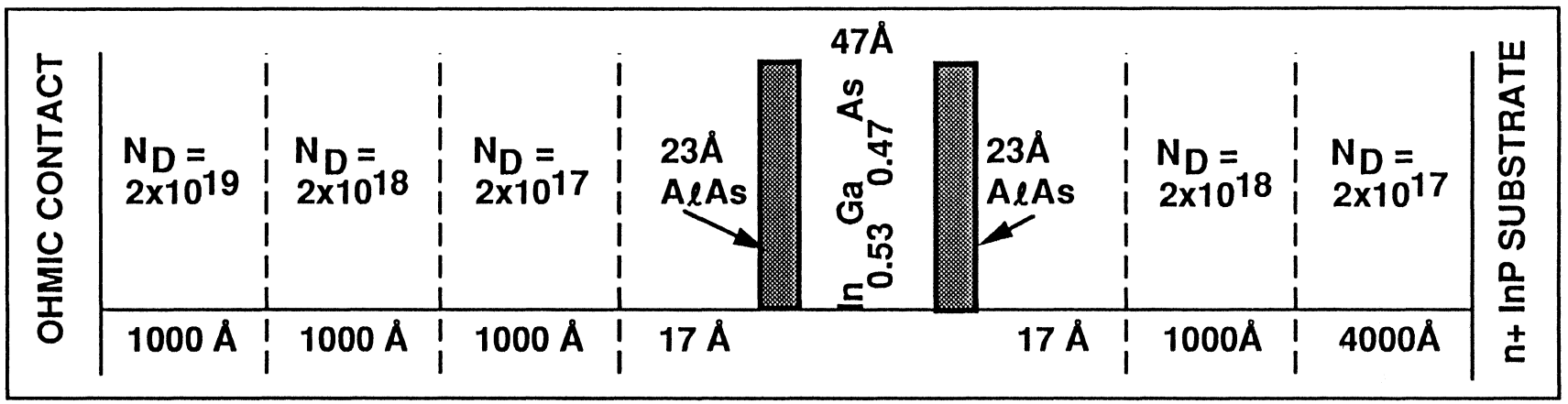

Device Parameters

Jp = $3x10^4$ A/cm ^{2}
Ip/Iv = 10:1
Diameter = 3 μm
Rs = 12 Ω
Ceff = 1/{1/Cmin - 1/Cmax} = 7 fF
fc = 1/2πRsCeff = 1890 GHz

Device I-V Curve

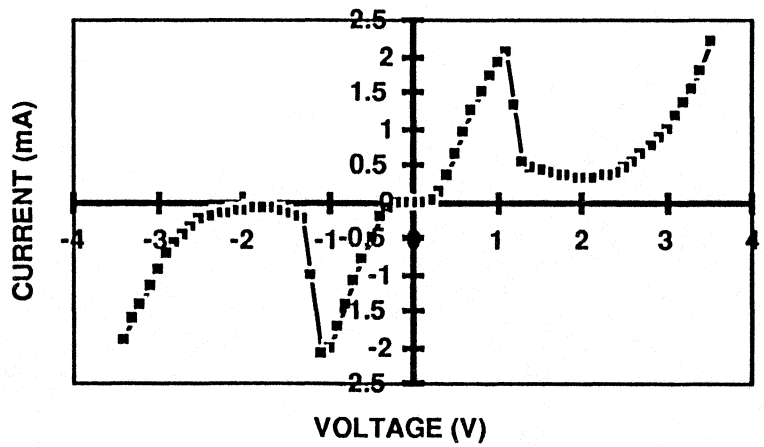

HYPOTHETICAL QUANTUM WELL RESONANT TUNNELING DIODE

DEVICE PARAMETERS

$J_p = 3 \times 10^5$ A/cm^2

$I_p / I_v = 10{:}1$

DIAMETER = 1 μm

$R_S = 5\Omega$

$C_{eff} = 1/\{1/C_{min} - 1/C_{max}\} = 1$ fF

$f_c = 1/2\Pi R_S C_{eff} = 29$ THz

MULTIPLIER OPERATION: WAVEFORMS

Low Frequency Case

GaAs/AlAs RTD

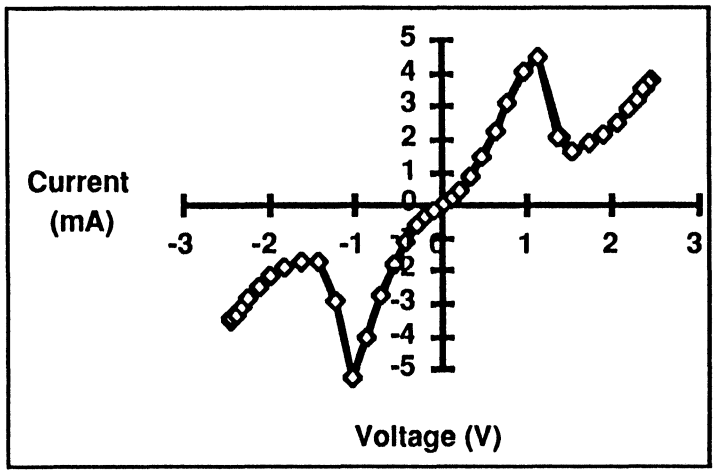

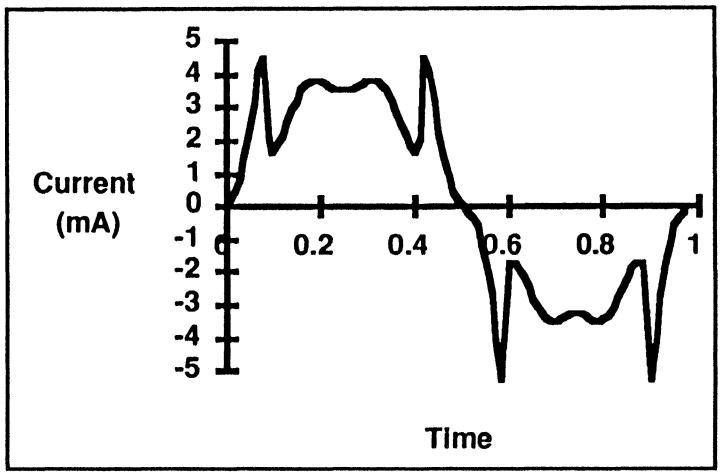

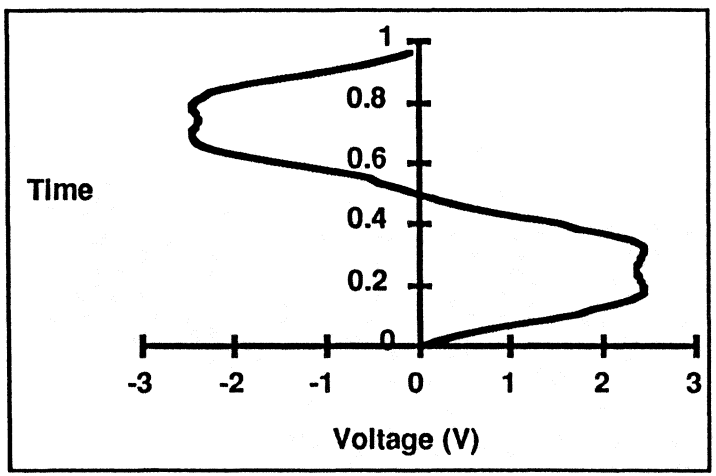

MAF 2-26-90

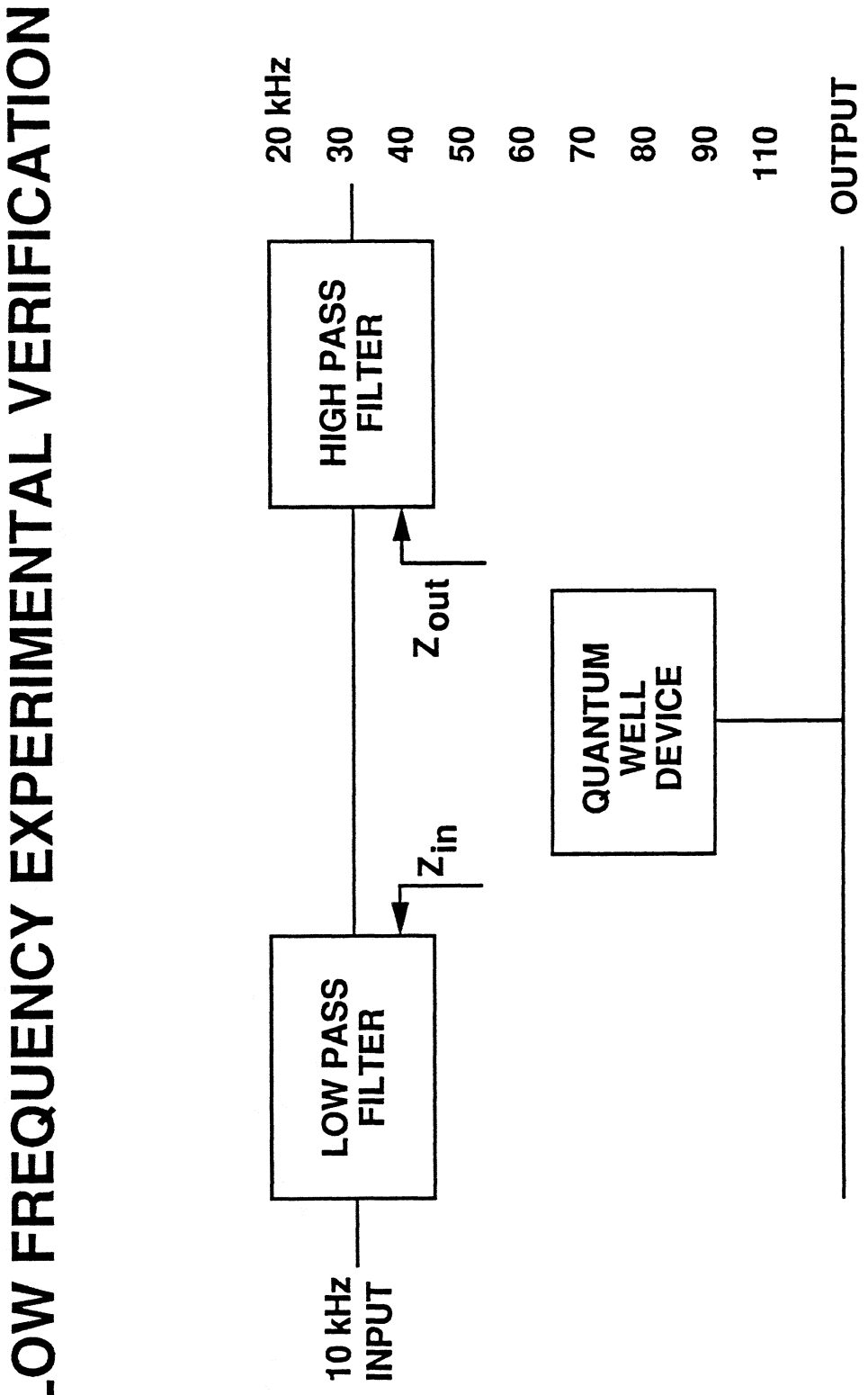
LOW FREQUENCY EXPERIMENTAL VERIFICATION
20 kHz
30
40
50
60
70
80
90
110
OUTPUT
HIGH PASS FILTER
Z_{out}
QUANTUM WELL DEVICE
Z_{in}
LOW PASS FILTER
10 kHz INPUT

LOW FREQUENCY VERIFICATION THEORY AND MEASUREMENT

GaAs/AlAs RTD

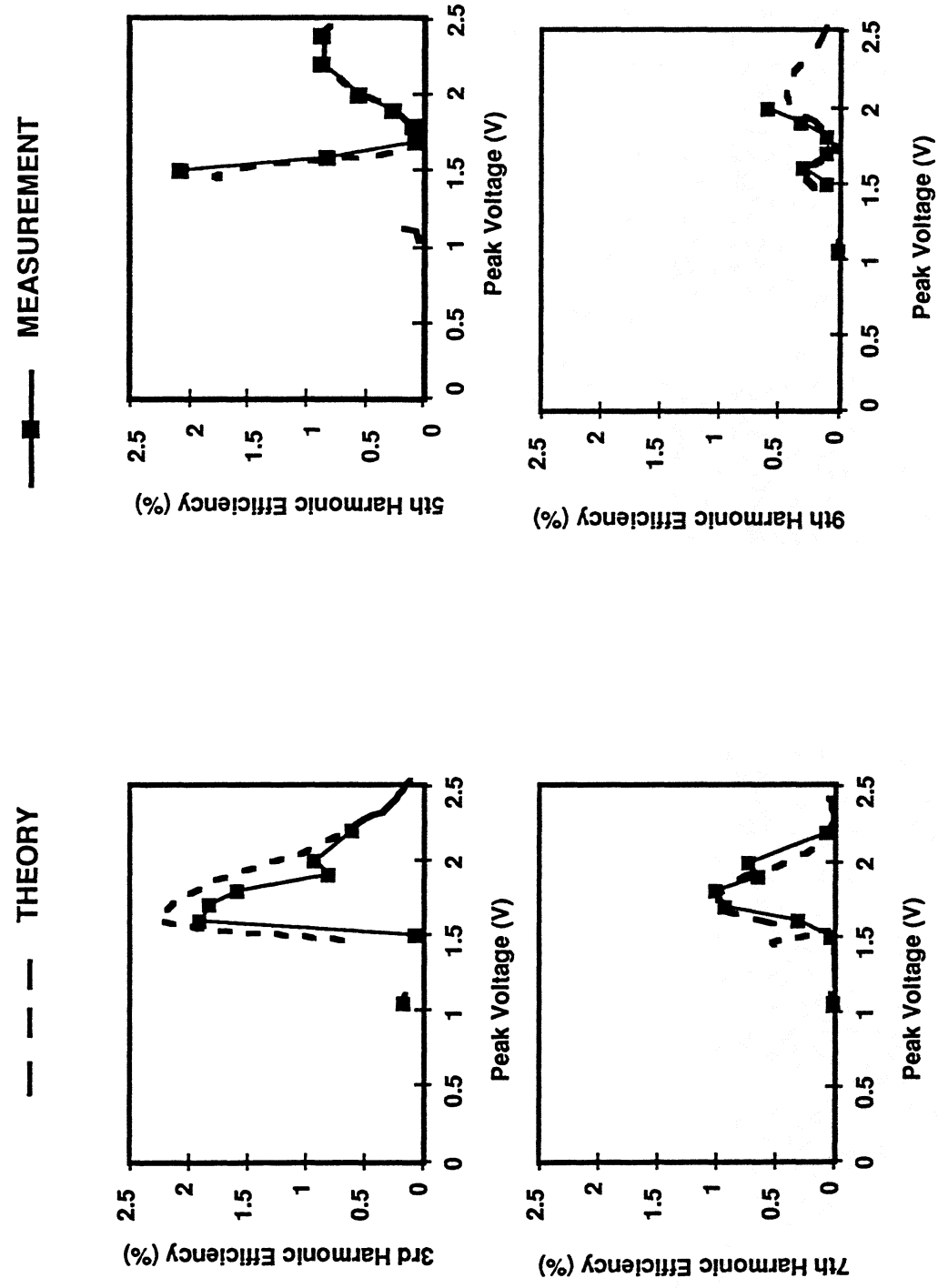

MAF 2-28-90

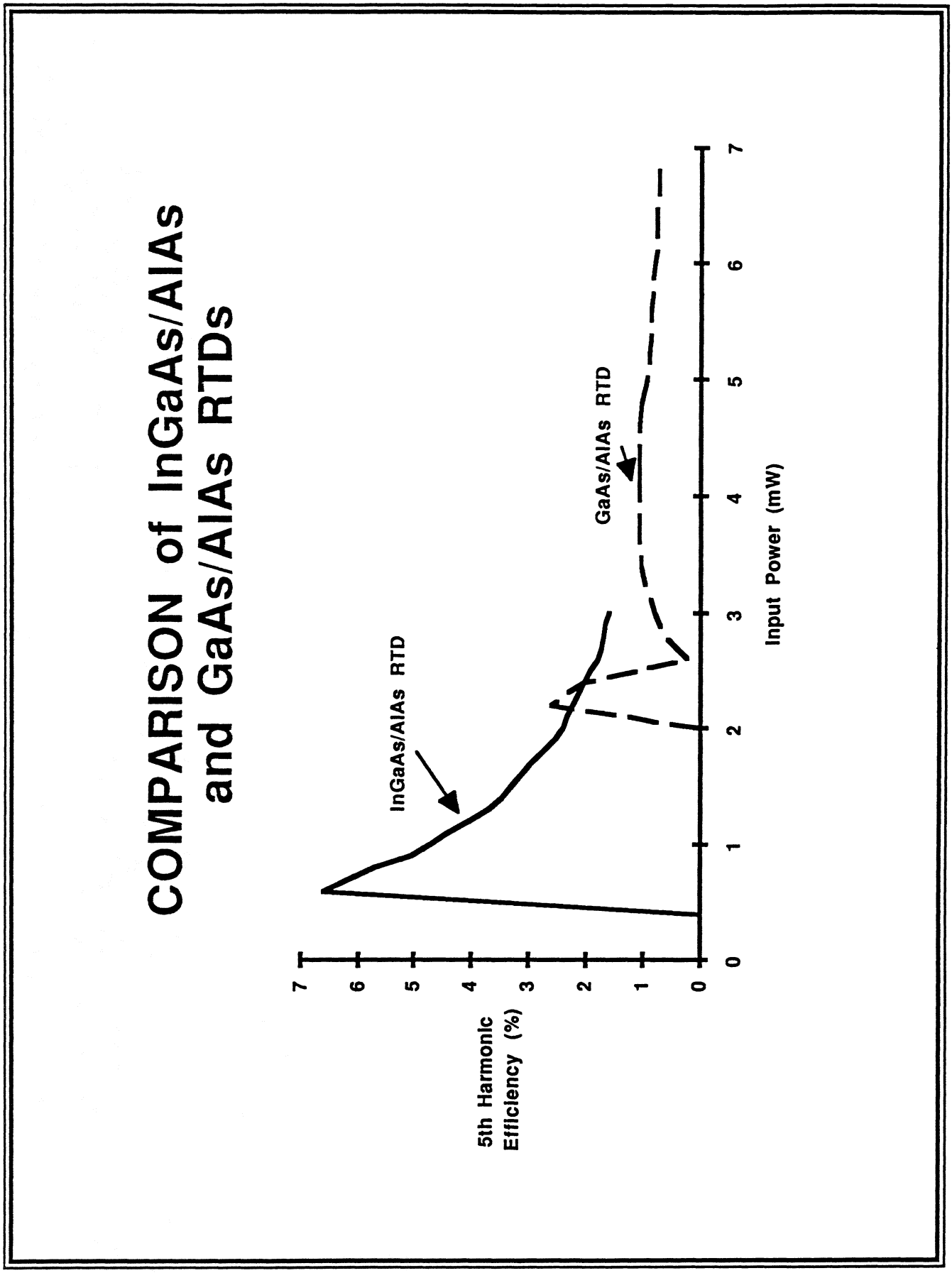
COMPARISON of InGaAs/AlAs and GaAs/AlAs RTDs
InGaAs/AlAs RTD
GaAs/AlAs RTD
5th Harmonic Efficiency (%)
Input Power (mW)
0
1
2
3
4
5
6
7

PARASITICS

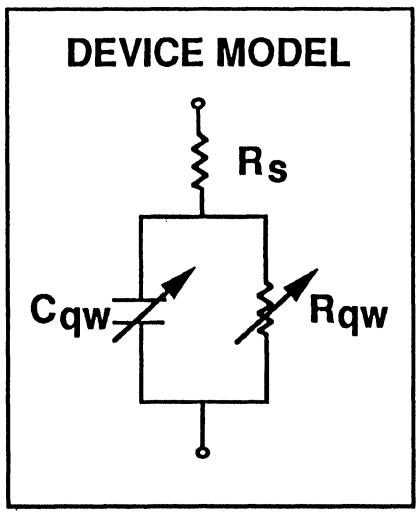

SERIES RESISTANCE

$$R_s = R_{contact} + R_{epi} + R_{spread}$$

$$R_{contact} = \rho_c / A$$

$$R_{epi} = \rho_{epi} L/A$$

$$R_{spread} = \frac{\rho_{substrate}}{2d}$$

SHUNT CAPACITANCE

$$C = \frac{\varepsilon A}{W + D}$$

$$C_{jo} = \frac{\varepsilon A}{W}$$

$$C = \frac{C_{jo}}{\sqrt{1 + \left(\frac{2\varepsilon}{eN_D W^2}\right) V}}$$

Quantum Well Double Barrier Diode C-V Curve

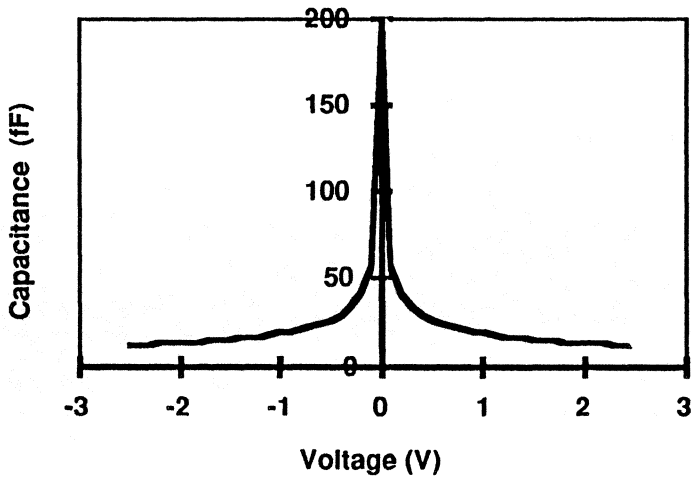

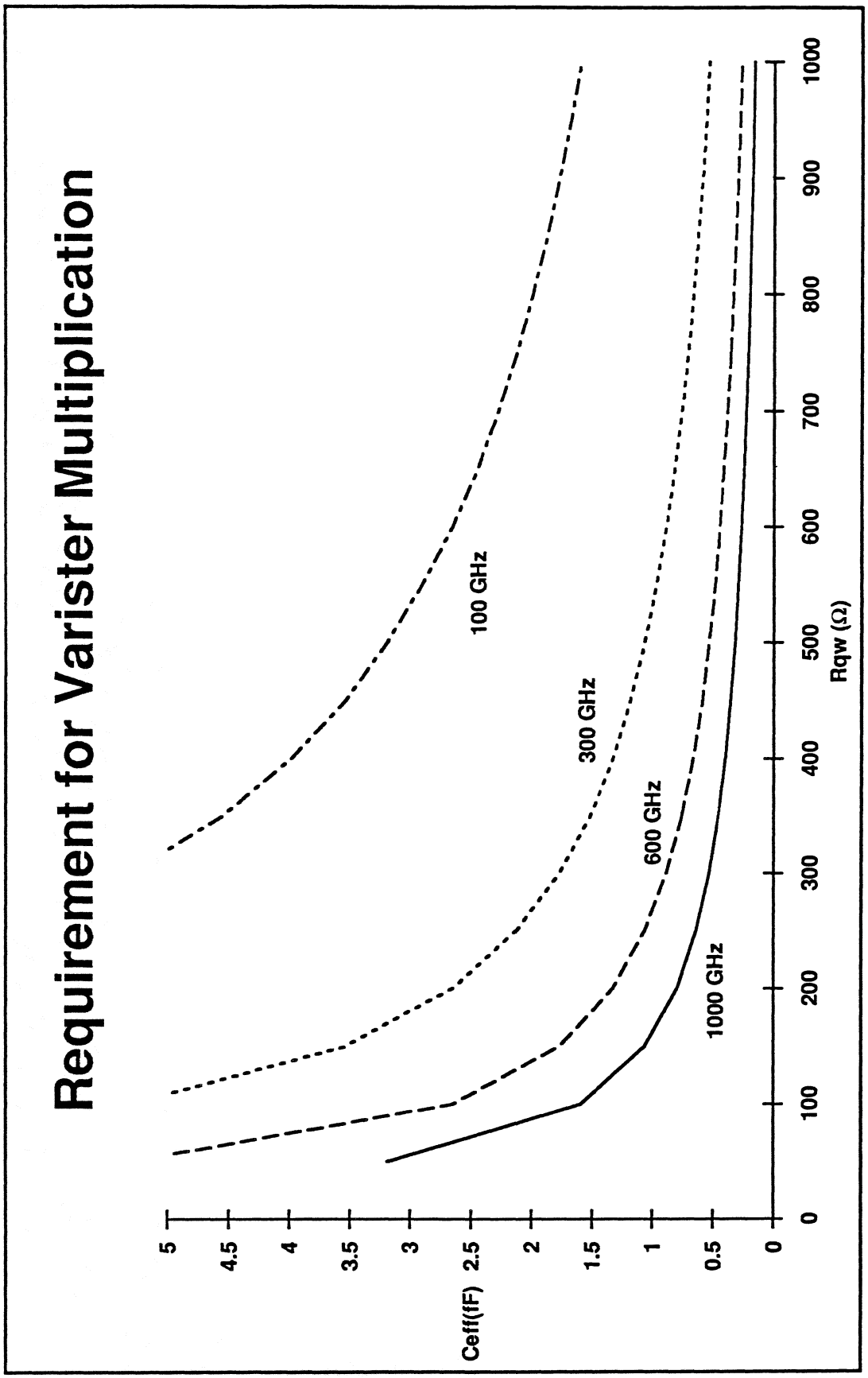
Requirement for Varister Multiplication
100 GHz
300 GHz
600 GHz
1000 GHz
Ceff(fF)
5
4.5
4
3.5
3
2.5
2
1.5
1
0.5
0
Rqw (Ω)
0
100
200
300
400
500
600
700
800
900
1000

MULTIPLIER OPERATION: WAVEFORMS

183 GHz Case

GaAs/AlAs RTD

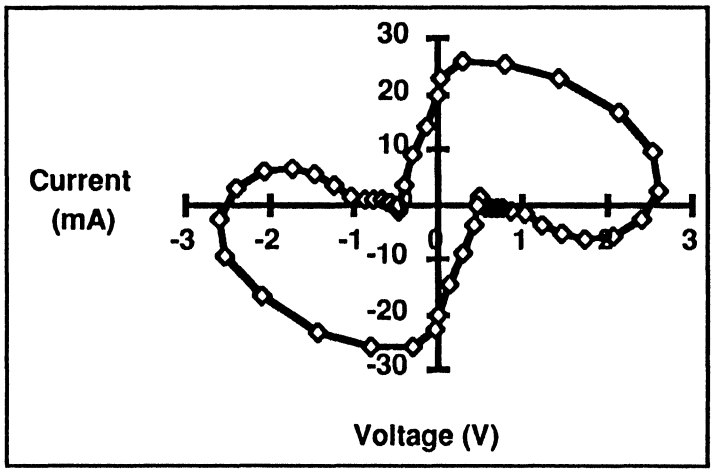

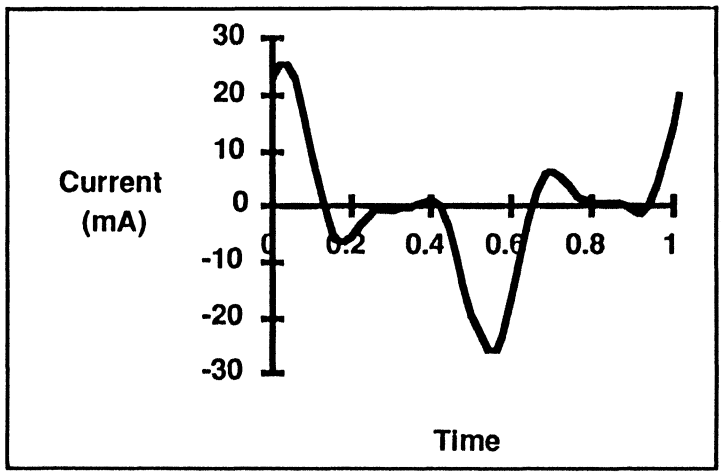

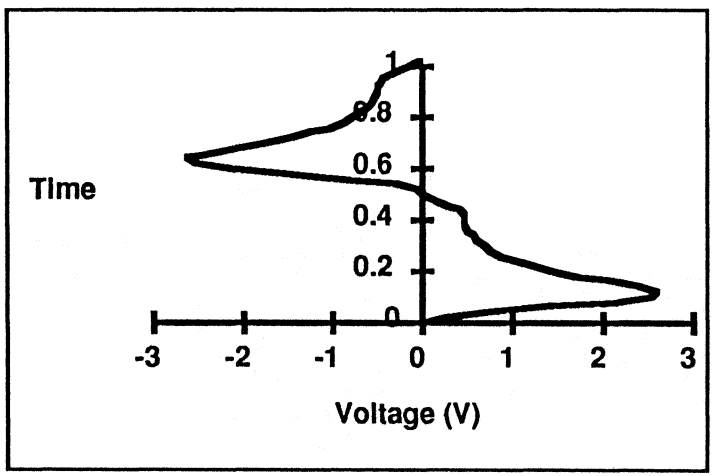

MAF 2-26-90

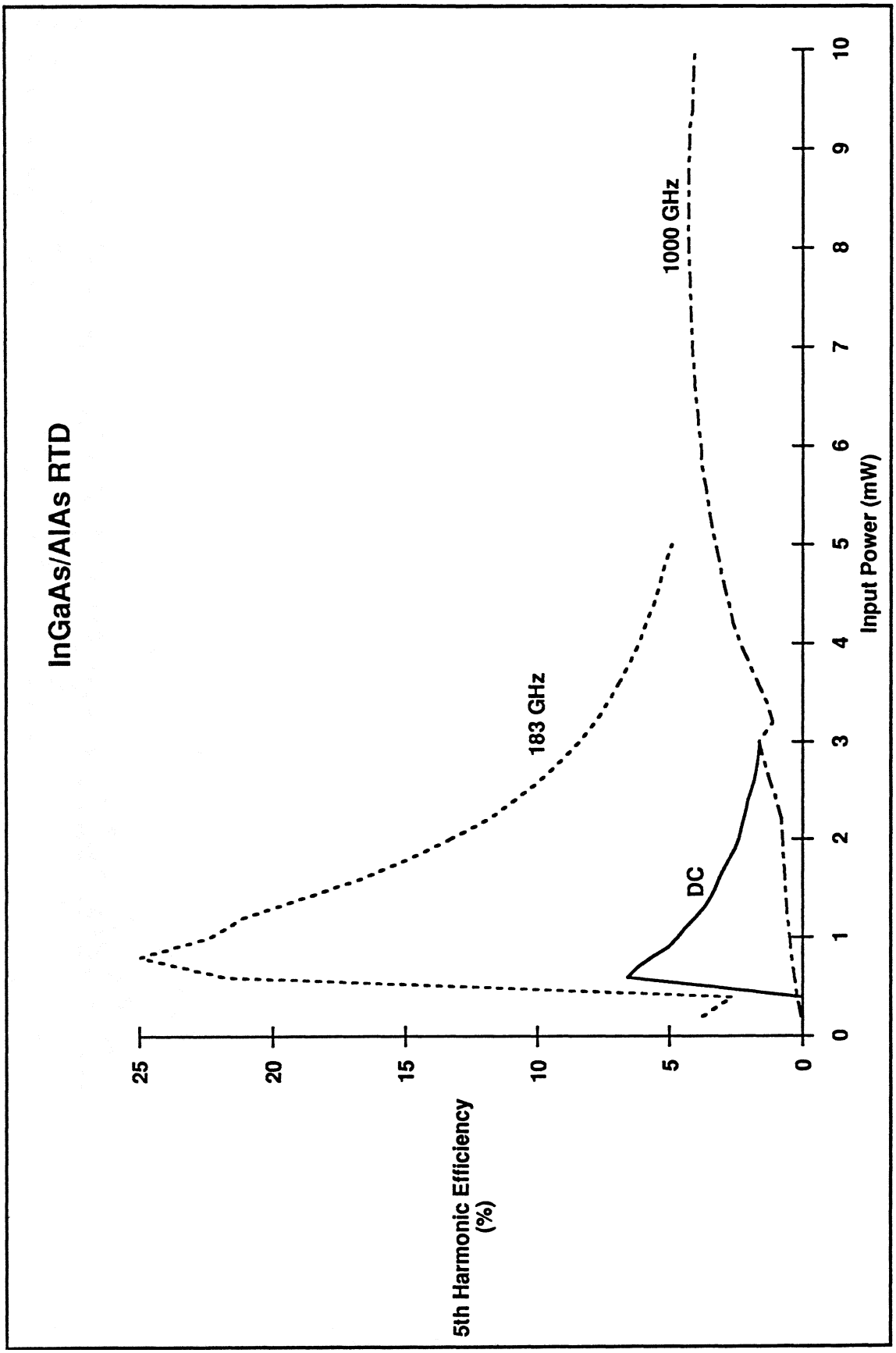
InGaAs/AlAs RTD
1000 GHz
183 GHz
DC
5th Harmonic Efficiency (%)
Input Power (mW)
0
5
10
15
20
25
0
1
2
3
4
5
6
7
8
9
10

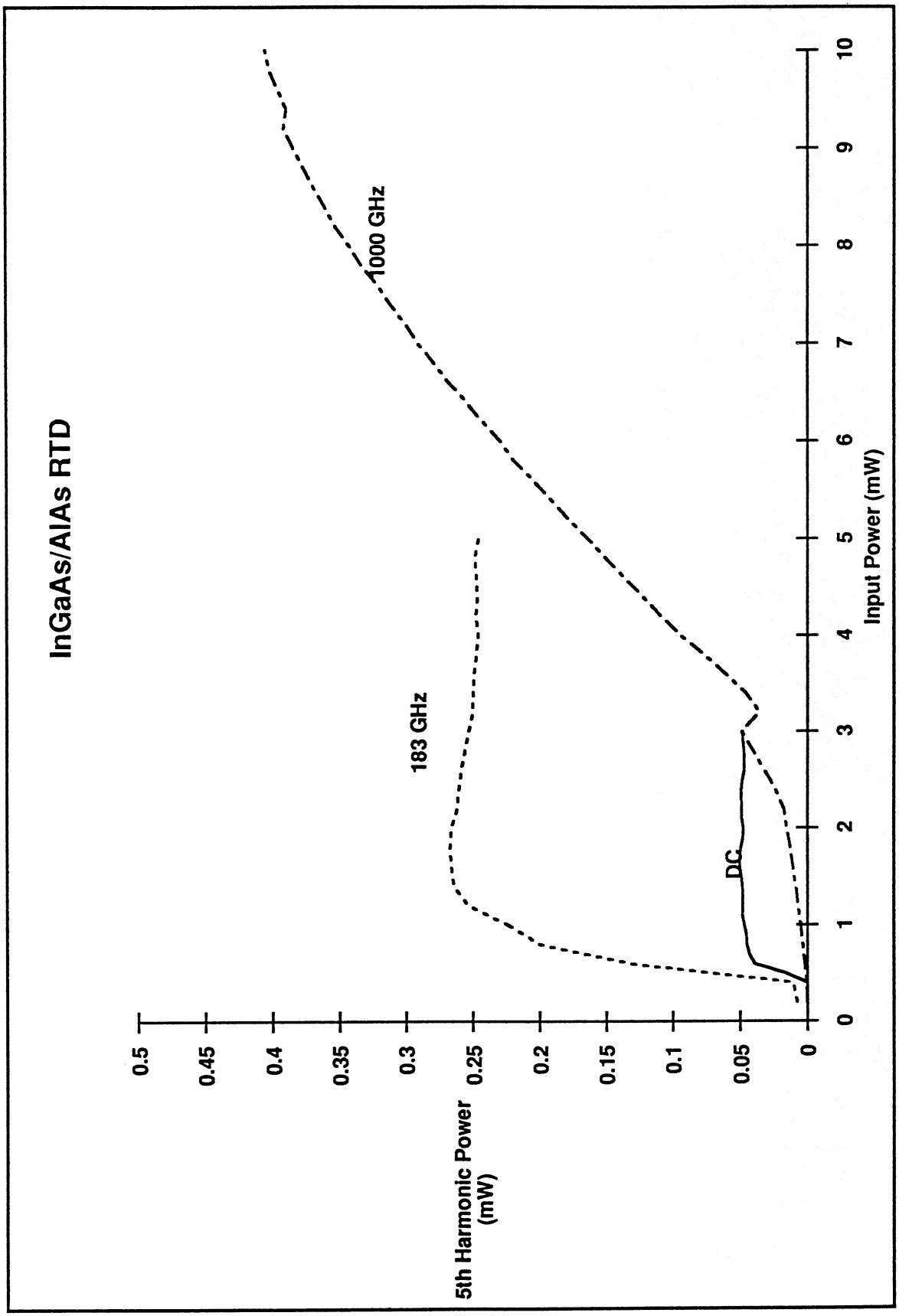
InGaAs/AlAs RTD
1000 GHz
183 GHz
DC
5th Harmonic Power (mW)
Input Power (mW)
0
0.05
0.1
0.15
0.2
0.25
0.3
0.35
0.4
0.45
0.5
0
1
2
3
4
5
6
7
8
9
10

SUMMARY

- Quantum Well Devices are a Promising Millimeter and Submillimeter Wave Frequency Multiplier
  - Tailorable Device
  - High Order Harmonic Generator
  - Odd Harmonics only
- Verified Varister Multiplication at Low Frequencies
  - Large Signal Analysis
  - Experimental Measurement
- Parasitics are Critical to High Frequency Performance
- Quantum Well Devices May Function as Varactors as well

MAF 2-28-90

SIS Receivers for Submillimeter Wave Astronomy

T. G. Phillips, Thomas H. Büttgenbach and Brian N. Ellison

Division of Physics, Mathematics and Astronomy, California Institute of Technology, Pasadena, CA 91125

We report on the development of broadband heterodyne receiver systems used at the Caltech Submillimeter Telescope (CSO) on Mauna Kea, Hawaii. All our receivers utilize Pb alloy superconductor insulator superconductor (SIS) tunnel junctions for the mixing element. Standard electron beam lithography for the masks and the tri–level photoresist stencil technique are used for the fabrication. Typical gap voltages of 2.4 mV and critical current densities of about 7000 A/cm^2 at 4.2 K are achieved. The junction overlap area is between 0.5 and 1.0 μm^2 yielding $\omega R_N C$ = 1 at about 150 GHz. These devices are fabricated in collaboration with Ronald E. Miller at AT&T Bell Laboratories (Figure 1). Receiver noise temperatures of about 65 K (DSB) at 220 GHz and 150 K (DSB) at 350 GHz are achieved.

Waveguide receivers

Two waveguide receivers are currently operated at the CSO (henceforth referred to as the 230 GHz and 345 GHz receiver). The receivers are designed to operate from 190 to 290 GHz (Ellison and Miller 1987) and 280 GHz to 420 GHz (Ellison et al. 1989). A schematic layout of the receiver system is shown in figure 2. The IF is 500 MHz wide and centered at 1.5 GHz. The three stage IF amplifier (Weinreb et al. 1982) has been modified to have a HEMT in its first stage yielding about 2 K noise temperature.

Both mixers have two noncontacting shorts, i.e. a backshort and an E plane tuner, in full height waveguide (Figures 3,4). The shorts are formed from a series of high and low impedance sections. Their design center frequency is 230 GHz and 345 GHz for the two receivers. Originally the SIS junction was mounted on the waveguide wall with an asymmetric filter structure (RF choke). Again the design center frequency for the RF chokes is 230 GHz and 345 GHz. Scale model measurements, which are discussed in more detail below, showed that the desired position for the junction is in the center of the waveguide. Both mixer blocks are now in that configuration.

The 230 GHz receiver has been tested successfully over its design frequency range (Figure 5). The best sensitivity obtained for this receiver is at 220 GHz with a double sideband (DSB) noise temperature of 65 K. Typical values are about 100 K. The 345 GHz receiver has yet not been tested above 370 GHz due to lack of local oscillator power. Its best performance is at 345 GHz with T_{DSB} = 150K and typical value of about 200 K (Figures 6,7). The performance of both receivers is best close to the design center frequency for the RF choke and the sliding shorts and degrades towards both ends of the band. Thus we conclude that the performance of the receivers far away from the center frequency is limited by the RF choke or the sliding shorts rather than the ability to match power into the junction mount. Figure 8 shows a comparison of the best reported noise temperatures of broadband heterodyne receivers. All numbers were converted to single sideband noise temperatures for purposes of comparison.

The waveguide blocks are mounted in hybrid cryostats using CTI closed cycle refrigerators to cool the IF amplifiers and radiation shields to 12 K and a liquid Helium reservoir to cool the mixer blocks (Ellison 1988, Figure 9). The 4 liter liquid helium reservoir has a hold time of 18 days.

Scale Model and theory for the waveguide receivers

The 230 GHz waveguide receiver in its original configuration showed a region of very high noise temperatures at about 250 GHz. We built a scale model of the mixer block (Figure 10) in order to investigate this resonance and the general performance of the two tuner waveguide structure (Büttgenbach et al. 1990). The two tuners allow access to a wide range of impedances as shown by the shaded area in Figure 11. The

dark circles are backshort circles, i.e. the E plane tuner was fixed and the back short moved. Figure 12 shows the performance over the fundamental waveguide band of the model. The transmission data was obtained by sending power into the waveguide port, where the horn antenna would be located in the full size mixer and taken out with the probes at the junction position. The tuners were optimized for each data point. Comparing Figure 12a with 12b shows that the transmission is highest where the area of accessible impedance values in the Smith chart is largest. Figure 12c demonstrates this by depicting the relative tuning area, i.e. the ratio of accessible tuning area to total area of the Smith chart. The qualitative behavior of the transmission and relative tuning area as a function of frequency is identical. Deducing the efficiency of a mount geometry by comparing the measured embedding impedances with the desired impedance for a device can be misleading. This is well demonstrated at the resonance frequency at 6.4 GHz. Depending on what one assumes for the embedding impedance of the SIS junction one could come to the conclusion that the SIS junction is well matched to the incoming radiation. As apparent from figure 12b this is not the case. The relative tuning area, however, is much more significant. This is due to the fact that a tuner has a zero reflection coefficient for a non propagating mode. The large range of impedance values available when moving the tuners allows good coupling to the propagating mode in the waveguide, which contains the energy of the incoming radiation.

Figure 13 shows the relative tuning area as a function of junction position in the waveguide. The resonance strength decreases significantly when the junction is centered. Numerical simulations (Büttgenbach et al. 1990) of the same waveguide structure showed the same effect. This resonance is due to cross modal coupling to all n=1 modes caused by the junction mount as represented by an obstacle in the waveguide. By centering the gap, i.e. the position where the junction is in the waveguide, the coupling to the n=1 modes can be eliminated and therefore the strength of the resonance reduced. This has been confirmed in the 230 GHz receiver, when the SIS junction was moved into the center of the waveguide. The noise temperature at the resonance frequency (250 GHz) is now only a factor of 1.5 higher than the average value in the vicinity.

According to theory the resonance frequency is inversely proportional to the waveguide height. The effective waveguide height at the mount is somewhat higher than the geometric height due to the dielectric substrate of the junction mount. The decrease of resonance frequency due to the substrate dielectric has been investigated and found to be in excellent agreement with the measured resonance frequency of the 230 GHz receiver.

Fabrication of reduced height waveguide components in the submillimeter region is very difficult, making it advantageous to maintain full height waveguide. However, a slight reduction in waveguide height ($\approx$ 20%) will push the resonance out of the frequency range of interest without increasing machining difficulty significantly.

Figure 14 shows a lumped element equivalent circuit derived from the theory. L_1 and C_1 correspond to the reactance due to the coupling to the n=1 modes. C and L contain the reactances of the coupling to all other modes, the lead inductances, the junction capacitance and the choke reactance. At the resonance frequency, i.e. where L_1 and C_1 resonate, the junction is shorted.

Quasi optical receivers

We are investigating a new technique of coupling the radiation from a telescope into an SIS detector by means of planar antennas instead of waveguide structures. This technique avoids the difficulty of fabricating waveguide structures in the submillimeter band, which become very lossy. Furthermore there is the potential for a receiver operating over several octaves. A major disadvantage is the lack of tuning capability thus requiring SIS junctions with low $\omega R_N C$ products at the operating frequency. We use a planar antenna mounted on a hyperhemispherical lens (Figure 15) as first suggested by Rutledge. Initial receiver tests (Wengler et al. 1985) using bow–tie antennas were promising. A continued investigation (Büttgenbach et al. 1989) using spiral antennas (Figures 16,17) gave noise temperature results that were almost as good as waveguide systems below 400 GHz and considerably better from 400 GHz to 760 GHz. These results were obtained with one single instrument. However, the coupling efficiency of the receiver to the light from the telescope was rather poor ($\approx$ 30%). This is due to the extremely fast beam launched by the spiral antenna and the problems associated with controlling that beam. We are currently investigating the optics for planar antenna structure receivers with the goal of improving the coupling efficiencies.

References

Büttgenbach, T.H., Groesbeck, T.D., and Ellison, B.N., "A Scale Mixer Model for SIS Waveguide Receivers," Int. J. of IR and MM Waves, vol. 11, no. 1, January 1990.

Büttgenbach, T.H., Miller, R.E., Wengler, M.J., Watson, D.M., Phillips, T.G., "A Broad-Band Low-Noise SIS Receiver for Submillimeter Astronomy, IEEE Trans. Microwave Theory Tech., vol. MTT-36, December 1988.

Ellison, B.N., and Miller, R.E., "A Low Noise 230 GHz Receiver," Int. J. of IR and MM Waves, vol. 8, no. 6, June 1987.

Ellison, B.N., Schaffer, P.L., Schaal, W., Vail, D., and Miller, R.E., "A 345 GHz Receiver for Radio Astronomy," Int. J. of IR and MM Waves, vol. 10, no. 8, 1989.

Ellison, B.N., "Hybrid liquid helium cryostat for radio astronomy use", Cryogenics, vol. 28, November 1988.

Weinreb, S., Fenstermacher, D.L., and Harris, R.W., "Ultra-low-noise 1.2 to 1.7 GHz cooled GaAs-Fet amplifiers", IEEE Trans. Microwave Theory Tech., vol. MTT-30, June 1982.

Wengler, M.J., Woody, D.P., Miller, R.E., and Phillips, T.G., "A Low Noise Receiver for Millimeter and Submillimeter Wavelength," Int. J. of IR and MM Waves, vol. 6, pp. 697-706, 1985.

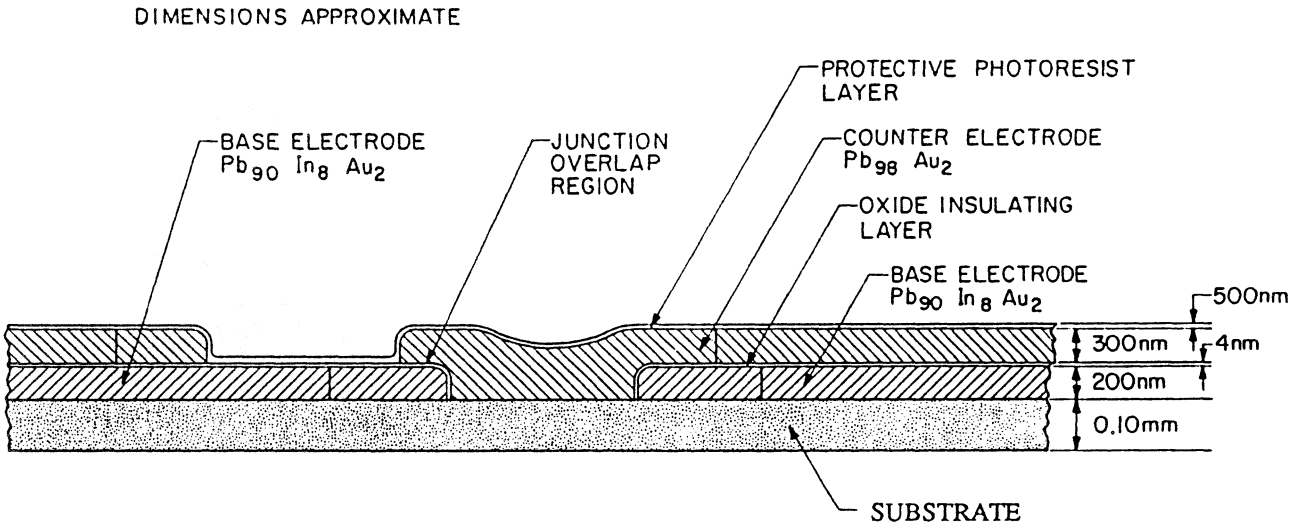
DIMENSIONS APPROXIMATE
PROTECTIVE PHOTORESIST LAYER
BASE ELECTRODE Pb_{90} In_8 Au_2
JUNCTION OVERLAP REGION
COUNTER ELECTRODE Pb_{98} Au_2
OXIDE INSULATING LAYER
BASE ELECTRODE Pb_{90} In_8 Au_2
500nm
300nm
4nm
200nm
0.10mm
SUBSTRATE

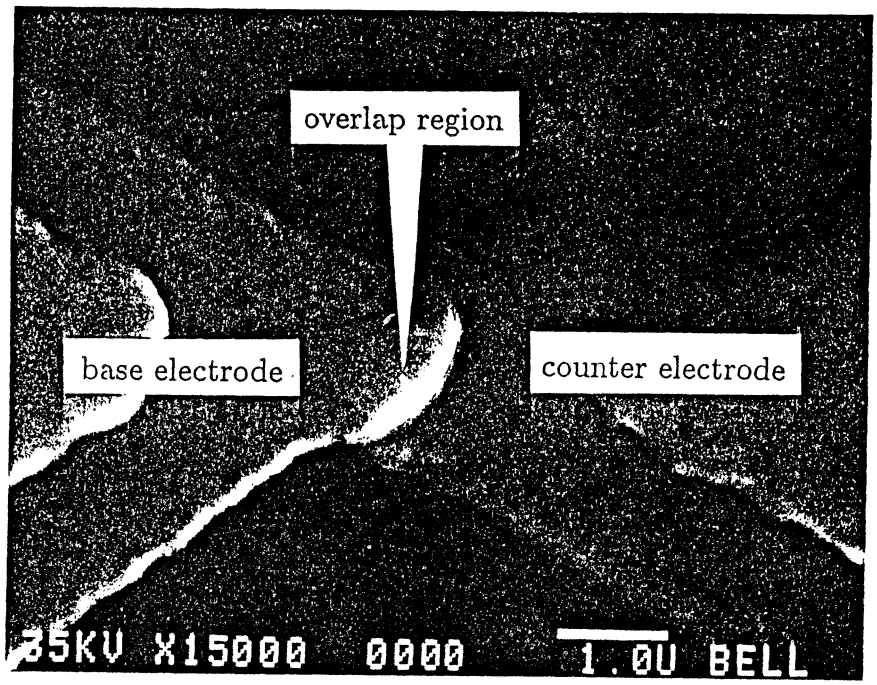
overlap region
base electrode
counter electrode
35KV X15000 0000
1.0U BELL

Figure 1

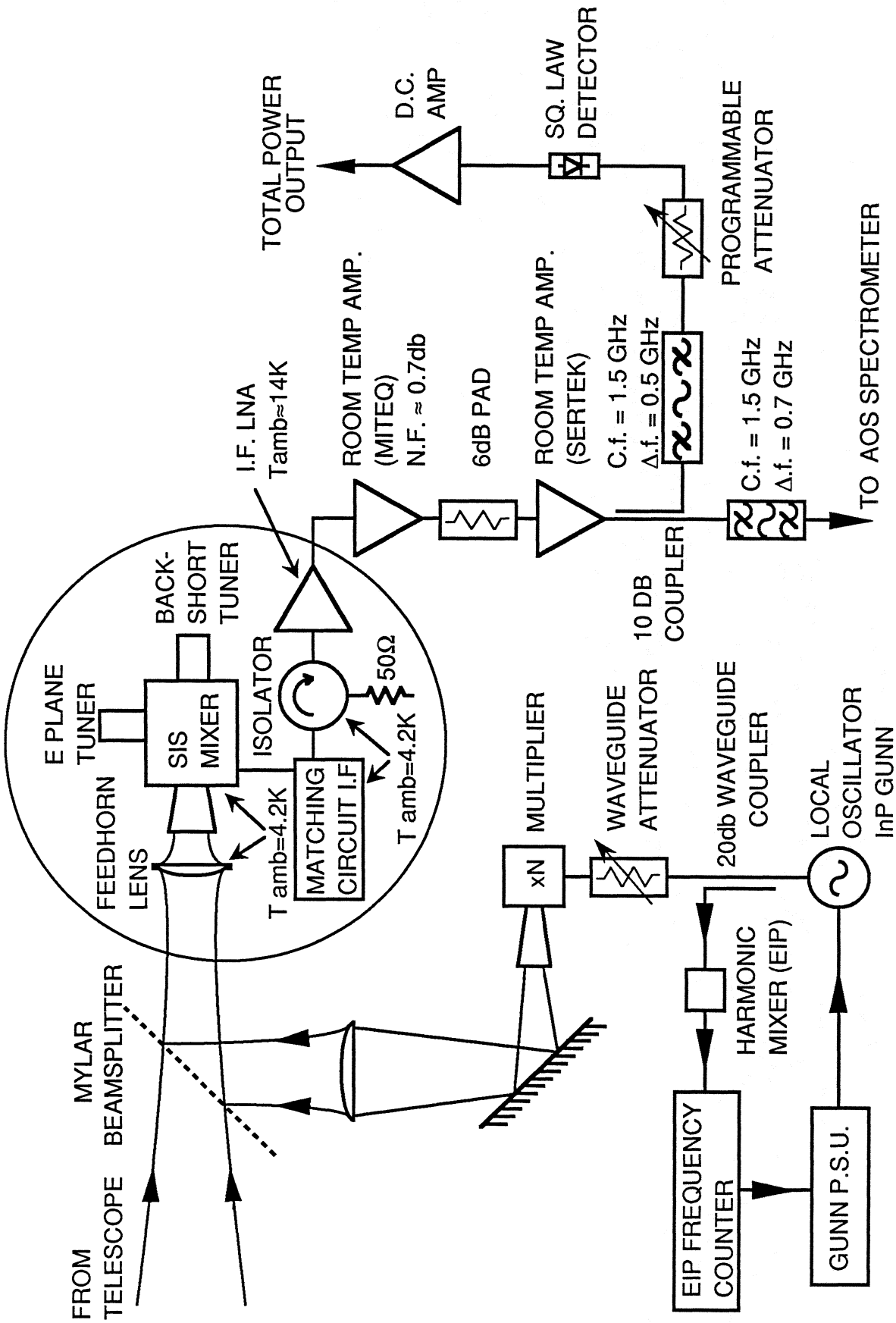
FROM TELESCOPE
MYLAR BEAMSPLITTER
FEEDHORN LENS
E PLANE TUNER
BACK-SHORT TUNER
SIS MIXER
ISOLATOR
50Ω
T amb=4.2K
MATCHING CIRCUIT I.F
T amb=4.2K
I.F. LNA Tamb≈14K
ROOM TEMP AMP. (MITEQ) N.F. ≈ 0.7db
6dB PAD
ROOM TEMP AMP. (SERTEK)
10 DB COUPLER
C.f. = 1.5 GHz Δ.f. = 0.5 GHz
C.f. = 1.5 GHz Δ.f. = 0.7 GHz
PROGRAMMABLE ATTENUATOR
SQ. LAW DETECTOR
D.C. AMP
TOTAL POWER OUTPUT
TO AOS SPECTROMETER
MULTIPLIER
xN
WAVEGUIDE ATTENUATOR
20db WAVEGUIDE COUPLER
LOCAL OSCILLATOR InP GUNN
HARMONIC MIXER (EIP)
EIP FREQUENCY COUNTER
GUNN P.S.U.

Figure 2

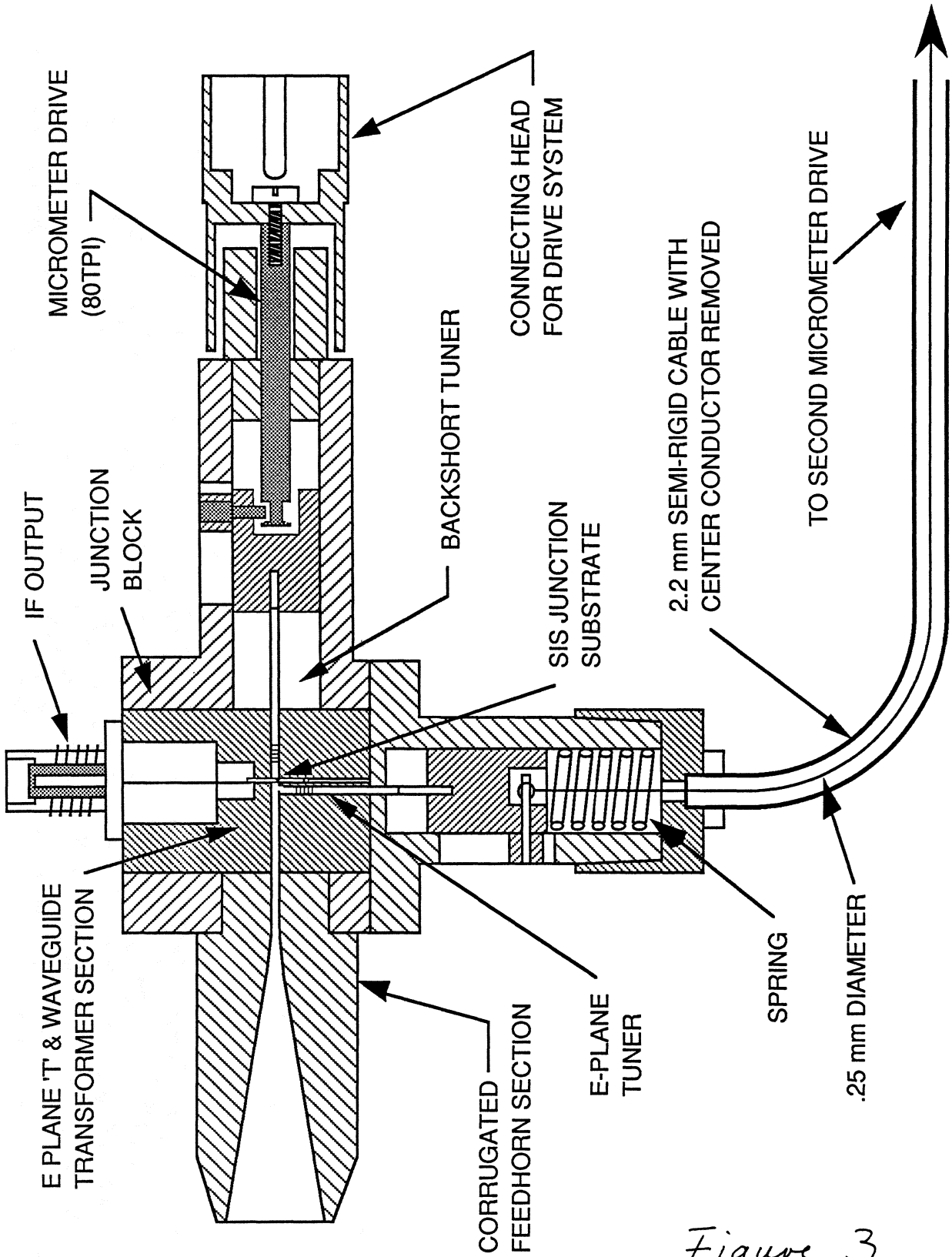
MICROMETER DRIVE
(80TPI)
CONNECTING HEAD
FOR DRIVE SYSTEM
IF OUTPUT
JUNCTION
BLOCK
BACKSHORT TUNER
SIS JUNCTION
SUBSTRATE
2.2 mm SEMI-RIGID CABLE WITH
CENTER CONDUCTOR REMOVED
TO SECOND MICROMETER DRIVE
E PLANE 'T' & WAVEGUIDE
TRANSFORMER SECTION
CORRUGATED
FEEDHORN SECTION
E-PLANE
TUNER
SPRING
.25 mm DIAMETER

Figure 3

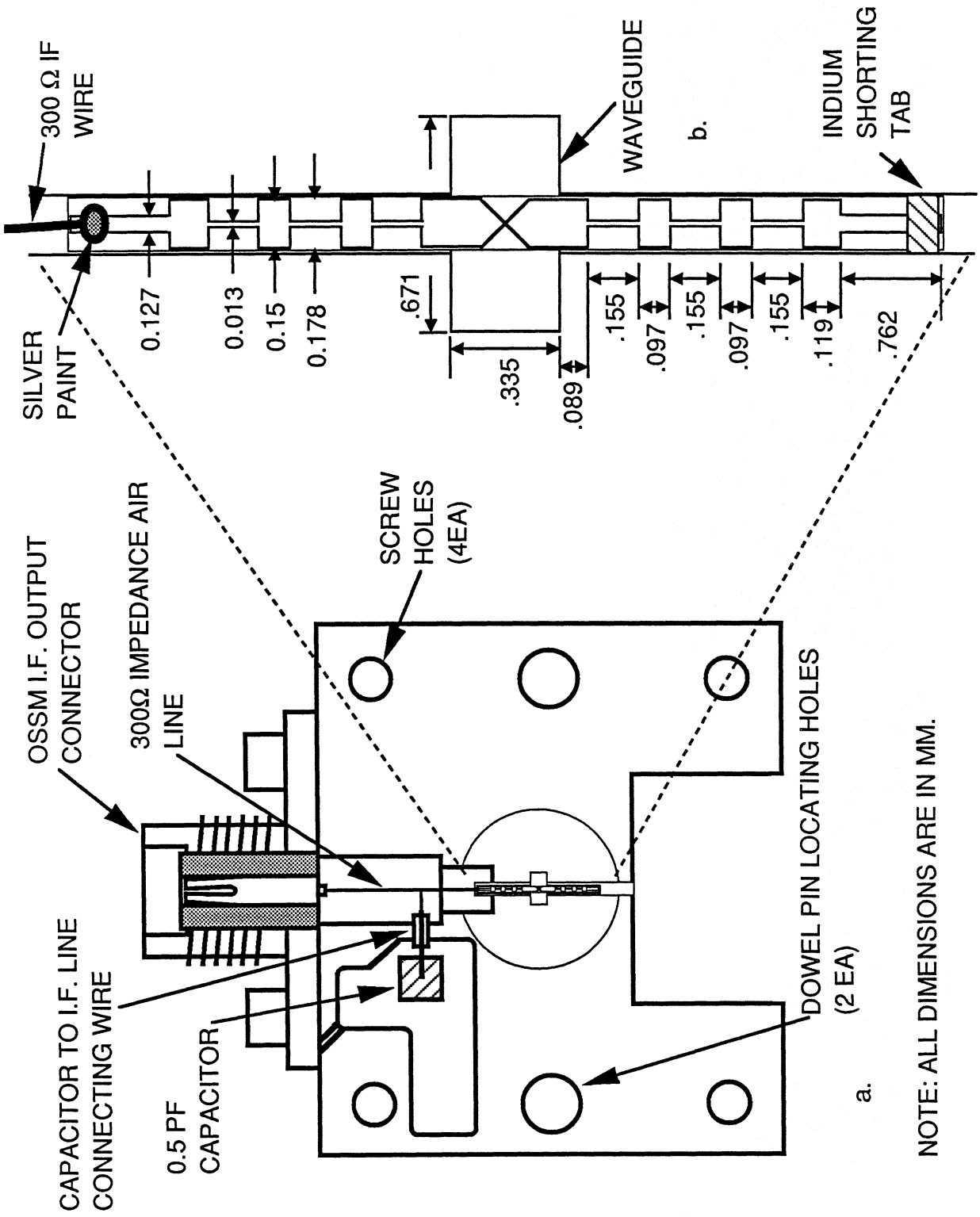
300 Ω IF WIRE
WAVEGUIDE
INDIUM SHORTING TAB
b.
SILVER PAINT
0.127
0.013
0.15
0.178
.671
.335
.089
.155
.097
.155
.097
.155
.119
.762
OSSM I.F. OUTPUT CONNECTOR
300Ω IMPEDANCE AIR LINE
SCREW HOLES (4EA)
CAPACITOR TO I.F. LINE CONNECTING WIRE
0.5 PF CAPACITOR
DOWEL PIN LOCATING HOLES (2 EA)
a.
NOTE: ALL DIMENSIONS ARE IN MM.

Figure 4

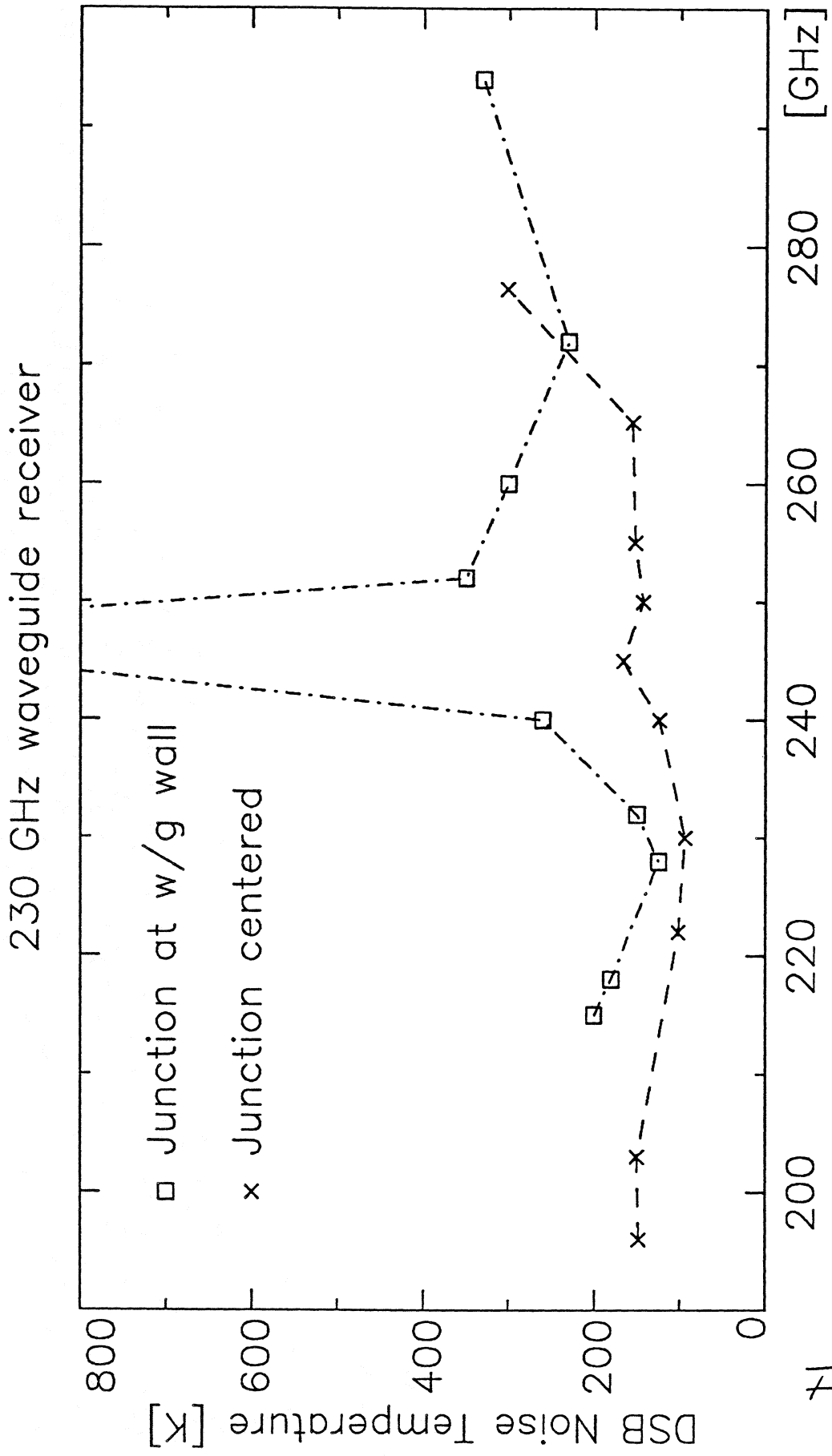
230 GHz waveguide receiver
□ Junction at w/g wall
× Junction centered
DSB Noise Temperature [K]
0
200
400
600
800
Frequency [GHz]
200
220
240
260
280
[GHz]

Figure 5

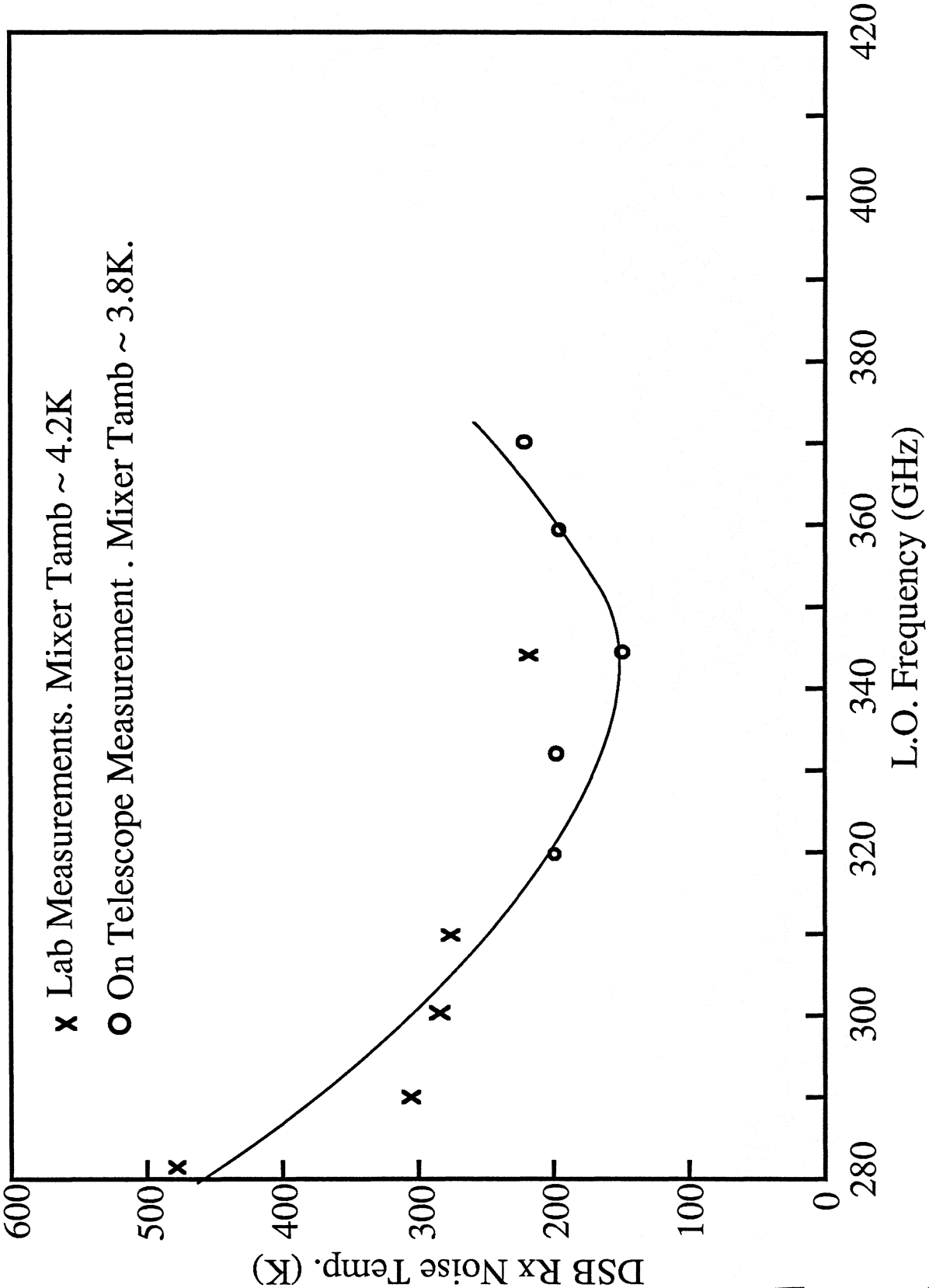
x Lab Measurements. Mixer Tamb ~ 4.2K
o On Telescope Measurement . Mixer Tamb ~ 3.8K.
DSB Rx Noise Temp. (K)
L.O. Frequency (GHz)
600
500
400
300
200
100
0
280
300
320
340
360
380
400
420

Figure 6

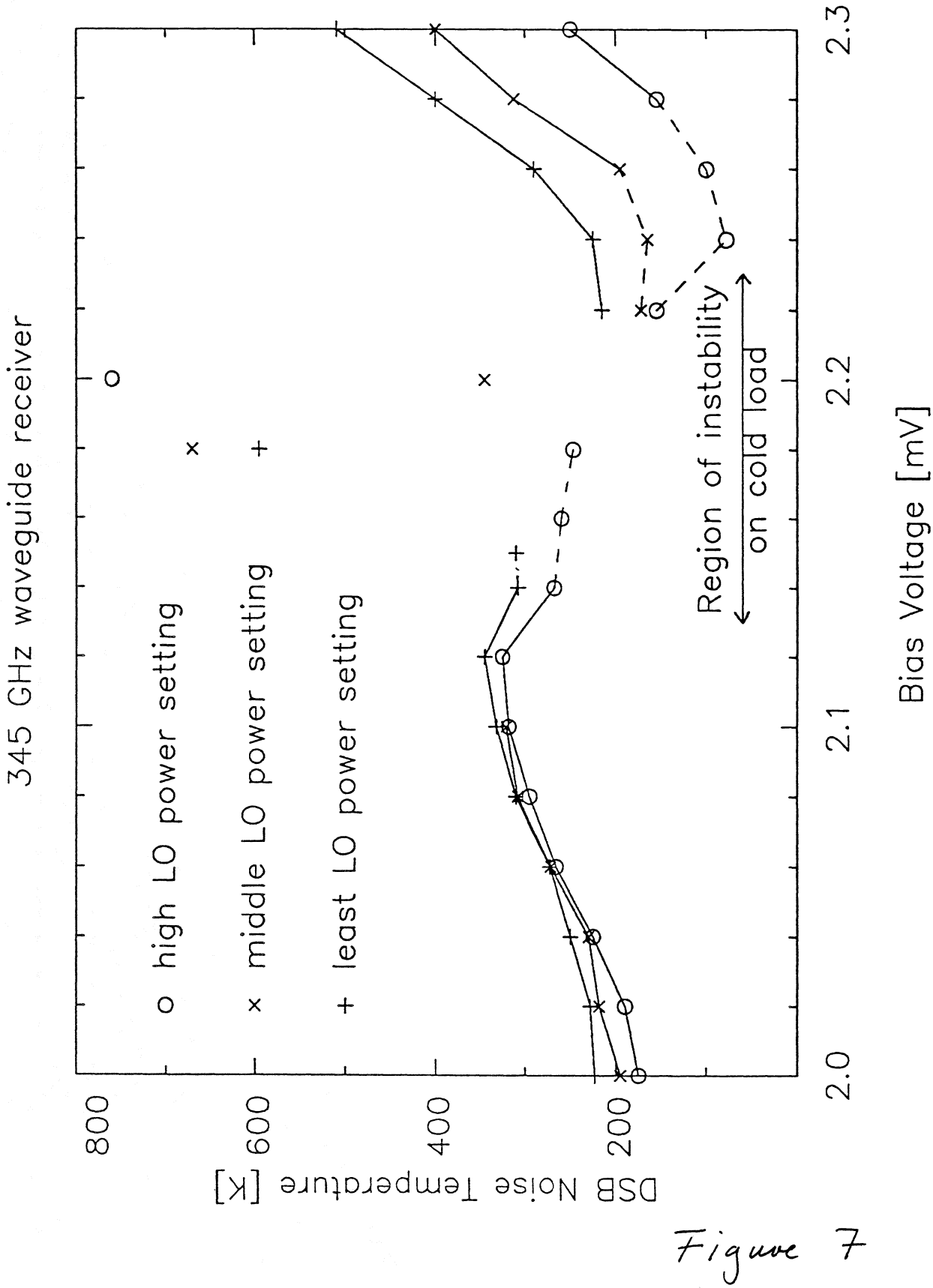
345 GHz waveguide receiver
o high LO power setting
x middle LO power setting
+ least LO power setting
Region of instability
on cold load
DSB Noise Temperature [K]
Bias Voltage [mV]
800
600
400
200
2.0
2.1
2.2
2.3

Figure 7

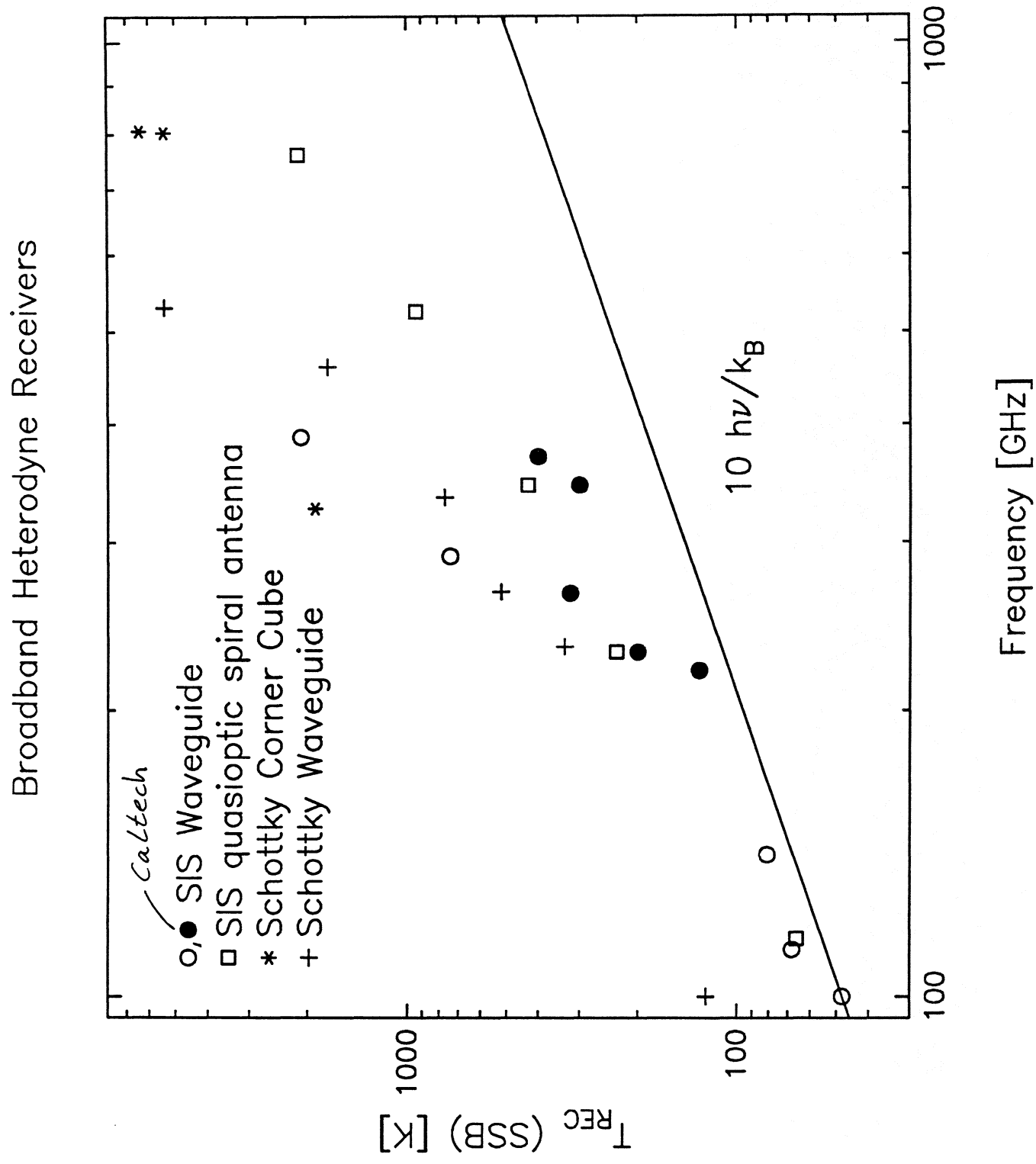
Broadband Heterodyne Receivers
Caltech
SIS Waveguide
SIS quasioptic spiral antenna
Schottky Corner Cube
Schottky Waveguide
10 hν/k_B
T_REC (SSB) [K]
Frequency [GHz]
1000
100
1000
100

Figure 8

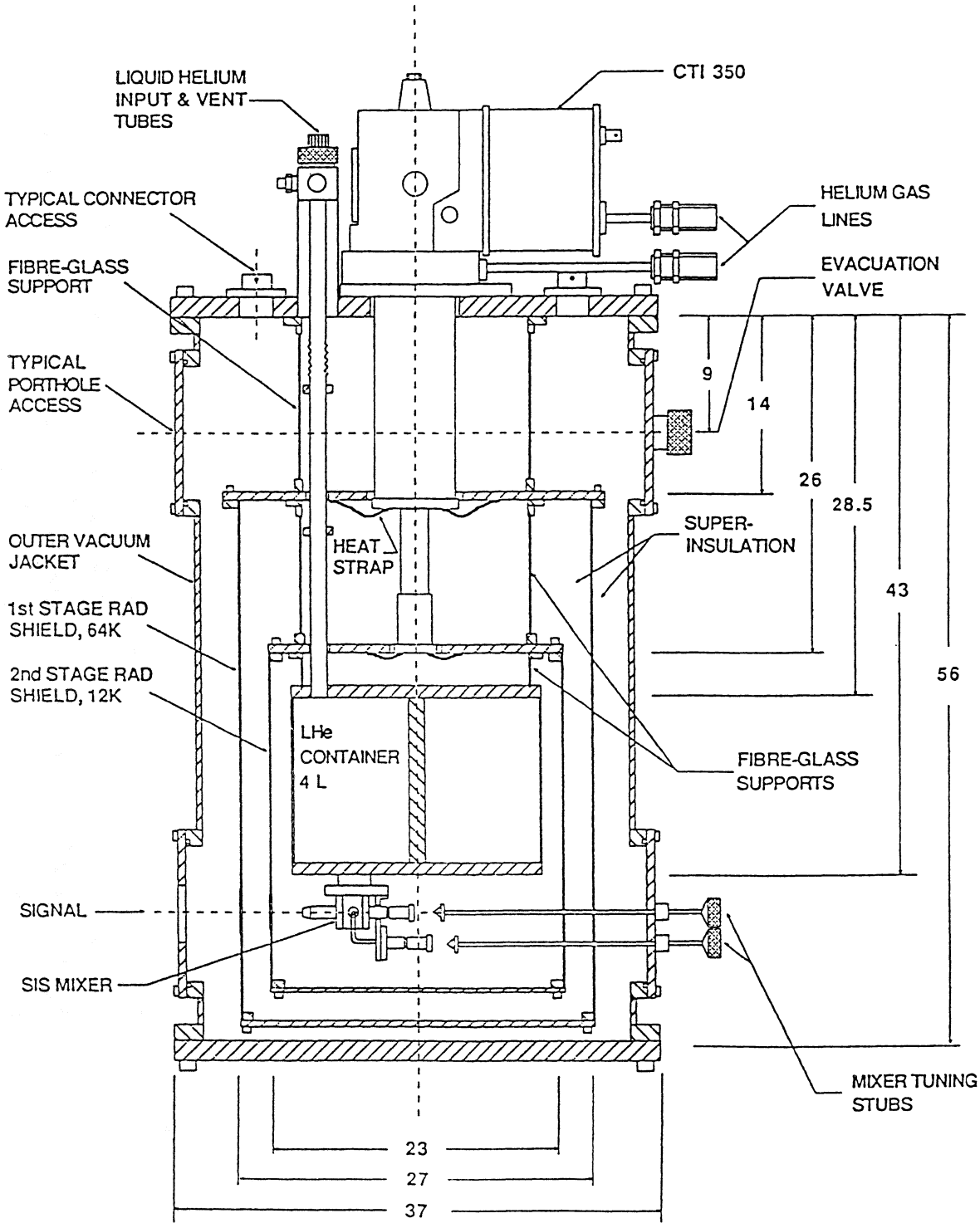
LIQUID HELIUM INPUT & VENT TUBES
CTI 350
TYPICAL CONNECTOR ACCESS
HELIUM GAS LINES
FIBRE-GLASS SUPPORT
EVACUATION VALVE
TYPICAL PORTHOLE ACCESS
9
14
26
28.5
43
56
SUPER-INSULATION
OUTER VACUUM JACKET
HEAT STRAP
1st STAGE RAD SHIELD, 64K
2nd STAGE RAD SHIELD, 12K
LHe CONTAINER 4 L
FIBRE-GLASS SUPPORTS
SIGNAL
SIS MIXER
MIXER TUNING STUBS
23
27
37

Figure 9

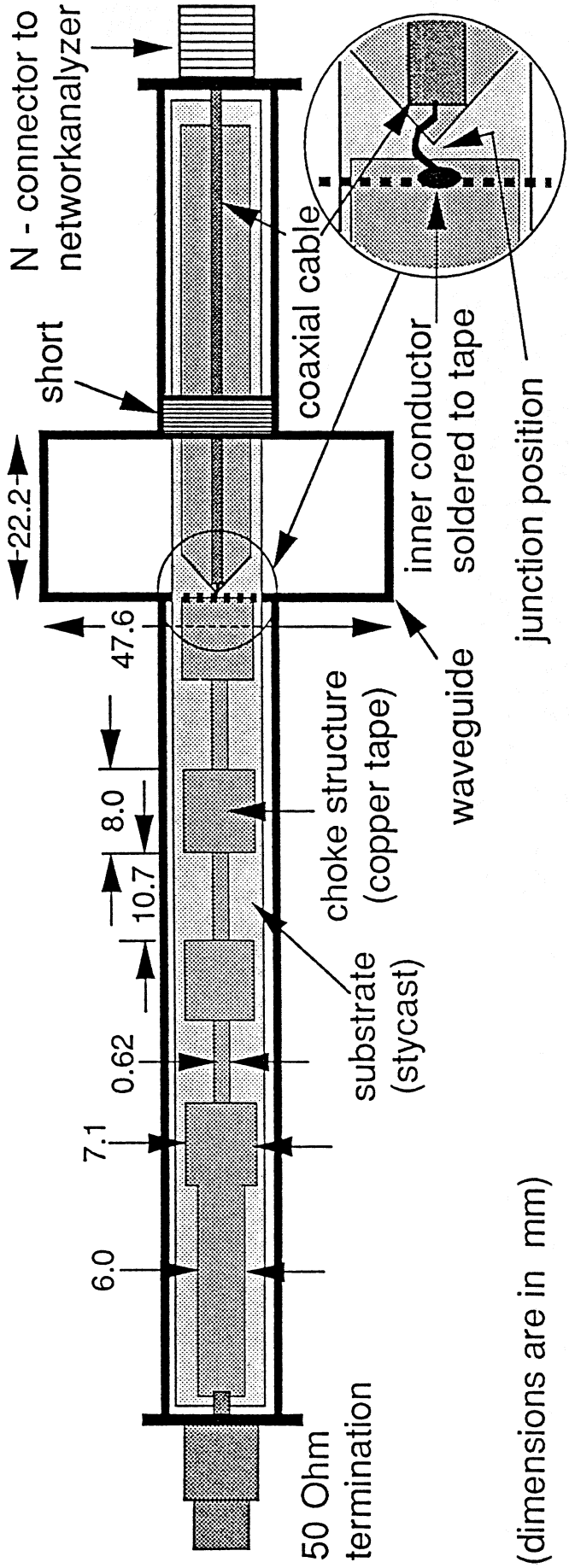
N - connector to networkanalyzer
short
coaxial cable
inner conductor soldered to tape
junction position
22.2
47.6
waveguide
choke structure (copper tape)
8.0
10.7
substrate (stycast)
0.62
7.1
6.0
50 Ohm termination
(dimensions are in mm)

Figure 10

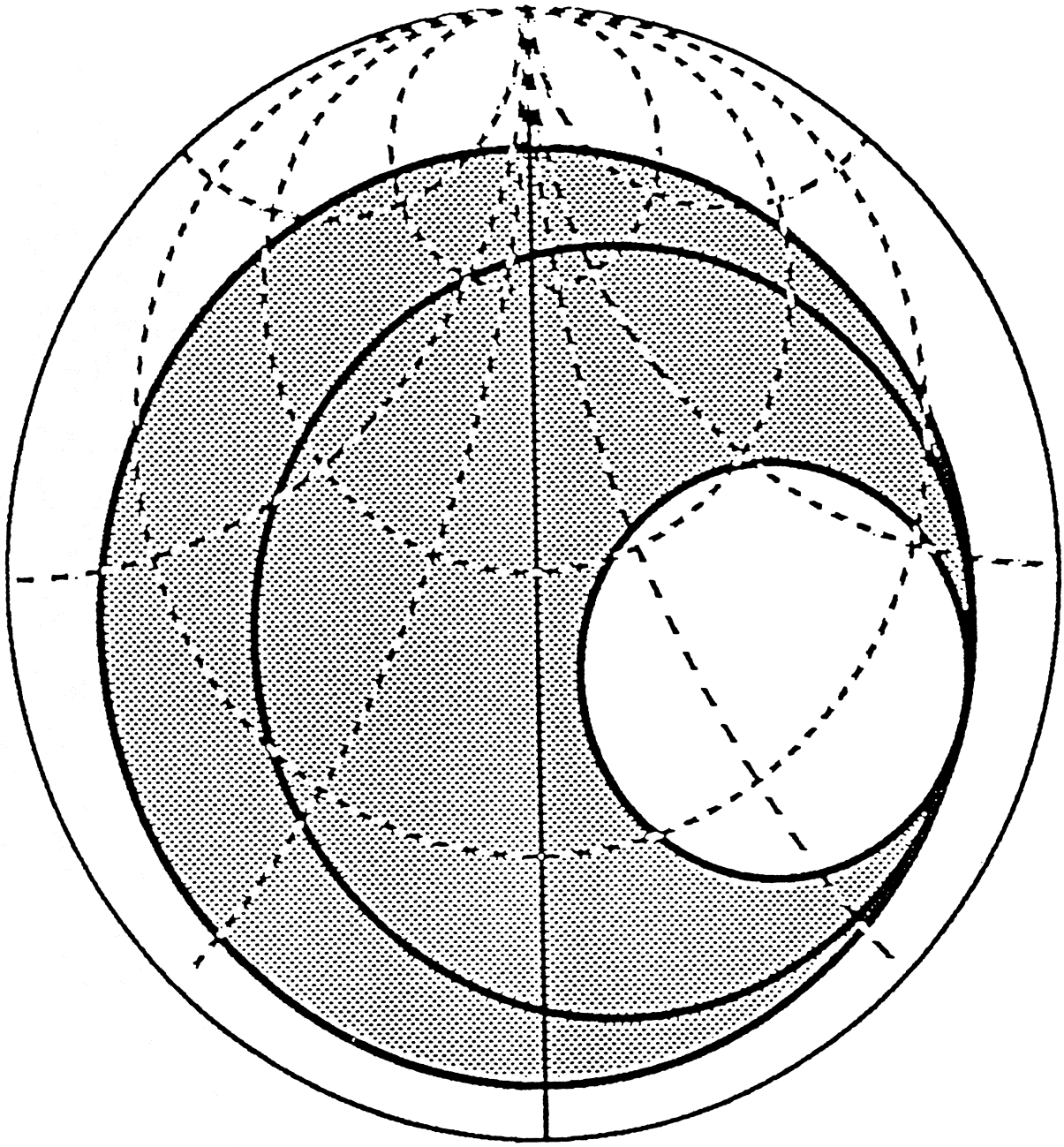

Smith chart normalized to 50Ω

Figure 11

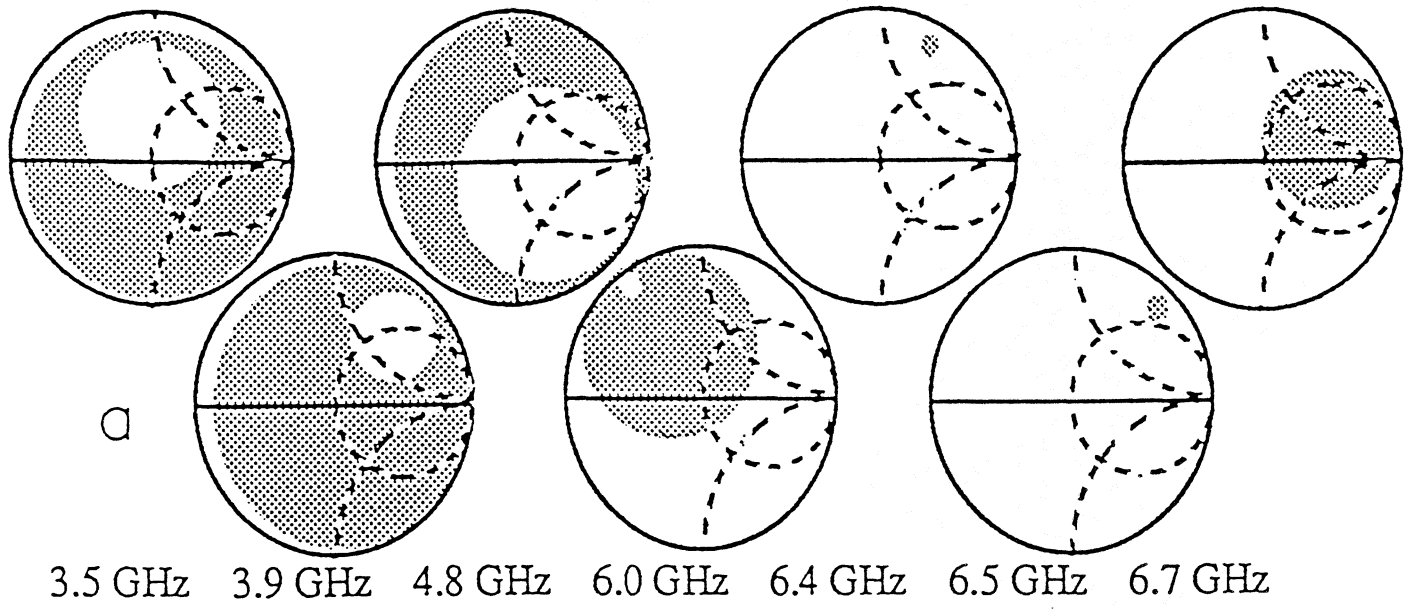
a
3.5 GHz
3.9 GHz
4.8 GHz
6.0 GHz
6.4 GHz
6.5 GHz
6.7 GHz

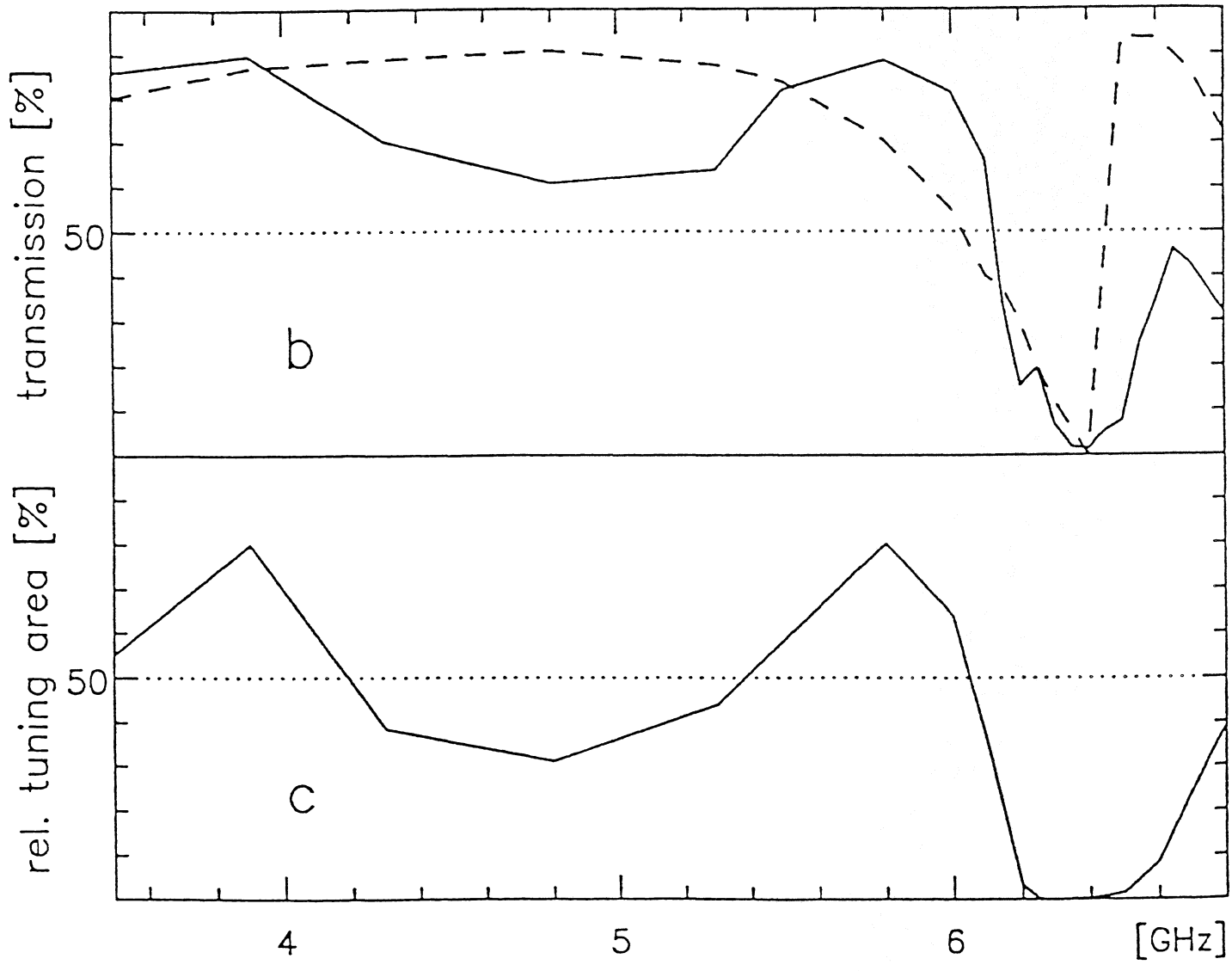
transmission [%]
50
b
rel. tuning area [%]
50
c
4
5
6
[GHz]

Figure 12

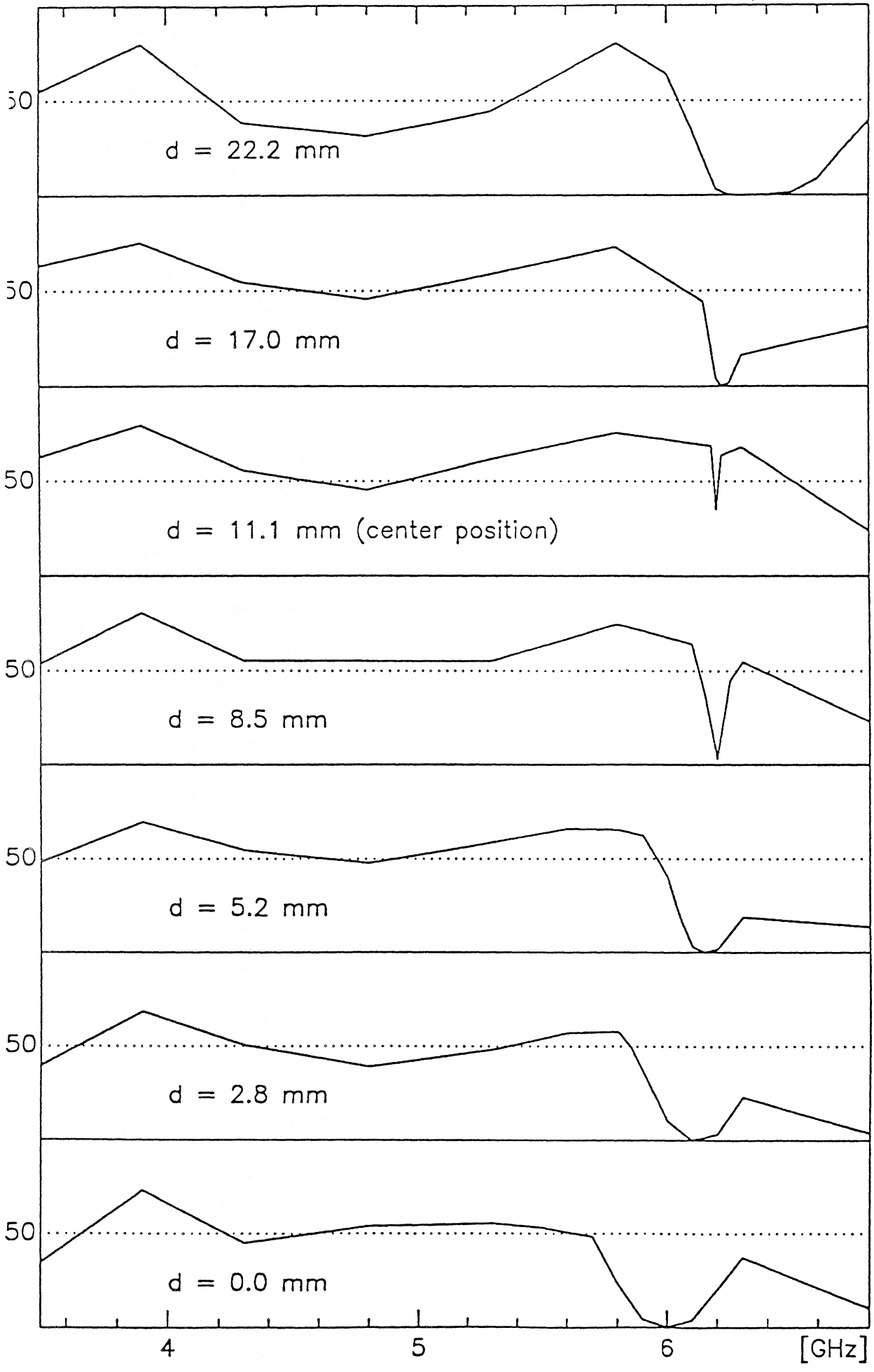
50
d = 22.2 mm
50
d = 17.0 mm
50
d = 11.1 mm (center position)
50
d = 8.5 mm
50
d = 5.2 mm
50
d = 2.8 mm
50
d = 0.0 mm
4
5
6
[GHz]

Figure 13

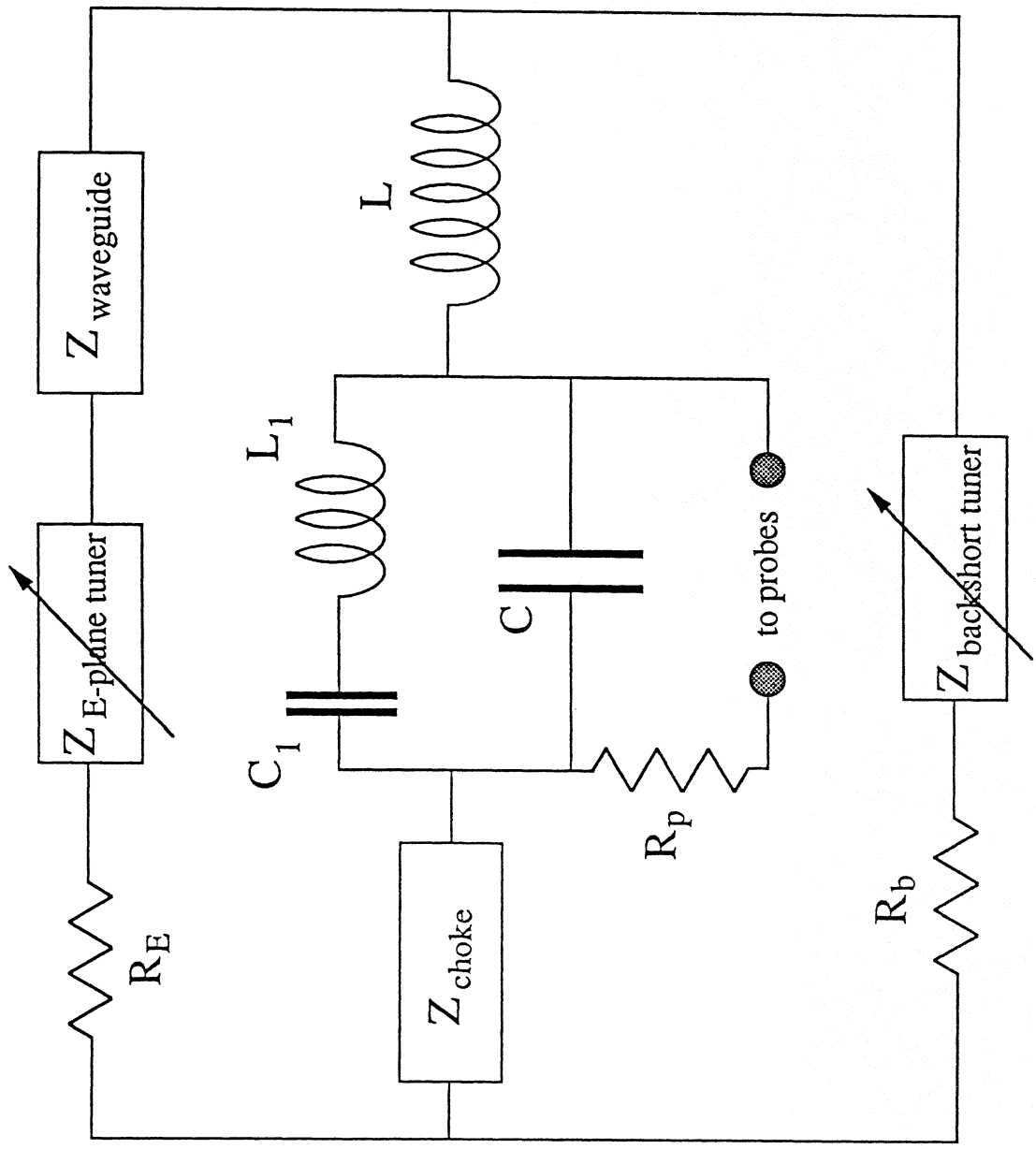
Z waveguide
Z E-plane tuner
R_E
L
L_1
C_1
C
to probes
R_p
Z choke
Z backshort tuner
R_b

Figure 14

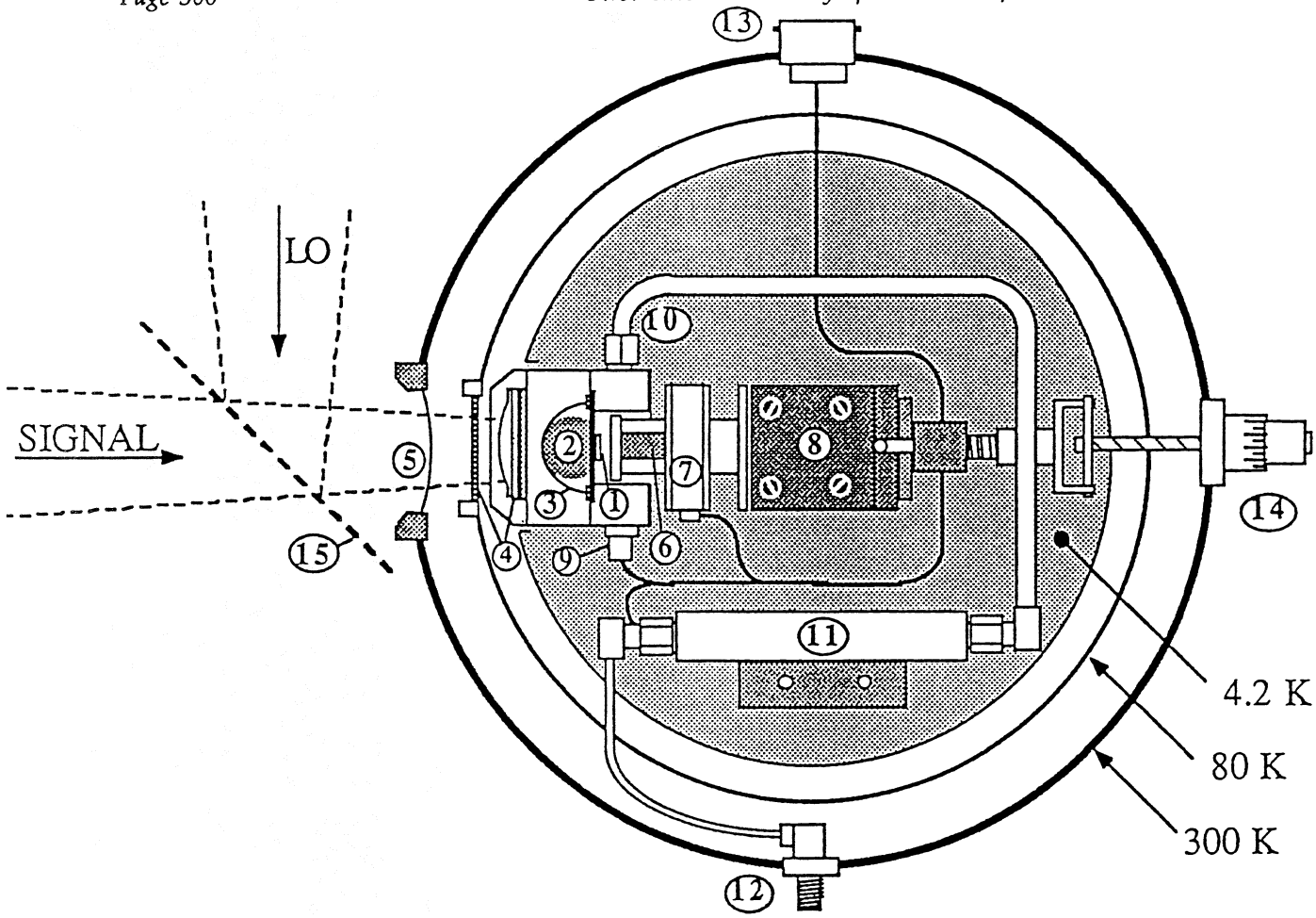

1 Spiral antenna with SIS junction
2 Hyperhemisphere
3 Anti reflection coating
4 IR filters and plastic lens
5 Mylar window
6 Conductive plane with Fe core
7 Coil for magnetic field
8 Translation stage
9 SIS junction DC-bias
10 Mixer IF output
11 IF preamplifier
12 IF output
13 Electronics connector
14 Conductive backplane drive
15 Beam splitter

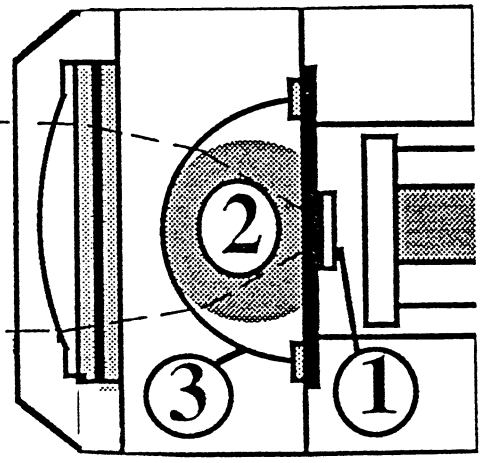

Mixer block

Figure 15

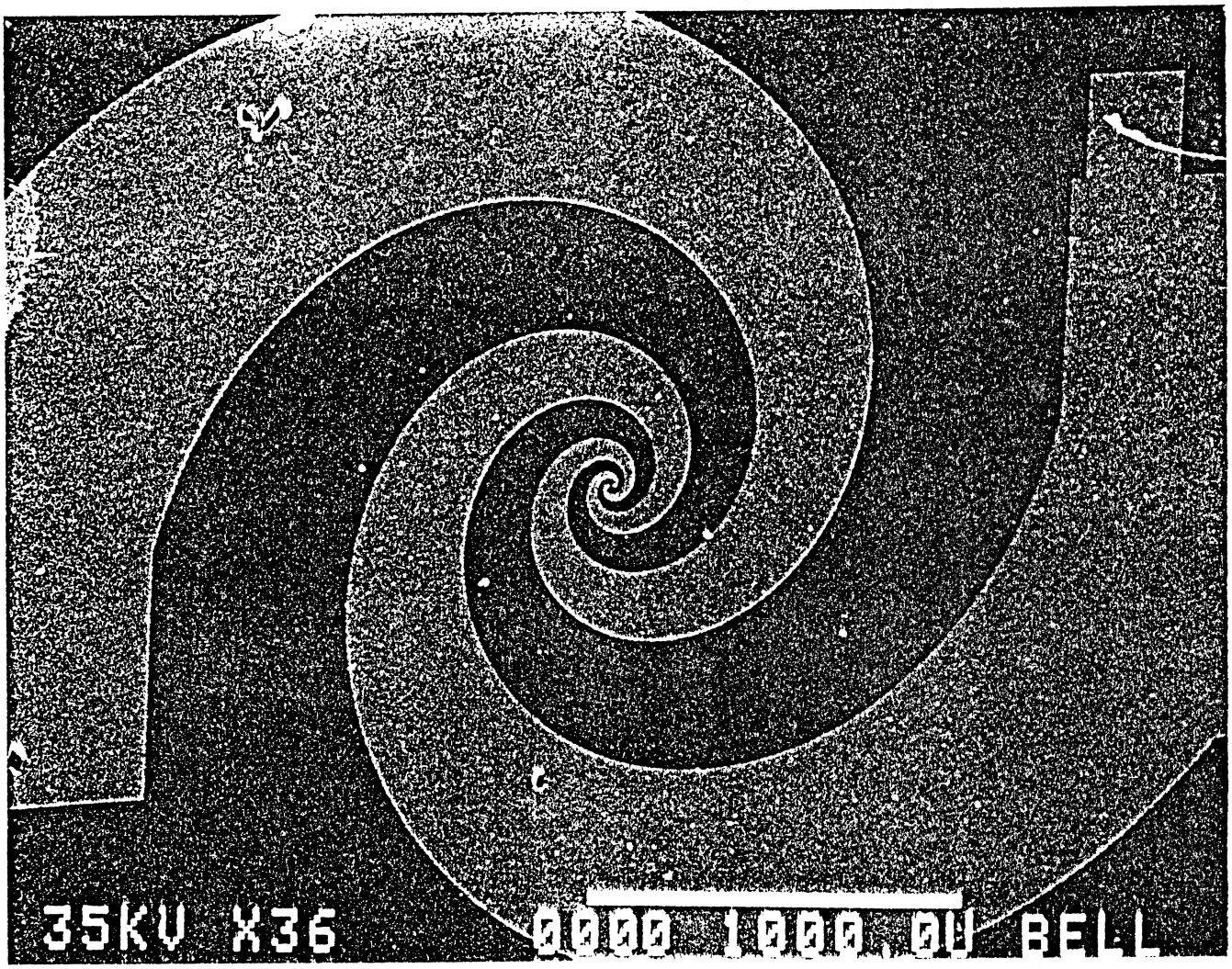

Figure 16

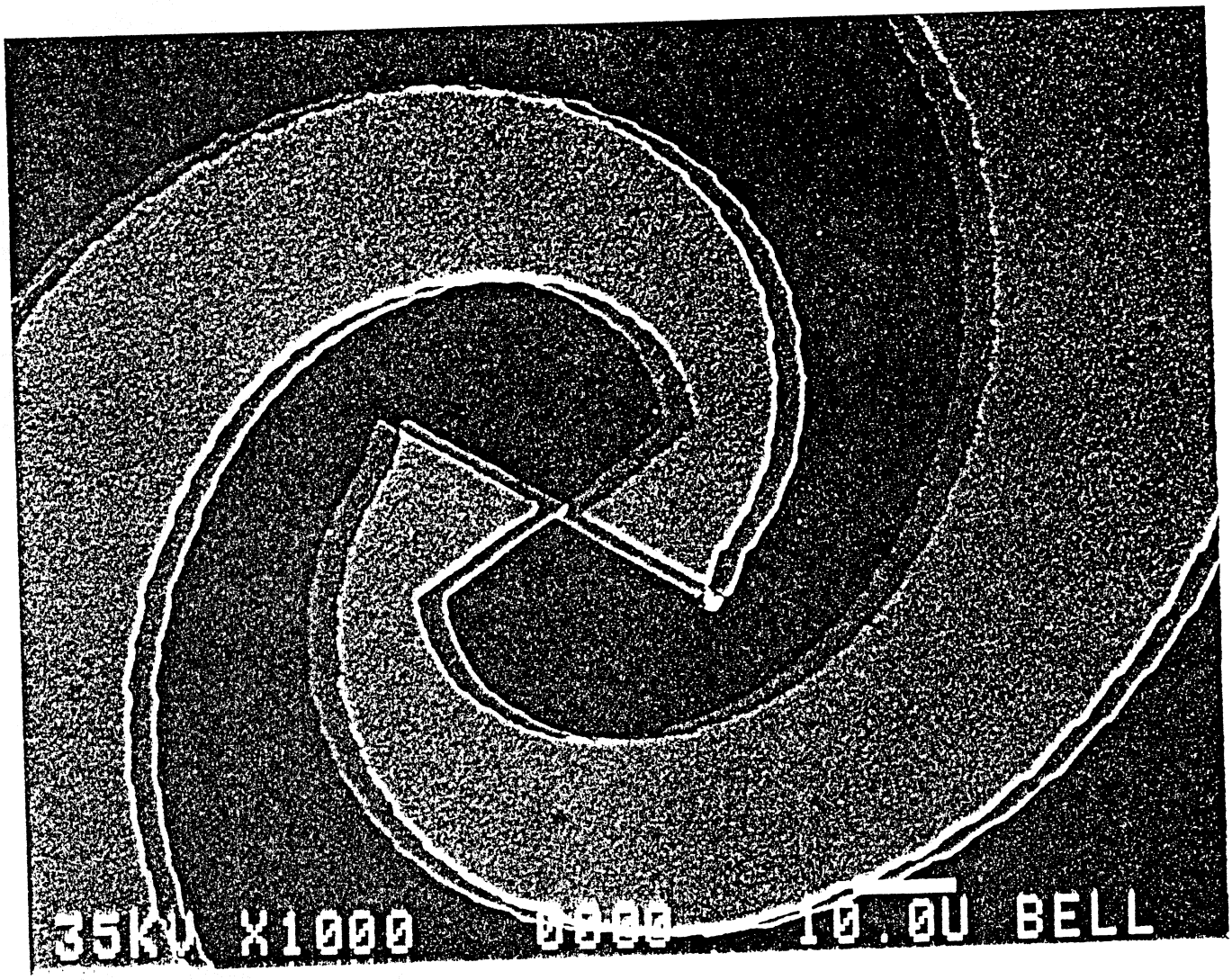

Figure 17

SOME RECENT DEVELOPMENTS IN THE DESIGN OF SIS MIXERS

A. R. Kerr and S.-K. Pan

National Radio Astronomy Observatory[1]
Charlottesville, VA 22903

ABSTRACT

This paper describes SIS mixers in use or under development at NRAO, and introduces a new design procedure for SIS mixers.

By using broadband waveguide-to-stripline transducers, it is possible to design SIS mixers which do not require reduced-height waveguide. At the shorter millimeter wavelengths this greatly simplifies mixer fabrication and allows the use of non-contacting waveguide tuners.

The use of superconducting circuit elements integrated with the junction (or array of junctions) to tune out the usually large junction capacitance has made possible a tunerless mixer which covers a full waveguide band.

The new design procedure for SIS mixers aims at meeting certain practical design constraints on noise temperature, conversion loss, input match, and load impedance. It is found that the ratio of normal resistance to source resistance, R_N/R_S, should have a 1/f dependence for mixers in the quantum-limited regime. The $\omega R_N C = 4$ rule is modified to $\omega R_N C = 4(100/f(\text{GHz}))$, which requires a critical current density $J_C \propto f^2$. The implications of this design procedure are examined for the case of Nb/Al-Al_2O_3/Nb junctions, and design curves are given for R_N, J_C, and junction size as functions of frequency.

---

[1]The National Radio Astronomy Observatory is operated by Associated Universities, Inc., under cooperative agreement with the National Science Foundation.

1. INTRODUCTION

Because of their high sensitivity, reasonable bandwidth, and small LO power requirements, SIS receivers are now widely used for millimeter-wave radio astronomy. To date about ten observatories worldwide are routinely using SIS receivers from 43 to 360 GHz, and in the near future this number will increase to at least fifteen. Despite their widespread use, many SIS receivers are little or no more sensitive than the best cryogenic Schottky diode mixer receivers, and few have approached the ultimate sensitivity limit imposed by the uncertainty principle.

Fig. 1 shows the noise temperatures reported for SIS receivers up to 400 GHz and, for comparison, the present limit for Schottky mixer receivers.

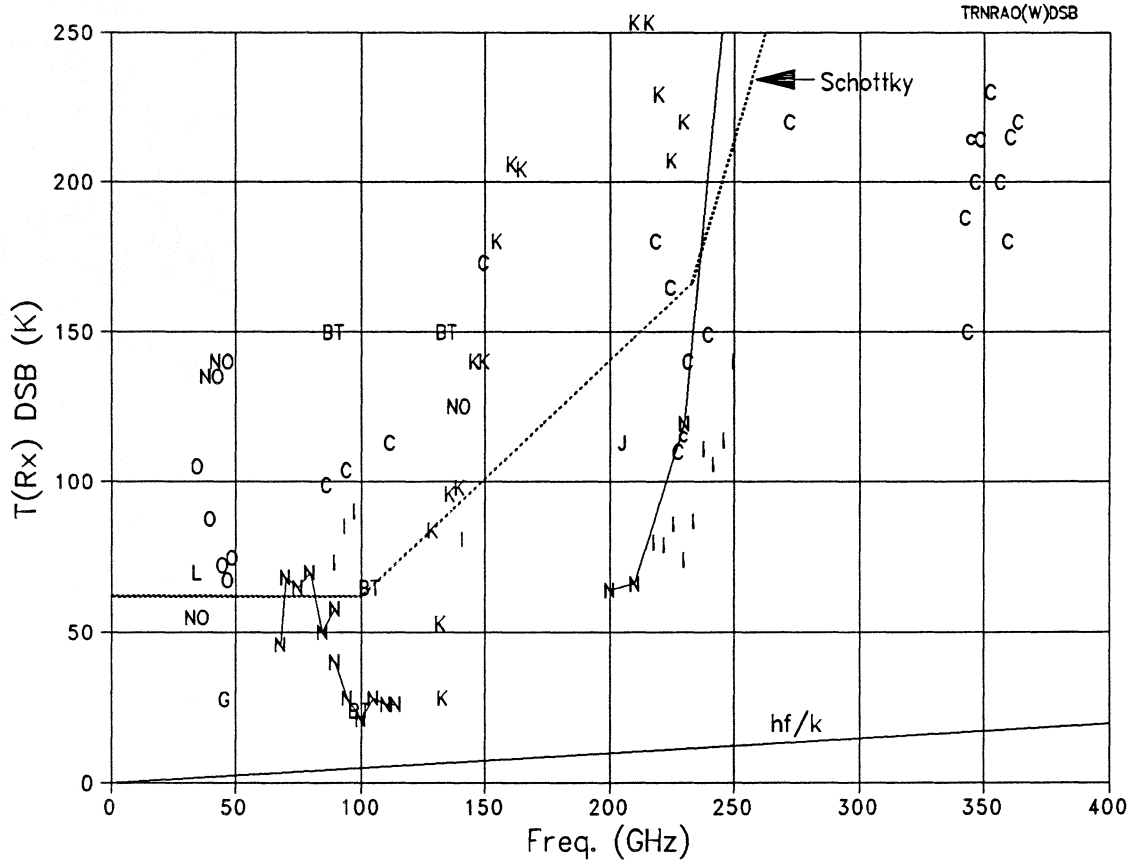

Fig. 1. Double sideband noise temperatures of the better SIS receivers in the frequency range 0-400 GHz. The following coding is used: BT=Bell Labs, C=CalTech, c=CalTech (quasi-optical), G=GISS/Princeton, I=IRAM, J=JPL, K=U. of Koln, L=LETI, N=NRAO, NO=Nobeyama. The performance of the best Schottky receivers is shown by the dotted line. Receivers developed at NRAO are indicated by a solid line, as is the photon noise temperature hf/k.

We believe there are two main reasons that SIS receivers have been slow to develop their full potential: the lack of high-quality SIS junctions with appropriate properties, and the difficulty of tuning out the usually large junction capacitance. In the following sections we describe the approach we have taken to designing SIS mixers at NRAO.

2. SOME NRAO SIS MIXER DESIGNS

2.1 The GISS Type-D, 90-116 GHz mixer

The GISS Type-D mixer [1,2] is shown in Fig. 2. In this mount a series array of SIS junctions is suspended across a reduced-height waveguide. Two waveguide tuners allow the embedding admittance seen by the junctions to be set anywhere in the complex plane except in the forbidden region indicated in Fig. 2(c). This design has been successful using SIS junctions with and without integrated circuits to tune out the junction capacitance [3]. Without integrated tuning circuits, the mixer can be tuned

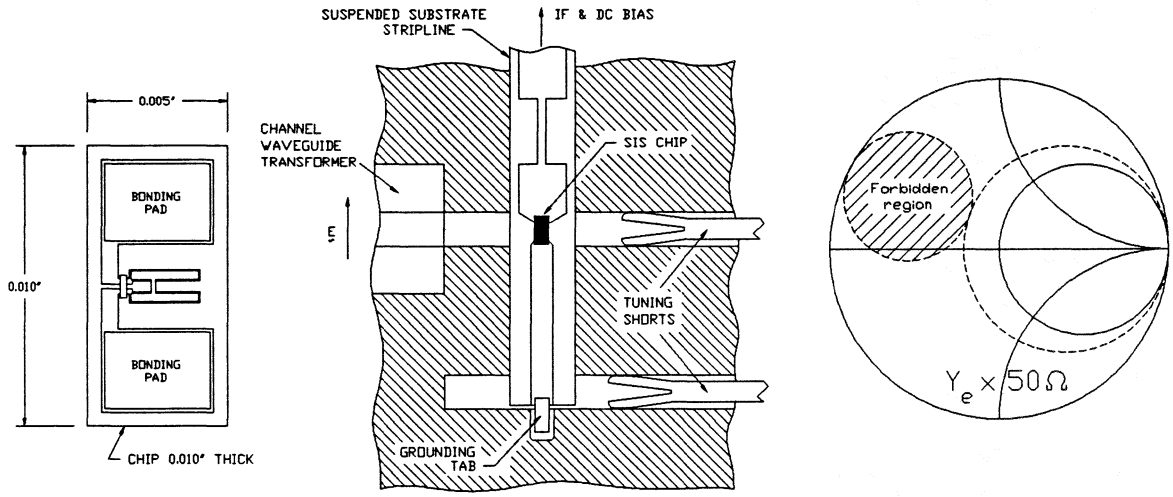

Fig. 2. The GISS Type-D, 90-116 GHz, SIS mixer uses a 0.005" x 0.010" chip (a) with a series array of 2 or 4 junctions, mounted across a 1/4-height waveguide on a quartz suspended-substrate stripline, as shown in (b). The mixer block is split along the middle of the broad walls of the waveguides. The stripline crosses a second waveguide containing an adjustable tuner which provides a variable reactance in series with the junctions. The embedding admittance can be adjusted to any value outside the forbidden region indicated in (c). A channel waveguide transformer [4] is used to reduce the waveguide height from 0.050" to 0.0125" in the vicinity of the junctions. The suspended substrate is fused quartz 0.023" wide x 0.003" thick. The SIS chip shown in (a) has a two-junction array with the integrated tuning circuit described in [2].

to obtain good performance and 20 dB image rejection. While this mixer can be scaled for use at lower frequencies, scaling to higher frequencies is difficult because of the small size of the 1/4-height waveguide and the poor quality of adjustable waveguide short-circuits in such small waveguides.

2.2 The NRAO-401, 140-260 GHz mixer

The NRAO-401 mixer for the WR-4 waveguide band was designed to overcome the limitations on scaling the GISS Type-D mixer to higher

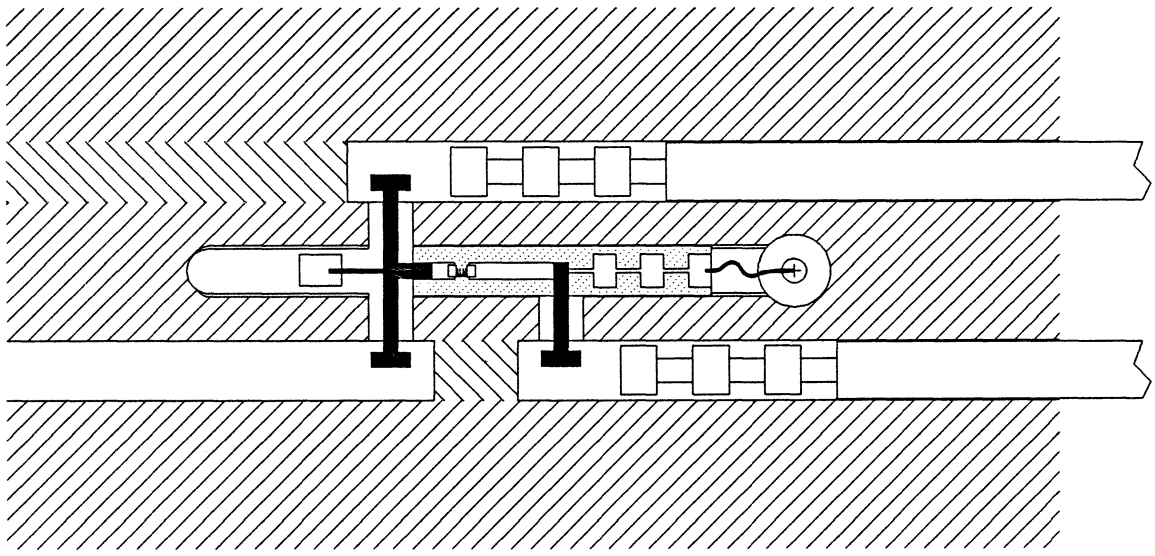

(a)

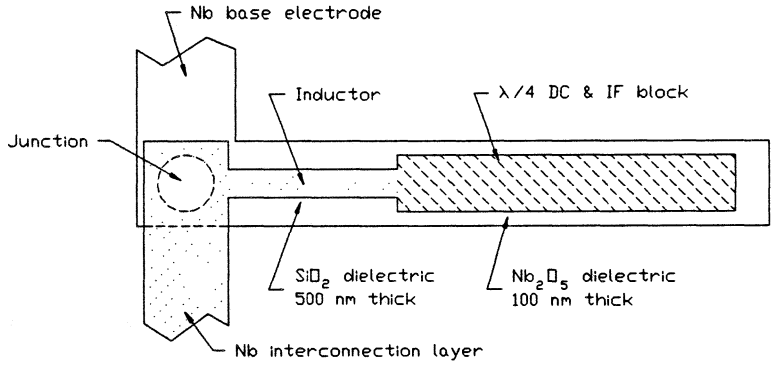

(b)

Fig. 3. NRAO-401, 140-260 GHz mixer. (a) The SIS junctions are on a 0.005" x 0.010" quartz chip which is soldered face-down on the larger fused quartz substrate (shown dotted) and then ground to a thickness of ~0.0005". The free-standing striplines (shown solid) are photo-fabricated from 0.001" copper and soldered to the main substrate. The main substrate is fused quartz 0.0025" thick x 0.018" wide. The waveguide height is 0.0215". The mixer uses a series array of individually tuned junctions [3], as shown in (b). An inductive tuning circuit with a DC/IF block tunes out the capacitance of each junction.

frequencies. Two adjustable tuners are again used, but these are in full-height waveguide in which non-contacting short circuits are practical [5]. Power is coupled from the input waveguide to the SIS junctions via a broadband transition to a 50-Ω self-supporting copper stripline, followed by a suspended-substrate stripline, as shown in Fig. 3(a). The two tuners are likewise coupled to the junctions and provide series and parallel tuning elements. At the left end of the diagram, a $\lambda/4$ stub to ground provides a DC and IF return. This mixer uses an array of individually tuned junctions as shown in Fig. 3(b) [3]. The mixer block is split along the middle of the broad walls of the waveguides. Fabrication of the block is relatively straightforward. The two halves are machined simultaneously: two long waveguide slots and the substrate slot are milled right across both halves, and the waveguides are later plugged as indicated by the reverse hatching in the figure.

2.3 A tunerless mixer for 75-110 GHz

The reduced size of a fully integrated SIS mixer circuit results in greatly reduced parasitic reactances compared with the mixers described above. It then becomes feasible to design a mixer with no adjustable tuners which covers a full waveguide band. The mixer shown in Fig. 4(a) [6] operates in the WR-10 band (75-110 GHz). The heart of the mixer, shown in Fig. 4(b), is a coplanar transmission line connected to a series array of individually tuned junctions (see Fig. 3(b)). The coplanar line makes a broadband transition to suspended-substrate stripline, which then couples into a waveguide via a broadband probe transducer.

In the form shown here, the mixer is coupled to an input waveguide, but the same basic coplanar design (Fig. 4(b)) is equally suitable for operation in more complex, fully planar systems, e.g., in a planar quasi-optical receiver with a slot, dipole, or spiral antenna.

The noise temperature of two receivers using mixers of this type is shown in Fig. 4(c).

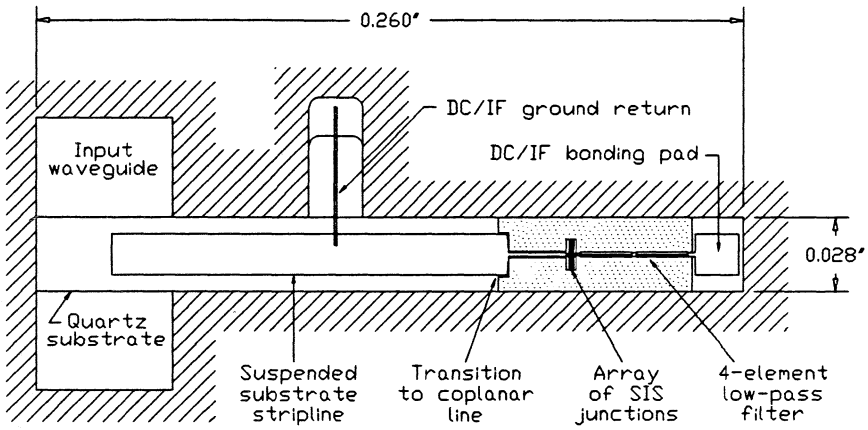

(a)

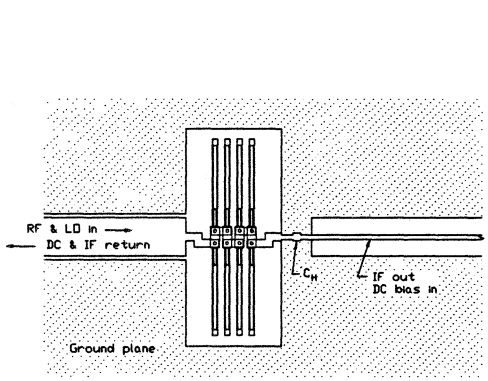

(b)

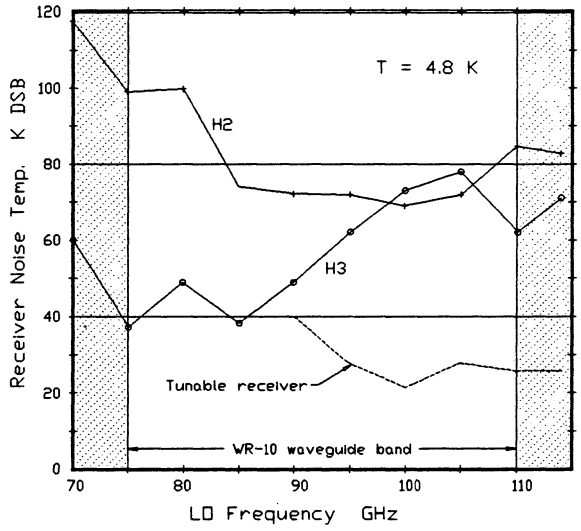

(c)

Fig. 4. The tunerless mixer for 75-110 GHz is on a 0.010" thick x 0.028" wide quartz substrate coupled to the WR-10 waveguide shown at the left in (a). Power from the waveguide is coupled to the SIS junctions via a broadband probe transducer to a suspended-substrate stripline, followed by a broadband transition to coplanar transmission line. The junctions are located in a hole in the ground plane metalization as shown in (b). The inductance of this hole is tuned out by the capacitance C_H. Contact between the edges of the ground plane and the shoulders of the substrate channel is made by gold wire gaskets. The SIS array has individually tuned junctions [3] as shown in Fig. 3(b). The noise temperature of a receiver using mixers with two different tuners is shown in (c), and the noise temperature of a tunable receiver using a GISS type-D mixer is shown for comparison.

3. A DESIGN PROCEDURE FOR SIS MIXERS

3.1 Design requirements

For most applications the following properties are desirable in SIS mixers:

(i) Low mixer noise temperature.

(ii) Low conversion loss (~ 0 dB SSB). While gain is possible in SIS mixers, substantial gain is usually undesirable because of the reduced dynamic range and greater likelihood of out-of-band instability.

(iii) A moderately well matched input (VSWR $\lesssim$ 2). A source impedance near 50 Ω is practical in many types of mixer mount.

(iv) Operation into a 50-Ω IF amplifier with no matching transformer is desirable. Note that this does not require the IF output impedance of the mixer to be 50 Ω; SIS mixers can operate well with a high output impedance driving a 50-Ω load.

3.2 RF source impedance

Using Tucker's theory in its three frequency approximation [7-9], we have investigated the behavior of SIS mixers as a function of LO frequency and amplitude for various source and load impedances. We assumed a low IF, and a broadband embedding circuit which tunes out the junction capacitance in the upper and lower sidebands. The bias point was taken as the middle of the first photon step below the gap voltage. Two types of junction were considered, Nb/Al-Al_2O_3/Nb trilayer junctions and Nb/oxide/PbInAu edge-junctions. The calculations were based on the I-V curves, shown in Fig. 5, of mixers which had given good results in the laboratory. (These I-V curves are actually for two- and four-junction series arrays; however, as series arrays are theoretically equivalent to single junctions, this is immaterial [9,10].)

From these calculations we have found that the design requirements above can normally be satisfied by the appropriate choice of the ratio (junction normal resistance)/(RF source resistance), R_N/R_S. Fig. 6 shows the dependence of the optimum value of R_N/R_S on frequency.

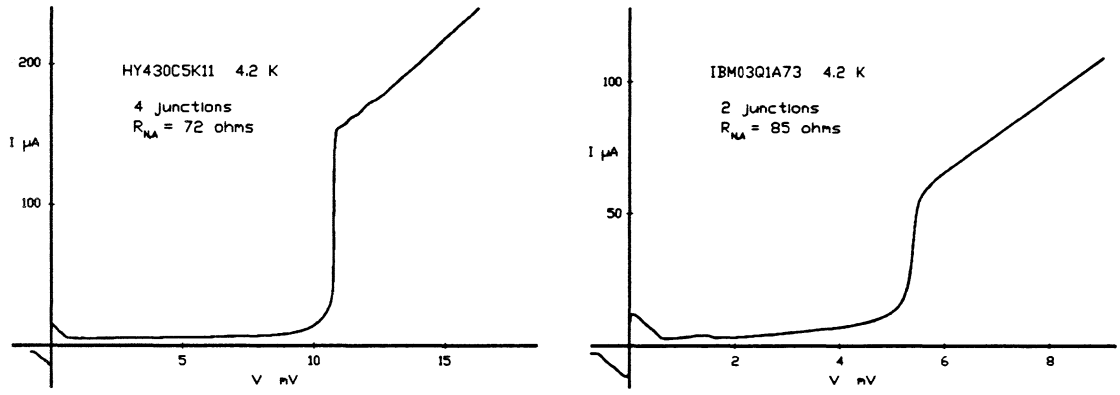

(a) (b)

Fig. 5. I-V curves of (a) a four-junction array of Hypres Nb/Al-Al_2O_3/Nb junctions, and (b) a two-junction array of IBM Nb/oxide/PbInAu edge junctions.

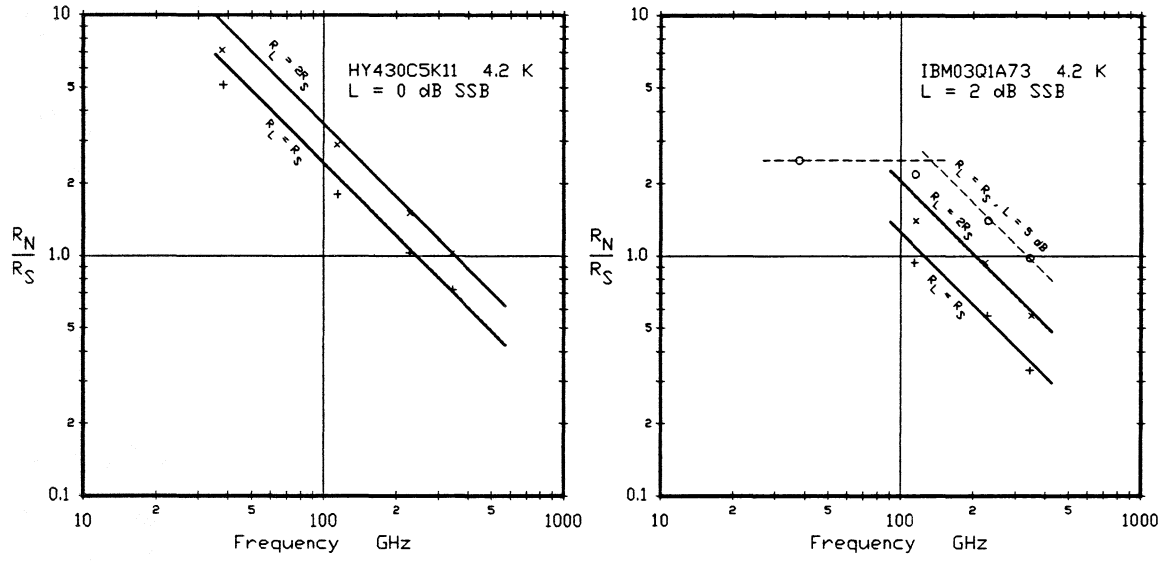

(a) (b)

Fig. 6. Optimum ratio of (array) normal resistance to source resistance, R_N/R_S, as a function of frequency. With the indicated R_N/R_S, the mixer can operate with low noise, gain near unity, and a reasonably well matched input. Graph (a) is for the Nb/Al-Al_2O_3/Nb junctions of Fig. 5(a) with IF load impedance $R_L = R_S$ and $2R_S$. For this case, the relatively sharp I-V curve allows mixer operation with strong quantum characteristics (e.g., L = 0 dB SSB) well below 100 GHz. Graph (b) is for the Nb/oxide/PbInAu edge junctions of Fig. 5(b) which have a much softer I-V curve. In this case it was not possible to obtain unity conversion loss at the lowest frequencies, so the criterion L = 2 dB was used in plotting the lower two curves which are for IF load impedances $R_L = R_S$ and $2R_S$. The upper curve is for L = 5 dB with $R_L = R_S$, and is included to show the clear break between the low-frequency region, where the mixer is predominantly classical and R_N/R_S is independent of frequency, and the high-frequency region, in which quantum effects are dominant and $R_N/R_S \propto 1/f$.

3.3 A modification of the $\omega R_N C = 4$ rule

A parameter widely used in characterizing SIS mixers is the $\omega R_N C$ product. Here ω is the LO frequency, R_N is the normal-state junction resistance, and C is the capacitance of the junction including overlap capacitance between the interconnection layer and base electrode. Based on analysis of published data [10] and simulated mixer results [11], mostly for mixers near 100 GHz, a value of $\omega R_N C$ near 4 appears to give the best SIS mixer performance. This is believed to be due to the low embedding impedance presented by C to LO harmonics and harmonic sidebands generated in the junction conductance. There is no reason to assume this optimum value of $\omega R_N C$ is not frequency dependent.

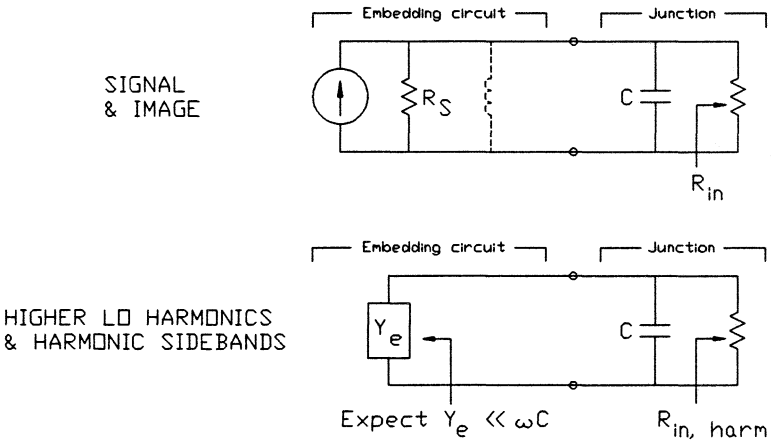

Fig. 7. RF equivalent circuit of an operating SIS mixer at the signal and image frequencies ($f_{LO} \pm f_{IF}$) (upper diagram), and at the LO harmonic (nf_{LO}) and harmonic sideband ($nf_{LO} \pm f_{IF}$) frequencies (lower diagram). In a practical circuit, it is almost certain that the junction capacitance C will dominate the embedding admittance at the LO harmonic and harmonic sideband frequencies.

Consideration of the RF circuit of an operating SIS mixer, as in Fig. 7, suggests that the quantity which governs the effect of the capacitance C at the LO harmonics and harmonic sideband frequencies is actually $R_{in,harm}$, rather than the DC normal resistance R_N. It should then be $\omega R_{in,harm} C$ rather than $\omega R_N C$ which is used as a frequency-independent parameter in designing mixers. $R_{in,harm}$ is related to the signal-frequency input impedance R_{in}, and

in the quantum-limited regime, with the mixer designed to meet the above design requirements, we expect $R_{in,harm}/R_{in}$ to be relatively independent of frequency. Hence, $\omega R_{in}C$ can be used as a frequency-independent parameter. If the input of the mixer is matched, $R_S = R_{in}$, so $\omega R_S C$ also becomes frequency independent. It is clear from Fig. 6 that in the quantum-limited regime, the optimum R_N/R_S is inversely proportional to frequency. It follows that the optimum $\omega R_N C$ is also inversely proportional to frequency, and hence the $\omega R_N C = 4$ rule for mixers near 100 GHz should be modified to include the frequency dependence:

$$\omega R_N C = 4 \frac{100}{f(GHz)} \quad . \tag{1}$$

3.4 Required junction area vs. frequency

For a particular type of junction – e.g., Nb/Al-Al_2O_3/Nb trilayer or Nb/oxide/PbInAu edge junctions – the specific capacitance C_s is almost independent of the critical current density J_C, and will be taken as constant. Given the RF source resistance R_S, the normal resistance R_N is obtained from Fig. 6. The junction capacitance C is then deduced from eq. (1). If stray (overlap) capacitance can be ignored, then for a single-junction mixer, the desired junction area is

$$A = \frac{400}{f(GHz)} \frac{1}{\omega R_N C_s} \quad . \tag{2}$$

In the quantum-limited regime, with $R_N \propto 1/f$ (at constant source resistance R_S), the junction area A is therefore inversely proportional to frequency. This is also obvious from the constraint, discussed in the previous section, that $\omega R_S C$ be independent of frequency.

For a mixer with a series array of N junctions, R_N in (2) is replaced by the normal resistance of the whole array $R_{N,a}$. Then for the individual junctions $R_N = R_{N,a}/N$, and the area of each junction is

$$A = \frac{400}{f(GHz)} \frac{N}{\omega R_{N,a} C_s} \quad . \tag{3}$$

3.5 Required J_C vs. frequency

Theoretically, the product $R_N I_C$ for a tunnel junction is a function only of the superconducting energy gap $\Delta(T)$. At 4.2 K, for Nb/Al-Al_2O_3/Nb trilayer junctions $R_N I_C \simeq 1.8$ mV, and for Nb/oxide/PbInAu edge junctions $R_N I_C \simeq 1.6$ mV. Given the junction area and normal resistance, the critical current density is

$$J_C = \frac{(R_N I_C)}{R_N A} \tag{4}$$

Under the design requirements discussed above, R_N and A are each inversely proportional to frequency for quantum-limited mixers, so $J_C \propto f^2$.

3.6 Design of Nb/Al-Al_2O_3/Nb mixers

As an example of the above design procedure, consider the design of Nb/Al-Al_2O_3/Nb trilayer SIS mixers for various frequencies. The I-V curve of Fig. 5(a) is assumed, with source and load impedances of 50 Ω, a specific capacitance $C_s = 45$ fF/μm^2 [12] and $R_N I_C = 1.8$ mV. The calculations are for a single junction.

(i) From Fig. 6(a), $R_N/R_S = 2.5 \times 100/f(GHz)$, so $R_N = 12500/f(GHz)$.

(ii) From eq.(2), the junction area $A = 113/f(GHz)$ μm^2.

(iii) From eq.(4), The critical current density $J_C = 0.13\ f^2(GHz)$ A/cm^2.

These results are shown graphically as functions of frequency in Figures 8 and 9.

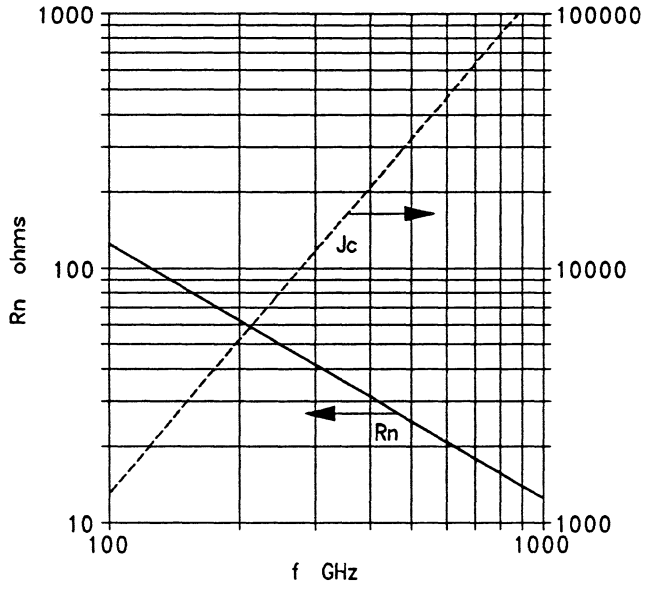

Fig. 8. Required normal resistance R_N and critical current density J_C (A/cm^2) for a mixer using a Nb/Al-Al_2O_3/Nb junction with 50-Ω source and load impedances. When a series array of junctions is used, R_N is the normal resistance of the array ($R_{N,a}$).

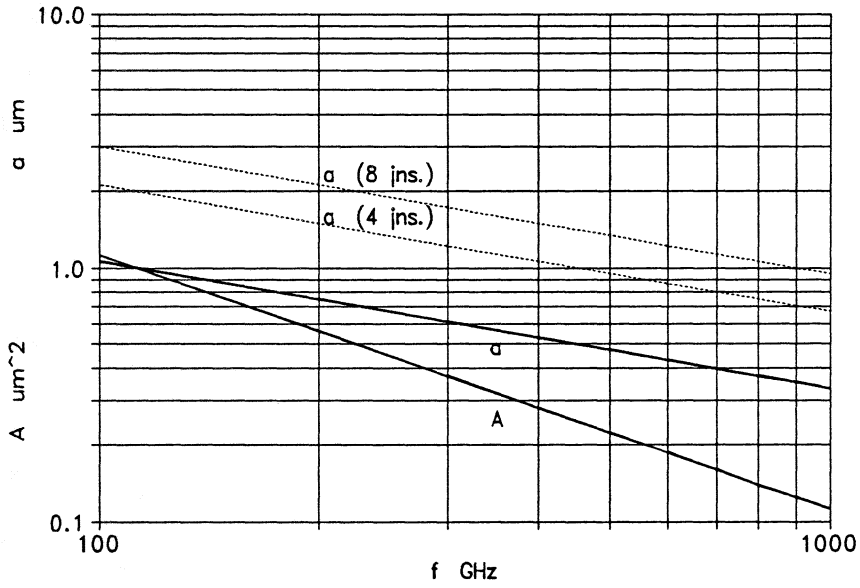

Fig. 9. Required junction area A (μm^2) and side a (μm) (assuming square junctions) for a mixer using a single Nb/Al-Al_2O_3/Nb junction with 50-Ω source and load impedances. The dashed curves give the size of junctions (a μm) required for series arrays of four and eight junctions.

4. SUMMARY

By using broadband waveguide-to-stripline transducers, it is possible to design SIS mixers which do not require reduced-height waveguide. At the shorter millimeter wavelengths this greatly simplifies mixer fabrication and allows the use of non-contacting waveguide tuners.

The use of superconducting circuit elements integrated with the junction (or array of junctions) to tune out the junction capacitance has made possible a tunerless mixer which covers a full waveguide band.

A new approach to SIS mixer design allows the mixer to have low noise, gain near unity, and a reasonably well matched input. The ratio of normal resistance to source resistance, R_N/R_S, is then inversely proportional to frequency. The $\omega R_N C = 4$ rule is modified to $\omega R_N C = 4(100/f(GHz))$, which requires a critical current density $J_C \propto f^2$.

The implications of this design procedure are examined for the case of Nb/Al-Al_2O_3/Nb junctions, and design curves are given for R_N, J_C, and junction size as functions of frequency.

5. ACKNOWLEDGEMENTS

The authors gratefully acknowledge the vital contributions to this work by S. Whiteley, M. Radparvar, and S. Faris of Hypres, Inc., and by A. W. Kleinsasser, J. Stasiak, R. L. Sandstrom, and W. J. Gallagher of IBM.

Parts of this work were performed under funding from AFOSR and ONR. We thank H. Weinstock and M. Nissenoff for their support and encouragement.

We thank N. Horner, Jr. and Françoise Johnson of NRAO for assembling the mixers described here, and Nancyjane Bailey for her work in testing them.

6. REFERENCES

[1] S.-K. Pan, M. J. Feldman, A. R. Kerr, and P. Timbie "Low-noise 115-GHz receiver using superconducting tunnel junctions," Appl. Phys. Lett., vol. 43, no. 8, pp. 786-788, 15 Oct. 1983.

[2] S.-K. Pan, A. R. Kerr, M. J. Feldman, A. Kleinsasser, J. Stasiak, R. L. Sandstrom, and W. J. Gallagher, "A 85-116 GHz SIS receiver using inductively shunted edge-junctions," IEEE Trans. Microwave Theory Tech., vol. MTT-37, no. 3, pp. 580-592, March 1989.

[3] A. R. Kerr, S.-K. Pan, and M. J. Feldman, "Integrated tuning elements for SIS mixers," Int. J. Infrared Millimeter Waves, vol. 9, no. 2, pp. 203-212, Feb. 1988. This paper was presented at the International Superconductivity Electronics Conference, Tokyo, Japan, Aug. 1987.

[4] P. H. Siegel, D. W. Peterson, and A. R. Kerr, "Design and analysis of the channel waveguide transformer," IEEE Trans. Microwave Theory Tech., vol. MTT-31, no. 6, pp. 473-484, June 1983.

[5] A. R. Kerr, "An adjustable short-circuit for millimeter waveguides," Electronics Division Internal Report, No. 280, National Radio Astronomy Observatory, Charlottesville, VA 22903, July 1988.

[6] A. R. Kerr, S.-K. Pan, S. Whiteley, M. Radparvar, and S. Faris, "A fully integrated SIS mixer for 75-110 GHz," to appear in IEEE International Microwave Symposium, Digest of Technical Papers, May 1990.

[7] J. R. Tucker, "Quantum limited detection in tunnel junction mixers," IEEE J. of Quantum Electron., vol. QE-15, no. 11, pp. 1234-1258, Nov. 1979.

[8] J. R. Tucker, "Predicted Conversion Gain in Superconductor-Insulator-Superconductor Quasi-Particle Mixers," Appl. Phys. Lett., vol. 36, pp. 477-479, 15 March 1980.

[9] J. R. Tucker and M. J. Feldman, "Quantum detection at millimeter wavelengths," Rev. Mod. Phys., vol. 57, no. 4, pp. 1055-1113, Oct. 1985.

[10] M. J. Feldman and S. Rudner, "Mixing with SIS arrays," Reviews of Infrared & Millimeter Waves, (Plenum, New York), vol. 1, p. 47-75, 1983.

[11] S. Withington and E. L. Kollberg, "Spectral-domain analysis of harmonic effects in superconducting quasi-particle mixers," IEEE Trans. Microwave Theory Tech., vol. MTT-37, no. 1, pp. 231-238, Jan. 1989.

[12] A. W. Lichtenberger, C. P. McClay, R. J. Mattauch, M. J. Feldman, S.-K. Pan, and A. R. Kerr, "Fabrication of Nb/Al-Al_2O_3/Nb junctions with extremely low leakage currents," IEEE Trans. on Magnetics, vol. MAG-25, no. 2, pp. 1247-1250, March 1989.

Multi-element Quasi-optical Oscillator Arrays for Terahertz Region

M.Nakayama, M.Hieda, T.Tanaka, K.Mizuno

Research Institute of Electrical Communication, Tohcku University, Sendai, 980 Japan

ABSTRACT

Multi-elements oscillator with quasi-optical resonator is reported. The resonator consists of a Fabry-Perot cavity with a grooved mirror. It has capability for power-combing of solid-state sources in the millimeter wave region. X-band models consisting of Gunn diodes or GaAs MESFET's are demonstrated. Power combining and frequency-locking of 18 diodes and 6 FET's have been successfully observed. 50GHz-band Gunn diode oscillator with the resonator is also reported.

INTRODUCTION

Recently many kinds of oscillators are developed in the millimeter and submillimeter wave region. Solid-state devices have many advantages: small size, light weight, and low-voltage requirements. As the frequency increases, however, output power becomes smaller. In addition, the dimensions of conventional waveguide cavities become very small and ohmic losses in the metal wall increases. Therefore coherent power combining of a large number of devices using quasi-optical resonator is attractive. Young and Stephan demonstrated power-combining in a quasi-optical resonator of two devices [1]. Popović et al. proposed and demonstrated power-combining using grid oscillators with GaAs MESFET's at 10GHz [2]. We have proposed a Fabry-Perot resonator with a grooved mirror for solid-state oscillators [3],[4]. In this paper, we report the results of the experiments with the X-band model consisting of Gunn diodes or GaAs MESFET's and the results of 50GHz-band Gunn diode oscillator with the resonator.

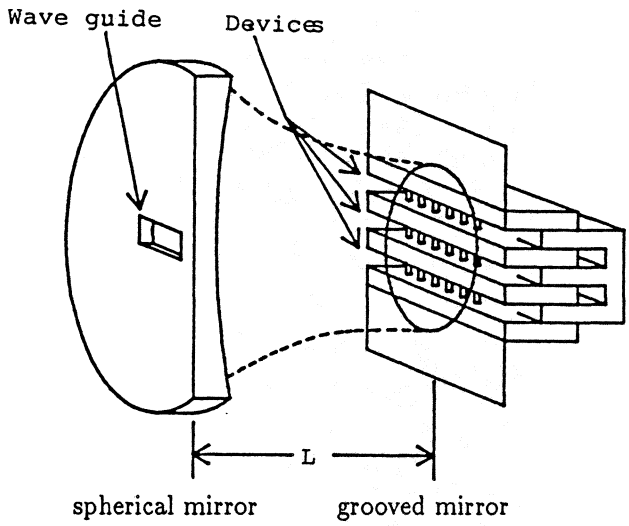

Fig. 1 Resonator configuration.

CONFIGURATION

The configuration of the model resonator is shown in Figure 1. It consists of a grooved mirror and a concave spherical mirror facing each other. Figure 2 shows the structure of the grooved mirror. The groove pitch D must be less than half of oscillator wavelength to avoid diffraction losses [5]. The Gunn diodes(JRC NJX4410) are mounted in grooves and biased by the top and the bottom plates of each groove (Fig.2a). These plates are insulated by thin (80μm)teflon tape. Similarly, FET's(Fujitsu FSX52-LF) are mounted on the surface of the groove. Gate and drain ribbons are connected to adjacent insulated plates. The groove depth t could be continuously changed to adjust the impedance of the groove. The size of the grooved mirror is $5.0\lambda \times 5.0\lambda$. This is large

enough for the beam waist size($2.5\lambda\phi$) on the mirror surface. Output power is taken out by a wave guide at the center of the spherical mirror.

The 50GHz-band resonator consists of plane mirror (100mm×100mm) or metallic mesh output coupler instead of concave spherical mirror.

The resonator proposed here has the following advantages: it has a large heat dissipation capacity, can mount large number of devices, is lager enough than wave length, and has simple bias circuit.

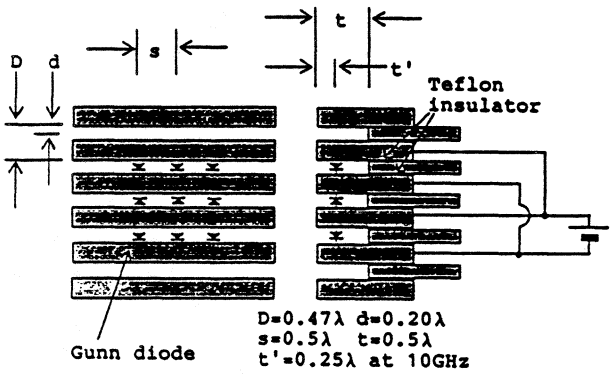

Fig. 2a Grooved mirror for diodes.

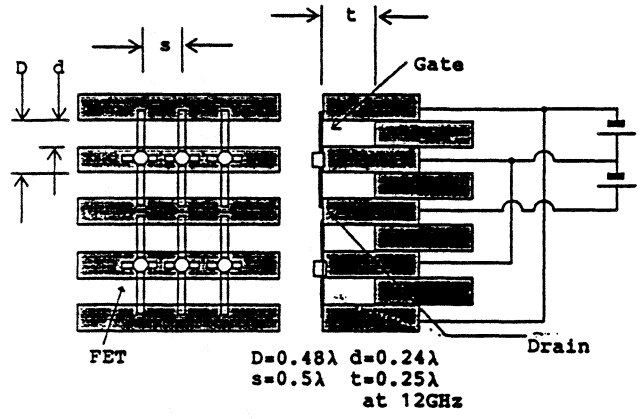

Fig. 2b Grooved mirror for FET's.

EXPERIMENTS

Figure 3 shows the spectra for diode oscillators. We have succeeded frequency locking and power combining. Further, it can be seen that the spectrum for nine diodes is much narrower than that for a single one. The similar phenomena were observed with FET oscillator. The optimum depth of each groove was about $\lambda/2$ for diodes and $\lambda/4$ for FET's. The optimum spacing between elements in a groove has been

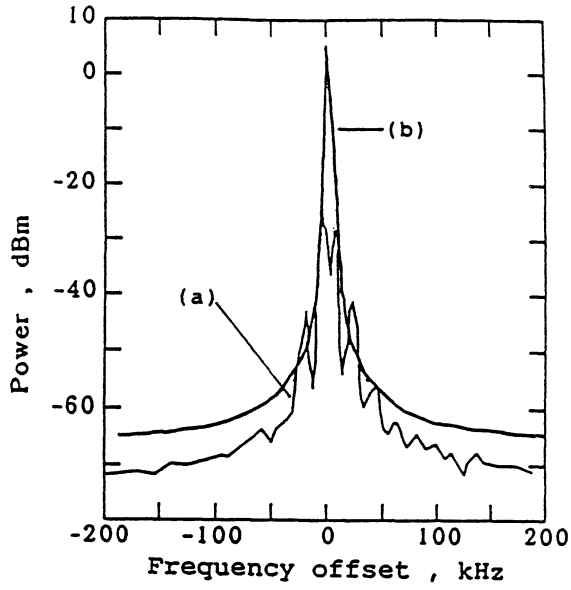

Fig. 3 Spectra of Gunn diode oscillators.
(a) Single diode. (L=107.2mm,fc=10.0336GHz)
(b) Nine (3×3 grid) diodes.
(L=104.2mm,fc=10.2293GHz)

chosen experimentally. We had good results with the spacing of $\lambda/2$. At present, we have succeeded in frequency locking and power combining for the 18 diodes (six by three grid) and the six FET's (three by two grid).

Figure 4 shows how the oscillation frequency varies with the length of the resonator with 6 FET's. The mechanical tuning range is about 5%. Oscillation frequency agrees with theoretical resonant frequency of the fundamental (TEM_{00}) mode of the Fabry-Perot resonator. The oscillation frequency of Gunn diode also agrees with resonant frequency. We have measured the field distribution through moving a small piece of absorber around in the resonator .

Figure 5 shows simplified equivalent circuit of FET oscillator. The ribbons are represented as inductance and capacitance. Phase change between port1 and 2 should be π at oscillation frequency, if the oscillation mode is the fundamental of Fabry-Perot resonator. This simple consideration predicts an oscillation frequency of 12GHz, which agrees with experiments.

Figure 6a shows the spectrum for 50GHz-band Gunn diode oscillator with the resonator consists of plane and grooved mirrors. The Gunn diode(Alpha DGB8266) is mounted at the center of the grooved mirror. Figure 6b shows the spectrum using the same Gunn diode with a waveguide cavity. It can be seen that the resoator has a higher Q-value than the waveguide.

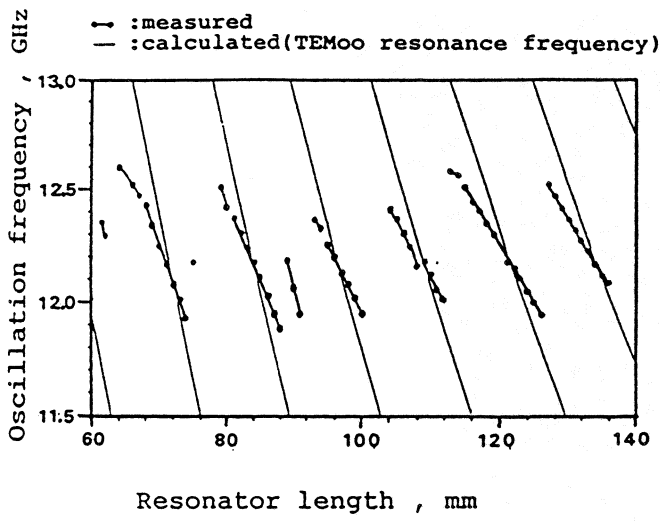

Fig. 4 Oscillation frequency of six FET's oscillator versus resonator length. Calculated line shows resonance frequency of TEM_{00} mode.

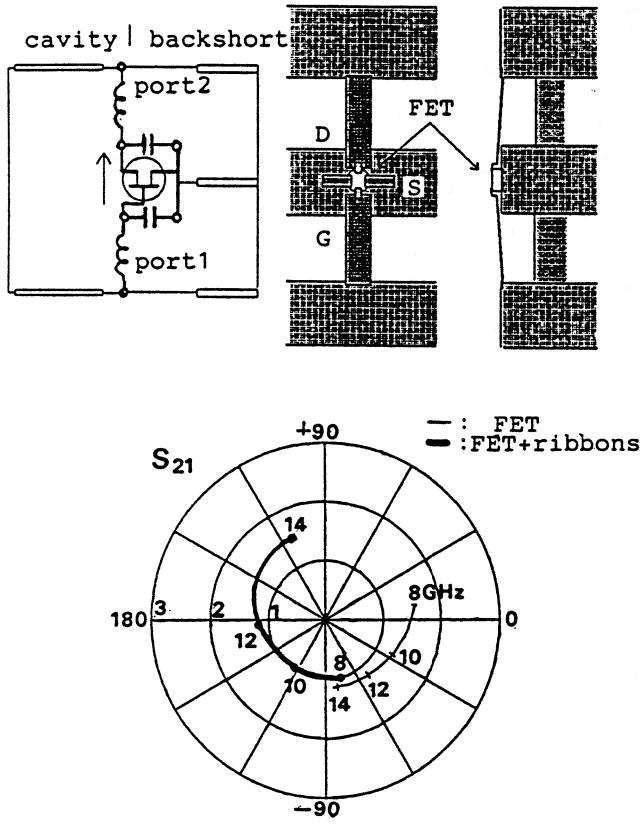

Fig. 5 (a) Equivalent circuit of FET oscillator. (b) S_{21}-parameters of FET(between gate and drain) and port1-2(including impedance of the ribbons).

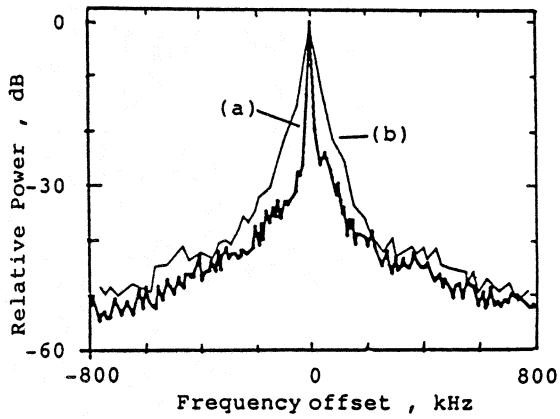

Fig. 6 Spectra of 50GHz-band Gunn diode oscillators.
(a) With quasi-optical resonator (fc=55.19GHz)
(b) With waveguide cavity (fc=55.72GHz)

CONCLUSION

We have demonstrated the utility of a quasi-optical oscillator with multi-elements. Its resonator consists of Fabry-Perot cavity with a grooving. It has capability for power combining of solid-state sources in millimeter and submillimeter wave regions. Frequency-locking and power combining of 18 Gunn diodes and 6 GaAs FET's have been successfully observed in X-band. Mechanical frequency tuning range is about 5%. The oscillation mode is the fundamental (TEM_{00}) mode of the Fabry-Perot resonator.

REFERENCES

[1] S.Young and K.D.Stephan, 'Stabilization and power combining of planar microwave oscillator', IEEE Microwave Symposium 1987, MTT-S Digest, pp185-188, 1987

[2] Z.B.Popović, M.Kim and D.B.Rutledge, 'Grid Oscillators', International Journal of Infrared and Millimeter Waves, Vol. 9, No.7, pp.647-654, July 1988

[3] K.Mizuno, T.Ajikata, M.Hieda, and M.Nakayama, 'Quasi-Optical Resonator for Millimeter and Submillimeter Wave Solid-state Sources', Electronics Letters, Vol.24, pp.792-793, June 1988

[4] M. Hieda, M. Nakayama, K. Mizuno, T. Ajikata, and D. Rutledge, 'Quasi-Optical Resonator for Millimeter and Submillimetere Wave Solid-State Sources', 13th International Conference on Infrared and Millimetere Waves, Conference Digest, pp.55-56, December 1988.

[5] K. Mizuno and S. Ono, 'The ledatron', in K. J. BUTTON (Ed.), Infrared and millimeter waves (Academic Press, 1979), 1, pp213-232

QUANTUM WELL AND QUANTUM BARRIER DIODES FOR GENERATING SUB-MILLIMETER WAVE POWER.

Hans Grönqvist*, Erik Kollberg* and Anders Rydberg**.
The Millimeter Wave Laboratory
Departments of Applied Electron Physics* & Radio and Space Science**
Chalmers University of Technology
S-412 96 Göteborg, Sweden

Abstract.

Quantum well diodes have been used for generating power at millimeter and submillimeter waves, both in negative resistance oscillators and in multipliers. In this paper, we will first discuss the power versus frequency and the maximum frequency of oscillation of "ordinary" quantum well oscillators. Possible methods of improving the power output and the maximum frequency of oscillation will be suggested. Quantum well diode multipliers will also be discussed. Realizing the importance of the non-linear capacitance for the quantum well diode multiplier efficiency we have investigated a quantum barrier diode in multiplier applications.

1. Introduction.

Quantum Well diode (QW-diode) oscillators have recently been shown to have a potential to generate power in the millimeter and submillimeter wave region [1,2]. The device used in these oscillators is a kind of tunnel diode with negative differential resistance, first suggested as early as 1970 by Esaki. They were, however, not implemented experimentally until 1974, [3], when MBE (Molecular Beam submillimeter) technique for making appropriately doped epitaxial Ga(Al)As was developed. The first experiments with QW diode oscillators were made by Sollner 1983 at microwave frequencies. The best QW oscillator results so far have been reported by Sollner et. al. [1] and by us [2]. The QW-diode can also be used in multipliers [4], and should have a possible application in negative resistance mixers with a potential of having conversion gain [5].

In paragraph 11 we will describe a new device, the *Quantum Barrier Varactor* (QBV) diode multiplier, which has high efficiency and interesting properties since only odd harmonics are created.

2. Device design.

A typical outline of a QW-diode is shown in Fig. 1. The doping profile and the band bending for a biased diode is shown in Fig. 2a. The tunneling current has a maximum for the bias voltage making the energy level in the well equal in energy with the Fermi level to the left of the QW. An approximate equivalent circuit of the QW-diode is shown in Fig. 2b. The parameters in the equivalent circuit are depending on the doping profile, bias conditions, and size of the diode. There are several possibilities to increase the output power. It has been suggested that more power will be available if the $\Delta I \cdot \Delta V$ product (ΔI and ΔV are the differences in current and voltage respectively, measured

between the peak and valley current points of the iv-characteristic) approximately determined from the iv-characteristic) can be increased by improving the device. However, the analysis given below, shows that ΔI is more fundamental than ΔV.

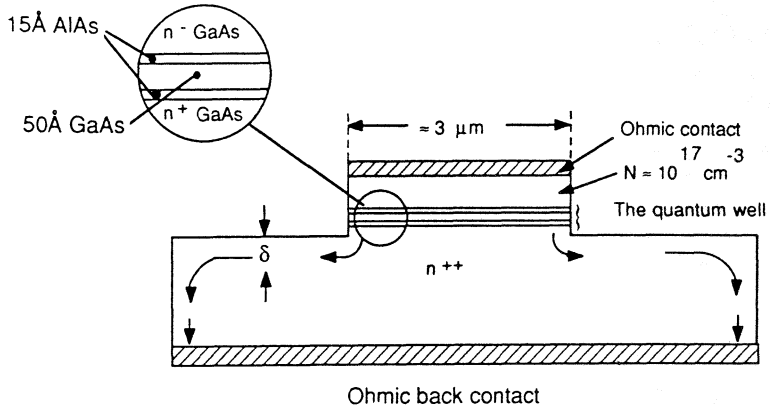

Fig. 1. Schematic diagram of a typical QW-diode.

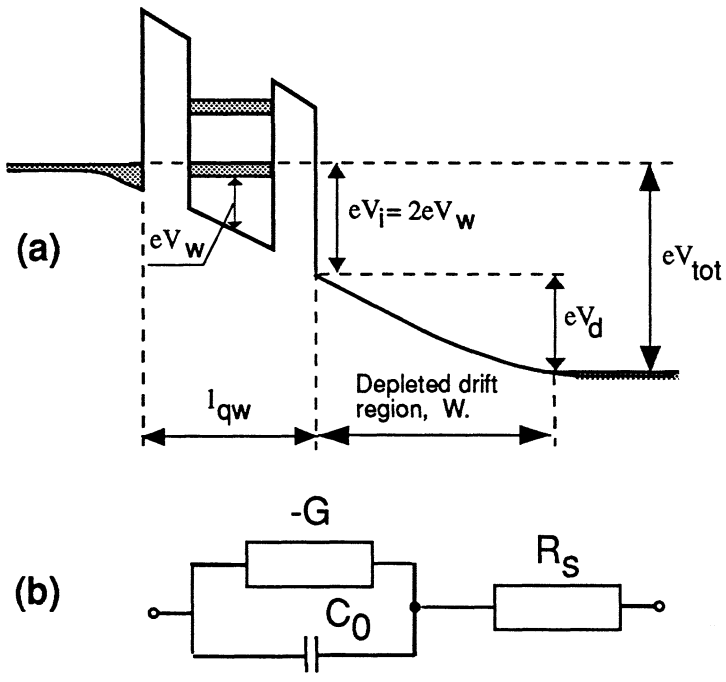

Fig. 2. Electron potential energy at the conduction band edge for a forward bias of $V_{tot} = V_{qw} + V_d$ (a), and the equivalent circuit (b).

3. The maximum frequency of oscillation.

A simplified equivalent circuit of a QW diode oscillator is shown in Fig. 3. When the oscillator starts oscillating, the voltage amplitude ΔV_{osc} will increase and the effective negative conductance G_{eff} will decrease until the requirements of the oscillator are satisfied, i. e. ΔV_{osc} will adjust itself so that [6]

$$G_{eff} = \frac{1}{2(R_l + R_s)} \cdot \left(1 - \sqrt{1 - [2(R_l + R_s)\,\omega\, C_o]^2}\right) \tag{1}$$

which requires $2(R_l+R_s)\omega C_o < 1$ i.e.

$$f < \frac{1}{4\pi (R_l + R_s) C_o} < \frac{1}{4\pi R_s C_o} \tag{2}$$

Hence, the maximum frequency of oscillation is

$$f_{max} = \frac{1}{2\pi} \cdot \frac{1}{2R_s C_o} \tag{3}$$

For this frequency the load resistance is zero, i.e. no power is delivered to the load. For low frequencies $G_{eff} \approx (R_l+R_s)(\omega C_o)^2$, and hence

$$G_{eff\,min} \approx R_s (\omega C_o)^2 \tag{4}$$

which ensures the largest possible voltage swing and maximum power at ω. G_{eff} will evidently increase with increasing frequency while the voltage swing will decrease. This phenomenon is illustrated in Fig. 4.

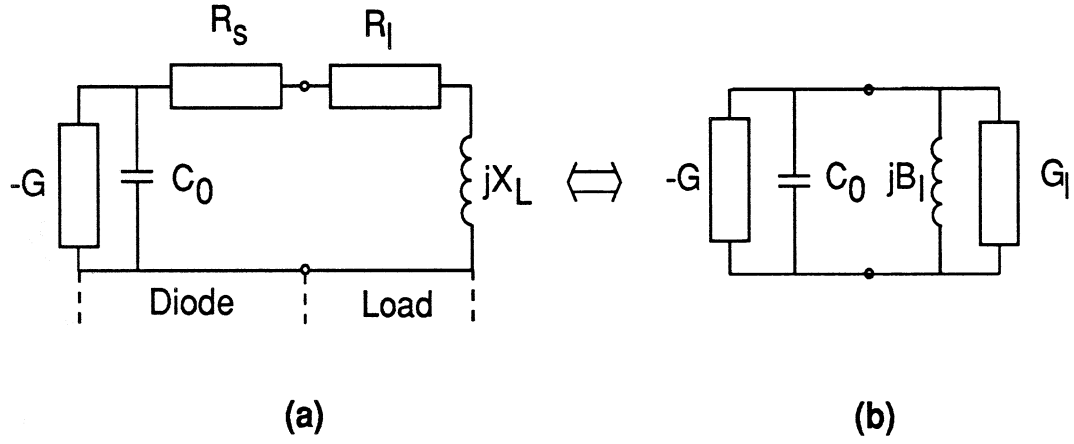

Fig. 3. Equivalent circuit of a QW-diode oscillator (a), and the derived equivalent parallel circuit (b) (to be used for evaluating relevant oscillator properties).

Both the diode negative conductance and the parallel capacitive susceptance are affected by the drift region and the space charge related to the conduction current through the diode. Assuming that the frequency is low in the sense that the drift angle $\theta = \omega W/v_s$ (where W is the length of the drift region, v_s is the mean velocity of the electrons traveling through the drift region) is small ($\leq \pi/3$) we may assume that the *large signal* admittance of the drift region can be expressed in the same way as for the

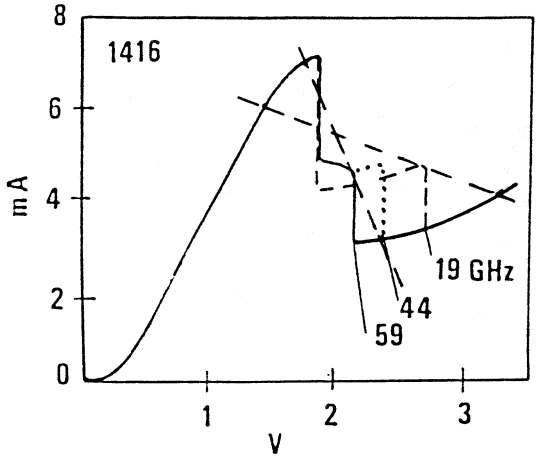

Fig. 4. DC iv-characteristic of a QW-diode in a 19, 44, and 59 GHz oscillator (from ref. [2]).The load-lines defined as $(1/G_l\text{-}R_s)$ (see paragraph 4 below) for 19 and 59 GHz are also shown.

small signal case, i.e. [6]:

$$Y = G + jB \tag{5}$$

$$G \approx A \cdot \left(\frac{W}{\sigma_e} + \frac{W^2}{2\varepsilon v_s}\right)^{-1} = \frac{A \cdot \sigma_e}{W}\left[1 + \frac{\sigma_e W}{2\varepsilon v_s}\right]^{-1} \tag{6}$$

$$jB \approx A \cdot \left(\frac{W}{j\omega\varepsilon} + \frac{\sigma_e}{j\omega\varepsilon}\frac{W^2}{2\varepsilon v_s}\right)^{-1} = j\frac{A\omega\varepsilon}{W}\left[1 + \frac{\sigma_e W}{2\varepsilon v_s}\right]^{-1} \tag{7}$$

where σ_e is then an effective (*large signal*)negative conductance related to the well region and characteristic of the oscillating diode and A the area of the diode. In these expressions the influence from the delay of the rf current with respect to the rf voltage is neglected. The term $\sigma_e W/2ev_s$ in equation (6) and (7) is due to the space charge. The effective capacitance of the diode is consequently larger for $\sigma_e < 0$ than the "cold" capacitance Ae/W. If the space charge term is large enough, it may cause a hysteretic form of the iv-characteristic [6]. Eq. (6) and (7) can also be derived using the impedance expression given in ref. [7], and using the same approach as in [6],we have found them approximately valid also for a punch through diode, i.e. the "depleted" drift region will reach the n^{++} -region.

When the diode oscillates, the oscillating voltage amplitude and current amplitudes adjust, i.e. σ_e obtains a certain value, such that $|G| = G_{eff}$ (see Eq.(1)). Hence, σ_e is determined. At the maximum frequency of oscillation, $R_l = 0$ and $|G| = 1/2\ R_s$, yielding a particular value for σ_e, which can be put into Eq.(7) for determining jB. Realizing that $j\omega C_o \equiv jB$, we now obtain for the maximum frequency of oscillation

$$f_{max} \approx \frac{1}{4\pi R_s C_o} = \frac{W}{4\pi R_s A \varepsilon}\left(1 + \frac{W^2}{4A\varepsilon v_s R_s}\right)^{-1} \tag{8}$$

Notice that R_S and A are inter-related and that v_S is a complicated function of W [12]. If R_S is dominated by the mesa contact resistance, $R_S \cdot A$ is approximately constant, and f_{max} is therefore independent of the diode area. However, in practice there are further contributions to R_S such as the spreading

resistance [8]. If A and R_S are fixed, and knowing $v_S(W)$, W can be optimized (either by choosing a certain doping concentration N_D which will determine the width of the depleted region. W, or designing the diode so that the drift region is "punch through" to the highly doped region). The capacitive susceptance jB for frequencies below f_{max} corresponds to a susceptance of $B=(1/2R_S)(f/f_{max})$.

Eq.(8) does not take into account the negative conductance $-G_{qw}$ and the susceptance B_{qw} of the QW itself. This influence is easily included, since the ratio $-G_{qw}/B_{qw} = -G/B$ [Eqs.(6) and (7)]. The conclusion is that Eq.(8) can just be modified so $W \rightarrow W+l_{qw}$ and $v_S \rightarrow v_S\ (1+l_{qw}/W)^2$ where l_{qw} is the extension of the QW (see Fig. 2). Consequently f_{max} will increase typically 10% by taking into account the influence of $-G_{qw}$ and B_{qw}. Evidently R_S and v_S are very important parameters for reaching the highest possible frequencies. In fact, the maximum frequency of oscillation will have a maximum, which for $R_S = 10\ \Omega$ and $v_S=0.6\cdot10^5$ m/s is 290 GHz with W = 700 Å, and for $R_S = 20\ \Omega$ is 210 GHz with W = 830 Å. Similar results as obtained with equation (8) were obtained by Brown et. al. [9]. We will return to this discussion in paragraph 8 below. Notice also that f_{max} is finite for $R_S = 0$. In this case, the power is dissipated in the space-charge resistance, $R_{spch}=W^2/(2\cdot A\varepsilon v_S)$ (see e.g. Ref.[6] or [7]). In fact, f_{max} can be expressed as (changing $W \rightarrow W+l_{qw}$ and $v_S \rightarrow v_S(1+l_{qw}/W)^2$):

$$f_{max} \approx \frac{W + l_{qw}}{4\pi\, A\varepsilon\, (R_s + R_{spch}/2)} \tag{9}$$

with

$$R_{spch} = \frac{(W+l_{qw})^2}{2\, A\, \varepsilon\, v_s} \tag{10}$$

4. Output power of the fundamental oscillator.

Let us assume that the oscillating current and voltage amplitudes adjust themselves such that Eq. (1) is satisfied, and that the rf current amplitude i_{rf} passing through the the negative conductance of the diode is the same as observed at DC, i.e. $i_{rf} = \Delta I/2$. At resonance this current must also pass through the load conductance G_l (Fig. 3b). The maximum power delivered to the load can then be calculated. Since G_l (= G_{eff} of eq. (1)) is a function of R_l we obtain using eq. (1)

$$P_{del} = \frac{\Delta I^2}{8}\frac{1}{G_l}\cdot\frac{R_l}{R_l + R_s} = \frac{\Delta I^2}{4}\frac{R_l}{1 - \sqrt{1 - [2(R_l+R_s)\omega C_o]^2}} \tag{11}$$

which increases with R_l and becomes maximum when

$$1 - 2(R_l+R_S)\,\omega C_o = 0 \tag{12}$$

The load conductance G_l approximately equals G of Eq.(6) and the ωC_o approximately equals B of Eq.(7). In a similar way as Eq.(9) is derived, one obtains now for the oscillation frequency

$$f = \frac{W + l_{qw}}{4\pi\, A\, \varepsilon(R_l+R_S+R_{spch}/2)} \tag{13}$$

and from Eq.(13), (3) and (9) one obtains

$$R_{lopt} = R_{spch}\frac{v_s}{W+l_{qw}}\left(\frac{1}{f}-\frac{1}{f_{max}}\right) \tag{14}$$

with which Eq.(11) and (12) yields the maximum power into R_l as

$$P_{delmax}=\frac{\Delta I^2}{8}\frac{W}{A\varepsilon}\left(\frac{1}{f}-\frac{1}{f_{max}}\right) \tag{15}$$

This equation is different to Eq.(20) of Ref.(6), the reason being that in Ref.(6) C_o was assumed constant and equal to the value for $f = f_{max}$. Noticing that ΔI is proportional to A, P_{delmax} as expected is proportional to the diode area A.

Eqns.(11)-(15) must be handled with some care. Eq.(15) seems to suggest that the power output goes to infinity for $f = 0$. The reason is that the model assumes the voltage swing ΔV over the diode to be $\Delta I/G_l = \Delta I/G_{eff}$, which is quite unrealistic when ΔV becomes significant larger than the voltage difference between at the peak and the valley current. It is obvious that zero load resistance leads to zero output power and too large load resistance means no oscillations.

5. Comparison with experiments.

Referring to our own work [10], mesa diodes with a diameter of ≈ 4 μm and a height of ≈ 0.5 μm were fabricated. Two different epitaxial designs have been tested so far. Diode #1 consists of 45 Å GaAs well surrounded by 20 Å AlAs barriers and a 50 Å spacer layer of GaAs outside each barrier. All of these layers are nominally undoped. Outside the spacer layers a region of low doped GaAs, Si doped to $2\cdot10^{17}$ cm^{-3}, with a length of 2000 Å is grown. The second diode, #2, differs in mainly one aspect: the region of low doping ($6\cdot10^{16}$ cm^{-3}) is 2250 Å, and grown on one side only.

The diodes were tested in both post and cap waveguide mount structures. We found that output power of the QW-diode #1 often was a harmonic, with the fundamental oscillation frequency below the cut-off frequency of the waveguide. Such harmonic operation modes were found to be due to resonances caused by the bias circuit of the mount. By improving the bias circuit it was possible to obtain fundamental oscillations at frequencies within the waveguide transmission band. In Fig. 5 is the output power as obtained from Eq. (15) compared with the experimental results for fundamental oscillations reported in ref. [2]. In these experiments we carefully checked if any subharmonic power could be detected in the bias circuit, as was the case for the "harmonic mode operation". Notice that the theoretical power is obtained choosing the load resistance R_{lopt} for maximum output power i.e. using Eq.(14)-(15). The experimental output powers are (of course) lower. By optimizing the embedding impedance of the mount, reducing the series resistance of the device and the losses in the mount, more output power should be achieved. Moreover, judging from our experiments and assuming that it should be realistically possible to match the circuit to a diode with $Re\{Z_o\} = 1\ \Omega$, it should be possible to increase the diode area with a factor of 70. Hence, the output power also should improve with a factor of approximately 70 (compare Fig. 5) to about 6 mW at 100 GHz.

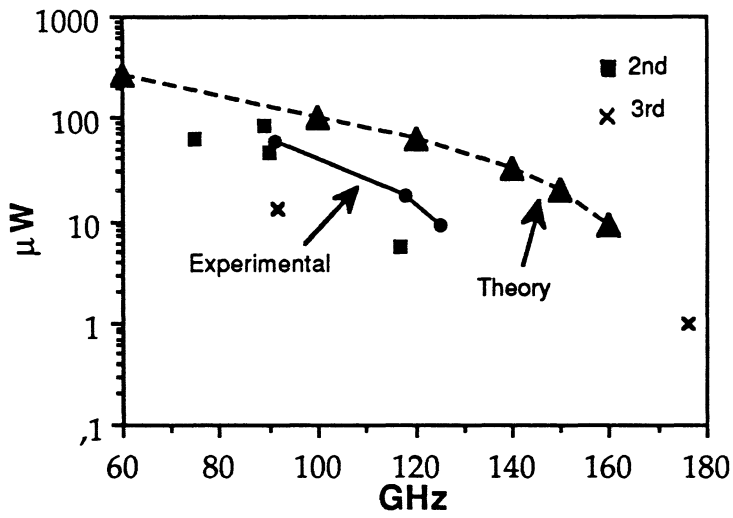

Fig. 5. The output power for a fundamentally oscillating optimized quantum well oscillator according to eq. (11) and as obtained experimentally (from ref. [2]). It is assumed that $A = 1.2 \cdot 10^{-11}$ m^2, $R_S = 20\ \Omega$, W = 1100 Å, and $\Delta I = 4$ mA. Also shown is the experimentally obtained output power for oscillators at the 2nd and the 3rd harmonic (also from ref. [2]).

An educational case is illustrated by the properties of the diode #2 with the low doping and a long depleted drift region. Quite a large space charge resistance is obtained for this diode. The iv-characteristic shows a large hysteresis, and the highest frequency of oscillation obtained experimentally (it was very difficult to get oscillations) was as low as 100 MHz. It was found that the measured hysteresis fits very well to what can be expected from the available fabricational data of the diode assuming it to be due to space charge effects. Applying Eq.(10) assuming $v_s = 6 \cdot 10^4$ m/s and $R_S = 20\ \Omega$ yields $f_{max} = 95$ GHz.

The iv-characteristic shown in Fig. 4 is typical and obtained with diode #1. It shows hysteresis as well as a characteristic step at the negative resistance slope part. Both phenomena can be explained assuming oscillations. The step can be explained as a mean current for this bias voltage range when the diode is experiencing oscillations. If the voltage swings approximately between the maximum peak current and the valley minimum, the resulting current should be of the order the mean of the maximum and the minimum current, as observed. The hysteresis is caused by the fact that oscillations can start as soon as the small signal negative σ (= di/dv in the bias point) has a large enough amplitude, and that oscillations once started may continue even if the small signal σ at the bias point is positive. This is due to the fact that for large voltage swing at increased bias the *effective* σ_e remains negative [6].

It is interesting too, to determine the load line, G_{eff}^{-1} for the oscillating diodes of Figure 4. The load line of the *active* part of the diode (the series resistance not included as part of the diode) is $(R_{lopt}+R_S)$, yielding 800 Ω for 19 GHz, 290 Ω for 44 GHz and 180 Ω for 59 GHz. In Figure 4 these load-lines are indicated (it would have been more accurate to modify the dc-iv-characteristic by subtracting the voltage drop over the series resistance, $i_{dc} \cdot R_S$).

6. Harmonic output power.

As already mentioned the nonlinear iv-characteristic and a large oscillation voltage amplitude will cause a large harmonic content in the resulting current waveform. Hence at "low" fundamental oscillation frequencies, when the voltage amplitude surely is large, the oscillator ought to be very efficient as a harmonic oscillator. Due to the symmetry of the iv-characteristic, the 3rd harmonic should have a comparatively large amplitude. This also agrees with the result shown in Fig. 5. Besides the nonlinearity of the iv-characteristic itself, another reason for a large harmonic content, is relaxation type oscillations (see e.g. Ref. [11]). One cannot expect a pure sinusoidal oscillation at any frequency, not even at the highest possible frequency of oscillation. Hence, one concludes that when output power is required at frequencies near and above f_{max} it is more advantageous to design the oscillator as a harmonic oscillator. The optimum fundamental oscillating frequency is then probably to be choosen at $f_{osc} \approx (1/3) \cdot f_{out}$.

Also notice that the current amplitudes at the harmonic frequencies should remain large up to frequencies *well above the maximum frequency of oscillation.* Important for the performance are the actual embedding impedances at these frequencies and the capacitance of the diode. Efficient multiplication should therefore be possible to obtain to quite high output frequencies.

7. Optimizing the diode.

The drift length over which the carriers have high velocity is limited and is a function of the electric field after the barrier and the injection energy. In Fig. 6 is shown f_{max} vs the length of the drift region for different mean velocities. Notice that the Figure may be used for other values of the series resistance than 10 Ω. For e.g. R_S=5 Ω (20 Ω), multiply (divide) the velocities and the frequency scale with 2.

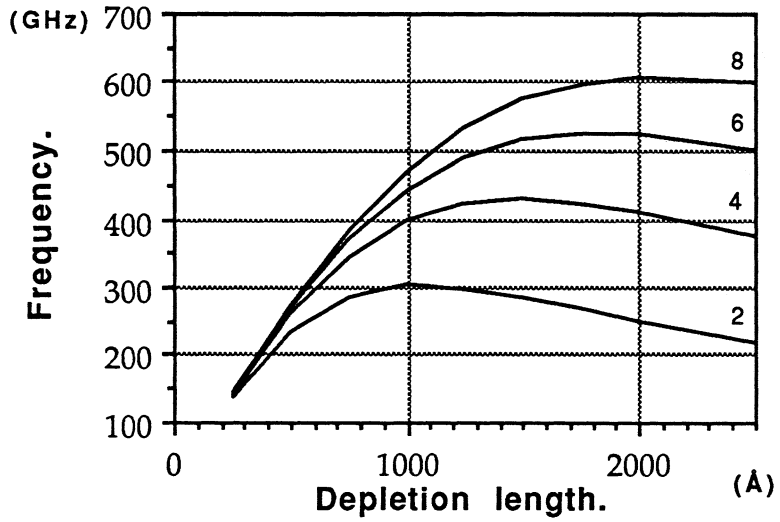

Fig.6. Calculated values for f_{max} as a function of depletion length for different carrier velocities using Eq.(11). The values for v ranges from $2 \cdot 10^5$m/s to $8 \cdot 10^5$m/s. The area A of the diode is 12 μm^2 and the series resistance R_S is 10 Ω.

For "ordinary" GaAs diodes a frequency of ≈ 600 GHz could probably be reached with a depletion length of 600 Å ($W+l_{qw}$=700 Å). However, in order to achieve this or higher frequencies, one must understand the fundamental problems in this context. We will also show that if InAs is used in the drift region, the higher achievable velocities will ensure a still higher f_{max}.

8. Optimizing the GaAs diode design.

In GaAs, electrons subjected to an electric field will travel much faster in the main Γ valley than in the L valley. Since the energy of the L valley is 0.31 eV above the bottom of the Γ valley it can be concluded that when carriers in an accelerating field have gained energy ≥0.31 eV, a transfer of the carrier to a higher valley will occur, and the velocity of the carrier drops. Monte Carlo simulations for GaAs [12] do show a velocity decrease when this requirement is fulfilled. Hence as a rule of thumb, the requirement

$$e \cdot V_{peak} \approx 0.31 \text{ eV} \tag{16}$$

should be fulfilled in order to maintain a high mean velocity through the drift region. The peak current voltage is the sum of the voltage over the accumulation layer in front of the QW, the voltage drop V_{qw} over the QW itself and the voltage drop V_d over the drift region. From Fig. 2 and simple geometrical arguments it is obvious that the injection energy for *peak current* and a symmetric double barrier structure $e \cdot V_i$ is related to the electron excess energy eV_w in the well viz. $eV_i = 2 \cdot e \cdot V_w$ ($=e \cdot V_{qw}$) and the accelerating field E_w in the drift region at the quantum well is

$$E_w = \frac{2 \cdot V_w}{(L_w + 2L_b)} \tag{17}$$

where L_w and L_b are the width of the well, and the width of the barriers respectively. If the potential in the drift region is parabolic, the voltage drop over the drift region becomes $V_d \approx 0.5 \cdot L_d \cdot E_w$ where L_d is the length of the drift region. Hence with equation (17) the requirement for the mean velocity to be as high as possible is

$$2V_w \cdot \left(\frac{L_d}{2(L_w + 2L_b)} + 1\right) \approx 0.31 \text{ eV} \tag{18}$$

We propose two possible ways of decreasing V_w: **i.** lowering V_w by increasing the width of the well, and **ii.** lowering V_w by doping the well with indium.

In order to determine the effect of increasing the width of the well, we have solved the Schrödinger equation for different well widths and no bias (Fig. 7). The barriers are taken as AlAs, giving the potential barriers equal to 1 eV. The bold line indicate the present device with 45Å well width and the circles show the two energy levels in that well. Although when the device is biased the well region does no longer have a simple square shape, Fig. 7 yields a reasonable estimate of the real situation. As is seen in the figure, the energy levels are lowered as the width of the well is increased.

Another approach to lower the energy level is to grow the well region with a lower band gap than GaAs. For $In_xGa_{1-x}As$ with small values of x, the difference in band gap is given by [13]

$$\Delta E = 0.2295x^2 - 1.1365x \quad (19)$$

in eV. Roughly 85% of this difference is in the conduction band, the rest in the valence band. The mixing of InAs with GaAs is slightly more complicated than the mixing of AlAs with GaAs since the lattice constant of InAs is different from that of GaAs. Thus a strained layer is formed and there is a limiting thickness to the layer that can be grown. This is discussed in [14] and it can be concluded that for a 45 Å well the maximum In content is ≈40%. The In-doping means that the potential barrier becomes higher, which should be accounted for in a more exact theoretical evaluation.

The best solution is to combine these methods and use a slightly wider well and a limited In content in the well.

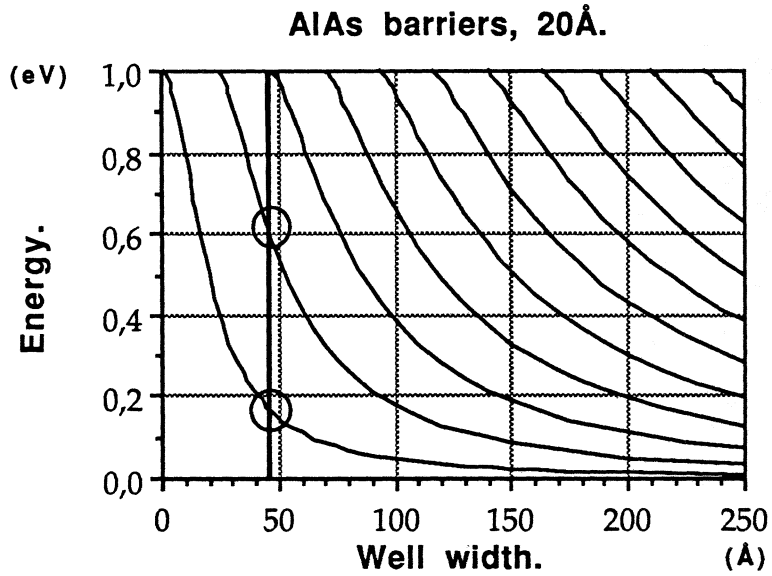

Fig.7. The energy levels for a square well potential for well widths up to 250Å. The bold line indicates the 45Å well currently used in the devices with the two energy levels, one at ≈0.17eV and one at ≈0.63eV.

In the table below, is given some examples on expected f_{max} of different designs all with diode areas of 12 μm^2. The original experimental diode yields an f_{max} of approximately 170 GHz.

Width Å	In %	V_W meV	E_W kV/cm	W_{opt} Å	v_s 10^5 m/s	R_s Ω	f_{max} GHz	Rem.
45	0	170	400	1000	1.0	20	170	Exp.diode
45	0	170	400	1000	1.0	5	≈230	
60	0	110	220	600	1.0	5	≈300	
60	7	32	64	600	8.0	5	≈600	
60	8	22	44	800	3.0	5	≈500	
60	8	22	44	800	3.0	20	≈200	

The diode we have have used in experiments was according to the upper one in the table, i.e. f_{max} was as low as 170 GHz. Improving the mean velocity by using In in the well and broadening the well itself, for the same series resistance f_{max} will become about 200 GHz, while if R_S can be 5 Ω, one may reach f_{max} = 600 GHz.

It is interesting to use Eq. (15) to predict the maximum output power at e. g. 400 GHz for the diode with f_{max}=600 GHz of the table above ($W+l_{qw}$=700 Å, $v_s=6\cdot10^5$ m/s) by choosing a larger area diode (R_S proportional to 1/A). It is reasonable to assume at that 400 GHz it is realistically possible to match the diode to a 5 Ω load resistance. This should allow us to use a 60 μm^2 area diode (R_S=1 Ω, $\Delta I \approx 20$ mA) yielding a maximum output power (Eq. (15)) of approximately 420 μW. Probably only of the order 200 μW will be available as useful output power. Whether it is possible to achieve still more output power at 400 GHz for a diode oscillating fundamentally at 133.3 GHz, is not clear. The maximum output power at 133 GHz for the same diode area should be about 7 times higher, i. e. 3 mW.

9. Using InAs in the drift region.

A way to get around the problem of decreasing velocity for electrons with high energies is to use a material combination where the lowest upper valley is higher up than the 0.31 eV in GaAs. The upper valley in InAs is more than 1 eV higher than the Γ valley [13] but this is not the sole benefit of that material system. The mobility is higher, ≈33000 cm^2/Vs compared to 8500 cm^2/Vs for GaAs at room temperature [15]. Moreover, the the series resistance in this material can be made lower, partly because the higher mobility but also since the band gap is lower it gives a lower ohmic contact resistance.

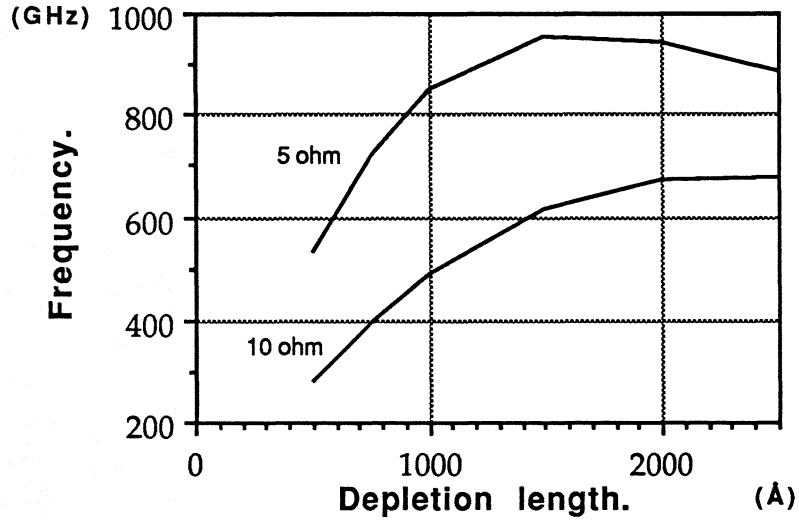

Fig. 8. Calculated values for f_{max} as a function of depletion length for two different series resistances 5 Ω and 10 Ω,.assuming v_s is 10^6 m/s and the area A of the diode is 12 μm^2. These parameters are probably obtainable for InAs.

Experiments on this material system with quantum well diodes have been performed with good results [16]. Large peak to valley ratios can be obtained, since barriers of AlSb in InAs are very high, ≈1.3 eV, compared to ≈1 eV for AlAs barriers in GaAs. Even though this is a new material and hardly tested it looks to be the most promising for the future because of the possibility to get high carrier velocity and low series resistance. The peak velocity for bulk InAs is $\approx 3.6\cdot10^5$m/s [13], around 60%

higher than GaAs $\approx 2.2 \cdot 10^5$m/s. For short distances in GaAs this peak velocity can be exceeded by two to three times, [12]. If the same is true for InAs the maximum velocity would be approximately $10 \cdot 10^5$m/s, and this without the necessity of having a low field outside the barriers. Due to the lower bandgap of InAs as compared to GaAs, better ohmic contacts should be obtainable. In Fig. 8, calculated values for f_{max} is presented with $v_s = 10 \cdot 10^5$m/s and the series resistance $R_s = 10\ \Omega$ and $R_s = 5\ \Omega$. A maximum frequency is then $\approx$900 GHz for a 5 Ω

Finally it is interesting to use Eq. (15) to predict the the maximum output power at e. g. 750 GHz for an optimized InAs diode with f_{max}=900 GHz (assuming $W+l_{qw}$=1500 Å, $v_s = 10 \cdot 10^5$ m/s, $R_s \approx 6\ \Omega$ for a 12 μm^2 area). Assuming that at this frequency it is possible to match the diode to a load resistance of 10 Ω (higher losses causes a larger load resistance), the maximum power to the load (Eq. (15))will be of the order 250 μW. Probably only a fraction of this power (may be 50 %) will be useful The optimum area of this diode is then about 15 μm^2, $R_s \approx 4.6\ \Omega$ and $\Delta I \approx 10$ mA. If a still lower R_s is possible to realize, of course still higher output powers can be achieved.

10. QW-diode Multipliers.

As was pointed out in paragraph 6, the QW oscillator may be very rich in harmonics. One should therefore expect potential high efficiency from a QW diode multiplier. We have designed a Quantum Well (QW) diode frequency tripler with more than 1.2 % efficiency and 0.8 mW output power at about 250 GHz [4]. A comparison between the experimental results and the theoretically calculated efficiency for a tripler using such a diode has been made. The multiplier mount used in our experiments is meant for Schottky-varactor triplers, and has a design similar to Erickson´s [17]. Due to the symmetric I-V characteristic of the QW-diode, see Figure 9, only odd harmonics are obtained for zero bias voltage using the QW in a multiplier. This means that the current of a QW-diode pumped by a sinusoidal signal contains mainly third and fifth harmonics. Thus the idler tuning used in this mount at the second harmonic is of no importance in this case if the bias voltage is zero. In Figure 10 the measured efficiency versus input power for the QW-diode at three different output frequencies is plotted. It can be seen that the efficiency increases with input power up to a certain level where it becomes more or less saturated. Maximum efficiency was obtained for zero voltage bias.

Using the large signal multiplier analysis program developed by Siegel et al. [18] and modified by us for the QW-diode, the efficiency of the diode was calculated as a function of the input power. A simple equivalent circuit consisting of a non linear capacitance in parallel with a nonlinear resistance was assumed for the QW-diode. A series resistance represents frequency dependent (due to the "skin effect") losses. The capacitance of the diode was assumed to vary inversely as a function of the length L of the depletion region. The parallel resistance of the QW-diode was assumed to follow the measured I-V characteristic of the diode, see Figure 9. The frequency dependent series resistance of the QW-diode was calculated to be between 22-32 Ω (at 83 GHz) depending on the contact resistance (measured to be between $2 \cdot 10^{-6}$ - $4 \cdot 10^{-6}\ \Omega cm^2$) of the chip.

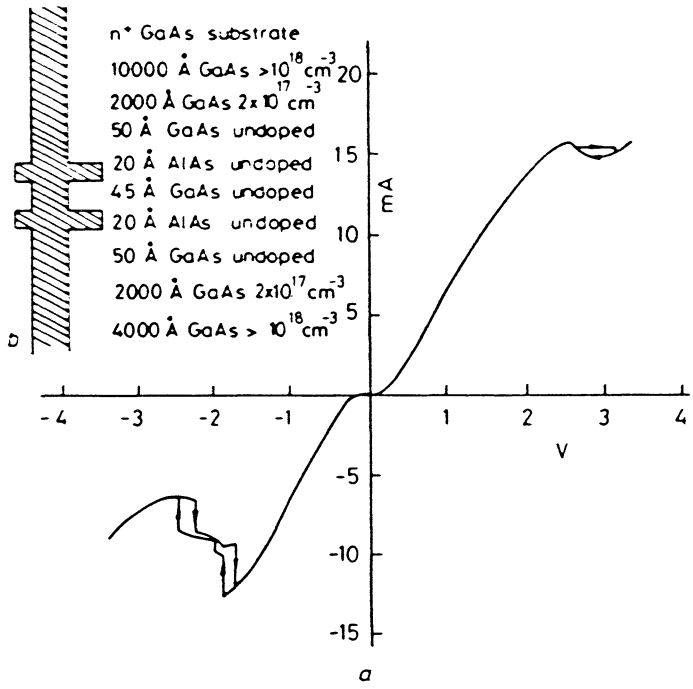

Fig. 9. The IV-characteristic of the QW-diode used in the multiplier experiments.

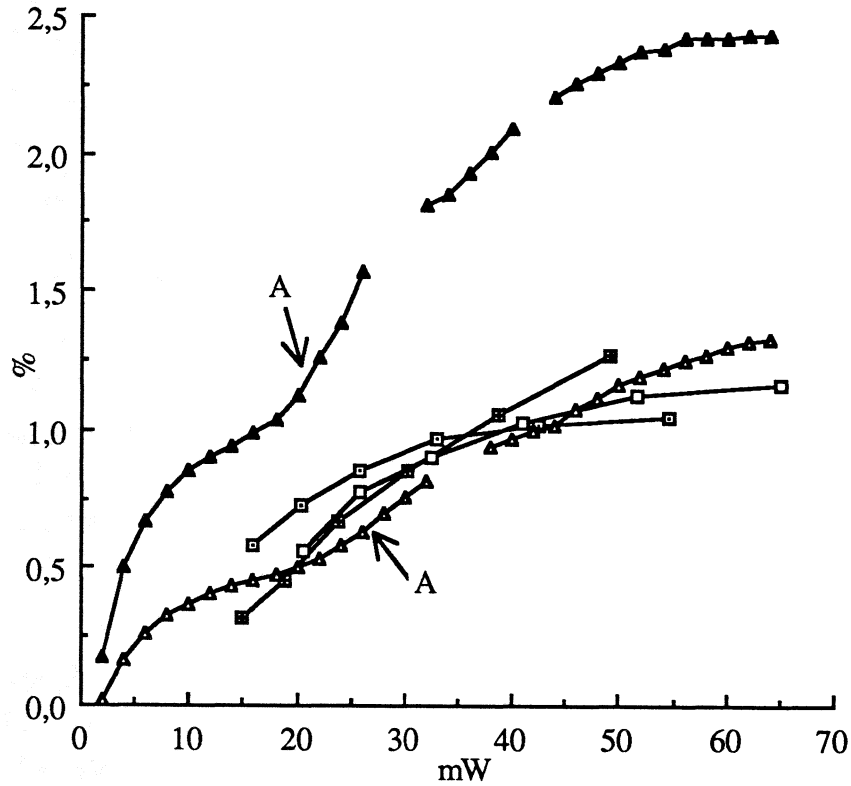

Fig. 10. Measured and calculated efficiency vs input power for the tripler.
(□): measured efficiency at 242 GHz.
(▣): measured efficiency at 249 GHz.
(▣): measured efficiency at 257 GHz.
(▲): calculated efficiency for 249 GHz, contact resistance is 2.10^{-6} Ωcm^2.
(△): calculated efficiency for 249 GHz, contact resistance is 4.10^{-6} Ωcm^2.

The theoretically calculated results at an output frequency of 249 GHz are shown in Figure 10 for -0.2V bias voltage (≈ zero bias). It is seen that one for a contact resistance of $4 \cdot 10^{-6}$ Ωcm^2 the experimental and theoretical curves agree. However, due to the negative differential resistance above about 2V (see Figure 9) the program did not always converge, as indicated by the broken line curve in Figure 10.

At the points "A" in Figure 10 the theoretically calculated efficiency starts to increase. This is due to the voltage swing of the pump signal across the QW-diode exceeds the voltage for peak current in the I-V characteristic of the diode, see Figure 9. Thus the negative differential resistance portion of the I-V characteristic of the QW enhances the efficiency of the tripler.

It can be seen that the general behaviour of the theoretical curves agree well with the measured ones. Thus the simple equivalent circuit applied here for the QW-diode could be used as a first approximation for the diode. The equivalent circuit of the QW-multiplier is further investigated in Ref. [19].

11. QBV-diode multipliers.

A new device, the Quantum-Barrier-Varactor diode (QBV-diode), has been proposed by us for use in multipliers for millimeter-waves [20]. Since the capacitance vs voltage characteristic is symmetric, only odd harmonics are obtained. Hence there is no idler circuit to consider for the tripler and only one for the quintupler. It is shown that for triplers and quintuplers, the theoretical efficiency using QBV's is comparable or possibly larger than using Schottky-varactor diodes.

By making the width and/or the height of the barrier in the QBV-diode such that the conduction current through the device is negligible for the voltage interval defined by the pump voltage swing, the device can be modelled simply as a voltage dependent capacitance.

A QBV-diode may be fabricated in the same way as the quantum well mesa diode, but with the epitaxial GaAs/AlGaAs/GaAs material designed as indicated in Fig. 11. The AlGaAs barrier will to a large extent prevent electrons to pass through the structure and will cause a depleted region with a voltage dependent width, which is associated with a voltage dependent capacitance C(V). When the diode is biased in the forward direction, the depleted region will appear on one side of the barrier, and the depletion capacitance of the device will decrease with increasing voltage. Since the diode is essentially symmetric, a reversed bias will in the same way cause a decrease of the capacitance of the device. Hence, the maximum capacitance is obtained for zero voltage and is determined by the thickness of the AlGaAs barrier. The minimum capacitance, which occurs for maximum bias voltage, is determined by the doping concentration and the extension of the low doped region "L" (see Fig. 11). In fact a similar capacitance swing vs voltage as for the Schottky-varactor diode is expected. It is obvious that in future work one should search for optimum doping profiles.

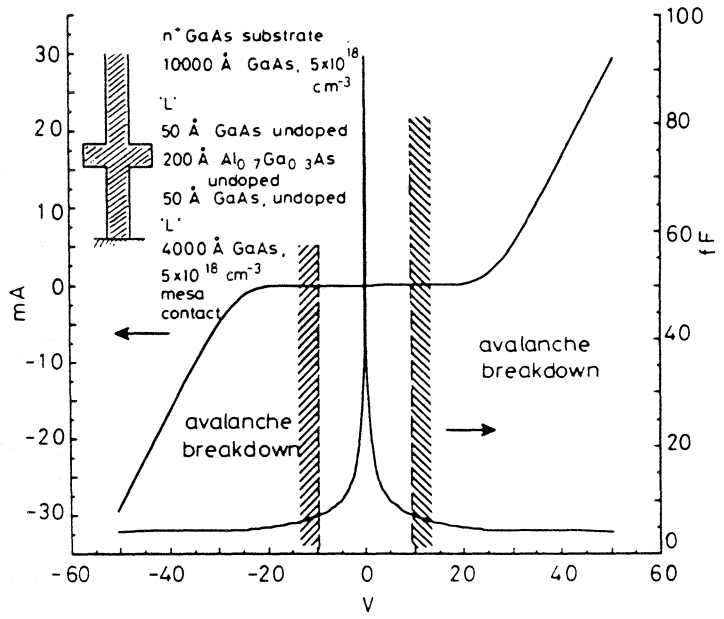

Fig.11 The doping profile of the mesa structure. Also shown is the I-V and C-V characteristic of the diode with Ø=4.5 μm, L=4000 Å, and $N_d=2\cdot10^{17}$ cm^2, assuming no avalanche breakdown. The avalanche breakdown will limit the allowable rf-voltage swing.

For the QBV-diode as well as for the Schottky-varactor diode, the series resistance $R_s(V)$ is bias dependent. In order not to overestimate the QBV-diode multiplier efficiency, we have in the calculations presented below, used a constant depletion region series resistance contribution equal to $R_{depl.max}$. Notice that for a Schottky-varactor diode tripler, the idler current at $2\cdot\omega_p$ will deteriorate the tripler performance, since any finite reactance termination will cause power losses in the series resistance.

An I-V profile for a quantum barrier alone, consisting of $Al_{0.7}Ga_{0.3}As$ with a length of 200 Å, has been determined from experiments [21]. Using this information, we calculated the I-V and C-V characteristics for a 4.5 μm device with this barrier followed by a 4000 Å low doped region ($N_D=2\cdot10^{17}$ cm-3) (see Fig. 11). Notice (Fig. 11) that the differential conductance defined as dI/dV is quite small compared to ωC.

Using a large signal multiplier analysis program based on the principle of harmonic balance developed by Siegel et. al. [18] and modified by us for the QBV-diode, the efficiency of the QBV-multiplier was calculated for a few different device structures as a function of input power. The equivalent circuit of the device and the procedure for optimization are very similar to those used for the Quantum Well multiplier in ref. [4].

The theoretical efficiency vs input power for a tripler to 105 GHz is shown in Fig. 12. The length of the region "L" is chosen to be 4000 Å and the doping of the region is used as the parameter in Fig. 12. As mentioned above the series resistance used in these calculations is $R_s = R_{depl.max} + R_{contact}$, where $R_{contact}$ is assumed equal to 3.14 Ω corresponding to a contact resistance of $0.5x10^{-6}$ ohm cm^2. The results presented in Fig. 12 show that the conversion efficiency is high for low input

powers using low doping in the depletion region. The highest efficiency of 54 % was obtained for $N_D=2\cdot10^{17}$ yielding a series resistance of 19.2 Ω (see Fig. 2). This result is comparable to the maximum efficiency of 60 % theoretically and 28 % experimentally for a 3x35 GHz Schottky-varactor tripler [22] with a series resistance of 10 Ω. We found that the maximum efficiency for a QBV-diode having a series resistance of 10 Ω is 64 %. It can be seen that the series resistance does play an important part in achieving optimum efficiency for a QBV-multiplier, which of course is also the case for a Schottky-varactor multiplier. A preliminary investigation of the QBV quintupler (output frequency 175 GHz), indicates efficiencies of more than 30 %. For a 175 GHz optimum Schottky-varactor quintupler a theoretical efficiency of 30 - 40 % has been predicted for the case when all idlers have optimum reactance loads, and 15 - 25 % when two idlers are optimized [22].

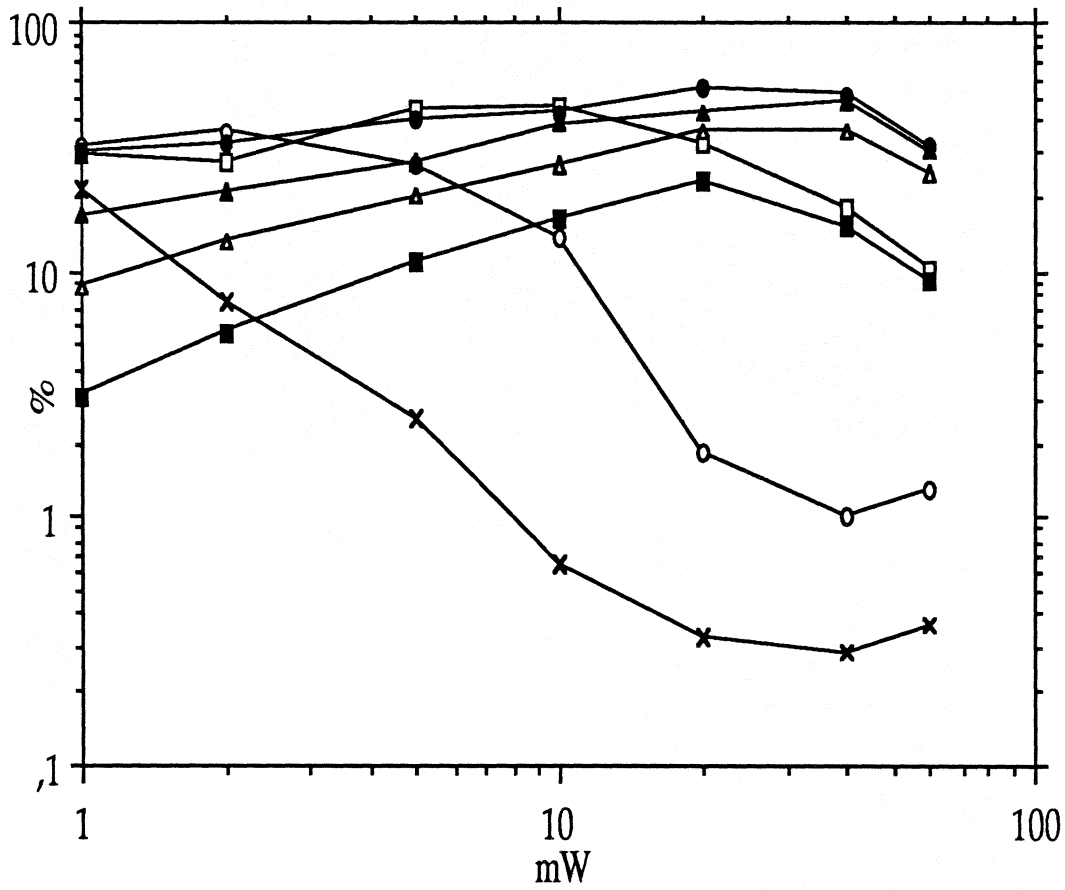

Fig. 12. Efficiency vs input power for a QBV-tripler. The doping N_D of region "L" in Fig. 1 is used as the as the parameter. The length of "L" is 4000 Å.

(✗): $N_d = 1\cdot10^{16}cm^{-3}$, $R_s = 51.2\Omega$.
(○): $N_d = 2\cdot10^{16}cm^{-3}$, $R_s = 37.1\Omega$.
(□): $N_d = 4\cdot10^{16}cm^{-3}$, $R_s = 25.5\Omega$.
(●): $N_d = 8\cdot10^{16}cm^{-3}$, $R_s = 19.2\Omega$.
(▲): $N_d = 2\cdot10^{17}cm^{-3}$, $R_s = 15.1\Omega$.
(Δ): $N_d = 4\cdot10^{17}cm^{-3}$, $R_s = 13.5\Omega$.
(■): $N_d = 8\cdot10^{17}cm^{-3}$, $R_s = 12.6\Omega$.

It is essential also that the ohmic contact is reasonably good, although at the high frequencies involved even a contact with poor dc-qualities will work well [23]. The optimum doping profile may actually be different for different frequencies of operation. The reason is that the doping profile has an influence on not only C(V), but also on the I-V characteristic, i. e. the conductance G(V)=dI/dV, which is in parallel with C(V). As a rule of thumb, G ought to be small as compared to the minimum parallel susceptance ωC for the whole bias voltage range.

We here fabricated a first batch of $\varnothing = 3$ μm QBV-diodes using MBE-material (from IMEC in Leuven, Belgium). The barrier consist of 210 Å AlGaAs with 70% Al. Outside the barrier a 50 Å undoped spacer layer of GaAs is grown. Outside these spacer layers on each side 5300 Å region of GaAs is grown, doped to $1 \cdot 10^{17}$ cm^{-3} followed by highly doped GaAs to provide good ohmic contacts. The initially measured IV-characteristics showed a current density about $8 \cdot 10^5$ times larger than expected. We intend to address this problem in the near future.

Despite the too large current density, the conversion efficiency was reasonably high. The experiments were conducted in a Schottky-varactor waveguide tripler structure of the same design as described in Ref.[17]. For an output frequency of 225 GHz a maximum efficiency of more than 5 % and an output power of more than 2 mW was measured. For a good Schottky-varactor diode tripler for the same frequency, using diodes from Univ. of Virginia (type 6P2), an efficiency of about 4.5 % was obtained. A theoretical analysis of the efficiency of the used diodes yielded $\eta \approx 6.4$ %, while a diode with the expected smaller current should offer $\eta \approx 13.6$ % efficiency for 32 mW input power. An ohmic contact resistance for the mesas of $3 \cdot 10^{-6}$ ohm cm^2 was assumed in the analyze [4].

12. Conclusions.

The work on applications of QW-diodes for millimeter waves and submillimeter waves have only started. Although the oscillator power obtained experimentally so far is low, it is sufficient in some applications such as for local oscillators in superconducting mixers or as a signal source for measurement systems. The main design problems are related to the device itself and the mm/submm-wave circuit, which should yield the optimum embedding impedance(s) required by the device. Besides oscillators and multipliers, mixers with gain can be constructed. However, it is not yet known whether it will be possible to achieve low mixer noise.

The QBV-diode is potentially a very competitive device in millimeter-wave multiplier applications. The obtainable multiplier efficiency with a QBV-diode is shown to be comparable to corresponding Schottky-varactor multipliers. The main advantage is that idler tuning is not required for a tripler, and only one (two) idler(-s) has to be considered for a quintupler (heptupler).

13. Acknowledgements.

The author would like to thank Dr. T. Andersson and Mr. J. Söderström for their kind supply of MBE-material for the experimental quantum well diodes and Prof. S. Yngvesson for useful discussions. Milena Mattas is acknowledged for her help in drawing most of the figures. The Swedish board for Technical Development and the European Space Agency (ESTEC contract RFQ/3-6172/88/NL/PB) are acknowledged for financial support.

References.

[1] T. C. L. G. Sollner, E. R. Brown, W. D. Goodhue and H. Q. Le, "Observations of millimeter-wave oscillations from resonant tunneling diodes and some theoretical considerations of ultimate frequency limits," Appl. Phys. Lett., vol. 50, pp. 332 - 334, 1987.

[2] A. Rydberg, H. Grönqvist, E. Kollberg, "A theoretical and experimental investigation on millimeter-wave quantum well oscillators," Microwave and Optical Technology letters, vol. 1, pp. 333 - 336, 1988.

[3] L. L. Chang, L. Esaki, R. Tsu, "Resonant Tunneling in Semiconductor Double Barriers," Appl. Phys. Lett., vol. 24, pp. 593 - 595, 1974.

[4] A. Rydberg and H. Grönqvist, "Quantum well high efficiency millimeter-wave frequency tripler," El. Lett. vol. 25, pp. 348 - 349, 1989.

[5] A. Mortatzawi, V. P. Kesan, D. P. Neikirk, and T. Itoh, "A self oscillating QWITT diode mixer", to be published in the Proceedings of the 19th European Microwave Conference, London, 1989.

[6] E. Kollberg, "Superconducting Devices and Quantum Well Diodes in Low Noise Heterodyne Receivers, Part 2: Quantum Well Diodes", Alta Frequenza, Vol. LVIII, No. 5-6, pp. 521-530, 1989.

[7] V. P. Kesan, D. P. Neikirk, P. A. Blakey, B. G. Streetman and T. D. Linton, "The influence of transit-time effects on the optimum design and maximum oscillation frequency of quantum well oscillators," IEEE Trans. on Electron Devices, vol. ED-35, pp. 405 - 413, 1988.

[8] E. R. Carlson, M. V. Schneider and T. F. McMaster, "Subharmonically pumped millimeter-wave mixers," IEEE Trans. Microwave Theory and Techniques, vol. MTT-26, pp. 706 -715, 1978.

[9] E. R. Brown, W. D. Goodhue and T. C. L. G. Sollner, "Fundamental oscillations up to 200 GHz in resonant tunneling diodes and new estimates of their maximum oscillation frequency from stationary-state tunnel theory," J. Appl. Phys., vol. 64, pp. 1519 - 1529, 1988.

[10] H. Grönqvist, A. Rydberg, H. Hjelmgren, H. Zirath, E. Kollberg, J. Söderström, and T. Andersson, "A millimeter wave quantum well diode oscillator," Proceedings 18th European Microwave Conference, Stockholm, pp. 370-375, 1988.

[11] M. A. Lee, B. Easter, and H. A. Bell, Tunnel diodes, Chapman and Hall, London, 1967.

[12] J.Y-F. Tang and K. Hess, "Investigation of Transient Electronic Transport in GaAs Following High Energy Injection.", IEEE Trans. Electron Devices, Vol.ED-29, pp.1906-1911, 1982.

[13] "Landolt-Börnstein, Numerical Data and Functional Relationships in Science and Technology.", Vol.17a, Springer-Verlag Berlin, 1982.

[14] T.G. Andersson, Z.G. Chen, V.D. Kulakovskii, A. Uddin, J.T. Vallin, "Variation of the Critical Layer Thickness with In Content in Strained InxGa1-xAs-GaAs Quantum Wells Grown by Molecular Beam Epitaxy.", Appl. Phys. Lett. Vol.51, pp.752-754, 1987.

[15] S.M. Sze, "Physics of Semiconductor Devices.", Wiley, 1981.

[16] J.R. Söderström, D.H. Chow, T.C. McGill, "InAs/AlSb Double Barrier Structure with Large Peak-to-Valley Ratio: A Candidate for High Frequency Microwave Devices.", To be published.

[17] N.R. Erickson, "A high frequency tripler for 230 GHz," Proc. European Microwave Conf. 1982, pp. 288-292.

[18] P.H. Siegel, A.R. Kerr and W. Hwang, "Topics in the Optimization of Millimeter Wave Mixers," Nasa Technical Paper 2287, March 1984.

[19] A. Rydberg, "On the Design of Quantum-Well Multipliers", Proc. 14th International Conference on Infrared and Millimeter Waves, Würzburg, BRD, pp. 467-468, 1989.

[20] E. Kollberg and A. Rydberg, "Quantum-Barrier-Varactor Diodes for High Efficiency Millimeter-Wave Multipliers.", Electronics Letters, Vol. 25, No. 25, pp. 1696-1697, 1989.

[21] I. Hase, H. Kawai, K. Kaneko and N. Watanabe, "Electron transport through the MOCVD grown GaAs/AlGaAs/GaAs heterojunction barrier," Electronics Lett., vol. 20, pp. 491-492, 1984.

[22] T.J. Tolmunen, "High efficiency Schottky-varactor frequency multipliers at millimeter waves," Thesis for doctor of Technology degree, Helsinki University of Technology, Report S 180, 1989. (Partly published in Int. J. of Infrared and Millimeter Waves, vol. 8, pp. 1313 - 1353 (1987) and vol 9, pp. 475 - 518 (1989))

[23] H. Zirath, "On the high-frequency behaviour of ohmic contacts," Proc. 19'th European Solid State Device Research Conference ESSDERC'89, Berlin, BRD, pp. 63-66, 1989.

LOW NOISE 500–700 GHZ RECEIVERS USING SINGLE–DIODE HARMONIC MIXERS

Neal R. Erickson

Millitech Corp.
P.O. Box 109
S. Deerfield, MA 01373

and

Five College Radio Astronomy Observatory
Dept. of Physics and Astronomy
University of Massachusetts
Amherst, MA 01003

ABSTRACT

A second harmonic mixer has been built using a single Schottky diode achieving an overall noise temperature only 25% higher than that of a fundamental mixer at the same frequency. This mixer has been built in two models for center frequencies near 600 GHz. These mixers are pumped by frequency multiplied InP Gunn oscillators providing about 2 mW output. The theory of mixer noise and conversion loss agree fairly well with the experimental results. The best results are a receiver noise temperature of 5300 K SSB at 550 and 665 GHz. This mixer design will be used in receivers for 490 and 550 GHz in the Submillimeter Wave Astronomy Satellite.

INTRODUCTION

Harmonic mixers have long been used to frequency convert signals at a frequency where it is inconvenient or impossible to obtain a fundamental local oscillator source. However they have not offered noise performance comparable to fundamental mixers except at low frequencies where two diode balanced designs are available [1]. Even these have proven difficult to make work at their full potential, because of the need to match the two diodes and embed them in a stripline structure. While single diode harmonic mixers are much simpler, previous single diode mixers have not been designed to achieve an optimum set of embedding impedances at the LO and signal frequencies, nor has any detailed theoretical study been done to investigate the full potential of such a mixer. In this work we have made a computer study of a submillimeter harmonic mixer using a single Schottky diode to determine the optimum LO and signal impedances and have

constructed a mixer for 550 GHz which largely agrees with this theory and compares favorably with a fundamental mixer at the same frequency.

THEORETICAL STUDIES

A mixer analysis program [2] may be used to derive the optimum embedding impedances, bias current and LO power for a single diode mixer using an idealized Schottky diode. While this program is written for fundamental mixing, its output may be used to predict harmonic mixing results as well. This program includes all diode parameters including junction capacitance, and allows inputs of circuit impedances at three harmonics of the LO. Mixer bias voltage and current are also parameters (and thus indirectly the LO power). Outputs are conversion loss for conversion products up to the third harmonic, and the mixer noise temperature.

One way to achieve a low conversion loss in harmonic mixing is to suppress fundamental mixing (conversion of the signal to a frequency near that of the LO in this case), by severly mismatching the diode at the LO frequency and then using large amounts of LO power. Since this work was aimed at a submillimeter mixer, this approach is not practical, as LO power is quite limited. In this analysis the program was modified to fix the available LO power in order to use it as a constraint. The LO power was chosen to be 2 mW since this is all that is typically available from multipliers near 300 GHz.

The goal of the original work was to build a harmonic mixer for a frequency of 550 GHz in single mode waveguide, using a crossed waveguide structure to bring in the LO power. This allows a free determination of the impedances at the LO and signal harmonics. We made the assumption of a mixer with a low IF having identical embedding impedances at the LO harmonics and the two adjacent signal sidebands. The impedance at the signal frequency was determined by scale modeling the signal waveguide in the mixer mount and determining in an iterative process the closest impedance match achievable without resorting to extreme dimensions in the mount. This impedance was determined to be $80 + 120j\,\Omega$ while the third harmonic impedance was chosen at an estimated value of $50 + 50j\,\Omega$ (this value is not critical). The important variable to be determined was then the impedance at the LO fundamental frequency. Once an approximate value was found, the mixer bias current was optimized and then fixed at this value of 0.2 mA.

At this point the conversion loss and mixer noise temperature were calculated for a range of fundamental impedances. The mixer noise is found to have a broad minimum

which is not coincident with the conversion loss minimum. The best compromise depends on the IF noise temperature, but in most cases favors the lower mixer noise. This results in a predicted mixer noise temperature of 2100 K SSB and a conversion loss of 11.5 dB, at an impedance of 50 + 150j Ω. A 1 dB lower loss may be achieved with a 10% increase in mixer noise at an impedance of 100 Ω. Even lower conversion loss may be reached at much higher impedances but at the cost of much higher noise. Over the region of minimum mixer noise, the effective diode noise temperature (the equivalent attenuator temperature of the diode) was found to be 200 to 250 K, which is lower than seen in most fundamental mixers in the submillimeter. In addition, the predicted conversion loss is only about 2 dB higher than predicted for a typical fundamental mixer, so the expectation is that a harmonic mixer should be fairly competitive, with perhaps a 25% higher noise. A practical single ended mixer also has input losses associated with coupling in the LO which are typically 10% in the submillimeter. One surprising result is that the IF impedance is predicted to be 1000 Ω, resulting apparently from the low bias current, and the relatively large LO drive. This makes IF matching over a wide bandwidth more difficult.

SCALE MODEL STUDIES

In order to design an actual mixer having the optimized impedances it was necessary to do some scale modeling in order to fully understand the waveguide embedding structure. Initially the signal waveguide dimensions and contact whisker length were chosen to achieve a reasonable impedance match at the signal frequency. With the diode mounted in the signal waveguide this problem may be separated from the LO waveguide if the filter coupling in the LO is assumed to present a short circuit at the signal frequency. The waveguide height was chosen to be as low as practical for reasonable fabrication (0.10 mm high for a width of 0.35 mm at the actual size) since even the lowest practical height was too great for optimum matching. These dimensions resulted in the signal frequency impedances used in the computer studies.

Using a computer aided design program, a three section coaxial filter with air dielectric was designed to present a short circuit at the top wall of the waveguide at the signal frequency but a nearly optimum LO impedance when the effect of the contact whisker and LO waveguide are taken into account. The LO backshort was assumed to be $\lambda/4$ away from the coupling post in this design to maximize the fixed tuned bandwidth and minimize losses. In designing this filter, coaxial impedances were constrained to the range 20 to 60 Ω to avoid excessively difficult construction. The LO waveguide

impedance was optimized at 150 Ω. The filter was then incorporated into the mount and its effect verified. The circles of impedance as the LO backshort is tuned pass near the expected optimum impedance, with fairly minimal frequency dependence.

The construction of the mixer is shown in Fig. 1. The filter uses variations in the inner and outer conductor diameters to achieve the largest impedance ratio. In addition only the first section of the filter is designed to be cut off to higher modes at the operating frequency. Note that the first section of the center conductor of the filter consists entirely of the diode chip, which is cut into a roughly circular shape. Another filter is used on the other side of the LO waveguide to eliminate loss of power out the IF port. The filter center pin is supported by a machinable ceramic (Macor) ring, with 50 Ω impedance through this ring (the highest impedance practical) to minimize problems with the IF match.

EXPERIMENTAL RESULTS

The mixers of this design were built with an electroformed signal waveguide with an integral conical feed horn. The LO waveguide was machined as a channel in a block attached to the electroform. The mixer diode in the first mixer for 550 GHz is a type 1E13 from the University of Virginia, with $C_j(0) = 1.5$ fF, $R_s = 22$ Ω and epitaxial doping optimized for room temperature operation. This diode was contacted by a 4 μm diameter NiAu wire with a length of 60 μm. Local oscillator power was provided by a frequency tripled InP Gunn oscillator, with about 2.5 mW output at 275 GHz. This mixer was used with a 1.4 GHz IF amplifier having a noise temperature of 50 K. An IF matching circuit was designed to provide an IF VSWR of less than 2:1 over a 500 MHz bandwidth. The unmatched IF impedance was measured to be 350 Ω, which is significantly lower than the prediction of 1000 Ω, but still higher than normal for a fundamental mixer at this frequency.

Local oscillator noise was found to be a potential problem with this mixer since there is no rejection of noise sidebands on the LO, which produce IF noise with a lower order mixing than that for the signal. However, this is found not to be a problem when an InP Gunn oscillator is used. When a GaAs Gunn is used the noise can be substantial, particularly at certain settings of the LO backshort, and thus these oscillators are not suitable for this application, unless perhaps a very high IF is used.

This receiver achieves a best noise temperature of 5300 K SSB at 550 GHz and a conversion loss of 12.8 dB with the mixer at room temperature. Optimum bias current is 0.2 mA as predicted, with the bias voltage varying from 0.5 to 0.65 V. The diode

effective noise temperature is 240 K, also as predicted. The higher than predicted conversion loss may result from input losses. The tripler was connected to the mixer with a 3.7 cm length of waveguide with a loss of 0.7 dB. While the mixer and tripler could be connected directly together, they could be made to work better with the long connecting guide because the length of the guide in combination with the tripler output mismatch modulates the LO impedance at the diode. If the phase is correct, the mismatch can favor coupling of LO power to the diode while simultaneously enhancing the impedance at the signal and image. With the incorrect phase the situation can be made worse. Thus the "low IF" approximation with identical impedances at all nearby frequencies used in this design is not strictly true.

The receiver noise temperature is 5300–7000 K across the frequency range 535 to 572 GHz with a ripple on a very fine scale due to the interaction with the LO multiplier. This frequency dependence is shown in Fig.2. No real trend is seen in the noise vs frequency. This mixer was also tested at 632 GHz where the noise is 6800 K. An identical mixer has been tested at just 637 GHz where it is about 5% noisier than the first. This bandwidth of operation with only backshort tuning exceeds that of fundamental mixers with similar waveguide dimensions. This may result from a higher operating impedance level which matches better to the relatively high mixer mount impedance. Since LO power is relatively difficult to obtain even for a harmonic mixer, we also measured the behavior of the conversion loss and noise as the LO power varies. A reduction of the tripler output by about a factor of two caused only a 10% increase in conversion loss and a 7.5% increase in receiver noise. Thus the mixing is fairly well saturated at 2 mW input, although more power will always work better, since the LO tuning may be altered to suit the power available.

A third mixer of identical design except scaled to higher frequency has been tested at 665 GHz using a U.Va. type 1I8 diode having a capacitance of 0.8 fF which also yields a best room temperature noise of 5300 K SSB. If the behavior as a function of frequency is the same as the first mixer tested, then similar results should be obtained up to 750 GHz. LO in this case is provided by an InP Gunn oscillator followed by a cascaded pair of frequency doublers producing 3 mW at half the signal frequency. This performance is superior to the 6300 K measured for a waveguide fundamental mixer of similar construction using a laser LO at 690 GHz, although the results are not directly comparable since this fundamental mixer was used with an older diode with $C_j(0) = 2$ fF. Use of the newer 1I8 diode in this mixer as well as in the 550 GHz harmonic mixer could be expected to lower the noise.

Two of these mixers were tested at lower temperatures to determine the noise

reduction with cooling. A temperature sensor was bolted to the mixer block and the complete mixer, IF amplifier and LO multiplier were slowly cooled in a styrofoam box partially filled with liquid nitrogen, with data taken over a range of temperatures. It is essential to cool the multiplier with the mixer since the connecting waveguide must be too short for effective thermal isolation. Multipliers have proven to be quite reliable at low temperature and even increase in output power. The Gunn oscillator was maintained at room temperature. Unfortunately, these tests were not begun with the diode contacts producing the very best results, so the room temperature noise was 6000 K SSB in both cases. However the cooling curve should be similar for all contacts. For the 665 GHz mixer the data showed a nearly linear decrease in noise with temperature, with a minimum value of 4300 K at 208 K. It became impractical to continue cooling below this temperature with such a crude setup. The 550 GHz mixer was also tested with the cooling continued down to 106 K in this case, resulting in a reduction of the receiver noise to 3100 K. This data is shown in Fig. 3. This noise is fit quite well by assuming that the mixer noise scales with ηT as measured from the dc IV curve, while the IF noise scales linearly with T. There is evidence from these curves and the IV data that even lower temperature operation would be beneficial, even though the diodes in these tests are very highly doped and show a rather nonthermal IV curve even at room temperature ($\eta = 1.2$–1.3). This doping is necessary in order to achieve the highest cutoff frequency and thus optimized coolable diodes are not presently practical for this frequency.

APPLICATIONS

The advantages of a harmonic mixer are quite substantial when the difficulties of producing the LO are considered. For Schottky diodes sufficient power is presently not available except from lasers for frequencies above 500 GHz. The constraints on the IF of a mixer used with a laser may significantly increase the receiver noise for many applications. The principal drawback of the harmonic mixer over a fundamental mixer is the higher IF impedance which limits the IF bandwidth for achieving a good match. A bandwidth of about 1 GHz with a VSWR of 2:1 is the best that can be done with the present design using the ceramic support ring. Also the interaction with the LO source would ideally require some way to adjust the phase of the LO path which appears a bit impractical for a widely tunable application.

The considerable simplicity of this design makes it very attractive for space applications, and it will be used in the Submillimeter Wave Astronomy Satellite (SWAS) in receivers for 490 and 550 GHz. We expect to operate these receivers at a temperature

of 100–150 K using passive cooling. Consideration is being given to this design for other space missions. The mixer tested at 665 GHz is intended for ground based observations in the 600–700 GHz window, particularly of molecular species such as ^{13}CO J = 6 → 5 not yet observed using laser LO's.

REFERENCES

[1]. Carlson, E.R., Schneider, M.V. and McMaster, T.F., "Subharmonically pumped millimeter–wave mixers," *IEEE Trans. Microwave Theory Tech.*, vol MTT–26, pp. 706–715, 1978.

[2]. Siegel, P.H., Kerr, A.R. and Hwang, W., "Topics in the optimization of millimeter–wave mixers," *NASA Technical Paper #2287*, 1984.

FIGURE CAPTIONS

Fig. 1. Cross section through the submillimeter harmonic mixer. The signal waveguide continues to an integral conical horn.

Fig. 2 Noise temperature vs. frequency of the harmonic mixer designed for 550 GHz. All data is taken at room temperature.

Fig. 3 Receiver noise temperature vs. physical temperature of two receivers using harmonic mixers tested at 550 and 665 GHz. Also shown is the best room temperature value for comparison.

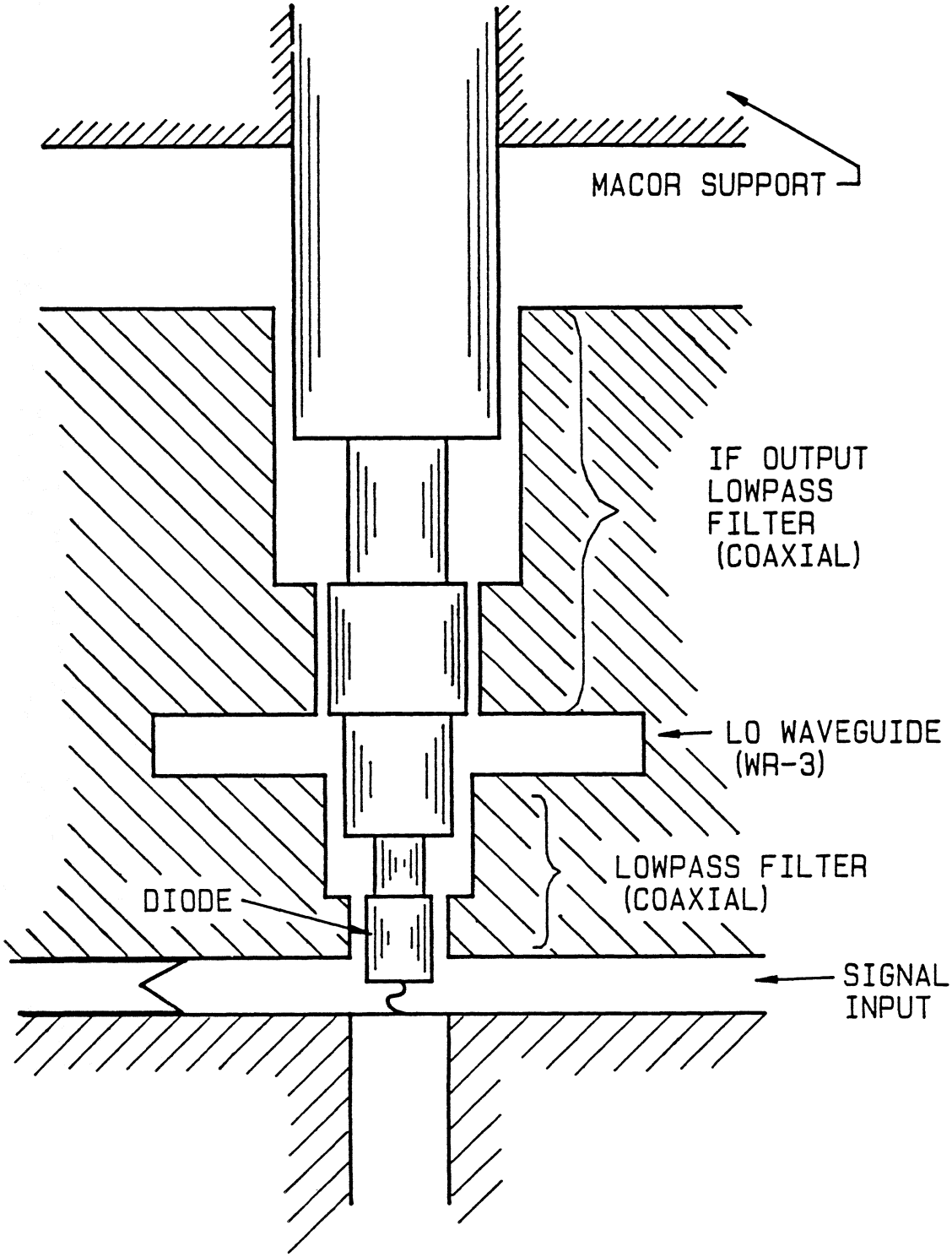
MACOR SUPPORT
IF OUTPUT
LOWPASS
FILTER
(COAXIAL)
LO WAVEGUIDE
(WR-3)
LOWPASS FILTER
(COAXIAL)
DIODE
SIGNAL
INPUT

Fig. 1

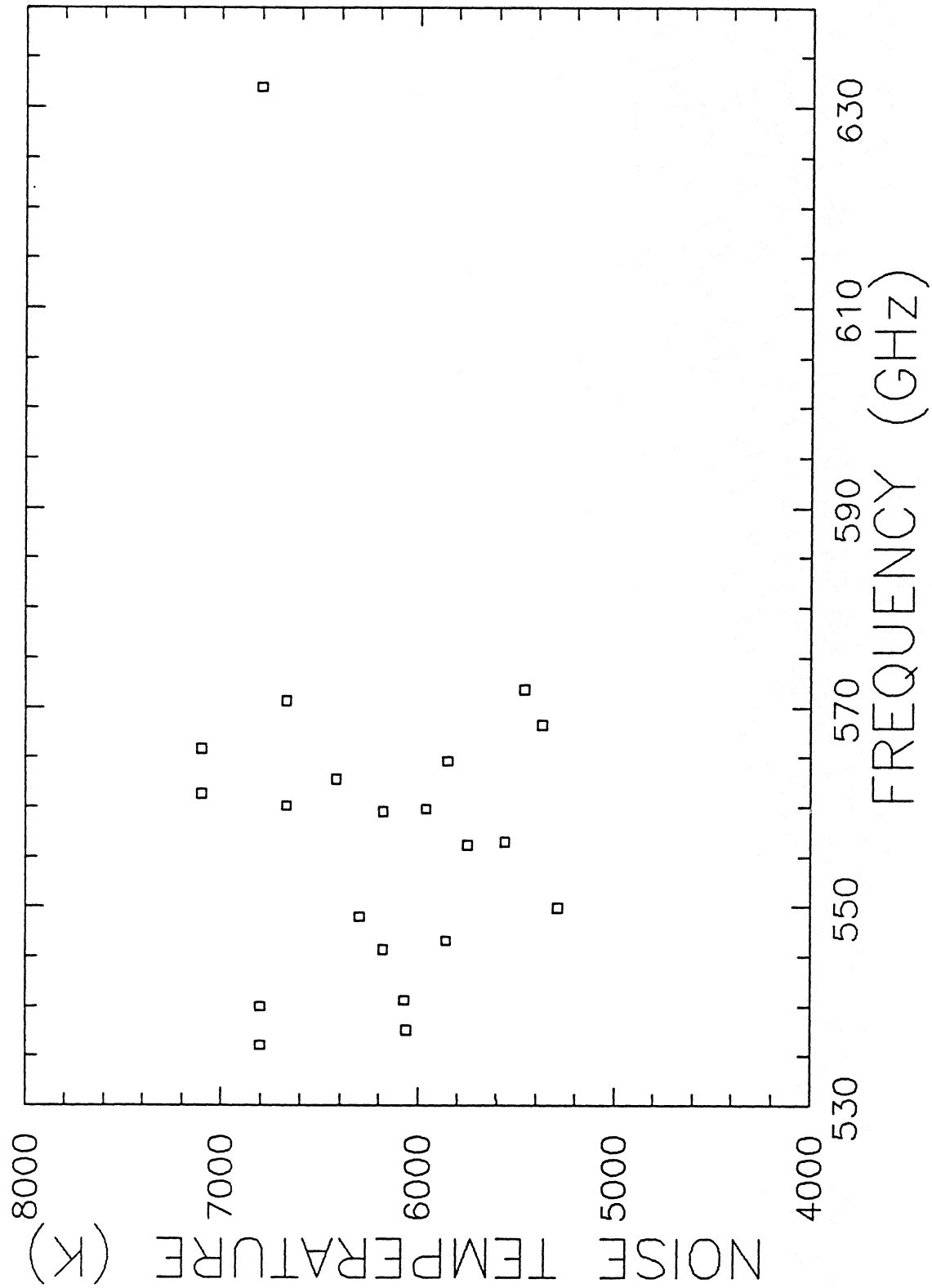
NOISE TEMPERATURE (K)
8000
7000
6000
5000
4000
FREQUENCY (GHZ)
530
550
570
590
610
630

Fig. 2

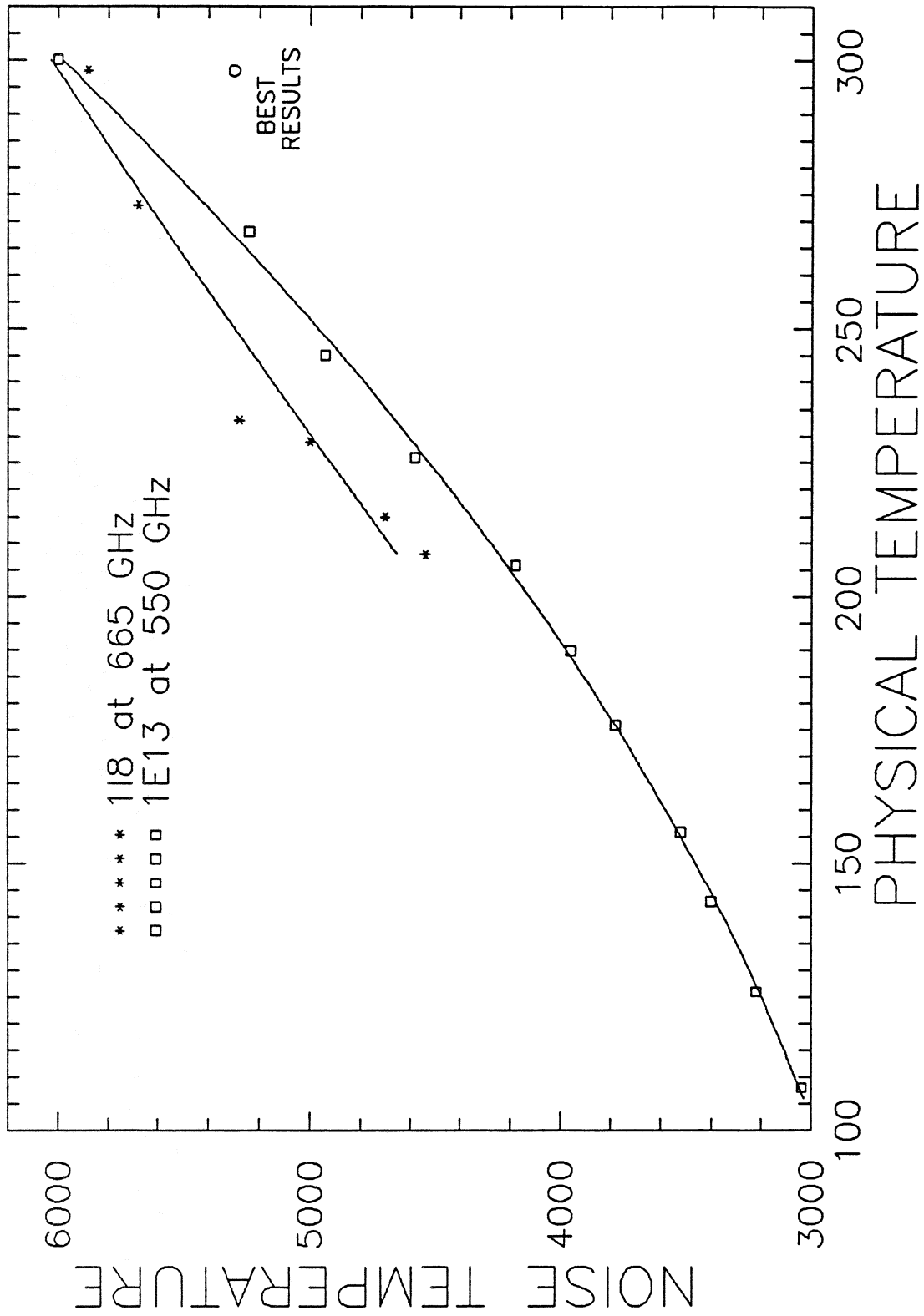
NOISE TEMPERATURE
6000
5000
4000
3000
100
150
200
250
300
PHYSICAL TEMPERATURE
BEST RESULTS
* * * * * 118 at 665 GHz
□ □ □ □ □ 1E13 at 550 GHz

Fig. 3

DEVELOPMENT OF A 600 - 700 GHz SIS RECEIVER

W.R. McGrath[1], K. Jacobs[2], J. Stern[3], H.G. LeDuc[1], R.E. Miller[4], M.A. Frerking[1]

1. Jet Propulsion Laboratory, California Institute of Technology Pasadena, CA 91109
2. I. Physics Institute. University of Koeln, Koeln, West Germany
3. Physics Department, California Institute of Technology, Pasadena, CA
4. AT&T Bell Laboratories, Murray Hill, NJ 07974

Abstract

We report here on the development of a 600 - 700 GHz SIS receiver employing a waveguide mount designed to tune a large junction capacitance. A large scale model was used to optimize the bandwidth and tuning range of the mount. A new design of noncontacting backshort has been developed for use at 600 GHz. It performs as well as competing conventional designs at 100 GHz but is easily fabricated for use at submillimeter wave frequencies. NbN tunnel junctions are being developed for this receiver. We have made a systematic study of the mixer gain and noise of these junctions shunted with microstrip lines as rf tuning elements. This has given values of junction capacitance of 85fF/μ^2 and magnetic penetration depth of 3800Å. Mixer noise temperature as low as 134K has been achieved which is the best reported to date for an NbN junction.

Introduction

Many important chemical species in the interstellar medium, including HCl, H_2O, and CO, produce molecular line emissions in the 600 - 700 GHz frequency range. However, few observations presently exist due to the lack of sensitive heterodyne receivers. The nonlinear tunneling currents in an SIS tunnel junction provide the lowest noise mixing element in receivers at millimeter wavelengths (1-4). Theory suggests these receivers should provide exceptional performance up to the energy gap frequency of the superconductor comprising the tunnel junction. We report here on the development of a 600 - 700 GHz SIS receiver employing a waveguide mount designed to tune a large junction capacitance. Large scale model measurements of the mixer mount will be discussed. A new design of noncontacting waveguide backshort has been developed for use at submillimeter wave frequencies. It has performed well in tests up to 100GHz. Niobium nitride (NbN) tunnel junctions are being developed for this receiver. High quality NbN junctions with microstrip stubs have been fabricated and the mixer gain and noise performance studied at 200-210 GHz as a function of the inductance provided by the stub. This has yielded values for the junction capacitance and magnetic penetration depth. Mixer noise temperature as low as 134K has been obtained for properly tuned junctions. This is the best noise performance ever achieved for an NbN SIS mixer.

The Receiver

Figure 1 shows a block diagram of the receiver. The mixer mount, coupling mirror, and low-noise HEMT IF amplifier are housed in a LHe vacuum cryostat (5). The mixer and IF transformer are mounted to the LHe tank and are shrouded by a 20K radiation shield. Room temperature radiation in the optical path is reduced by cooled quartz and fluorogold far-IR filters. The signal and local oscillator are focussed onto the dual-mode conical feed horn of the waveguide mount by an off-axis mirror. This arrangement reduces standing waves which can become significant at these frequencies with conventional on-axis lenses.

The local oscillator (LO) power is generated by a Gunn oscillator operating at 105 GHz followed by a frequency doubler and tripler combination (6). The output power has been roughly measured at 40μW. This is sufficient power to properly to drive the SIS mixer. The Gunn oscillator frequency is stabilized to better than 2 parts in 10^8 by a phase lock system. The signal and local oscillator (LO) source will be diplexed using either a Mach-Zehnder interferometer or a simple mylar beamsplitter, depending on the strength of the LO source and the rf coupling efficiency of the mixer mount. The interferometer gives a low LO transmission loss, however our experience with 205 GHz SIS mixers (7) suggests that a 95% beamsplitter may be sufficient.

The receiver is calibrated by chopping between ambient temperature and cold (77K) blackbodies made from Eccosorb. The receiver gain and noise can thus be measured for each spectral channel. The sky temperature is then measured by chopping the sky against the cold blackbody.

The IF output power from the mixer is coupled to the low noise IF system by a microstrip impedance transformer. Excellent coupling efficiency to the 50Ω IF system with sufficient bandwidth can be achieved with properly optimized transformers. The first stage of the IF system is a cooled HEMT amplifier with a bandwidth of 1.1 - 1.7 GHz, a gain of 33dB, and a noise temperature about 6K. Room temperature amplifiers are then used to obtain sufficient power to drive an acousto-optic spectrometer.

The SIS Mixer Mount

An important figure of merit for an SIS tunnel junction is the relaxation parameter ωRC where ω is the angular frequency, R is the junction resistance, and C is the junction capacitance. Experimentally it has been found (1) that best results are usually obtained for $\omega RC > 1$, which implies a large junction capacitance which must be properly tuned by the mixer mount. We have chosen a waveguide mount with an adjustable backshort and E-plane tuner in order to accomodate large values of ωRC. A 130X

scale model of this mount is used in conjunction with a 3-6 GHz network analyzer to optimize the mount design (8). The effects on the rf tuning range produced by the size of the coupling hole in the waveguide broad wall, the size of the substrate, and the shape of the rf filter metallization have been studied. In addition, a 2000X scale model of the SIS junction with an integrated microstrip line as a tuning element has also been investigated.

Figure 2 shows a photo of the large scale model. The model waveguide dimensions are 47.5mm x 22.1mm. The mixer block is split along the center of the waveguide broadwall to simplify the machining and construction. A symmetrical channel 17mm wide x 9.5mm deep is cut in each half of the block to hold the junction substrate which is 14.3mm wide x 7mm thick. These substrate dimensions were chosen to correspond to 0.11mm x 0.054mm in the actual mixer. Thinner substrates would become increasingly difficult to fabricate and handle. The substrate is in the E-field direction with the junction metallization parallel to the narrow wall of the waveguide. A microstrip rf filter was designed to provide a short circuit at the wall where the substrate enters the waveguide. The length of the first filter sections were subsequently adjusted to optimize the tuning range of the mount. A 0.86mm diameter coaxial cable was soldered to the rf filter metallization and used to sample the mount impedance at the position of the junction. The E-plane tuner is located about one guide wavelength in front of the junction at 4.8GHz (corresponding to 624GHz in the final mixer).

This mount configuration gives an acceptably broad range of imbedding impedances from 4.55 GHZ to 5.30 GHZ (593GHz to 690GHz). Just above or below these frequencies, the range of impedances shrinks to an unacceptably small region of the Smith chart, but only over a narrow range of frequencies. This effect is related, at least in part, to the large hole in the waveguide produced by the substrate channel. Decreasing the depth of the channel in one half of the block to 6mm extended the acceptable tuning range to 5.57GHz (725GHz). Also, reducing the substrate width to 11.4 mm increased the range of accessible impedances at 5.57GHz. Thus the tunable bandwidth of this mount is about 20%.

This is sufficiently broad as it greatly exceeds the tuning range of the LO sources at these frequencies.

The rf filter metallization must taper down to the junction area. The angle of this taper was found to affect the size of the forbidden tuning region (9). A 90° taper produced a large forbidden region centered 35° above the real axis and encompassing real impedances from 38Ω to 1000Ω at 4.8 GHz(624GHz). A 45° taper significantly reduced the size of the forbidden region and rotated it clockwise around the Smith chart. The shaded area in Fig. 3 shows the final tuning range obtained for the mount. RF junction resistance as low as 5Ω and $\omega RC < 6$ for R=50Ω can be tuned.

Figure 4 shows a photo of one half of the mixer block. The waveguides are cut with conventional machining techniques and then polished to the final dimensions 0.366mm wide x 0.170mm high. This gives a fundamental mode waveguide band of 410GHz - 820GHz. Radiation is coupled into the mixer block with a dual mode conical horn. These horns are fabricated using an electroform technique and their properties have been previously reported (10). The far-field pattern has a 3dB half angle of 6° which allows for easy coupling to telescope feed optics.

New Backshort Design

Contacting backshorts are normally used at these high frequencies due to the very small dimensions of the waveguides. Figure 5(a) shows a conventional contacting backshort. The contact area is critical and must make good contact to produce an acceptable short circuit. These backshorts are excellent in that they provide a short circuit over the entire waveguide band. However, the contacting areas can eventually degrade from sliding friction. It is also difficult to get a uniform contact with the waveguide walls at high frequencies where the waveguide dimensions become fractions of a millimeter.

Another approach commonly used is the noncontacting backshort shown in Fig. 5(b). A thin mylar insulator prevents contact and allows the backshort to slide smoothly. In order to produce an rf short circuit, and hence a large reflection, this backshort has a

series of high impedance and low impedance sections which are usually $\lambda_g/8$ to $\lambda_g/4$ in length (where λ_g is the guide wavelength). However, at very high frequencies the thin high impedance sections become too thin to easily fabricate and the backshort is no longer strong enough to slide snugly in the waveguide. An alternative approach is needed.

A new noncontacting backshort design has been developed (11) and is shown in Fig. 6. In order to obtain a large reflection, a noncontacting backshort must provide a periodic variation of guide impedance on the correct length scale. This is accomplished in the new design by either rectangular or circular holes with the proper dimension and spacing cut into a metallic bar. This bar is dimensioned to form a snug fit in the waveguide with a mylar insulator. The holes replace the thin high impedance sections in the conventional design shown in Fig. 5(b). The new design is easy to fabricate and can be used at any waveguide frequency between 1GHz and 1000GHz. For very high frequencies, above a few hundred GHz, the metallic bar is a piece of shim stock polished to the correct thickness. The holes can be formed by drilling, punching, or can be etched using common fabrication techniques.

Several backshorts were built and tested at 3.1-6.2 GHz and 75-115 GHz with a variety of hole sizes and spacings. Figure 7 shows the reflection for a backshort with rectangular holes. The reflection coefficient is > 0.99 over a 40% bandwidth. This is as good as a conventional backshort. The center frequency is estimated to be 3.87GHz. This implies the high impedance section lengths are $0.16\lambda_g$ and the low impedance section lengths are $0.14\lambda_g$. The presence of the mylar modifies the waveguide modes. The guide wavelengths, λ_g, for the high and low impedance sections were estimated using an approach outlined in references 12 and 13. Figure 8 shows the reflection for a backshort with three circular holes. The reflection is >0.99 over a 26% bandwidth with a center frequency of 4.3 GHz. As can be seen in both of these figures, there are regions of reduced reflection at either the high or low end of the frequency range. These result

from power which leaks through the short due to the complex mode structure produced by the holes.

In order to test if the designs could be scaled to millimeter wave frequencies, a backshort with rectangular holes was fabricated for 75-115 GHz. The results are shown in Fig. 9. As can be seen, this figure is similar to Fig. 7 which implies the design can be scaled to high frequencies.

SIS Junctions

This receiver system will use either Pb-alloy tunnel junctions produced at AT&T Bell Laboratories or NbN-MgO-NbN junctions produced at JPL. It is desirable to use integrated tuning elements with the junctions to resonate out the junction capacitance over a broad bandwidth. We have chosen an open-circuited microstrip stub to provide an inductive susceptance (14). Figure 10 shows the suspended photoresist bridge technique used to produce the Pb-alloy junctions. Since a microstrip stub cannot be easily added after the junction fabrication steps, we have developed the geometry shown in fig. 11. The center conductor is put down first on the substrate. This is covered by an SiO layer, and then the junction and rf filter layer are deposited last to form the ground plane for the line.

A 2000x scale model of this geometry has been investigated. Plane A is the reference plane for the stub. The length of center conductor from A to B forms an inductance L_1 and the rf filter metallization from B to the junction completes the circuit with an inductance L_2. These inductances to good approximation add directly to the inductance L_t of the stub to resonate with the junction capacitance. Figure 12 shows the equivalent circuit. At resonance the real part of the junction impedance is reduced by the factor $n = (L_1+L_t \; / \; L_1+L_2+L_t)^2$. We estimate L_1 =1.4pH and L_2 = 0.6pH for a 5μ wide stub and A-to-B distance of 5μ. This yields typically n = 0.5 - 0.7 depending on junction capacitance and hence L_t. Model measurements at 312 MHz confirm the effect of L_1 and L_2 on the resonant frequency and the value of n. These results indicate that at frequencies near 600GHz, micron scale

features near the junction must be properly included in the rf circuit.

All niobium nitride (NbN) tunnel junctions with MgO barriers are being fabricated at JPL (15). NbN is a chemically stable and mechanically rugged refractory metal which makes it well suited for practical receiver applications. In addition, the high energy gap of 5 mV will allow for operation near 1000GHz and for easier descrimination against interferring Josephson effects. However, the high specific capacitance of these junctions is best tuned with a microstrip stub. Proper design of the stub requires accurate knowledge of the junction capacitance and the magnetic penetration depth in the superconducting film. These parameters are well known for the extensively developed Pb-alloy junctions, but are less accurately known for the new NbN junctions. We have fabricated high quality NbN junctions with microstrip stubs and studied the mixer gain and noise performance at 200-210 GHz as a function of the inductance provided by the stub. This has yielded values for the junction capacitance and magnetic penetration depth.

The phase velocity in the stub determines the length and is calculated using the expression (14)

$$\upsilon/c = (\varepsilon_r \left(t_d + \lambda_1 \coth(t_1/\lambda_1) + \lambda_2 \coth(t_2/\lambda_2)\right) / t_d \ll 1 \quad (1)$$

where ε_r is the dielectric constant, t_d is the dielectric thickness, λ_1 and λ_2 are the magnetic penetration depths in the top and bottom electrodes respectively, and t_1 and t_2 are the thicknesses of the top and bottom elecrodes respectively. For our stubs, the magnetic penetration depth (3000Å - 4000Å), the film thickness (3000Å), and the dielectric thickness (1500Å) are comparable. In this case, υ and hence the resonant frequency are sensitive to λ. Thus λ must be accurately known to properly design the resonant circuit.

Small area, high current density NbN-MgO-NbN tunnel junctions are fabricated using a recently developed trilayer process which

is fully described elsewhere (15). The junctions have an area 1x1 μ^2, a current density J_c = 5000 - 10,000 A/cm^2, and a normal state resistance R_n = 50-70Ω. The gap voltage is V_g = 4.8 mV at 4.2K, and the width ΔVg of the quasiparticle current rise at V_g is typically about 1 mV. This is slightly larger than the characteristic photon voltage of 0.875 mV at 205 GHz. Figure 13 shows a typical I-V curve.

Each junction was fabricated with a microstrip stub. Stubs 75μ, 80μ, and 86μ long by 4.5μ wide, and 75μ by 7μ were tested. The total capacitance each stub would resonate with is calculated using $C = 1/(\omega^2 L)$ where L is the stub inductance.

Accurate measurements of mixer gain and noise are required to properly characterize the rf effects of the stubs. We have built a specially designed test system to perform these measurements. Figure 14 shows a block diagram of the mixer test system which is mounted in a commercial vacuum cryostat. It employs variable-temperature blackbodies (loads) at the rf input and IF output of the mixer. The novel feature is the IF load (16) which is cryogenically-coolable and is placed in the cryostat close to the mixer thus minimizing errors due to transmission line losses. Mixer gain and noise temperature can be measured to better than ±8%. These measured values include the small losses due to the LO diplexer, mylar vacuum window, and fluorogold IR filter for the current NbN mixer tests. The mixer block is a full height waveguide mount (17) employing a noncontacting backshort and E-plane tuner. Due to the low LO power requirements, a simple mylar beamsplitter is used to reflect about 2% of the incident LO power into the cryostat. The LO source consists of a 68GHz Gunn oscillator driving a x3 frequency multiplier which employs a whisker contacted Schottky barrier diode. A similar arrangement is used to provide monochromatic signals to optimize the mixer.

A cooled coaxial switch allows power from either the mixer or IF load to enter the IF system. A 20dB bidirectional coupler allows test signals to be injected for evaluating the mixer IF mismatch and the IF system gain. A cooled isolater is used to minimize the effects of impedance changes on the noise of the IF

system. The first gain stage is provided by a HEMT amplifier with a gain of 38dB and a noise temperature of 6K. Room temperature bandpass filters with a center frequency of 1.4 GHz and a bandwidth of 100 MHz are used for the noise measurements.

Using high quality Pb-alloy SIS tunnel junctions, this mixer test system has given overall double-sideband receiver noise temperatures as low as 113K (7). This is comparable to the performance reported for fully optimized receivers in this frequency range (3,17,18).

Mixer Performance of NbN Junctions

Figure 15 shows the mixer noise temperature versus the capacitance tuned by the stub. Without a stub, values above 1000K were obtained. However, T_m below 200K was obtained for stubs which tuned a capacitance near 85fF which agrees well with previously reported data (19) using a SQUID interferometer technique. Mixer gain was also found to improve from -19dB without a stub to -11dB with one.

Figure 16 shows mixer noise temperature versus frequency at 4.2K and 1.5K. The best result is T_m = 134K at 202.5 GHz. Mixer noise improved by about 50K on cooling the junction to 1.5K. The mixer gain also improved by 2-3dB. Mixer performance is expected to change with changes in the shape of the I-V curve (20). In these junctions, ΔVg showed almost no change, and the subgap current decreased 10% - 50% depending on bias voltage. A decrease in subgap current could improve mixer noise but may not fully account for the improvements in mixer gain. Detailed calculations with Tucker's quantum mixer theory (21) are required to fully interpret changes in the I-V curve.

Another possibility is ac losses in the superconductive stubs. Kautz (22) has published calculations for losses in superconductive microstrip and shown that these losses can be strongly temperature dependent even below half the superconducting transition temperature. Since the Q of our stub tuned junctions is relatively high, about 8, even a small loss would strongly affect the performance. Using a simple lumped element model of the junction shunted with a lossey microstrip

stub, we calculate that resistance of 2-5Ω would degrade the mixer return loss to less than 10dB. Figure 17 shows the results. We are currently investigating the losses in our microstrip lines.

The propagation velocity υ on the stub was determined by a method (14) using the ac Josephson effect in the junction as a voltage controlled oscillator to sample the resonances of the circuit. The frequency spacing of these resonances is given by $\upsilon/2l$ where l is the length of the stub. This method gave λ = 3800Å for our films, which is significantly larger than the previously reported value of 2800Å (19). This led to stub lengths of 75-80μ for best mixer performance.

Summary

A 600-700 GHz SIS receiver employing a waveguide mount is being developed. A large scale model was used to optimize the bandwidth and tuning range of the mount. A new design of noncontacting backshort has been developed for use at 600 GHz. It performs as well as competing conventional designs at 100 GHz but is easily fabricated for use at submillimeter wave frequencies. NbN tunnel junctions are being developed for this receiver. We have made a systematic study of the mixer gain and noise of these junctions shunted with microstrip lines as rf tuning elements. This has given values of junction capacitance of 85fF/μ^2 and magnetic penetration depth of 3800Å. Mixer noise temperature as low as 134K has been achieved which is the best reported to date for an NbN junction.

Acknowledgements

This work was supported in part by the Jet Propulsion Laboratory, California Institute of Technology under contract with the National Aeronautics and Space Administration, and the Strategic Defense Initiative Organization.

References

1. Tucker, J. R. and Feldman, M. J. *Rev. Mod Phys.*, **57**, p. 1055 (1985).

2. Pan, S.-K.; Kerr, A. R.; Feldman, M. J.; Kleinsasser, A. W.; Stasiak, J. W.; Sandstrom, R. L.; Gallagher, W. J. *IEEE Trans. Microwave Theory Tech.*, **MTT-39**, 580 (1989).

3. Blundell, R.; Carter, M.; Gundlach, K. H. *Int. J. IR & mm Waves*, **9**, p. 361 (1988).

4. Buttgenbach, T. H.; Miller, R. E.; Wengler, J. J.; Watson, D. M.; Phillips, T. G. *IEEE Trans. Microwave Theory Tech.*, **MTT-36**, 1720 (1988).

5. Ellison, B. N. *Cryogenics*, **28**, 779 (1988).

6. The local oscillator source was developed at Radiometer Physics, Bonn, West Germany under contract to the Jet Propulsion Laboratory.

7. McGrath, W. R.; Byrom, C. N.; Ellison, B. N.; Frerking, M. A.; Miller, R. E. *Digest 13th Int. Conf. Infrared and Millimeter Waves*, p. 98 (1988).

8. Jacobs, K. A.; McGrath, W. R. *Digest 14th. Int. Conf. Infrared and Millimeter Waves*, p. 540 (1989).

9. Collins, R.E. *Foundations for Microwave Engineering*, McGraw-Hill (1966).

10. Pickett, H. M.; Hardy, J. C.; Farhoomard, J. *IEEE Trans. Microwave Theory Tech.*, **MTT-32**, p. 936 (1984).

11. McGrath, W. R., Jet Propulsion Laboratory, Notice of New Technology Case No. JPL I.R. 30-18091/7600 (1990).

12. Brewer, M. K. and Raisanen, A. V. *IEEE Trans. Microwave Theory Tech.*, **MTT-30**, 708 (1982).

13. Harrigton, R. F. *Time-Harmonic Electromagnetic Fields*, McGraw-Hill, pp. 158-161 (1961).

14. Raisanen, A. V.; McGrath, W. R.; Richards, P. L.; Lloyd, F. L. *IEEE Trans. Microwve Theory Tech.*, **MTT-33**, p. 1495 (1985).

15. Stern, J. A.; Hunt, B. D.; LeDuc, H. G.; Judas, A.; McGrath, W. R.; Cypher, S. R.; Khanna, S. K. *IEEE Trans. Magn.*, **MAG-25**, p. 1054 (1989).

16. McGrath, W. R.; Raisanen, A. V.; Richards, P. L. Int. J. IR & mm Waves, **7**, p. 543 (1986).

17. Ellison, B. N.; Miller, R. E. *Int. J. IR & mm Waves*, **8**, 608 (1987).

18. Woody, D. G.; Giovanine, C. J.; Miller, R. E. *IEEE Trans. Magn*, **MAG-25**, p. 1366 (1989).

19. Shoji, A.; Aoyagi, M.; Kosaka, S.; Shinoki, F.; Hayakawa, H. *Appl. Phys. Lett.*, **46**, p. 1098 (1985).

20. McGrath, W. R.; Richards, P. L.; Face, D. W.; Prober, D.; Lloyd, F. L. *J. Appl. Phys.*, **63**, p. 2479 (1988).

21. Tucker, J. R. *IEEE J. Quantum Elec.*, **QE-15**, 1234 (1978).

22. Kautz, R. *J. Appl. Phys.*, **49**, 308 (1978).

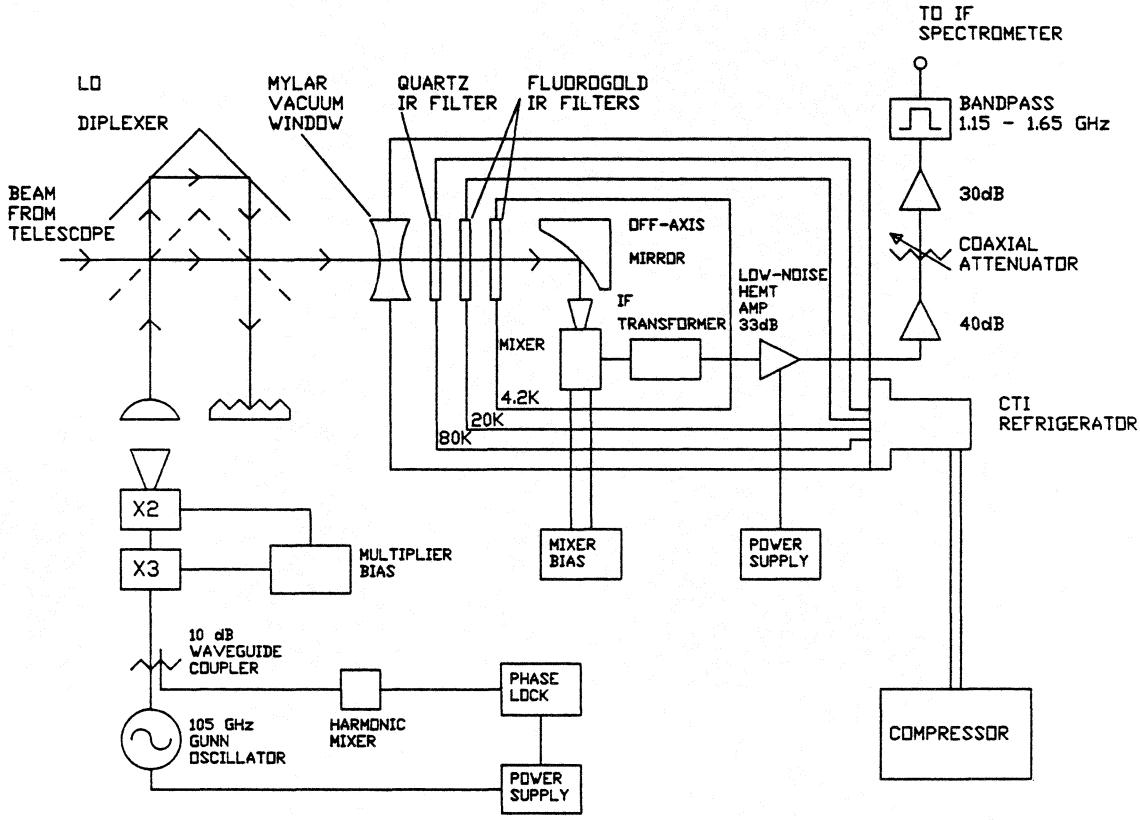

Fig.1 Block diagram of 600-700GHz SIS receiver.

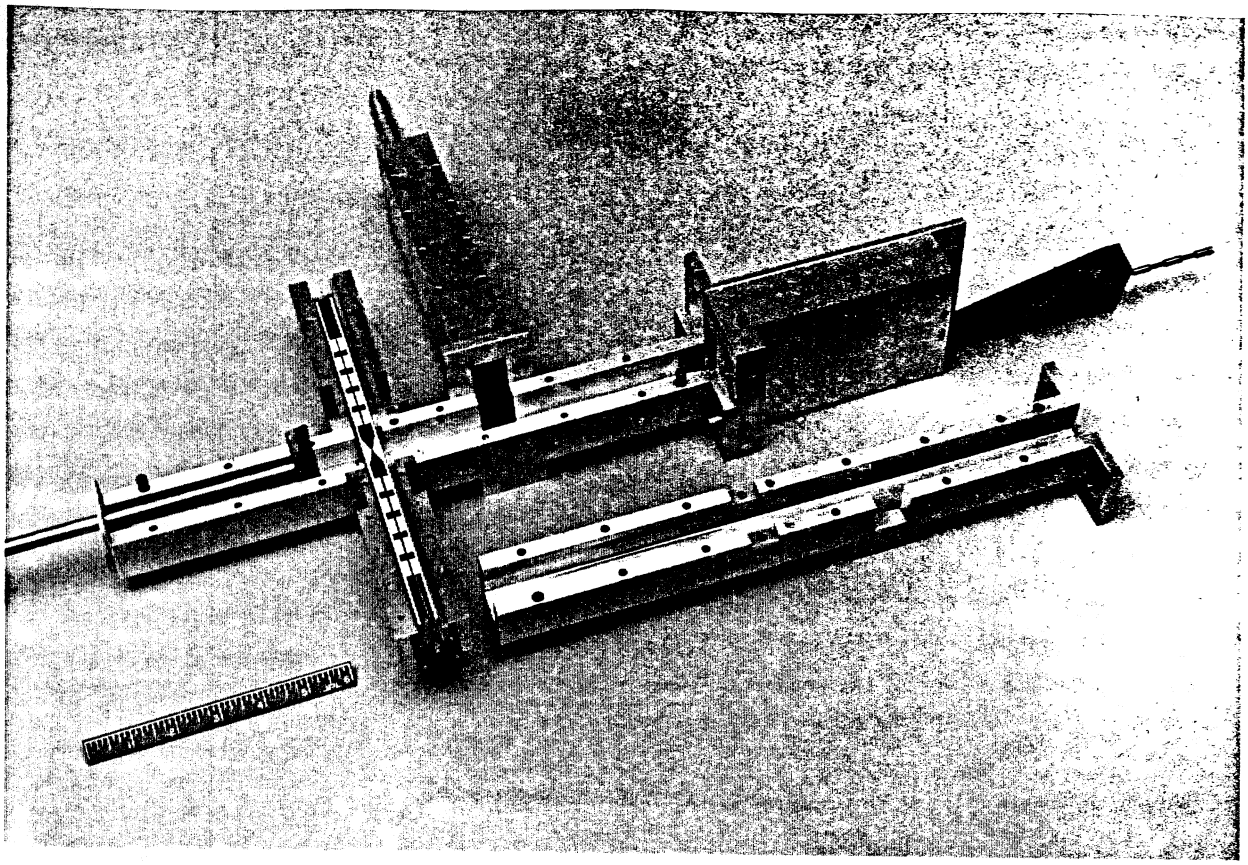

Fig.2 Large scale, 3-6GHz model of waveguide SIS mixer mount.

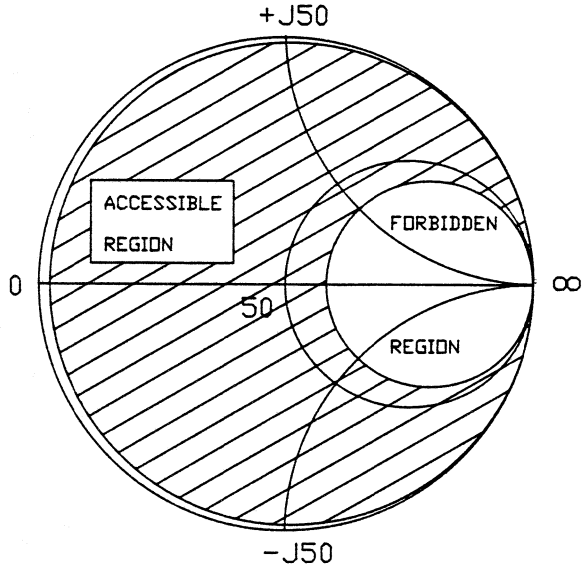

Fig.3 Impedance Smith Chart showing tuning range of mixer mount.

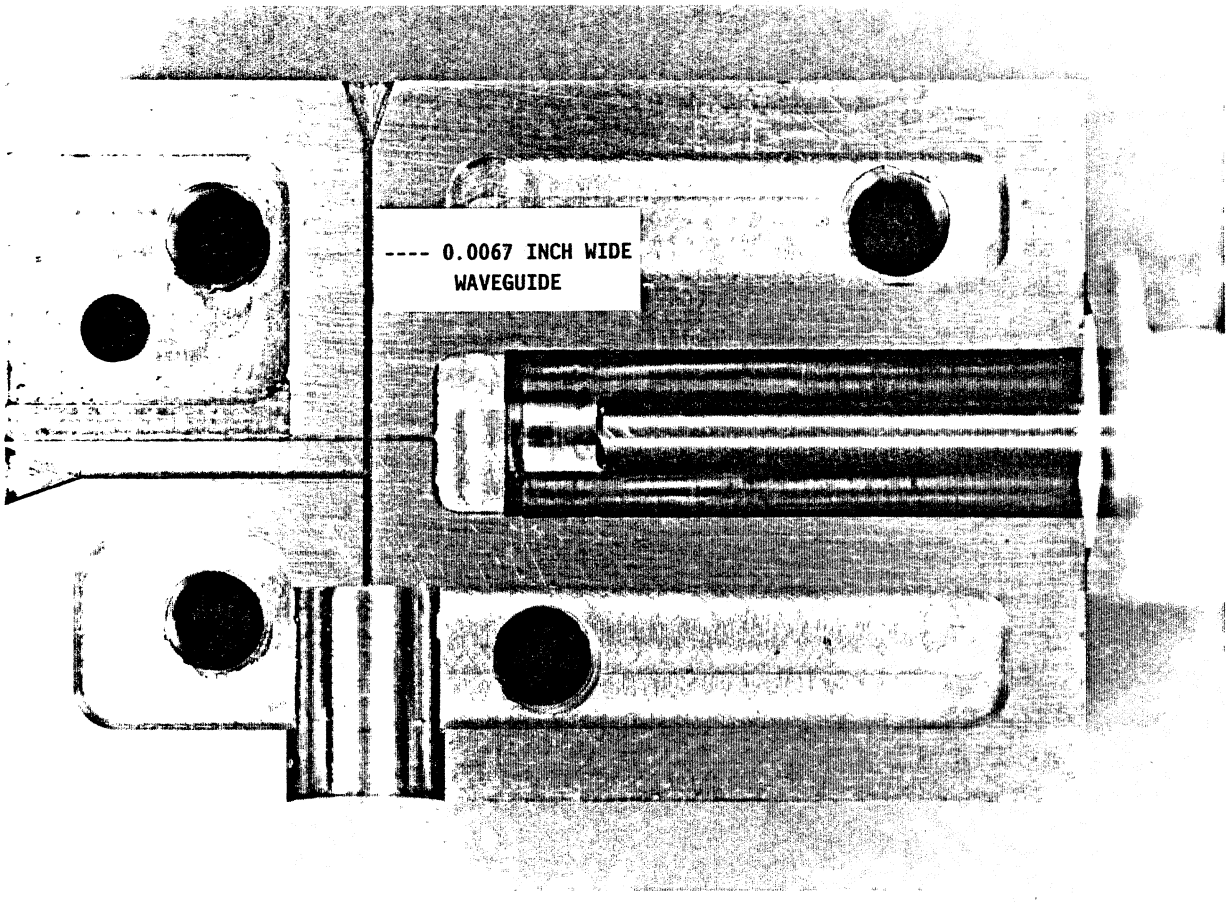

Fig.4 Photo of one half of mixer block. The waveguides are flared at the ends to assist insertion of backshorts. The conical horn fits into the cylindrical cavity at the lower end of the main waveguide.

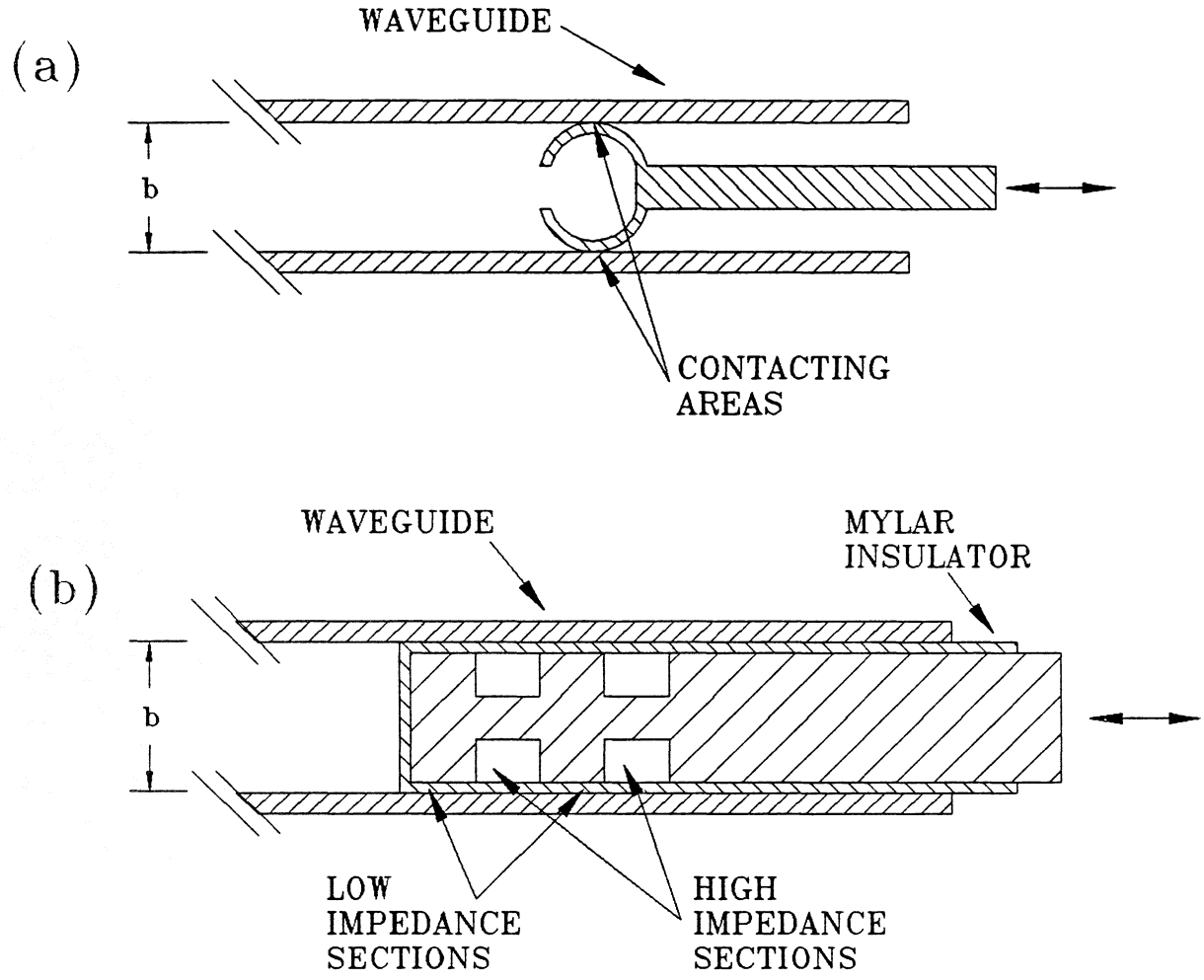

Fig.5 Schematic diagram of conventional backshort designs. (a) contacting backshort; (b)noncontacting backshort.

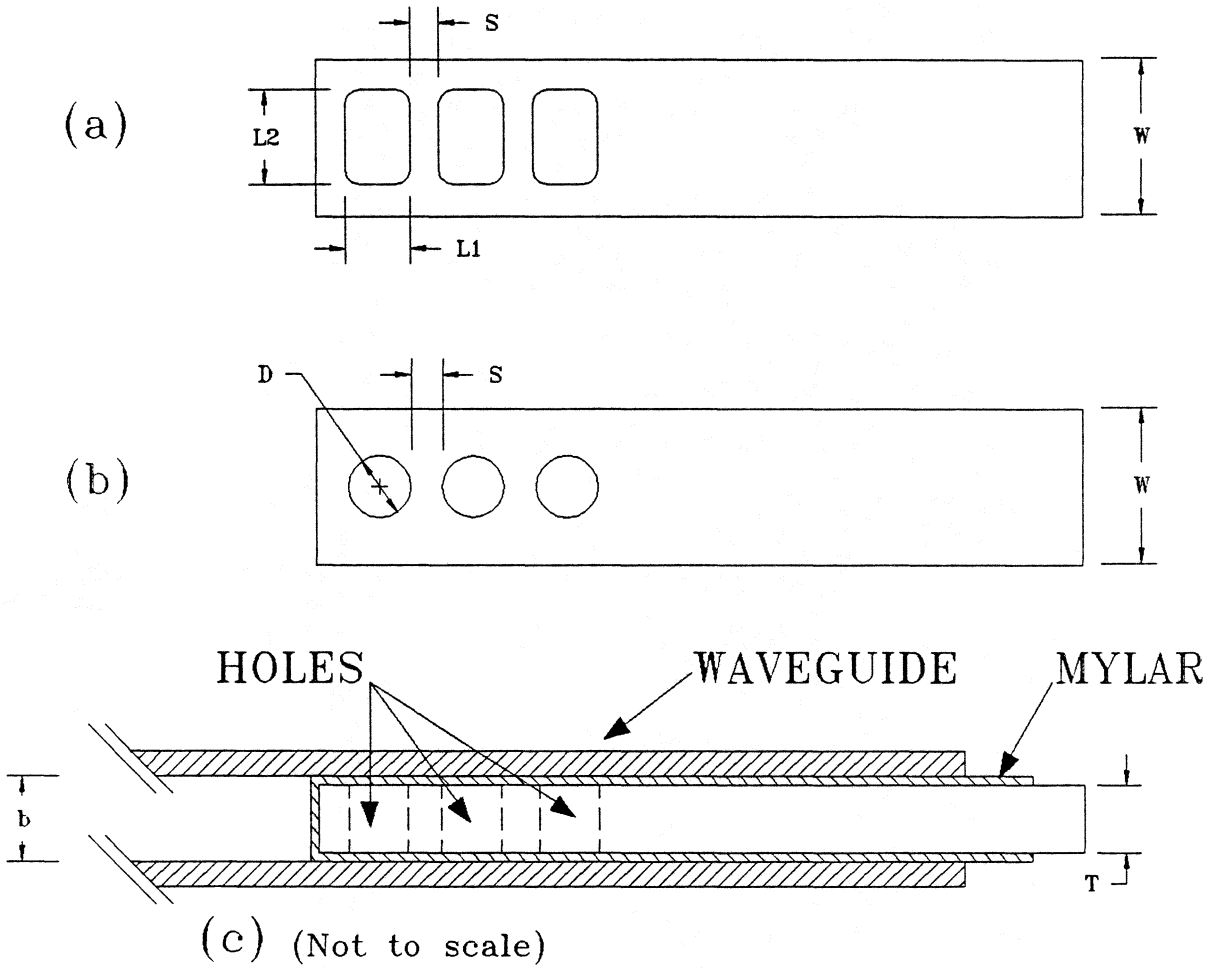

Fig.6 New backshort design employing (a) rectangular or (b) circular holes to provide the proper impedance variation for a large reflection. (c) Cross sectional view in waveguide.

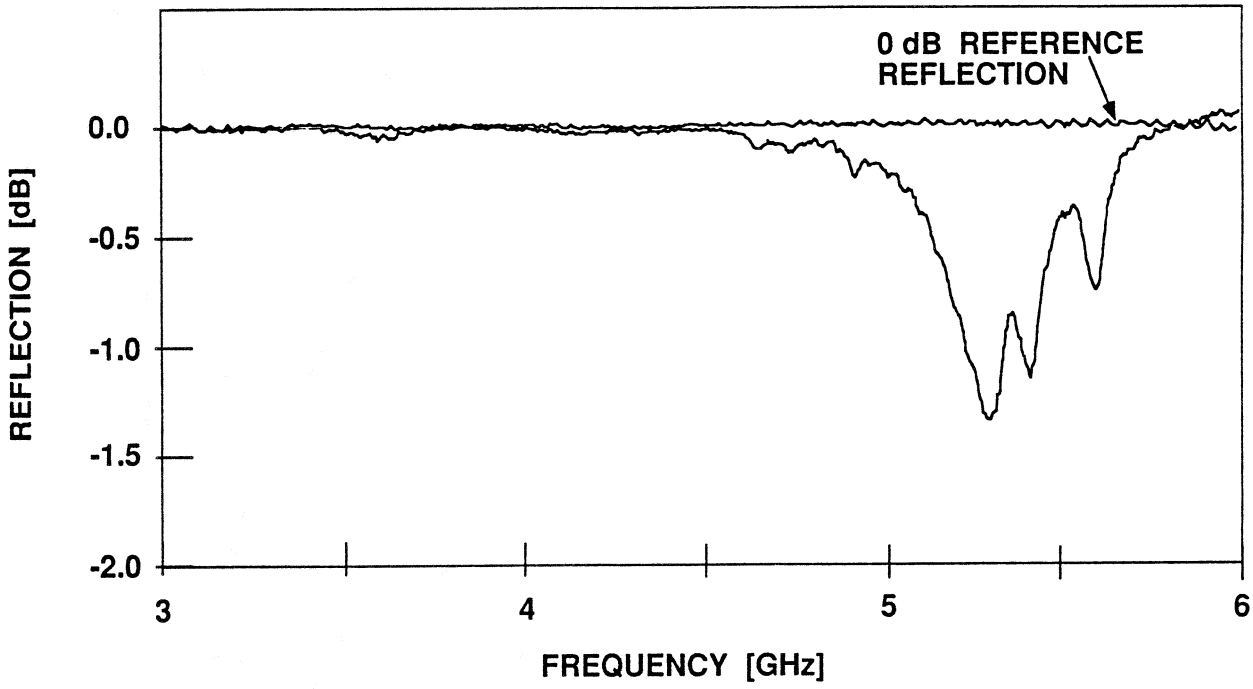

Fig.7 Reflection from model backshort with 3 rectangular holes.

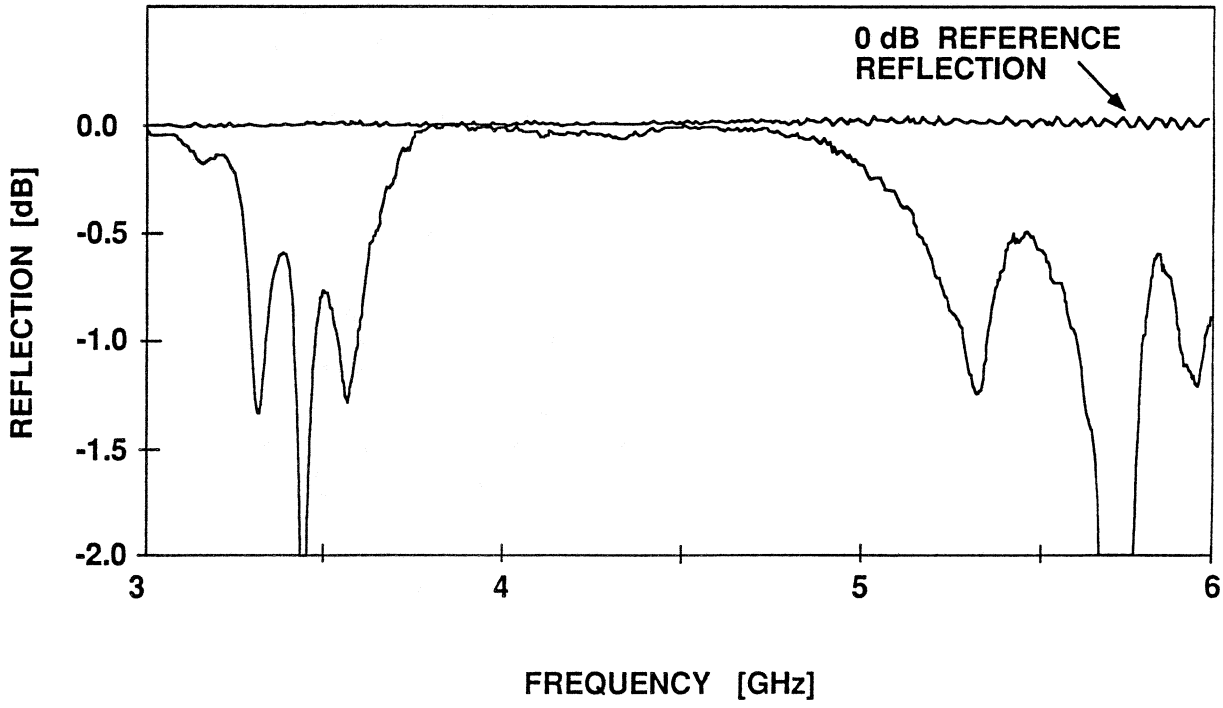

Fig.8 Reflection from model backshort with 3 circular holes.

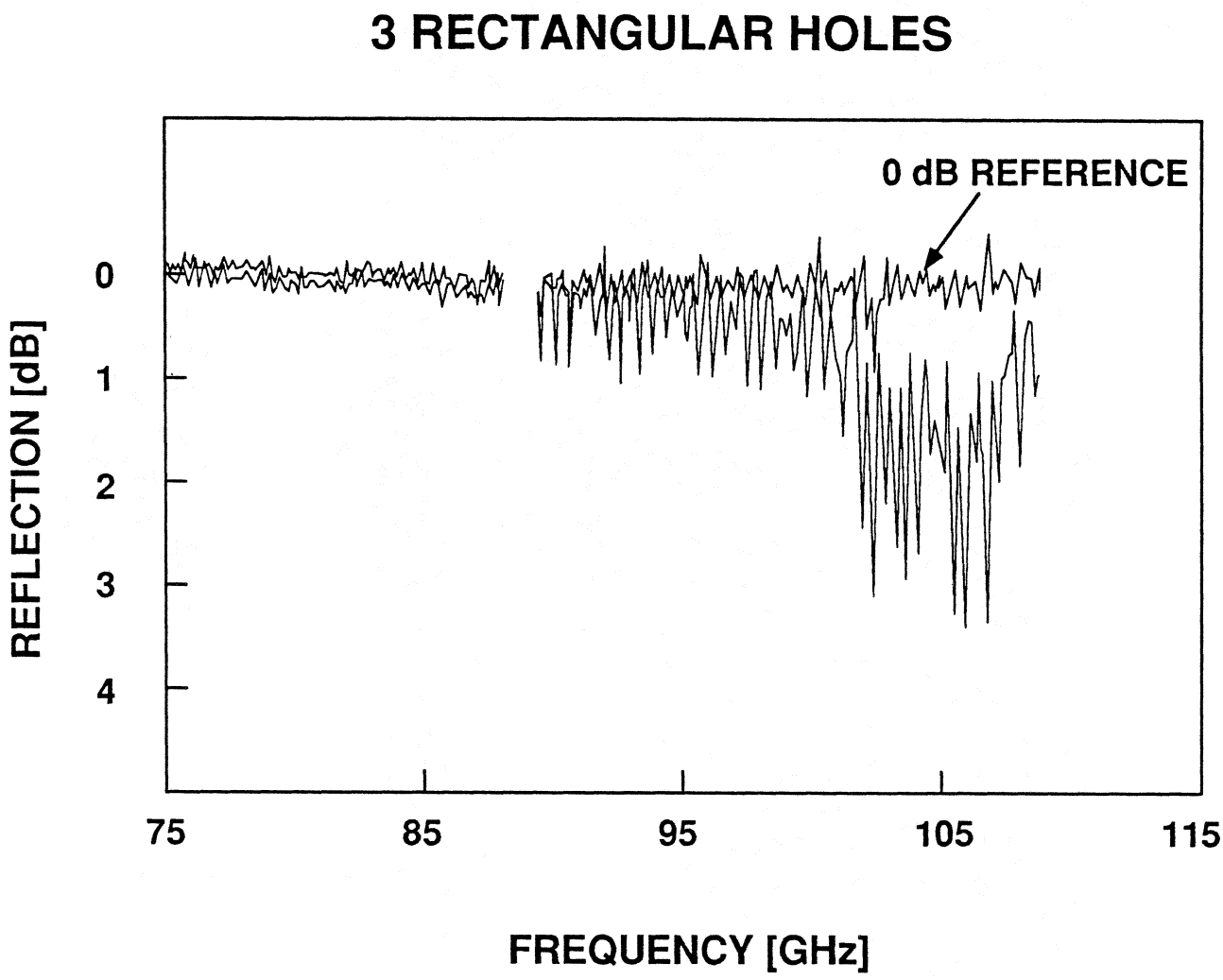

Fig.9 Reflection from millimeter wave backshort with rectangular holes.

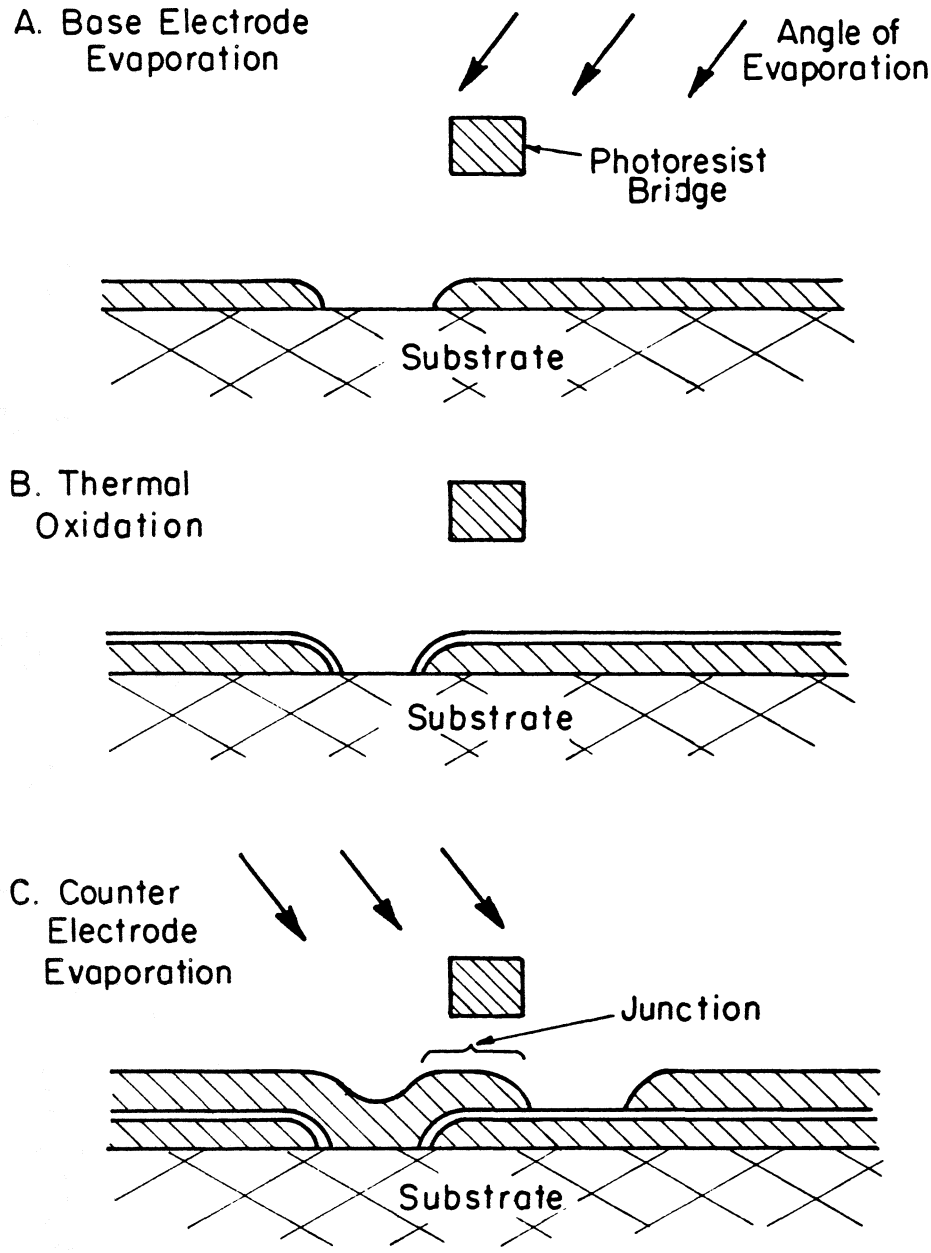

Fig.10 Fabrication of Pb-alloy tunnel junctions using photoresist bridge technique.

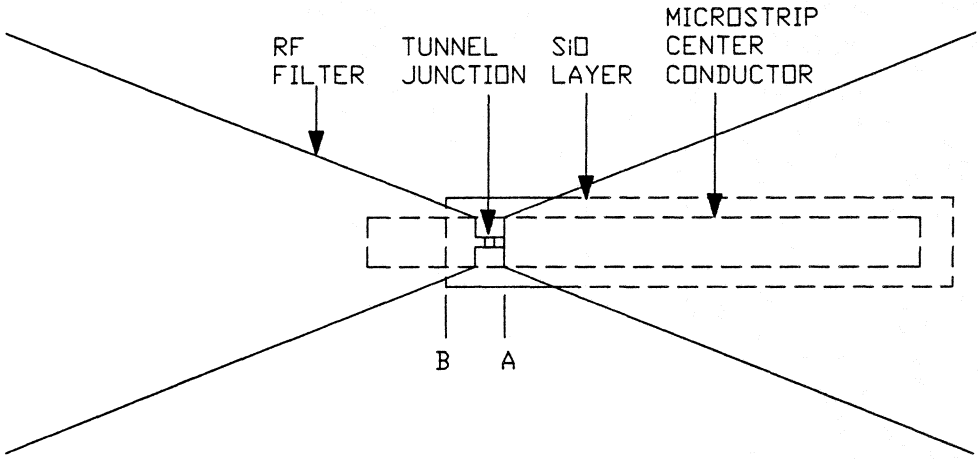

Fig.11 Diagram of microstrip tuning stub integrated with Pb-alloy junction.

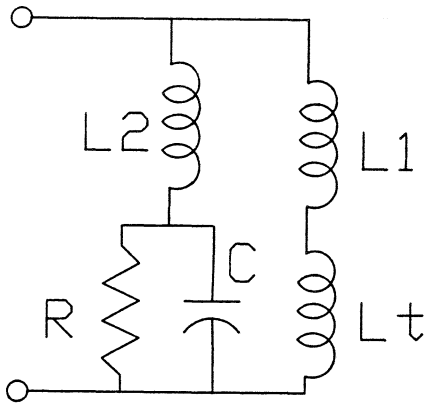

$L1+L2+Lt$ RESONATE WITH C

$Rrf = nR$

$n = (L1+Lt/L1+L2+Lt)^2 = 0.5-0.7$

Fig.12 Equivalent circuit of stub tuned junction.

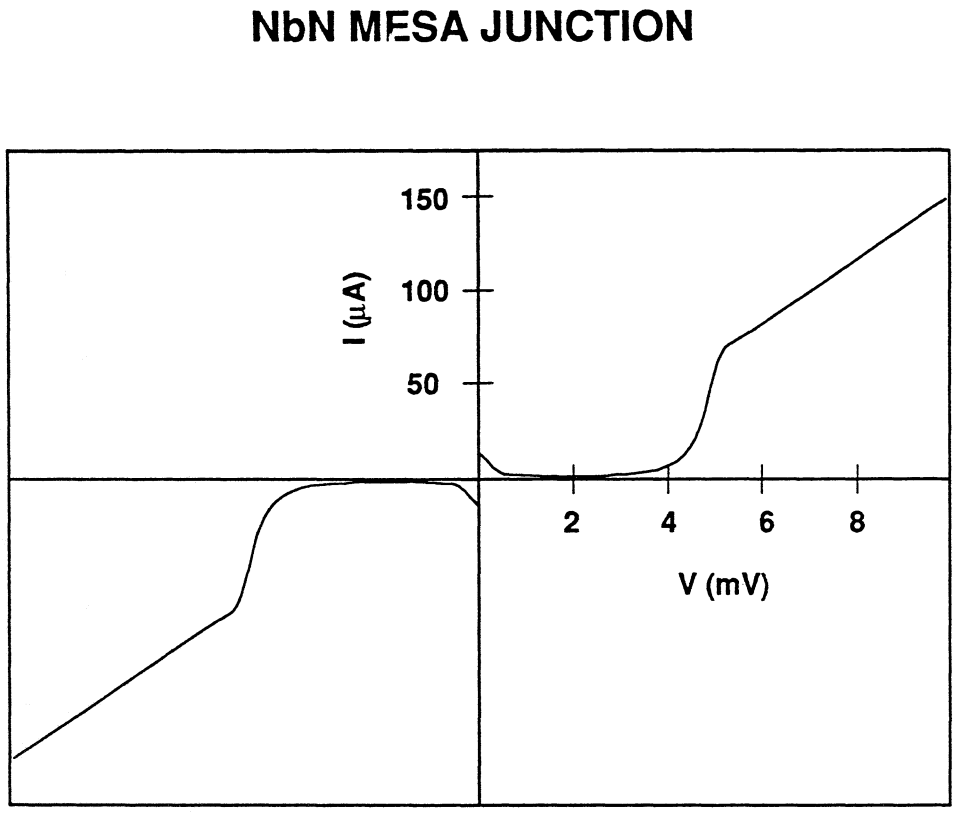

Fig.13 Typical I-V curve for NbN-MgO-NbN tunnel junction.

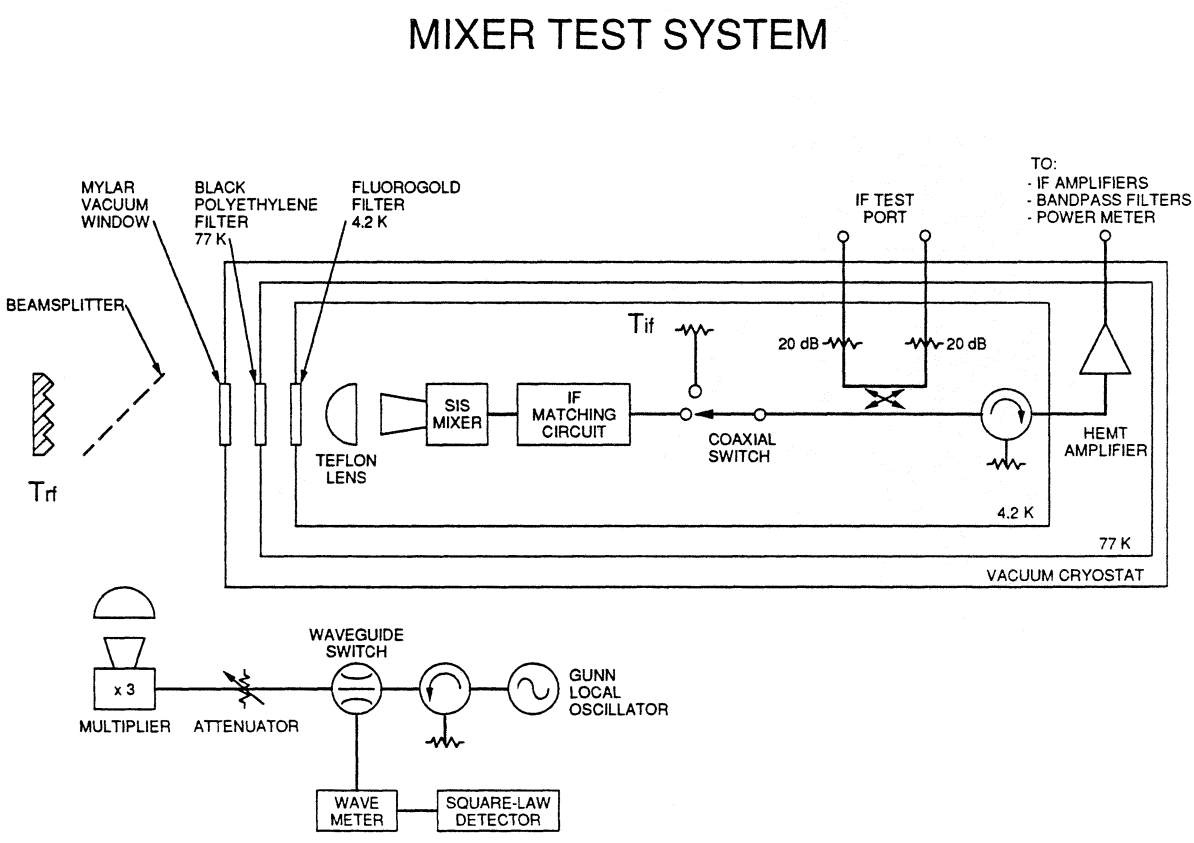

Fig.14 Test system employing cooled IF load to characterize mixer performance.

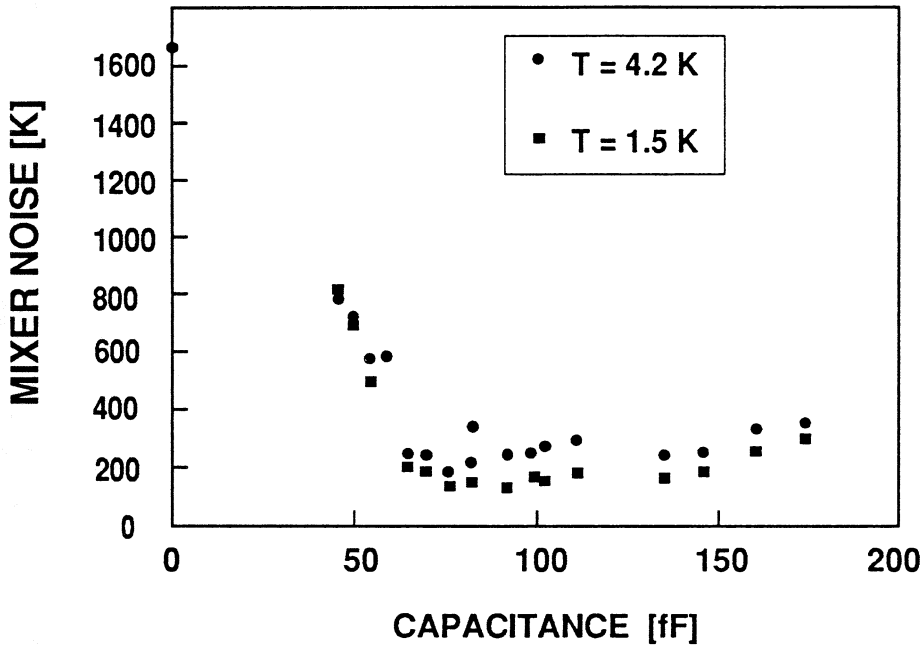

Fig.15 Mixer noise temperature versus capacitance tuned by the microstrip stub.

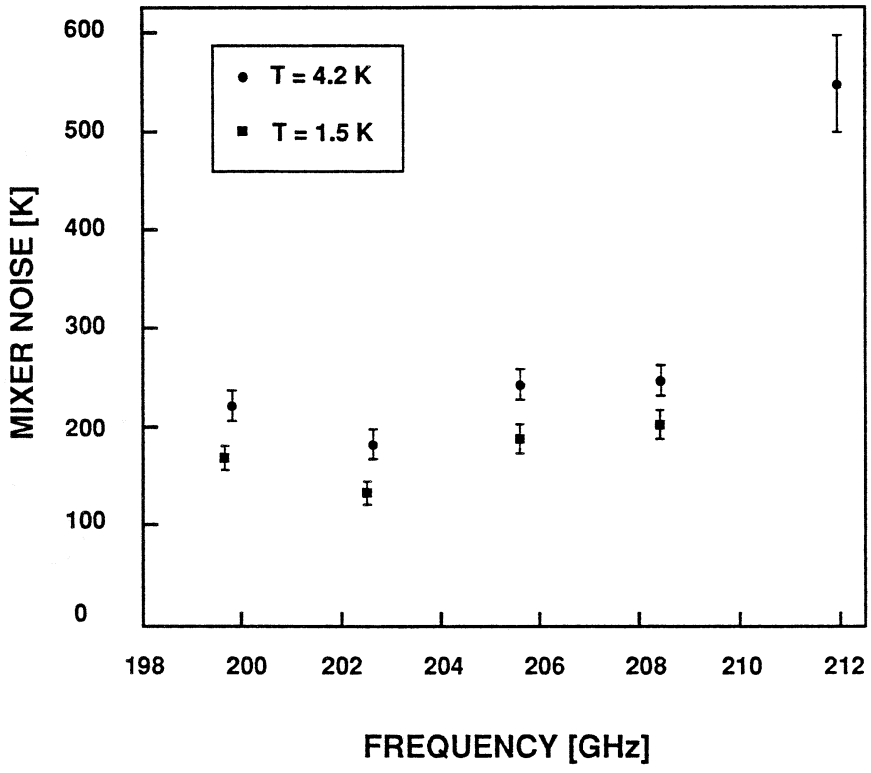

Fig.16 Mixer noise temperature versus frequency at two physical temperatures: 1.5K and 4.2K.

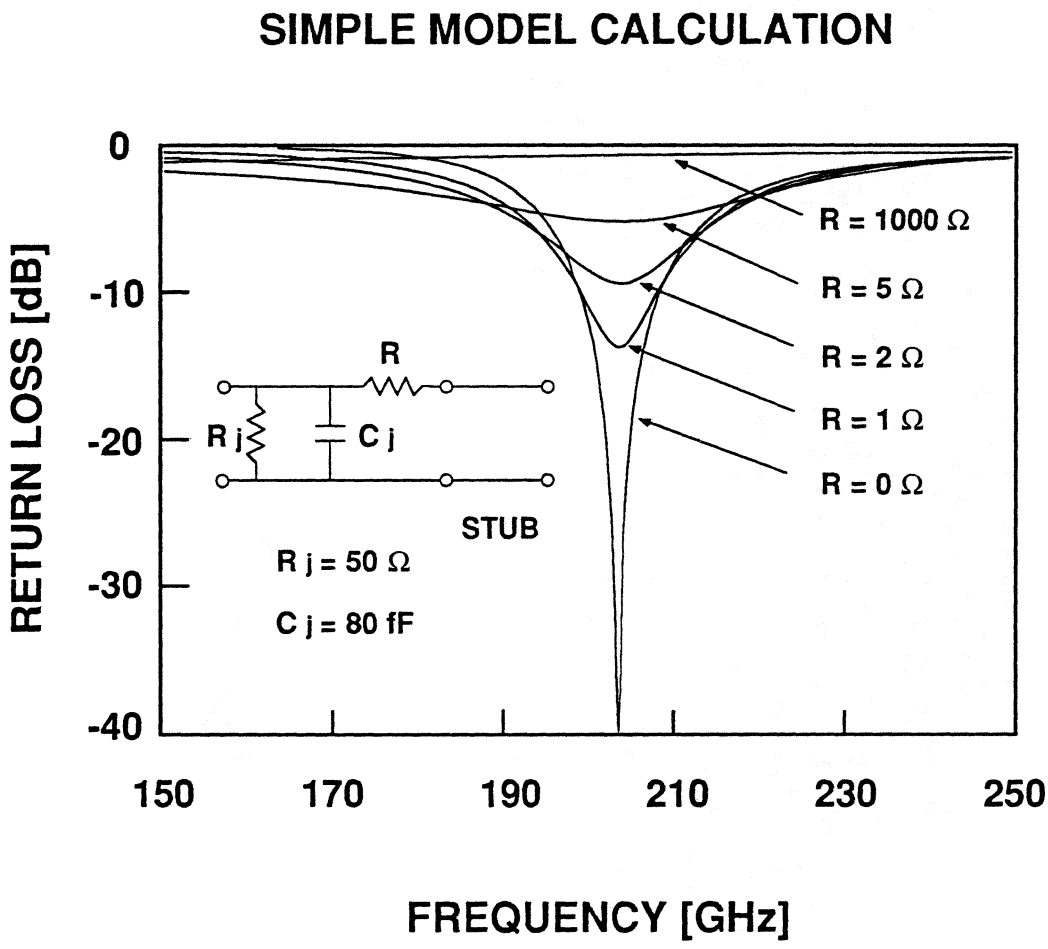

Fig.17 Simple calculation of the effect of loss in the stub on mixer rf coupling.

Submillimeter Astronomy in France

P. ENCRENAZ

Laboratoire de Radioastronomie Millimétrique

OBSERVATOIRE DE PARIS - Section de Meudon

92195 - MEUDON FRANCE

ABSTRACT :

Submillimeter astronomy has been selected as the top priority for the next decade by the french space agency (CNES). A balloon borne telescope of 2m of diameter is built by Matra-Space, using the lightest CFRP materials. The petals of the telescope have been recently delivered: the telescope will be diffraction limited at 150 μm, and the pannels will be adjusted during flight. A pointing accuracy of 5" is anticipated. The first flight from Sicily to Spain is scheduled for 1992 with a set of bolometers cooled to He_3. The first heterodyne receiver will fly in 1993. It consists of a cooled schottky receiver at 380 GHz to observe simultaneously H_2O and O_2. The trilayer $Nb/Al_2O_3/Nb$ junctions may be used for the first flight.

In collaboration with Cal Tech and Jet Propulsion Laboratory, a proposal for a small submillimeter satellite called SM_3 (T. Phillips in the P.I) has been selected for a phase A by CNES. Related technological developments are funded in the area of cryo coolers, adjustable pannels in flight, quantum well devices and local oscillator sources, and manufacturing of SIS junctions.

Work on different subsystems of the cornerstone FIRST is also in progress.

PRONAOS :

A French Balloon - Borne Space Project

1) Generalities :

PRONAOS is a scientific space project for astrophysical observations in submillimeter wavelength region with instrumentation borne on a stratospheric balloon gondola.

The PRONAOS architecture consists of three parts :

- a carry away vehicle : the stabilized gondola
- a common facility : the submillimeter telescope
- a scientific payload : 2 focal plane instruments

A 900 000 m^3 balloon will permit first flights in transmediterranean campaigns from Sicilia to south Spain (about 20 hours of ceiling at an altitude of 40 km and a latitude of 38° N), in july 1992 and 1993.

2) "Naps" gondola :

The main characteristics of the vehicle are :

- an azimuthal gondola with two stages stabilization delivering a diurnal pointing with an accuracy RMS in arc seconds on two axes :
  - . absolute 7"
  - . stability 5"
  - . drift rate 5" (1 hour)
- the dry mass is 1600 kg for a lauching mass of 2200 kg
- the mass of the pointed set including Telescope, 1 focal-plane instrument and various equipments is approximatly 500 kg.
- The gondola dimensions are typically : 4m x 4m x 7m (see Fig III-1.1 and 1.2) and the on-board energy permits a capacity of 30 kWh by a set of lithium batteries.

PRONAOS NAPS - TEL

Fig III - 1-2

FIG. II-1-1 : ENSEMBLE NACELLE ET BALLON

3) The telescope :

It is a 2m class submillimeter telescope. The main characteristics are :

Cassegrain type telescope with a focal length of 20m, with f/0,9 primary aperture and 2.8 m back focus. The pointing (accuracy goal : 5 arc second) is obtained by stellar sensor.

The 2m of diameter primary mirror has a surface accuracy of 10 μm RMS including all defects.

The image quality of the telescope will be limited by the diffraction at 300 μm .

Light weight technology is used for the primary mirror realization : carbon fibre by a replica-technique.

The mirror, segmented in 6 parts semi-active (in flight, aligment of the 6 segments considered as rigid, controlled by an on-board servo-loop), is equiped with 18 actuators and 30 dispacement captors.

Each segment is realized in composite structure (carbon fibre : honeycomb and skins) on a replica mould : the mass is 3.3 kg, with a coating of 0.15 μm thickness gold deposit.

4) Instruments :

Two instruments could be used on the focal plane of the telescope :

SPM : (Multiband Photometric System)
The spectral resolution $\nu/\Delta\nu$ is 1 to 10 on the field : 200 μm to 1.5 mm (in 5 bands).
The photometer employs cooled bolometers at 0.5 K (or 0.1 K).

SMH : (Heterodyne Spectrometer)
With a high spectral resolution ($\nu/\Delta\nu \simeq 10^6$)

The submillimeter heterodyne radiometer will operate in the first generation at 380 GHz with a next goal of operating to 550 GHz. Noise temperatures as low as 500 K at the lower frequency and 1000 K at the high end of the frequency range are expected. The heterodyne radiometer mixes the input signal with a local oscillator (LO) signal at approximately the same frequency to generate an output at the difference or intermediate frequency (IF) which is then amplified and processed.

An ambient thermal load and a cold load will be used for absolute calibrations of the radiometer. The mixer subsystem consists of a cooled Schottky diode, or three element arrray of superconducting - insulating - superconducting tunnel junctions (SIS)

operating at 3.5 K. The IF subassembly includes the cooled low-noise preamplifiers which are followed by warm amplifiers. The LO subsystem contains the injection optics, a set of frequency multipliers, Gunn oscillator to drive the multipliers , and a phase locking system for the Gunn oscillator.

Acousto-optic spectrometers (AOS) will be used for the spectral analysis of the heterodyne radiometers. The instrument block diagram is shown in Fig. III-2. Following are descriptions of the heterodyne radiometers and the AOS.

5) SMH main characteristics and description :

The first interstellar molecules in galactic sources studied with SMH are H_2O and O_2 at 380.2 and 368.5 GHz respectively.

Atmospheric attenuation for different sites, shown on Fig. III-3, indicates the necessity to observe from space.

Using the double side band operation on the submillimeter heterodyne receiver, both lines will be observed simultaneously by a optimized choice of the intermediate frequency of the receiver (see picture below) :

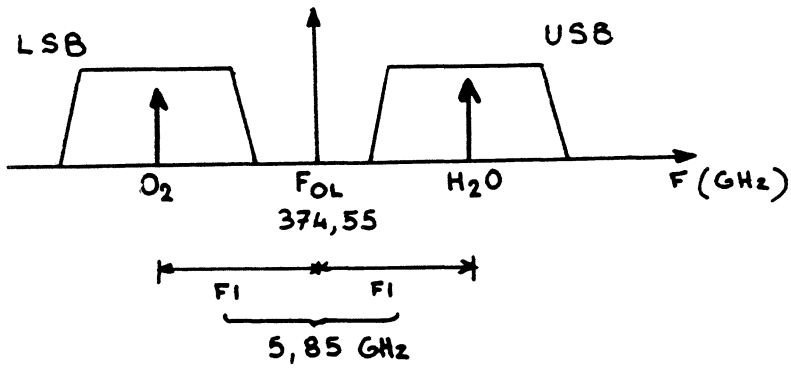

Sensivity of the instrument : is given by the choice of the mixer technology. At first a cooled Schottky diode followed by an HEMT 6 GHz amplifier will be used. In this case a over-all 500 K noise temperature will permit to detect a line in half of hour. For the second flight, an SIS mixer will be used to increase the sensitivity.

Local oscillators :

Optimum performance of a Schottky or an SIS mixer is achieved with an absorbed LO power of about 300 μW in the first case or less 10 μW in the second case. To provide

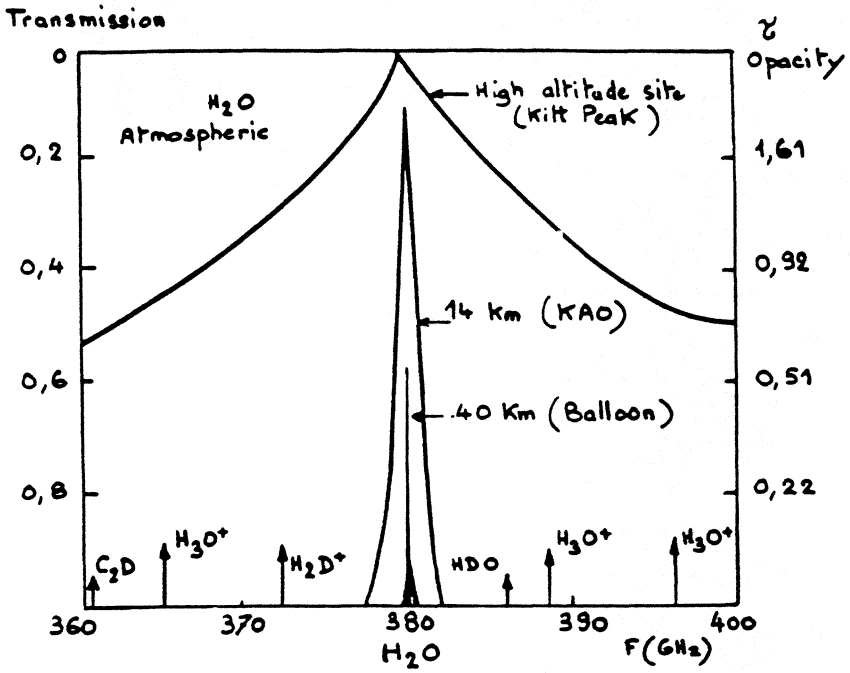

Fig III-3. **Atmospheric transmission**

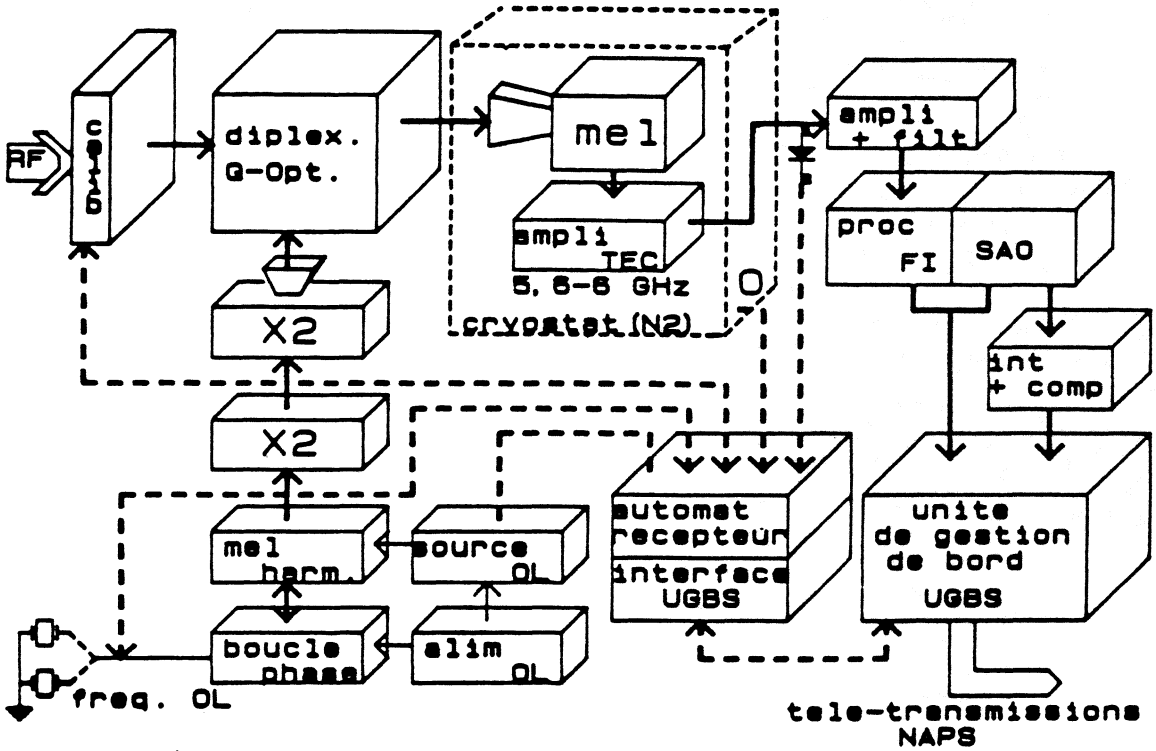

PRONAOS/SMH - synoptique du recepteur -

Fig III-2

even this level of power over the 300 GHz band is a challenge ; however, an approach based on frequency multiplication of phase-locked solid-state millimeter-wave sources is adequate and should be sufficiently reliable for space applications.

IF amplifiers :

The IF frequency will be set at about 6 GHz with a bandwidth of 500 MHz . To take advantage of the low noise performance of the mixers devices, the first IF stage, with 30 dB gain, will be cooled to about 40 K and located close to the mixers. HEMT devices are being developped in the frequency range with noise temperatures less than 20 K and low power dissipation.

Spectrum analysis :

Acousto-optic spectrometers (AOS) will be used to analyze the spectra from the heterodyne radiometers. In the AOS, the IF signal modulates a transducer which generates a beam of acoustic waves in a crystalline material. These acoustic waves diffract a separately injected laser beam. The deflected laser light is then detected by a linear array of photodiodes to integrate the signal power in each frequency channel.The signals from each diode are read out to a computer for the processing of the spectral data.

The spectrum resolution of 500 kHz with 1000 pixels is obtained by 2 acousto-optical spectrometers (Fig III-4). The AOS bandwith is 180 MHz with a $PbMoO_4$ bragg cell.

To obtain high spectrum resolution, all local oscillators are stabilized by a phase and frequency loop on a quartz reference. (stability of 10^{-8} is required).

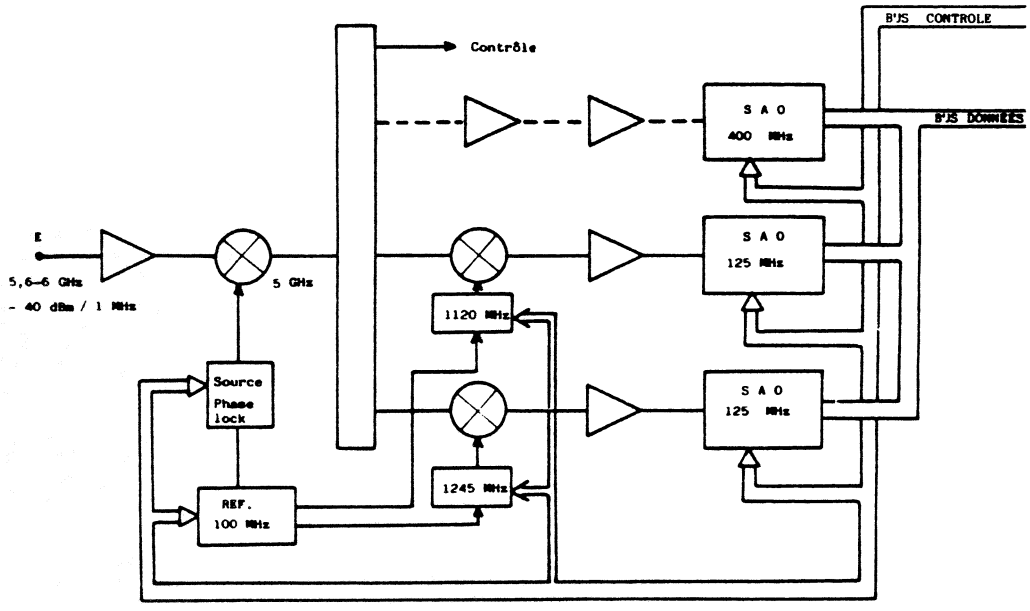

Fig : III-4

Data acquisition and controls : An in-board computer can control the receiver (house keeping) and compact the data to send them to the ground station. The transmission flow from the instrument is about 150 kbyte/s.

Cryogenics :

The constraints and requirements for the cryogenic system 3.5 K operating temperature with a 40 hours lifetime. The baseline design is a liquid Helium Dewar with a 40 K stage for the IF cooled amplifier.

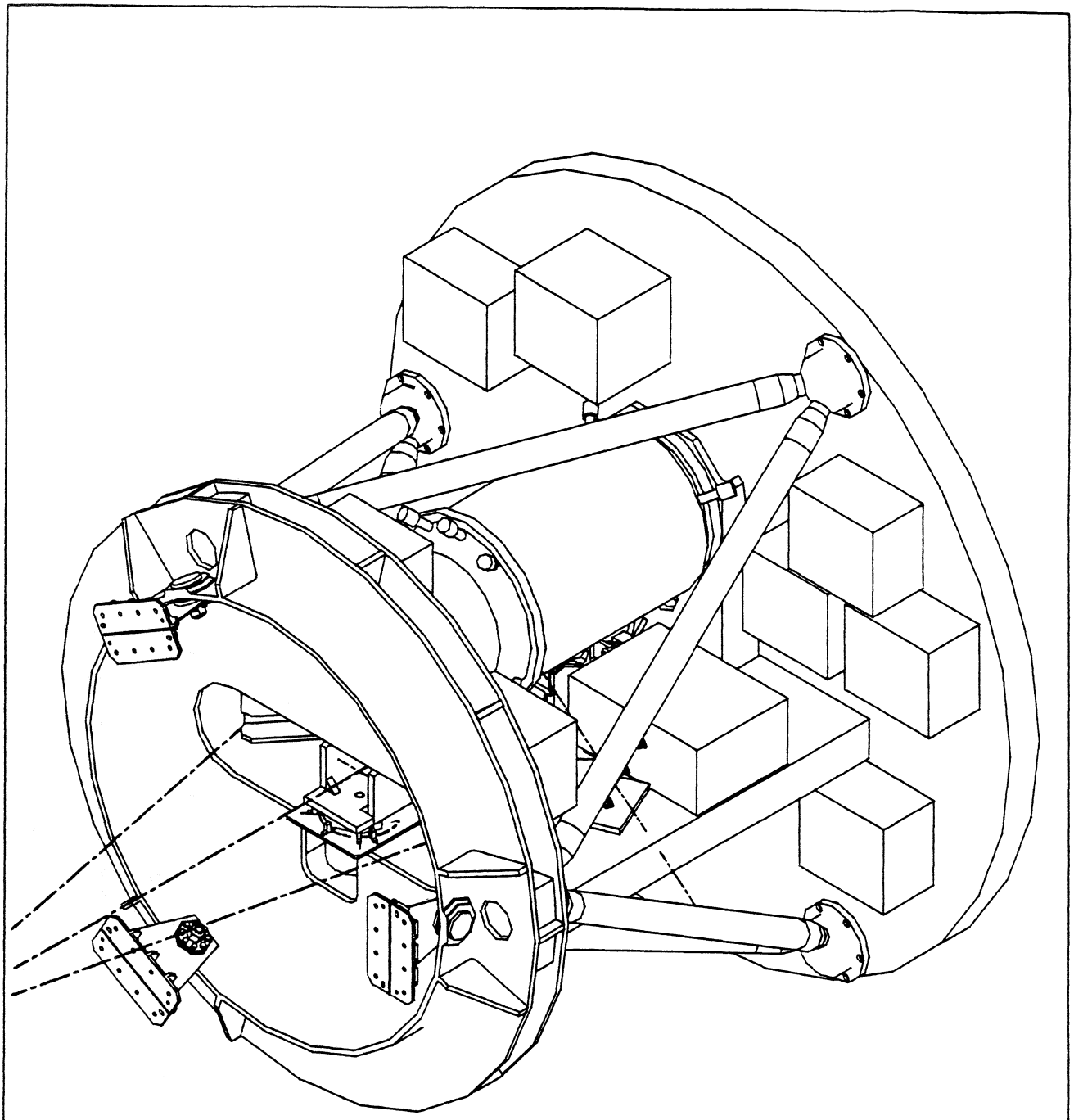

DATES	VISAS	MODIFICATIONS	IND.

USINAGE : 6.3
TRAITEMENT :
ARETES CASSEES : 0.25 A 45°
TOLERANCES GENERALES : JS13- js13
TEMPERATURE DE REFERENCE : 20° C
PROTECTION :

MATIERE :
POIDS : ECH. : 1/15
DATE : 23/4/90 DESSINE : MORIN
DESIGNATION : PRONAOS AXD

OBSERVATOIRE DE PARIS-MEUDON
S.E.R.T

MATRA ESPACE

"FIRST" ANTENNA DEPLOYMENT

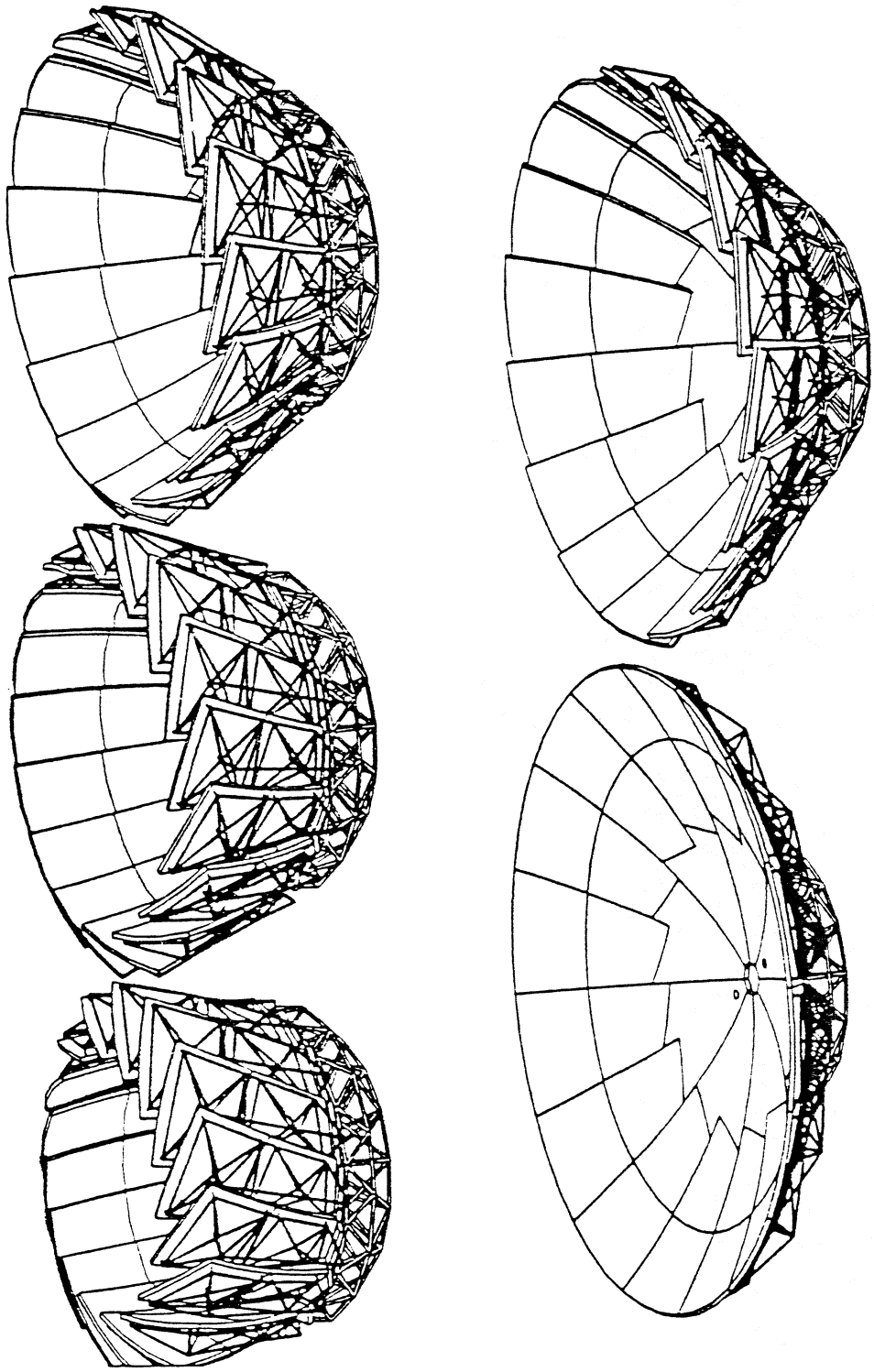

JPL

SUBMILLIMETER/INFRARED LINE SURVEY SPACECRAFT SYSTEM

LAUNCH CONFIGURATION*

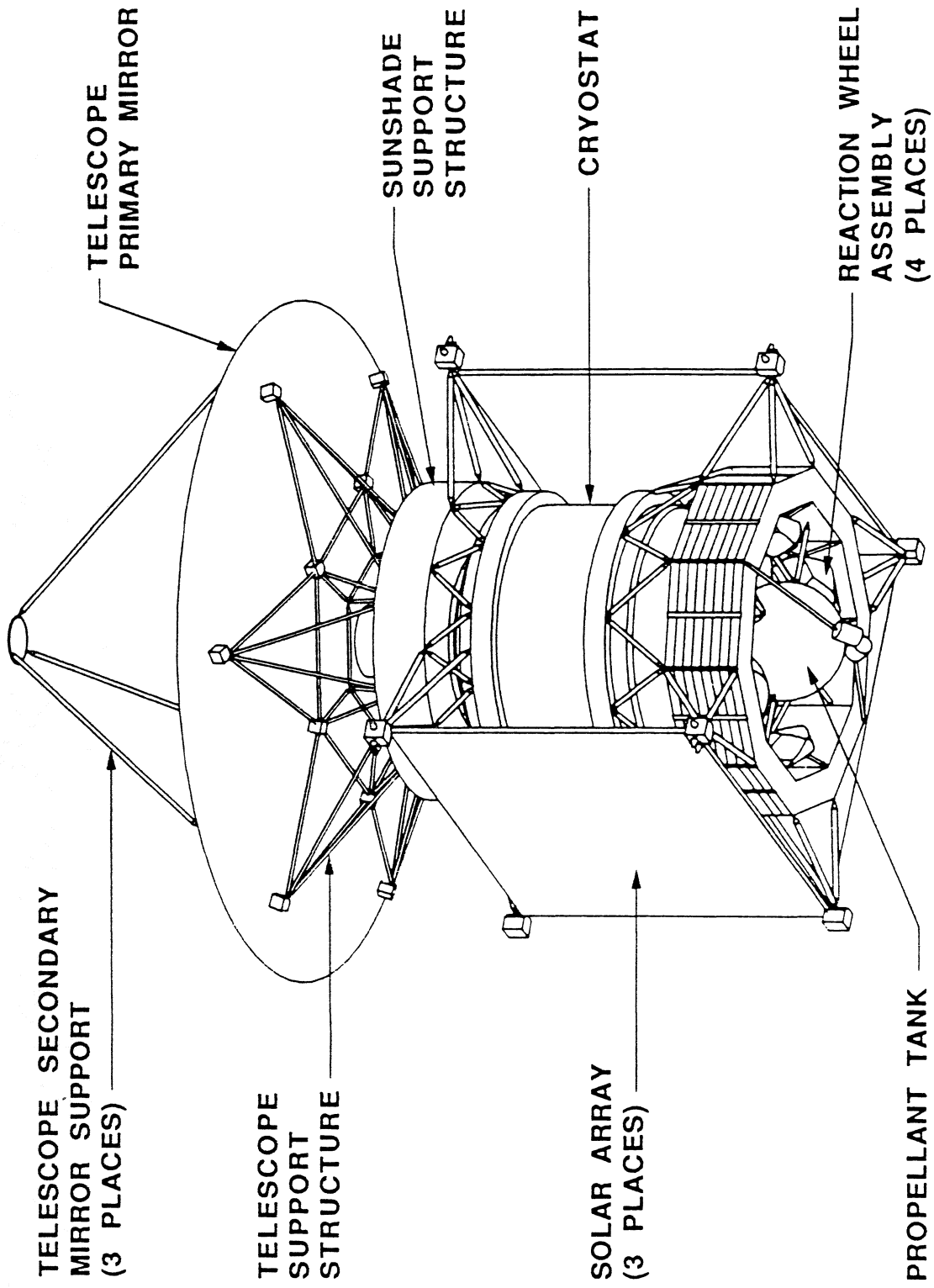

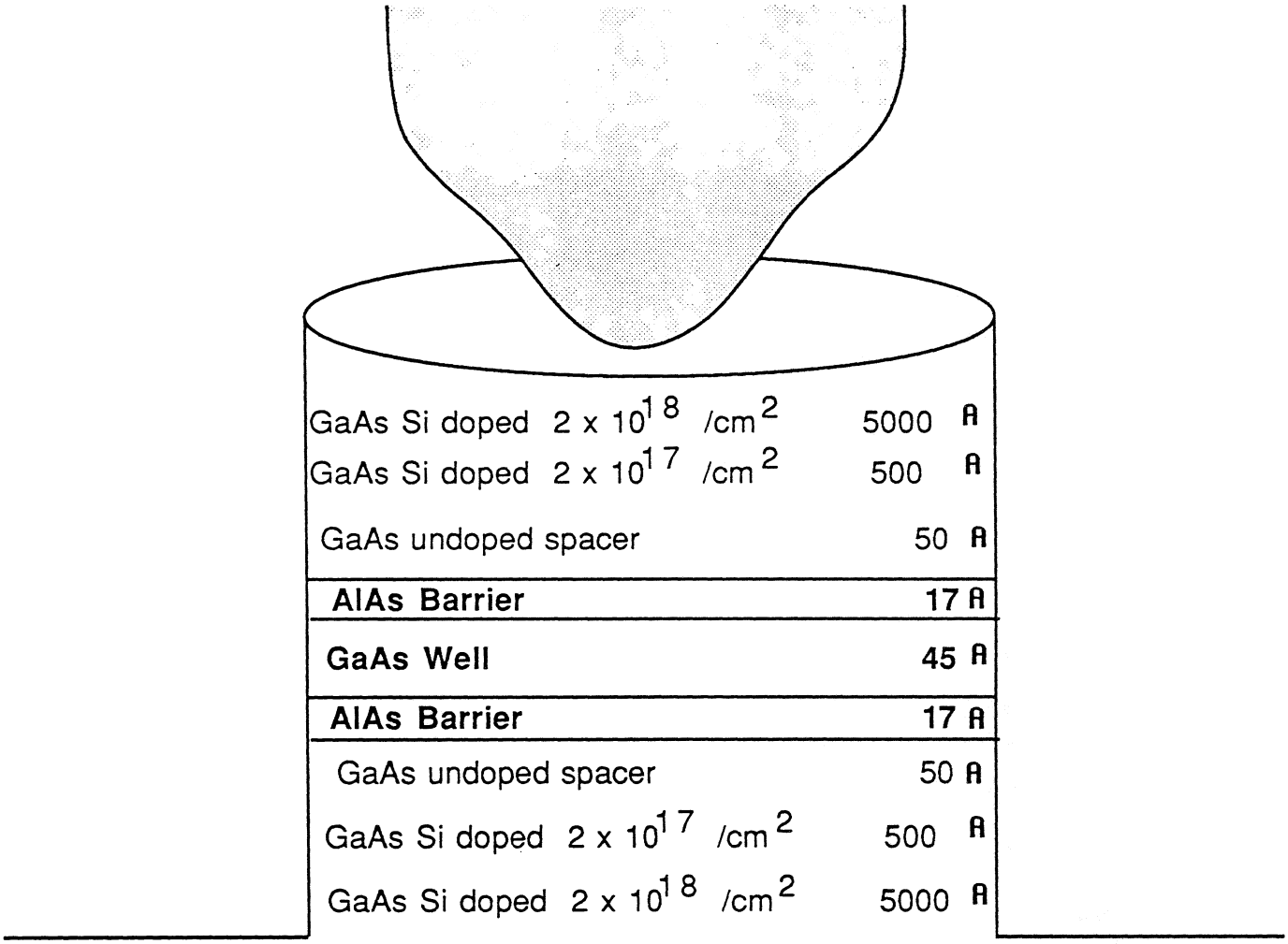

Resonant Tunneling Diode

AlAs/GaInAs Resonant Tunneling Diode

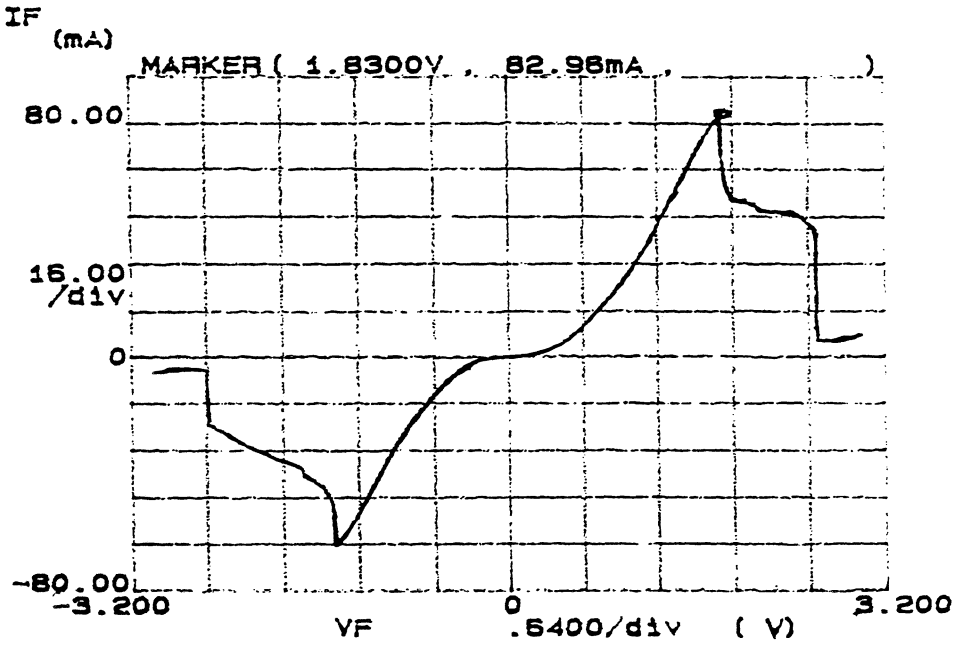

AlAs Barrier 25A
GaInAs Well 50A

Room Temperature
30 μm X 30 μm area

$$300K \quad \frac{J_p}{J_V} = 15.8 , \quad J_p = 9.1 \text{ KA/cm}^2$$

at 77K 80 μm X 80 μm area

$$\frac{J_p}{J_V} = 37.5 , \quad J_p = 7 \text{ KA/cm}^2$$

Ecole Polytechnique Federale de Lausanne
Thomson CSF-LCR
Ecole Normale Superiéure

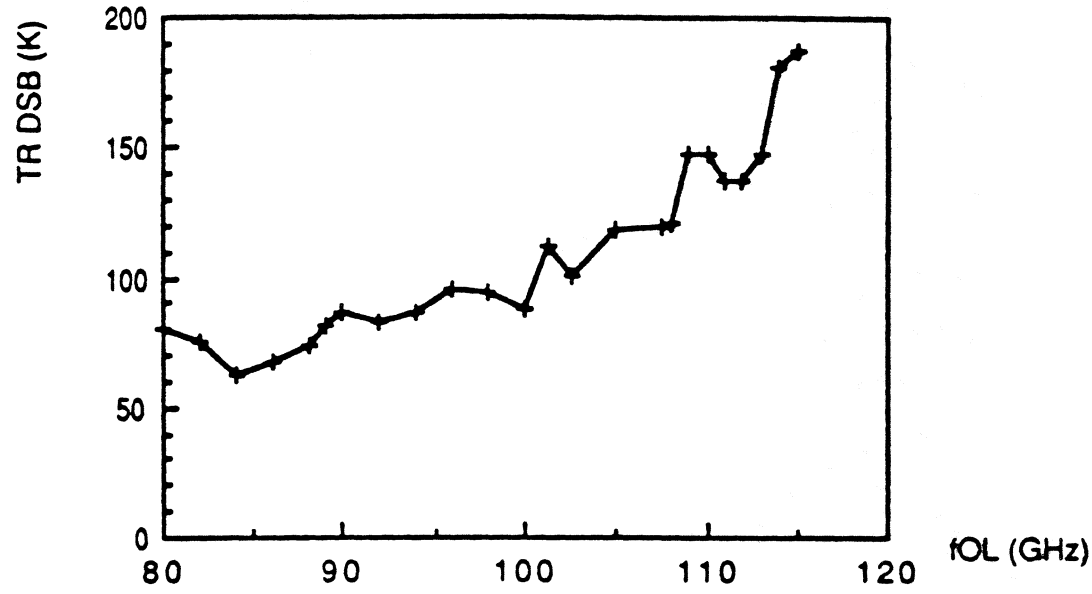

Fig.4. Receiver noise temperature (DSB) with the $2\mu m^2$ all Nb junction as a function of LO frequency.

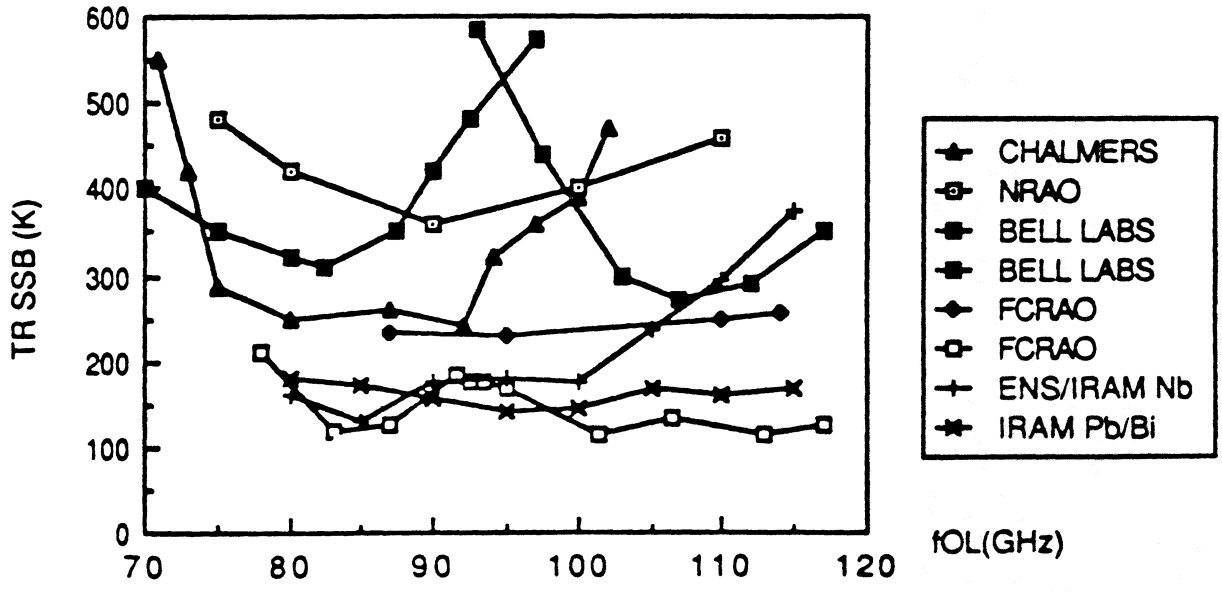

Fig.5. Frequency response of 3-mm cooled mixers. Single sideband receiver noise temperature are plotted over the 70 to 120 GHz range for the NRAO mixer, the Bell Telephone Laboratory system, the Chalmers University system and the Five College Radio Astronomy Observatory Schottky receiver (after (20)).Also shown on this figure the data obtained with IRAM receiver using Nb/Al-AlOx/Nb junction and Pb/Bi junction.Filled symbol are SSB temperature and the others are twice DSB results.

MATRA ESPACE

4 METERS SBMM SEGMENTED MIRROR
TENTATIVE BASELINE

. SEGMENTATION GEOMETRY :
  . HEXAGONAL 19 SEGMENTS

. SEGMENTS :
  . MADE OF CFRP : UHM GY70/PITCH 100S 2 SKINS ISOTROPIC LAYUP
    DISTANCIATED BY CFRP HONEYCOMB CURED ON ZERODUR GLASS MOLD (X3)
  . OPTICAL SURFACE OBTAINED BY REPLICA TECHNIQUE TH = 0.1 MM

. REFLECTIVE COATING :
  . VACUUM DEPOSITION OF GOLD TH = 0.15 MICRON

. SUPPORTING ACTUATORS :
  . 3 PER SEGMENT - TOTAL NUMBER : 57
    STEPPER MOTOR ASSOCIATED TO GEAR REDUCTION AND SPINDLE RESOLUTION : 0.1 MICRON

. INTER-SEGMENT SENSORS :
  . 12 PER SEGMENT - TOTAL NUMBER : 84
  . CAPACITIVE TYPE - DIFFERENTIAL MEASUREMENT
  . ELECTRODES MADE IN ZERODUR/GOLD COATED RELATIVE TYPE.

. CONTROL :
  . RELATIVE TYPE
  . SURFACE ACCURACY OF THE MIRROR KEPT BY MINIMIZING THE DEVIATION
    OF SENSORS INFORMATIONS WRT REFERENCE VALUES.

4 METERS - SBMM SEGMENTED MIRROR SURFACE ACCURACY BUDGET

CONTRIBUTORS	ALLOCATION (RMS IN MICRON)
A/ CRFP SEGMENTS MANUFACTURING :	
A1-SEGMENT DEVIATION WRT BF PARABOLA	1,5
A2-SEGMENT RADIUS OF CURVATURE SCATTERING	1,5
B/ SEGMENTS DIMENSIONAL STABILITY	
B1-THERMAL (WORKING T : 100K -50 K+ 10K . DIAMETRAL GRADIENT = 5K . TRANSVERSAL GRADIENT = 3K)	1,0
B2-MOISTURE RELEASE	2,3
B3-GRAVITY RELEASE	0,5
B4-LACK OF ISOSTATICITY OF SEGMENT FIXATIONS	0,2
C/ STABILITY OF SUPPORTING STRUCTURE (BETWEEN 2 CORRECTIONS)	0,1
D/ SEGMENTS INITIAL ALIGMENT ACCURACY	1,0
E/ CONTROL LOOP ACCURACY	1,0
F/ TOTAL	
$= \left[A1^2 + A2^2 + (B1 + B2 + B3 + B4)^2 + (C + D + E)^2 \right]^{1/2} =$	5,0

4 METERS SBMM SEGMENTED MIRROR CONTROL ALGORITHM

. GEOMETRY : 19 SEGMENTS

. ACTUATORS : 3 x 19 = 57 POSITIONS OF THEM ARE DEFINED BY A VECTOR P

. SENSORS : 12 PER SEGMENT - TOTAL NUMBER = 84 - ALL OF THEM WORKING IN DIFFERENTIAL
(MONITORING OF RELATIVE POSITION OF ASEGMENT WRT ADJACENT ONES.
SENSOR INFORMATIONS ARE DEFINED BY A VECTOR Z

. GEOMETRY OF THE SYSTEM = = > INFLUENCE MATRIX M = = > Z = M.P

. RECIPROCALLY Z BEING THE SENSORS INFORMATIONS ASSOCIATED TO NOISE COVARIANCE MATRIX : N

. ALGORITHM WILL DERIVE P VECTOR MINIMIZING THE VARIANCE

$$\text{MIN}\left[{}^{T}(Z - MP)\ N\ (Z - MP)\right] = = > {}^{T}M.N.^{-1}\ M.P = {}^{T}M.N^{-1}.Z$$

RIGID BODY MOTIONS OF THE MIRROR IS NOT DETECTED BY THE SYSTEM
= = > ${}^{T}M.N.^{-1}$ M IS SINGULAR (ORDER 3)

SELECTED SOLUTION = = > PISTON AND TILTS = 0 = = > P = CZ

4 METERS - SBMM SEGMENTED MIRROR CONTROL LOOP ACCURACY BUDGET

. CONTRIBUTORS	SURFACE ACCURACY DEGRADATION (RMS IN MICRONS)
. SENSORS AND ASSOCIATED ELECTRONIC ACCURACY	0,2
. STABILITY OF DISTANCE SENSOR/OPTICAL SURFACE	0,2
. STABILITY OF BEST PLANE/SENSORS PLANE	0,2
. ALGORITHM ACCURACY	0,2
. ACTUATORS ACCURACY	0,2
TOTAL (LINEAR SUMMATION)	1,0

MATRA ESPACE

4 METERS SBMM SEGMENTED MIRROR
MASS/POWER BUGETS ESTIMATE

MASS		POWER	PEAK	STAND BY
. SEGMENTS (19) :	47.5 KG (2.5KG/SEGMENT)	SENSORS ELECTRONIC	60 W	160 W
. ACTUATORS (57) :	34.2 KG (0.6 KG/ACTUATORS)	ACTUATORS	30 W	30 W
. SENSORS (84) :	21.0 KG (0.25KG/SENSOR)		190W	160W
. ELECTRONICS :				
. SENSORS	10.0K6			
. ACTUATORS :	7.0KG			
. HARNESS :	13.0KG			
. CONTINGENCY :	12.0KG (9%)			
	144.7KG			

ASSUMPTION :
ACTUATORS DRIVEN
BY GROUP OF 3 (TBR)

. SURFACIC MASS	11.5KG/M2
. GOAL	10 KGM2

MATRA ESPACE

4 METERS SBMM SEGMENTED MIRROR

SURFACE ACCURACY MIRROR

CONTRIBUTORS	ALLOCATION	PERFORMANCE ESTIMATE	REMARKS
A/ CFRP SEGMENTS MANUFACTURING			
A1/ SEGMENT DEVIATION WRT BF PAROBOLA	1.5	1.5	PER = SPEC
A2/ SEGMENT RADIUS OF CURVATURE SCATTERING	1.5	1.5	
B/ SEGMENT DIMENSIONAL STABILITY			
B1/ THERMAL (WORKING TEMP T = 100K - 50K + 0K DIAM GRAD = 5K/TRANS GRAD 3K)	1.0	0.84	CORRESPONDING TO ISO TYPE ORBIT
B2/ MOISTURE RELEASE	2.3	0.12	
B3/ GRAVITY RELEASE	0.5	0.22	
B4/ LACK OF ISOSTATICITY OF SEGMENT FIXATIONS	0.2	0.14	
C/ STABILITY OF SUPPORTING STRUCTURE	0.1	0.1	PERF = SPEC
D/ SEGMENTS INITIAL ALIGNMENT ACCURACY	1.0	1.0	
E/ CONTROL LOOP ACCURACY			
E1/ SENSOR & ASSOCIATED ELECTRONICS	0.2	0.05	SENSOR ALONE = +/- 25 nm
E2/ STABILITY OF DISTANCE SENSORS/OPTICAL SURFACE	0.2	0.2	
E3/ STABILITY OF BEST PLANE/SENSORS PLANE	0.2	0.2	
E4/ ALGORITHM ACCURACY	0.2	0.2	
E5/ ACTUATORS ACCURACY	0.2	0.065	ACTUATOR ALONE = +/- 0.05 micron
$TOTAL = \left[A1^2 + A2^2 + (B1 + B2 + B3 + B4)^2 + (C + D + E1 + E2 + E3 + E4 + E5)^2 \right]^{1/2}$	5	3.1	

SUBMILLIMETER WAVELENGTH ASTRONOMY MISSIONS FOR THE 1990s

S. Gulkis
Jet Propulsion Laboratory
California Institute of Technology
Pasadena, CA 91109

ABSTRACT

The submillimeter spectral band between wavelengths of 100 μm and 1000 μm is of key importance for the investigation of a wide range of astronomical topics. These include star-forming molecular cloud regions, planetary atmospheres, galaxies, and cosmic background radiation. Space telescopes will ultimately be required to study these objects at submillimeter wavelengths with complete freedom from the interference due to the terrestrial atmosphere. Ground based, airplane, and balloon observations have been and will continue to be important in developing the field. Several small and modest-sized astronomical space projects for the 1990s have been studied which could dramatically open the window on the submillimeter and far infrared spectral ranges. This paper presents an overview of the science and instrumentation under discussion for these 1990s projects.

1. INTRODUCTION

Our knowledge of the sky will take a large step forward during the decade of the nineties due to the operation of a number of submillimeter and far infrared astronomy space missions, starting first with the COSMIC BACKGROUND EXPLORER (COBE) launched in late 1989. The submillimeter spectral region, defined here to range from 100 to 1000 μm (micrometers), is important to studies of most aspects of astronomy including the solar system, the galaxy, extragalactic objects, and cosmology. This spectral region has not been explored in any detail to date because of the high opacity (and variability) of the terrestrial atmosphere in the submillimeter range due primarily to H2O, O2, and O3. Melnick (1988) gives a good discussion of the atmospheric transparency in the submillimeter range. He also discusses the unique role that balloons can make in helping to study the sky in the era before the large space based submillimeter telescopes come into being. This paper presents and overview of the science and instrumentation for a number of submillimeter and far infrared space missions currently under discussion.

2. SUBMILLIMETER SPACE MISSIONS

TABLE I lists six submillimeter/far infrared space missions for the decade from 1990-2000 and their estimated (nominal) observation times in orbit. Of the six mission, only one, COBE, is presently in orbit. The others are in varying states of approval and readiness.

TABLE I

SUBMILLIMETER / FAR INFRARED SPACE MISSIONS

PROJECT NAME	ESTIMATED ORBIT TIMES (YEARS)
COSMIC BACKGROUND EXPLORER(COBE)	1989-1990
INFRARED TELESCOPE IN SPACE(IRTS)	1993
SUMILLIMETER WAVE ASTRONOMY SATELLITE(SWAS)	1994-1995
INFRARED SPACE OBSERVATORY(ISO)	1993-1994
SUBMILLIMETER MISSION(SMMM)	1999-2001
SPACE INFRARED TELESCOPE FACILITY(SIRTF)	1999-2004

In addition to these space missions, a number of balloon projects and astronomy research aircraft will allow considerable access to the submillimeter sky. These vehicles will serve as platforms for instrument development and modest research projects during the decade. The newest of these projects, the Stratospheric Observatory of Infrared Astronomy(SOFIA), will provide a considerable improvement in capability if approved. SOFIA is planned to carry a warm, 2.5 meter telescope to heights of 14 km.

Two additional space submillimeter projects are also in the planning stages but launch dates will probably not take place until the next century. These are the ESA-Far infrared Space Telescope(FIRST) and the Large Deployable Reflector(LDR). A submillimeter lunar interferometer is also under discussion at the present time. These three missions are critically dependent on the development of terahertz technology.

The COBE mission is designed to study cosmic background radiation over the wavelength range from 1 μm to 1 centimeter. Primary mission objectives are to search for angular anisotropies in the cosmic microwave background, to measure the spectrum of the background radiation, and to search for diffuse infrared emission from the first stars and galaxies. The COBE spacecraft was launched into a polar orbit in November 1989 and is designed to have nominal lifetime of 1 year. The COBE spacecraft carries three instruments, a set of differential microwave radiometers at 31GHz, 53 GHz, and 90 GHz, a polarizing Michelson interferometer which operates over the wavelength range 1 cm to 100 μm, and a diffuse infrared experiment which measures in ten bands from 1 μm to 300 μm. The microwave instruments are based on Schottky Diode receivers. The receivers at 53 and 90 GHz are radiatively cooled to about 135 K. The Michelson interferometer and diffuse infrared experiments are both located inside a 600 liter cryostat which contains liquid helium.

IRTS is a Japanese mission with potential for U.S. participation. IRTS will study galactic and extragalactic radiation on angular scales of 0.1 degrees. The primary light collector is a 15 cm cryogenically cooled telescope. Mission lifetime is two to three weeks. The data collected from IRTS will be complementary to the COBE data.

The mission objectives for SWAS are to study cloud chemistry, energy balance, and structure of galactic molecular clouds by studying emission from four submillimeter spectral lines: 1)the ground state ortho transition at 556.936 GHz, 2)the 487.249 GHz transition of O2, 3)the ground state fine structure transition of carbon at 492.162 GHz, and 4)a rotational transition of 13CO at 550.926. SWAS plans to use a 55 cm, ambient temperature, off-axis Casegrain telescope. Passive radiators will be used to cool the Schottky diode receivers to temperatures near 100 K. An acousto optical spectrometer(AOS) will be used to provide the spectral line backend.

The ISO mission is an ESA mission with potential for collaboration with U.S. astronomers. The ISO spacecraft will contain four focal plane instruments (1 camera, 2 spectrometers, and 1 photopolarimeter) which cover the wavelength interval from 3 to 200 μm. The expected launch vehicle is an Ariane 44 which will place the spacecraft into a highly elliptic (1000 - 70500 km) orbit having an inclination of 5 degrees. The telescope is a 60 cm, Ritchey-Chretien telescope cooled to less than 3.2 K.

The submillimeter mission(SMMM) is designed to make physical and chemical studies of high red-shift galaxies, molecular clouds, star forming regions and planets. SMMM will utilize a roughly 4 meter ambient temperature telescope with a liquid helium cooled focal plane. It will achieve a complete submillimeter spectroscopic survey of a large number of sources between 100 and 700 μm. Heterodyne techniques will be used at the longer wavelengths to provide this spectroscopic capability. Direct detection in conjunction with a far-infrared spectrometer will be used for spectroscopy at the shorter wavelengths. SMMM will also carry a far-infrared camera with a bolometer array. Superconduction tunnel junction (SIS) detectors will form the basis for the heterodyne receivers. The expected lifetime is about 2 years. This mission is critically dependent on the development of terahertz technology.

The Space Infrared Telescope Facility(SIRTF) planned for the later part of the decade will perform astronomical studies including imaging, photometry, and spectroscopy over the wavelength range of 1.8 to 700 μm. The telescope is a helium cooled 0.85 meter system. SIRTF will carry three scientific instruments, a multiband imaging photometer which operates in the band 3 to 700 μm, an infrared array camera that operates from 1.8 to 30 μm, and an infrared spectrograph that operates in several bands from 2 to 200 μm. The highest spectral resolution is about 2500.

3. TECHNOLOGY EVOLUTION

Many new technologies(including new applications in space) are going to be needed to fully exploit the submillimeter spectral range. Future space projects will certainly require the knowledge and heritage gained from predecessor space missions. Table II shows the evolutionary technology trends in the current mission set.

TABLE II

SPACE-BASED SUBMILLIMETER TECHNOLOGY EVOLUTION

COOLED FIR SCANNING SPECTROMETER	COBE	ISO		
SCHOTTKY MIXERS	COBE			
SPECTROMETERS(AOS)		SWAS		
GUNN MULTIPLIERS				
CARBON EPOXY PANELS			SMMM	
WAVEFRONT SENSING				
SIS RECEIVERS(500GHz-1.2 THz)				
IMAGING SIS RECEIVERS				FIRST/LDR
YEAR	1990	1995	2000	2005

4. CONCLUSIONS

The scientific arguments for submillimeter astrophysics space missions are compelling and multi-disciplinary. Science objectives include studies of planetary and satellite atmospheres, comets, the interstellar medium, star formation regions, stars, galaxies, and cosmology. Terahertz technology will play a crucial role in the planning and implementation of space missions. The instrument requirements for space astronomy are very challenging. A great deal of laboratory and field work must be done to meet the requirements of future space missions. The technology evolution built into the present mission set for the 1990s provides an orderly transition of technology from the laboratory to space.

REFERENCES

Melnick, G. J. ,"ON THE ROAD TO THE LARGE DEPLOYABLE REFLECTOR(LDR): THE UTILITY OF BALLOON-BORNE PLATFORMS FOR FAR-INFRARED AND SUBMILLIMETER SPECTROSCOPY", International Journal of Infrared and Millimeter Waves, Vol. 9, No. 9,1988.

ACKNOWLEDGEMENTS

The research described in this paper was carried out at the Jet Propulsion Laboratory, California Institute of Technology, under contract with the National Aeronautics and Space Administration.

SUBMILLIMETER WAVE ASTRONOMY SATELLITE

Paul F. Goldsmith
Five College Radio Astronomy Observatory
Department of Physics and Astronomy
University of Massachusetts, Amherst
and
Millitech Corporation
South Deerfield, Massachusetts

Abstract

The Submillimeter Wave Astronomy Satellite (SWAS) was selected in 1989 by NASA, for a scheduled Scout launch in 1993. The objectives of this mission within the Small Explorer Program are to study dense clouds in the interstellar medium via critically important transitions of molecular and atomic species which can be observed only at submillimeter wavelengths. SWAS will thus observe transitions of water vapor at 557 GHz, molecular oxygen at 487 GHz, atomic carbon at 492 GHz, and carbon–13 monoxide at 554 GHz. These frequencies are totally or largely opaque from the ground, and a space–based survey of molecular clouds throughout our galaxy will yield important new information about the chemistry in very dense clouds in the Milky Way, and the process of star formation. The SWAS instrument employs a 55–cm diameter offset Cassegrain antenna with a nutating secondary reflector. The receivers are second harmonic downconverters, using Schottky diodes as the mixing elements, with phase locked InP Gunn devices as the local oscillator sources. The receiver front ends are passively cooled to $\simeq$ 150 K. Spectral analysis is performed by an acousto–optical spectrometer with 1.4 GHz bandwidth, which covers the four lines simultaneously. SWAS represents the first space–borne system operating in the submillimeter range, and as such is providing considerable impetus for development of highly reliable, compact, components which have low mass and power consumption. We see SWAS as the precursor of more elaborate submillimeter astronomy missions, and complementing work done from airborne platforms and dry sites on the Earth's surface.

Participants in the SWAS project:

G. Melnick, A. Dalgarno, G. Fazio, P. Thaddeus, Smithsonian Astrophysical Observatory

P. Goldsmith, N. Erickson, R. Snell, University of Massachusetts, Amherst

D. Hollenbach, NASA Ames Research Center

G. Winnewisser, University of Cologne, F.R.G.

M. Harwit, National Air and Space Museum

D. Neufeld, University of California, Berkeley

Industry contractors:

Ball Aerospace Systems Group (antenna, pointing, thermal design,integration)

Millitech Corporation (submillimeter frontend)

OBJECTIVES FOR SWAS PROJECT

SWAS IS AN OUTGROWTH OF INTEREST OF SCIENTISTS IN EXPLOITATION OF THE SUBMILLIMETER WAVELENGTH REGION FOR ASTRONOMY

IT WILL BE A PIONEERING STEP IN SUBMILLIMETER ASTRONOMY IN SPACE

SUBMILLIMETER CONTINUUM OBSERVATIONS, WHILE PAINFUL, CAN TAKE ADVANTAGE OF "WINDOWS"

THUS, THE FOCUS OF **SWAS** IS ON SUBMILLIMETER SPECTRAL LINES OF ASTROPHYSICAL SIGNIFICANCE WHICH CANNOT BE STUDIED USING GROUND–BASED TECHNIQUES

THE CHOICE OF FREQUENCIES IS ALSO IMPACTED BY REQUIREMENT THAT TECHNOLOGY BE AVAILABLE

* **Long wavelength submillimeter heterodyne receivers**
  - Schottky diode mixers
  - Solid state local oscillators
* **Acousto–optical spectrometer**

SWAS SPECTRAL LINES

Species	Transition	Frequency (GHz)	Wavelength (Microns)
O_2	$3(3) - 1(2)$	487.249	615.7
CI	$^3P_1 - {}^3P_0$	492.162	609.6
^{13}CO	$5 - 4$	550.926	544.5
H_2O	$1_{10} - 1_{01}$	556.936	538.7
$H_2{}^{18}O$	$1_{10} - 1_{01}$	547.545	547.9

SPECIES SELECTED FOR OBSERVATION BY **SWAS** ARE IMPORTANT BECAUSE

(1) THEY ARE PREDICTED TO BE MAJOR RESERVOIRS OF CARBON AND OXYGEN IN DENSE INTERSTELLAR CLOUDS

(2) THEY SHOULD BE VALUABLE PROBES OF PHYSICAL CONDITIONS IN THESE REGIONS

(3) THEY *SHOULD* PLAY A MAJOR ROLE IN DETERMINATION OF TEMPERATURE IN INTERSTELLAR CLOUDS

(4) THEY PROVIDE IMPORTANT TESTS OF CHEMICAL MODELS OF WELL–SHIELDED REGIONS IN MOLECULAR CLOUDS AND OF REGIONS WHERE PHOTOCHEMISTRY IS IMPORTANT

WATER AND CARBON MONOXIDE ARE THOUGHT TO BE THE MOST

IMPORTANT COOLANTS OF GAS IN INTERSTELLAR MOLECULAR CLOUDS

AT HIGH DENSITIES IN CLOUD CORES $n(H_2) \geq 10^5$ CM^{-3}

H_2O IS THE MOST IMPORTANT GAS COOLANT

THE **557 GHZ $1_{10} - 1_{01}$ GROUND STATE TRANSITION** PLAYS A KEY ROLE

THIS TRANSITION SHOULD BE READILY OBSERVABLE WITH **SWAS**

IN GMC CORES THROUGHOUT MILKY WAY

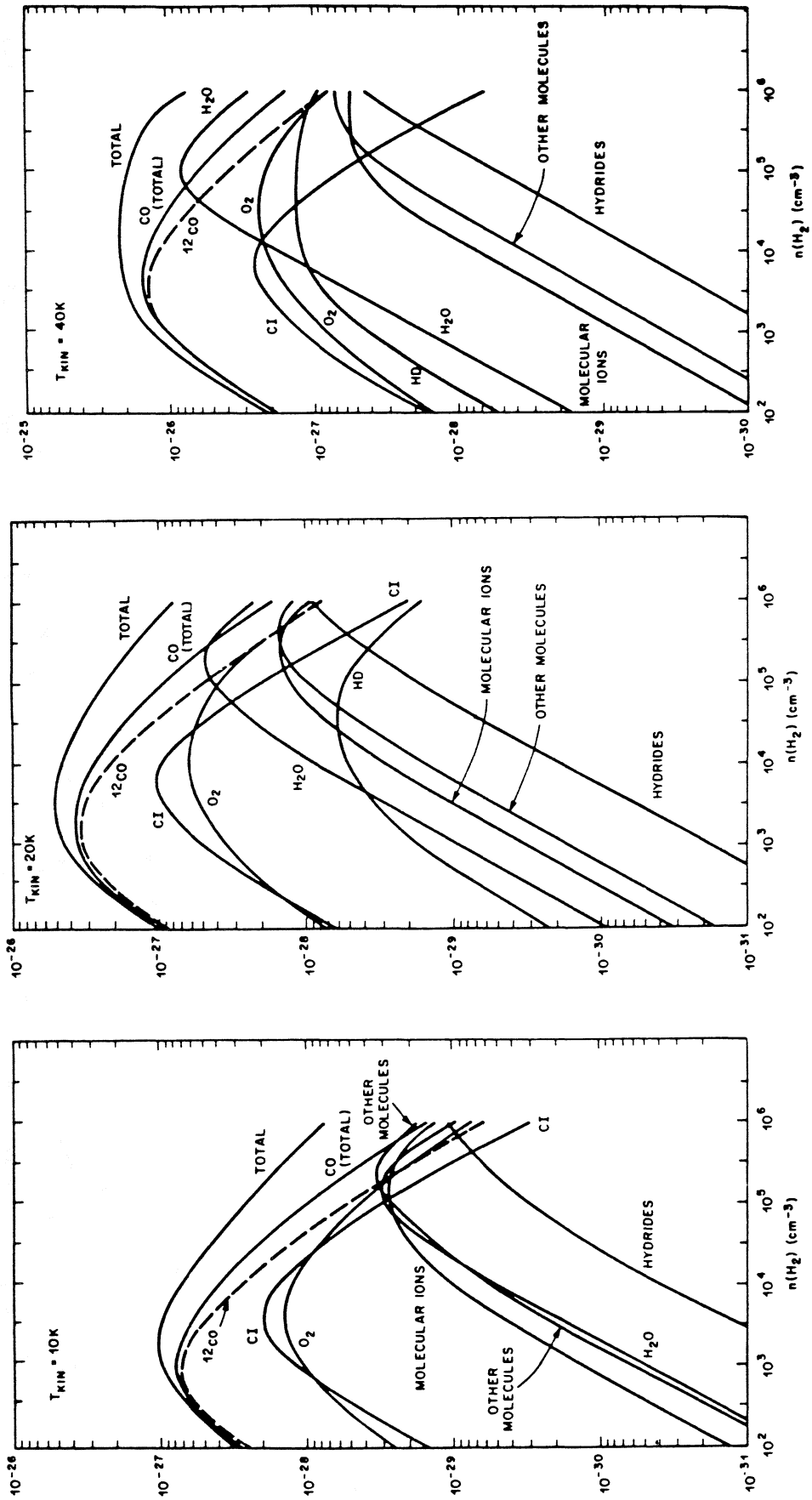

COOLING FROM ATOMS AND MOLECULES IN DENSE CLOUDS IN THE INTERSTELLAR MEDIUM

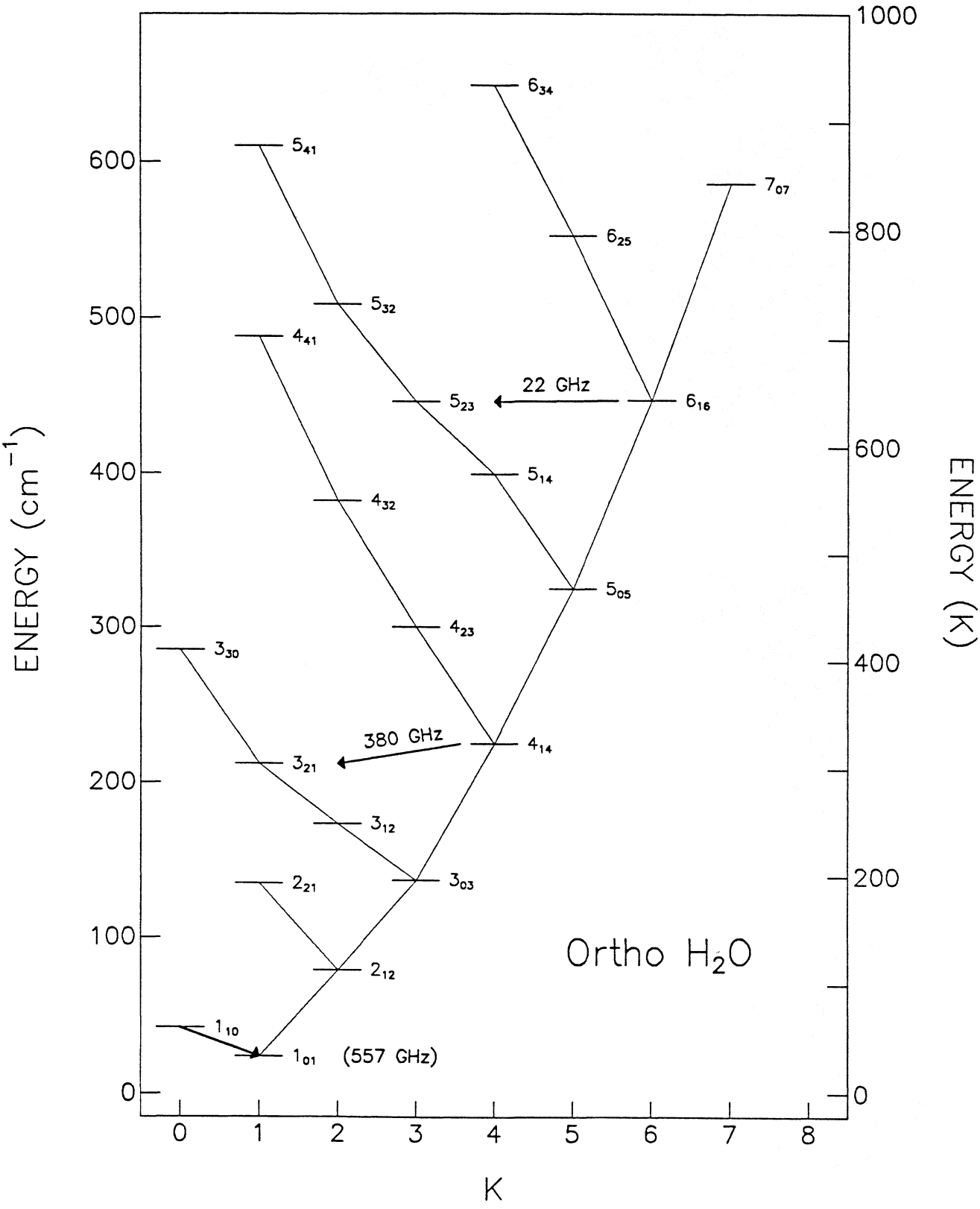
ENERGY (cm^{-1})
ENERGY (K)
K
0
100
200
300
400
500
600
0
200
400
600
800
1000
0
1
2
3
4
5
6
7
8
6_{34}
5_{41}
7_{07}
6_{25}
5_{32}
4_{41}
22 GHz
5_{23}
6_{16}
5_{14}
4_{32}
5_{05}
4_{23}
3_{30}
380 GHz
4_{14}
3_{21}
3_{12}
2_{21}
3_{03}
2_{12}
1_{10}
1_{01} (557 GHz)
Ortho H_2O

NEUTRAL CARBON IS A VERY VALUABLE PROBE OF THE EFFECTS OF PHOTOCHEMISTRY ON THE STRUCTURE OF MOLECULAR CLOUDS

THIS MAY NOT BE RESTRICTED TO CLOUD EDGES, BUT IF DENSITY OF A CLOUD IS VERY NON–UNIFORM (HIGHLY CLUMPED), THERE MAY BE PHOTOCHEMICALLY–DOMINATED REGIONS THROUGHOUT A LARGE FRACTION OF CLOUDS' VOLUME. THIS WILL HAVE A PARTICULARLY IMPORTANT EFFECT WHEN THERE ARE HII REGIONS NEARBY

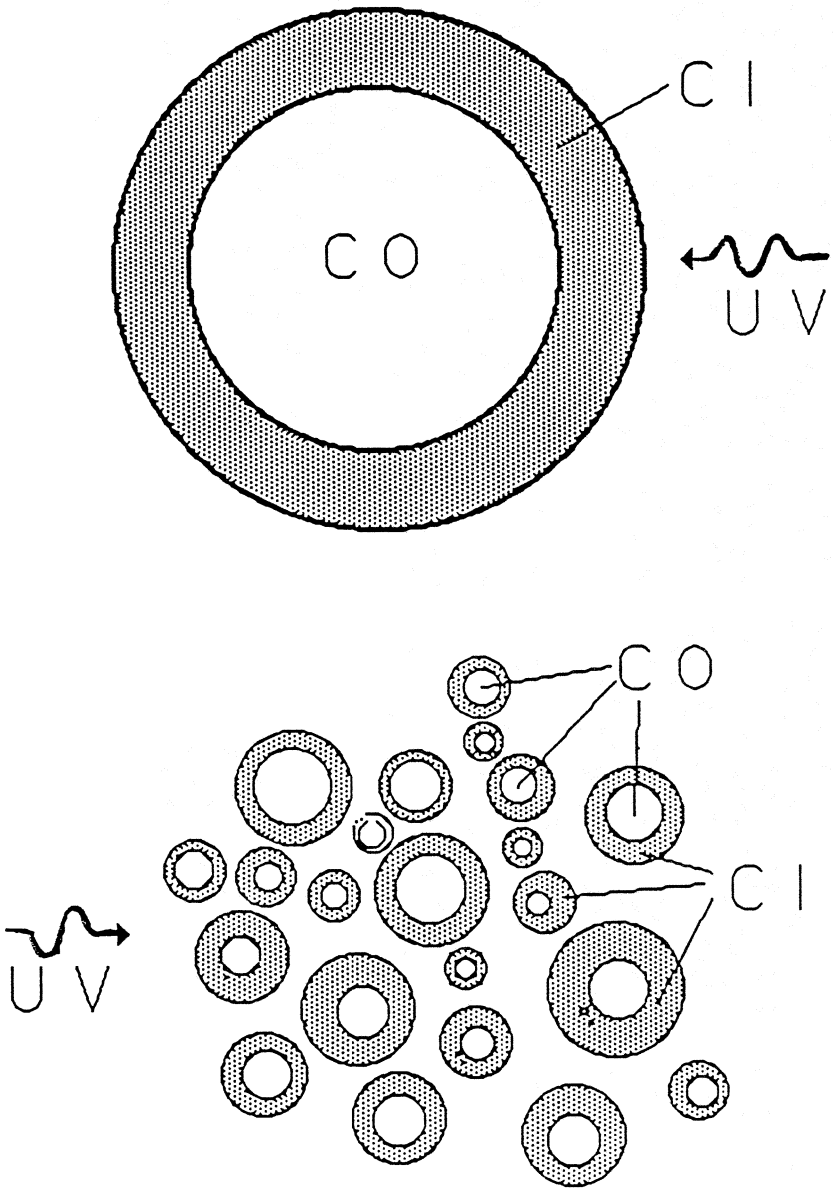

HIGHLY CLUMPED MODEL OF INTERSTELLAR CLOUD WHICH

ALLOWS PENETRATION OF UV

^{13}CO J = 5–4 TRANSITION AT 551 GHZ IS SENSITIVE TO REGIONS WITH HIGH TEMPERATURE AND DENSITY

THE UPPER LEVEL IS 80 K ABOVE GROUND STATE

SPONTANEOUS DECAY RATE IS 1.1×10^{-5} s^{-1}

IN CONJUNCTION WITH OTHER PROBES, IT SHOULD BE A VERY EFFECTIVE TRACER OF WARM MATERIAL IN GMC's

MOLECULAR OXYGEN IS AN IMPORTANT SPECIES TO OBSERVE BECAUSE FORMATION AND DESTRUCTION PATHWAYS ARE INTIMATELY LINKED WITH OTHER MAJOR CARBON- AND OXYGEN- BEARING SPECIES INCLUDING CI, CO, AND H_2O

FORMATION OF O_2

$H_2 + CR \rightarrow H_2^+ + e^-$

$H_2^+ + H_2 \rightarrow H_3^+ + H$

$H_3^+ + O \rightarrow OH^+ + H_2$

$OH^+ + H_2 \rightarrow H_2O^+ + H$

$H_2O^+ + H_2 \rightarrow H_3O^+ + H$

$H_3O^+ + e^- \rightarrow \mathbf{H_2O} + H$
$\rightarrow OH + H_2$

$OH + O \rightarrow \mathbf{O_2} + H$

DESTRUCTION OF O_2

$C + O_2 \rightarrow CO + O$

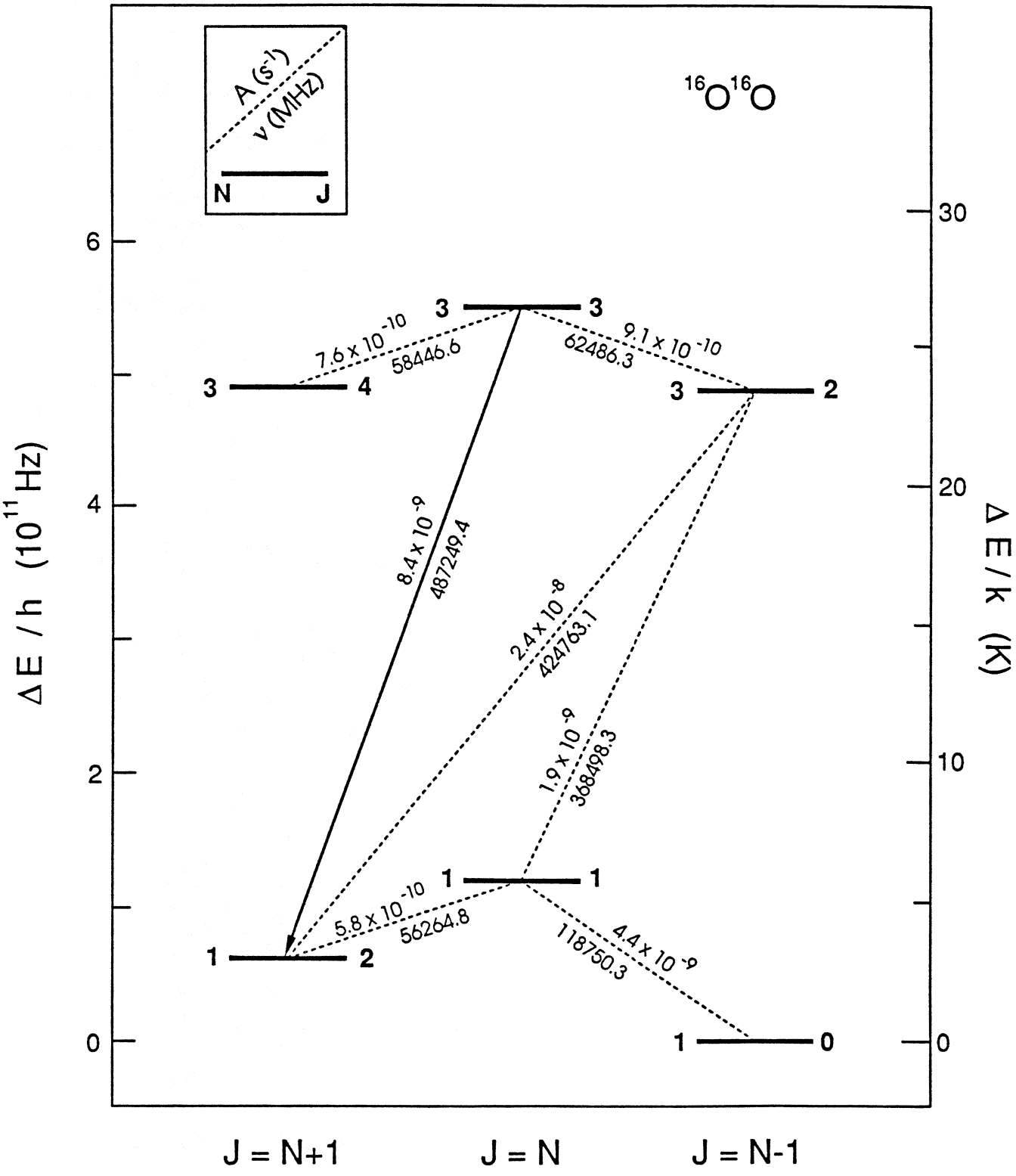
A (s-1)
ν (MHz)
N
J
16O16O
ΔE / h (10^11 Hz)
ΔE / k (K)
0
2
4
6
0
10
20
30
3 3
3 4
3 2
1 1
1 2
1 0
7.6 x 10-10
58446.6
9.1 x 10-10
62486.3
8.4 x 10-9
487249.4
2.4 x 10-8
424763.1
1.9 x 10-9
368498.3
5.8 x 10-10
56264.8
4.4 x 10-9
118750.3
J = N+1
J = N
J = N-1

SWAS MISSION PROFILE

I. QUICK–LOOK CHEMISTRY

10 POSITIONS IN EACH OF 5 GIANT AND DARK CLOUD CORES FOR 1200 s

4 POSITIONS IN EACH OF 5 GIANT AND DARK CLOUDS FOR 45,000 s

Total time approximately 10 days

II. MINI–SURVEY OF GMC's in GALAXY

1000 POSITIONS FOR 5000 s PER POSITION

NEUTRAL CARBON MAPPED THROUGHOUT REGIONS

EXPECT TO DETECT ALL GMC CORES IN H_2O, ^{13}CO, AND O_2

Total time approximately two months

III. MAPS OF LOCAL CLOUDS

10 LOCAL CLOUDS FOR SPATIAL DISTRIBUTION OF VARIOUS SPECIES

TRACE VARIATIONS AS FUNCTION OF τ, RADIATION FIELD, etc.

Orion, Monoceros, Taurus, Perseus, Chamaeleon, Ophiuchi, Cygnus...

Total time approximately four months

IV. ADDITIONAL STUDIES

DEPEND ON INTENSITIES AND ABUNDANCES FROM PHASES I – III

HIGH SPATIAL RESOLUTION STUDIES– –NYQUIST–SAMPLED MAPS

FULL SURVEY OF CLOUDS IN THE GALAXY

EXTRAGALACTIC SOURCES

Nominal mission lifetime is 2 years

SWAS ANTENNA AND OPTICS

Observe Four Spectral Lines Simultaneously

* Two Receivers operating in orthogonal polarizations
* Wire Grid Diplexer sends two lines to each mixer
* Local Oscillator frequencies fold a pair of lines into each IF
* Two IF's diplexed into spectrometer

Antenna

* 55 cm diameter offset Cassegrain
* $\Delta\theta_{fwhm} = 4.4$ arcmin at 610 μm and 3.9 arcmin at 540 μm
* $f_e/D_m = 4.8$
* Nutating secondary mirror (1 degree chop at 1/60 Hz)
* Approximately Gaussian illumination with conical feedhorns

Calibrations

* Internal using ambient load and cold sky: $\Delta T \simeq 160$ K
* External using planets (unresolved) and Moon

Spectrometer

* Acousto–Optical Spectrometer (AOS)
* 1400 elements covering 1.4 GHz
* Redundant laser diodes and CCD readouts

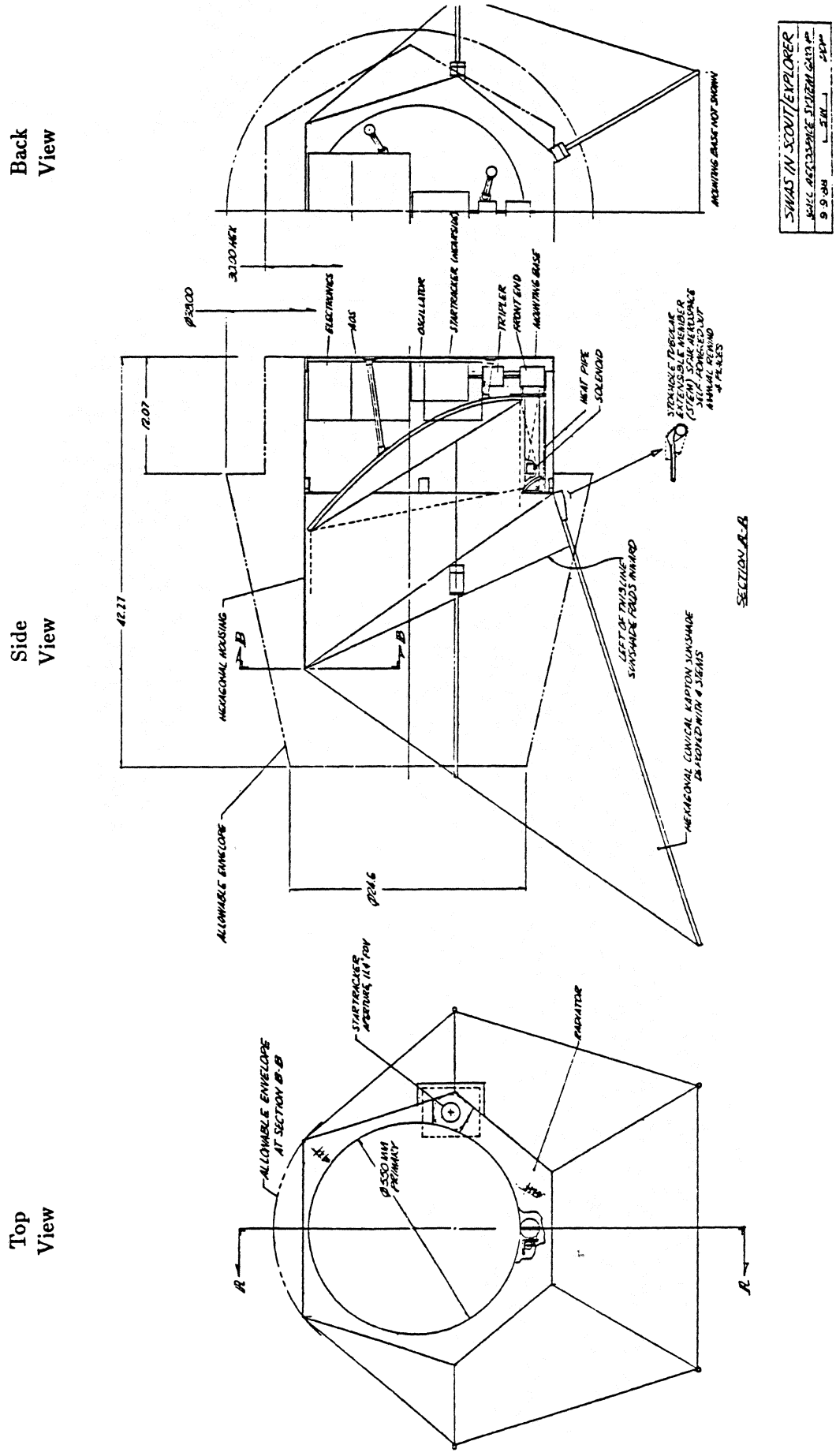

Layout of the SWAS intrument relative to the payload envelope.

SWAS RECEIVERS

*** Second harmonic mixers pumped by frequency–tripled Gunn oscillators**

Oscillator frequencies are 81.5 GHz and 92.3 GHz for the two receivers

The two Gunn oscillators are phase locked to a single (but redundant) reference oscillator at 5.114 GHz

Doppler tracking is obtained by synthesizer employed for PLL loop reference

*** HEMT amplifiers for first IF stages**

2.1–2.8 GHz for low band (O_2–CI) receiver and 2.7–3.4 GHz for high band (H_2O–$C^{13}O$ receiver)

*** Input optics, mixers, and first IF amplifiers are passively cooled to a temperature of between 120 and 160 K** (the value depends on thermal design)

*** Use of harmonic mixers significantly reduces system complexity**

Eliminates frequency doubler for second harmonic mixer and input diplexer

Approximately 1 dB (1.26x) higher conversion loss for second harmonic mixer than for fundamental mixer

*** 557 GHz (modified for 547 GHz) prototype successfully flown on KAO**

*** Expected receiver temperatures when cooled $<$ 2500 K Single Sideband**

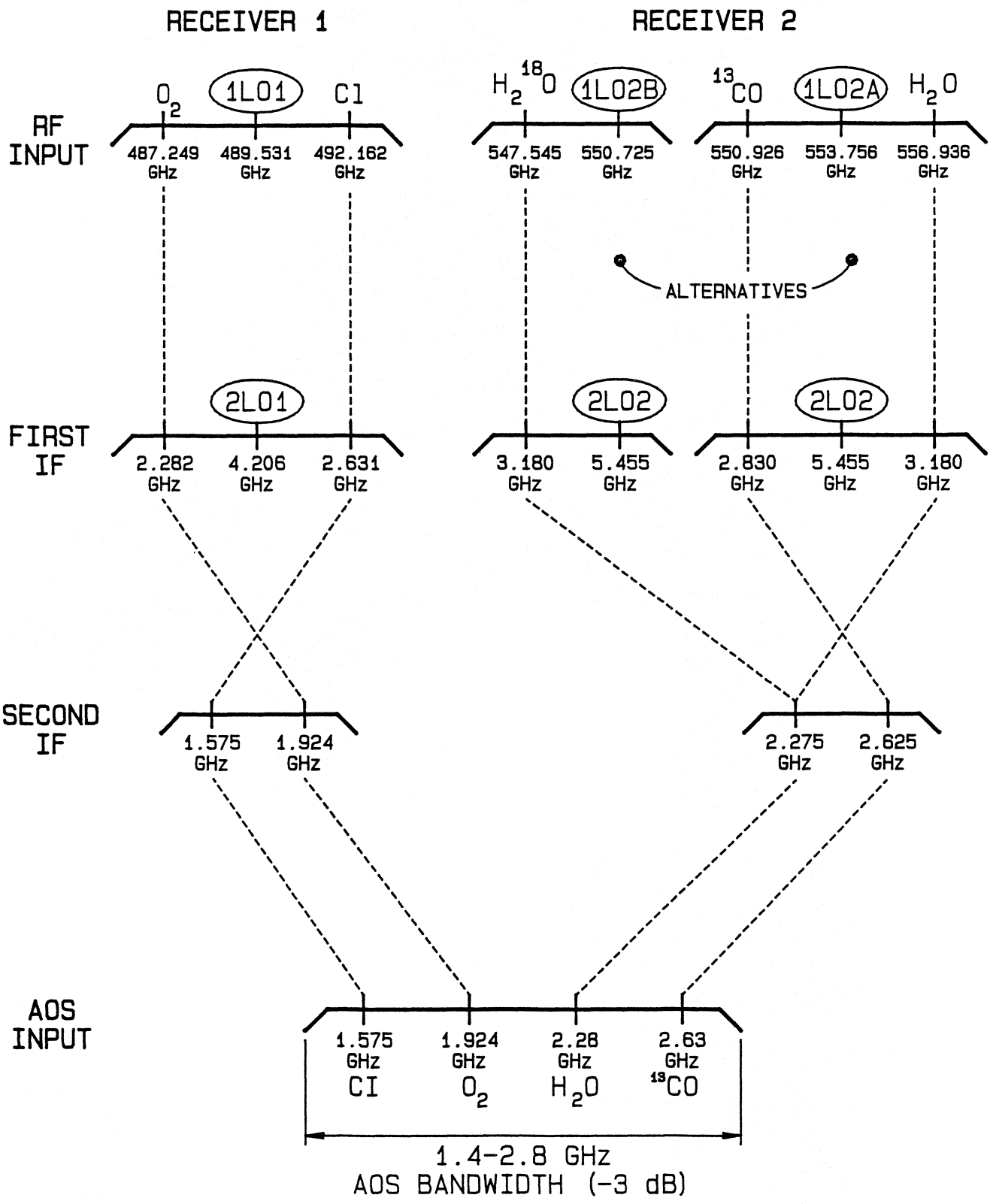

SWAS SUBMM RECEIVER FREQUENCIES

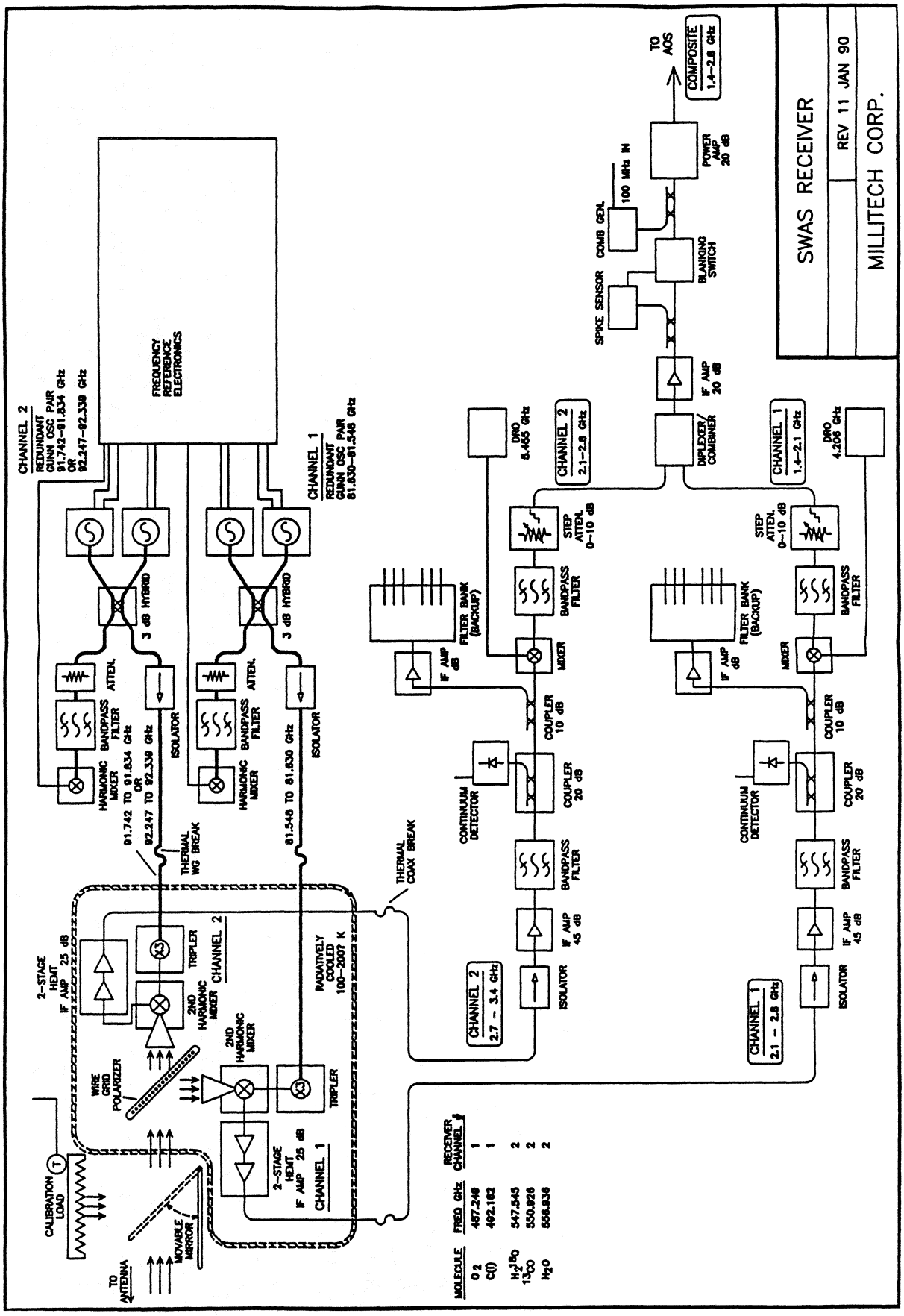
SWAS RECEIVER
REV 11 JAN 90
MILLITECH CORP.
CHANNEL 2
REDUNDANT GUNN OSC PAIR
91.742–91.834 GHz
OR
92.247–92.339 GHz
CHANNEL 1
REDUNDANT GUNN OSC PAIR
81.630–81.548 GHz
FREQUENCY REFERENCE ELECTRONICS
3 dB HYBRID
ATTEN.
BANDPASS FILTER
HARMONIC MIXER
ISOLATOR
91.742 TO 91.834 GHz OR 92.247 TO 92.339 GHz
81.548 TO 81.630 GHz
THERMAL WG BREAK
THERMAL COAX BREAK
2-STAGE HEMT IF AMP 25 dB
TRIPLER
2ND HARMONIC MIXER
CHANNEL 2
CHANNEL 1
WIRE GRID POLARIZER
MOVABLE MIRROR
CALIBRATION LOAD
TO ANTENNA
RADIATIVELY COOLED 100–200? K
MOLECULE FREQ GHz RECEIVER CHANNEL #
O2 487.249 1
C(I) 492.162 1
H2 18O 547.545 2
13CO 550.926 2
H2O 556.936 2
DRO 8.465 GHz
DRO 4.206 GHz
STEP ATTEN. 0–10 dB
MIXER
COUPLER 10 dB
COUPLER 20 dB
CONTINUUM DETECTOR
IF AMP 45 dB
CHANNEL 2 2.7 – 3.4 GHz
CHANNEL 1 2.1 – 2.8 GHz
CHANNEL 2 2.1–2.8 GHz
CHANNEL 1 1.4–2.1 GHz
DIPLEXER/ COMBINER
IF AMP 20 dB
SPIKE SENSOR
COMB GEN.
100 MHz IN
BLANKING SWITCH
POWER AMP 20 dB
COMPOSITE 1.4–2.8 GHz
TO AOS

SWAS MISSION AND SPACECRAFT

* **Two year lifetime to accomplish scientific objectives**

  requires perigee altitude $\geq$ 530 km

  An equatorial orbit is most favorable for lifetime, but has problems including telemetry stations and launch site status. Still under discussion

* **Pointed observations using solid state star tracker – 0.01 deg pointing accuracy**

* **Mass minimized by use of**

  deployable metallized plastic sunshade
  ribbed graphite epoxy primary mirror (1.5 kg)

* **Overall instrument mass is 60 kg**

  includes antenna, receiver, and spectrometer

  with spacecraft, the total mass is 200 kg

  may be reduced by lightening of AOS support structure

* **Power consumption is 50 W**

  allowing for converter efficiency, this is just within SMEX limit

* **Launch vehicle has not been definitely selected**; it could be a Scout, an Augmented Scout, or a new launcher such as Pegasus

* **Launch currently scheduled for August 1994**

SUBMILLIMETER REMOTE SENSING OF STRATOSPHERIC GASES

Joe W. Waters

Jet Propulsion Laboratory, California Institute of Technology
Pasadena, CA 91109

ABSTRACT

Technology is now becoming available to develop submillimeter wavelength heterodyne radiometric experiments for remote sensing the stratosphere from space. Such experiments can provide many essential measurements for assessing the depletion of stratospheric ozone by pollution from industrial products. A millimeter wavelength experiment for this purpose is now ready for launch on the NASA Upper Atmosphere Research Satellite (UARS). An enhanced version, which operates at submillimeter wavelengths, is in study for the future NASA Earth Observing System.

keywords: remote sensing, stratosphere, submillimeter

INTRODUCTION

Microwave remote sensing of Earth's atmosphere from satellite was initiated in the early 1970's [1]. Technology advances and increased satellite accommodation capability have now made possible its use in limb sounding mode, and at submillimeter wavelengths, to study Earth's upper atmosphere [2]. This is timely, as stratospheric ozone shields life from solar ultraviolet radiation but can be depleted by pollution from industrial activities [3].

MICROWAVE LIMB SOUNDING

Microwave limb sounding measures atmospheric thermal emission spectra at millimeter and submillimeter wavelengths as the instrument field-of-view (FOV) is scanned through the limb from above. Atmospheric profiles of molecular abundances, temperature, pressure, wind, and magnetic field can be determined from the measured emission spectra. Intensity of the emission provides abundance and temperature. Measured linewidths, and emission from temperature-insensitive O_2 lines, provide pressure. Differentiation of measured pressure with respect to measured height differential (obtained from the instrument FOV scan encoder) also provides temperature through atmospheric hydrostatic equilibrium (which relates temperature to pressure and height differential). Doppler shifts of spectral lines provide wind, and Zeeman splitting of the magnetic dipole lines of O_2 provides magnetic field. Limitations on spatial resolution are $\sim$2 km in the vertical and $\sim$300 km in the horizontal direction along the line-of-sight, as can be determined from the appropriate weighting functions.

General features of microwave limb sounding, some of which are shared by other techniques, are:

1. Many upper atmospheric molecules, especially chemical radicals important in ozone destruction, have spectral lines which can be measured.

2. The viewing geometry optimizes vertical resolution and signal strengths.

3. Thermal emission is observed, allowing measurements at any time without requiring background sources (*e.g.*, the sun) or intermediate processes (*e.g.*, backscattering).

4. Spectral resolution can be made arbitrarily fine, so the only limitation in resolving spectral features is the overlapping of atmospheric lines. This allows spectral channels to be selected which contain only radiation from optically-thin atmospheric regions and provide better vertical resolution than from channels which contain radiation from optically-thick regions.

5. The spectroscopy data base [4] is generally more accurate than in other spectral regions. This is due to the fact that line strengths are determined from the permanent dipole moment of the molecule, which can be measured in the laboratory to better than 1% from Stark or Zeeman effects without requiring simultaneous measurement of the abundances in the laboratory cell. Uncertainties in quantum-mechanical calculations of matrix elements for individual line transitions are also typically less than 1%.

6. Measurements require no simultaneous ancillary data. Spectral lines for composition measurements can be chosen which have temperature-insensitive limb thermal emission, so that highly-accurate temperature measurements are not required for deducing abundances. The data contain atmospheric pressure information, as discussed above, so that precise platform pointing information is not essential. Aerosols and ice clouds have negligible effect, so their measurement is also not needed.

7. Instruments can be developed for orbiting satellites which have long (many years) operational lifetime and reliable long-term calibration.

Microwave heterodyne technology is rapidly advancing to higher frequencies [5,6,7,8,9, for example]. The maximum frequency at which long-lived space instruments can be implemented is increasing by more than 3× each decade. In 1970 this frequency was ~60 GHz [1], in 1980 it was ~200 GHz, and now it is ~700 GHz. Large improvements in microwave sensitivity and ease of fabrication are also being made. The new superconductor-insulator-superconductor (SIS) mixers are rapidly becoming operational. These will give significantly improved sensitivity and require much less local oscillator power, considerably simplifying instrumentation. Current SIS mixers must be cooled to <10 K, and developments are underway [10] which could lead to the reliable light-weight coolers necessary for SIS systems operating for many years in Earth orbit. Intermediate frequency amplifiers are now available which cover a bandwidth of ~10 GHz or greater [M. Pospieszalski, National Radio Astronomy Observatory, private communication], allowing a much larger portion of the spectrum to be observed instantaneously. Advances are also being made in systems to spectrally analyze these broadband signals: acousto-optic spectrometers can now analyze bandwidths of 1 GHz with ~1000 spectrally-resolved channels [11]; units with 1000 channels output can be made small ($< 2\times10^{-4}$ m^3) and with low (<10 W) power requirements [M. Koontz, Harris Corporation, private communication].

THE UARS MICROWAVE LIMB SOUNDER

The UARS Microwave Limb Sounder (MLS) measures ClO (~25–45 km), O_3 (~15–80 km), H_2O (~15–85 km), and pressure (~30–60 km)[2,12]. The ClO abundance is a good measure of ozone destruction by chlorine, since ClO is the rate limiting molecule in the chlorine destruction cycle. ClO measurement on a global scale, to be done by the MLS,

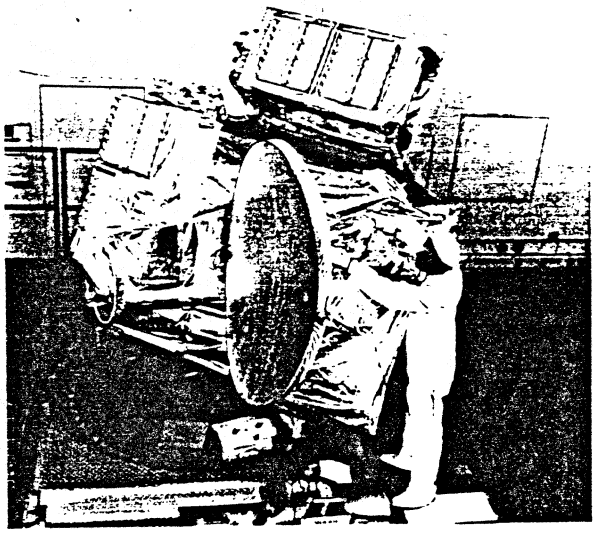

Figure 1: UARS MLS flight instrument

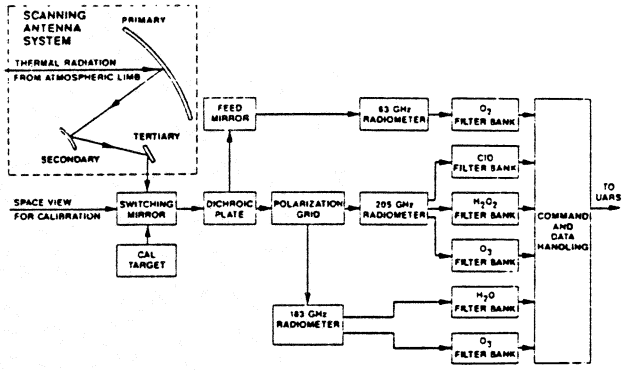

Figure 2: UARS MLS signal flow block diagram.

is crucial for understanding and monitoring chlorine depletion of ozone. Simultaneous measurements of O_3 and H_2O provide additional important information on stratospheric ozone chemistry. The H_2O and O_3 measurements will be to higher altitudes than previously explored on a global basis, and will provide new information on chemistry in the mesosphere. The pressure measurements provide the vertical reference for composition measurements. Secondary MLS measurement goals include H_2O_2, HNO_3, temperature, and one component of wind in the mesosphere. All measurements are made simultaneously and continuously, at all times of day and night. The experiment is being developed and implemented by the Jet Propulsion Laboratory in collaboration with the UK Heriot-Watt University, Edinburgh University and Rutherford Appleton Laboratory. Prior development included aircraft [13,14] and balloon [15,16,17] experiments.

Figure 1 is a photograph of the flight instrument, and Figure 2 shows its signal flow block diagram. The 1.6 m vertical dimension of the antenna gives a 205 GHz FOV which has full width at half-maximum of 1.3×10^{-3} radians (0.07°), corresponding to 3.5 km vertical extent at the limb. The switching mirror accepts radiation either from the antenna, from an internal target, or from space. The space and target views provide radiometric calibration of the instrument using optimized algorithms [18]. A dichroic plate following the switching mirror separates a signal for 63 GHz measurements of pressure (O_2). A polarization grid then separates signals for 183 GHz bands (O_3 and H_2O measurements) and 205 GHz bands (ClO, O_3, and possibly H_2O_2 and HNO_3 measurements). Ambient-temperature Schottky-diode heterodyne radiometers are used [19]; the local oscillator is coupled to the mixer by a quasi-optical ring-resonator [20]. The signal bands are frequency converted (in two steps) to 500 MHz wide bands centered at 400 MHz. These bands are then input to six filter banks: each separates the signal into 15 spectral channels, measures the power in each channel, and digitizes the result

for telemetry. Individual filter widths vary from 128 MHz on band edge to 2 MHz at band center. The instrument integration time is ~2 s, and a vertical scan is performed each minute. The instrument has three assemblies: sensor, spectrometer, and power supply. Thermal control of the sensor and spectrometer is radiational by louvers, with designed in-orbit temperature stability of 0.015° C per minute, or better, to provide sufficient stability for 'total power' measurements. The overall instrument mass is 280 kg, its power consumption is 163 W, and its output data rate is 1250 bits/s. The noise temperature for the most critical ClO band, referenced to the switching mirror input, is ~1200 K double sideband.

THE EOS MICROWAVE LIMB SOUNDER

An enhanced MLS is in definition phase study for the future NASA Earth Observing System (Eos). Most of the Eos MLS measurements are planned to be from the spectral region around 600 GHz. This region is very rich in spectral lines of atmospheric interest, and includes the first rotational line of HCl, and the strongest emission lines of ClO and many other molecules. Figure 3 summarizes the expected measurement capability (vibrationally excited states of O_3, O_2, and possibly of other molecules, will also be measured). All measurements are made simultaneously and continuously, at all times of day and night, with ~2 km vertical resolution. Latitude coverage is 82°S–82°N on each orbit.

Scientific information from the Eos MLS measurements includes trend detection, chemistry, dynamics, and climatology of the stratosphere and mesosphere. Trend detection is essential for ascertaining mankind's impact on the upper atmosphere. Mid-latitude ozone at 40 km decreased 3–9% between 1979 and 1986, which is within the range of predicted depletion due to chlorine from industrial CFCs [3]. Simultaneous measurements of O_3, and the radicals ClO, HO_2, and NO_2 which limit its destruction rate should, based on current theory, establish a cause-and-effect relationship of any measured O_3 depletions. A topic of major current interest is the springtime Antarctic ozone hole [21]. Of concern is its long-term growth and the extent to which similar processes might be occurring elsewhere. Heterogeneous chemistry in polar stratospheric clouds causes the hole by converting HCl and $ClONO_2$ to active chlorine which then catalytically destroys O_3 [22,23,24]. The Eos MLS can, since its signals are only slightly affected by ice clouds, measure many of the gas-phase abundances needed to study such processes. Simultaneous measurements of ClO, HCl, and O_3 on each limb scan can provide crucial monitoring of such processes in both the antarctic and arctic regions. Measurements of HNO_3, HCl, and H_2O also provide vital data on when these molecules condense onto, or evaporate from, ice clouds. N_2O measurements provide information on vertical transport in this region, which can separate dynamical and chemical effects.

ACKNOWLEDGEMENTS

I thank my many colleagues at JPL and in the UK for their support over the many years we have spent developing the MLS experiments. This work was performed by the Jet Propulsion Laboratory, California Institute of Technology, under contract with NASA.

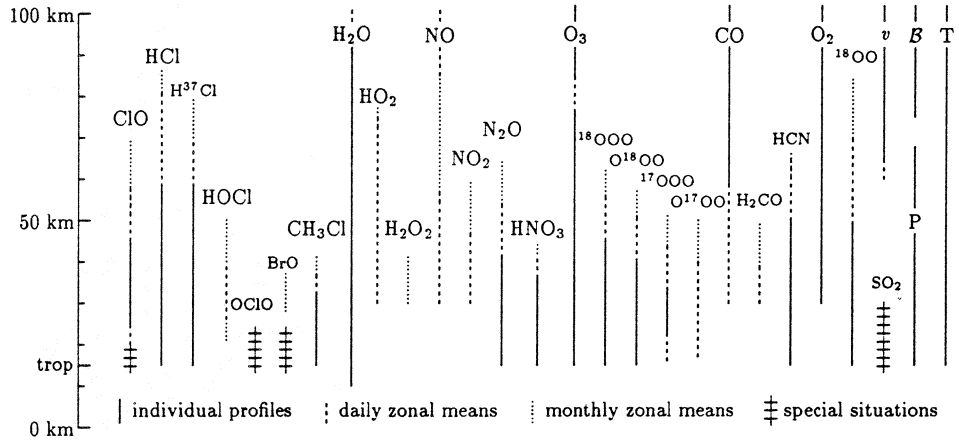

Figure 3: Expected measurement capability of Eos MLS. Molecules are indicated by their chemical formulae and P is pressure, T is temperature, v is one component of wind (from emission line Doppler shifts), and $\mathcal{B}$ is magnetic field (from Zeeman splitting of O_2 emission lines). 'Individual profiles' are for measurements on each limb scan, taking ~40 s for a complete limb scan covering 0–120 km tangent heights. 'Special situations' refer to the springtime Antarctic ozone hole for the halogen molecules, and to volcanic injections for SO_2.

REFERENCES

[1] D. Staelin, A. Barrett, J. Waters, F. Barath, E. Johnston, P. Rosenkranz, N. Gaut, and W. Lenoir, "Microwave spectrometer on the Nimbus 5 satellite: meteorological and geophysical data," *Science*, vol. 182, pp. 1339–1341, 1973.

[2] J. Waters, "Microwave limb-sounding of earth's upper atmosphere," *Atmospheric Research*, vol. 23, pp. 391–410, 1989:

[3] R.T. Watson and Ozone Trends Panel, M.J. Prather and Ad Hoc Theory Panel, and M.J. Kurylo and NASA Panel for Data Evaluation, "Present state of knowledge of the upper atmosphere 1988: an assessment report (NASA reference publication 1208)," Tech. Rep., NASA Office of Space Science and Applications, Washington DC, USA, 1988.

[4] R. Poynter and H. Pickett, "Submillimeter, millimeter and microwave spectral line catalog," *Appl. Opt.*, vol. 24, pp. 2235–2240, 1985.

[5] P. Goldsmith and N. Erickson, "Waveguide submillimeter mixers," in *Instrumentation for Submillimeter Spectroscopy, SPIE vol. 598*, (E. Kollberg, ed.), pp. 52–59, 1986.

[6] H. Roeser, R. Wattenbach, E. Durwen, and G. Schultz, "A high resolution heterodyne spectrometer from 100 μm to 1000μm and the detection of CO ($J = 7 - 6$), CO ($J = 6 - 5$), and ^{13}CO ($J = 3 - 2$)," *Astron. Astrophys.*, vol. 165, pp. 287–299, 1986.

[7] T. W. Crowe, "GaAs schottky barrier mixer diodes for the frequency range 1–10 THz," *Int. J. Infrared and Millimeter Waves*, vol. 10, pp. 765–777, 1989.

[8] A. Harris, J. Stutzki, U. Graf, and R. Genzel, "Measured mixer noise temperature and conversion loss of a cryogenic Schottky diode mixer near 800 GHz," *Int. J. Infrared and Millimeter Waves*, vol. 10, pp. 1371–1376, 1989.

[9] J. M. Payne, "Millimeter and submillimeter wavelength radio astronomy," *Proc. IEEE*, vol. 77, pp. 993–1017, 1989.

[10] T. Bradshaw, "Miniature stirling cycle refrigerators for space use," *J. British Interplanetary Soc.*, vol. 39, pp. 224–227, 1986.

[11] R. Schieder, V. Tolls, and G. Winnewisser, "The Cologne acousto optical spectrometers," *Experimental Astronomy*, vol. 1, pp. 101–121, 1989.

[12] J. Waters, G. Peckham, R. Suttie, P. Curtis, B. Maddison, and R. Harwood, "The microwave limb sounder for the upper atmosphere research satellite," in *IGARSS '88 Symposium*, pp. 937–940, IEEE, 1988.

[13] J. Waters, J. Gustincic, R. Kakar, H. Roscoe, P. Swanson, T. G. Phillips, T. DeGraauw, A. Kerr, and R. Mattauch, "Aircraft search for millimeter wavelength emission by stratospheric ClO," *J. Geophys. Res.*, vol. 84, pp. 6934–7049, 1979.

[14] J. Waters, J. Gustincic, P. Swanson, and A. Kerr, "Measurements of upper atmospheric H_2O emission at 183 GHz," in *Atmospheric Water Vapor*, (Wilkerson and Ruhnke, eds.), pp. 229–240, New York: Academic Press, 1980.

[15] J. Waters, J. Hardy, R. Jarnot, and H. Pickett, "Chlorine monoxide radical, ozone, and hydrogen peroxide: stratospheric measurements by microwave limb sounding," *Science*, vol. 214, pp. 61–64, 1981.

[16] J. Waters, J. Hardy, R. Jarnot, H. Pickett, and P. Zimmermann, "A balloon-borne microwave limb sounder for stratospheric measurements," *J. Quant. Spectrosc. Radiat. Transfer*, vol. 32, pp. 407–433, 1984.

[17] J. Waters, R. Stachnik, J. Hardy, and R. Jarnot, "ClO and O_3 stratospheric profiles: balloon microwave measurements," *Geophys. Res. Lett.*, vol. 15, pp. 780–783, 1988.

[18] G. Peckham, "An optimum calibration procedure for radiometers," *Int. J. Remote Sensing*, vol. 10, pp. 227–236, 1989.

[19] M. Frerking, J. Hardy, W. Wilson, and P. Zimmermann, "A broadband low noise 205 GHz radiometer for a satellite receiver," in *IEEE MTT International Microwave Symposium Digest*, pp. 110–112, 1983.

[20] H. Pickett and A. Chiou, "Folded fabry-perot quasi-optical ring resonator diplexer: theory and experiment," *IEEE Trans. on Microwave Theory and Techniques*, vol. MT-31, pp. 373–380, 1983.

[21] J. Farman, B. Gardiner, and J. Shanklin, "Large losses of total ozone in Antarctica reveal seasonal ClO_x/NO_x interaction," *Nature*, vol. 315, p. 207, 1985.

[22] M. Molina, T. Tso, L. Molina, and F. Wang, "Antarctic stratospheric chemistry of chlorine nitrate, hydrogen chloride, and ice: release of active chlorine," *Science*, vol. 238, pp. 1253–1260, 1987.

[23] S. Solomon, "The mystery of the Antarctic ozone 'hole'," *Rev. Geophys*, vol. 26, pp. 131–148, 1988.

[24] J. Anderson, W. Brune, and M. Proffit, "Ozone destruction by chlorine radicals within the Antarctic vortex: the spatial and temporal evolution of ClO–O_3 anticorrelation based on in situ ER-2 data," *J. Geophys. Res.*, vol. 94, pp. 11,465–11,479, 1989.

Atmospheric Remote Sensing in the Terahertz Region

Prof. Paul B. Hays and Hilary E. Snell
Center for Space Terahertz Technology
Space Physics Research Laboratory
Department of Atmospheric, Oceanic, and Space Sciences
Ann Arbor, MI 48109-2143

Abstract

Remote Sensing of major and minor constituents gases is of very great importance in understanding the atmospheres of earth and planets. Of the minor gases in an atmsophere the most difficult species to observe are often the radicals such as atomic oxygen, hydroxyl, chlorine monoxide and species such as hydrogen chloride, hydrogen fluoride, among others. Observations in the terahertz region of the spectrum have been successful in determining the density of many of these species including the hydroxyl radical. However, the instruments used to date are complex and in general not suitable for spaceflight on small satellites. This study has as its primary goal the presentation of a simple, compact scanning Fabry-Perot interferometer which has the capability to make observations of minor constituents in an atmosphere competative with larger and more complex instrumentation. We illustrate the use of this new instrument by showing how the hydroxyl in the earth's stratosphere can be detected from observations taken at balloon altitude.

1. Introduction:

Development of small and rugged remote sensing instruments to observe the constituents in the planetary atmospheres is of very great interest to the geophysical community. On earth this interest is in part generated from the need to understand the state of the atmosphere in an era where we have just begun to reach an awareness of the impact that man has on the global environment. However, the overriding reason for the interest in the state of the atmosphere is the recognition that our present understanding of this important geophysical system is at best in its infancy. In many cases increased knowledge will come from exploration using new techniques. The most difficult species to observe are often the radicals such as atomic oxygen, hydroxyl, and chlorine monoxide among others.

The hydroxyl radical (OH) is used here to illustrate the capabilities of the instrument that we are developing because it is an important member of the HO_X family and it is very difficult to detect. Hydroxyl is a highly reactive species

which enters in many atmospheric chemical reactions including the catalytic cycles of HO_X, NO_X, and ClO_X which lead to the destruction of ozone. In these cycles OH is strongly involved in determining the partition between radicals and reservoir species in the atmosphere.

Observations in the terahertz region of the spectrum have been successful in determining the density of many stratospheric species including the hydroxyl radical [1]. However, the instruments used to date are complex [2] and in general not suitable for spaceflight on small satellites. We show in this paper that a old instrumental concept, the Fabry-Perot interferometer, when applied in a new way, can make a serious contribution to observations of a number of minor gases in the atmosphere.

2. Multiplex Fabry-Perot Interferometer

The instrumental study presented in this paper is of a new type of interferometer to examine extended spectral regions in a manner similar to done with a Michaelson interferometer. This new interferometer, called the Multiplex Fabry-Perot Interferometer (MFPI)[3,4,5,6,7] , will produce the same information that is obtained from a high resolution Fourier Transform spectrometer operating at resolutions of the order of $0.003cm^{-1}$. However, this instrument is much smaller and does not require large mirror stroke of a Michelson Interferometer. In the terahertz where many of the radical species can be observed this new instrument is a metal mesh Fabry-Perot interferometer with a mirror stroke of less than 10 cm. The results shown in this study are preliminary numerical simulations of the instrument function and inversions of simulated spectra obtained with such an instrument. During the next year this numerical model will be used to complete the final design specifications for a balloon flight instrument.

The choice of the Fabry-Perot interferometer for our investigation is based on the experience that exists at the University of Michigan in the design, construction, and operation of this type of instrumentation for ground based observations [8] and for space flight[9].

3. Instrument Concept

Conceptually the MFPI is very elementary, consisting of two very flat partially reflecting surfaces that are moved apart over a distance of about 10 cm. while maintaining their parallelism. This device is illustrated in figure 1 shown below. We note that in addition to the components show there is a metal mesh filter in the dewar to isolate the spectral region of interest.

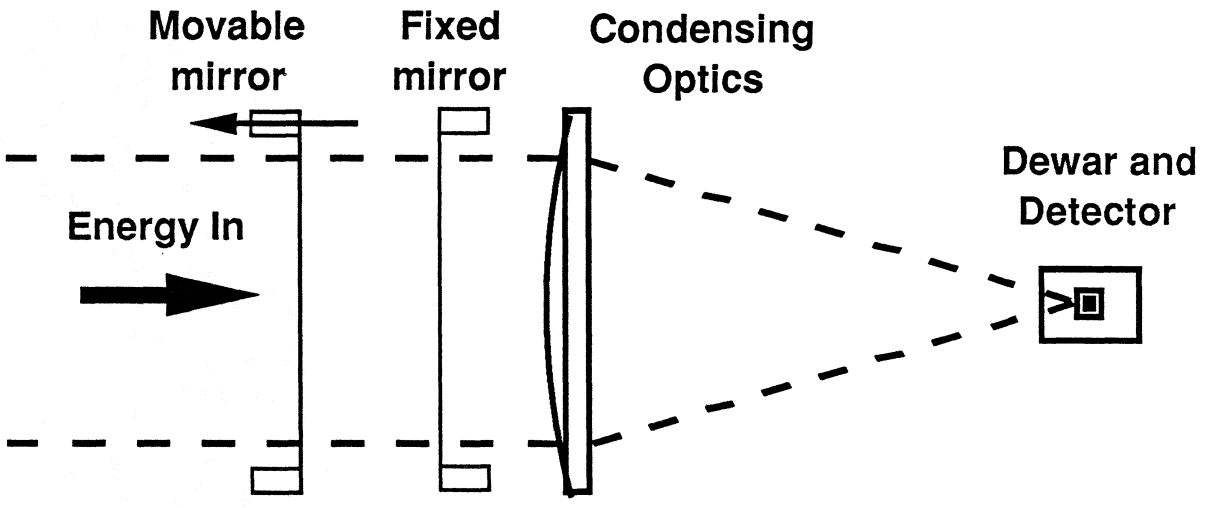

MULTIPLEX FABRY - PEROT INTERFEROMETER

Figure 1

The mirror or etalon will be moved using a simple linear translator and piezoelectric actuators to move the grids during a scan of the instrument. The requirements for parallelism in the terahertz region is relaxed compared to the task in the visible where we have had considerable experience. This cavity, or etalon, acts as a comb filter with a comb separation in the spectrum that is dependent on the separation of the two partially reflecting surfaces. As the surfaces move further and further apart the resolution of the spectrum increases. Consequently, during the beginning of a scan when the etalon surfaces are nearly in contact a low resolution spectrum is determined, and at the end of the motion when the surfaces are far apart the high frequency portion of the spectrum is identified. Throughout the scanning processes the transmitted energy is focused on a cooled detector and a set of fundamental temporal harmonics are extracted

from this signal. The interesting characteristic of the multiple pass interferometer is that each reflection of the incoming beam of energy is passed with a unique temporal frequency, thus allowing us to obtain a signal that is equivalent to that of several Fourier Transform spectrometers operating simultaneously as the etalon cavity length is varied.

4. Measurement Technique

The actual measurement is taken by detecting all of the energy that passes through the etalon as one of the etalon plates is moved through a relatively large optical distance.

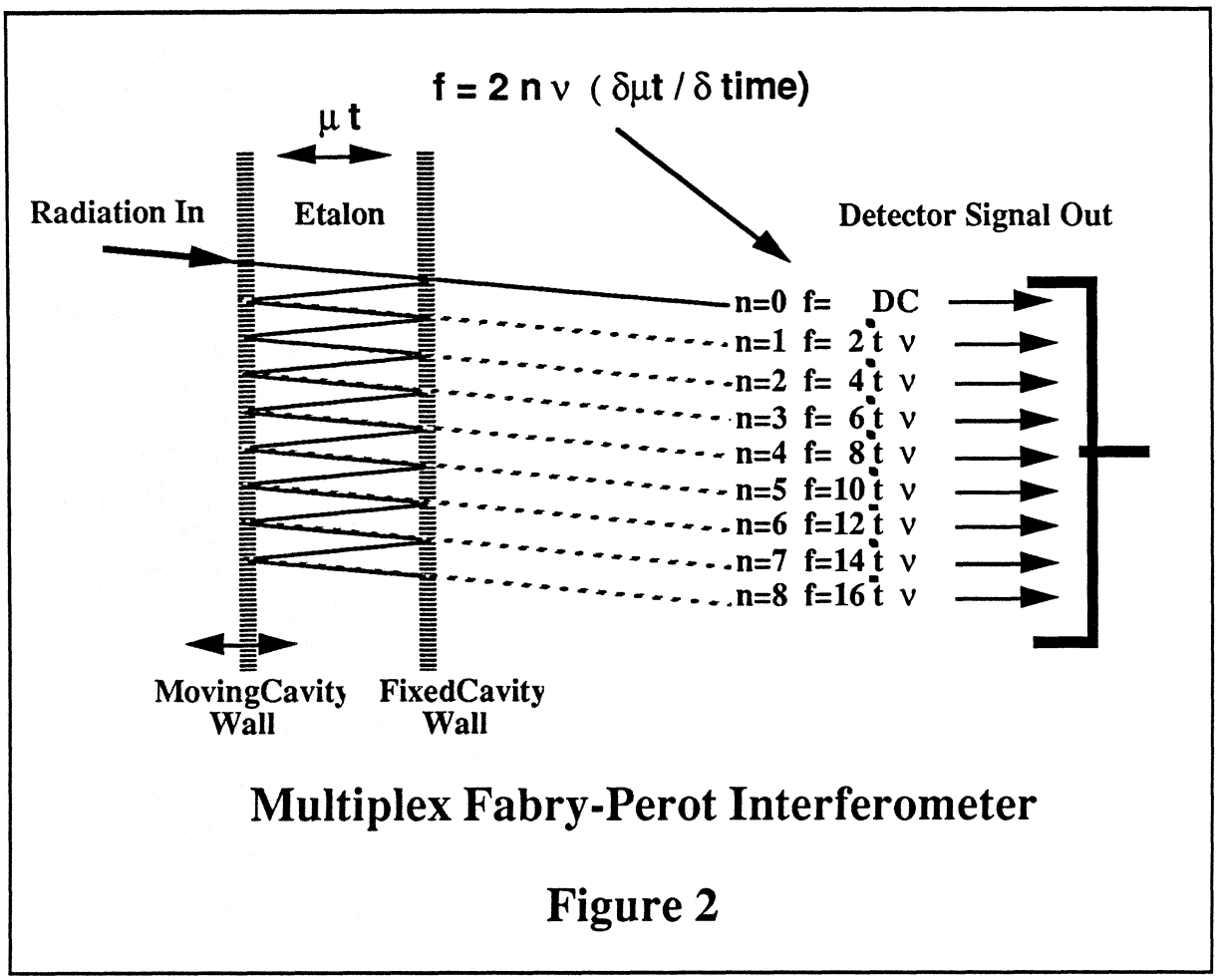

Multiplex Fabry-Perot Interferometer

Figure 2

The energy transmitted to the detector is modulated by a carrier frequency, f, that depends on the number of times the light has been reflected inside the etalon, or optical cavity. The energy is self-heterodyned within the cavity and the signal can be separated by the number of reflections within the cavity, n, by this frequency of modulation. It is also important to note that the rate of change of path length is directly related to the velocity of the moving cavity wall and also with the number of reflections within the optical cavity.

The energy passing through the etalon with one reflection gives a signal that is equivalent to a Michelson in which the optical path difference between the plates has doubled. The energy passing through the etalon after five reflections is equivalent to that of a Michelson where the path difference has been changed by a factor of ten, and so on. Thus by moving one of the cavity walls over a small distance, e.g., 10 cm, one can measure a signal that is equivalent to moving a Michelson plate over a considerably larger distance. The advantage of using this multiplex technique is thus easy to understand.

The measured signal is the convolution of the atmospheric signal and the instrument function. Numerical simulations have shown that the broadening is considerably narrower for the MFPI than that produced by a Michelson Interferometer.

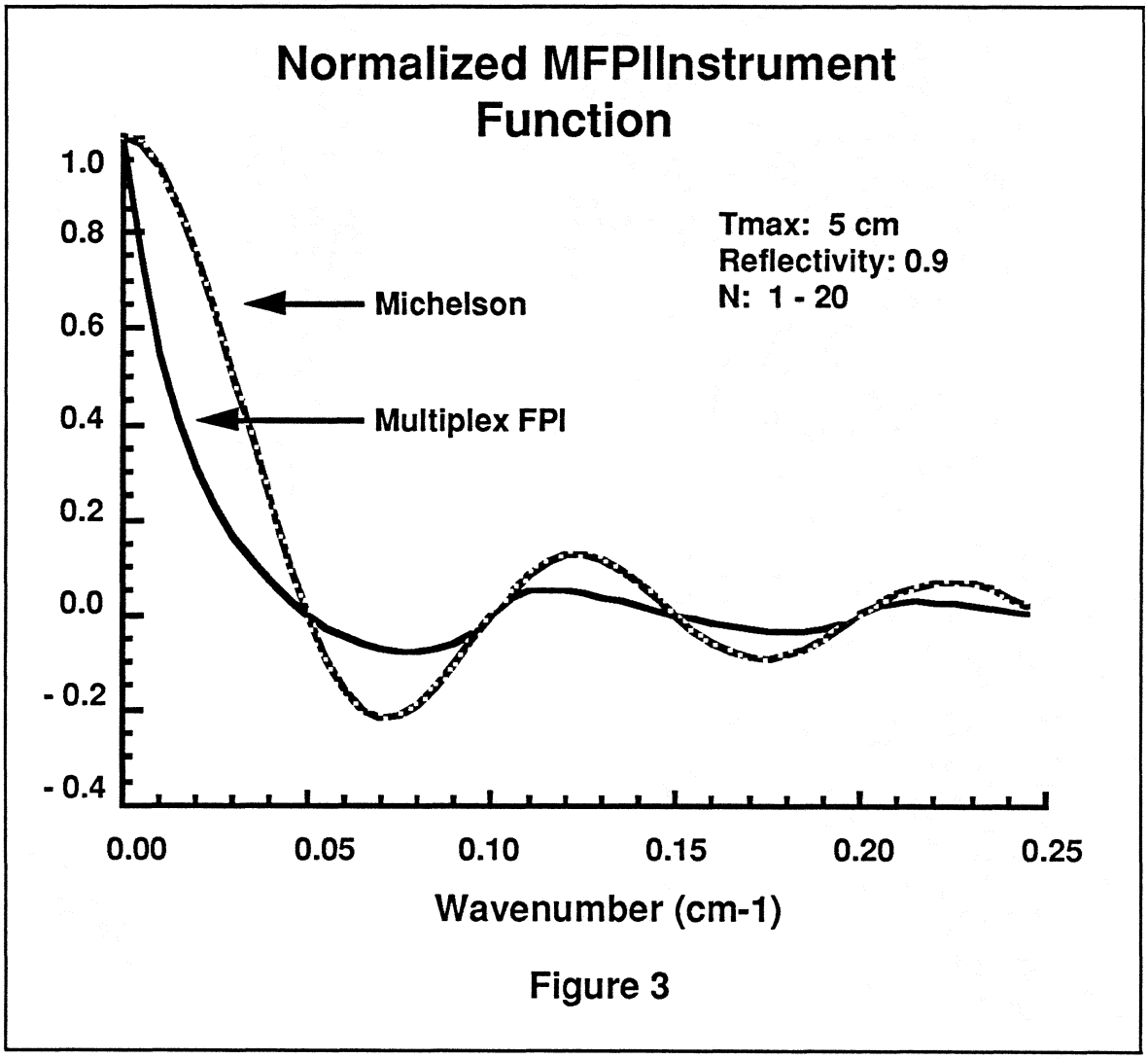

Figure 3

Furthermore, if the signal to noise ratio is sufficiently high the lower harmonics can be ignored. The resulting spectrum has even less broadening than when all of the harmonics are used.

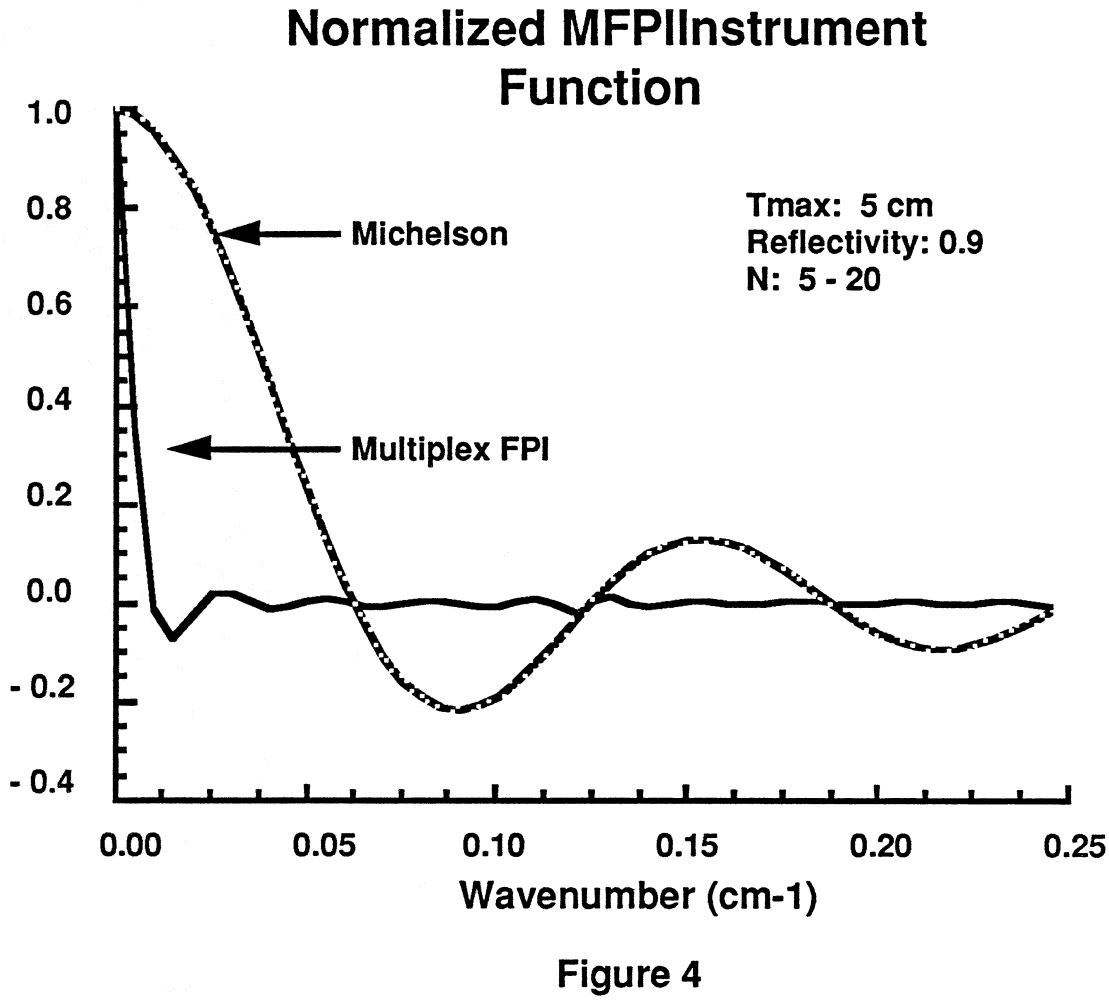

Figure 4

We have developed a radiative transfer code to allow us to examine the spectrum of the earth's atmosphere throughout the terahertz spectral region[10]. This will allow us to identify the important spectral intervals in which to observe the radical species of interest. This code allows us to model the atmospheric spectrum and the solar absorption spectrum when viewed from any point in or above the atmosphere. To test our ability to reconstruct a portion of the spectrum we chose a spectral region around 118 cm^{-1}

because is contains transition lines of O_3, H_2O, and OH.

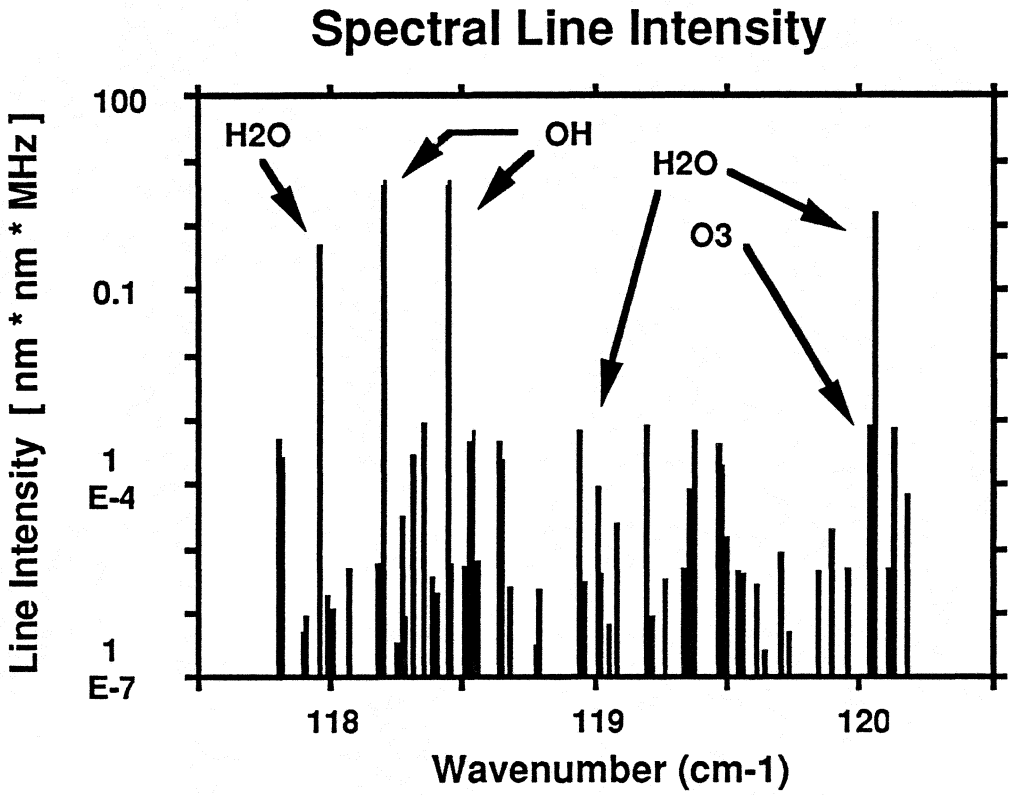

Figure 5

The important spectral lines in this region are shown in figure 5. The OH transitions here are quite intense, however, the brightness of these transitions is small due to the low mixing ratio of OH. In practice this may not be a desirable region in which to measure OH, but for this test case it will allow us to illustrate that it is possible to resolve very weak spectral features. The simulation used the brightness spectrum obtained from our radiative transfer code and determined the instrument response to this spectrum. We then reconstructed the spectrum from the instrumental output using all of the temporal frequencies without weighting. This inversion is elementary and results in the unapadized spectrum shown in figure 6. We note that the comparison is satisfying.

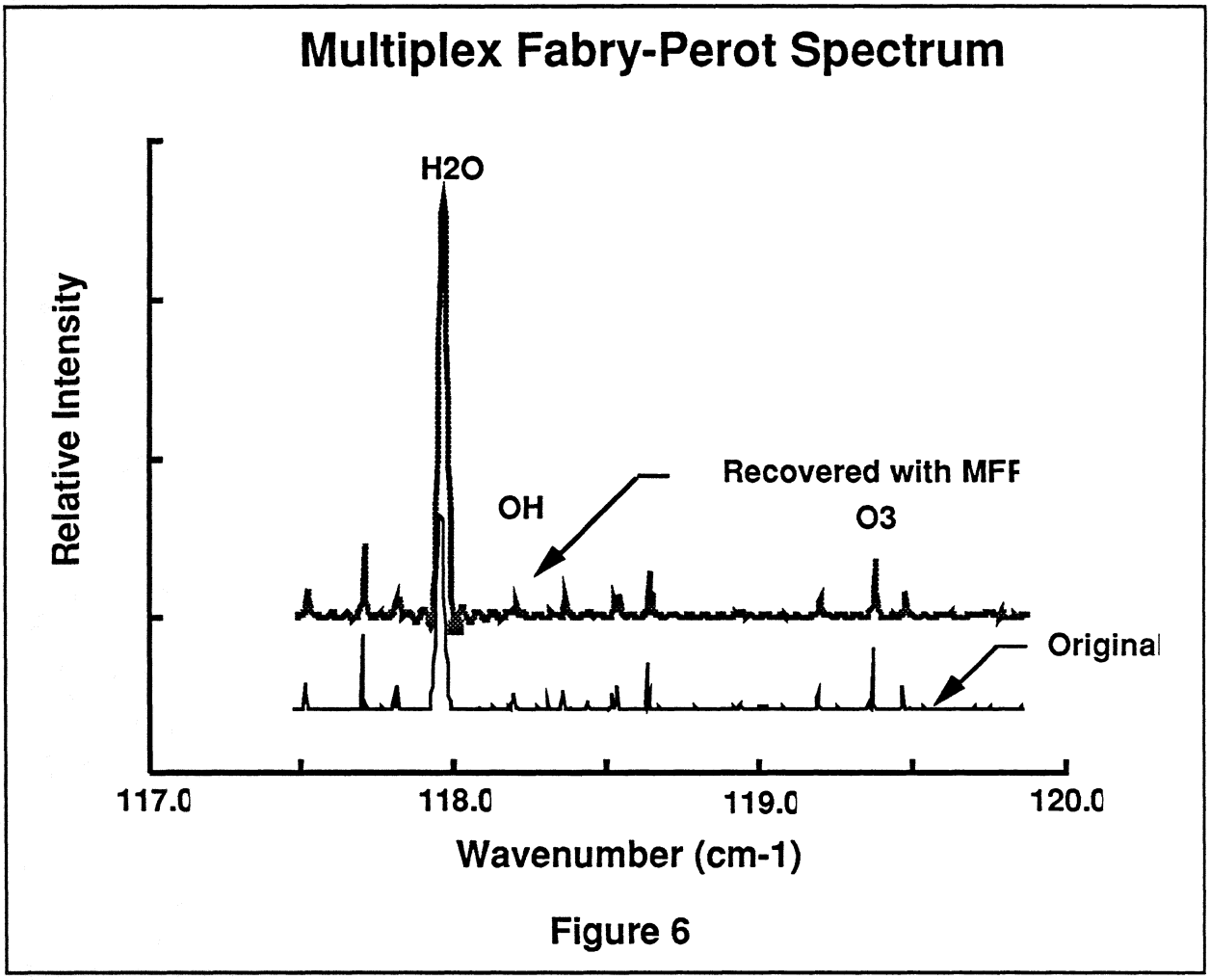

Figure 6

The amplitudes of the retrieved lines are proportional to the area under the spectral feature as illustrated by the water vapor signal. The reconstruction of this spectrum simulated with our radiative transfer model is quite good.

5. Summary

This short paper has illustrated the use of a Fabry-Perot interferometer to observe a modest spectral interval in the terahertz region of the spectrum. We have illustrated that this instrument has the capabilities of a Michaelson interferometer with a much larger mirror motion than is required for the Multiplex Fabry-Perot. We are currently in the preliminary stages of designing an actual instrument for balloon flight and we expect that this new instrumental technique will prove to be very important for both earth and planetary observations.

[1]Bruno Carli, Massimo Carlotti, Bianca M. Dinelli, Francesco Mencaraglia, and Jae H. Park, " The Mixing Ratio of the Stratospheric Hydroxyl Radical from Far Infrared Emission Measurements", J. Geophys. Res., 94, 11040, 1989.

[2]Bruno Carli, Francesco Mencaraglia, and Alberto Bonetti, " Submillimeter High-resolution FT Spectrometer for Atmospheric Studies", Applied Optics, 23, 2594, 1984.

[3]G.Hernandez, 'Fabry-Perot Interferometers', Cambridge Studies in Modern Optics, Vol.3, Cambridge University Press, New York, 1987.

[4] Kunio Yoshihara and Atsuo Kitade, "Far Infrared Spectroscopy by the Fabry-Perot Interferometer", Japan J. Appl. Phys., 17, 1895, 1978.

[5] Kunio Yoshihara and Atsuo Kitade, "Far Infrared Spectroscopy by the Fabry-Perot Interferometer. II", Japan J. Appl. Phys., 18, 2327, 1979.

[6] Kunio Yoshihara and Atsuo Kitade, "Far Infrared Spectroscopy by the Fabry-Perot Interferometer", Optica Acta, 26, 1049, 1979.

[7] Kunio Yoshihara and Atsuo Kitade, "Far Infrared Spectroscopy by the Fabry-Perot Interferometer. III", Japan J. Appl. Phys., 19, 2523, 1980.

[8]Meriwether, J. W. Jr., C. A. Tepley, S. A. Price, and P. B. Hays, "Remote ground-based observations of terrestrial airglow emissions and thermospheric dynamics at Calgary, Alberta, Canada" , Opt. Eng., **22**, 128-131, 1983.

[9]Hays,P.B., T.L.Killeen, and B.C.Kennedy, "The Fabry-Perot Interferometer on Dynamics Explorer" , Space Sci. Instrum., **5**, 395, 1981.

[10] Bruno Carli, "The High Resolution Submillimetre Spectrum of the Stratosphere", J. Quant. Spectrosc. Radiat. Transfer, 32, 397, 1984.